CRANFIELD UNIVERSITY

C. O. EKUNDAYO

1994

HEAT TRANSFER IN ENCLOSURES: OVENS

SCHOOL OF MECHANICAL ENGINEERING

PhD THESIS

CRANFIELD UNIVERSITY

SCHOOL OF MECHANICAL ENGINEERING

DEPARTMENT OF APPLIED ENERGY

PhD THESIS

Academic Year 1994-5

Author: C. O. Ekundayo

Title: Heat Transfer in Enclosures: Ovens

Supervisor: Dr. M. Newborough

December 1994

This thesis is submitted in partial fulfilment of the requirements for the Degree of Doctor of Philosophy

ABSTRACT

The use of natural convection to effect heat transfers in enclosures is limited principally because of its low heat transfer coefficients. This study aimed to establish a better understanding of the heat transfers occurring in enclosures which are heated by cylindrical heat sources and to identify preferred heating arrangements for improving the rates of natural convection heat transfers.

Experimental investigations including interferometric observations were carried out on a square-sectioned enclosure containing a rectangular-sectioned, isothermal inner body and cylindrical, sheathed electrical heating elements. The locations of the heaters were varied and the effects on natural convection heat transfers established. The findings conformed to intuitive expectations, concluding that the maximum position for natural convection heat transfer was with the heaters located in the lower half of the sidewalls.

The flow patterns and heat transfer characteristics of a single horizontal cylindrical (9.5mm dia) heater in a square-sectioned enclosure were studied by traversing the heater both horizontally and vertically across the enclosure at distinct Rayleigh numbers ($7.5x10^4$ and $1.1x10^5$). Optimal positions for maximum and minimum Nusselt numbers were established with respect to heater diameter and vertical height, and horizontal offset from a vertical wall. Flow and interferometric observations were also carried out on an enclosed single tubular 55mm dia. heater, and two 55mm dia. heaters. Improved arrangements for enhanced heat losses by natural convection from horizontal tubular arrays were deduced, applicable to arrays either totally enclosed or in the proximity of a vertical wall.

A square-sectioned (350x350x1700mm) tunnel oven was designed which would withstand operations under vacuum. Within this enclosure, the heating arrangements were located and varied essentially in the lower half of the enclosure, flow and thermal profiles obtained, a multi-surface radiation model developed and the convective heat transfers validated by evacuating the enclosure. At oven temperatures, over 40% of the heat input was achieved by natural convection.

ACKNOWLEDGEMENT

The author would like to express his thanks and appreciation to Dr. M. Newborough, for his advice, suggestions and generosity with his time through this project.

Thanks are also due to all those who helped with various aspects of the practical phase and especially to the following:

Mr. R. H. Dewar, for his advice and patience through the various periods of the design, drawing and construction of the rigs; to Mr. D. Brown for his invaluable advice on the rig fabrication techniques; to other members of the workshop staff for their speedy attention to the various aspects of the rig construction and finishing; and to Mr. C. Knight, for helping with various components.

Finally, I would like to express my special thanks and gratitude to Prof. S. D. Probert for his enthusiasm and support throughout this study.

CONTENTS

LIST OF FIGURES (Dimensions in mm)

NOTATION

A	Area (m^2)
c1, c2	Constants, for Ra or Gr
c_p	Specific heat ($J\ kg^{-1}\ K^{-1}$)
csa	Cross-sectional area
d	Diameter
F_{1-2}	View factor (from surface 1 to surface 2)
Gr	Grashof number ($\rho^2 g\beta\Delta T L^3/\mu^2$)
g	Gravitational force (ms^{-2})
h	Natural convection heat transfer coefficient ($Wm^{-2}K^{-1}$)
H	Height (m)
k	Thermal conductivity ($Wm^{-1}K^{-1}$)
L	characteristic length, as defined (m)
$\dot{m}$	mass flow rate
Nu	Nusselt number hL/k
Pr	Prandtl number ($\mu c_p/k$)
q	Heat flux, Q/A (Wm^{-2})
Q	Total heat transfer(W)
R_i	Radius of inner body
R^2	Reliability of correlation
Ra	Rayleigh number ($\rho^2 g\beta\Delta T L^3 c_p/\mu k$)
S	Separation gap or offset, (m)
t	thickness (m)
T	Temperature (K)
ΔT	Temperature difference, as defined (K)
W	Enclosure width (m)
$\sin\alpha$	View factor angle
$\cos\beta$	Angle for view factor (radians)
τ	Transmissivity
ρ	Density
β	Coefficient of volumetric expansion (1/K)
ε	Emissivity
μ	Dynamic viscosity ($kg\ m^{-1}s^{-1}$)
θ	temperature difference

σ	Stefan-Boltzmann constant (5.67×10^{-08} $Wm^{-2}K^{-4}$)
Ψ	Heat ratio for uncertainty analysis
j	number of view factor sub-surfaces
CC	Separation of cylinder-to-cylinder centres
CW	Cylinder-wall separation
FD	Finite difference
FE	Finite element
IB	Inner body
LOE	Located on edge
LOF	Located on flat
MZI	Mach-Zehnder Interferometer

Subscripts

con, conv	convection
cond	conduction
rad	radiation
h	horizontal
i	inner body
insul	insulant
m	mean
v	vertical
H	hot
C	cold

INTRODUCTION

1. INTRODUCTION

The effectiveness and efficiency of industrial, commercial and domestic equipment can often be improved by studying their thermal performance. The use of natural convection for achieving enhanced, uniform heating in enclosed spaces such as in high viscosity oil tanks, ovens and furnaces, or for cooling electronic components and refrigerator condensers, eliminates the necessity for recirculating pumps or fans which are expensive, require power input and increased maintenance.

In the transfer of thermal energy, three distinct mechanisms of heat transfer may be distinguished [1]: conduction, convection and radiation. In enclosures, all the modes of heat transfer may be present simultaneously. It is then normal to determine the heat transfers separately, adding them to obtain an estimate of the total rate of heat transfer.

The primary aim of this investigation is to determine, by experimental means, the heat-transfers and the temperature distributions within an air-filled enclosure with protruding or line heat sources and an inner body. By employing different heating arrangements, the changes which occur in the natural convection heat transfers could be examined through temperature field data and flow visualisation. This should provide a basis from which commercial and industrial enclosures and ovens could be further developed to achieve more effective natural convection, and hence improved performance.

1.1 GENERAL CONSIDERATIONS

1.1.1. Theoretical Considerations

The procedure of optimising the performance of heat transfer equipment often requires a theoretical study and analysis of the detailed mechanisms governing the heat transfer processes. The analytical basis of steady-state heat conduction in a solid is Fourier's Law:

$$Q = -kA\frac{\partial T}{\partial x} \qquad (1\text{-}1)$$

(see Fig. 1-1a), which can be simplified to:

$$q = \frac{Q}{A} = \frac{k}{t}A(T_1\text{-}T_2) \qquad (1\text{-}2)$$

following the notation indicated in Fig.1-1b.

If a solid surface is placed in the path of a stream of fluid, a narrow region of the fluid near the surface is slowed down (see Fig.1-1c). It was postulated by Prandtl [2] that within this zone or boundary-layer, the velocity changes from the stream velocity to zero at the stationary surface (for a no-slip condition). Prandtl's boundary layer theory was extended to explain the mechanism of convective heat transfer [3]. When a temperature difference exists (e.g. with the fluid warmer than the surface), a thermal boundary layer exists (similar in profile, but thinner than the velocity boundary layer), across which most of the temperature difference occurs (see Fig. 1-2a). The convective heat transfer across the fluid layer is analogously presented as in equation (1-2). However, because measurement of the boundary layer thickness is difficult, the convective heat transfer is usually written as:

$$Q = hA(T_1 - T_2) \qquad (1\text{-}3)$$

where h is a convective coefficient for the transfer between the surface and the body of the fluid.

If a heated vertical plate is positioned in a quiescent fluid, the fluid near the hot surface will rise by natural convection, while remaining stationary at the surface and outside the boundary layer (see Fig.1-2b). The heat transferred is similarly represented by equation (1-3).

To increase the rate of heat transfer by convection, the temperature difference could be increased (which may be unacceptable for the product), or the surface area of the object to be heated increased (which may be inconvenient). Therefore attempts at increasing h ($\approx k/t$) could include:

(a) increasing the fluid's thermal conductivity (e.g. by the choice of an alternative fluid), or
(b) reducing the boundary layer thickness t (e.g. by increasing the fluid's velocity).

Increasing the velocity of the fluid can be accomplished either by the use of fans or pumps (forced convection), or by enhancing buoyancy forces from a suitable arrangement of the heating surfaces. The choice of equipment (i.e. oven selection) may be heavily influenced by the required speed of operation, or by the constraint of energy (primary, or electricity) requirement. It is now seen that convective heat-transfer calculations are complicated because:

(a) the fluid motion plays an important part in the heat transfer, and

(b) solving the resulting governing equations usually presents considerable mathematical difficulties.

To try to overcome the latter, heat transfer data are commonly expressed in non-dimensional ratios consisting of geometrical and fluid properties which exert an influence on the rates of heat transfer in the system under consideration. The Nusselt number, Nu, is the ratio of the convective to conduction coefficients where:

$$\mathrm{Nu} = h\frac{L}{k}$$

and L is a characteristic length. This can be related by analytical means or dimensional analysis to the fluid properties by the Prandtl (Pr) and Grashof (Gr) numbers. The Rayleigh number which is the product (GrPr) gives an indication of the flow range within which the calculated convective heat transfers would be comparable with those for similar-category systems:

$$\mathrm{Ra} = \mathrm{GrPr} = [\rho^2 g\beta(\Delta T)L^3 c_p]/\mu k \qquad (1\text{-}4)$$

where ΔT is the temperature difference between a hot surface and the cold surface. The relationship between the convective heat-transfer, and the varying fluid properties and buoyancy is frequently presented in the form of a correlation as:

$$\mathrm{Nu} = c_1 Ra^{c_2} \qquad (1\text{-}5)$$

In an enclosed system, other parameters, such as the physical dimensions of the enclosure and the locations of the heat sources may be incorporated. A sustained and justifiable reservation concerning the use of dimensionless relations [4] is brought about by the fact that the variables are not truly independent because both sides of the equation contain common factors (e.g. k and L). Consequently, if one is not careful in the interpretation, spurious correlations may be produced [5].

Unlike conduction and convection, radiation does not require a medium for energy transfer. The mechanism of heat transfer for this mode is electromagnetic radiation, which is emitted by all matter above absolute zero of temperature. Although the spectrum includes microwave radiation which is also used for heating, it is a form of energy transformation which is practically limited in applicability to certain objects (e.g. moist products). Therefore, the primary interest in this study is confined to thermal radiation.

For an ideal (blackbody) surface, the heat emitted is proportional to the fourth power of its absolute temperature:

$$Q \propto \sigma A T^4 \qquad (1\text{-}6)$$

where σ is the Stefan-Boltzmann constant [6]. The blackbody is an ideal case because surfaces covered by carbon black are known to approximate to this, whereas glossy or shiny surfaces emit much less than the blackbody at identical temperatures. To take account of non-black or grey body radiation, a surface parameter is introduced, the emissivity, which is the ratio of emitted radiation to that which would be emitted by a black body. If a surface at temperature T_1 is completely enclosed by a much larger surface at T_2, the net radiant exchange can be expressed as:

$$Q = \varepsilon_1 \sigma A_1 (T_1^4 - T_2^4) \qquad (1\text{-}7)$$

If the thermal radiation heat transfer occurs other than in a vacuum, that is in the presence of a medium such as air, the net radiant exchange may be reduced. In practice, some gases such as air are generally transparent to thermal radiation over a broad range of wavelengths in the electromagnetic spectrum. Others, such as CO_2 and H_2O absorb and emit weakly, and only within narrow bands of the spectrum, but are important considerations in combustion ovens and furnaces.

Other important considerations include the proportion of emitted radiation which directly falls upon another surface, the type of surface (e.g. food products susceptible to absorption and penetration by thermal radiation, or metallic products), the directional dependence of the thermal radiation, the optical characteristics - long wave, surface-absorbing infra-red radiation (3→6μm) or the more penetrating shorter-wave radiation (0.1→1.0 μm) [7] , and whether the surfaces behave as diffuse, or specular reflectors. Although heat-transfer calculations involving thermal radiation are well established, the reliability of predictions from them depends to a large extent upon accurate temperature and emissivity measurements.

The proportion of thermal radiation incident on another surface is usually unevenly distributed, so that concentrated hot-spots may be produced. However, heat is transferred more uniformly by convection [8] and this is the principal reason for trying to augment the proportion of heat transfer by convection.

1.1.2. Limitations of analytical methods for enclosed natural convection

Conventional methods of analysing convective heat transfers assume that the fluid external to the boundary-layer is stationary in natural convection, or that it is moving with the stream velocity in forced convection. That is, the region exterior to a

boundary-layer is unaffected by the boundary-layer (see Fig.1-2c), so that the boundary layer theory enables simplifying assumptions to be made which would aid in estimating the convective heat-transfers. These assumptions are valid for some external flows; there are many practical applications where a boundary layer analysis adequately describes the convective behaviour.

However, there are also many examples of convective heat-transfers which cannot be described adequately by the boundary-layer model. Such regions are found in the wake of separated flows around blunt bodies; in natural convection of gases at low Rayleigh numbers ($<10^4$); in natural convection from horizontal surfaces; and in most moderately-sized internal convection situations [9].

This is because for natural convection in an enclosure, the boundary-layer is not fully developed; the core region is not stationary (see Fig.1-2d), and eddies, vortices, cells, oscillation of cells and flows may exist there. Natural convection has been shown to be extremely sensitive to changes in enclosure size and geometry and the imposed thermal boundary-conditions, so the use of data derived for similar problems for design purposes can be dangerously unreliable [10]. Hence there is no accepted valid analytical or numerical method for analysing natural convection in enclosures. Most design tools which embrace natural convection in enclosures are derived from empirical data [11].

1.1.3. Limitations of numerical methods

Preliminary analyses or computations are often useful to obtain ball park figures when designing an experimental apparatus. This may result in a more appropriate experimental rig, possibly leading to reductions in equipment cost, necessary data-acquisition and analyses. Although numerical analyses can sometimes be undertaken to provide more information, the solutions often require idealistic assumptions to be made concerning the boundary conditions (e.g. isothermal or adiabatic walls, constant value fluid properties, instantaneous or radiative boundary conditions). Numerical solutions are therefore frequently limited in applicability.

1.1.4. Requirement for experimental methods

The most reliable information about a heat-transfer process is often given by real measurements particularly where natural convection forms a significant proportion of the total rate of heat transfer [4]. Experiments have the advantage of being applicable to

internal and unsteady flow, and turbulence. While they may be time consuming, expensive in resources, and sometimes difficult to reproduce, experiments are still indispensable.

1.1.5 Preliminary experimental considerations

Within enclosed air-spaces, having one vertical wall which is maintained at a higher temperature than the other, heat is transferred from the hot wall to the cold wall primarily by gaseous conduction and radiation when the air layer thickness W, is small, (i.e. with the convection inhibited) - the principle employed in double glazing (see Fig.1-3a). As W increases, air motion begins with the heated air rising up the hot wall due to density differences, (see Fig.1-3b) and the cooler air descending along the cold wall [12]. Eventually, further increases in W lead to slight reductions on the rates of heat transfer.

If a horizontal layer of air is uniformly heated from above, the density gradient is parallel to, and in the same direction as the gravitational force. Conditions are stable and no natural convection flow will exist (Fig.1-3c). Conversely, one would expect that uniform heating from below should instantly promote unstable conditions and generate flows. However, the upward or buoyancy force created by the thermal gradient must first overcome the viscosity and mass of air above it (see Fig. 1-3d); that is convection currents will result only if the buoyancy force exceeds a critical value, which depends on the height of the enclosure H, the temperature difference between the top and bottom surfaces, and the fluid properties. When ΔT exceeds a critical value, flow is initiated with a tessellated pattern of rolls (see Fig. 1-3e) [13]. A heated, inclined surface or a cylinder is an example of both mechanisms at work because the buoyancy force would have a component in both the tangential and normal directions.

Alternatively, a concentrated heat source could be positioned at a discrete point along a wall, either flush-mounted or protruding (as in electronic circuit boards), or mounted at some distance, clear of the wall (as in high viscosity oil tanks, ovens and furnaces). If more than one heat source is utilised, interactions from the plumes will exist, as well as from any adjoining wall, which may influence the rate of convective heat transfer. The size and location of the heating elements or hot wall are then crucial to the generation of buoyancy forces.

1.2 OBJECTIVES OF THE PROJECT

All too often, improvement in one mode of heat transfer in enclosures can only be achieved at the expense of another. Studies into raising the thermal performance and throughput of ovens and furnaces have included consideration of thermal insulation, wall emissivity and thermal conductivity, heater configuration, and heater design. For example, earlier experimental studies [14],[15], confirmed that the use of low-emissivity oven walls increased the heating efficiency of a standard test block. However, when the findings were applied to a cubical oven configuration, with the heaters positioned near the roof and base and containing low diffusivity baking items, the quality of the finished product was sometimes unsatisfactory because local hot spots were produced [15].

The initial conjecture was to associate this deterioration with non-uniform irradiance on the baking plane. As a result of the increased radiative heat transfer, the proportion of natural-convective heat-transfer in the enclosed system was conversely reduced. Convection is a proven means of improving temperature uniformity of an object being heated in an enclosure [8]. Of course, the use of forced-convection equipment could improve temperature uniformity, but the need for a fan and the associated electrical load should still encourage the development and use of natural convection ovens.

In order to overcome the problems which occurred, it was considered essential to investigate some of the interactions occurring under steady-state conditions and configurations in order to gain a better understanding of the basic governing processes. It had previously been impossible to obtain sufficiently-accurate results by analytical or computational means, and by experimental methods involving:

(a) a cubical enclosure [15], and
(b) a rectangular-sectioned enclosure with a cooled but non-isothermal inner body [16].

These revealed a need for a fundamental type of investigation to be carried out to quantify the heat transfer processes occurring with specific heating arrangements in an enclosure. Consequently, some experimental work would be carried out to determine and analyse the temperature distribution and air flow. To facilitate this, it was considered essential to employ an isothermal inner body within a square-sectioned enclosure fitted with protruding heat sources operated under steady-state conditions.

Fig.1-1 Conduction and convection characteristics

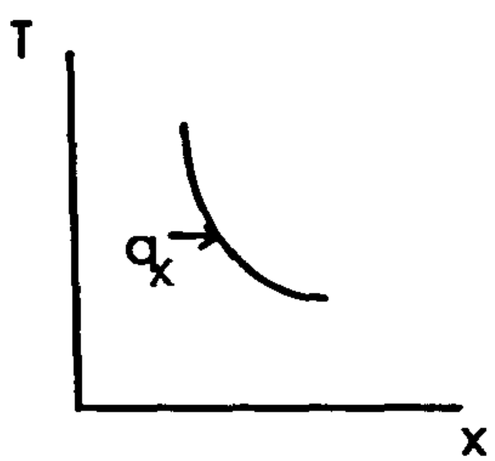

(a) Heat flow direction (linear scales)

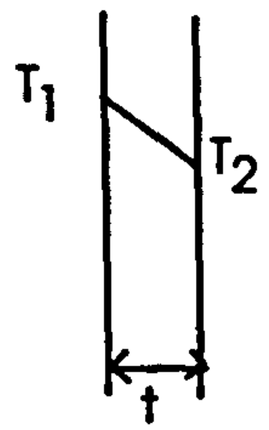

(b) 1-D steady-state conduction

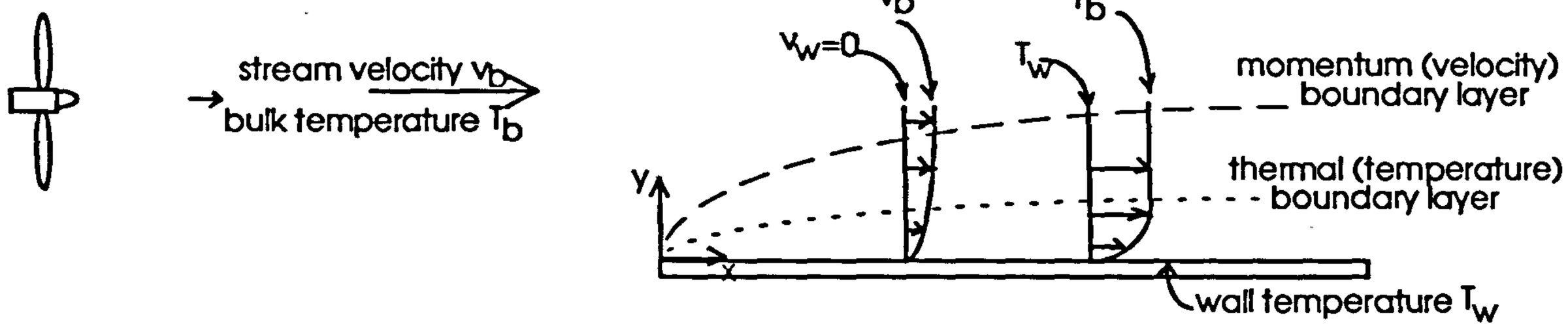

(c) Momentum and thermal boundary layers on a solid wall (forced convection)

Fig. 1-2 Boundary layer profiles

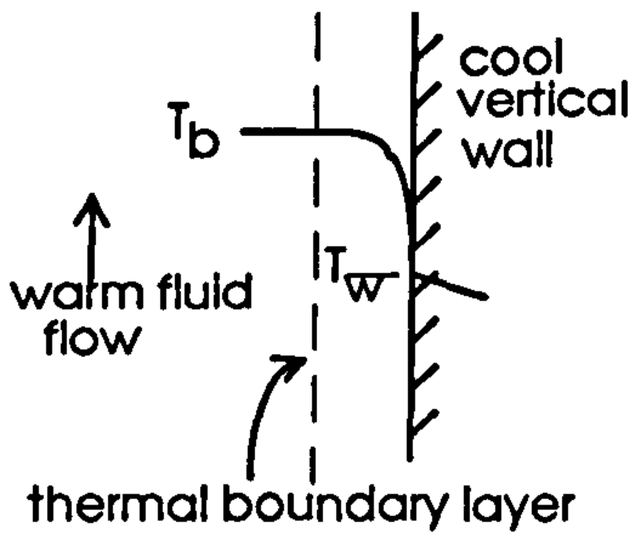

(a) temperature profile within thermal boundary layer (forced convection)

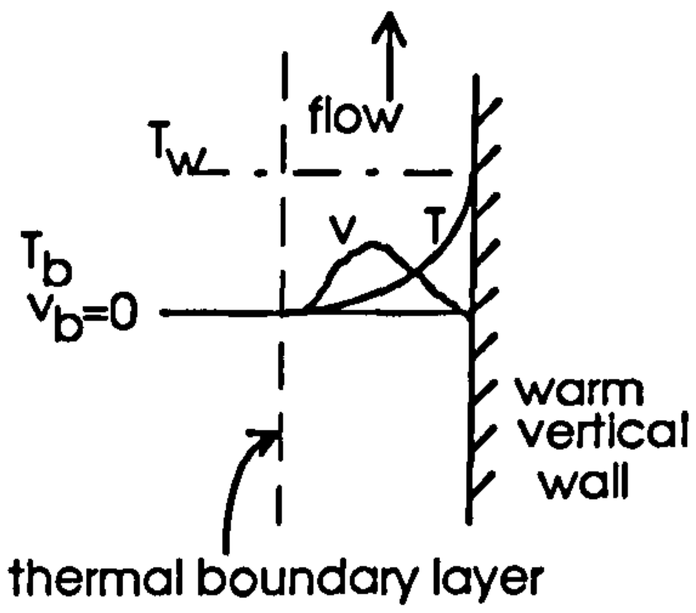

(b) velocity and temperature profiles within boundary layer (natural convection)

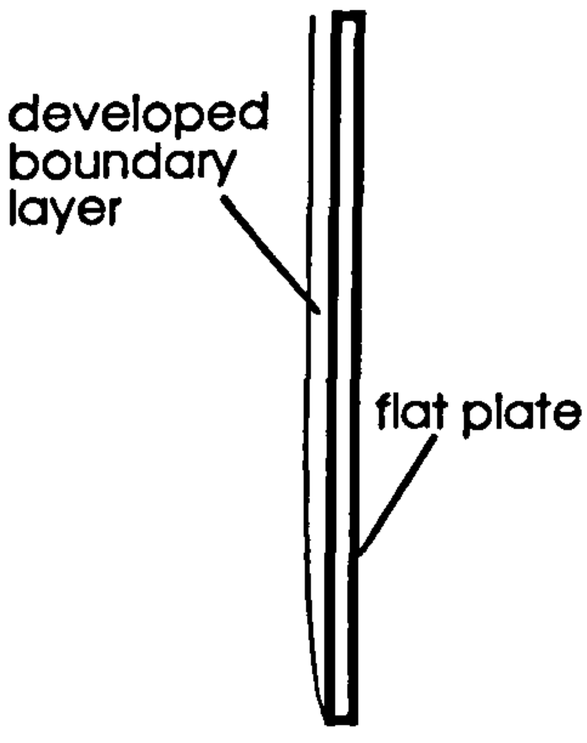

(c) developed boundary layer on a flat plate

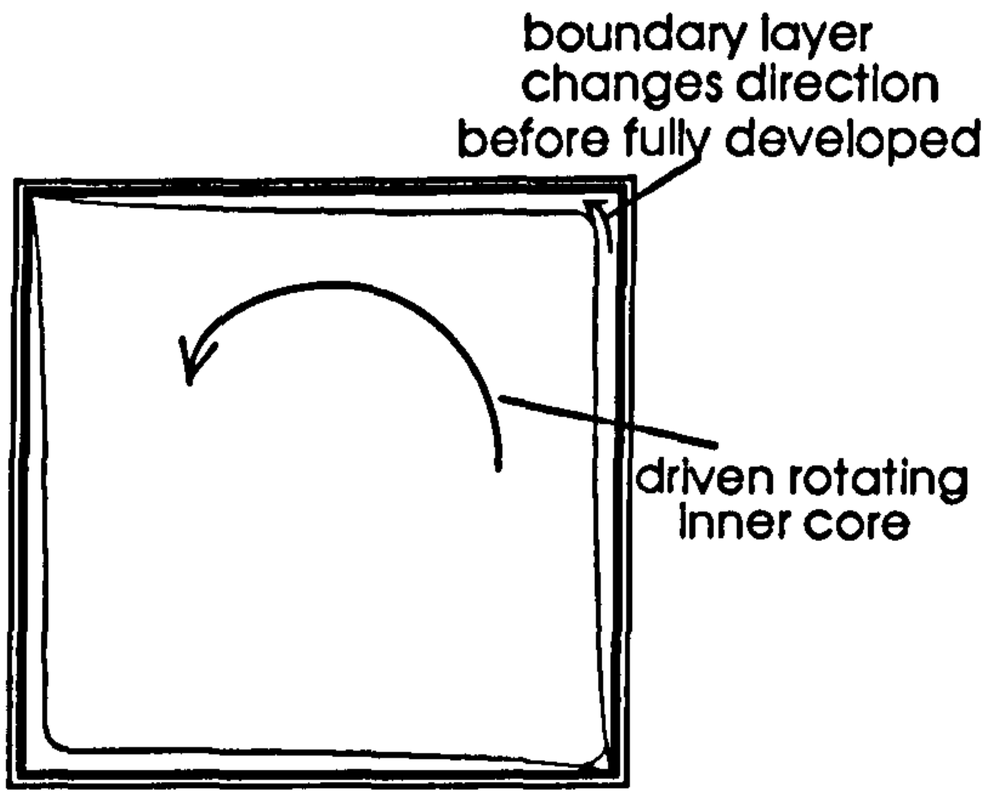

(d) 2-D enclosure flow

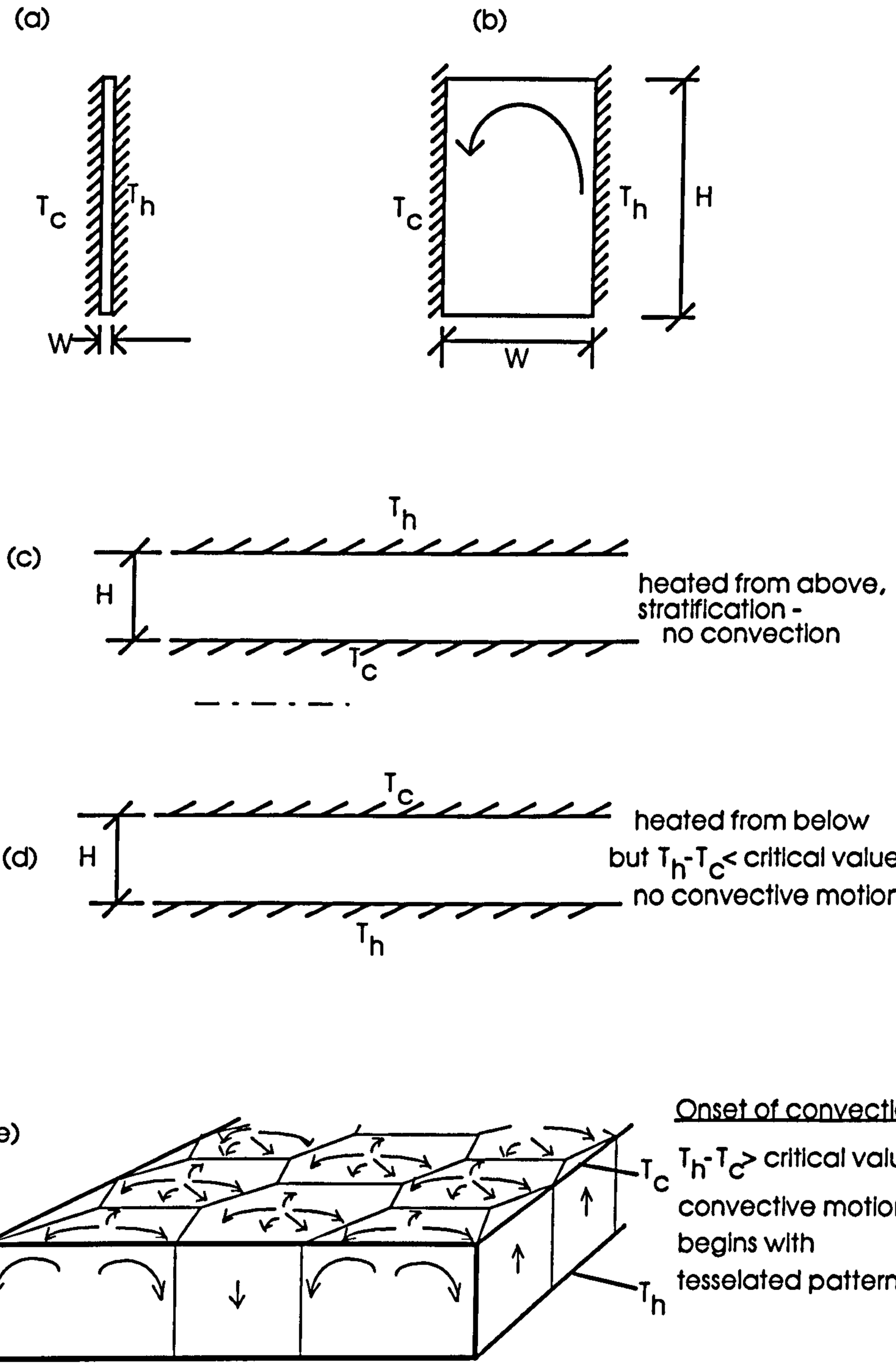

Fig.1-3 Convective heat transfer in enclosed spaces

2. REVIEW OF LITERATURE

2.1 INTRODUCTION

In the literature, there are many papers concerning experimental studies of natural convection heat transfers in enclosures. Technological needs, increased awareness of and the necessity for energy thrift have led to recent extensive research efforts being devoted to obtaining improved heat transfers by natural convection. But several of these studies have dealt with enclosures with inner bodies as cylindrical annuli. Very few have considered rectangular enclosures containing concentrated heat sources.

However, if a load is centrally positioned in an enclosure at a different temperature, a symmetrical pattern of flow will be observed (see Fig. 2-1a-c), so that the flows in half of the enclosure can be somewhat analogous to those in an empty (plain) enclosure. Thus the results from existing experimental studies involving cavities is of relative importance. It is also a stepping stone to the general symmetrical inner body case, which naturally progresses into medium temperature processes such as encountered in ovens, where the significant effects of radiation must be taken into account.

Also, because some of the external flow results for concentrated heat sources can give a general insight into internal flow behaviour, it will be helpful to examine some of the existing studies. Similarly, results from enclosed-cavity data can be helpful in interpreting those for an enclosure with an inner body.

2.2 ENCLOSED CAVITIES

In the experimental and numerical study of a uniformly heated wall of an enclosed cavity, the results of Hamady et al [17] were correlated as $Nu=0.175Ra^{0.275}$, $10^4<Ra<10^6$. If a flush-mounted heat source is employed [18] on a vertical wall at some distance y, from the lower horizontal wall, similar convective flow patterns will ensue with the heated air rising along the hot wall (see Fig.2-2a). When the heated zone was positioned nearer to the lower horizontal wall, a more symmetrical flow pattern was observed than when positioned closer to the upper horizontal wall. Although no experimental correlation was given to supplement the flow visualisation, the optimal heater location was estimated numerically as y/H=0.35, measured from the lower

horizontal wall, and the general variation of Nu was given as $0.7<Nu<2.6$ at ($10^3<Ra<10^5$), for a heater strip size to wall height of 0.2.

When a concentrated flush-mounted 'cold' source was employed [19] in a similar configuration (i.e. to [18]), the flow was reversed (see Fig. 2-2b) and, by simultaneously heating the opposite vertical wall, a larger Ra ($6.3x10^6$) was possible. For a heater strip located where $y/H>0.25$, there was virtually no further increment in the value of Nu. Two characteristic lengths were employed: the heater (chilled surface) height or the vertical wall height. The correlation presented for a square enclosure with the characteristic length based on the vertical distance of the cooled strip from the horizontal wall (i.e. $Nu=0.575Ra^{0.26}$) was some 60% higher than in free space. However, when adjusted using the heater vertical height as the characteristic length, and ΔT as the temperature difference between the heater surface and the cold surface, the resulting correlation, $Nu=0.257Ra^{0.25}$, was only 50% of that in free space. The prediction [18] that the non-dimensionalised vertical distance for optimal convective heat transfers would be 0.4 was also confirmed experimentally for larger Ra values.

Multiple flush-mounted heat-source arrays, discretely located flush on the vertical wall of an air-filled enclosure, have also been investigated numerically and experimentally [20] (see Fig.2-3a). Generally, the upper heaters had lower heat transfer coefficients than the lower heaters except for $Ra\leq10^3$, where the uppermost but one had the lowest coefficient. An increase in the aspect ratio of the enclosure resulted in a substantial drop in heat dissipation from the discrete heaters, which in turn led to a significant rise in the heaters' surface-temperatures. A mean correlation was obtained as $Nu=0.99Ra^{0.2}$. This finding is important for an enclosure with a large inner body where the vertical space is reduced to that of a large-aspect-ratio slot, resulting in restricted convective flow.

Protruding heat source arrays in a liquid-filled vertical enclosure with an aspect ratio (H/W) of 7.3 were studied experimentally [21]. The flow structure revealed similar primary and secondary cavity flows to those in reference [20]. But there were also secondary cells in the gaps between the protrusions (see Fig. 2-3b). It was concluded with the aid of the correlation ($Nu=0.0796Ra^{0.237}$), that degradation of convection occurred when compared with flush-mounted heaters. The reduction could be as a result of the inter-heater recirculatory secondary flow. Therefore, if line source heaters are located horizontally along a wall, reduction in convective flow may be expected.

2.3. HEAT TRANSFER RATE VARIATIONS WITH HEATING ARRANGEMENTS

The positioning of cylindrical heaters relative to each other and to the interacting walls has received some attention [22-28]. Previous studies have shown that when two horizontal heaters were placed vertically in line above one another in an external flow, the convective heat transfer of the upper heater became lower [22], whereas when horizontally offset by up to half the cylinder diameter (see Fig.2-4), there was an enhancement of natural convection heat transfers. The enhancements or otherwise were also shown to be a function of the spacing between the heaters.

For large spacings between the heaters, the rate of heat transfer increased with the vertical spacing by up to 30% [23]. This is because the rising buoyant flow had more time to accelerate, and so it entrains more air from the cooler surroundings, thereby reducing the plume temperature of the ensuing mixture before reaching the next heater situated above.

However, as reported by Sparrow and Boesneck [24], when the vertical separations ($S_v/d>5$; $S_h/d>1$) were large, the rate of heat transfer was hardly affected by small changes (offsets) in the vertical separations, and only marginally responsive to larger offsets. Similarly, as the horizontal offset increased beyond a critical value, ($\approx S_h/d > 2$) depending upon the vertical separation, the effect of the lower cylinder plume became so small, that there was hardly any increase in the convective heat transfers. Consequently, for ($0<S_h/d>2$), a small offset was only required to effect an enhancement.

When the heaters were positioned between two, or next to one vertical wall, enhancement of heat transfers by natural convection occurred when compared with free space data [26], and optimal arrangements were feasible [25,27]. For horizontal walls, when a heater was mounted either above, or below, a reduction in convection generally ensued [28]; when too close to a vertical wall, reduction similarly occurred. For heaters above a horizontal wall it can be surmised that a sufficient vertical gap should exist in order for air to flow into and around the heater for increased convective heat transfers.

The variations in the rates of heat transfers by natural convection are further examined in Chapter 4.

2.4. ENCLOSURE WITH INNER BODY

The presence of an inner body has also been investigated most especially as cylindrical (2-D) [29,36], or spherical (3-D) annuli [30], but works involving rectangular and cubical enclosures [31,32], are relatively limited, and when available, the inner body was maintained at a higher temperature than the enclosure.

The stages of flow development for the symmetrical cases are similar to those for plain rectangular enclosures bounded by two vertical planes with one side cooled and the other heated. At small Ra values ($< 2x10^3$ using the annular gap as the characteristic length), the fluid flow in a horizontal annulus is so small that the principal mode of heat transfer is by conduction. As Ra is increased (generally by increasing either the gap width or ΔT), a laminar boundary layer flow is established with the flow tending to move in a thin layer near each surface with a central core positioned above the horizontal line of symmetry.

In the experimental studies of Warrington and Powe [31], particular emphasis was placed on how the enclosure affects rates of heat transfer from a variety of hotter inner body shapes (sphere, cube, cylinder). Although a low emissivity aluminium enclosure (267x267x267mm) was utilised, the proportion of radiative heat transfers was still as large as 70% of the total heat supplied. This analysis was achieved by evacuating the test rig to less than 20μm Hg ($2x10^{-2}$ torr), thereby eliminating any convection heat transfers. The conduction loss through the leads and support structures was obtained via a one-dimensional analysis.

The findings revealed that the temperature profiles along the boundaries were remarkably similar, for the different inner body types and the cubical enclosure. This was also verified for the spherical enclosure. While the enclosure shape had less effect on the overall heat transfer, the enclosure size (specifically the annulus or the gap between the inner body and the enclosure) had a more significant influence on the results.

Another study involved four cylindrical heaters in both horizontal and vertical configurations mounted in an isothermal cubical enclosure [32]. The cylinders were 177.8mm in length and 41.2mm diameter. The horizontal configurations had the heaters positioned in the quadrants to make the geometry axisymmetrical (see Fig.2-5), and the results from the vertical central plane would approximate somewhat to a 2-D profile.

The heat transfer results were somewhat similar to that for cylindrical heaters in external flow. In this case the upper heaters achieved a Nu value of 84% of that achieved by the lower heaters (as against 87% in external flow [23]). With the cylinders oriented in a vertical (standing) position, there was an overall decrease of 15% in the heat transfers when compared with that for the horizontal configuration. For a single cylinder the reduction in the natural convection heat-transfer was about 10%.

These results are similar to free space experimental studies [26] where reduction in the natural convection heat transfers ensued for inclined (8%,45°) and vertically oriented (46%,85°) cylindrical heaters. These confirm that placing cylindrical heaters in the horizontal position in an enclosure will give better convective heat-transfers. All the flow visualisation and temperature-profile data showed fully-recirculating flows, so indicating that there was no stratification. As the heaters were fixed within a single enclosure, it was not possible to ascertain the variability of heat transfers with heater-wall proximity.

An experimental study of a cylindrical heater (28mm dia.) in a square-sectioned enclosure (100x100x635) employed a Mach-Zehnder Interferometer for the heat-transfer analyses [33]. The motivation was the need to reduce heat losses from an underground heating pipe. This influenced the trend of the experimental study whereby the position for the minimum heat loss was found to be along the vertical centre-line, the cylindrical heater eccentrically being positioned in the upper half of the cavity at $S_H/d \cong 2.5$. A study of differentially-heated cylinders in a rectangular enclosure [34], which was also motivated by the need to minimise heat losses from district-heating piping, established that by placing the cylindrical heaters the hotter one above the other, the minimum rate of heat losses could be achieved. The converse occurred if they were placed side by side. The deduction from this is that there could be an optimising arrangement of cylindrical heaters in rectangular-sectioned enclosures which would produce maximum convective heat-transfers.

Using the same enclosure and similar experimental techniques to obtain the convective component of heat transfers as in reference [32], cylindrical arrays in the form of tube bundles were tested [35] (see Fig.2-6). When a constant heat flux rather than an isothermal boundary condition was imposed on the cylinders, the temperatures of the upper rows of cylindrical heaters increased.

Table 2.1. Heat Transfer Correlations

Free space or infinite atmosphere

cube and sphere	[31]	$Nu=0.618Ra^{0.25}$	Adjusted from $Nu=0.52Ra^{0.25}$ (L for infinite atmosphere)
vertical plate	[58]	$Nu=0.52Ra^{0.237}$	

Enclosures

Square enclosure - one vertical wall heated	[17]	$Nu=0.175Ra^{0.275}$	Air $10^4<Ra<10^6$
Heated fraction of wall height	[19]	$Nu=0.168Ra^{0.25}$	Air
Flush-mounted array(heaters on vertical wall)	[20]	$Nu=0.99Ra^{0.2}$	Air $10^4<Ra<10^6$

Inner body

(a) annuli, (2-D)

Cylindrical annuli	[29]	$Nu=0.11Ra^{0.29}$	2-D

(b) spherical, (3-D)

Spherical annuli	[30]	$Nu=0.228Ra^{0.226}$	heat transfer greater than cylindrical annuli

(c) cubical, (3-D)

Cubical inner body	[31]	$Nu=0.590Ra^{0.235}(L/R_i)^{0.235}$	Gap effect $1.3<L/R_i<2.2$
		$Nu=0.622Ra^{0.235}$	$L/R_i=1.3$
		$Nu=0.678Ra^{0.235}$	$L/R_i=2.0$
cubical enclosure and four horizontal heaters	[32]	$Nu=0.496Ra^{0.245}$	3-D

While this temperature characteristic of the upper heaters was similar to that in free space, the local heat-transfer data indicated higher heat transfers, which contrasted with the free-space studies. This was explained by the increased convective activity in the upper zones caused by the enclosed space. Not only was this finding distinctly different from that in free space, it surprisingly contradicted the study using only four heaters in the same enclosure (as reported above) [32]. This then poses a different dilemma for the designer of heat-transfer equipment as to the best position of single, or multiple heated objects in enclosed spaces. The uncertainty would also be more serious for the inner bodies which would be at a lower temperature than their enclosure and heat sources.

More recently Warrington et. al. [36] further extended and co-ordinated the available data by studying the bounding effects, so as to determine the limits, with respect to gap width, within which the various correlations could be utilised for internal and external conditions. Although these results were mainly for 3-D configurations, attempts were made to normalise and combine them with 2-D data. In the process of trying to generalise the results in the form of universal correlations, they were later shown to be limited in applicability [48].

The reviewed correlations are tabulated (see Table 2.1).

2.5. NUMERICAL STUDIES AND CONFIGURATIONS

The recent advances in computer hardware have stimulated an increase in numerical methods for analysing heat transfers. However, the advances made for heat transfer problems involving the present subject of study have been disappointing, principally because the poor validities of several mathematical models have restricted the usefulness of computations mainly to situations where the temperature differences have been relatively low. Even then, the different methods of formulations and solutions can produce vastly different and conflicting results. There is, therefore, a dearth of reliable information in this area. Although some other configurations have emerged (see Fig.2-7), the most extensive studies concern, as stated before, horizontal annuli with idealised boundary conditions.

Kuehn & Goldstein [37] presented both experimental and pioneering numerical studies of horizontal annuli. The governing equations were formulated in polar cylindrical coordinates and the finite-difference approach was used to express the differential

equations in terms of values at discrete points. The successive over-relaxation technique was chosen as the method of solution. From the extent of the numerical analysis which converged (for $Ra<10^5$), the predictions largely agree with experimental results. The inner cylinder radial temperature was similar to that of a single cylinder in free atmosphere, with the boundary-layer thickness increasing as the flow moved up around the cylinder. The air data was correlated as $Nu=0.159Ra^{0.272}$. A somewhat updated and improved study was carried out [38] which compared favourably with available experimental data, and extended the eccentricity results.

In the studies of Chang et al [39], a hot square-sectioned cylinder was conceptually placed concentrically within a circular cylinder. The finite-element (FE) method was employed to solve the ensuing boundary-value problems using quadratic triangular elements, with linear interpolation applied for the pressure field. When the inner body was in a located-on-edge (LOE) position such that its walls were each inclined at 45^0 to the vertical (see Fig.2-7a), a boundary-layer flow occurred along the inner body surfaces. When the inner body was in a located-on-flat (LOF) position so that its side walls were vertical (see Fig.2-7b), the rising flow separated at the edge from the top horizontal surface, and overall, was of lower velocity than the previous configuration. When the inner body was simulated as being relatively large, so that the gap was small in the LOE position, co-rotating sub-vortices were found for $Ra\cong10^5$. Although this was barely distinguishable in the plotted streamlines, it was clearly visible in the experimental smoke visualisation, which was carried out to verify the numerical flow-results.

Therefore, if an enclosed heat transfer system consists of a non-uniform annulus, such that the mid-plane horizontal gap is small, not only would the convective flow be inhibited, but also the upper and lower zones would behave as if they were independent, with associated local flow characteristics. Although the LOE position always resulted in higher convective heat-transfers, it was also noticed that as the inner body size was reduced (inner body width with respect to enclosure diameter) from 0.4 to 0.2, the difference in heat transfer from the inner body to the enclosure, with respect to orientation, became marginal (from 8% to 2%). Therefore, the overall heat-transfer became little affected by the attitude of the inner cylinder, that is, the inner object was small enough so that the environment could not distinguish its shape, behaving like a circular cylinder which has no directional dependence. Therefore, it can be inferred that ovens designed to produce uniform heating of a small object may not necessarily produce uniform heating of larger objects.

Oosthuizen [40] studied the natural convection of a uniformly-heated, square-element mounted and protruding from one wall of a square enclosure (see Fig. 2-7c). Another 2-D study [41] employing similar FE techniques to those of reference [40] considered a prismatic inner body of variable aspect-ratio, placed symmetrically inside a square enclosure (see Fig. 2-7d). The flexibility of numerical techniques was amply demonstrated by varying the inner body shape from a thin flat-plate (aspect ratio H/W≈ 0) to a square-sectioned LOE prism of variable aspect ratio (see Fig. 2-7b).

Larson et al. [42] compared their numerical methods for enclosed natural-convection problems (which employed both finite difference, FD, and FE methods) with holographic interferometry. The interferograms were obtained from experimental studies of a heated circular cylinder positioned at the base of an isothermal rectangular-section enclosure. A hexagonal cylinder replaced the circular cylinder for a second configuration (see Fig.2-7e). Although the two computational methods yielded similar quantitative results, the FD routines gave a better agreement with the holographic interferometric measurements than the FE solutions. However, they were both within 10% of the measured temperature data. The identified numerical errors include the use of constant properties in the models, assumptions of isothermal conditions along the walls, and the variations in the mathematical formulations between the FE and FD grids. Also, only the lower section of the cavity was studied.

Another arrangement which has been considered was that of two horizontal cylindrical inner bodies in a rectangular enclosure cooled from above [43]. The results (for $Ra=10^4$ and $Ra=10^6$), showed an increase in convective activity at the upper corners at the larger Ra.

In general, where natural convection was concerned, numerical studies were largely undertaken complementary to experimental undertakings. The numerical exercises provided more detailed information including the velocity field; changes to shape and configuration were usually less difficult to incorporate. They can also provide invaluable information in the design of experimental equipment. However, experiments have the advantage of being applicable to unsteady flow and turbulence, beyond the Rayleigh range where the numerical computations become unstable [37].

2.6. RADIATIVE HEAT TRANSFERS

Radiative heat transfers within enclosures continue to receive increased attention both experimentally and numerically [44-50]. Where there is uniform heating from an upper horizontal surface, the temperatures increase on the adjacent upper vertical walls because of radiative heat transfers. If radiation is ignored, there is no fluid motion at steady-state because the air is stratified and gaseous conduction is the only mode of heat-transfer. However, when radiation is super-imposed from the hot wall, the general effect is to disturb the stratified conditions by creating a temperature gradient on the adjacent vertical walls and increasing the temperature of the cold wall, thereby reducing the overall ΔT.

2.6.1 Radiation-Convection Interactions

2.6.1.1. Absorbing medium

In the numerical results of Zhong et al [44] where CO_2 flows in a rectangular enclosure were studied, symmetrical flow fields were established (see Fig.2-8), the upper vortex flows being considerably weaker than the lower flows. It was subsequently established that absorbtion of radiation by CO_2 was low ($Ra \leq 10^6$), and that surface radiation was still the dominant feature. This therefore suggests that some of the findings should be applicable to those for a gaseous medium, where the upper horizontal wall is the hot surface.

The results indicated that the dissipation of heat by radiation through a weakly-absorbing medium:

(a) reduced the maximum temperature of the hot wall;

(b) increased the temperature gradients of the adjacent vertical walls; and

(c) initiated fluid flow by natural convection because the CO_2 is directly heated by radiation before ever contacting any walls.

It also follows that, if the thermal conductivity of the wall is high, the heat would be rapidly conducted along the walls, thus altering the local radiative flux, as well as attenuating the vertical surface temperature gradient; the generation of buoyancy forces

by the wall will also be affected. This is the influence or interaction by thermal conductivity on the system multi-mode heat transfers.

In the study of a top-heated cylindrical enclosure [45], valuable information was provided regarding flow patterns, velocities and temperature distributions. A borosilicate vertical cylinder was employed, covered by a plane, upper horizontal heated copper wall and a cooled base. From the photographs of the smoke flow visualisations, streamlines were drawn using an electromagnetic digitizer, and vortex location and flows cell sizes (cross-sectional areas) determined. Symmetrical flow fields were also observed similar to those predicted numerically, despite the inherent 3-D characteristics of the apparatus.

In the numerical study of a square-sectioned enclosure by Kassemi and Naraghi [46], the streamlines produced at $Gr=1.0x10^4$ were similar in shape to those of Zhong et al [44]. However, the flow directions were reversed, which virtually ensured a different convective heat-transfer coefficient, a potential nightmare in thermal equipment design where numerical results have previously been faithfully adhered to.

The vital fact remains that two different numerical methods gave conflicting results each with its own apparently logical explanation. Although Kassemi and Naraghi [46] employed the discrete exchange factor method which is more versatile than the zone method employed by Zhong et al [44], one of the methods which could have resolved the conflicting results would be to have carried out, simultaneously, experimental studies to provide a check on the applicability of the mathematical models for the chosen conditions, as suggested by Chu et al [18].

2.6.1.2 Radiation-Convection-Conduction Interactions

Zhao et al [47] considered the case of three cylinders in a rectangular enclosure. This was to establish the optimal heat-transfer rates from multiple electrical cables positioned inside rectangular trays. Unlike some of the earlier studies, which neglected other modes of heat transfer, both convection and radiation were considered in the numerical formulations. Although the cylinders were in contact with the base of the enclosure, conduction was assumed to be small and ignored in the numerical formulation. After expressing the resulting equations in finite difference form, they were solved in one half of the physical domain (due to symmetry), by the alternating direction implicit method. At each time step, utilising the new values of the dimensionless temperatures, the

radiation equations were solved for dimensionless radiosity or surface leaving flux, q_{rad}: the latter was obtained and used to update boundary conditions.

The results were compared favourably with a complimentary experimental study [48], where the flow visualisation was practically identical to the computed streamlines, and the average deviation of the mean cylinder temperature from the experiment was less than 2%. It was also pointed out that the correlations deduced via the experimental study contradicted the universal correlation of Warrington and Powe [31]. The presence of radiation was observed to enhance the heat transfer rate from the cylinders and the middle cylinder was marginally hotter. However as in reference [43], the temperatures of the inner bodies can be considered to be relatively similar. Therefore, none of the inner cylinders could be regarded as a heater, transferring heat simultaneously between itself and the enclosure walls, and to any other inner object.

2.6.2. Inner body interactions - oven and furnace configurations

Although combustion systems may introduce improved convection to the inner objects, industrial heat treatments often require the use of electric or tube ovens and furnaces, or in situations where atmospheric control is essential. Convection plays a significant part in enclosure heat transfers, but as the radiative component depends on quartic powers of the temperatures, the radiative component increases more rapidly than convective heat transfers as the system temperature increases. The effect of increased radiation on the system efficiency has also been studied, but systems operating above oven temperature (i.e. > 800^0C) are usually classified as radiation systems [6].

Studies by Scheitlin and De Witt [14] concentrated on optimising radiative heat transfers from a low-emissivity ('Bi-radiant', highly reflecting) cubical oven, under both transient and steady-state conditions. This study demonstrated the effect of wall properties, specifically the emissivity of both the heating elements and the enclosure's walls on the rate of heat transfer to an inner object. Protruding heaters were fitted just clear of the horizontal walls. With some variations in the heating element shape and arrangements, the influence of wall emissivity on the transient response of the oven was experimentally and numerically deduced.

High-emissivity (low reflectivity) walls were observed to heat up faster because of the greater absorptance of incident flux, but this should mean that the heat flux available to the interior of the enclosure (surrounding air) was temporarily reduced during the

transitory period. It was also observed that a thinner, and consequently hotter heating element (reduced from 6.6mm to 3.0mm dia.), improved the radiative supply to the interior of the cavity, thereby increasing the efficiency of the transient system from 17.9% to 35.3%. The natural convection component of the total heat transfers was less than 15% of that which was accounted for by radiation, (i.e. > 20% for a tested conventional oven [14]). However, the convection in the 'Bi-radiant' oven was determined using a universal correlation [26],[49] with a large uncertainty. Other factors which affected the system efficiency, were the overall thermal mass and the insulant's thermal conductivity; lower values improving the efficiency.

The vast majority of convection ovens are of the forced-convection variety, but a few models are still manufactured using natural convection (and radiation). Existing models include domestic electric ovens with lower sidewall-mounted heating-elements [50] (see Fig. 2-9a). Current models have similar configurations, but with an extra element in the upper quadrant [51] (see Fig. 2-9b). Other commecially-available configurations include top and bottom-mounted heaters (see Fig. 2-9c). But no related comprehensive heat-transfer analysis exists in the open literature.

The use of high-emissivity enclosure coatings was widely assumed to lead directly to high rates of net heat transfer, and implicitly to higher efficiencies. This influence of emissivity on furnace performance has been investigated both theoretically and experimentally [52]. The theoretical model, which showed good agreement with the experimental studies was extended to investigate the effect of varying the wall emissivity of an indirectly-heated furnace, and a radiant-tube furnace.

A muffle furnace was employed, whereby the heat supply by combustion or otherwise took place outside the furnace (see. Fig. 2-10), to enable a uniformly-heated and controlled internal atmosphere. The net heat-transfer to the inner body or the stock for the indirectly heated furnace was calculated using only a 2-surface model because the muffle permitted the assumption of uniform temperatures over most of the enclosure surfaces. The model input involved the stock covering the floor (surface 1), and the walls and the roof (surface 2) (see Fig. 2-10). Fixed data were used for the stock, while varying those for the wall and roof (see Table 2.2).

The findings for steady-state conditions, and for given values of the temperature of walls and roof show that:

a) increasing the emissivity of the walls and roof will increase the heat transfer to the stock; and

b) this increase is greater for larger temperature differences between the wall and stock.

Table 2.2. Data used to calculate heat transfer through refractory wall

	Emissivity	Temperature (K)
Walls and roof	0.1 to 0.9 (varied by steps each equal to 0.1)	1173 to 1573 (varied by steps each equal to 100)
Stock	0.85	973

The net heat transfer to the stock from an array of radiant tubes or heating elements in the roof was calculated using a 3-surface model. The model input involved the stock plane (surface 3), (see Fig. 2-11) but only the walls were assumed to be coated to alter their emissivity. Fixed data were used for the stock, as well as the effective emissivity of the imaginary radiant plane (see Table 2.3).

Table 2.3. Data used to calculate heat transfer from roof heaters.

	Emissivity	Temperature (K)
Roof (radiant plane)	0.66	1173 to 1673 (steps of 100)
Walls and roof	0.1 to 0.9 (step = 0.1)	1173 to 1673 (steps of 100)
Stock	0.85	973

It was essential to incorporate the effect of insulation on the heat transfers conducted away from the interior of the walls.

The findings show that the net heat-transfer to the stock does not change with emissivity for values of the insulant's thermal conductivity of less than 1.0 $Wm^{-1}K^{-1}$ during steady-state operation, but decreases slightly with poor ($k>5$ Wm^{-1} K^{-1}) insulation. This shows that for steady-state conditions, involving higher temperatures,

the effectiveness of the insulation of a highly-emissive enclosure will determine the system's efficiency.

2.7. CONCLUSIONS

If an entire wall of an enclosure is uniformly heated, improved convective heat transfers would result relative to employing flush, or protruding discrete heaters on the wall. Experimental results from free space show that when cylindrical heaters are mounted close to a vertical wall, improved convective flow and heat transfers can occur, more than if the heaters were to be situated at the base or along the upper horizontal wall. This has not yet been fully verified in a totally enclosed space.

Enclosure data have shown that convective heat transfers from a uniformly heated vertical wall would be higher than from a vertical wall with flat, discrete heaters at similar Ra. The maximum convective transfers would occur when a discrete heater is flush-mounted on a vertical wall at y/H=0.4.

It has also been shown that natural-convection heat transfers decrease when a heater is positioned close to a lower horizontal wall, rather than when it is positioned horizontally and close to a vertical wall. Although it is common for ovens to incorporate base-mounted heaters, the conditions under which enhancement or otherwise of convection would occur have not been established in the open literature.

In an enclosure fitted with an inner body, the total heat-input by protruding heaters or line heat-sources must be accounted for by the heat absorbed by the inner body, and that lost through the enclosure. Consequently, a reduction in heat loss by insulating the enclosure should result in increased heat gain by the inner body for the same total power input. Also, an enhancement in one mode of heat transfer could cause a reduction in other modes, if the total heat input remains the same. It has also been established that thermal mass and insulation properties played a more significant part during transient conditions than when steady-state conditions have been achieved.

While the process of calculating radiative heat-transfers in a non-absorbing medium is well established, that for natural convection has yet to evolve into universal acceptability. With radiation and convection interactions, more parameters than equations often prohibit a numerical solution. Various problems, notably instability and

oscillations, have limited the application of most numerical methods to regions of low values of Ra, and attempts at obtaining solutions for higher Ra and conditions where turbulence would exist have often met with conflicting results. It is therefore necessary to continue to rely on experimentally-derived solutions.

Convection improves temperature-uniformity of inner bodies, and from an energy standpoint, there may be significant advantages if this were to be achieved by natural rather than by forced convection. By varying the location of discrete line heaters in an enclosure, it should be possible to quantitatively determine the contribution of convection to the overall heat-transfers.

The present study will investigate experimentally, the heat transfers in an enclosure fitted with an inner body and cylindrical, sheathed electric heating-elements, with the aim of augmenting the transfer of heat uniformly to the inner body by natural convection. Experimental investigations will be carried out to examine the variability of natural convection heat transfers with heater location within an enclosure. An improved method of quantifying the convective component of the heat transfers will also be investigated.

Fig. 2-1 Enclosure with symmetrical inner body and parallel wall flow

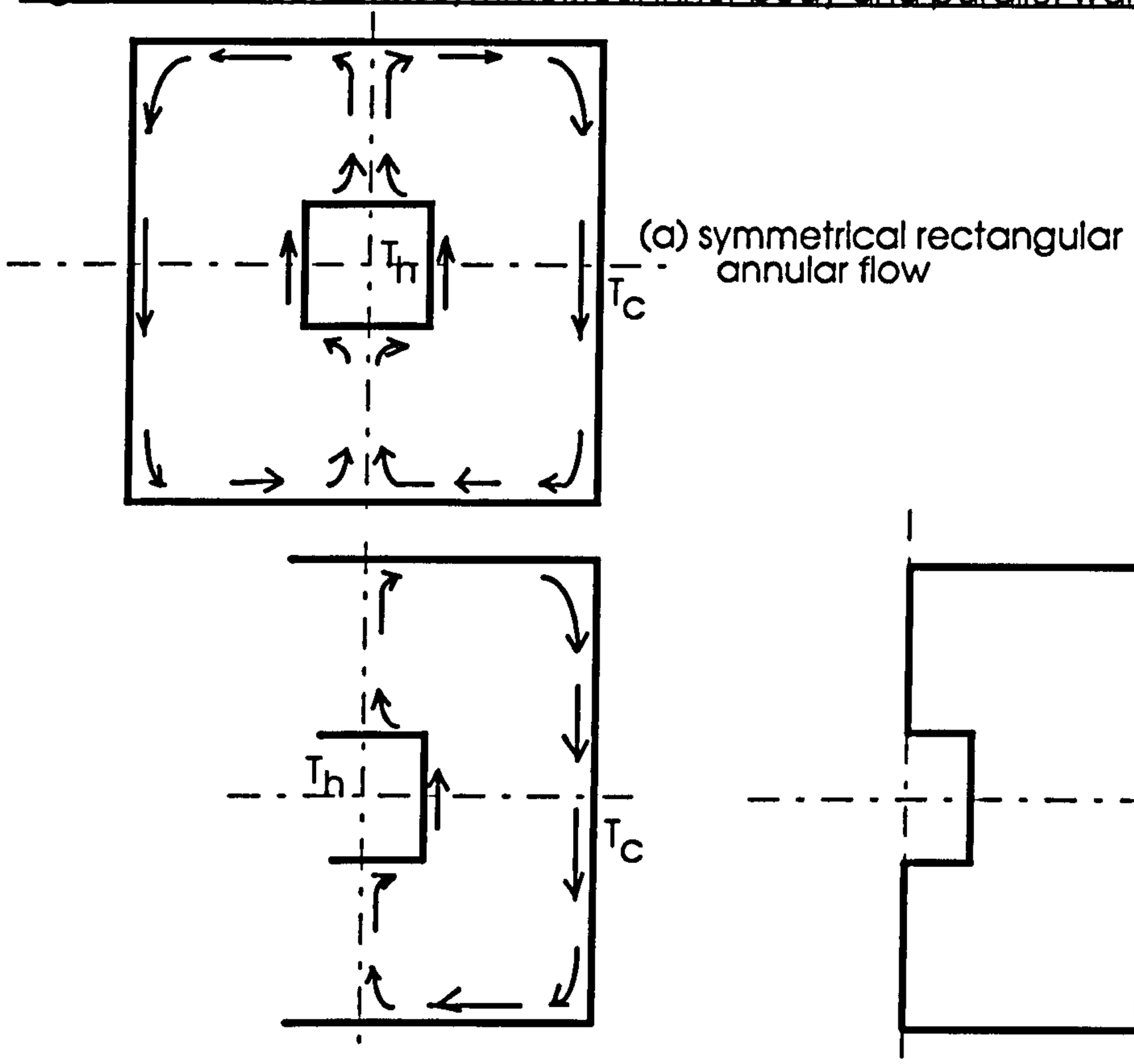

(a) symmetrical rectangular annular flow

(b) half of flow in enclosure

(c) approximate parallel wall configuration

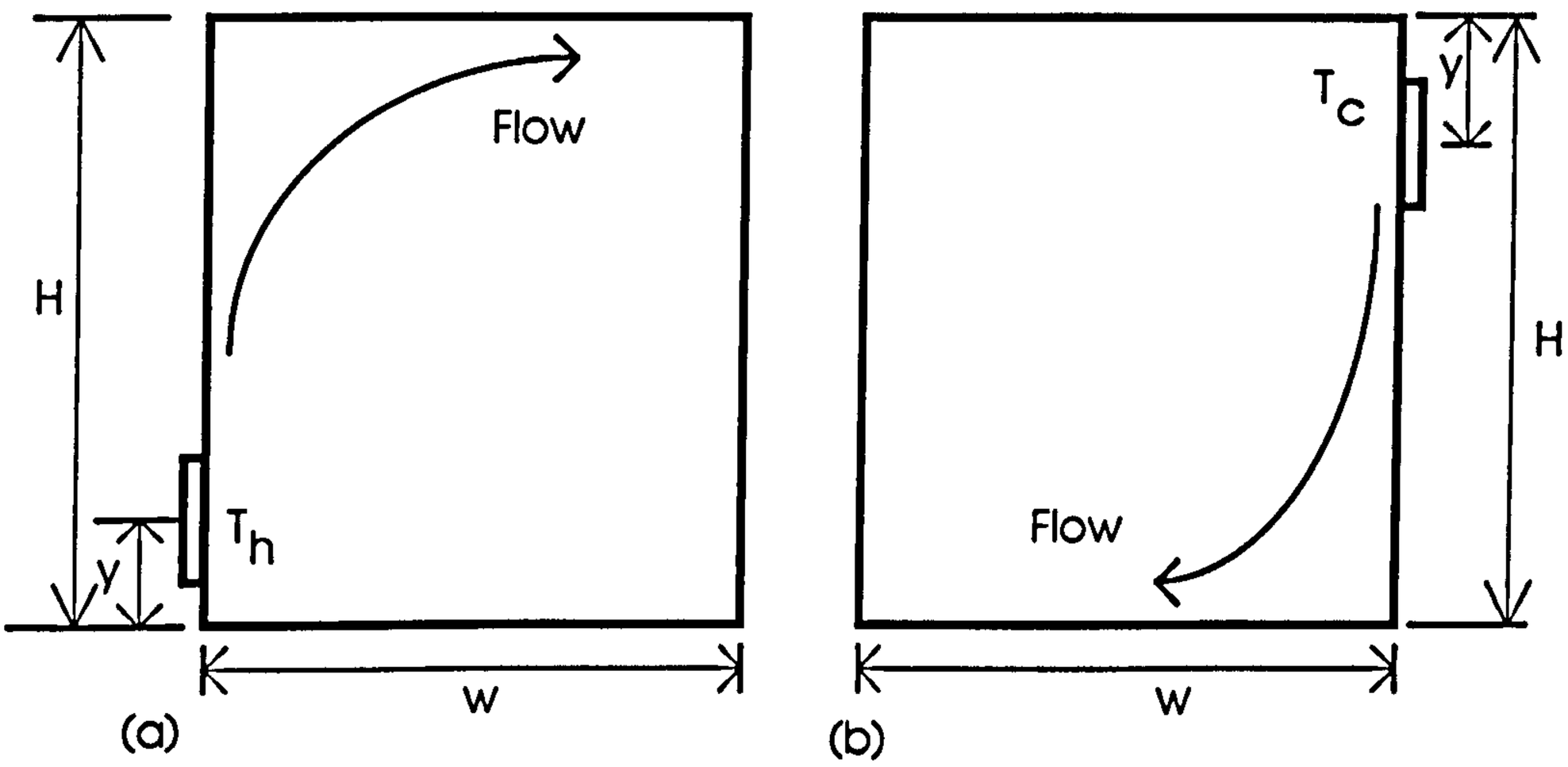

Fig.2-2 Concentrated, flush-mounted heat/cold source in an enclosure

Fig.2-3 Flush-mounted(discrete) and protruding heat sources in an enclosure

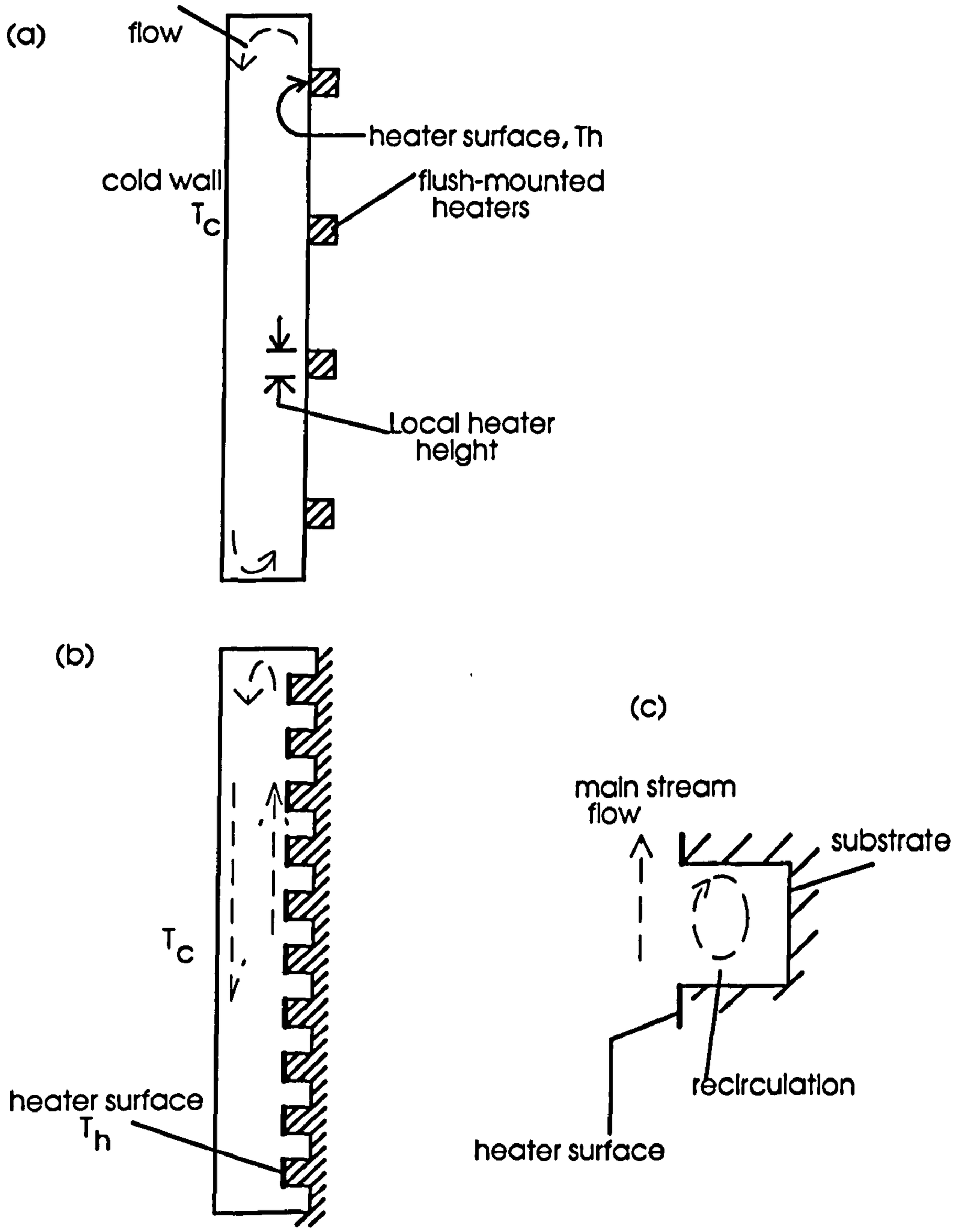

Fig. 2-4 Horizontal cylinders in free space

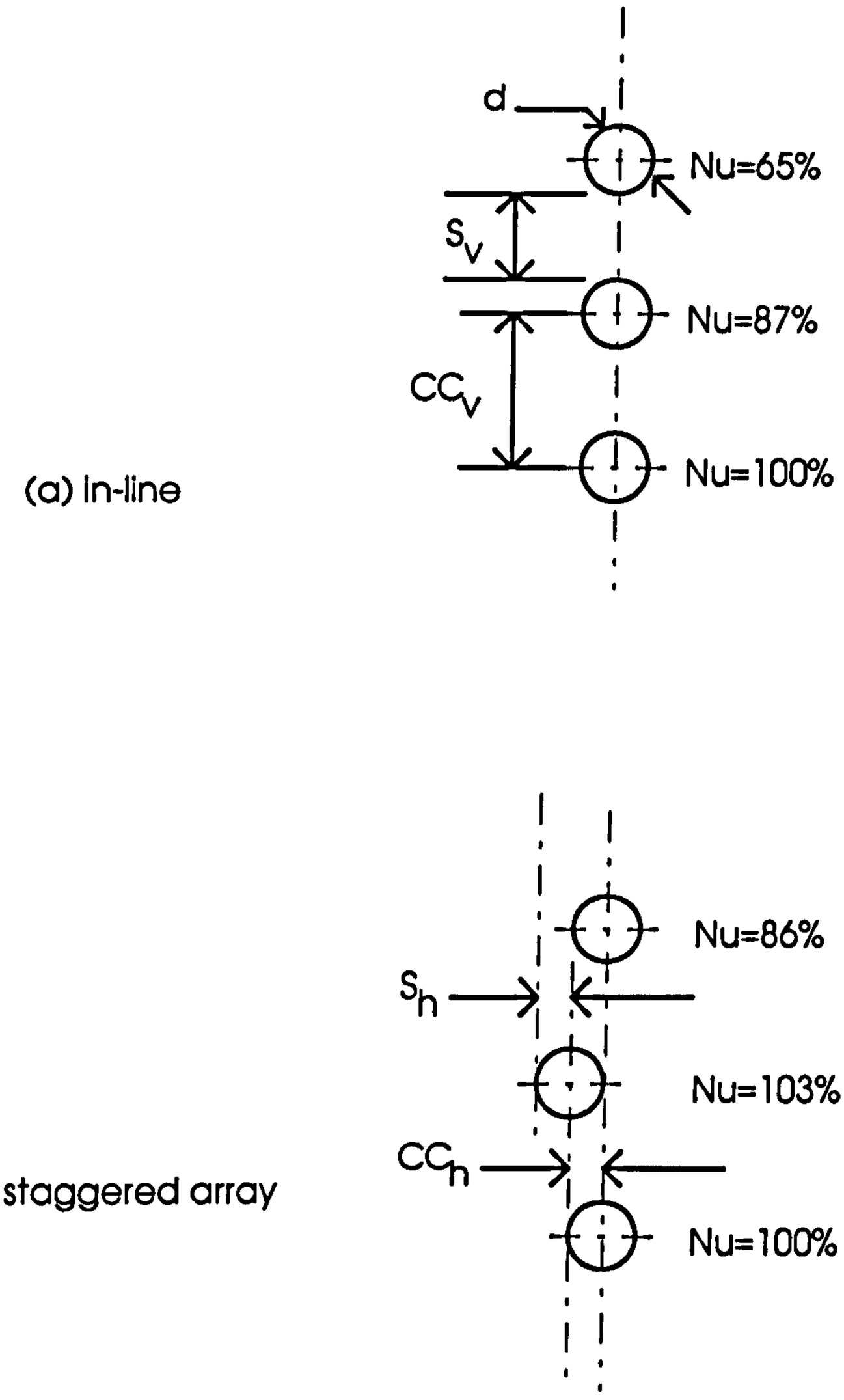

CC - cylinder centre-to-centre spacing

S - peripheral surface-to-surface separation

Fig.2-5 Cylindrical heaters in a cubical enclosure

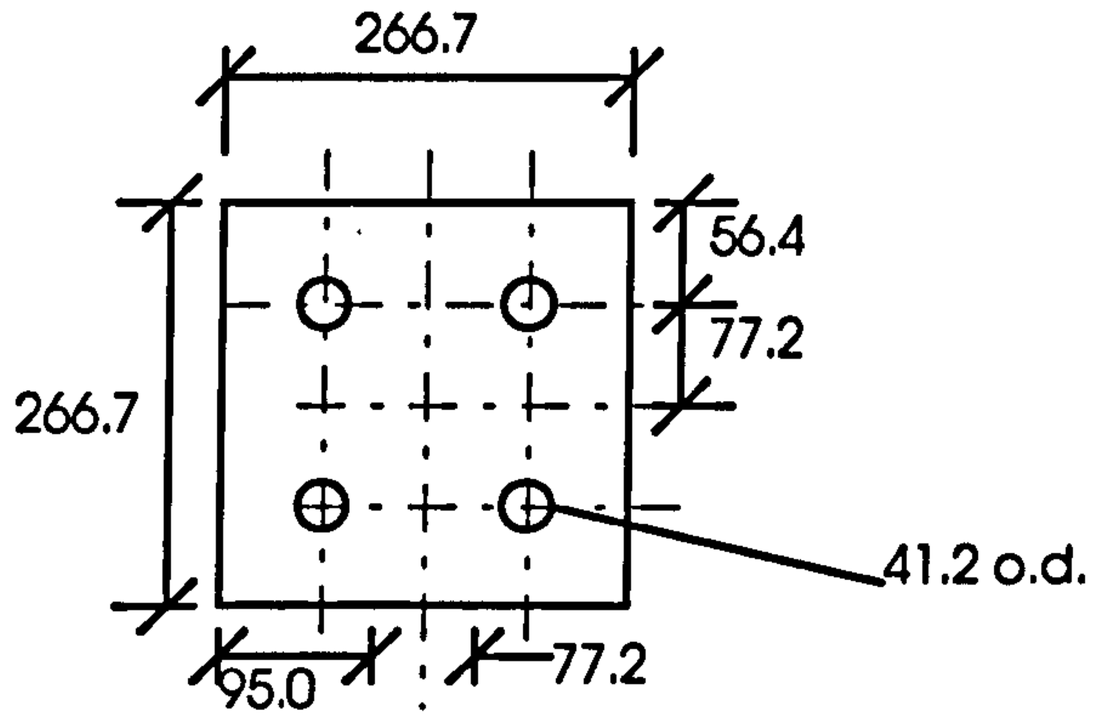

Fig. 2-6 Configurations of arrays of Horizontal Cylinders in Enclosures

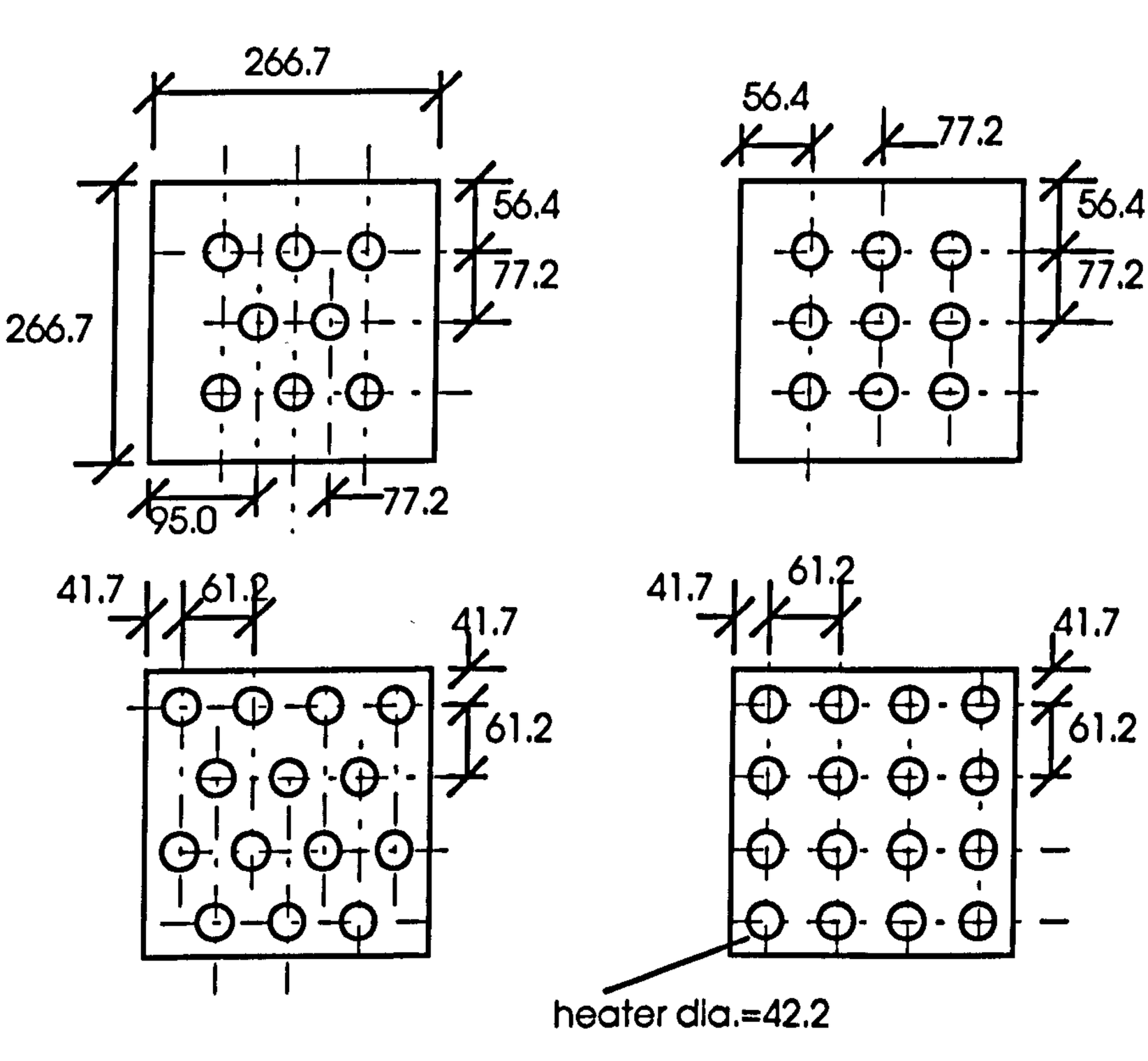

Fig.2-7 Some configurations in the numerical studies

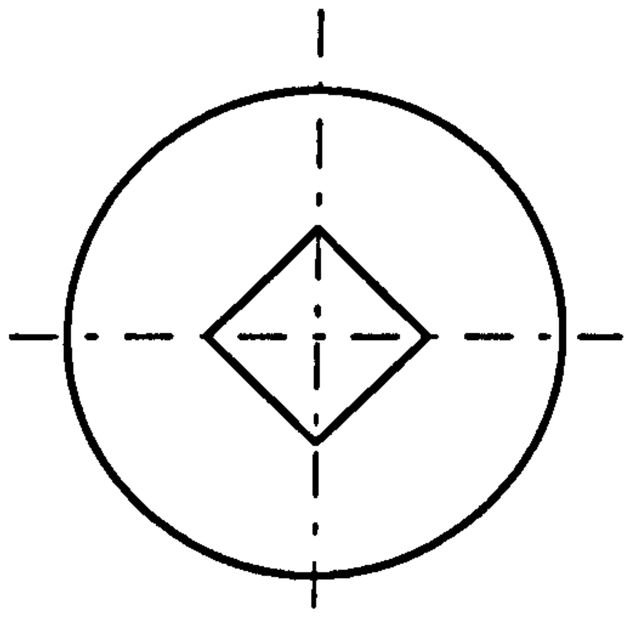

(a) square-sectioned cylinder
located on edge (39)

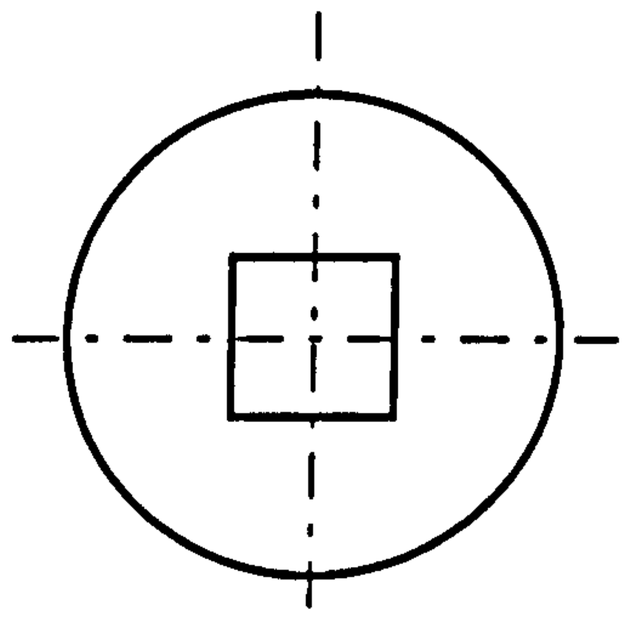

(b) square-sectioned cylinder
located on surface (39)

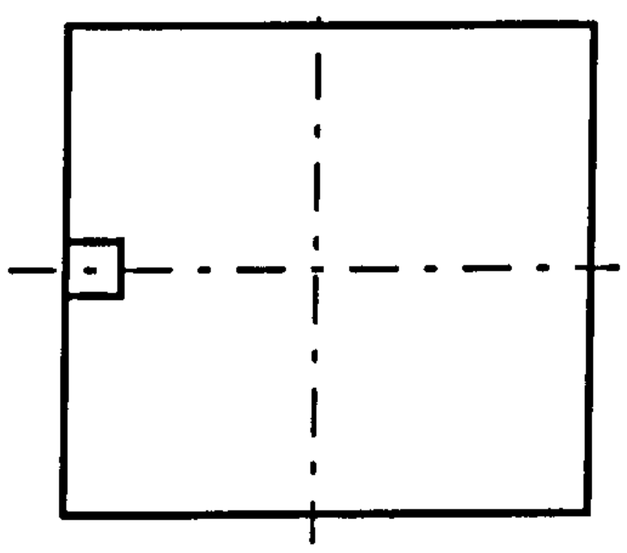

(c) square element in
an enclosure
(40)

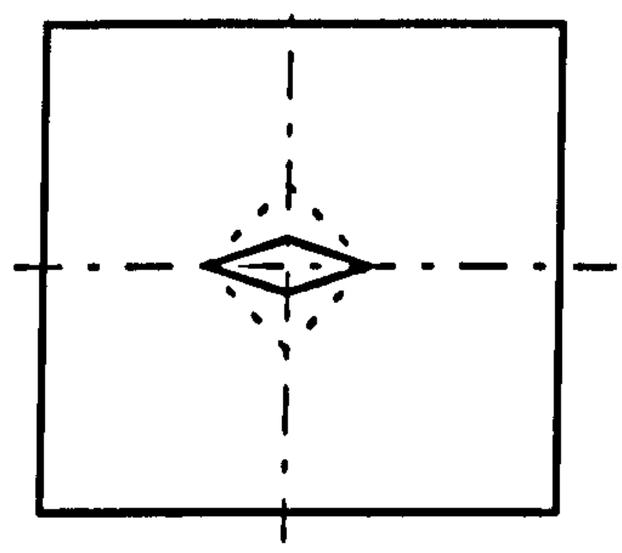

(d) prismatic inner body
(with variable aspect ratio)
(41)

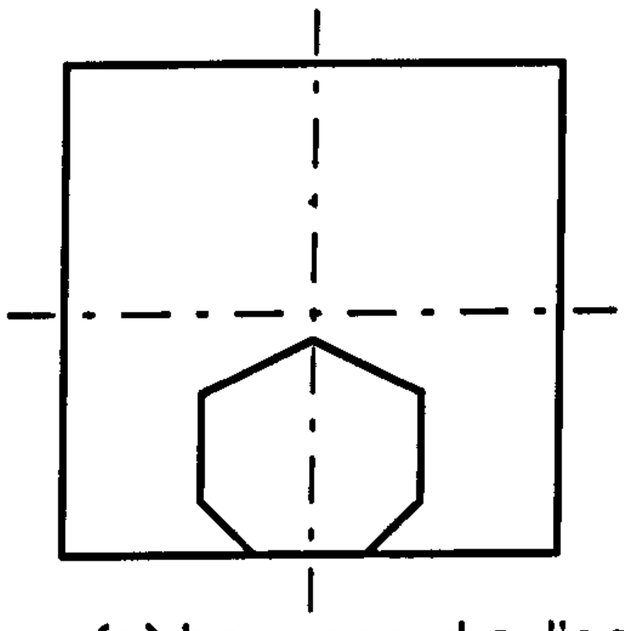

(e) hexagonal cylinder
at the base
(42)

Fig.2-8 Influence of radiation in destroying stratification

(in the presence of a weakly absorbing media)

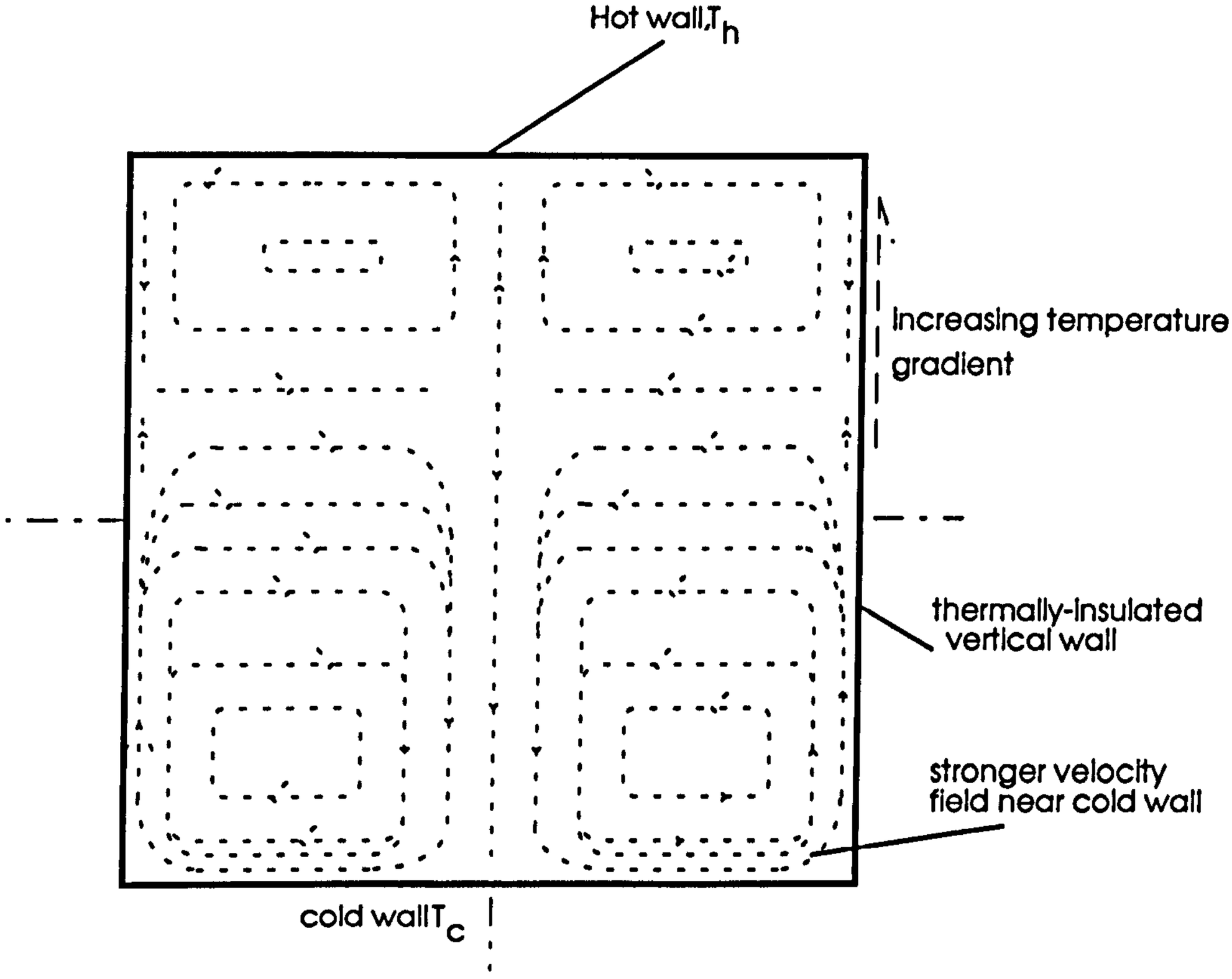

CO_2

$Ra=10^6$

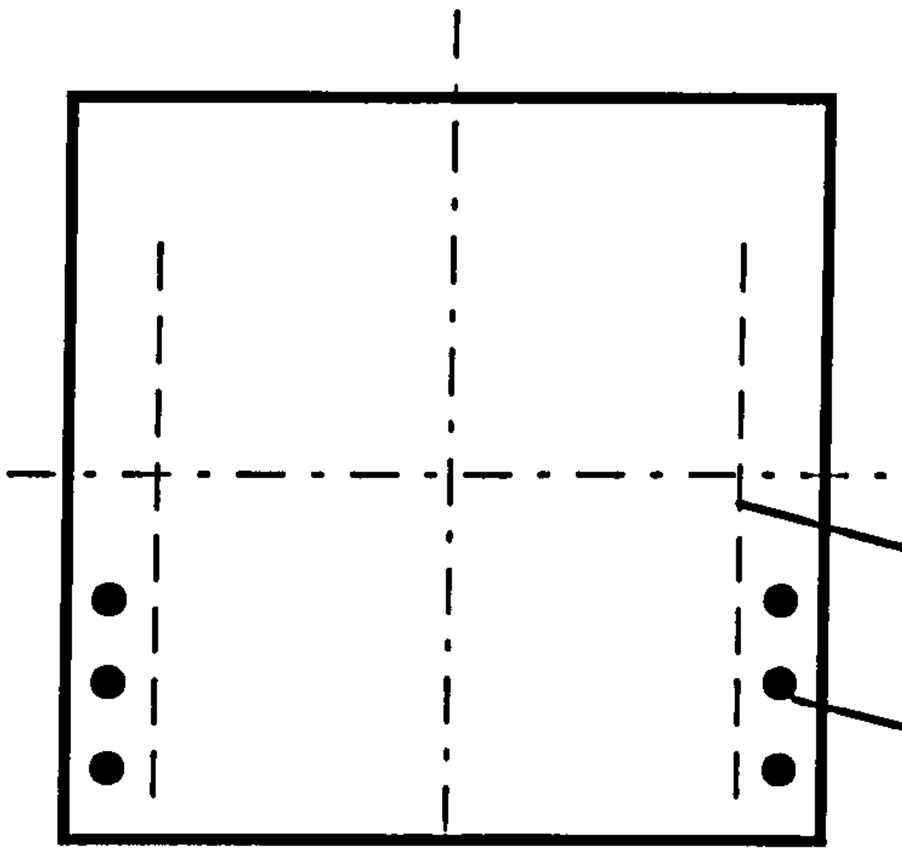

Fig. 2-9a

Natural convection configuration
Sidewall heating elements
Belling Compact 4, 'Belling'

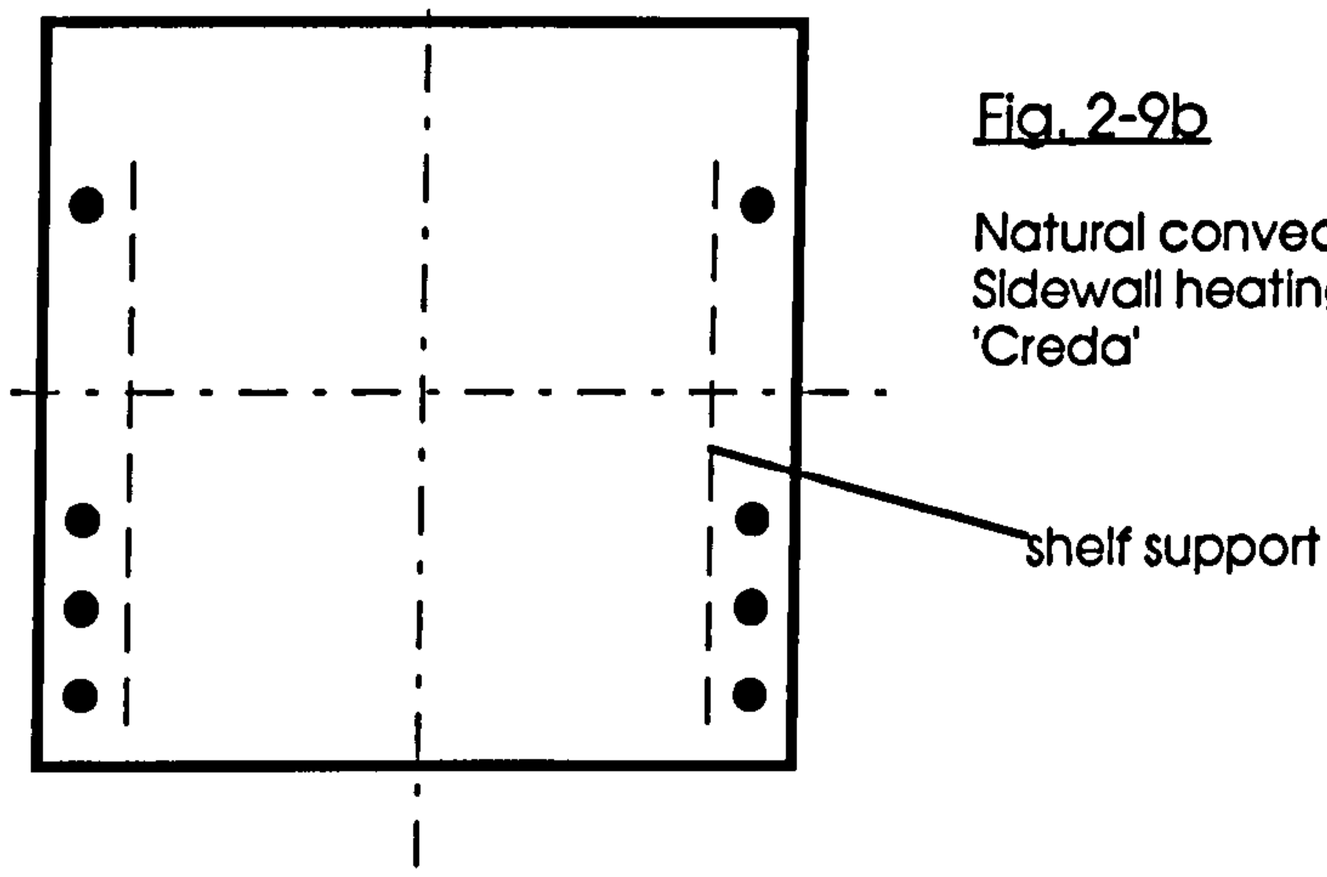

Fig. 2-9b

Natural convection configuration
Sidewall heating elements
'Creda'

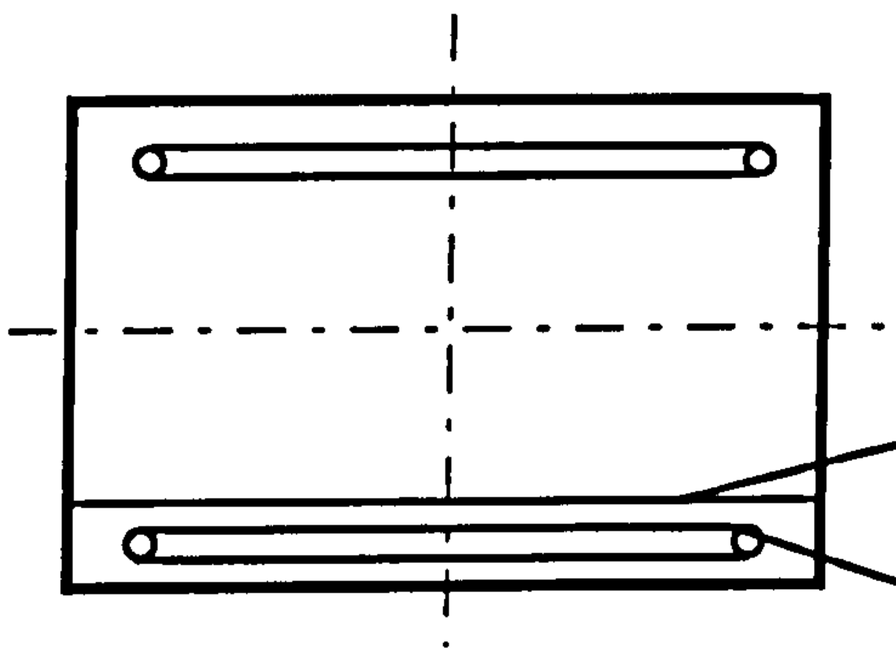

Fig. 2-9c

Natural convection configuration
Upper and Lower Heating Modes
'Hotpoint' and 'Creda'

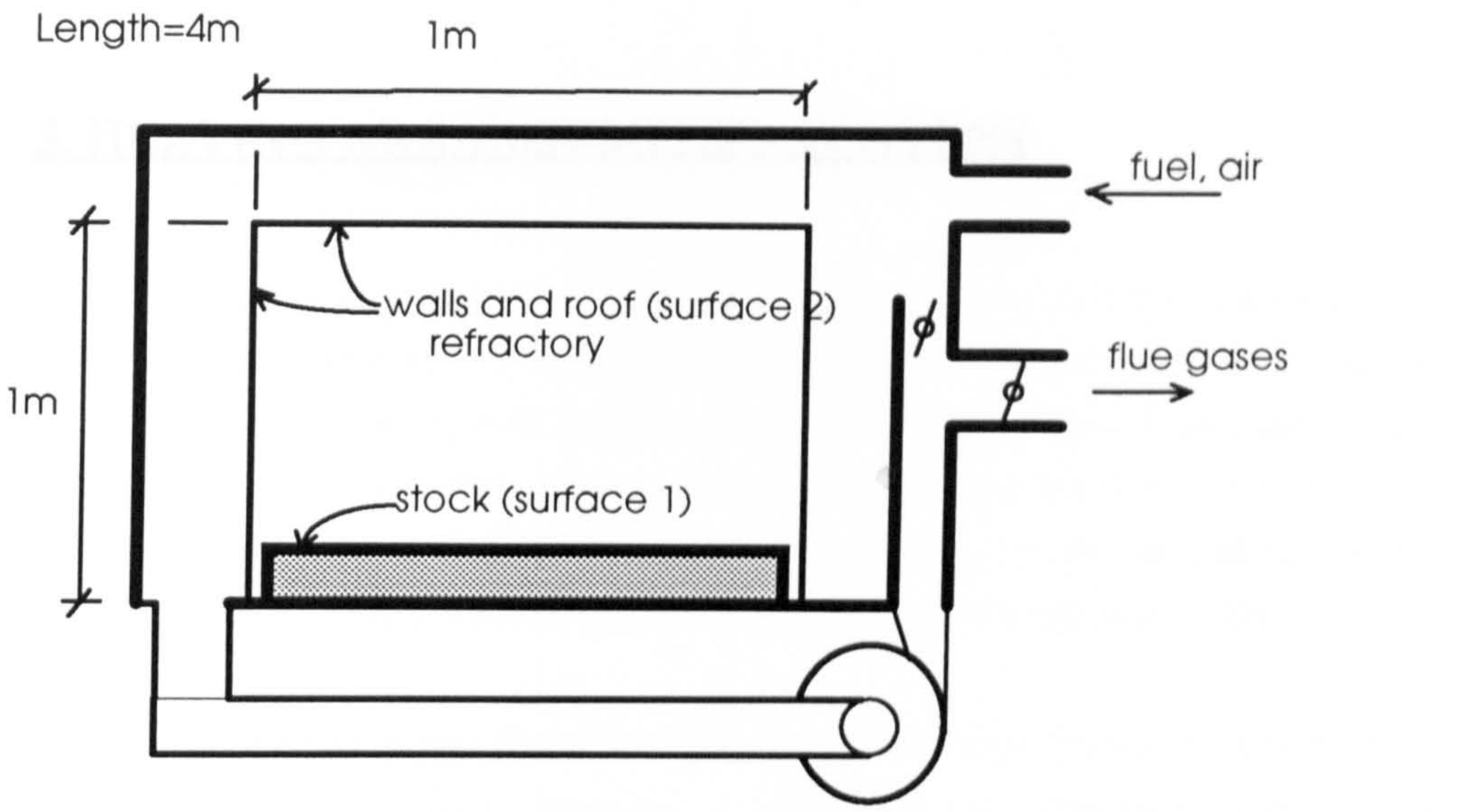

Fig. 2-10 Schematic representation of a metallurgical heat-treatment furnace (with controlled atmosphere)

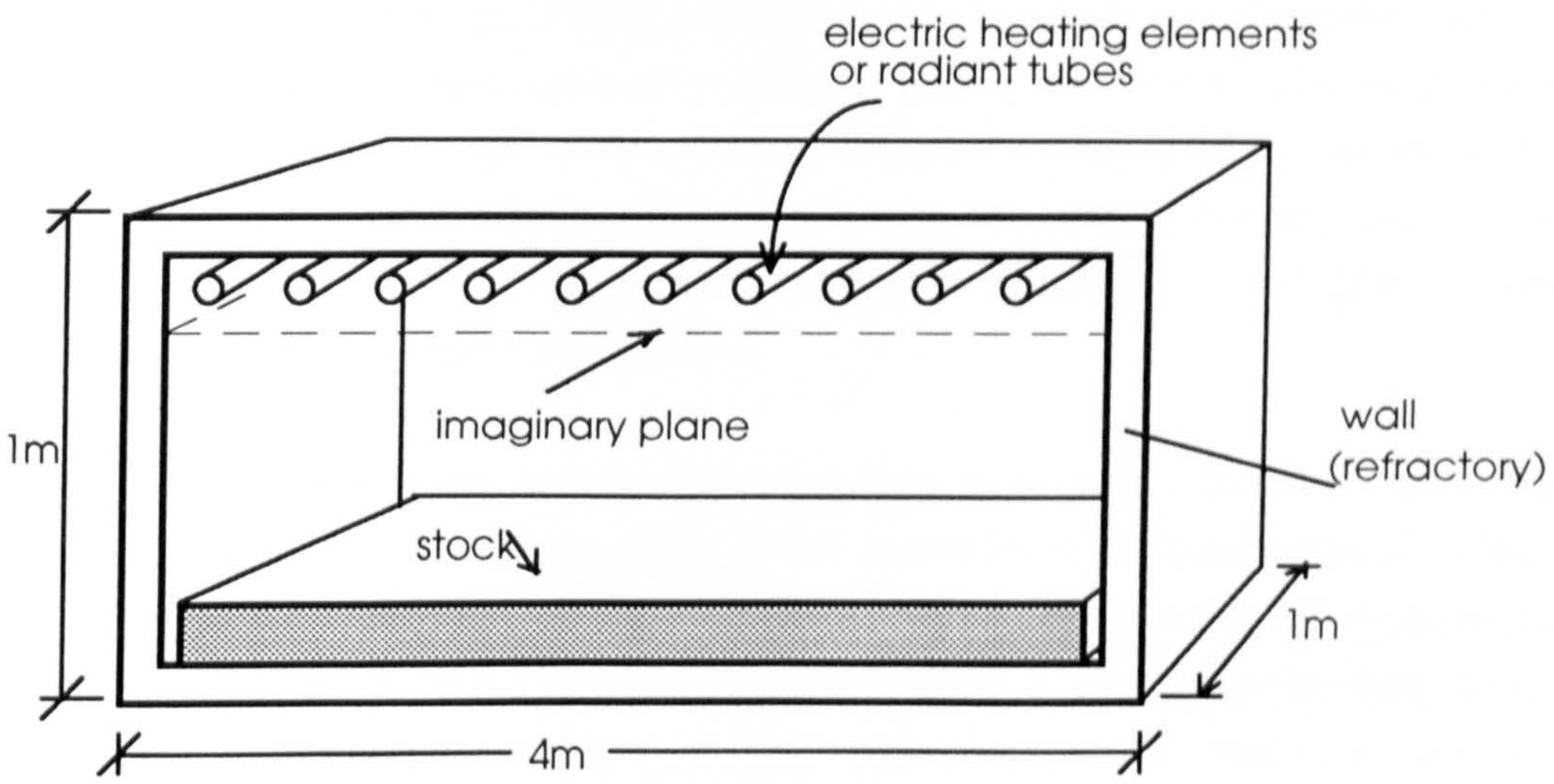

Fig. 2-11 Furnace heated by roof-mounted cylindrical heaters

3. HEATING ARRANGEMENTS IN OVENS

3.1. INTRODUCTION

From Chapter 2, it is clear that by varying the positions of heaters in an enclosure, the proportion of heat transferred by natural convection would be altered. For example the use of four horizontal cylindrical heat sources produced a Nusselt number of only 84% for the upper heaters when compared with those of the lower heaters [32], whereas when the number of tubes were considerably increased, Nu was actually reported to be marginally higher for the upper cylinders, using identical enclosures [35].

If these assertions were to be maintained at elevated temperatures, such as encountered in ovens, then it would be possible to effect heating arrangements which enhance natural convection. The enhancement may also be applicable to natural convection heating of higher viscosity fluids such as in lubricating and heavy fuel-oil storage tanks. Since a fan or pump would no longer be required, there are benefits with respect to energy usage, manufacturing and life-cycle costs. There are operational benefits as well which bear directly on comfort (noiseless operation in domestic ovens) [53], and demand side management, where only a non-inductive load need to be considered during electrical energy management and policy.

The principle behind the heating arrangements in ovens is not altogether unknown, with, for example, some convective domestic cubical ovens [50] utilising protruding heating-elements mounted (often behind a radiation vented shield or tray supports) at the lower half of the vertical walls and some with extra elements along the upper half of the vertical walls [51]. However, a comprehensive comparative analysis of various configurations has hitherto been elusive.

Many ovens and some electric furnaces have protruding, concentrated heating-elements mounted clear of the walls, rather than flush or uniformly heated walls. An earlier investigation [16] utilised a variant of such heating-elements in a rectangular-sectioned oven. It was indicated that while crown-mounted protruding heating-elements produced a stratified heating arrangement, the other accompanying configurations studied improved the proportion of natural convection.

However, because these assertions were not backed up by any quantitative analyses, the degree of improvement could not be ascertained. It was also not possible to determine the degree of stratification for the top-heated enclosure due to the lack of flow visualisation. A further survey of the literature did not unearth any prior work that undertook a comparative quantitative analysis.

To address these and earlier problems would require exploring some existing, as well as untried heating arrangements, which would necessarily culminate in quantitative and comparative analyses. This would also allow a better assessment and understanding of the practicalities or limitations of attempting to augment natural convection in ovens.

3.2. THE EXPERIMENTAL RIG

The experimental rig employed for the present investigation consisted of a steel oven enclosure, with glazed ends, an arrangement of 7.9mm diameter electric heating-elements, a water-cooled hollow inner body, a thermo-circulator to keep the temperature of the inner body uniform to within $\pm 0.1^0$C, a stabilised power supply, and the associated data acquisition equipment (see Fig. 3-1). The apparatus was developed from that used by Cheung [16]. However, as it incorporated a new and improved inner body which was designed to be operationally isothermal, thermally-insulated enclosure walls, and more comprehensive instrumentation, a brief discussion of the test rig is presented here.

3.2.1. Enclosure

The 750mm long, 350x350mm square-section enclosure, (see Fig. 3-2) was constructed from 1.2mm thick mild steel, and finished with high temperature black paint (ε=0.85). The effective working-length of the heated enclosure was assumed to be 580mm, the heater lengths.

Theoretically a two-dimensional enclosure has infinite depth and no temperature gradient in that direction, whereas radiation is inherently three-dimensional. However, 3-D effects are usually negligible, as deduced through the studies of Ozoe et al [54], provided that the third dimension is over twice the height or width [44]. For this enclosure with an inner body, the appropriate dimension to consider is the annulus, formed between the inner body and the enclosure's width. In the present study, no guard end heating compensation was employed, but the effects of the third dimension were investigated by noting the proportion of heat losses occurring via the glazed ends.

A single layer of Rockwool (k=0.06) was utilised for the insulation of the enclosure. It was applied in sections so that only the areas disturbed when the heater positions were changed would need to be replaced. Requirements for flow visualisation necessitated the use of 6mm-thick, flat, high temperature pyrex glass plates, to cover the ends. These glass end-plates were not insulated so that the flow visualisation results could be used to aid in the understanding of the steady-state thermometric results.

3.2.2. Inner Body

The rectangular-section inner body (158 x 70mm), 650mm long (see Fig.3-3), was designed to be concentric with the outer enclosure. Internally, the perforated water inlet and outlet pipes, which protruded through approximately 85% of the length of the inner body were mounted via thin internal supports. Water was led in through the lower pipe perforations, and through a baffle/deflector plate to the upper outlet pipe, and then back to the closed circuit thermo-circulator. An external means of supporting the cooling water entry and exit pipes, and hence the inner body, permitted precise adjustment of the position of the inner body inside the enclosure, in order to achieve concentricity. To prevent end losses, and to reduce any local air circulation currents occurring at the ends in the y- or z-direction, the end faces of the inner body were thermally insulated with fibrous blocks of identical cross-sectional dimensions as the inner body. These blocks virtually abutted the glass end plates.

3.2.3. Heating-elements Configurations

3.2.3.1 Heating-elements

The design of the enclosure permitted the installation and re-arrangement of the heating-elements (see Fig. 3-4) to form various heating configurations, each heater hole transversely separated by 70mm, and longitudinally, by 580mm. The 50mm "cold ends" of each heating-element were bent through 90 degrees so as to project outwards through appropriate cylindrical couplings mounted in the walls of the enclosure. Provision was made for up to five heating-elements to be mounted along each sidewall.

3.2.3.2. Basis of the heating-element configurations

From the literature survey, it was found that arranging heaters above generally produced stratified heating, heat being transferred to the inner body primarily by radiation and gaseous conduction. Arranging heaters along the sidewall, or at the base, would produce convective heating. The heater configurations investigated in the present studies utilised these basic principles, as well as mixing these to produce combined effects.

For instance, C8 was obtained from C7 by raising the lower mounted heaters from the base to the lower section of the sidewall; C7 in turn was a combination of crown- and

base-mounted heaters, as employed in multi-deck electric ovens [55] and in domestic top ovens although with the lower floor heated by flush or concealed heaters [51]. Nine experimental configurations were investigated (see Fig.3-5). Seven of these consisted of four heating-elements while the other two (C3 and C6) had only three (see Table 3.1). Due to design constraints, each heater was set at 35mm from the nearest enclosure wall, (i.e. ≈30mm peripheral distance to wall).

Table 3.1 Heating-element arrangements

Configuration	Heater arrangement	No. of heaters	Maximum Qin
C1	2 along each sidewall	4	805
C2	1 along each wall	4	805
C3	3 along the crown	3	603
C4	3 along the crown and 1 along the base	4	805
C5	1 along the crown, 3 along the base	4	805
C6	3 along the base	3	603
C7	2 along the crown, 2 along the base	4	805
C8	2 along the crown, 2 along the lower sidewall	4	805
C9	2 along the lower sidewall, 2 at the lower corners	4	805

3.2.4. Control and Instrumentation

The requirements for steady-state conditions and various power inputs necessitated the use of an automatic a.c. voltage stabiliser and an auto-transformer. A thermo-circulator closed-cycle system consisting of a chiller, heater, pump and associated water circuit was employed to regulate the inner body temperature to an initial set temperature of 50°C.

3.2.4.1. Thermometric measurements

Data-loggers were used to collect data from the various type K thermocouples which were positioned around the external body of the enclosure and in the air spaces (see Fig. 3-6). The 0.2 mm diameter thermocouples employed for measuring the air space temperatures were not shielded from direct radiation because of the anticipated complicated flow directions in the enclosure.

3.2.4.2. Interferometric measurements

Another method for obtaining the temperature distribution or heat transfer coefficients within the annulus is by interferometry. A collimated laser beam is split into two paths - the reference and the working beams - and then recombined as shown (see Fig. 3-7). This principle is utilised in the Mach-Zehnder Interferometer (MZI) [56]. If the beams intersect at an angle, or traverse unequal path lengths, there will be bright lines where the peaks of the waves reinforce and dark lines where the troughs coincide, giving a series of light and dark lines (or fringes).

If the lengths traversed in each path are equal and the beams recombine identically, they will form a uniformly lit (or dark) frame on an output screen. This is the infinite fringe mode. Adjusting to obtain the infinite fringe mode can be difficult, and an improved adjusting procedure with rapid path convergence, optimised from the existing adjusting procedure [57,58] specifically for the MZI available at Cranfield University, is included (see Appendix A).

A path length can be altered by changing the refractive index of the fluid medium. One of the factors which govern the refractive index is the temperature of the medium. If a cell at a different temperature (e.g. from ambient) is introduced into one of the paths - the working path - fringes will be produced on the output screen which can be related via the density differences and the refractive index to the temperatures within the test rig (see Appendix A).

The use of the MZI would normally possess several advantages chiefly [56]:

a) the air flow remains undisturbed because there is no introduction of thermojunction leads and

b) there are no inertial errors because of instantaneous mapping of the thermal profiles.

However, the enclosure was much larger than the ellipse (180x150mm) produced by the interferometer. This required taking multiple frames, which neutralised the latter advantage of inertial errors. The large glass end plates were also found not to be sufficiently optically flat, so that irregular fringes were introduced. Another set of glass end plates which was optically flat ($\lambda < 1/5$), but which covered only one-half of the enclosure width was utilised. Two dedicated jigs to be mounted on the enclosure ends were constructed from plywood to accommodate the smaller sets.

3.3. TEST PROCEDURES

3.3.1. Preliminary and Thermometric Tests

A preliminary test was carried out before insulating the enclosure to investigate the performance of the new inner body, the heating-elements' temperature uniformity, the outputs of the thermojunctions, and to test various heating-element configurations. Unused heating-element mounting holes were covered. The power input was temporarily varied from zero to 70% of the installed power (i.e. 1575W of the available 2250W), using C1. Subsequent operations were limited to a maximum of 60% of the installed voltage (Qin=201 W/element) to ensure that various components remained within their prescribed limits.

The enclosure was insulated on the four walls, with 50mm-thick Rockwool ($0.038<k<0.079$ $Wm^{-1}K^{-1}$, $50<T<250^0C$) and additionally wrapped with reflective aluminium foil to reduce the radiative losses. By installing thermocouples between the foil and the insulant, the ambient convective flow could also be ignored when the heat losses through the insulation were analysed. The glass end plates remained uninsulated.

3.3.2. Flow Visualisation

A light projector was centrally positioned 2.5m from one end of the rig, while a Praktica LTL3 35mm camera was placed at the opposite end, in the shadow cast by the inner body, to eliminate glare. A tube was passed through one of the unused heating-element mounting holes and manipulated so that smoke could be guided to enter at the centre of the lower region of the enclosure. The outer end was connected, via a suitable flexible hose to the smoke tube and bellows.

For each configuration, two smoke visualisation tests were carried out at the power inputs of 200W and 800W (150W and 600W for 3 element configurations). Between each injection of smoke, the glass end plates were removed and cleared of any adhering smoke particles in order to ensure continued photographic transparency. The enclosure cavity walls and the inner body were also thoroughly cleaned regularly in order to retain the existing surface emissivities. Subsequent recovery to steady-state conditions took up to 12 minutes. The smoke patterns were then recorded.

3.3.3. Interferometric Tests

The enclosure rig was located on a milling machine so that for the interferometric tests, the rig could be accurately traversed across the working beam, both horizontally and vertically. The glass end plates were first removed, the holders disassembled, and replaced by the smaller, optically-flat plates, located in the wooden jigs. This process was only necessary once as only the convective configurations subsequently recommended were required for these tests. Therefore, the main high temperature tests were completed before commencing on the interferometric tests. The temperature difference to which the smaller, optically-flat plates were subjected was kept below 70^0C.

The possible enclosure (half) aperture was 185mm wide and 350mm high. The ellipse obtained from the parallelogram arrangement of the MZI was 180mm high by 150mm wide. Therefore, six photographic frames were required to thermally map the symmetric vertical half of the enclosure because of the enclosure angular corners. The elapsed time between each re-positioning of the rig and taking photographs was very large (approximately 50s). However, the validity of the interferograms were not unduly affected because no quantitative analyses were utilised from the tests.

3.4. DATA REDUCTION AND CALCULATIONS

In order to estimate the total rate of heat transfer, it is customary to calculate the rate of heat transfer separately for each mode. The total heat flux to the inner body can be written as:

$$q = q_{conv} + q_{cond} + q_{rad}$$

$$= h(T_2-T_1) + \frac{k}{t}(T_2-T_1) + \varepsilon\sigma(T_2^4- T_1^4) \qquad (3\text{-}1)$$

In the case of higher temperature enclosures, ovens and furnaces in particular, it is also useful to compare the proportion of heat transfer for each mode, and the proportion intercepted by the different surfaces of the inner body, for design analysis and onward operational modifications.

3.4.1. Radiation Heat Transfers

In an enclosure, heat transfer by radiation involves successive reflections and absorptions by the surfaces of the inner body and enclosure. These consist of the incident flux, that portion of it which is reflected, that which is transmitted, and the flux which is emitted by virtue of the surface's temperature. For most engineering materials, the transmissivity is negligible except when the end plates are of glass, as in this instance. An allowance was made for the heat losses through the glass end plates due to the transmissivity of pyrex (borosilicate glass). The enclosure surface was painted black (ε=0.85) so that, in conjunction with the emissivity of the inner body (ε=0.7), re-radiation (which in the extreme would be proportional to an effective emissivity of 0.3x0.15=0.045) was assumed to be negligible.

The radiation view factor [6] given by the equation

$$F_{1\text{-}2} = (1/\pi A_1) \int_{A1}\int_{A2}(\cos\beta_1\cos\beta_2 dA_1 dA_2)/s^2 \qquad (3\text{-}2)$$

represents the fraction of radiation emitted by the surface A_1 which is intercepted by another surface A_2 which see each other. This is purely a function of the surface geometries. The net heat arriving at the inner body is then:

$$Q_{1\text{-}2} = \sigma\varepsilon_1 F_{1\text{-}2} A_1 (T_1^4- T_2^4) \qquad (3\text{-}3)$$

This enables the heat flux intercepted by each of the four surfaces of the inner body to be determined. From equation 3-3, only $\varepsilon_{12}Q_{1\text{-}2}$ was absorbed by the inner body. However, in order to calculate the radiative heat transfers, it is necessary to determine the view factors.

Integrating equation (3-2) can be tedious, or even impossible, except for simple geometries. One of the pioneering simple techniques for obtaining view factors, derived and developed by Hottel [6] for two-dimensional, parallel, infinitely long systems is the "Crossed-String" method. This method is also applicable to non-infinitely long radiating areas if:

a) the lengths of the exchange areas are much greater than both their cross-sections and the separation between the surfaces, and
b) the cross-sections do not change along their respective lengths.

For example, the direct-exchange area per unit length between the two surfaces 1 and 2 (see Fig. 3-8a) is obtained from a product of the view factor and the emitting area as:

$$A_1F_{1\text{-}2} = 0.5x\{\Sigma(\text{crossed strings})-\Sigma(\text{uncrossed strings})\}$$
$$= 0.5x\{(AD+BC)-(AC+BD)\}$$

Greater accuracy and simplification is obtainable for non-equal areas by taking the smaller area as surface 1. As the width of surface 1 tends to zero, the crossed strings method then reduces to:

$$F_{1\text{-}2} = 0.5(\sin\alpha_2+\sin\alpha_1), \text{ for Fig. 3-8b} \qquad (3\text{-}4)$$
$$F_{1\text{-}2} = 0.5(\sin\alpha_2-\sin\alpha_1), \text{ for Fig. 3-8c} \qquad (3\text{-}5)$$

where α is the angle between the normal to the centre-line of surface 1 and the lines connecting the centre of surface 1 to the edges of surface 2. From Fig. 3-9, using eqn(3-4), the view factor from the central heating-element of C3 to the upper inner body was found to be 0.55.

Some view factors already exist in the open literature [6],[59] in graphical or tabulated format, from which certain related geometries can be deduced by view factor algebra. By making suitable approximations, other view factors such as from the cylindrical heating-elements to the planar inner body can be obtained. However, the use of some of the documented view factor formulae resulted in serious errors particularly those

involving non-planar surfaces (see Appendix B). The view factors employed were therefore calculated using the crossed strings method. The method used to obtain the view factors, together with the tables are presented in Appendix B. The view factors were checked and modified by the area integral method, subsequently developed (see Appendix F).

With the aid of an emissometer, an average emissivity value for the inner body was measured as 0.70.

3.4.2. Natural convection heat transfer

One of the most intractable problems in convective heat transfer analyses is the choice of a characteristic length. Several experimental investigations have employed inner bodies which were warmer than their respective enclosures, so that the selection of the characteristic length was based on a variation of that as proposed by either King[60], McAdams[61], or Sparrow and Stretton[62], essentially based upon the heat leaving the hot wall. In this instance, however, the hot walls were not isothermal, and, together with the heating-elements, form a multiple heat input system. Another serious problem which is encountered when heaters are in close proximity to a wall, is how to separately determine the contribution of either the heaters or the walls to the generation of buoyancy forces. In order to circumvent this, all the analyses were based upon the heat flux arriving at the uniform-flux, cold (inner body) surface. Consequently, the characteristic length utilised was the sectional perimeter of the inner body (L=0.46).

For an ideal gas the volumetric coefficient of thermal expansion, β, can be calculated from $\beta=1/T$, where T is the local temperature. The enclosed air was treated as an ideal gas, with the air temperature T_m, as the average of the cold wall (inner body temperature) and the mean hot wall temperature. T_m was approximated by evaluating the arithmetic mean of the temperature of the heaters and the mean temperature of the enclosure, and the temperature of the inner body, i.e.

$$T_m = 0.5\left[0.5\left(\frac{1}{4}\sum_{HTR=1}^{HTR=4} T_{heaters} + \frac{1}{Z}\sum_{1}^{Z} T_{enclosure}\right) + T_{innerbody}\right] \qquad (3\text{-}8)$$

Other air properties were also evaluated at this mean value and the properties obtained from standard thermodynamic tables [63].

It must be borne in mind that the Boussinesq approximation, employed in estimating the value of Ra, is only valid at very low temperature differences, such that $\beta\Delta T<<1.0$, (i.e. $\beta\Delta T<0.1$) [64]. For instance, the temperature difference for C3 when the power supply was only 151W (3450Wm^{-2}), was 75K, (250K at 604W); β (~1/323) was 0.003096; thus $\beta\Delta T=0.232$. Even, when the average, absolute, hot wall temperature (T_H=403K) was used, $\beta\Delta T=0.186$ ($\beta\Delta T=0.436$ at 604W) still clearly too high, but the use of T_H in preference to the cold wall temperature gave an average numerical value much closer to the approximation across the power input range. This implies that the limiting criteria was relaxed to $\beta\Delta T<0.45$ in the present study. The effect of exceeding the strict limit would be that the calculated flow rates for the buoyancy field (Ra) would be progressively lowered as the temperature differences increase [65].

However, the correlations have been given, where feasible, as trends between the convection and heat input.

The total heat input was dissipated by heat transfers through the enclosure insulation and heat input to the inner body, and is written as follows in self-explanatory subscripts:

$$Q_{input} = Q_{inner\ body} + Q_{enclosure\ loss} \quad (3\text{-}9)$$

$$Q_{enclosure\ loss} = Q_{walls} + Q_{glass} \quad (3\text{-}10)$$

$$Q_{walls} = 4*(k/t_{insulation})*A*(\Delta T_{insulation}) + \{hA(T_{wall}-T_{ambient})\} \quad (3\text{-}11)$$

$$Q_{glass} = \frac{k}{t}A(\Delta T_{glass}) + \{hA(T_{glass}-T_{ambient}) + \varepsilon\sigma A(T^4_{glass}-T^4_{ambient})\} + \tau(F_{12}\sigma\varepsilon A(T^4_{enclosure}-T^4_{ambient})) \quad (3\text{-}12)$$

The first two terms of (3-12) have a common Q, so that if two temperatures within any of the terms could be measured, then only that term need be calculated. Within the experimental work, when the attachment of the thermojunctions to the inside surface of the glass end windows was of questionable integrity, the second {convection/emissivity} term was utilised.

The emissivity of the pyrex glass varied between 0.64 and 0.95 across the temperature range 300<T<500K, and the value of h (infinite atmosphere) was obtained from

standard flat plate correlations [11]. As the inner body was extended to abut the glass end plates, a distinct temperature gradient was created between the upper and lower walls for all the configurations except C5, C6, and C9. Therefore, it was necessary to zone the heat loss from the end plates.

The heat absorbed by the inner body was evaluated from

$$Q_{\text{inner body}} = Q_{\text{rad}} + Q_{\text{conv}} \; (+ Q_{\text{conduction,C3(upper space)}}) \qquad (3\text{-}13)$$

Q_{conv} was then obtained by subtraction:

$$Q_{\text{conv}} = Q_{\text{in}} - Q_{\text{enclosure}} - Q_{\text{rad}} \; \{- (Q_{\text{conduction,C3}})\} \qquad (3\text{-}14)$$

It is later shown (3.6.1) that C3 is a special case where all the three modes of heat transfers were distinctly present simultaneously, convective flow at the base being separated from the stratified gaseous conduction at the upper cavity, in addition to the calculated radiative heat transfers. Qconv for equation 3-14 would then represent the value at the lower space. Therefore, for C3 only, $Q_{\text{conduction}}$ was calculated by assuming gaseous conduction across the upper cavity. This varied between 1.5% and 6% because of the increase in thermal conductivity of air with temperature. The rate at which heat was absorbed by the inner body was finally checked against the heat gained by the circulating water, i.e.,

$$Q_{\text{inner body}} = \dot{m} c_p \Delta T \qquad (3\text{-}15)$$

However, this was applicable only at the highest power input, because the temperature difference was too small at the lower power inputs for the required thermometric sensitivity and accuracy to be achievable.

3.5. RESULTS

Nine experimental configurations (see Fig.3-5) were investigated, seven consisting of four electrical heating-elements, and the other two only three. Total power inputs were varied from 201W to 805W (151 to 604W for the 3-element configurations). At 805W the temperature of the thermocirculator approached its design limit, but this was at the required oven temperatures. 140 temperature data-points were recorded for each configuration. For configurations 1 to 7, more data were acquired at discrete, intermediate power inputs, and this permitted more flexible correlations to be deduced. Measurements of the air temperatures inside the enclosure were carried out for both horizontal and vertical profiles, at the mid-section of the enclosure where any 3-D effects would be at a minimum. Some of the configurations previously studied were compared with that obtained by Cheung [16], in order to ascertain the usefulness of the new, isothermal inner body.

3.5.1. Temperature Profile of the Inner Body

The thermocouples used for measuring the surface temperatures of the inner body were each shielded from direct radiation by contact aluminium tape. These were positioned centrally along the length, (z-plane) of the inner body, on each of its four walls.

Recorded temperature variations along the length of the inner body were small (the inner body was almost isothermal). Although it was still possible to discern subtle differences in the response of the inner body to radical changes in the configuration of the heating-elements (see Fig. 3-10), the inner body was an obvious improvement on the previous one [16], the largest difference between the lowest and highest temperatures along the length of the inner body sidewall being less than 5^0C as against 93^0C. The higher temperatures were recorded at the extreme ends. Therefore, it was concluded that some partial flow stagnation occurred at the ends of the inner body where it was impractical to position any holes for improved water circulation.

Along the top and bottom surfaces, C1, C2 and C5 had the highest variation on the upper surface but C1 and C2 had the least along the base, being virtually flat (see Fig. 3-10b,c). It is to be recalled that fluid was fed into, and out of the inner body along its entire length via drilled holes on the inlet and outlet pipes respectively (see Fig. 3-3). This led to the conclusion that the apparently haphazard nature of the upper and base

surface profiles, as graphically depicted was a reflection of the proximity of the flow sources and sinks within the inner body chamber. However, the temperature variations along the top and bottom surfaces were generally within $\pm 2.5^0$C.

3.5.2. Vertical air space temperature profiles (y-axis)

The vertical air space temperature profiles for all the configurations at 805W (600W for the 3 element configurations) are shown in Fig. 3-11a.

The widest temperature difference between the top and bottom air spaces was obtained from C3 (configuration 3 with only 3 elements). As expected, stratified conditions were deduced with the lighter, hotter air remaining at the top, and air motion within the enclosure at a virtual standstill. Thus, heat was transferred by radiation and gaseous conduction through the air layers. The addition of a fourth heating-element at the base, C4 induced buoyancy-driven convective flows because this provided a less steep vertical temperature gradient in the lower half of the enclosure (see Fig. 3-11a). Although the maximum temperature was only marginally higher, the lower half also attained much higher temperatures than for C3.

The respective reverse configurations to C3 and C4, that of C6 and C5, with concentrated heat sources at the base clearly achieved more uniform vertical air temperatures throughout the enclosure (see Fig. 3-11a). The air was not stratified and the air temperature towards the base of the enclosure was slightly higher than that recorded in the uppermost region for both of these configurations. C5 achieved the most evenly distributed, air temperature profile. Also the temperature difference between C6 and C5 was consistently maintained from the base to the crown, because the effect of the additional heating-element at the top was to raise the mean temperature of C5.

The trends of C3,C4,C5,and C6 have been combined and shown separately (see Fig.3-11b) from that of C1,C2,C7, and C8, (Fig.3-11c) for greater clarity.

C9 was the only configuration other than C5 and C6, which achieved a near-uniform vertical air temperature profile (see Fig. 3-11c). C8 and C7 produced nearly identical vertical air temperature profiles except at the base where C8 was less effective in increasing the base air temperatures. The rise in the air temperature with elevation achieved by C1 was almost linear, a form of compromise between C5 and C4 (see Fig.

3-11a). C2 produced similar temperatures to C1 despite the temperature drop which occurred 140mm from the base (see Fig. 3-11c). This drop in temperature at this section for C2 occurred throughout the entire power range. Because this section of the experimental work was repeated with identical results, it was concluded that cool air flows descending via the inner body were somehow responsible for this drastic deviation from normal expectation.

3.5.3. Horizontal air space temperature profiles (x-axis)

3.5.3.1. Upper Region

The relatively higher temperatures exhibited near the walls by C1 can be attributed to the vertically rising hotter air having passed in series through two heating-elements vertically positioned one above the other. A dip in the horizontal temperature profile in the central section occurred with C1, in contrast to the high temperatures towards the sides of the enclosure (see Figs.3-12a-c). The general increases towards the central position exhibited by C2 and C5, conform to expectations due to the centrally positioned heating-elements on the crown, producing high, local radiative flux. A slight temperature profile reduction at the sidewalls was produced by C3,C4,C5 and C8. The pronounced dip in the profile of C9 could be attributed to the descending air flows which have passed via the inner body.

3.5.3.2. Lower Region

As might be expected the results of C3 and C6 were interchanged, when compared with the upper space temperatures, with C6 producing the higher, and C3 the lower temperature profiles (see Figs.3-13a-c). In fact, the inner body was at about the same temperature as the air temperature in the lower air space for C3 when the power input was low (<400W), suggesting that there would be no localised convection. The highest (peak) temperature profile was produced by C9 near the walls, as a result of the closely-spaced, vertically-positioned heating-elements at this zone; the lower heating-elements were also located very close to the base (30mm) and thus the nearest thermocouples adjacent to each lower vertical wall were exposed to the combined, relatively high radiative fluxes.

The profiles of C1 and C8 were similar but their mean temperatures in this zone were rather low, as a result of the lower heating-elements being far from the centre. The

profile of C2 and C4 reflected the presence of the single element at the base. Along with C3, C6 had three heating-elements concentrated on one horizontal wall, but unlike C3, C6 did not produce a stratified profile because of the inherent instability due to the density gradient inducing buoyancy flow. The effect of the single extra element in C5, was to raise the overall temperature profile in accordance with increases in power output.

3.5.4. Flow Visualisation

The main air-flow patterns were similar to intuitive expectations. Generally the flows, like the heating-element configurations, were symmetrical about the central vertical axis in the x-y plane (see Figs. 3-14a-i). When heating-elements were present along the side walls(C1,C2,C8,C9) or base (C5,C6), there was a general tendency towards vigorous convective flows. The flows induced by the heating-elements appear to be dominant as they foreshadowed those which must have been induced by the hot enclosure walls. Rapid smoke dispersion necessitated a schematic recording and presentation of the results of the flow visualisation. This is comparatively depicted by the photographs of C3, C4 and C9 (see Fig. 3-15a-f) where the sharpness in the smoke streak lines of the stratified configurations of C3 and C4, were subdued in that of the convective C9.

The most buoyant flows were obtained from C5, C6, and C9 where the lower region was warmer than the upper zone. For C6, the rising air currents moved upwards on both sides of the inner body and, upon reaching the crown of the enclosure immediately descended symmetrically, apparently without touching at the upper centre-line (see Fig.3-14f). The general pattern at the lower space was duplicated somewhat by C5 (with a fourth element centrally positioned at the top space), but the effects of the fourth heating-element at the crown were to draw the flows closer to the centre-line, and also to split them, creating secondary, horizontally-elongated closed-loop cells along the crown (see Fig. 3-14e).

Because C5 air flows seem to be more tightly wrapped around the inner body than those of C6, a more active convective heat transfer was assumed. The air flows appeared to follow the inner body angular shape, descending without any separation from contact with the inner body; but these suggest much lower velocities than C6. It was also assumed initially that C5 would produce a more uniformly heated load. However, a high proportion of the convective heat would have been dissipated by the

slower flows around the mid-section of the inner body top surface, so that, in conjunction with the high radiative flux at the same central position, it is then seen here that the top surface of the inner body may be subjected to a higher degree of non-uniform heat flux. Therefore, the disadvantages of the centrally-positioned heating-element were that:

(a) there was a concentration of irradiance from both the heater and the backwall on the central portion of the inner body upper surface;
(b) the air flow rate was lower because the buoyancy forces generated by the lower heaters appear to be opposed by those of the upper heater, and
(c) thermal energy was expended to create the recirculations at the crown.

For the case of C7, in addition to vertical symmetry, each of the four enclosure quadrants had distinct vortices (see Fig. 3-14g), but they were more pronounced for the upper corners. Each upper corner had two cells, the lower of the two forming a completely closed cell. It is often assumed that the presence of cells and eddies promote good convective heat transfers. However, it was observed that the upper cells prevented the rising main stream from direct contact with the upper heating-elements before descending towards the inner body. Consequently, the presence of the upper angular corners at the top, which promoted the hot recirculating cells, would reduce the convective component of the heat transfers. Convective flow was also observed to be generally slower at the upper space of the inner body.

Another phenomenon noticed was the influence of the unsteady, oscillating cells (01 and 02 in Fig. 3-14g) just above the inner body edges, on the flow across the upper surface of the inner body (03 and 04). The main stream flows were observed to rise and fall in sympathy with the oscillating cells, thus periodically creating rarefied pockets at the upper surface edges. Therefore, it can be inferred that improved temperature uniformity of the upper surface of the inner body would be more difficult to achieve. This is further discussed (see 3.8.1).

The vertical distance between C9's heaters was the shortest (70mm), so the lower heater plume impinged directly on the upper heater surfaces with virtually little entrainment of the surrounding cooler air, and consequently a higher upper heater temperature. It was therefore expected that this configuration should produce the hottest mean air temperatures in the cavity. But as can be seen from the vertical air

space temperature profile (see Fig. 3-11a), the increase over C7 air temperature was only marginal. However, C9 still produced a visually more convective flow than C7.

C1 had its upper and lower zones well mixed with only a faint trace of eddies at the top corners, but there were several rotating cells between the inner body and the enclosure sidewalls. The cells below and above the inner body were very unstable and oscillated virtually at all power inputs, as shown (Fig.3-14a). The traditional assumption that eddies and vortices promote good convective heat transfers is probably justified for the middle vortices because they are located between streams of high temperature differences. However, the flows at the lower enclosure's quadrants were weak and poorly directed.

In the case of C8 (see Fig.3-14h), a relatively large space below the inner body had very weak, or no convective flow patterns indicating poor convective heat transfers within this zone. The lower angular corners are again seen here as redundant, rounding off being justifiable. However, when compared with C7, the elevated lower heating-element was seen to promote a more active convective flow, not only at the sides, but also at the upper zone.

The flow patterns of C2 (see Fig.3-14b) also indicated active convection to the top and base of the inner body. However, there was a distinct absence of air flows at the sides of the inner body. This indicated that heat was being transferred mainly by radiation, and suggests that the inner body side walls were exposed to concentrated radiative fluxes from the heating-elements, without the possible smoothening effect of convective flows. With the benefit of this flow visualisation, it is now possible to understand why the air temperature in the vertical direction, about 140mm from the base (see Fig.3-14c), was colder than the air temperature at the base. The air flowing downwards through this section had just passed over the upper surface of the cooler inner body. The interaction between this and the air ascending towards the central heating-element was seen to be responsible for the oscillating cell just below the heating-element.

Although there appeared to be no vortices at the top corners, there was a relatively large cell positioned about half-way between the top corners of the inner body and the top corners of the enclosure. The effect of wall-enclosure-heater interactions are clearly demonstrated here for the heating-element along the vertical walls. Instead of

the plumes rising straight upwards, they were deflected away from the vertical walls by the vortices at the corners.

This latter pattern also applied to C8 and in the region of the lower heating-element in C1. From this it may be appreciated that the recirculating air cells located at the top corners of the enclosure were clearly deflecting the adjacent rising stream towards the inner body. On the other hand, the rising air flows emanating from the upper heating-elements of C9 were not as forcefully deflected, partly because:

(i) there were no eddies or recirculating flows in-between the heating-elements, and,
(ii) the velocity of the rising plume was relatively high so that the recirculation at the top corner was not sufficiently effective in initiating a pronounced deflection.

Overall, C9 achieved a uniform, relatively vigorous convective flow distribution in both the upper and lower spaces.

This phenomenon of deflected plumes cannot be encountered in external natural convection studies because the upper horizontal wall is seen to be responsible for creating the recirculation at the upper quadrants, which deflect the main flow away from the vertical towards the interior of the enclosure. For three of these configurations (C1, C2, and C8), the deflected air flows demonstrate the additional complications encountered in the analyses of flows and heat transfers of rectangular enclosures with protruding heaters.

The flow visualisation photographs of C3 (see Fig.3-15a-b) show the effect of stratification. The test was conducted with C4's base-mounted heater in place, but switched off, and it can be seen that when suitably shielded, the base heater would not contribute to natural convection, because the heater, shielded from direct radiation by the inner body, remained at the surrounding low air temperatures.

When smoke was introduced, there was, initially, a rapid, thin layer, flowing along the enclosure vertical walls which quickly subsided into a stable stationary boundary layer. Then the thin boundary layer slowly expanded at the upper air space, and drifted inwards towards the centre-line of the enclosure in two distinct layers; there were two horizontal layers in this upper space, one along the upper edge of the inner body and the other just below the crown-mounted heating-elements (see Fig.3-15b). The drift, horizontal and normal from each vertical wall towards the central portion occurred

very slowly, (3 minutes to travel a distance of approximately 110mm or about 0.6mm/s), and then remained virtually stationary for over 20 minutes, never quite reaching the centre-line.

This indicated highly stratified, stable conditions, with very low rates of convective heat transfer. The two spaces between the three heaters and the upper wall contained two weak stationary cells, an indication that a limited air flow existed, and was probably responsible for giving an initial impetus to the introduced smoke which clearly depicted the stratified layers. Other factors which contributed to the smoke flow were the differential temperature and density differences between the hot air and the introduced cooler smoke.

These stratified patterns therefore indicate that heat transfer was by radiation and gaseous conduction from the heating-elements to the inner body and the upper enclosure side walls, and that convective heat transfer was principally restricted to the enclosure lower space. Here, two counter-rotating cells were weakly distinguishable. As the power was increased the motion of cell rotation which was barely perceptible ceased and the direction of flow reversed. The lower air space of C3 could be considered as an empty enclosed space with the inner body at a lower temperature forming the upper horizontal wall. The rate of air flow remained particularly low as the temperature difference between the enclosure base and the corresponding vertical walls ($\approx 80^0$C) and the inner body base (50^0C) was not particularly significant and this explains the limited convective flows attained at the base.

When compared with C3, the fourth single element which was mounted at the base to create C4 (see Fig.3-9d), served to increase the rate of air flow at the base, as well as to promote some limited recirculatory flow in the middle air space between the inner body sidewall and the enclosure sidewall. This is clearly depicted in the smoke visualisation photographs (see Fig. 3-15c,d).

While there was an obvious improvement in natural convection relative to C3, completely stratified patterns were still observed in the upper zone, similar to C3. The photographs of the flow visualisation for C9 is shown in Fig. 3-15(e-f). It can be seen that rapid smoke dispersion, coupled with visual perspective (3-D) distortion attenuated the smoke streak lines; hence the schematic presentation of the flow visualisation in Fig. 3-14(a-i).

3.5.5. Surface Temperatures of the Enclosure

Monitoring of the enclosure's surface temperatures enabled wall temperature distributions to be determined. These varied according to the heating configuration and the proximity of the heating-elements to the walls. The contribution of each of the enclosure's walls to the generation of buoyancy forces could be examined. For these reasons, and for the contribution to radiative heat exchange, the wall temperature profiles are of particular interest in thermal design.

The thermocouples were positioned both on the inside surfaces and also on the outer surfaces between the thin enclosure's wall and the insulant. The outputs of the outer thermocouples were only 0.6^0C or so lower than those of the corresponding inner ones, but because there were no spurious readings from the outer ones, their outputs were utilised.

3.5.5.1. Vertical Sidewalls, (y-axis)

The sidewall temperatures reflected the trend in the air temperatures, being generally warmer at the upper zone (Fig.3-16a). This temperature profile was true for all configurations except C5 and C6 where the base was slightly warmer than the top. The sidewall temperature of C3 showed the widest difference between the base and the top.

3.5.5.2. Base (x-axis)

C5, C2, and C6 produced the highest temperatures while, as expected, C3 with no lower elements produced the lowest. Also for C3, the temperature at the centre of the base was lower than at the corners adjacent to the vertical walls (see Fig.3-16b), because the central section was shielded from the heating-elements by the inner body.

3.5.5.3. Crown (x-axis)

With the exceptions of C1 and C6, the central section of the enclosure's crown recorded the highest temperatures, but reduced towards the sidewalls (see Fig.3-16c). Although, in general, the crown temperature profiles indicated a very wide temperature variation between the central portion and the ends, the profile for C6 was virtually flat. Therefore, uniform emission of radiative heat transfers could be assumed.

For C7, the temperatures of the crown adjacent to the vertical wall recorded average temperatures of 160^0C whereas the vertical air temperature, (see Fig.3-11c) was about 200^0C so the top elongated cell and the associated lower cell were transferring heat by convection from the top heating-element mostly to the crown, and not to the main stream convective flows, which remained at about 165^0C (see Fig.3-12c). This confirms that eddies, cells, and vortices located at enclosure corners contribute little to the enhancement of convective heat transfers, and this justifies the rounding-off of the right-angled corners of ovens.

3.5.5.4. Surface temperatures in the z-direction

Along the length in the z-direction, (see Figs 3-17a-c), the temperatures were significantly lower at the ends than in the central section, more so for the base (see Fig. 3-17b). A longer rig, and double-glazed (as used for inspection doors in ovens), or insulated end-plates are desirable, if the effects of the 3-D convection effects around the glazed ends were to be suppressed. However the flat profile in the central portion of the enclosure roof (see Fig. 3-17c) demonstrates the usefulness of the aforementioned data for the purpose of 2-D analyses.

3.6. HEATING CONFIGURATION ANALYSES

The foregoing analyses have served the preliminary purpose of classifying the various configurations into stratified or convective, as well as to providing a general insight into the complex convective activities within the enclosure. However, the degree of convective heat transfers could only be surmised from these analyses. By reducing the data into convective and radiative heat ratios, it would be possible to compare them with each other and to the heat input. The reliability of the regression was generally higher for the correlations involving Q than those involving Nu and Ra, as discussed in section 3.2, and, to reduce repetitive analyses, are tabulated in Table 3.2.

For the order of presentation, the stratified configuration C3 is first analysed, which is then followed by C4 in order to provide a coherent background for analysing the other configurations concisely.

3.6.1 Configuration 3

Although the primary source of heat was directly supplied by the three heating-elements, the inner body consistently received more radiative flux from the crown (heater backwall) than from the heaters (see Fig. 3-18a). Direct radiation from the heating-elements was less than 35% of the total absorbed radiation by the inner body throughout the power input range (see Fig. 3-18a). Conversely, the backwall and the upper sidewalls provided over 50%, effectively the largest steady-state source of heat, due to their large radiating areas. This agrees with the findings [14] where wall emission became the largest source of heat flux at the inner body. A power ratio of 0.30 to 0.70 (heating-elements:total radiation) was fairly constant throughout the power input range.

It was noticed from the flow visualisation that limited convection occurred at the lower space. At the low power input, the inner body temperature was higher than the enclosure base temperature; thus accounting for the negative heat transfer to the inner body (Qbase/Qin in Fig. 3-18b). The proportion of heat absorbed by the inner body surfaces to the total heat supplied also showed that most of the heat was to the upper surface. Also as the power input increased, the ratio absorbed by the inner body upper surface to that of the lower surface (see Fig. 3-18c) decreased, against expectations, from about 8:1 at 200W to about 4:1 at 600W. This occurred because the rate of

increase of the upper region heat transfers was lower than the rate of increase of the combined convective and radiative heat transfers at the lower region.

With the aforementioned data, it can be confidently surmised from this steady-state trend that, for grill type ovens which somewhat approximate to this configuration, the ratio of heat input to the top surface compared to the bottom of an inner body would be exceptionally high if there were no pre-heating, especially for low thermal conductivity, thick, or frozen products.

C3 is also a typical furnace heating arrangement, though commonly without the benefit of a lower space convective heating, except when the load is skid-supported instead of resting on a hearth. While this heating arrangement may be suitable for metallic loads of high thermal conductivity, it may however prove unsatisfactory for ceramics or plastics because of the highly disproportionate imbalance between the heat received by the upper surface of a relatively low conductivity inner body to that of the lower surface. The temperature rise at the base of the enclosure was certainly the result of re-radiation by the enclosure and subsequent conductive heat transfers by the high conductivity enclosure walls. Therefore a configuration which generates a higher degree of convective flow would be necessary for low conductivity products. It was observed however, that the intensity of direct radiation was attenuated due to conduction along the crown and the side walls to the base.

As the power input increased, Ra (L=0.46 for the total enclosure and inner body) decreased (see Fig. 18d). The value of Ra obtained by considering the limited convection at the lower space (L=0.16 i.e. the width of the inner body base) increased slightly with increased power input (see Fig. 3-18f). It is to be noted that the maximum temperatures obtained at this zone was less than 100°C.

3.6.2. Configuration 4

The fourth element which was mounted at the base to transform C3 to C4 was earlier seen from the flow visualisation tests to improve the convective activity, although it was limited to the lower and middle spaces. Nevertheless, the value for Ra was large (see Fig. 3-19a-c), because the whole cavity was considered in obtaining the characteristic length, and not the lower and middle sections of the annulus to which convection was restricted. It was also observed as expected, that the proportion of the

heat losses via the insulation to power input, decreased as the power input increased, so the enclosure steady-state efficiency was consequently seen to rise.

3.6.3. Configuration 6

This configuration had three base-mounted heating-elements and was earlier observed from the flow visualisation tests to be highly convective (see Fig. 3-14f). The temperature of the central heating-element was slightly higher than the average. This was attributed to radiative exchange with the other two outboard heaters as well as reduced air inflow, due to demand by the outboard heaters. As the input power was increased, however, the ratio of convective to radiative heat transfer decreased (see Fig. 3-20(a-b)) until the heat transfer by radiation became dominant. This point was reached rather earlier during the process of increasing the power input than anticipated. The ratios of the radiative and convective heat transfers to that of the power input are compared in Fig. 3-20b, and it is clear that at this power, (300W), the proportion of heat transfer by radiation became dominant. In the investigated range, Nu increased with Ra (see Fig.3-20c), but Ra and Nu decreased as the power input was increased. The high exponent (see Table 3.2) indicated a drastic reduction in the value of Ra.

3.6.4. Configuration 5

The presence of an extra heating-element mounted at the crown to transform C6 to C5 served to raise the overall temperature of the system, and inevitably the radiative component of the heat transfers as well. Beyond the power input of 300W the radiative heat transfers began to dominate (see Fig. 3-21(a-d)). Using power ratios Qconv/Qrad, radiation started to be dominant at 0.34 for the 3-element C6 and at a comparable 0.354 for C5. The convection heat ratio profile was flat even though the power input steadily increased. Similar correlations to that of C6 were obtained (see Table 3-2).

3.6.5. Configuration 2

The convective/radiative ratios followed similar trends to those of C5, Nu increasing with Ra, although it is necessary to reiterate that Ra and Nu decreased as Qin increased. At a power input of only 220W, the proportion of convection/radiation heat transfers was below unity (see Fig.3-22(a-d)), which indicated the power where radiation became the dominant mode of heat transfer.

3.6.6. Configuration 7

Although radiation was virtually dominant throughout the entire power input range for this base-and-crown-mounted heating-element configuration, the convective heat transfers obtained with this configuration (see Fig.3-23(a-d)) was much higher than that for C5 with three elements mounted at the base and one at the crown. The relationship between the convective heat transfers and convective flow activity (Nu vs Ra), showed a general trend of uniform proportionality, Nu increasing with Ra although Ra decreased as the power input was increased.

3.6.7. Configuration 8

There was improved convective heat transfers on C7 (see Fig. 3-24(a-d)). The lower heaters, which were slightly raised and mounted along the lower walls have previously been shown from the flow visualisation (see Fig. 3-14h) to increase convection, but this was more noticeable at the lower power (200W). It is shown here that the marginal superiority of C8 convection over C7 was retained right to oven temperatures (800W). The proportion of convection to radiation (see Fig. 3-24b) was similar to, though still marginally higher than that of C7. The reduction in the radiative heat transfer was accounted for via the lower enclosure base temperature.

3.6.8. Configuration 1

This sidewall-mounted configuration produced a very high proportion of convective heat transfers, convection being dominant for more than half of the entire power range (see Fig. 3-25(a-d)). The direct radiative view factors from the heaters were slightly lower for this arrangement, which contributed to the reduction in the calculated radiative heat transfers.

3.6.9. Configuration 9

This proved to be the most convective of all the configurations (see Figs. 3-27(a-d), partly because the direct view factor from the heaters to the inner body was the lowest, and partly because the heater mean temperatures were also the lowest. Additionally, the average wall temperatures were lower than most of the other configurations, so

that the total radiative fluxes and losses through the insulation were correspondingly lower.

3.6.10. Correlations

The correlations deduced are presented in Table 3.2. It is clear then that the correlations involving heat and heat ratios have a much improved reliability over that which employed Nu and Ra. The rapid decline in the value of Ra with increase in temperature can now be seen to give a very high exponent, with a correspondingly low constant c_1. This distortion occurred for various reasons, but principally as a result of the breakdown of the approximation in the buoyancy term (because $\beta\Delta T>>0.1$), the type of flow, which was turbulent, (c_2=0.25 with laminar flow), with flow discontinuities along the solid boundaries, and 2-D data distortion due to the transmissivity of the glass. These rendered the comparison of the deduced correlations

Table 3.2 Deduced correlations:

	$Nu=c_1Ra^{c_2}$			$\frac{Qconv}{Qin}=(c_4)(q_{in})^{c5}$			$Q_{conv}=c_6Ln(Q_{in})+c_7$		
	c_1	c_2	R^2	c_4	c_5	R^2	c_6	c_7	R^2
C1	1E-11	1.423	0.91	21.24	-0.454	0.997	85.2	-350	0.99
C2	9E-12	1.423	0.94	476	-0.874	0.997	10.5	22	0.9
C5	9E-17	1.974	0.986	52.2	-0.602	0.986	42.6	-142	0.96
C6	5E-17	2.164	0.865	163.6	-0.622	0.865	39.2	-120	0.98
C7	2E-12	1.613	0.99	55.9	-0.603	0.99	42.9	-146	1
C3				2E-10	1.93	0.864	43.26	-221	0.93
C4				143	-0.772	0.996	14.13	-21.5	0.956
	$Nu=c_1Ra+c_2$			$\frac{Qconv}{Qin}=(c_4)(q_{in})^{c5}$			$Q_{conv}=c_6Ln(Q_{in})+c_7$		
	c_1	c_2	R^2	c_4	c_5	R^2	c_6	c_7	R^2
C8	4E-07	-22.1	1	32.69	-0.516	1	856	-3736	1
C9	3E-07	8.63	1	16.3	-0.406	1	110.8	-468	1

with those in lower temperature systems impracticable. However, especially important are the correlations which involved Qconv/Qin or Qconv directly, as these instantly

provide a thermal design engineer with a trend in the convection heat transfer, with respect to each configuration, to a specified power input.

3.7. INTERFEROMETRY

Having established that C9 was the most convective, interferometric tests were then carried out to obtain its two-dimensional thermal profile. The photograph of half of the vertical symmetry of C9 is shown (see Fig.3-27). The temperature of the lower heater was only 55^0C, and that of the inner body 25^0C. Each heater is seen to be surrounded by densely-packed fringes, an indication of boundary layer formation. The lower heater plume is seen to deviate from the vertical towards the sidewall. The upper plume initially rose vertically but then deflected towards the middle of the enclosure.

A further analysis was carried out by raising the two upper heaters until they were well above the centred horizontal axis (see Fig.3-28). This was to observe the changes in the isotherms and the probable improved contribution to heat transfers to the upper surface of the inner body. The lower heaters were retained in the lower corners. The lower plume still deviated slightly towards the sidewall, but the upper plume was seen to deviate towards the upper corner instead of towards the inner body, suggesting much more wasteful convective activity at the quadrants. Therefore, there would be no further benefit for convective flows if the upper heaters were to be raised above the central horizontal line.

Attempts to improve the transient response of a domestic (cubical) oven include the installation of an extra element (as part of the continuous loop along a sidewall) (see Fig. 2-9b) above the lower horizontal arrays. However, the foregoing analyses have demonstrated that, while this extra element would increase the upper cavity temperature, and therefore improve the transient response of the system, it could also reduce the convective component of the heat transfers as demonstrated by the roof-mounted heating-element in C5.

This observation is valid for exposed heating-elements along the vertical wall of an oven. But the same may not necessarily apply to heaters which are shielded, by louvered shelf supports [51], because these would be subject to different convection characteristics [25].

3.8. DISCUSSION

3.8.1. Improved uniform heating by natural convection

It was pointed out in the Introduction (Chapter 1) that studies of low emissivity ovens with aluminium test blocks [14,15] indicated higher efficiencies, but that when the findings were applied to low diffusivity baking items, the finished products were unsatisfactory because of hot spots on the upper surfaces. The ovens had heating-elements mounted at the base and the crown. The nearest configuration from the present 2-D study which closely resembles the tested cubical ovens of Scarisbrick et al [15] is C7. The air temperature analyses, which were supplemented by the flow visualisation analyses improved the understanding of the flow activities which occurred in C7.

As explained in section 3.5.4, the main stream along the upper surface of the inner body was influenced by the activities of the cells above it. The flows across the upper surface of the inner body were observed to rise and fall in sympathy with the oscillating cells located between the inner body upper edges and the enclosure top corners (see 01 and 02 in Fig. 3-14g), which caused the main stream to lift as it approached that edge. Thus the main flow intermittently touched the upper surface rather than sweeping the entire surface at a uniform velocity. Stagnant pockets were formed periodically, at various points on the inner body upper surface. Additionally, noting that the irradiance from the heaters would be additive to that from the enclosure backwall, it was therefore concluded that hot spots were created because the attenuating effect of convective flows were localised.

3.8.2. Transient Thermal Response

In the course of the experimental work, it was observed that C2 with one element mounted on each enclosure wall achieved a steady-state condition most rapidly with the shortest transient response. On the contrary, C9 required a fairly lengthy delay before steady-state conditions were achieved. The mean distance of the heating-elements of C2 to the inner body walls was the lowest. Consequently, C2 had the highest direct view factors from the heaters, and C9 the lowest (see Appendix B). The transfer of heat by thermal radiation is instantaneous. Therefore, it is hereby partially

associated with the faster transient response of each configuration, and not to the wall properties, which were common in each study.

3.8.3. The effect of the angular corners.

It was noted during the flow visualisation, particularly for C7 that the upper corner recirculation could not be beneficial to convection heat transfers. This is because thermal energy required to drive the flow should have been available in the interior of the cavity, nearer the inner body. It was also observed in some cases that the recirculations actually prevented direct contact of the main stream with the upper heaters, thereby reducing the convective effectiveness of the configuration. It has been shown in this study that the benefit of generous rounding of the corners should provide considerable benefits for natural convection ovens, although this could be at the expense of a reduced volumetric capacity.

3.8.4. Inner body isothermality

The inner body utilised in this study was considerably difficult to fabricate because of the incorporation of a deflecting baffle, as well as the drilled pipes immersed within the inner body. Therefore, the necessity for isothermality was assessed by comparing some of the main thermal profiles with those achieved when the inner body was not isothermal.

Because a more pronounced temperature gradient of the inner body in the z-direction occurred [16], it was concluded that a significant 3-D effect was generated which would alter the flow and heat transfer characteristics of the system. The changes would not be limited to the 3-D flow at each end orthogonal to the main flow, but extend to the conduction effect between each flow, reaching well into the interior of the enclosure, and reducing the portion of the enclosure interior which could be classified as 2-D.

Upon comparison of the vertical air temperature profiles, however, it was found that for some of the configurations - 2,3,6, (i.e. identical configurations to [16]), the shape of the curves were somewhat similar although the maximum temperature difference of each curve was marginally lower than that obtained in [16]. Similar trends were noticed for the horizontal air temperature profiles, although the temperatures recorded

were again lower in the present study, because of the slightly lower wall temperatures of both the inner body and the enclosure.

It can be deduced therefore, that for a very simple temperature profile evaluation, the stringent requirement for inner body isothermality can be relaxed.

The significance of this finding is that the extra resources required to obtain an isothermal inner body would be avoided. However, when a thermal analysis is required, it is imperative that uniform boundary-conditions be obtained, since the considerable radiative exchange is subjected to the inner body surface temperatures, which in turn would influence the enclosure wall temperatures.

3.8.5. End plate heat losses

Referring back to the flow near each of the end plates noticed during the flow visualisation, it is assumed here that had there been further temperature gradients in the z-direction, then the 3-D flow and the attendant conduction effects would have been much more considerable, and of different intensities and depth of penetration to the interior from both ends. So, while the air temperatures appear to be similar to those presented in [16], the steady-state thermal analyses would have been much more complicated because of the need to use different temperatures and view factors for the inner body walls.

Although the flow visualisation was carried out under more or less identical conditions as to that of the thermometric measurements, the penalty paid was a 17% steady-state heat loss through the thin pyrex-glass end plates. The major influence in the original choice of glass end plates was to employ an interferometric technique in analysing the heat transfer data. However, because the glass end plates were not as highly polished and flat as was necessary for interferometry, and the attendant fringe distortion was too large, interferometry was not wholly employed in the thermal analyses. Additionally, interferometry would have produced too high a fringe density at the temperatures encountered in this study [56], which would have equally made the fringe analyses difficult.

If the enclosure end plates had been fully insulated, or double-glazed as in [19], the 2-D integrity of the data would have been considerably enhanced because the proportion of the enclosure length exhibiting a uniform temperature would have been higher.

Therefore, these observed limitations should be taken into account before the correlations obtained in this study are employed.

3.8.6. Uncertainty in the experimental data

To obtain Qconv, Qrad and Qinsul were subtracted from Qin. The data employed for the uncertainty in Qin was 1.5%, Qrad 7%, and in Qinsul 3%. The largest possible variation in the uncertainty simultaneously, would be cumulative, i.e. +0.07Qin, -0.07Qrad, -0.03Qinsul. So when the numbers employed to obtain Qconv were numerically close to Qin so that Qconv was very small, the ratio in uncertainty was found to be comparatively magnified (see Appendix C). The uncertainties for the convective configurations are listed in Table C.4.

Attempts to obtain correlations based on standard concepts were shown to be unsuccessful because the value of Ra declined rapidly. Because of the interactions of the enclosure corners and the inner body, and the increased influence of radiative heat transfers, it would be appropriate to refer to these problems not as a natural convection problem, but as all-modes heat transfer problem [28]. As the temperature of a system rises, the proportion of heat transfers by radiation increases because of its quartic dependence on temperatures and simultaneously, the proportion by convection falls because of the inherent characteristics of air properties (see Appendix D).

3.9. CONCLUSIONS AND RECOMMENDATIONS

3.9.1 Conclusions

Substantial improvements on convection heat transfers were made by altering the location of discrete heaters in an enclosure fitted with a symmetrical inner body. The flow visualisaton and the comparative analyses enabled certain problems to be examined and analysed. The highest convective heat transfers were obtained with wall-mounted configurations C9 (34%) and C1 (28%), while the fastest response was provided by C2, with a single element centrally-positioned along each enclosure wall.

The cause of localised overheating was identified from an examination of the flow visualisation which was carried out in the 2-D rig. It was discovered that oscillating cells located elsewhere in the enclosure have an adverse effect on the flow along the solid boundaries. Thus, the inconsistency in flow path caused localised overheating, which compromised the attenuating effect of convection upon the non-uniformly heated upper surface of the inner body.

3.9.2. Recommendations

The development of ovens is product-dependent. The range of configurations experimentally studied also indicate the complexity of natural convection flows in enclosures, and that any minor changes in heating arrangements could result in considerable changes in heat transfer coefficients. However, further development could arise as a result of the need to augment natural convection in enclosures, or specifically ovens, or the need to obtain faster response from natural convection ovens.

Therefore, C9, C1, or variants of these, could be further studied for a more accurate quantitative analyses of the various modes of heat transfers, as well as to improve, still further, the convection heat transfers by altering the heater-to-wall spacings.C2 should be studied in order to examine the influence of a faster response configuration on the uniformity of heated products.

The thermometric method employed to obtain the convective component of heat transfers was found to lead to large uncertainties particularly when the convective component of the heat transfers was small. Therefore, improved methods to obtain the convection, such as by evacuation, should also be explored.

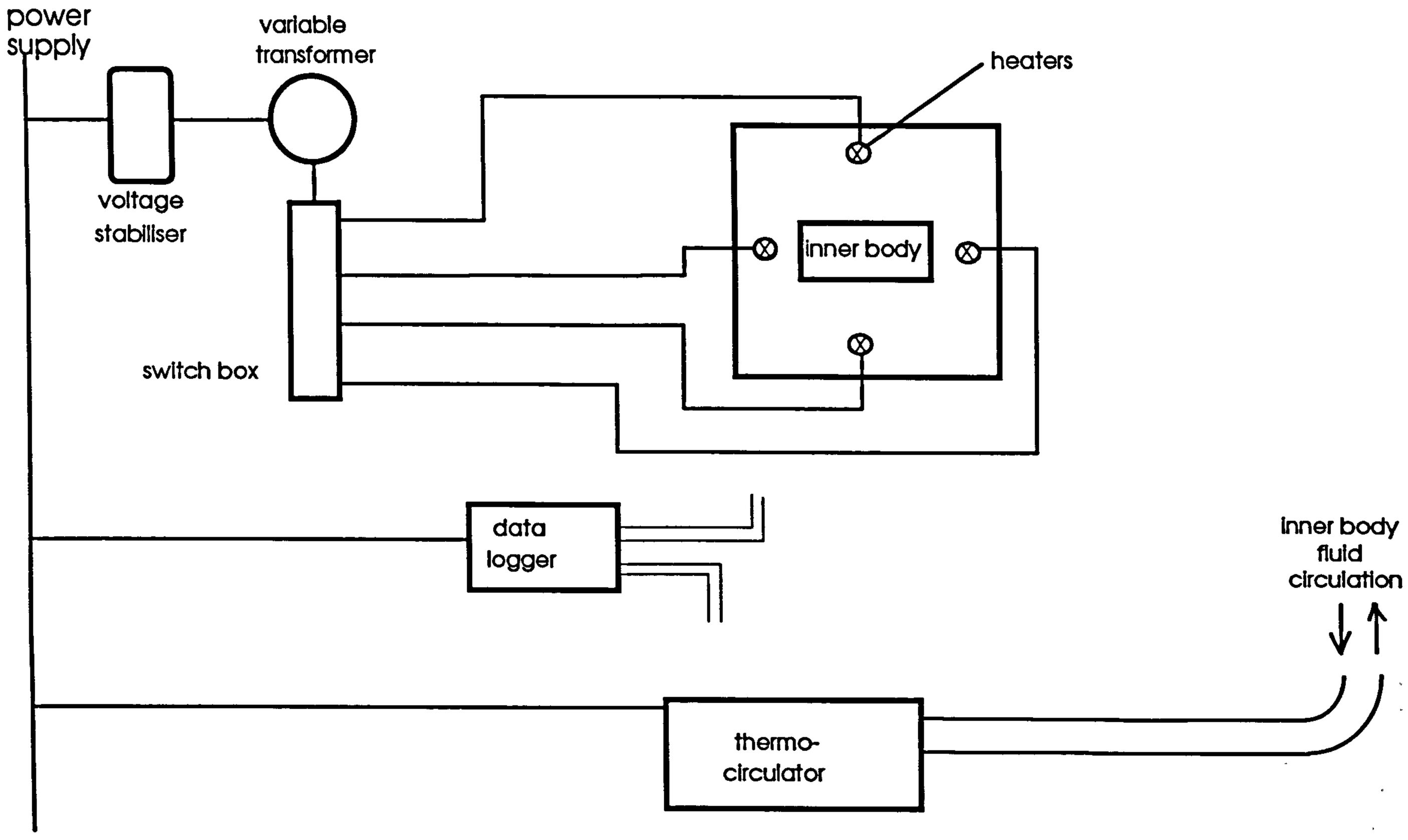

Fig. 3-1 Arrangement of the experimental rig

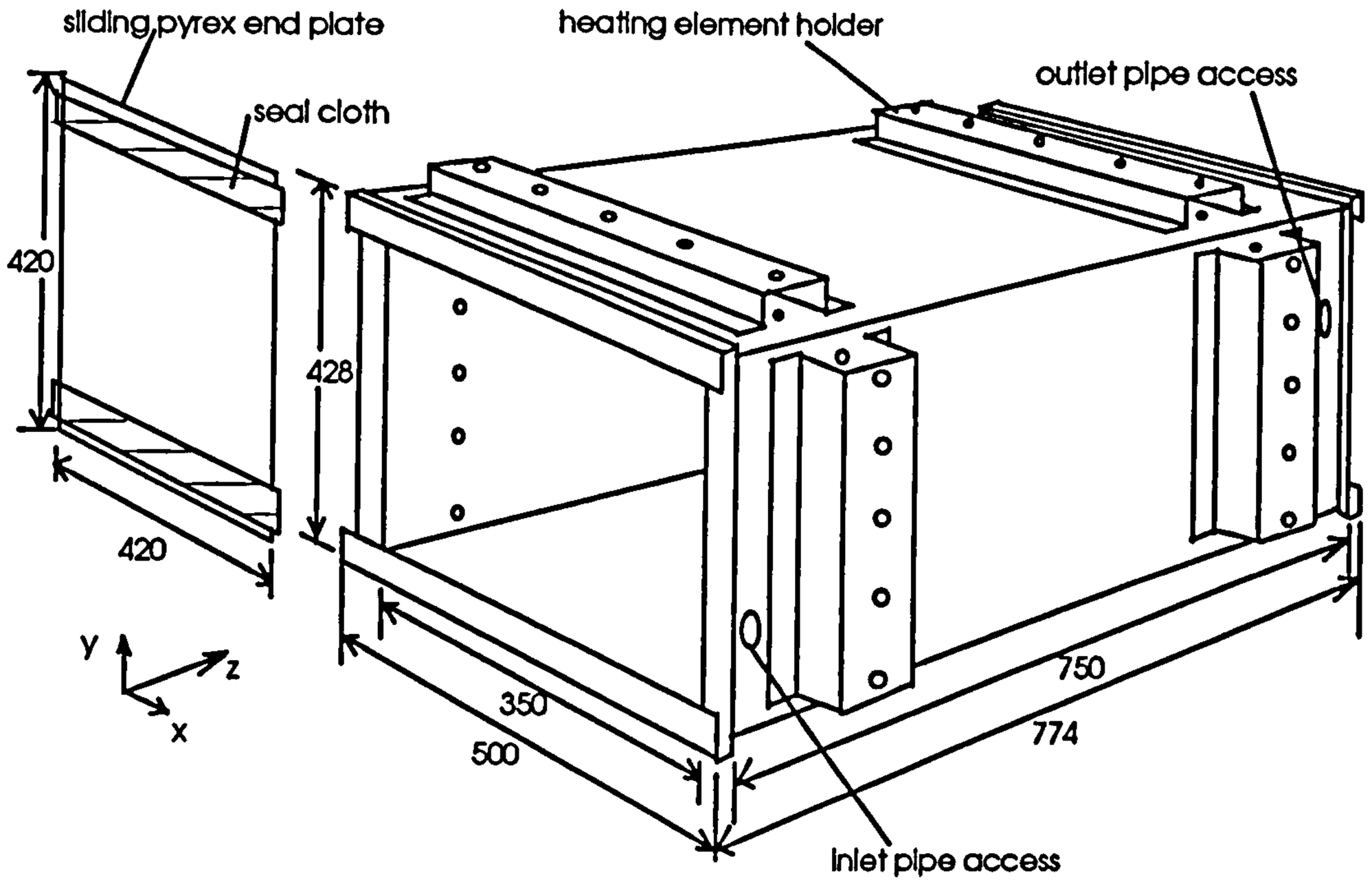

Fig. 3-2 Enclosure test rig

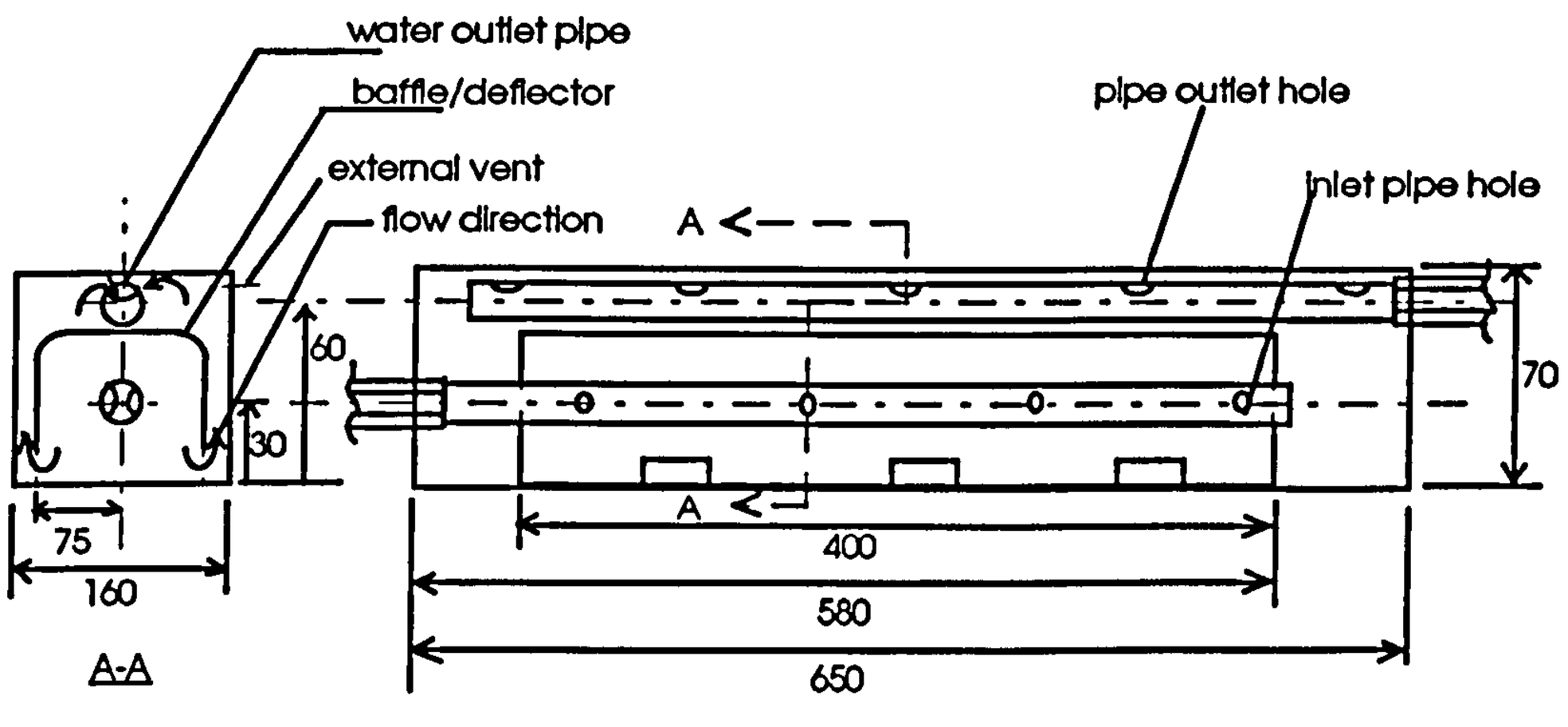

Fig. 3-3 Innerbody

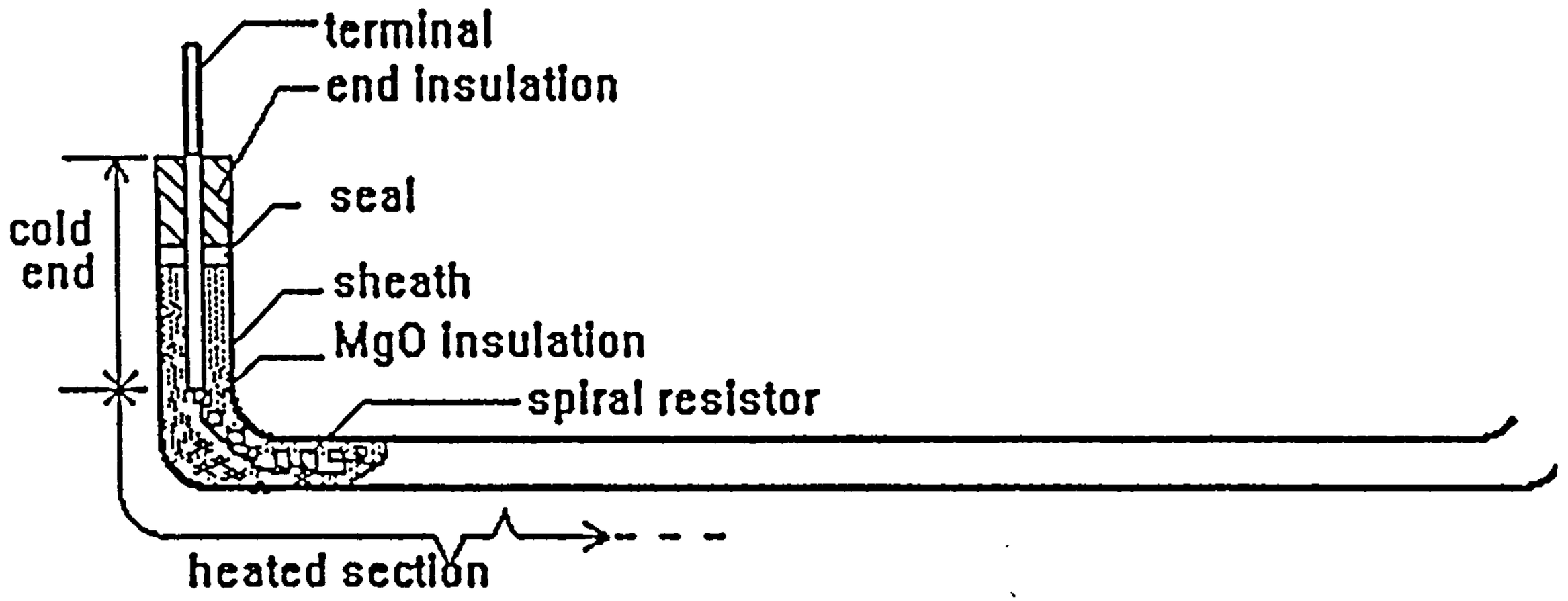

Fig. 3-4 Heating Element

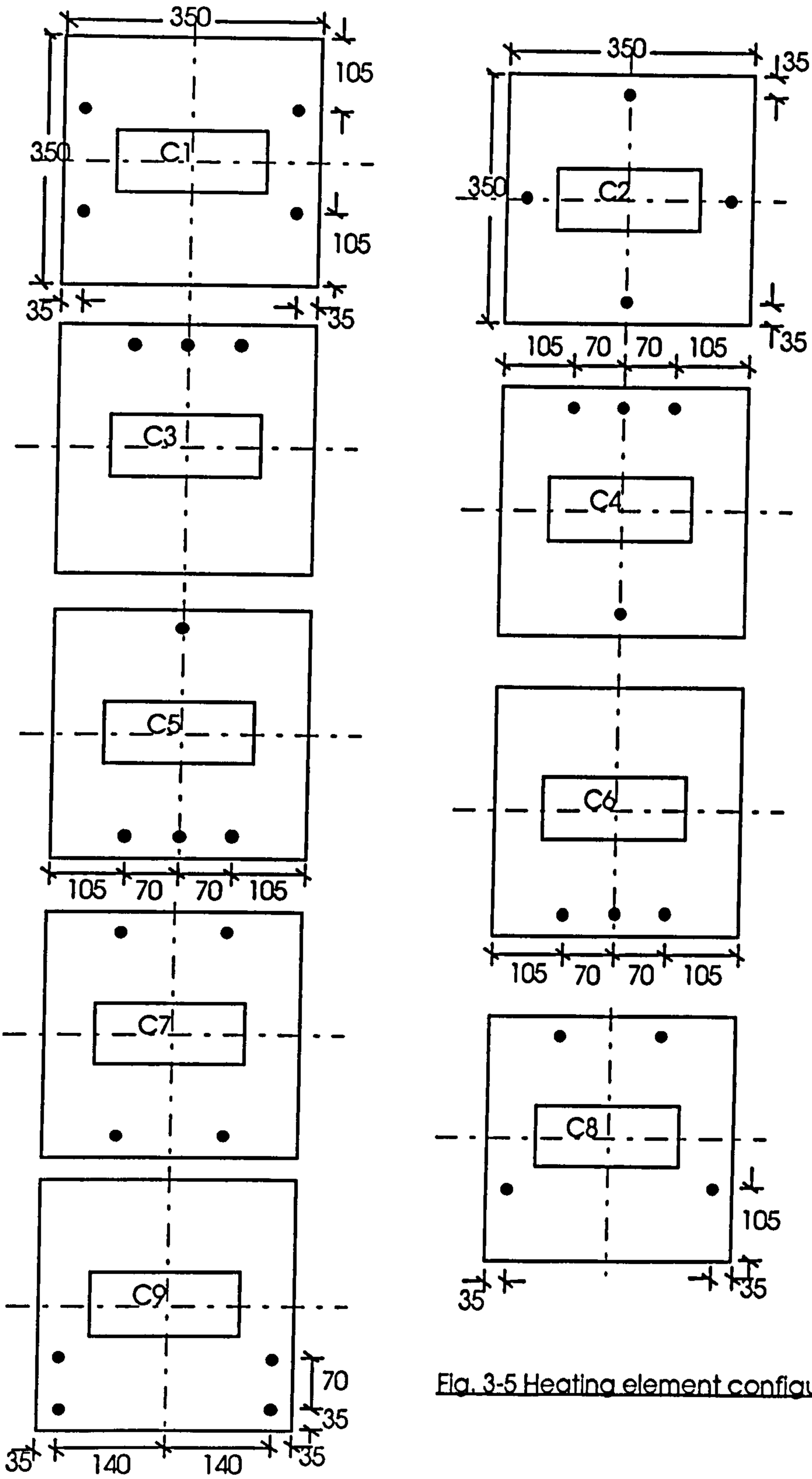

Fig. 3-5 Heating element configurations

Fig. 3-6 Thermojunction locations for data acquisition

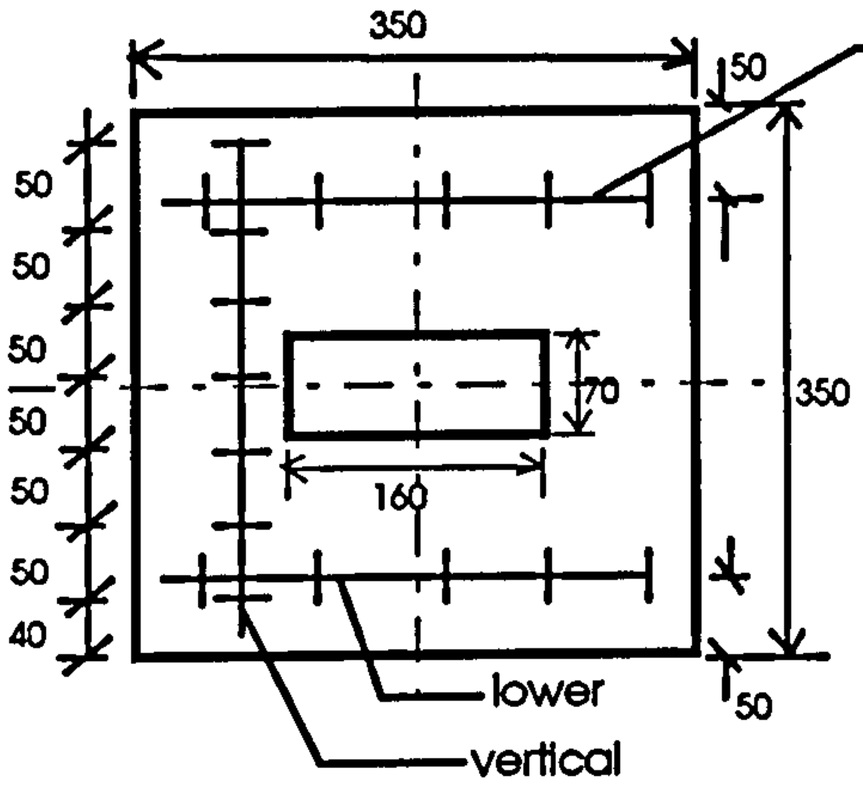

Data points:

Air space temperatures

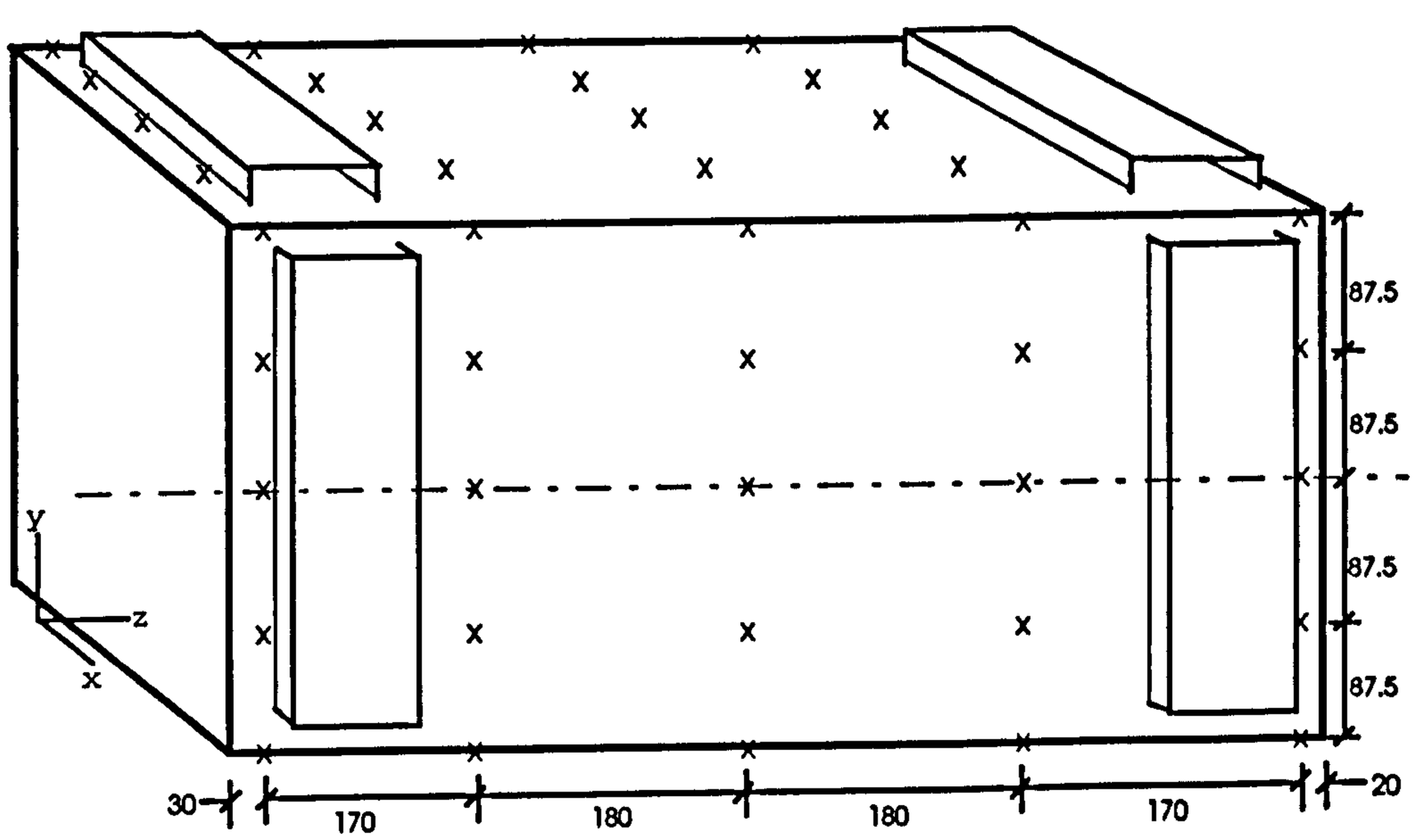

Data points:

Enclosure wall temperatures

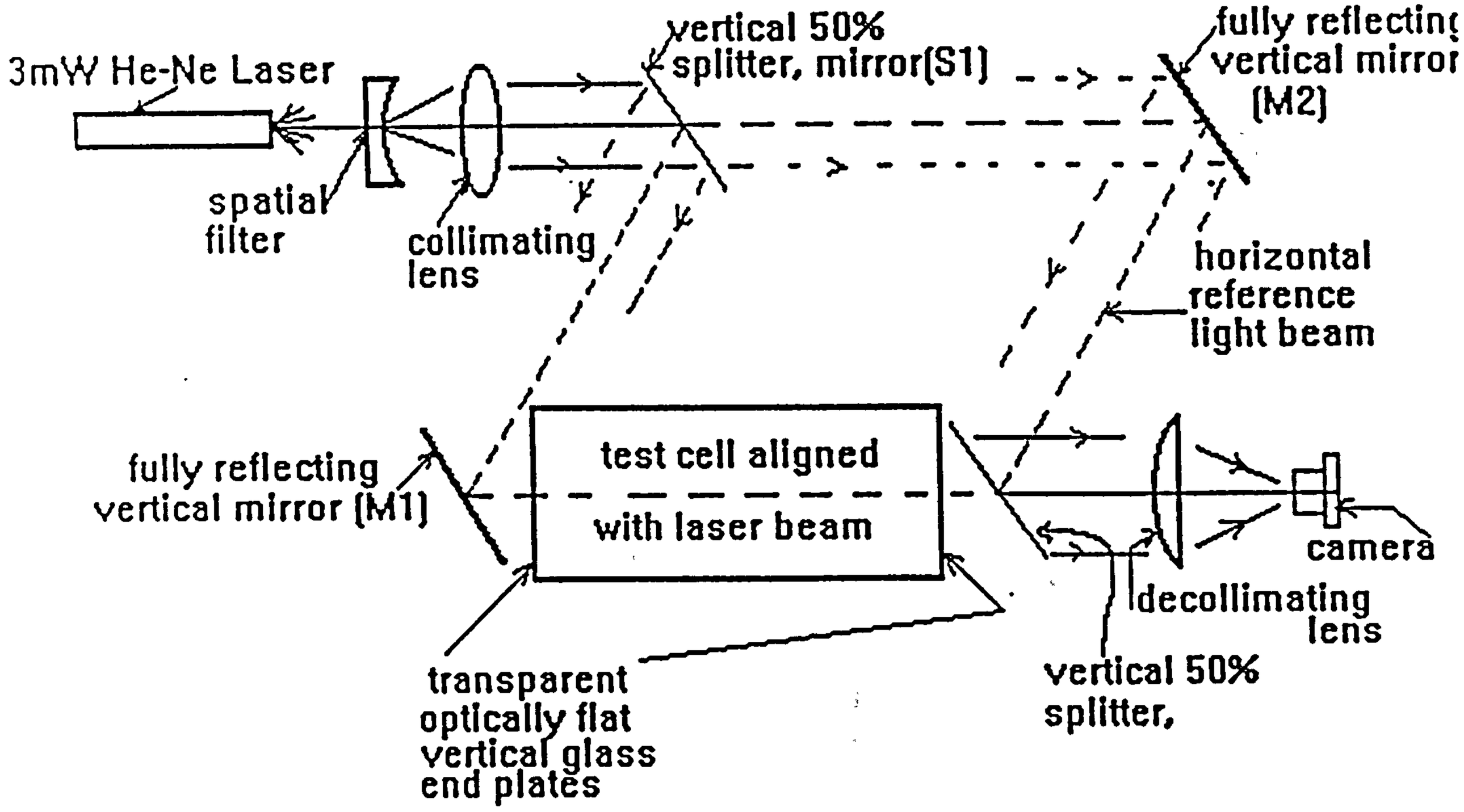

Fig. 3-7 Arrangement of the MZI and test rig

Fig. 3-8 Crossed strings method

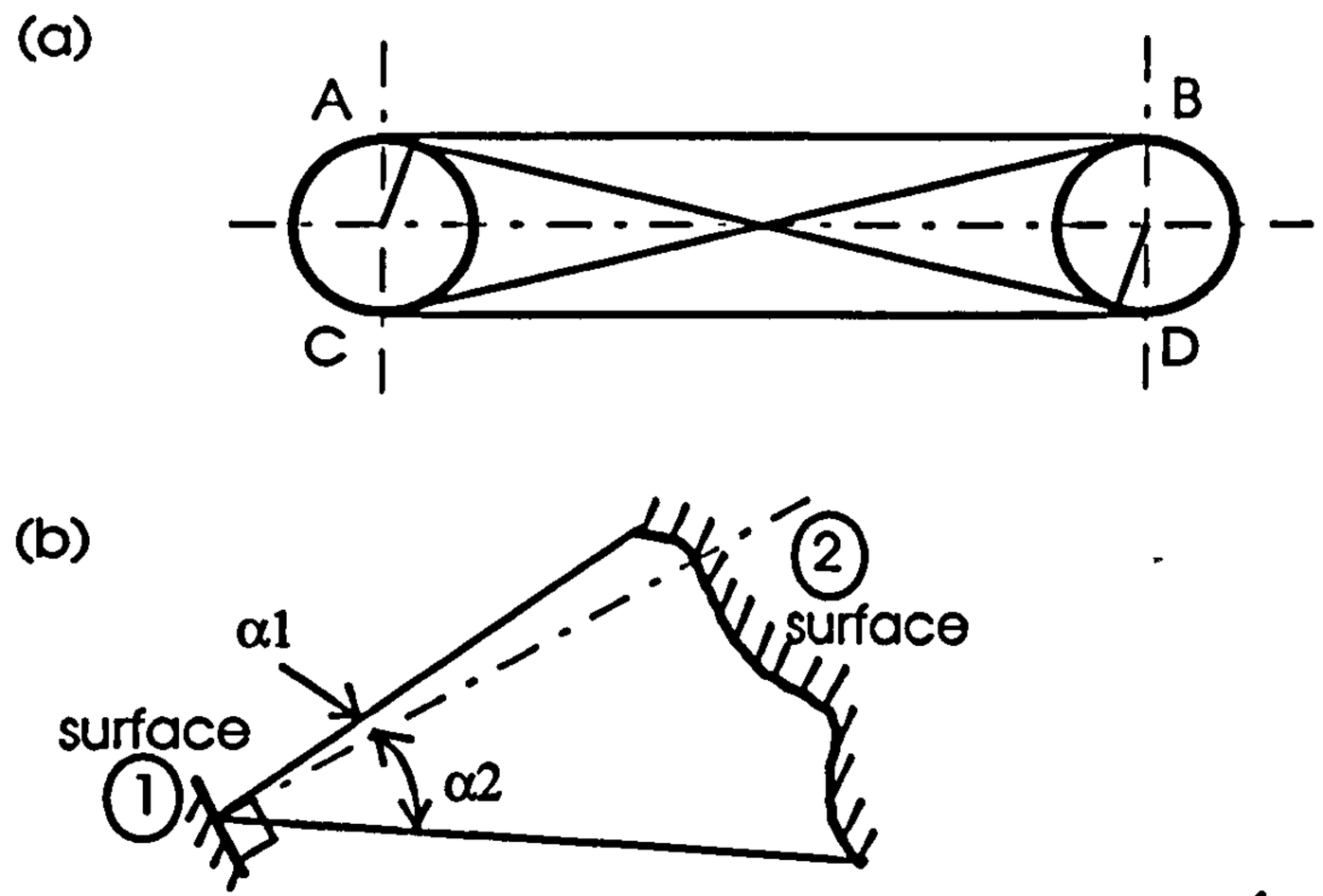

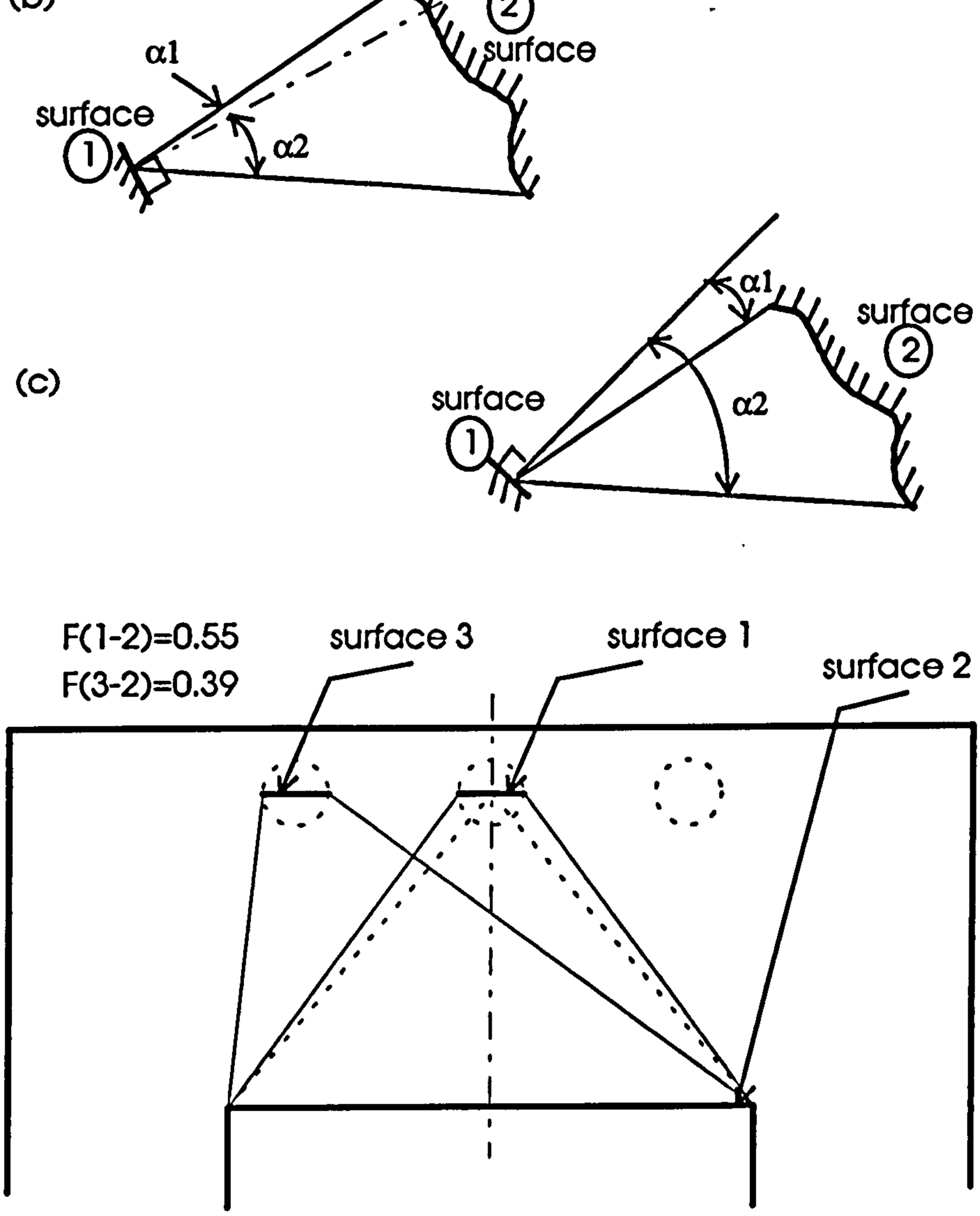

Fig. 3-9 View factor example

Fig. 3-10a: Innerbody temperature profile (sides, mean)

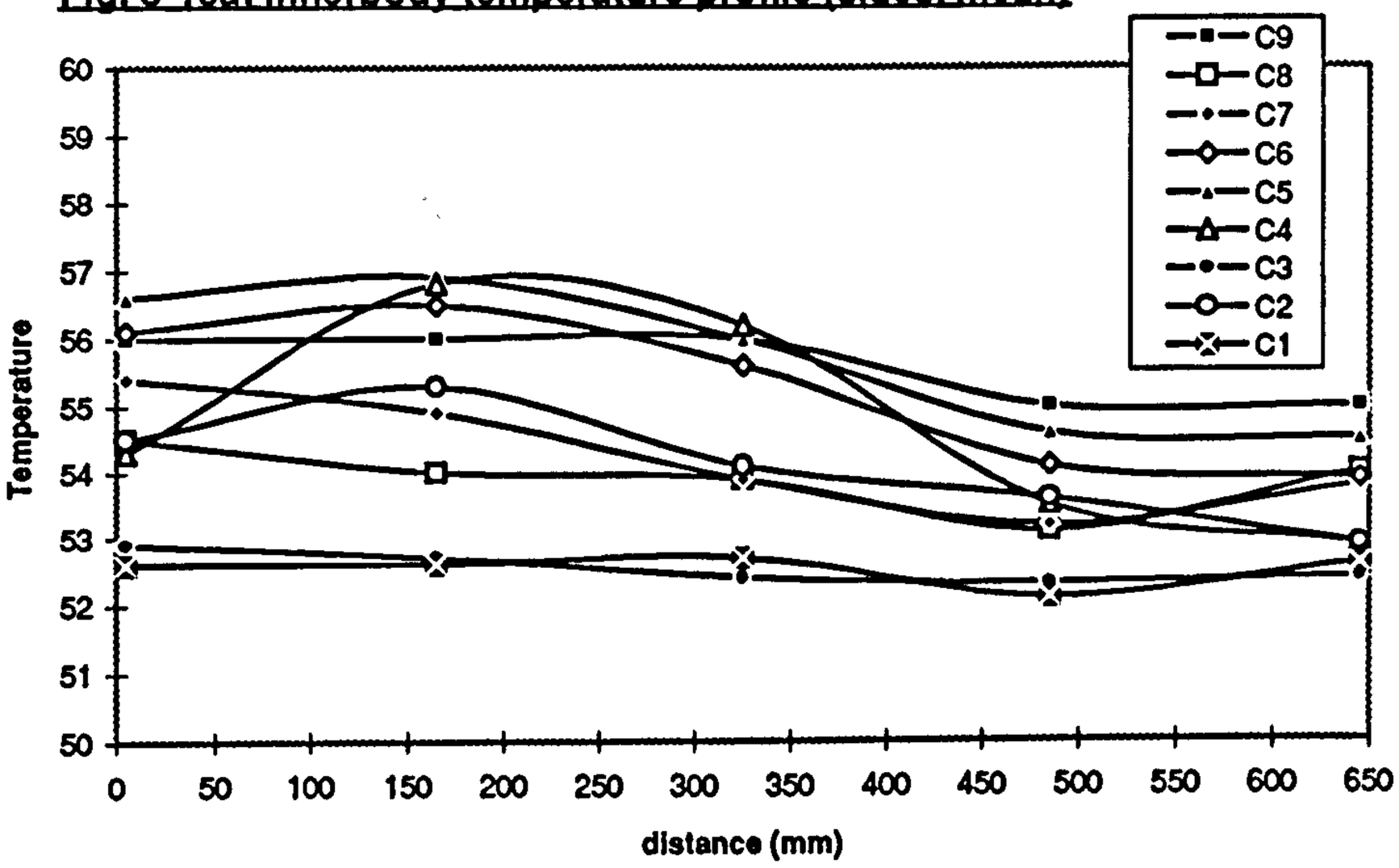

Fig. 3-10b: Innerbody temperature profile (top surface)

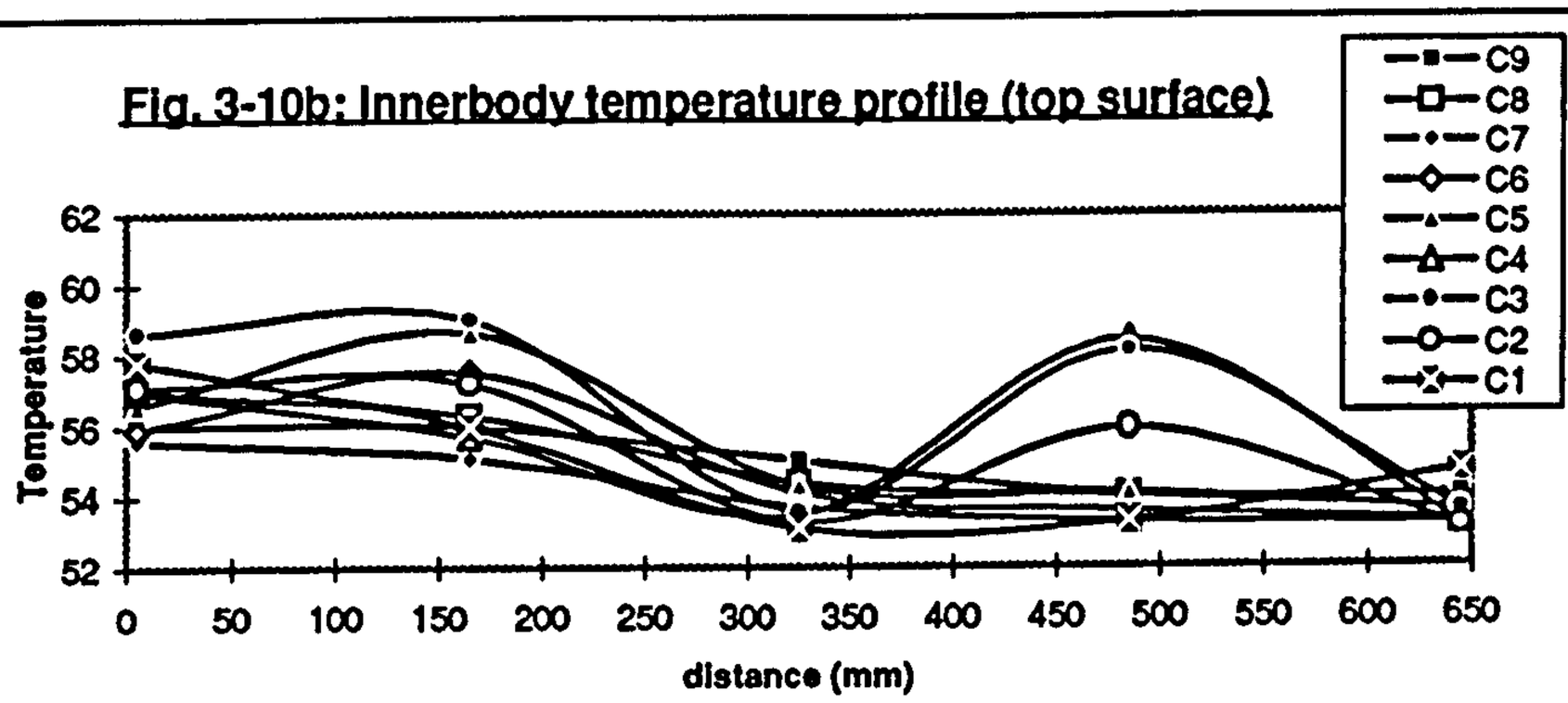

Fig. 3-10c: Innerbody temperature profile (base)

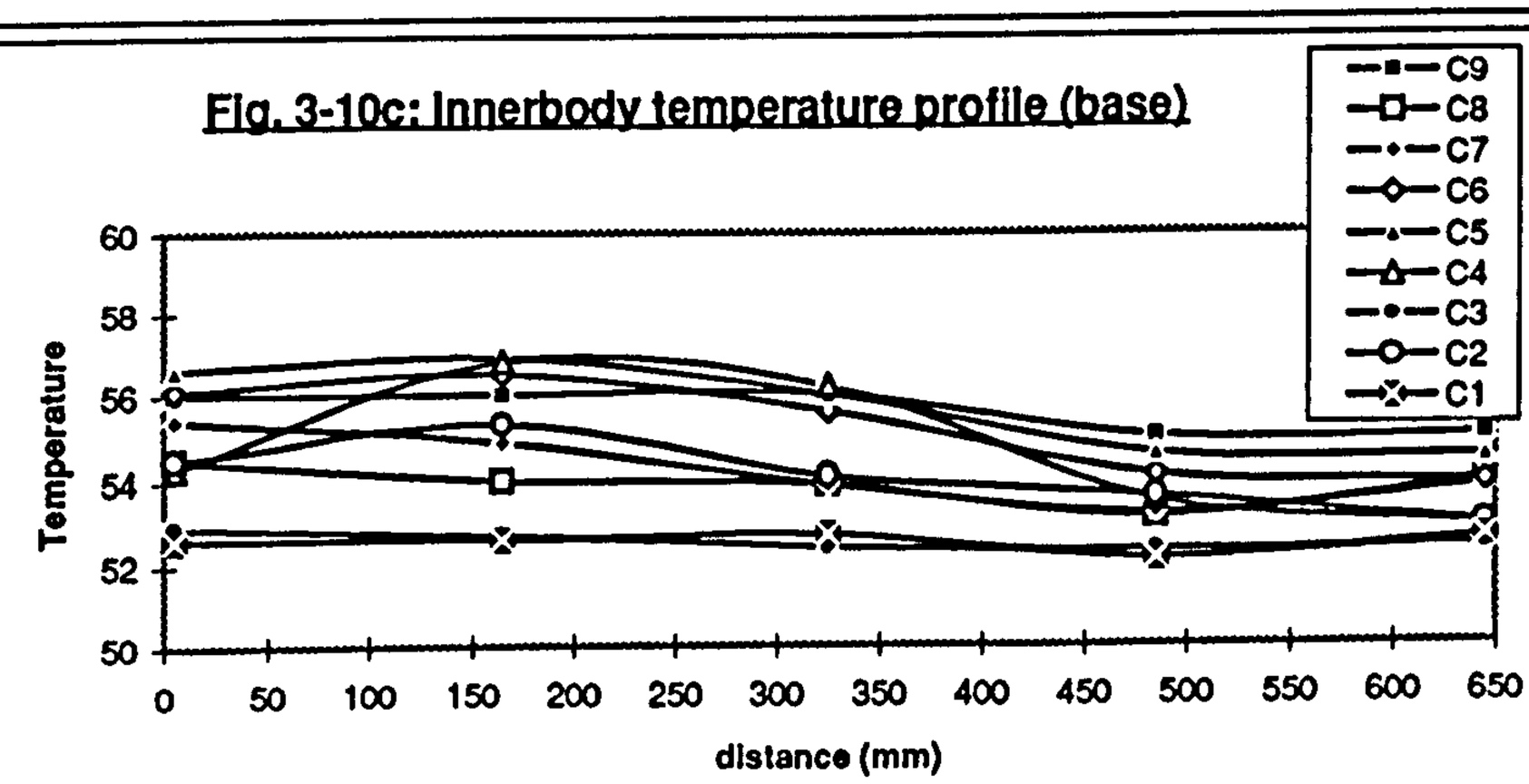

Fig. 3-11a: Enclosure air temperatures, vertical, y-axis

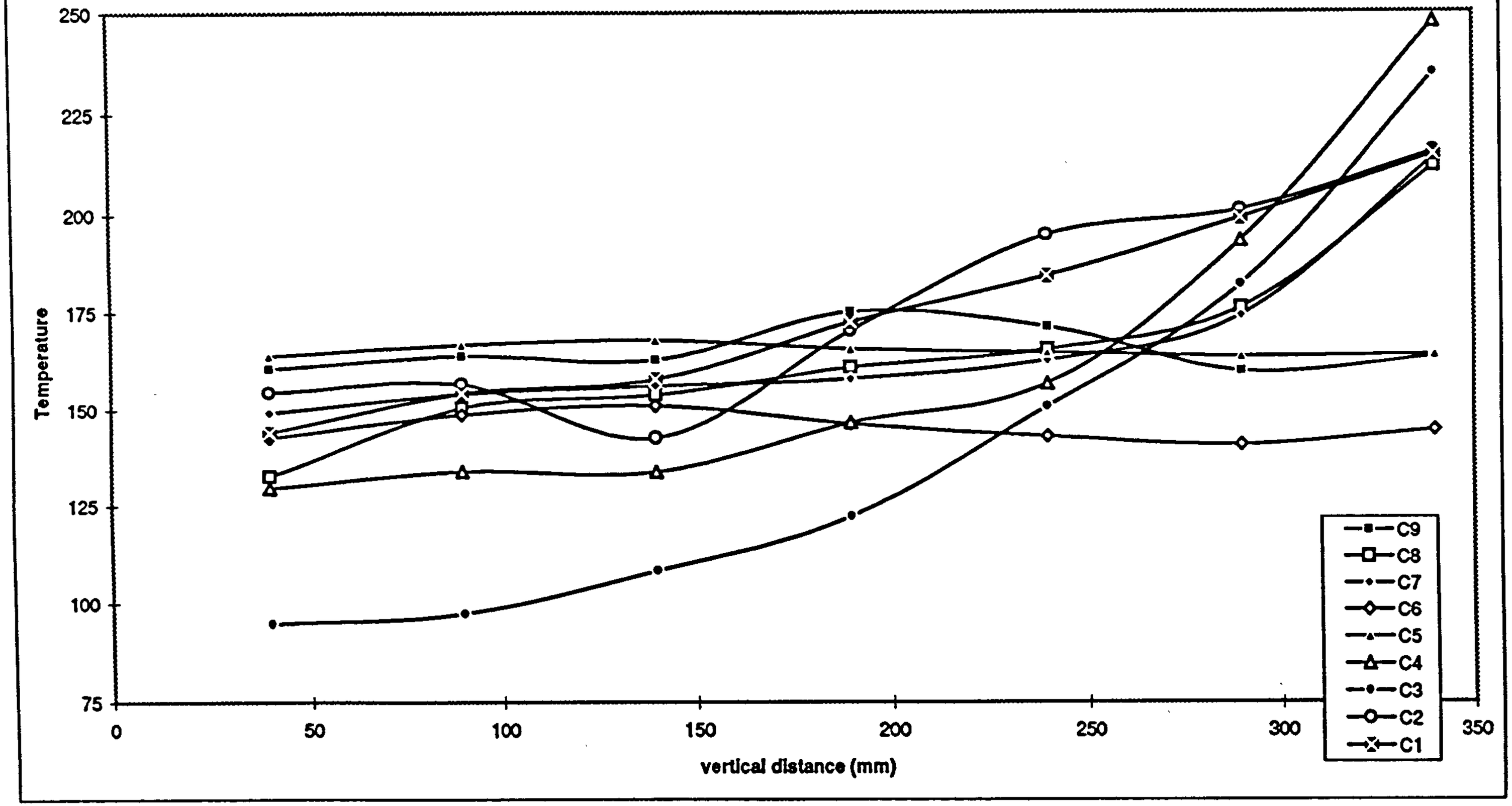

Fig. 3-11b: Air space temperatures (vertical) C3,4,5 & 6

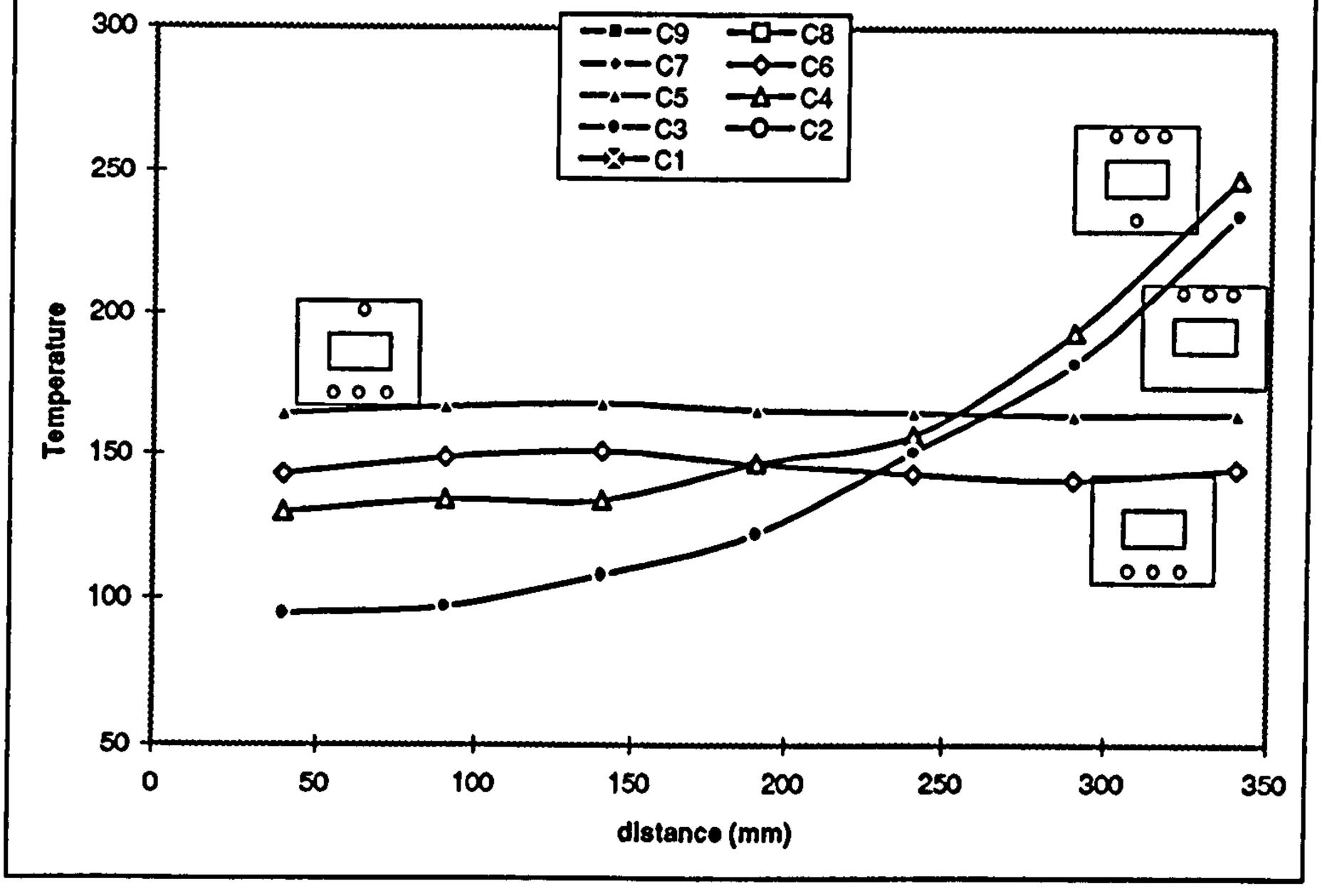

Fig. 3-11c: Air space temperatures (vertical), C1,2,7,8 & 9

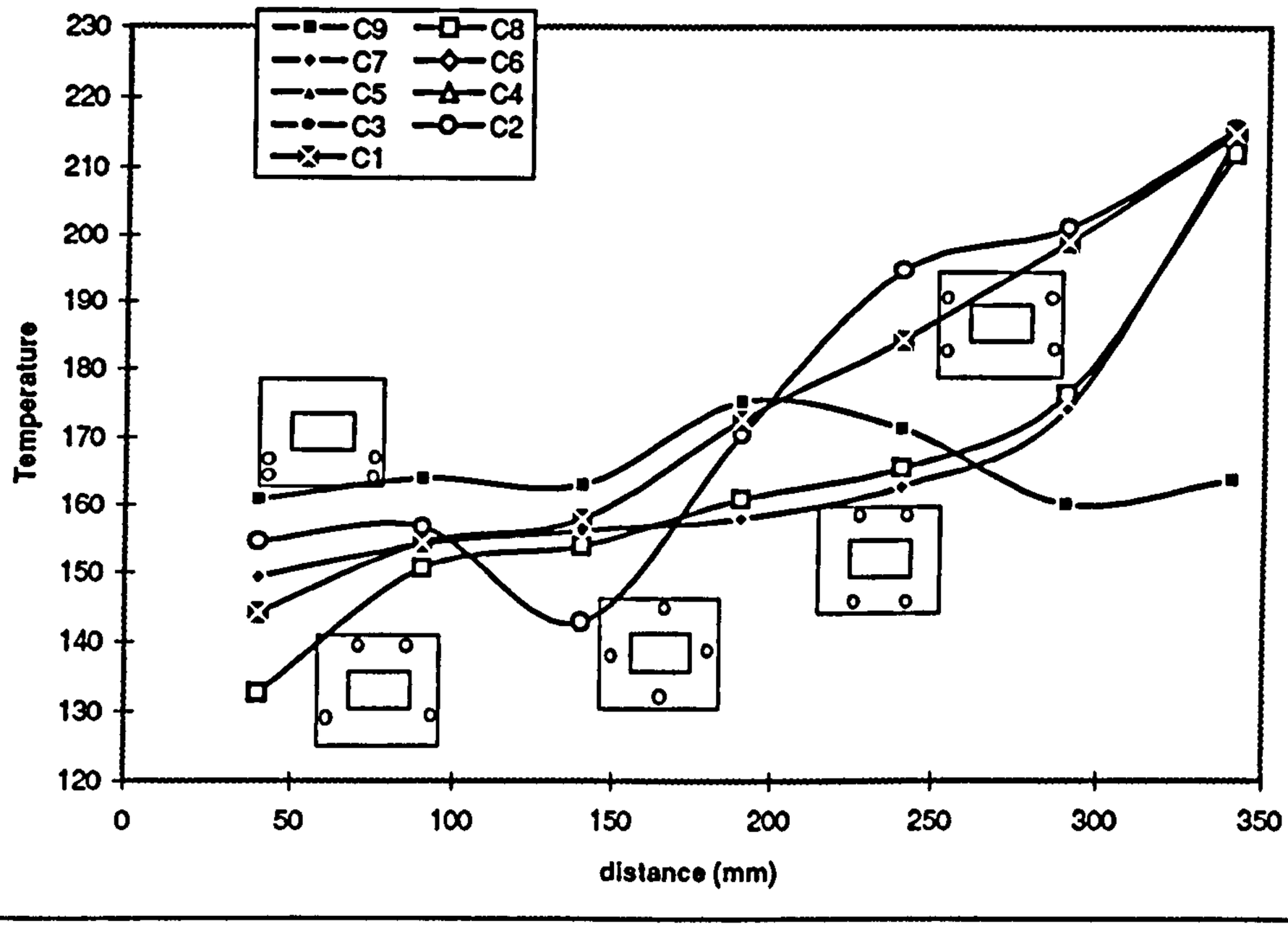

Fig. 3-12a: Air space temperatures,upper, x-axis

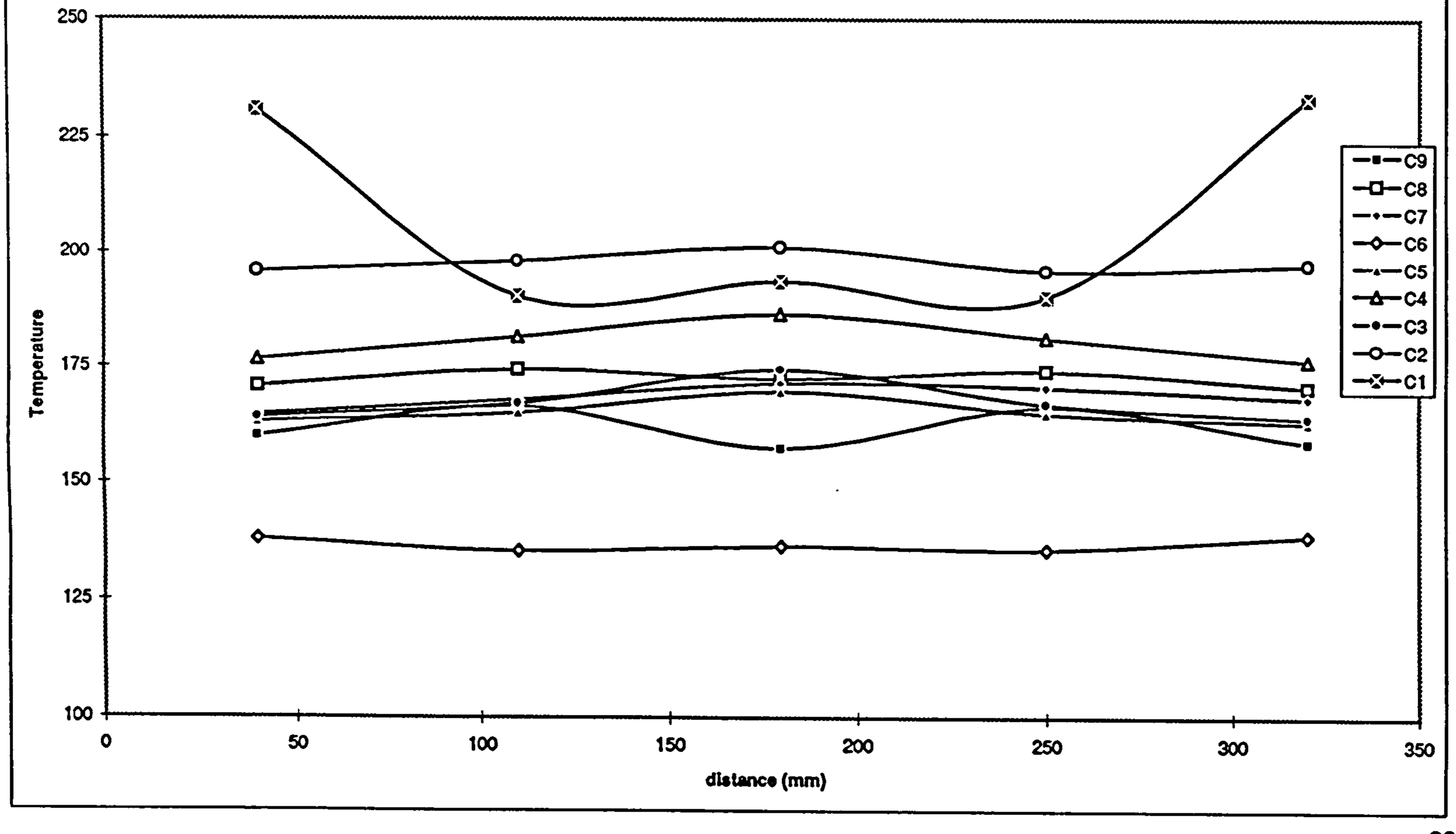

Fig. 3-12b: Upper air space temperatures (x-axis), C3,4,5 & 6

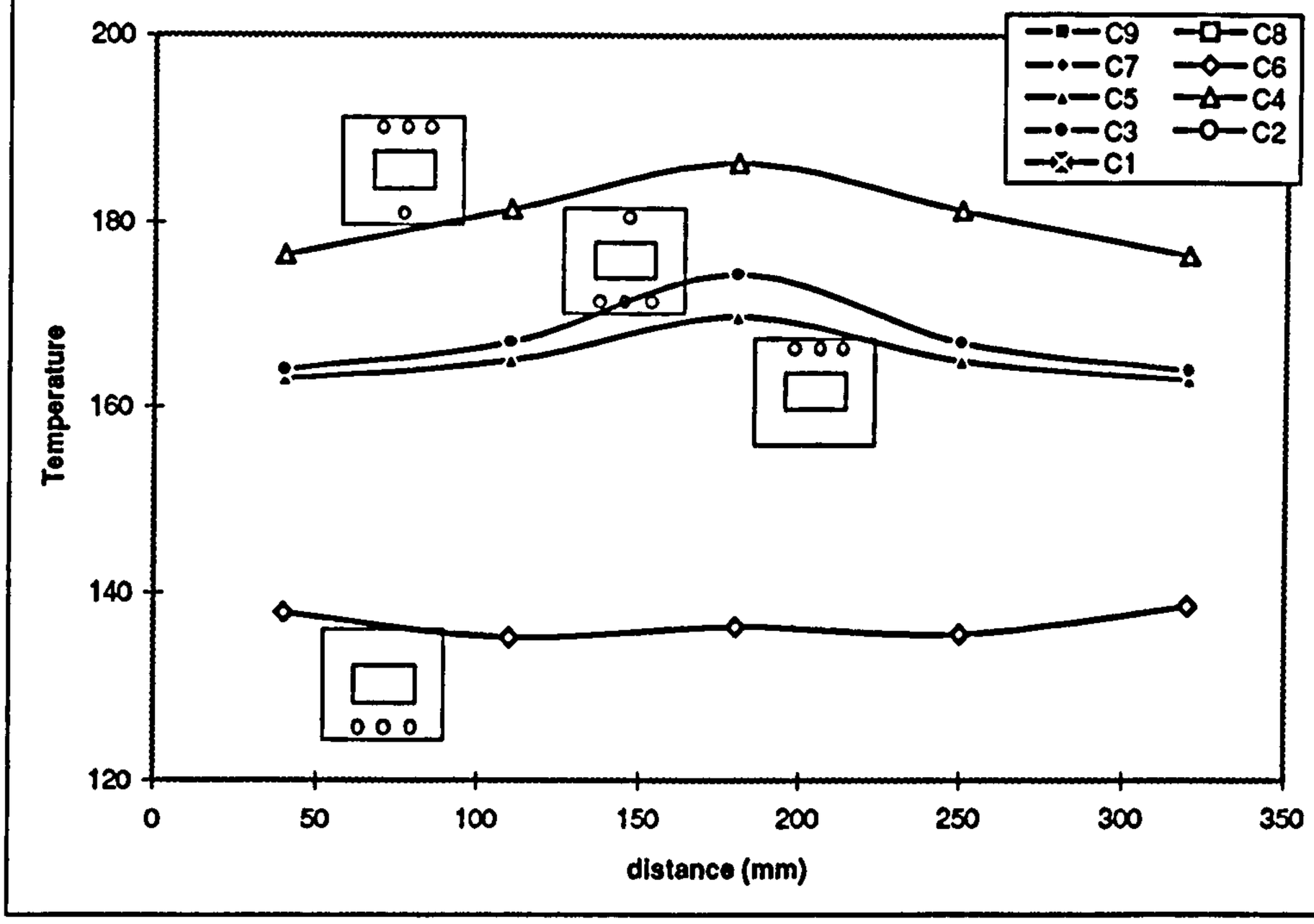

Fig. 3-12c: Upper air space temperatures (x-axis) C1,2,7,8 & 9

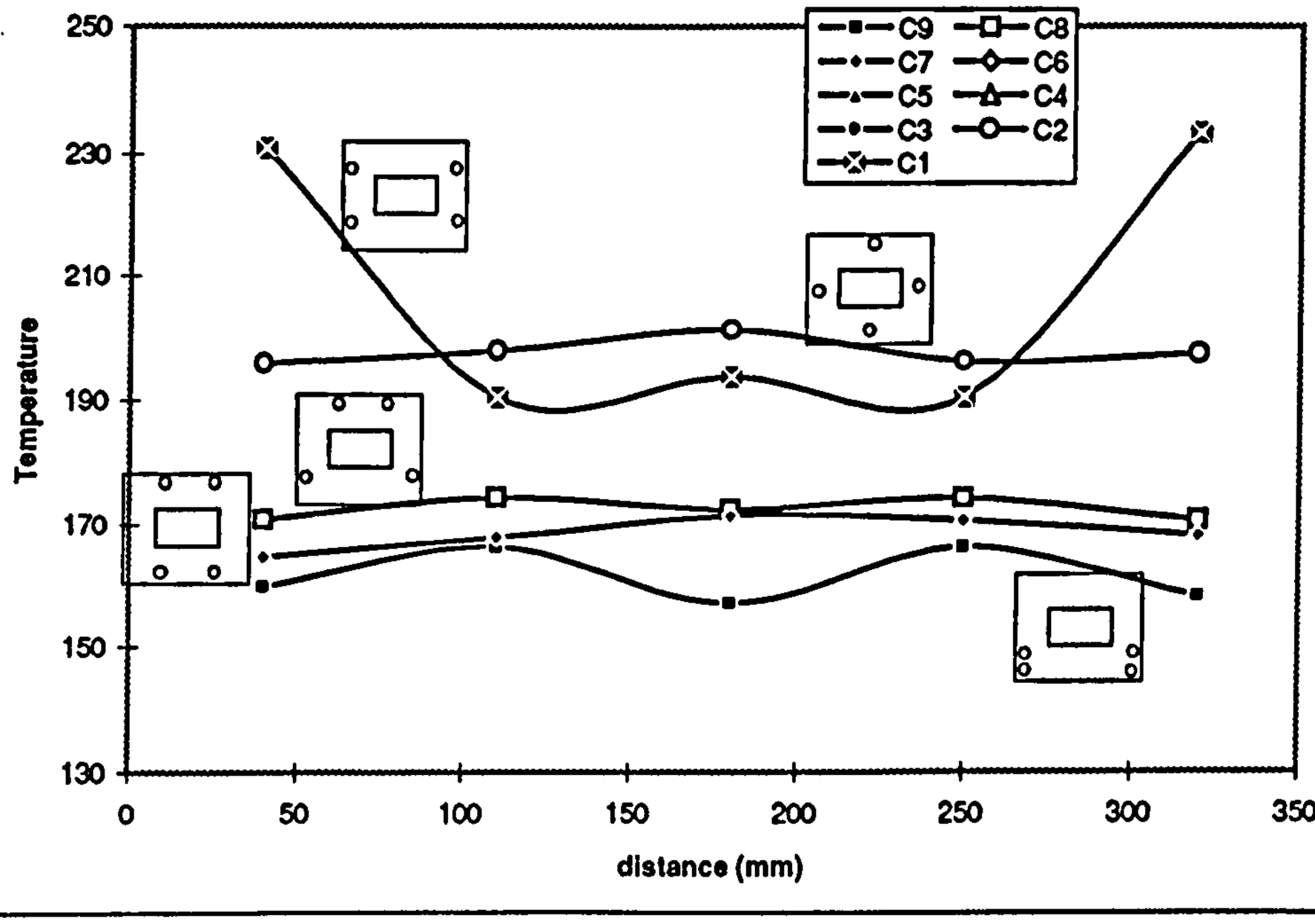

Fig. 3-13a: Air space temperatures, lower, x-axis

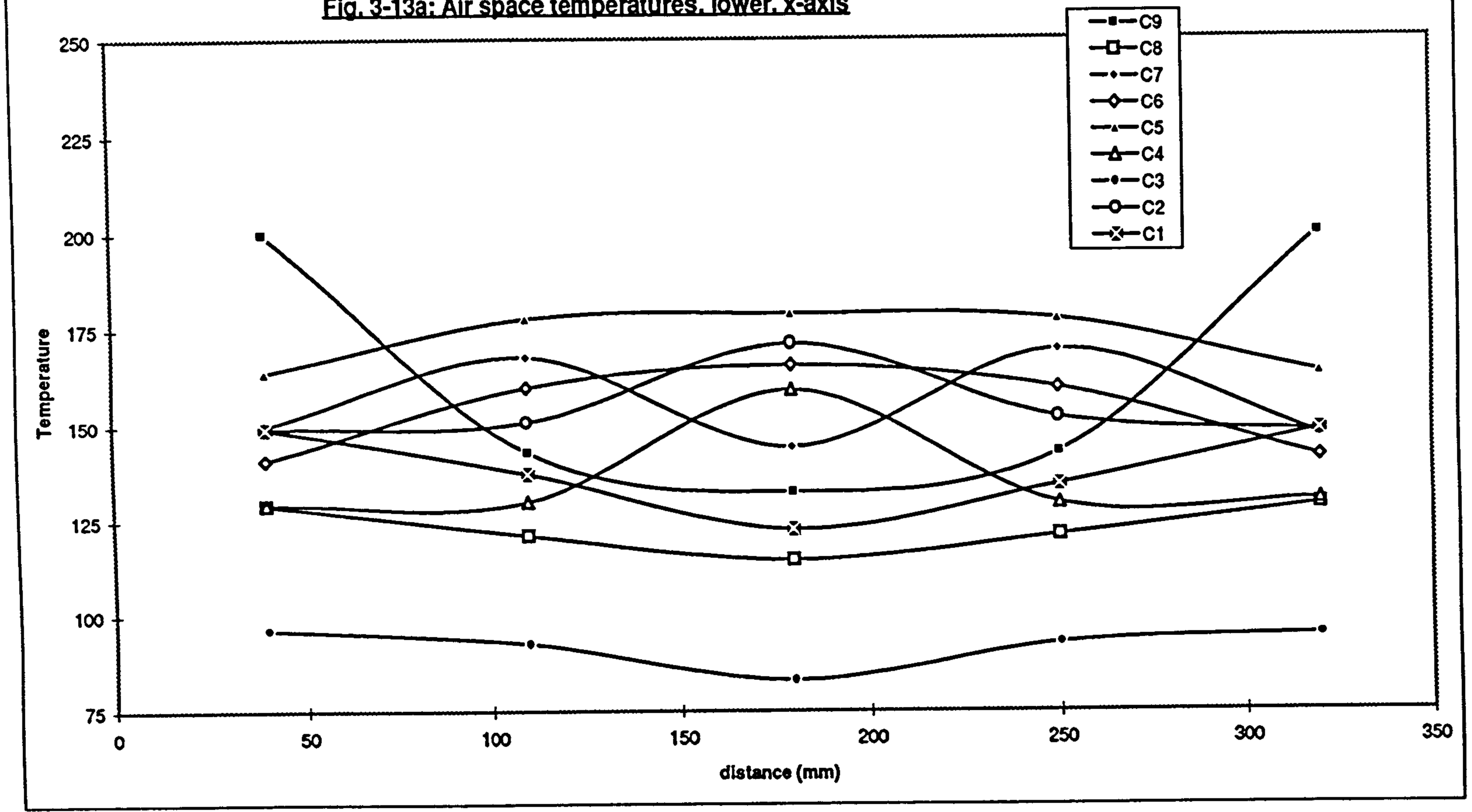

Fig. 3-13b: Lower air space temperatures (x-axis) C3,4,5 & 6

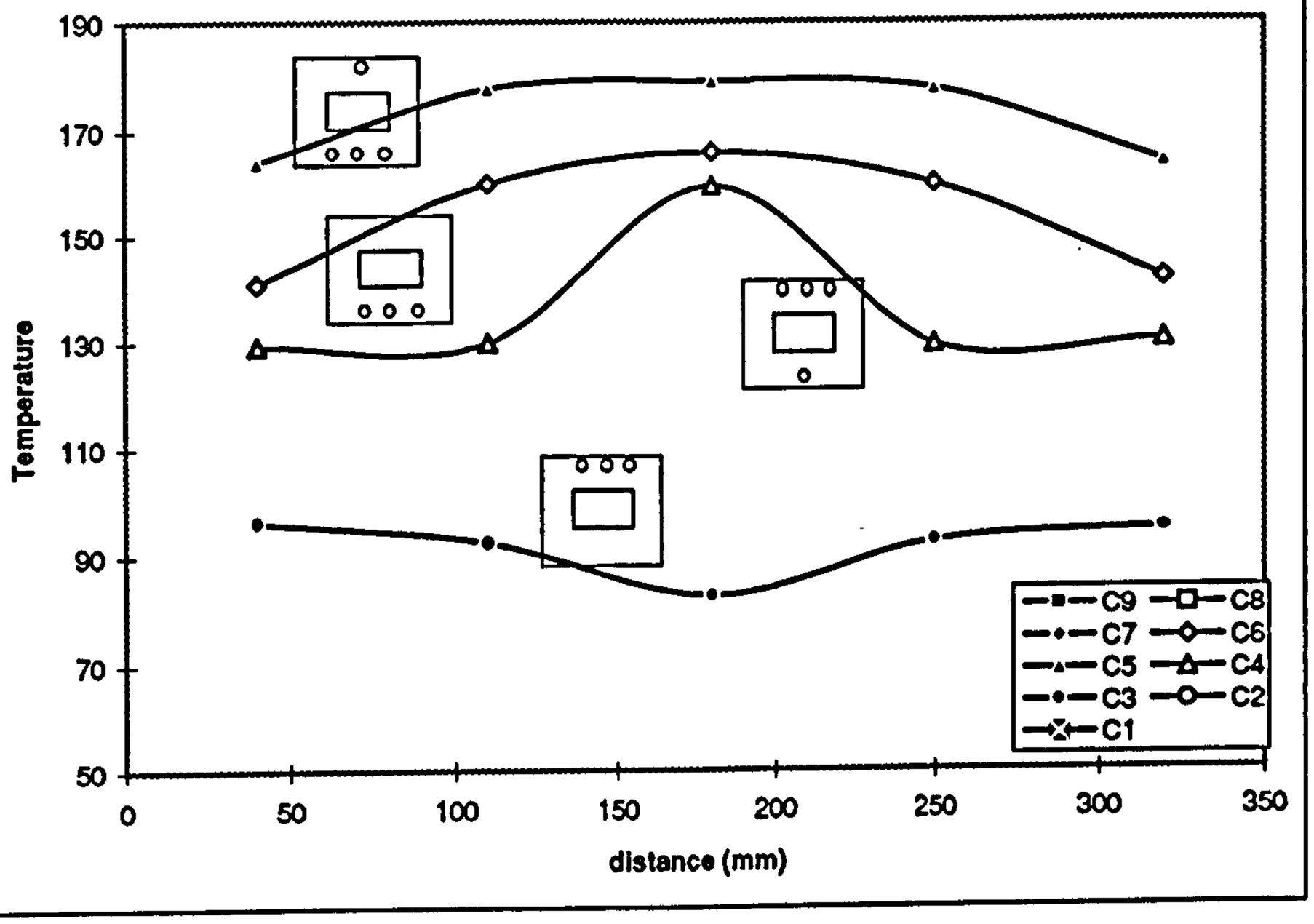

Fig. 3-13c: Lower air space temperatures (x-axis) C1,2,7,8 & 9

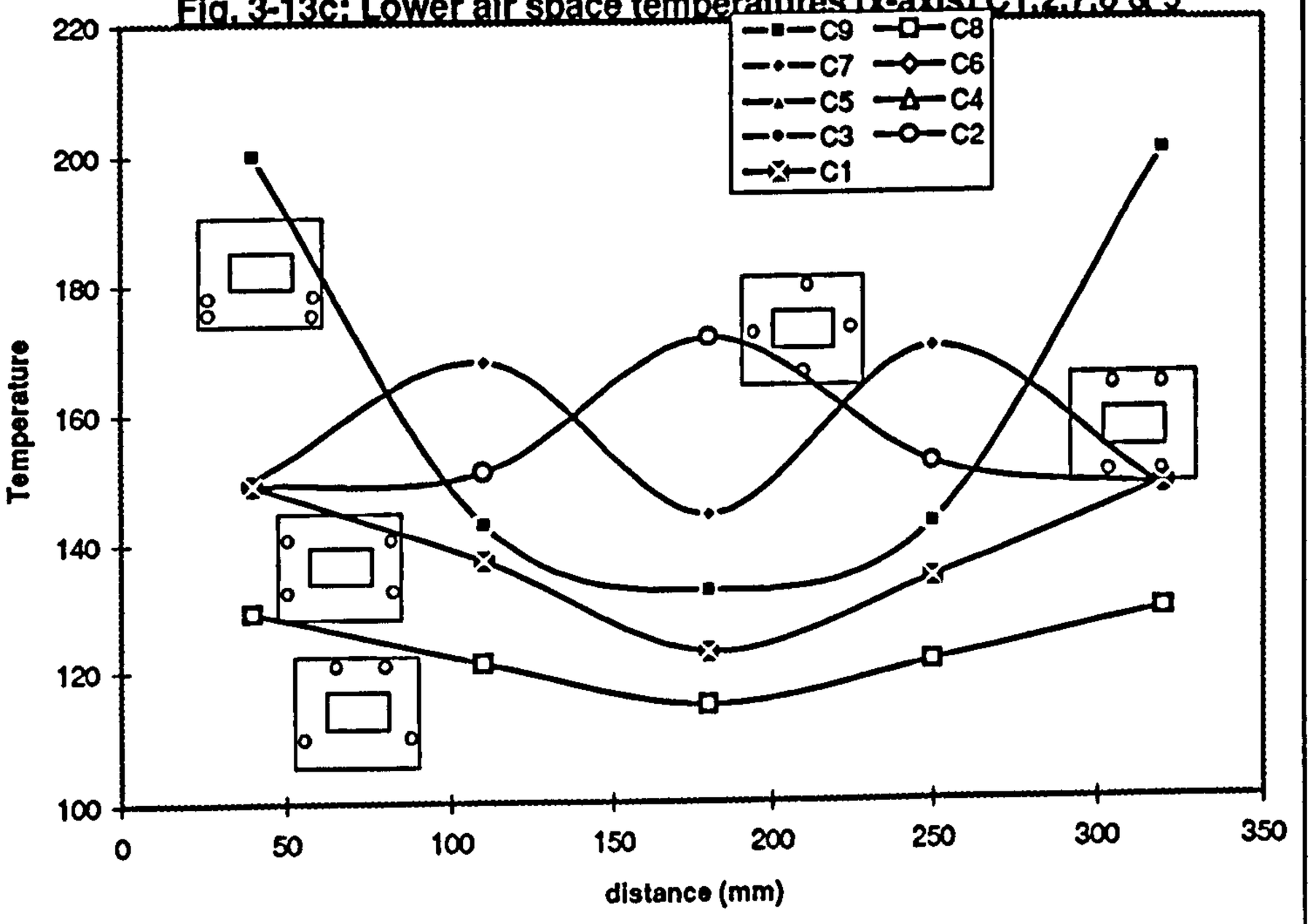

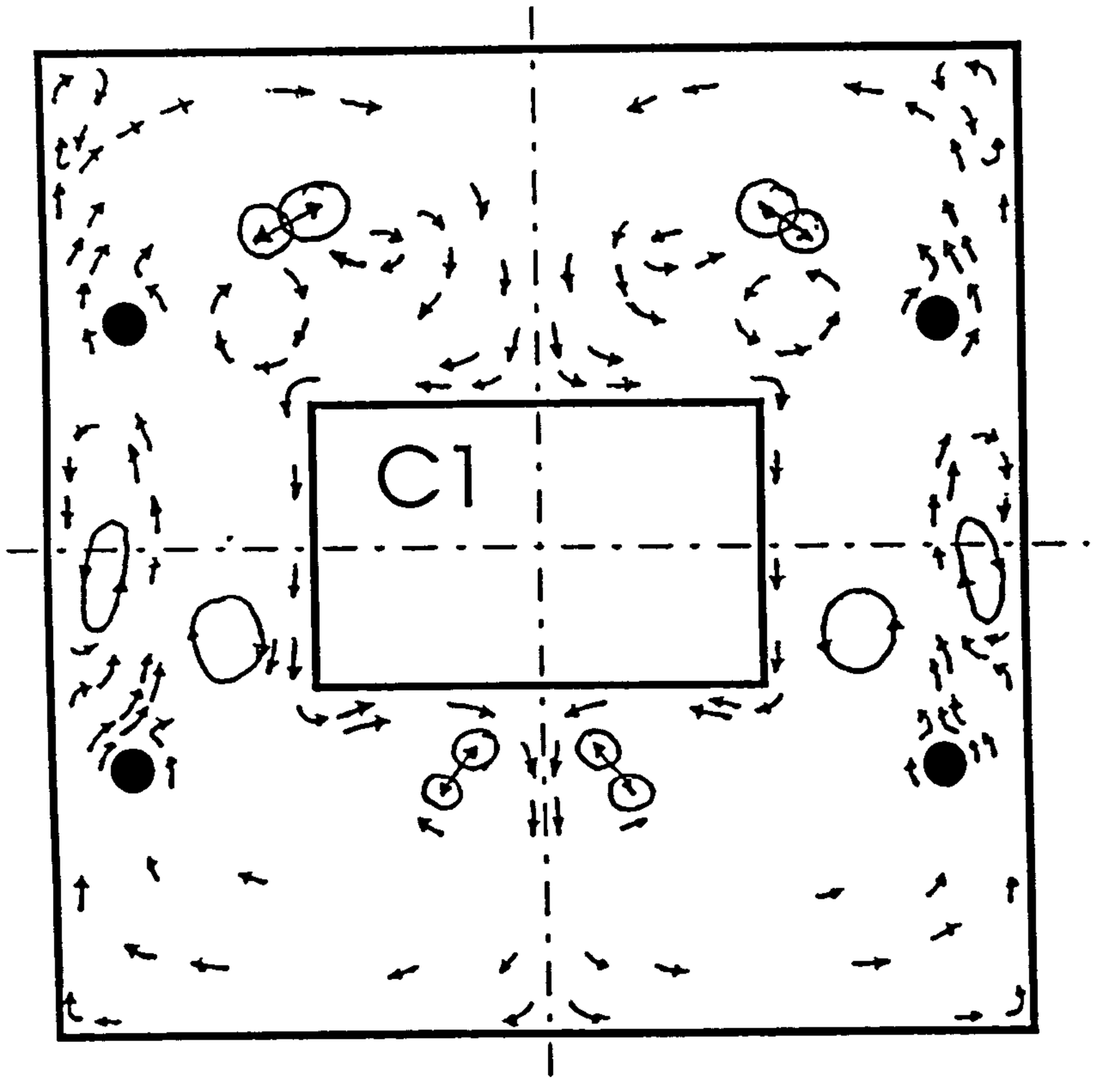

Fig. 3-14a Flow visualisation, C1.

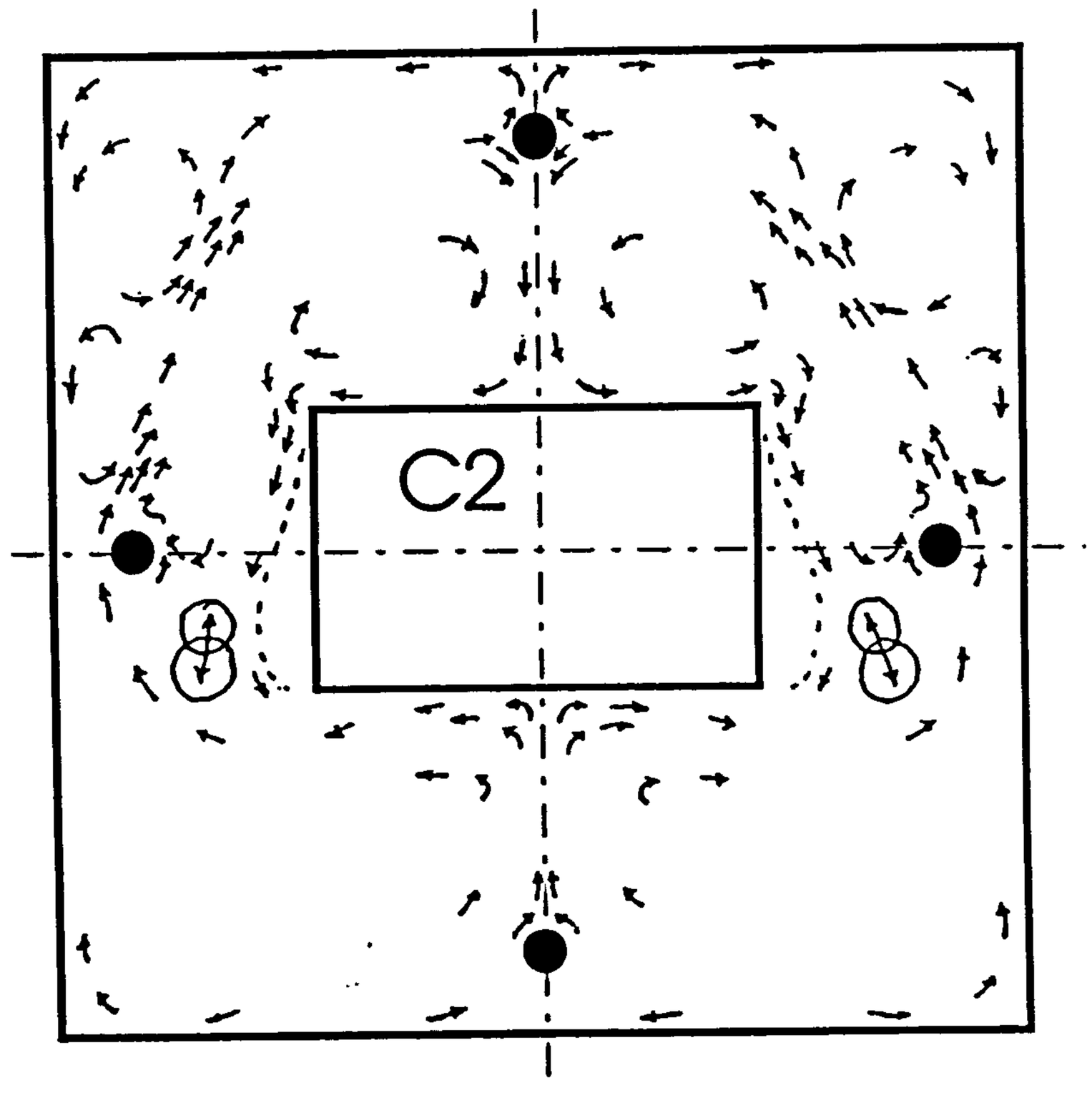

Fig. 3-14b Flow visualisation, C2

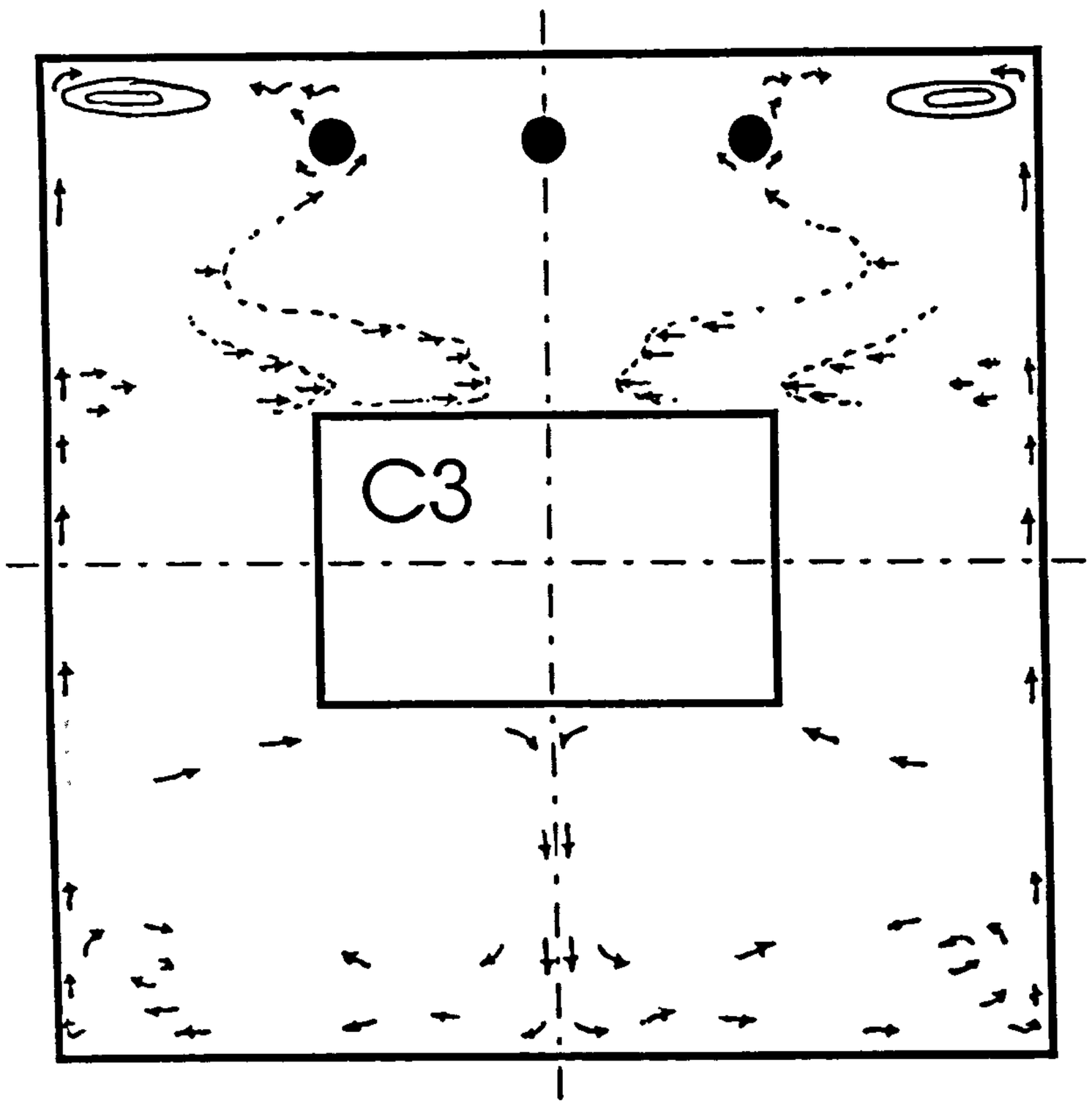

Fig. 3-14c Flow visualisation, C3.

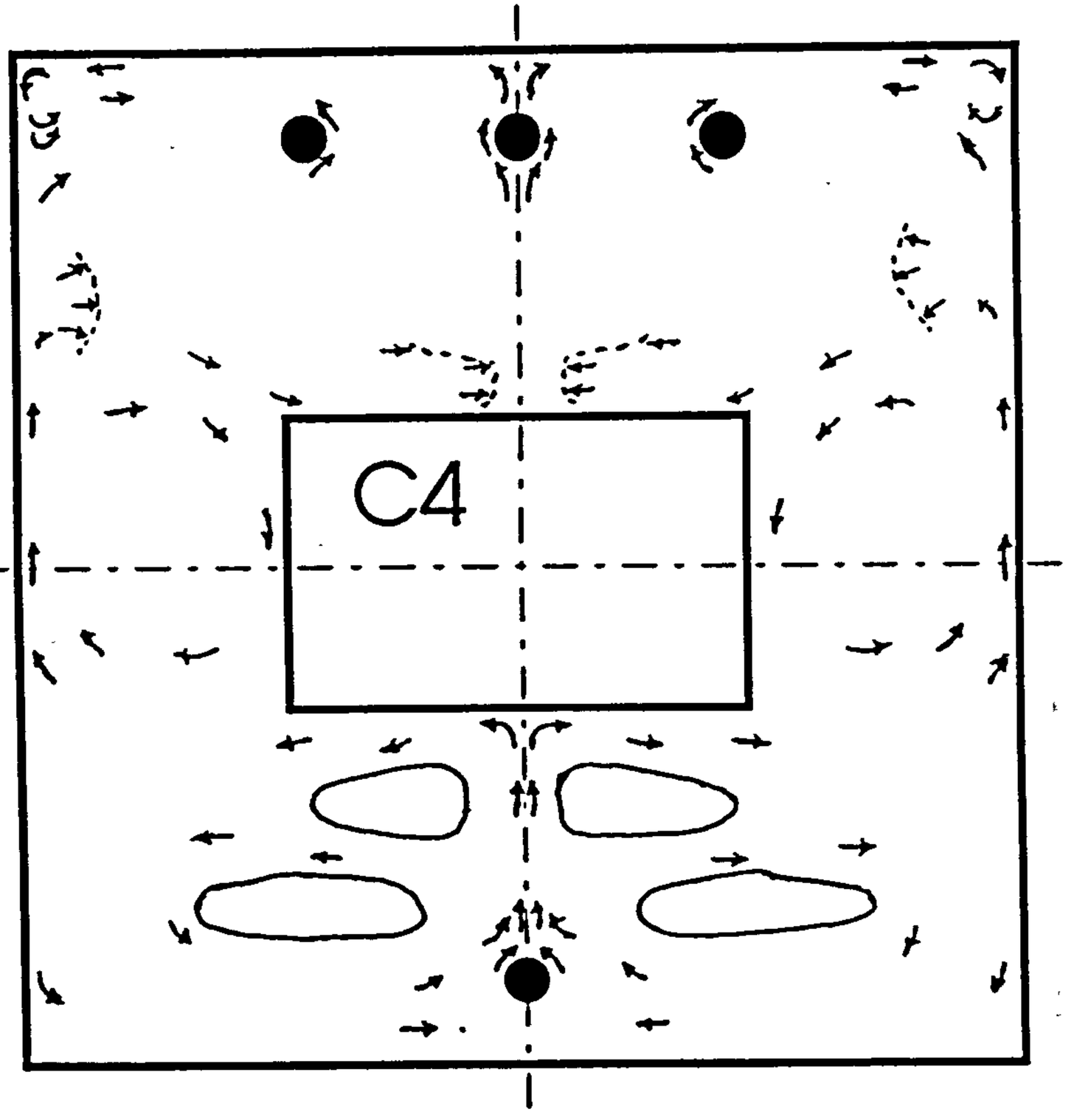

Fig. 3-14d Flow visualisation, C4

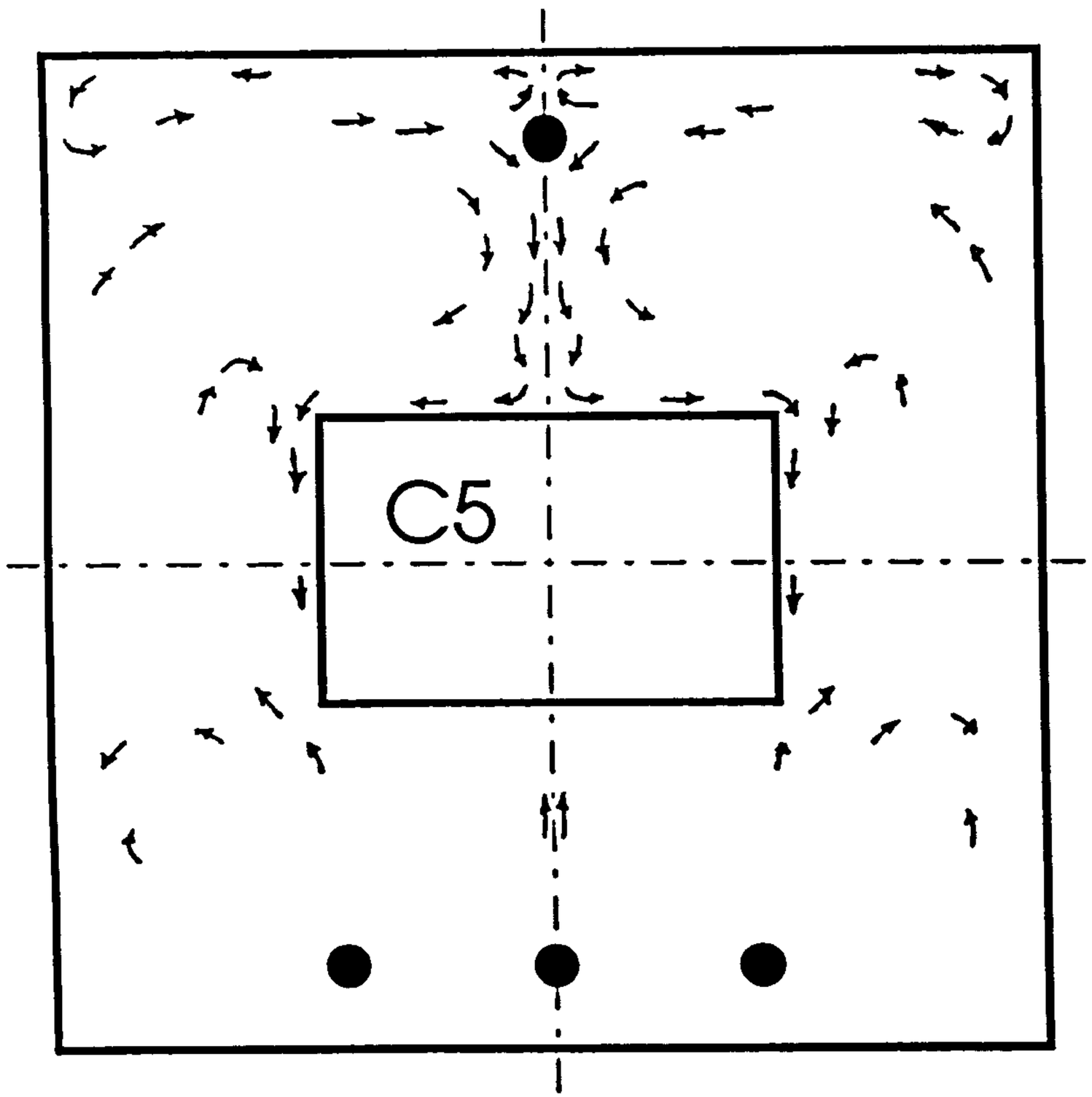

Fig. 3-14e Flow visualisation, C5.

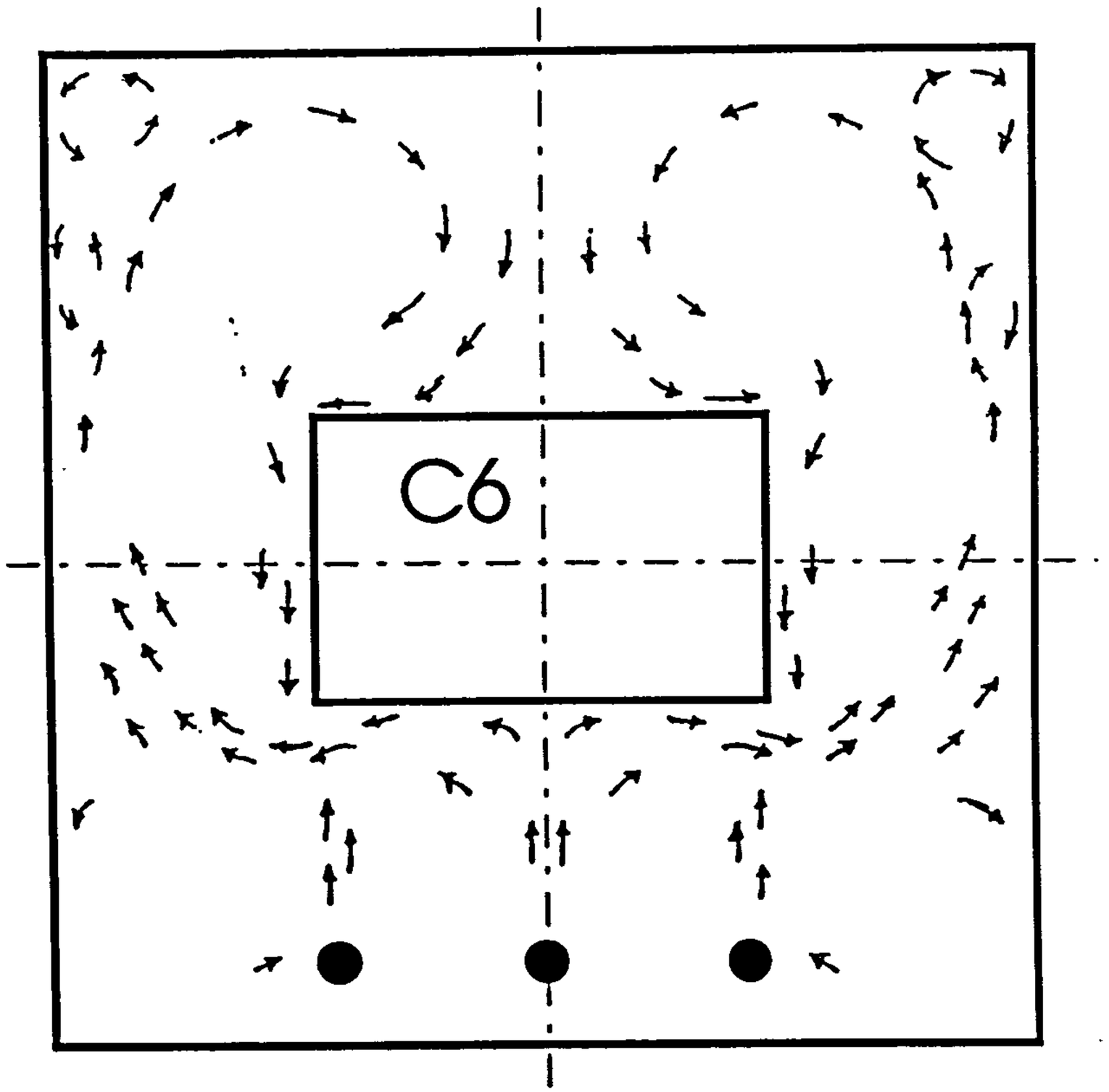

Fig. 3-14f Flow visualisation, C6

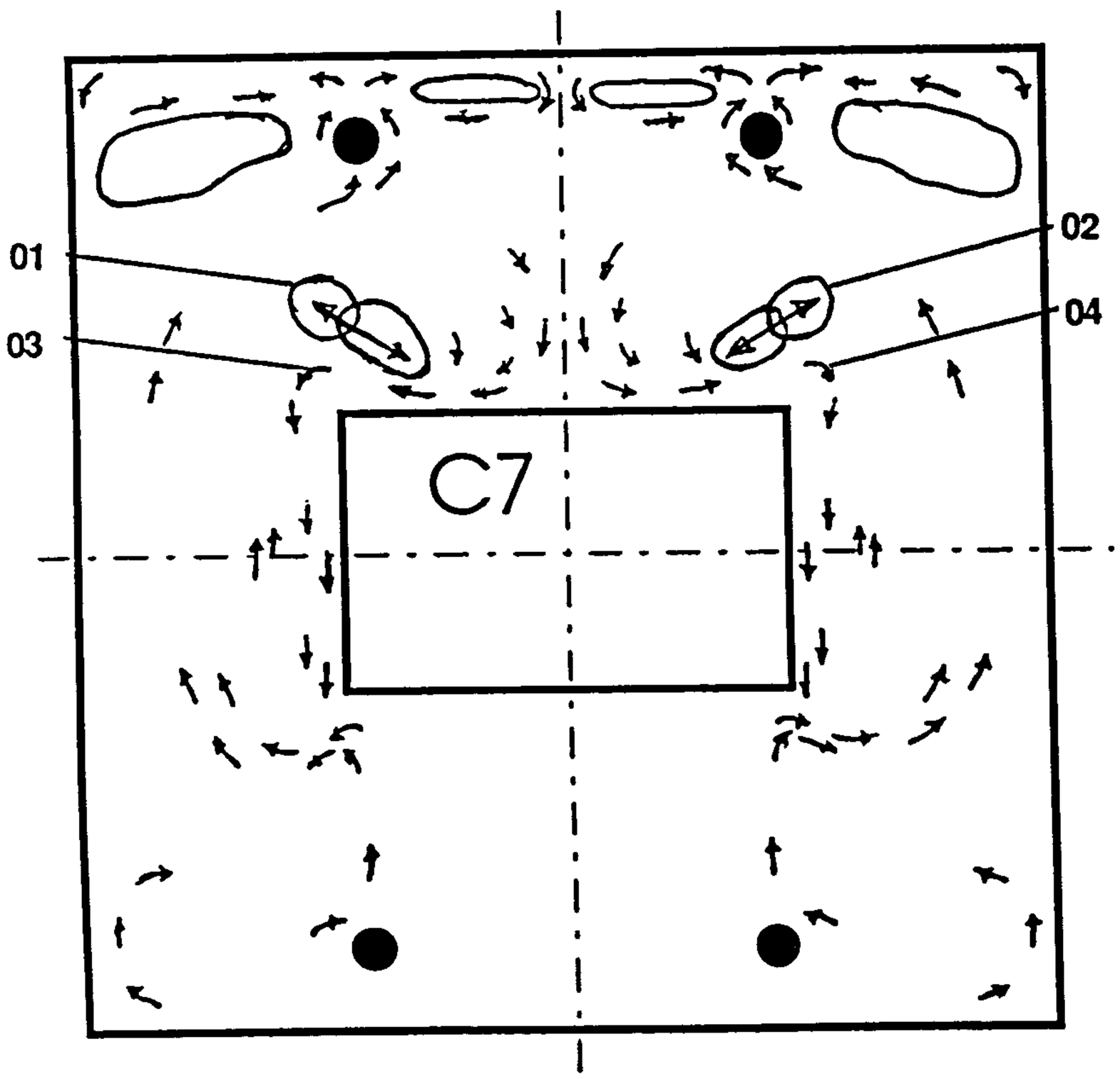

Fig. 3-14g Flow visualisation, C7

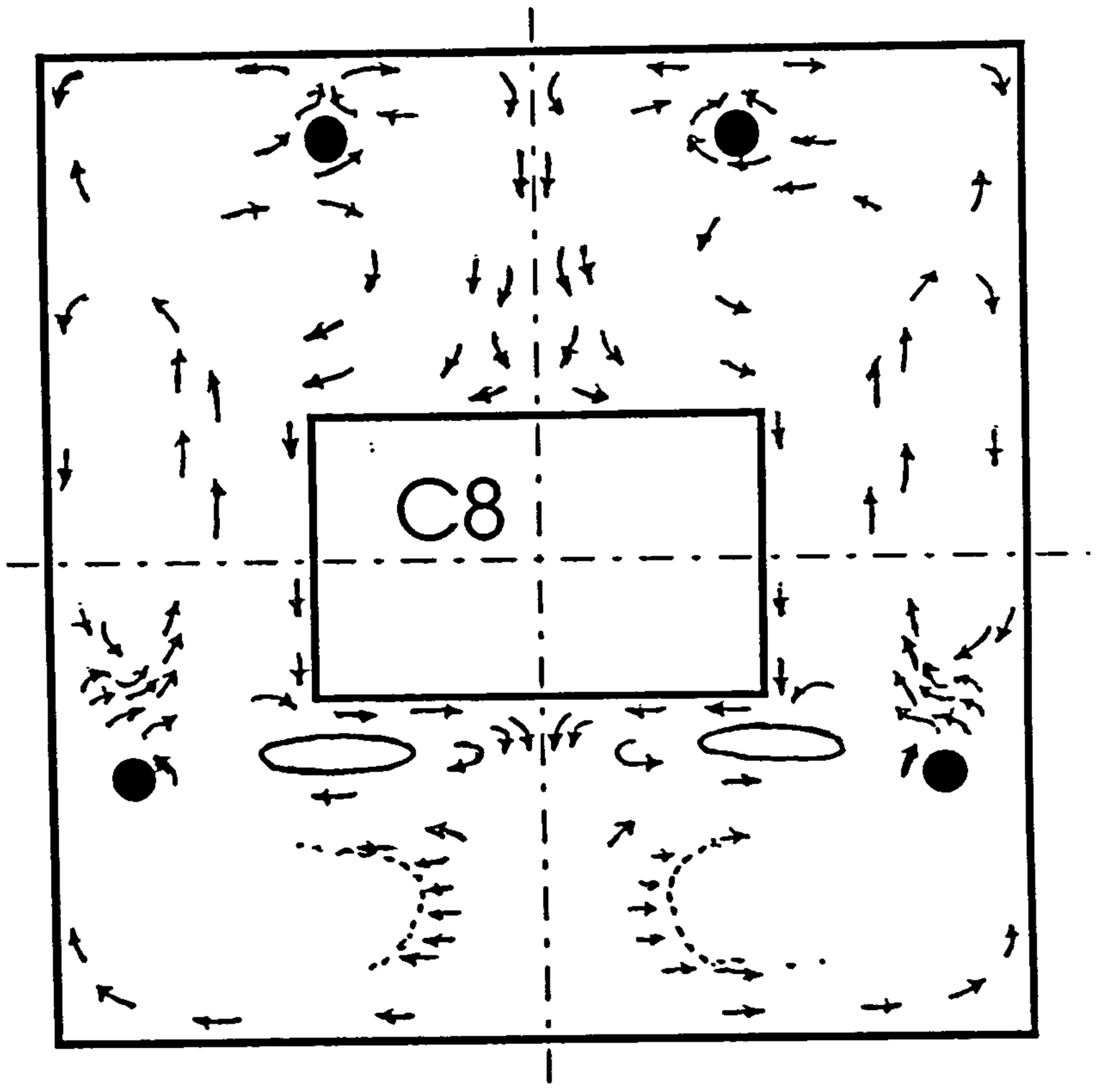

Fig. 3-14h Flow visualisation, C8

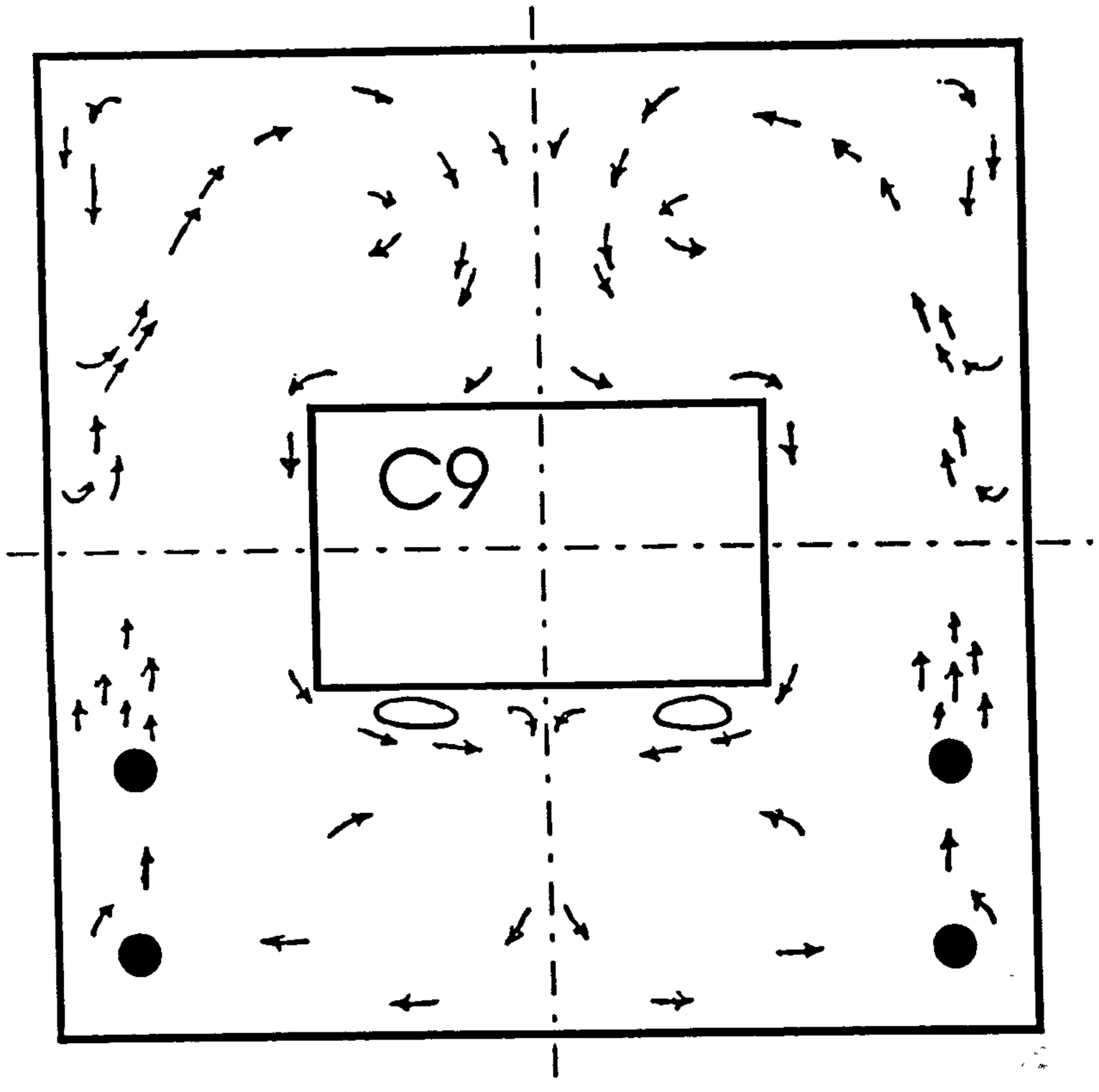

Fig. 3-14i Flow visualisation, C9.

Fig. 3-15. Flow visualisation, C3.

a

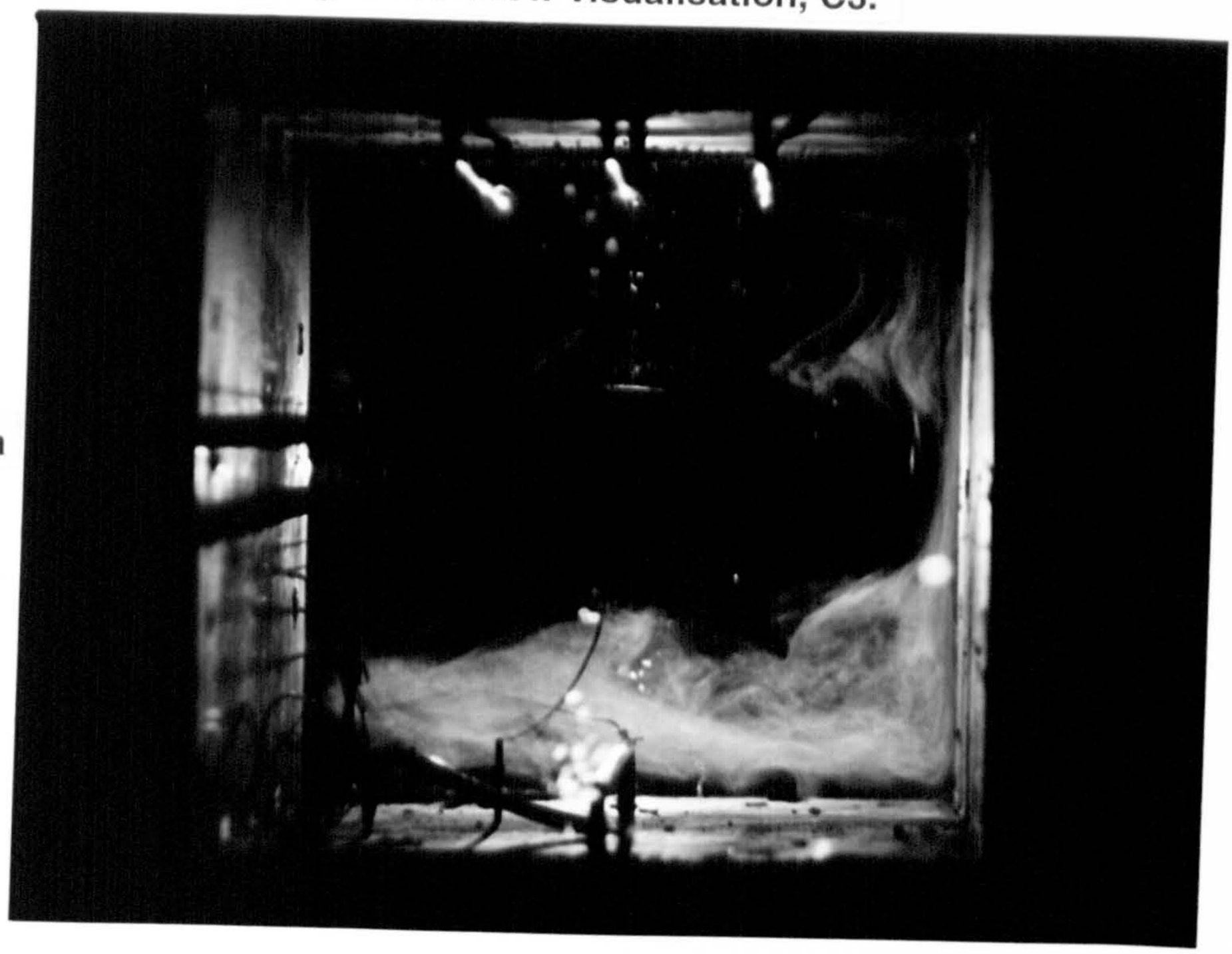

b

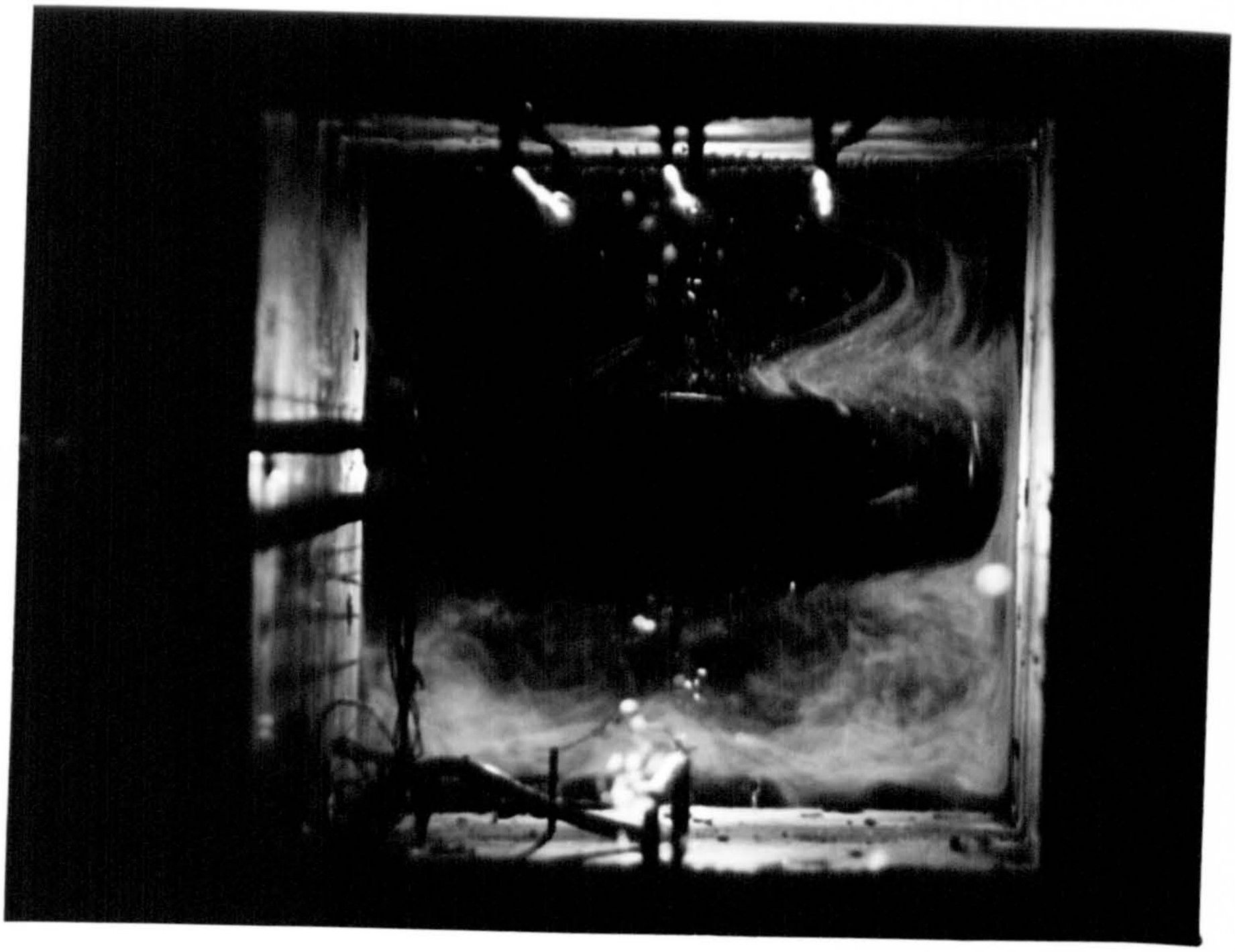

Fig. 3-15. Flow visualisation, C4.

c

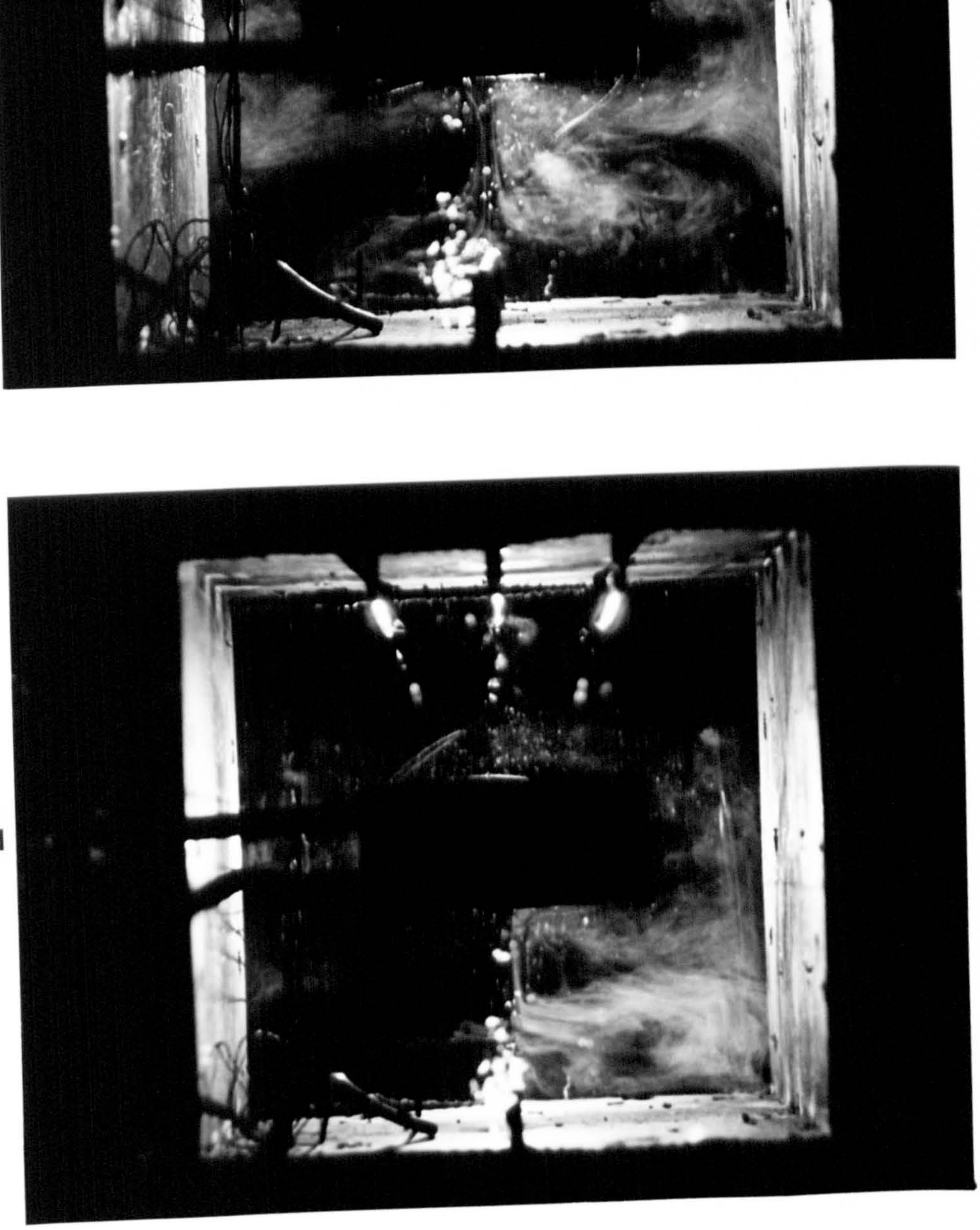

d

Fig. 3-15. Flow visualisation, C9.

e

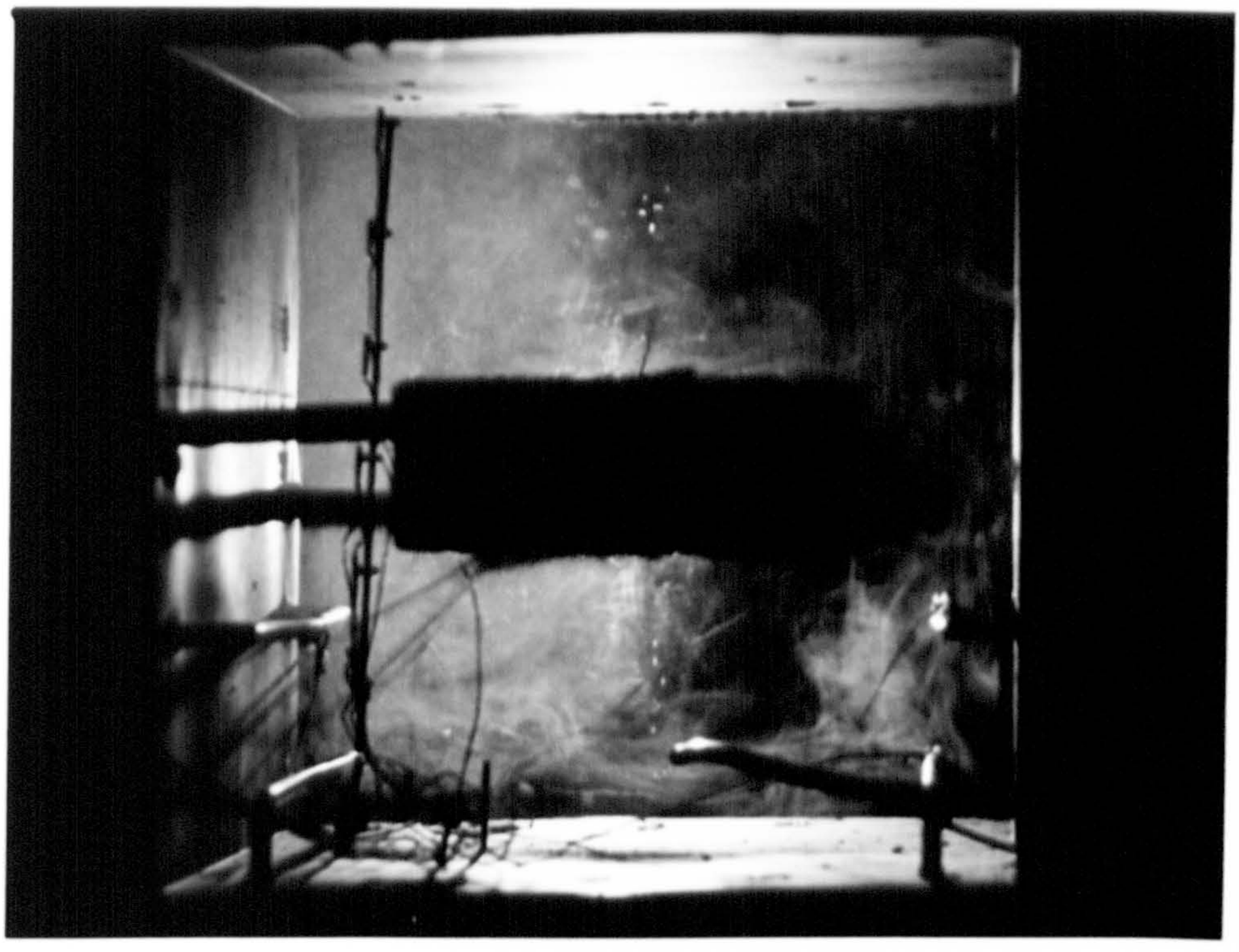

f

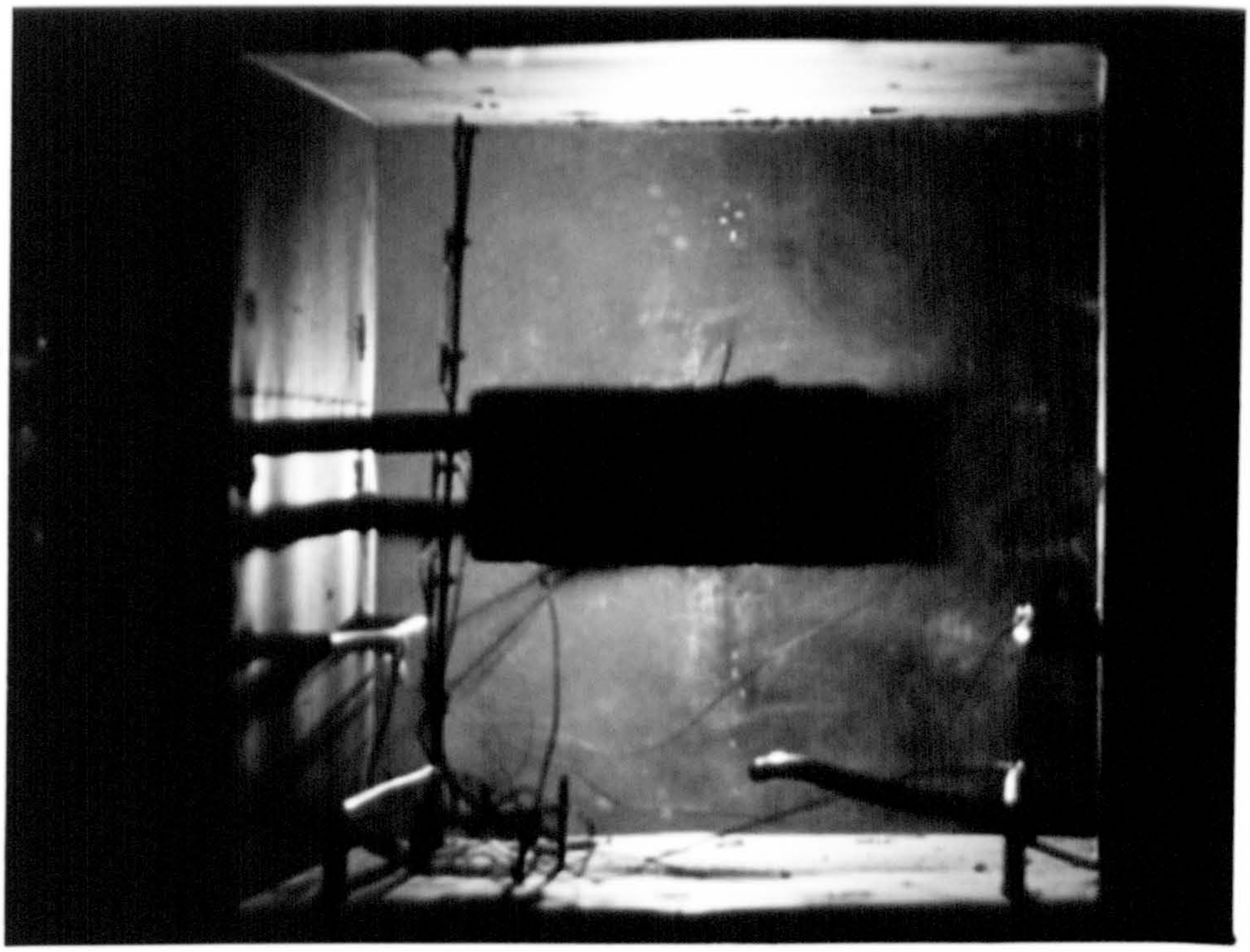

Fig. 3-16a: Enclosure wall temperatures, sidewall, y-axis

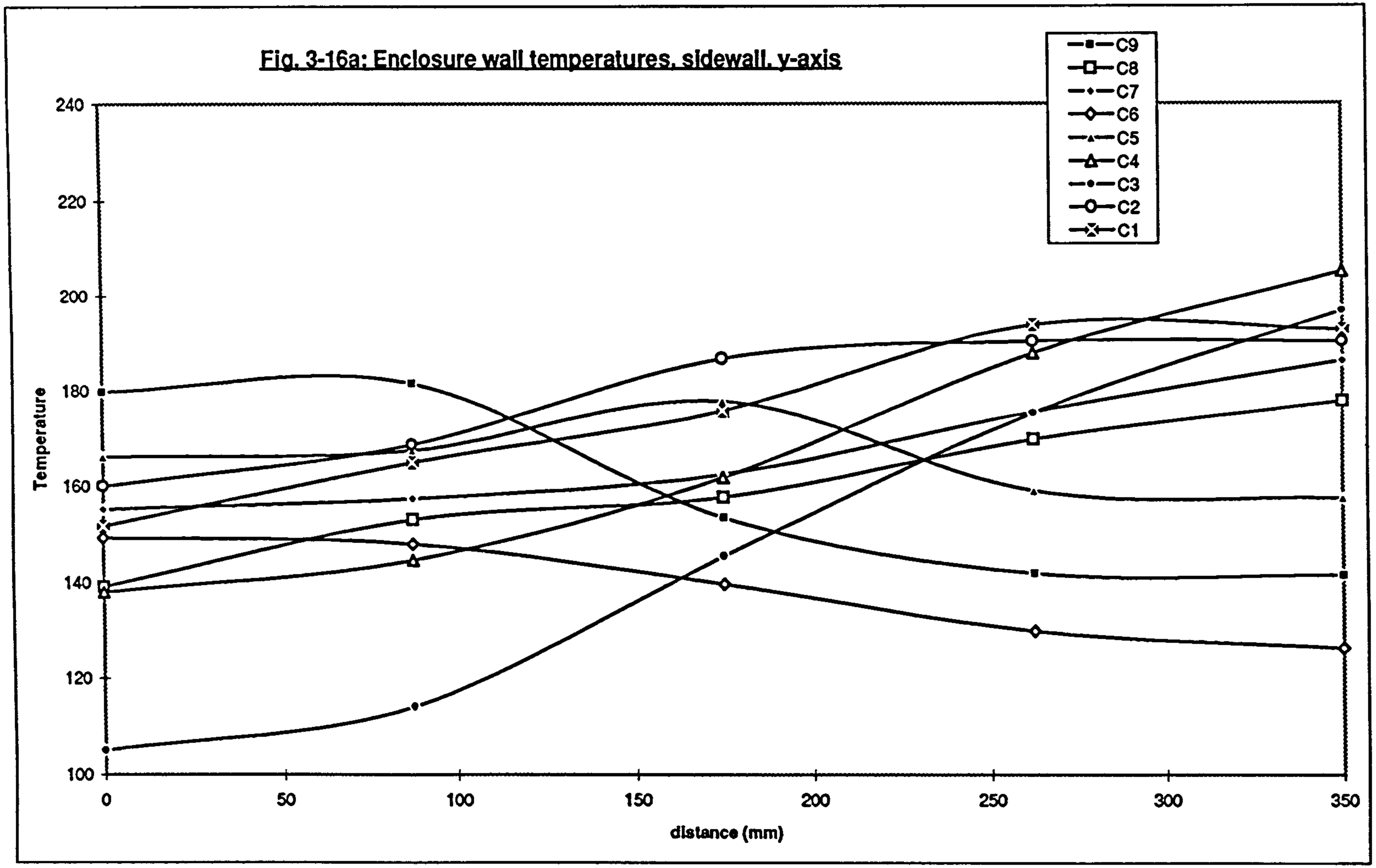

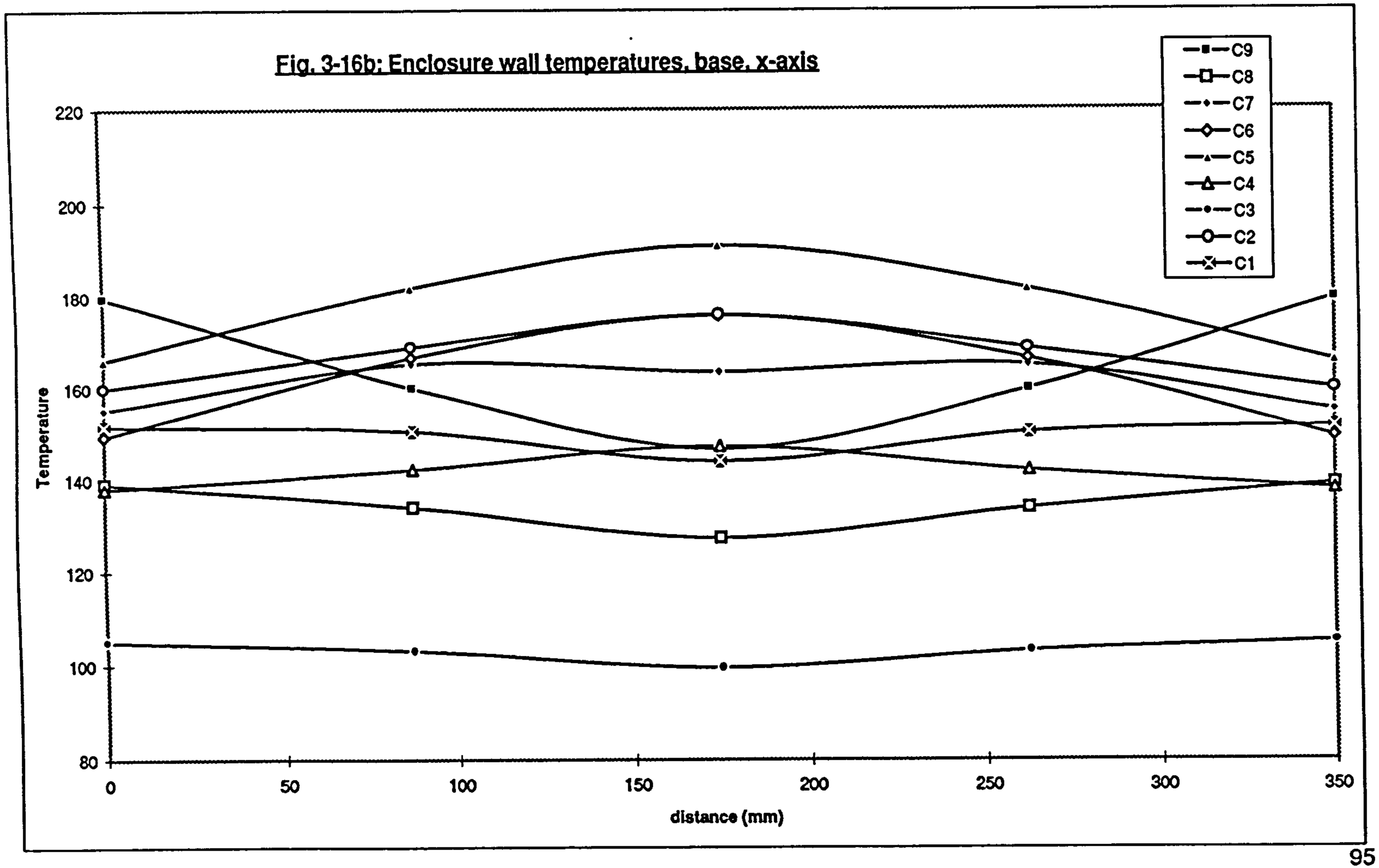
Fig. 3-16b: Enclosure wall temperatures, base, x-axis
C9
C8
C7
C6
C5
C4
C3
C2
C1
220
200
180
160
140
120
100
80
Temperature
0
50
100
150
200
250
300
350
distance (mm)

Fig. 3-16c: Enclosure wall temperatures, roof, y-axis

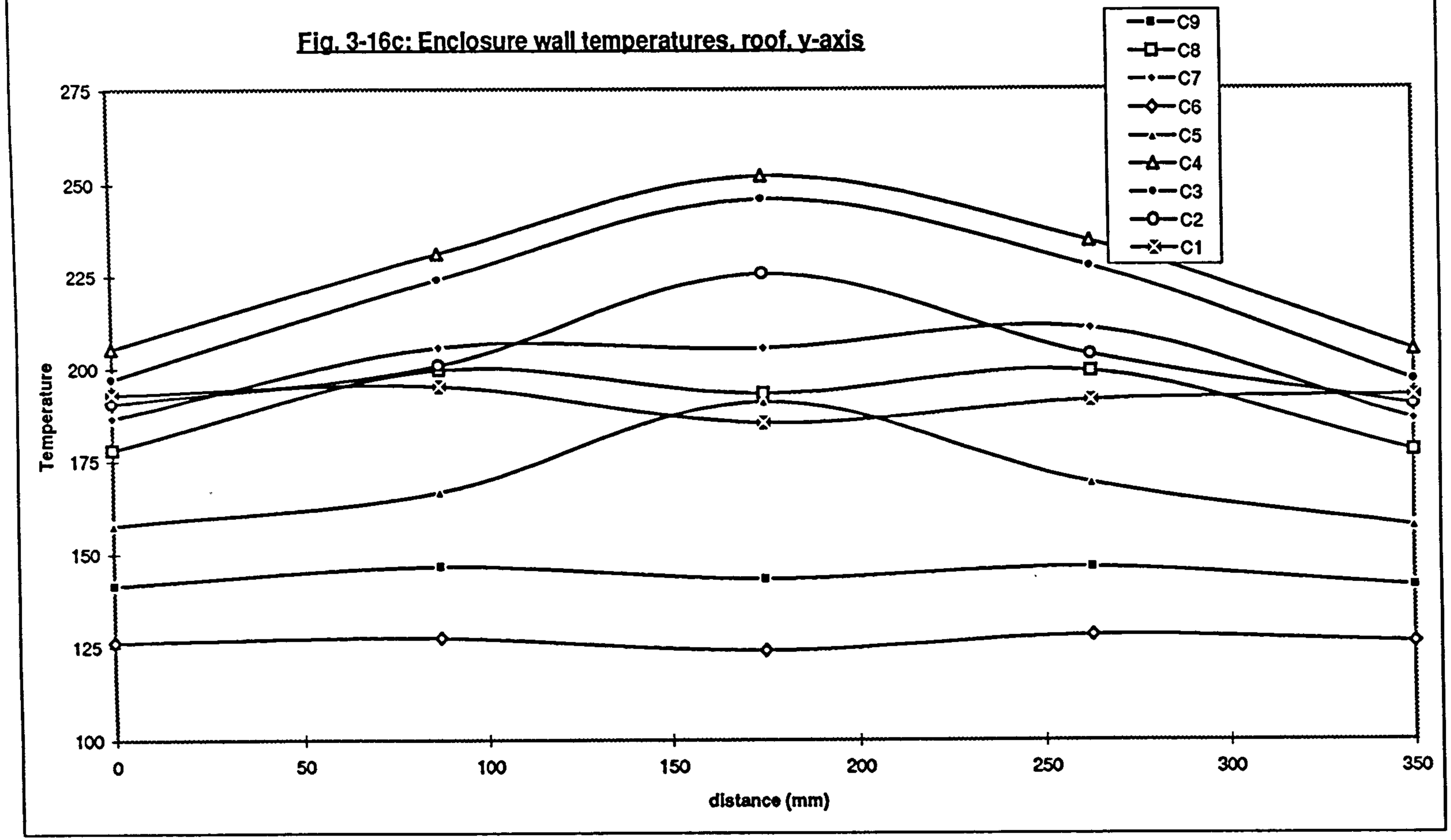

Fig. 3-17a: Enclosure wall temperatures, sidewall, z-axis

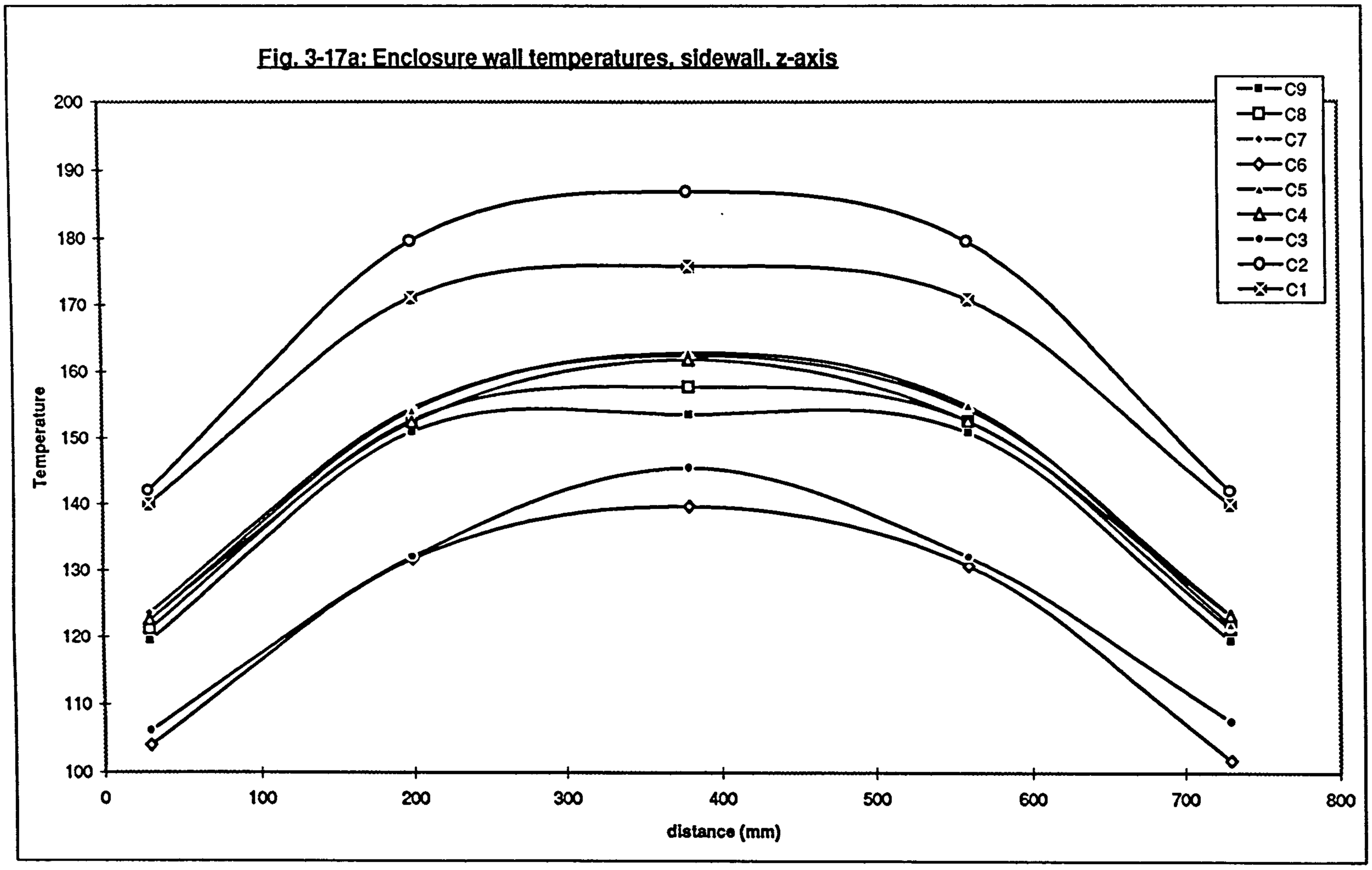

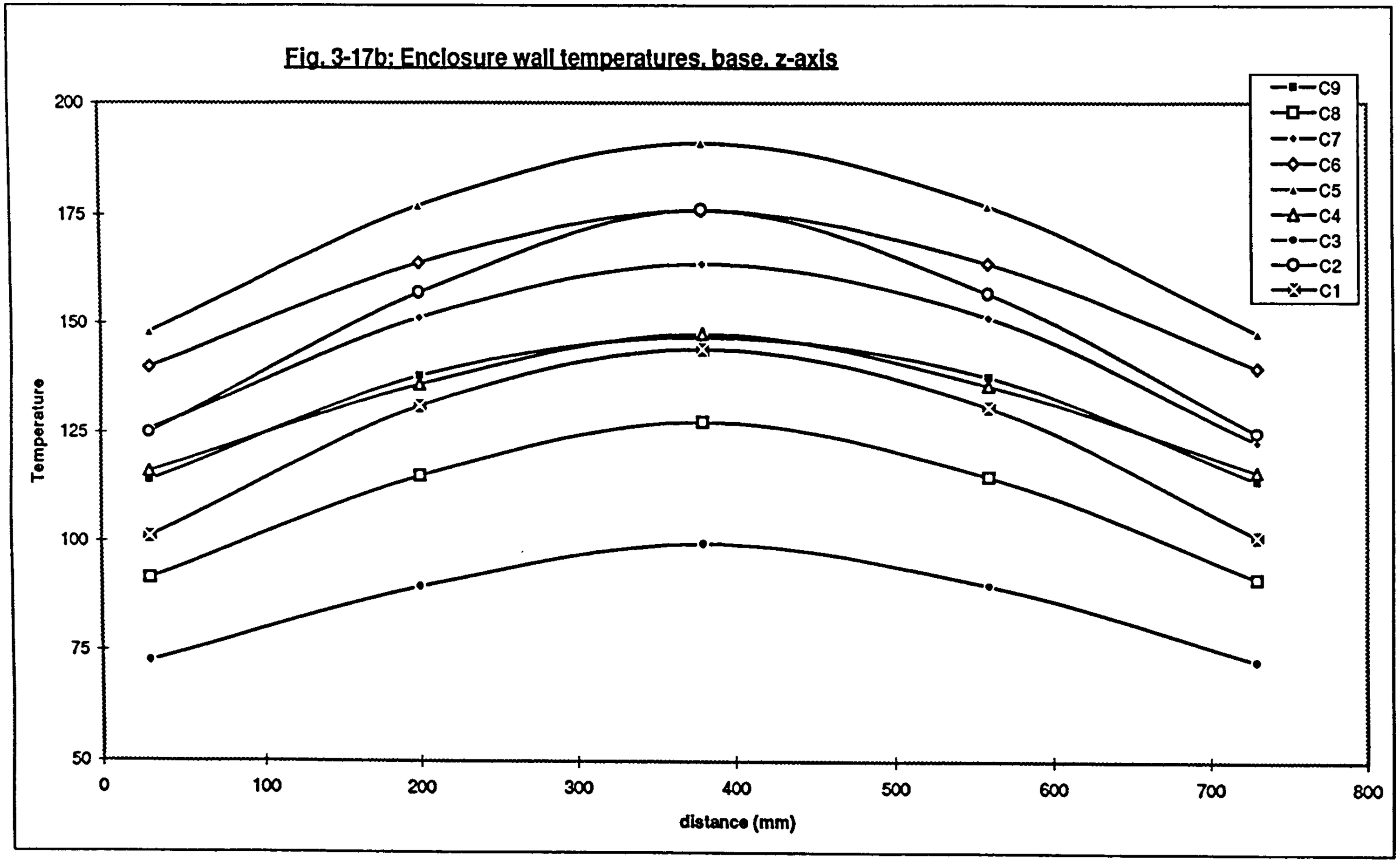
Fig. 3-17b: Enclosure wall temperatures, base, z-axis
C9
C8
C7
C6
C5
C4
C3
C2
C1
200
175
150
125
100
75
50
Temperature
0
100
200
300
400
500
600
700
800
distance (mm)

Fig. 3-17c: Enclosure wall temperatures, roof, z-axis

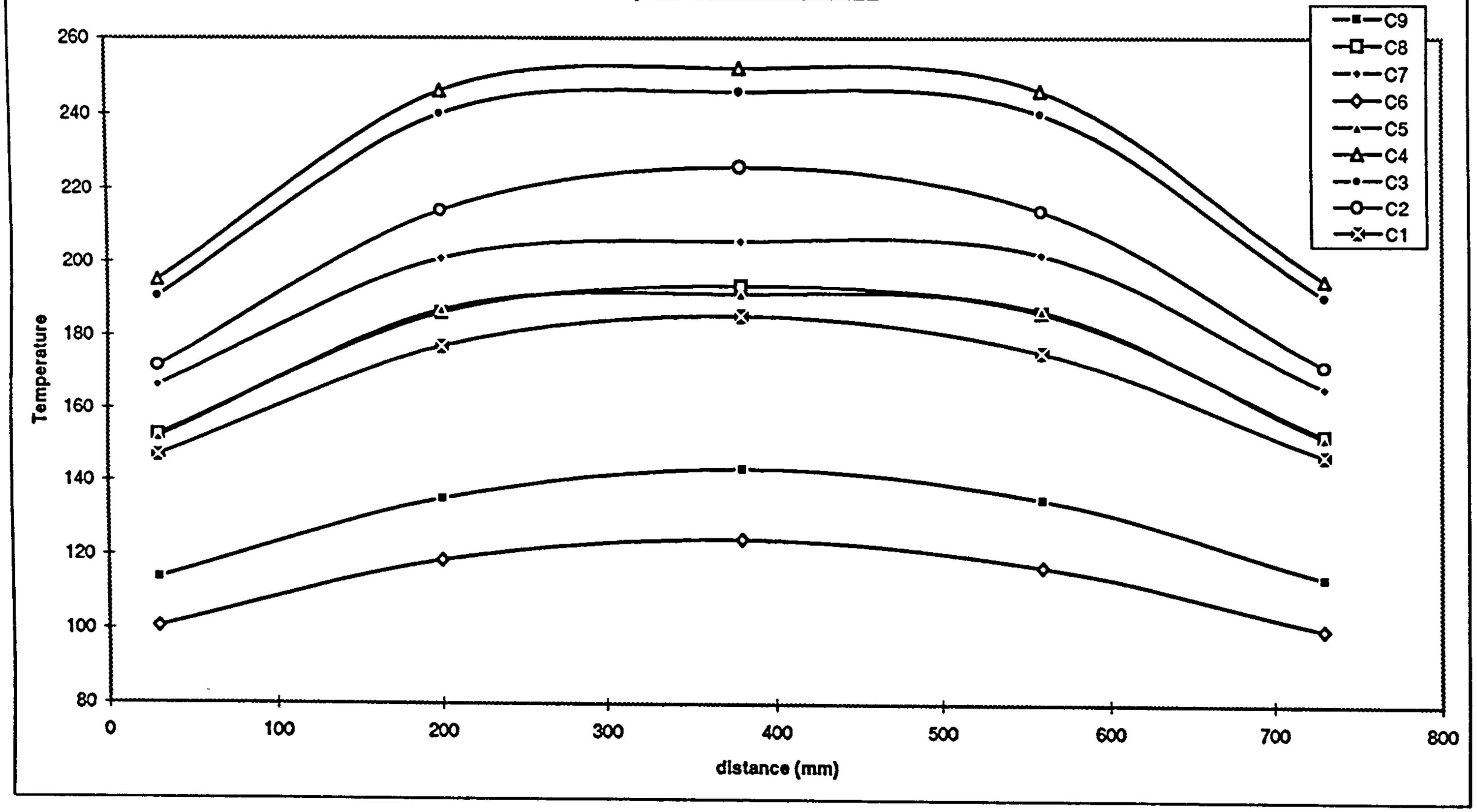

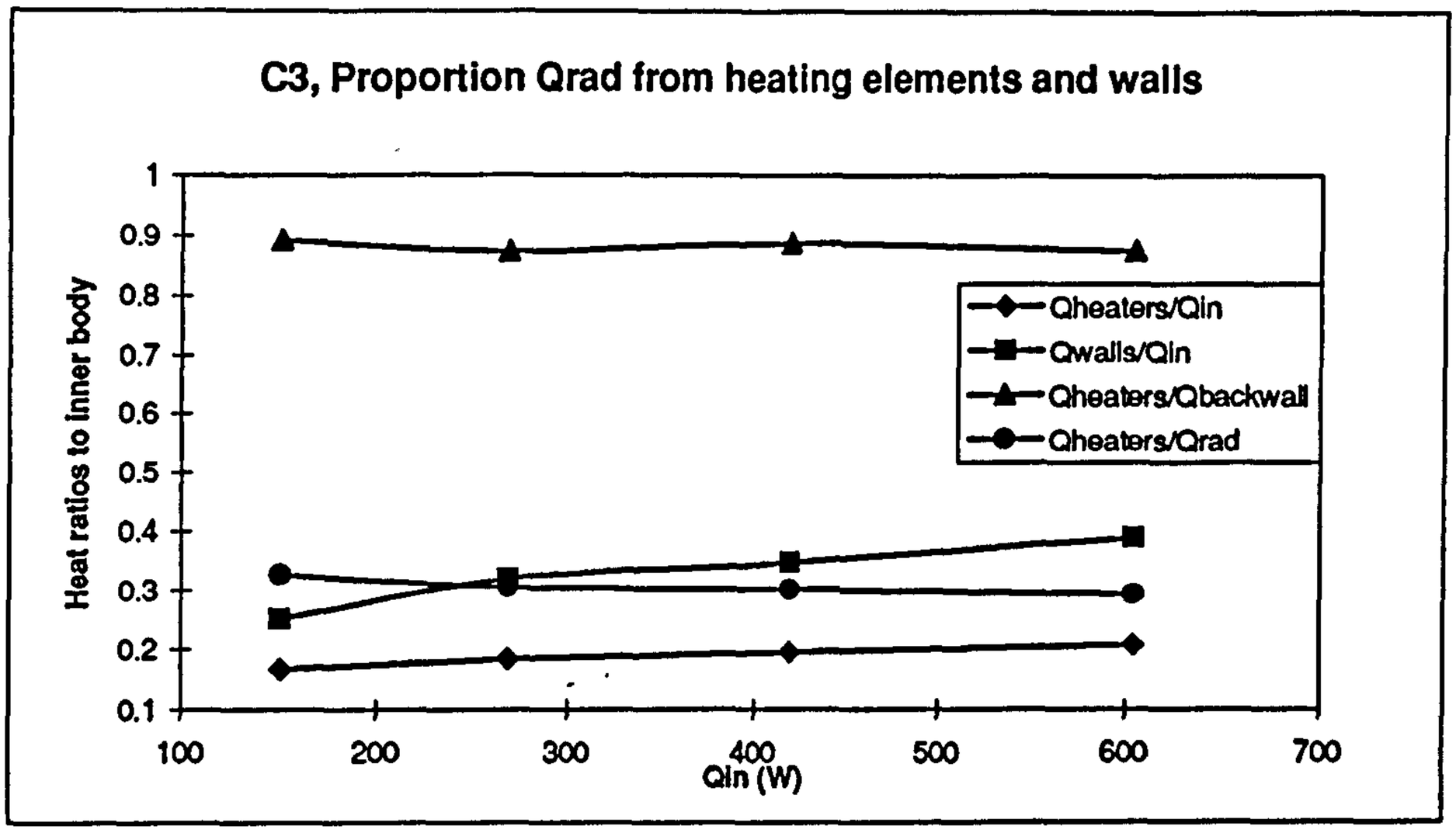
C3, Proportion Qrad from heating elements and walls
Heat ratios to inner body
1
0.9
0.8
0.7
0.6
0.5
0.4
0.3
0.2
0.1
100
200
300
400
500
600
700
Qin (W)
Qheaters/Qin
Qwalls/Qin
Qheaters/Qbackwall
Qheaters/Qrad

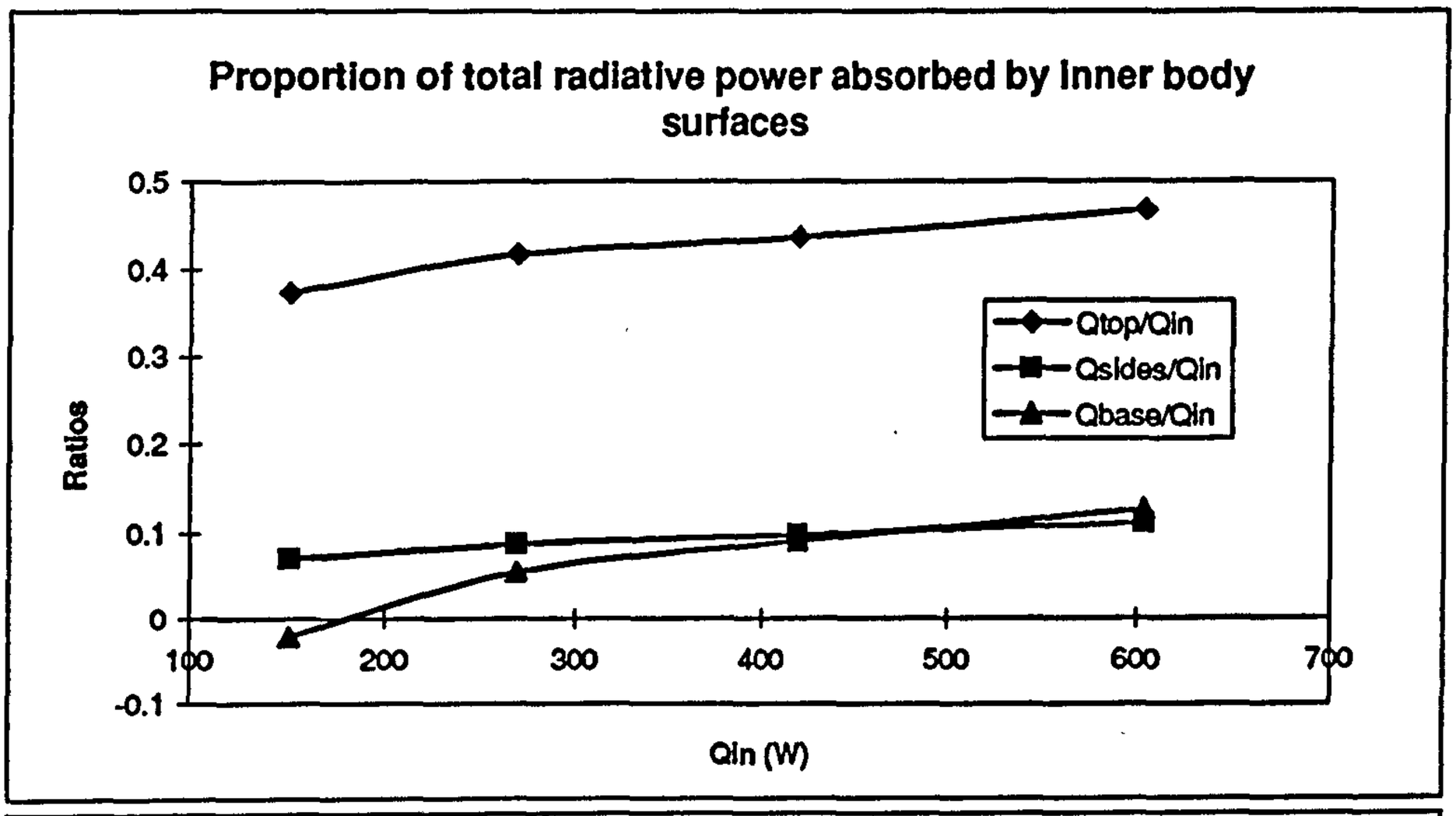
Proportion of total radiative power absorbed by inner body surfaces
Ratios
0.5
0.4
0.3
0.2
0.1
0
-0.1
100
200
300
400
500
600
700
Qin (W)
Qtop/Qin
Qsides/Qin
Qbase/Qin

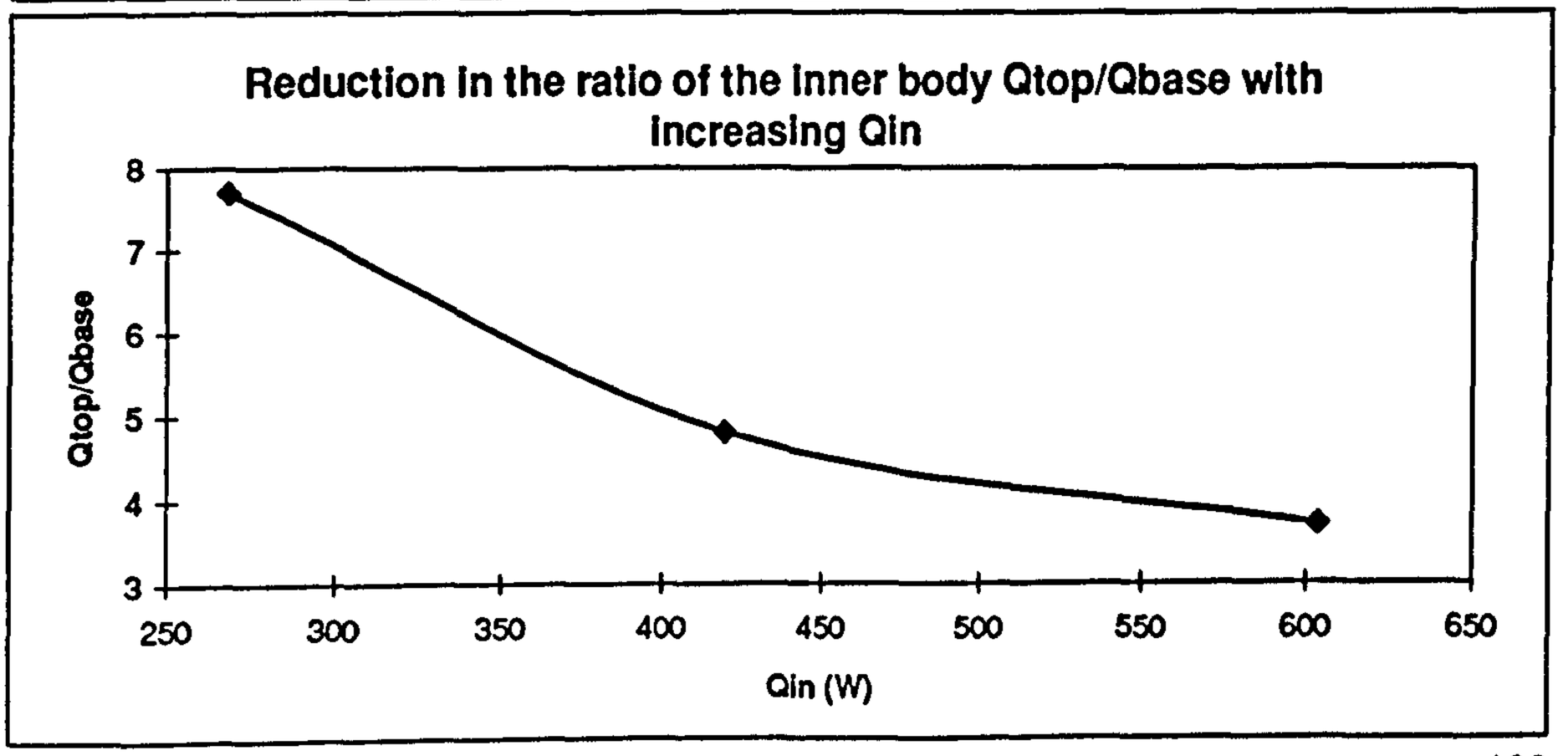
Reduction in the ratio of the inner body Qtop/Qbase with increasing Qin
Qtop/Qbase
8
7
6
5
4
3
250
300
350
400
450
500
550
600
650
Qin (W)

Fig. 3 - 18(a-c)

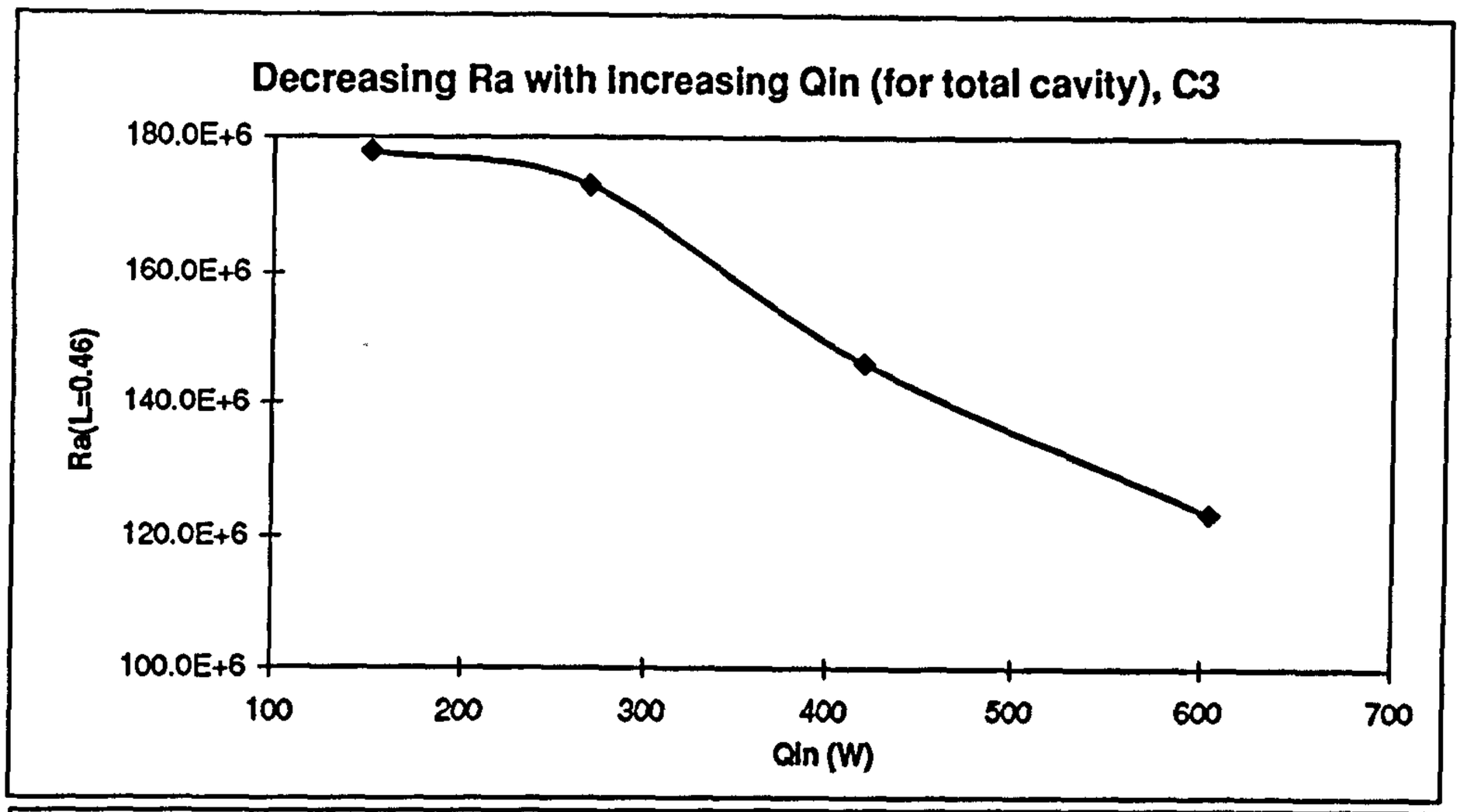
Decreasing Ra with Increasing Qin (for total cavity), C3
180.0E+6
160.0E+6
140.0E+6
120.0E+6
100.0E+6
Ra(L=0.46)
100
200
300
400
500
600
700
Qin (W)

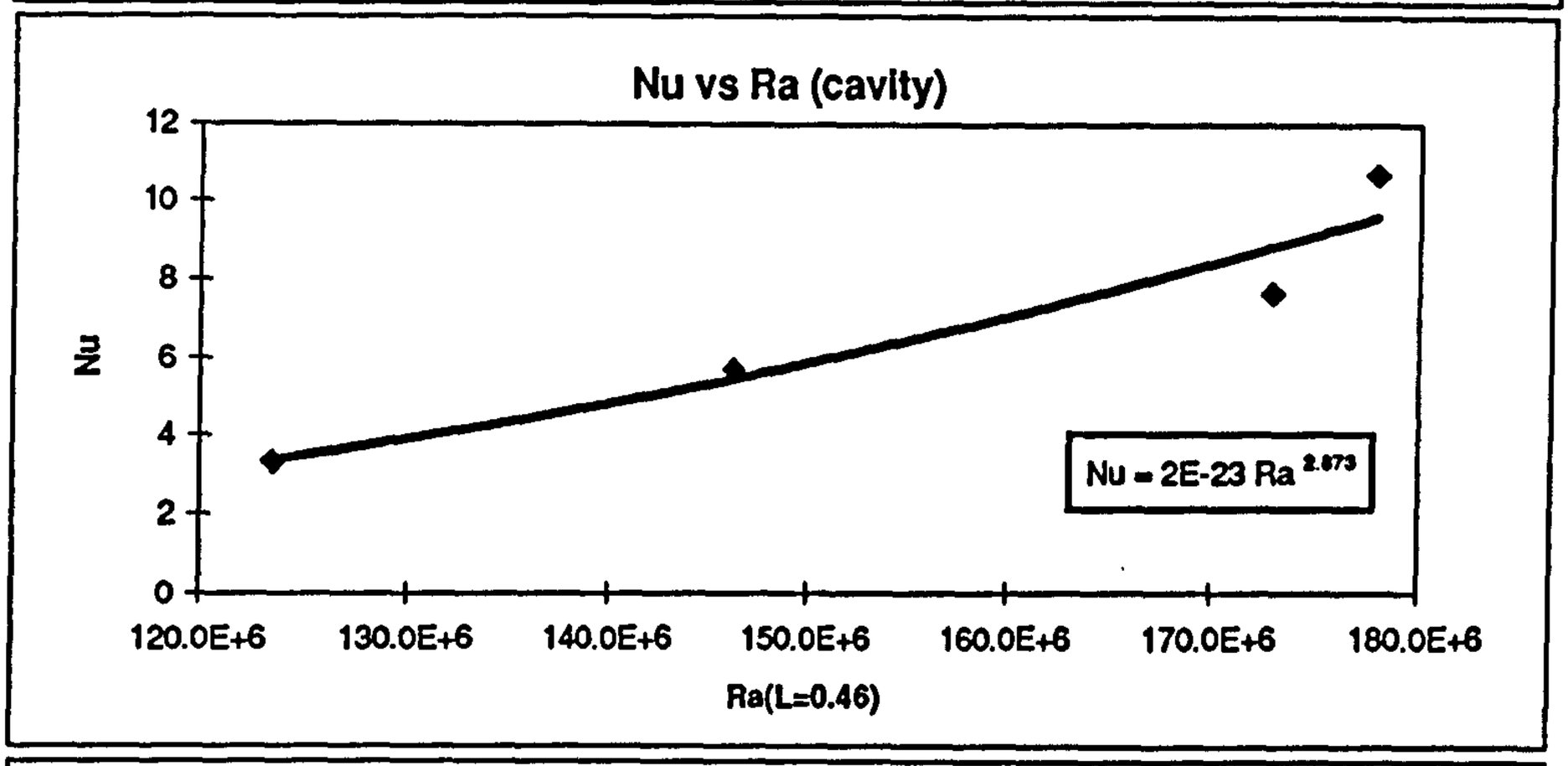
Nu vs Ra (cavity)
12
10
8
6
4
2
0
Nu
Nu = 2E-23 Ra 2.673
120.0E+6
130.0E+6
140.0E+6
150.0E+6
160.0E+6
170.0E+6
180.0E+6
Ra(L=0.46)

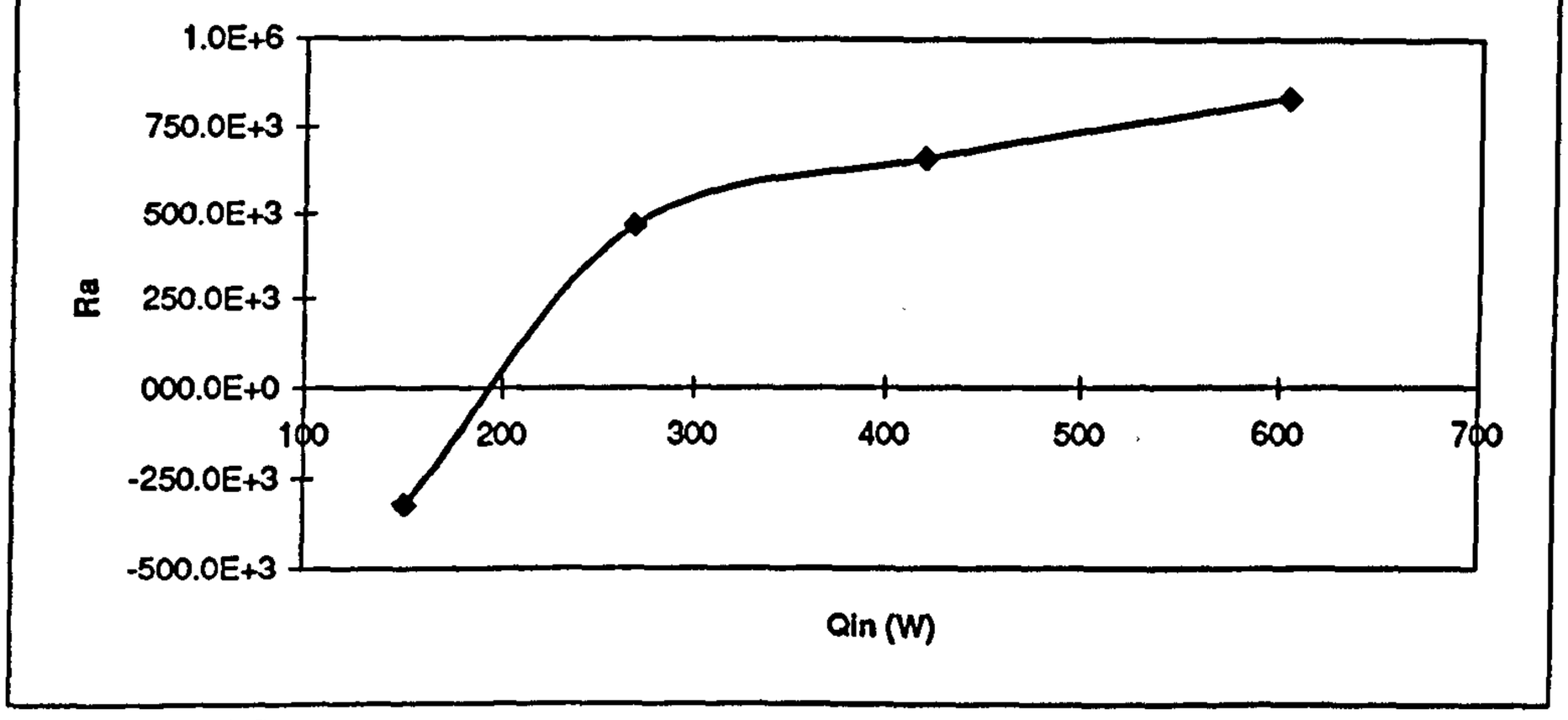
Increase of Ra with power input (C3, lower space)
1.0E+6
750.0E+3
500.0E+3
250.0E+3
000.0E+0
-250.0E+3
-500.0E+3
Ra
100
200
300
400
500
600
700
Qin (W)

Fig. 3 - 18(d-f)

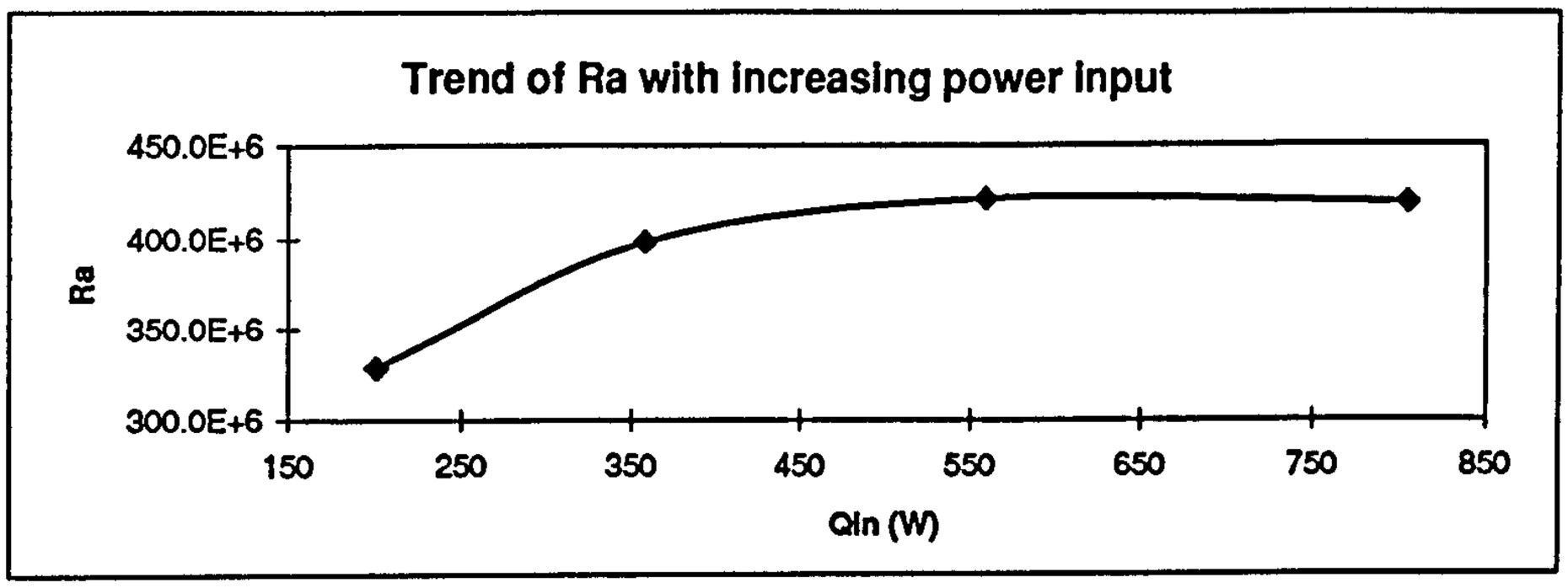
Trend of Ra with increasing power input
450.0E+6
400.0E+6
350.0E+6
300.0E+6
Ra
150
250
350
450
550
650
750
850
Qin (W)

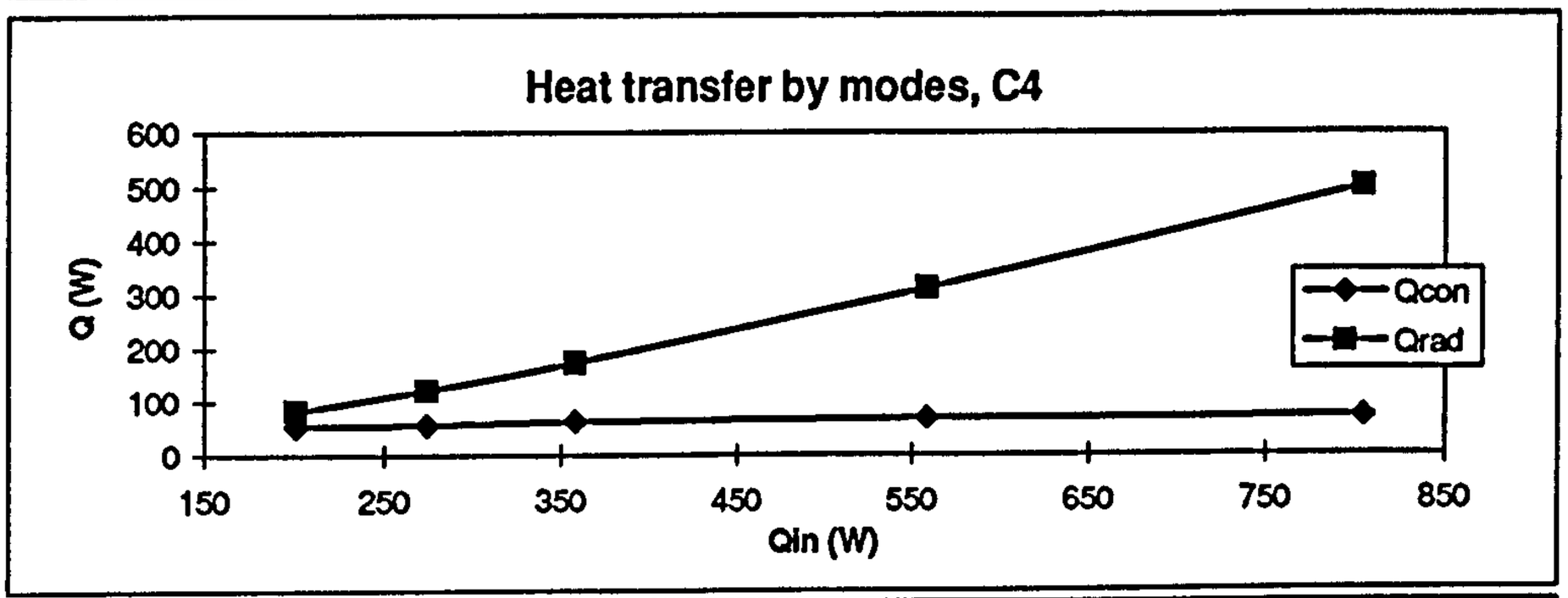
Heat transfer by modes, C4
600
500
400
300
200
100
0
Q (W)
150
250
350
450
550
650
750
850
Qin (W)
Qcon
Qrad

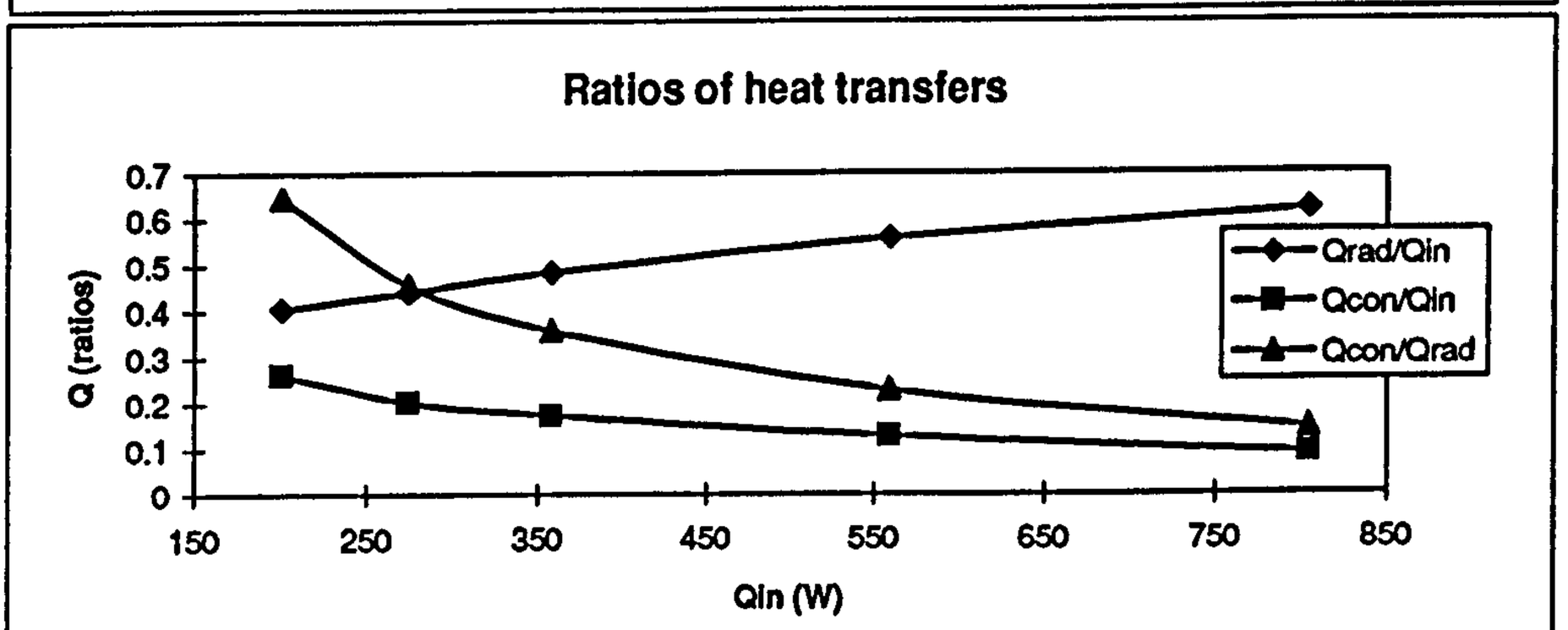
Ratios of heat transfers
0.7
0.6
0.5
0.4
0.3
0.2
0.1
0
Q (ratios)
150
250
350
450
550
650
750
850
Qin (W)
Qrad/Qin
Qcon/Qin
Qcon/Qrad

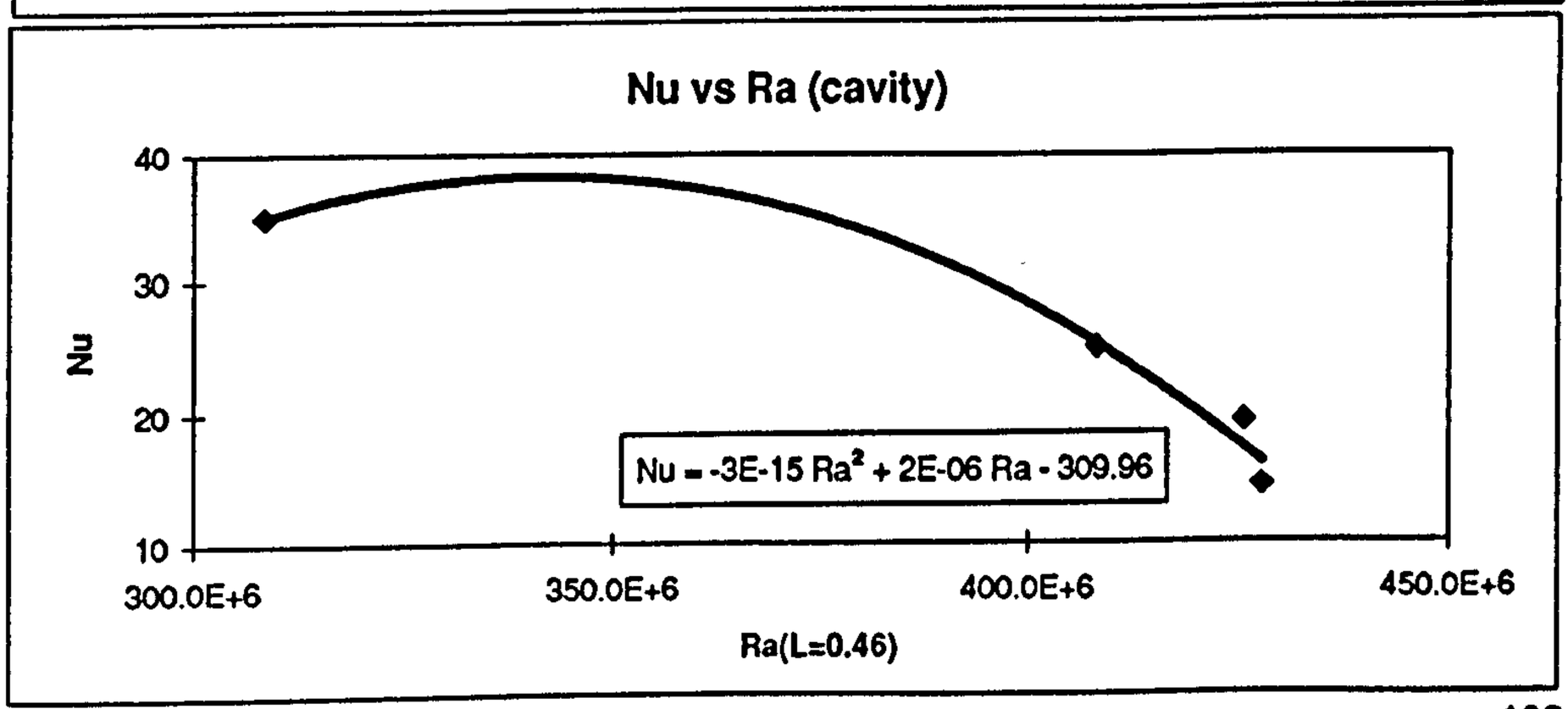
Nu vs Ra (cavity)
40
30
20
10
Nu
300.0E+6
350.0E+6
400.0E+6
450.0E+6
Ra(L=0.46)
Nu = -3E-15 Ra² + 2E-06 Ra - 309.96

Fig. 3-19(a-d)

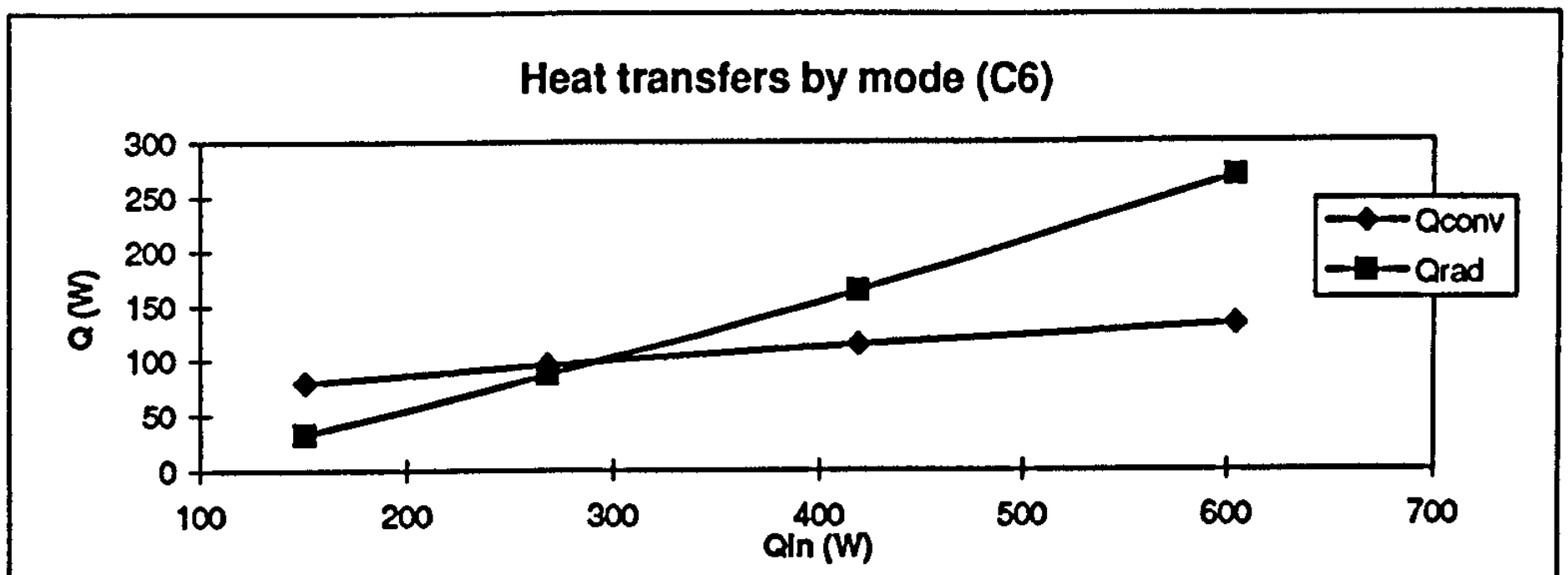
Heat transfers by mode (C6)
Q (W)
300
250
200
150
100
50
0
100
200
300
400
500
600
700
Qin (W)
Qconv
Qrad

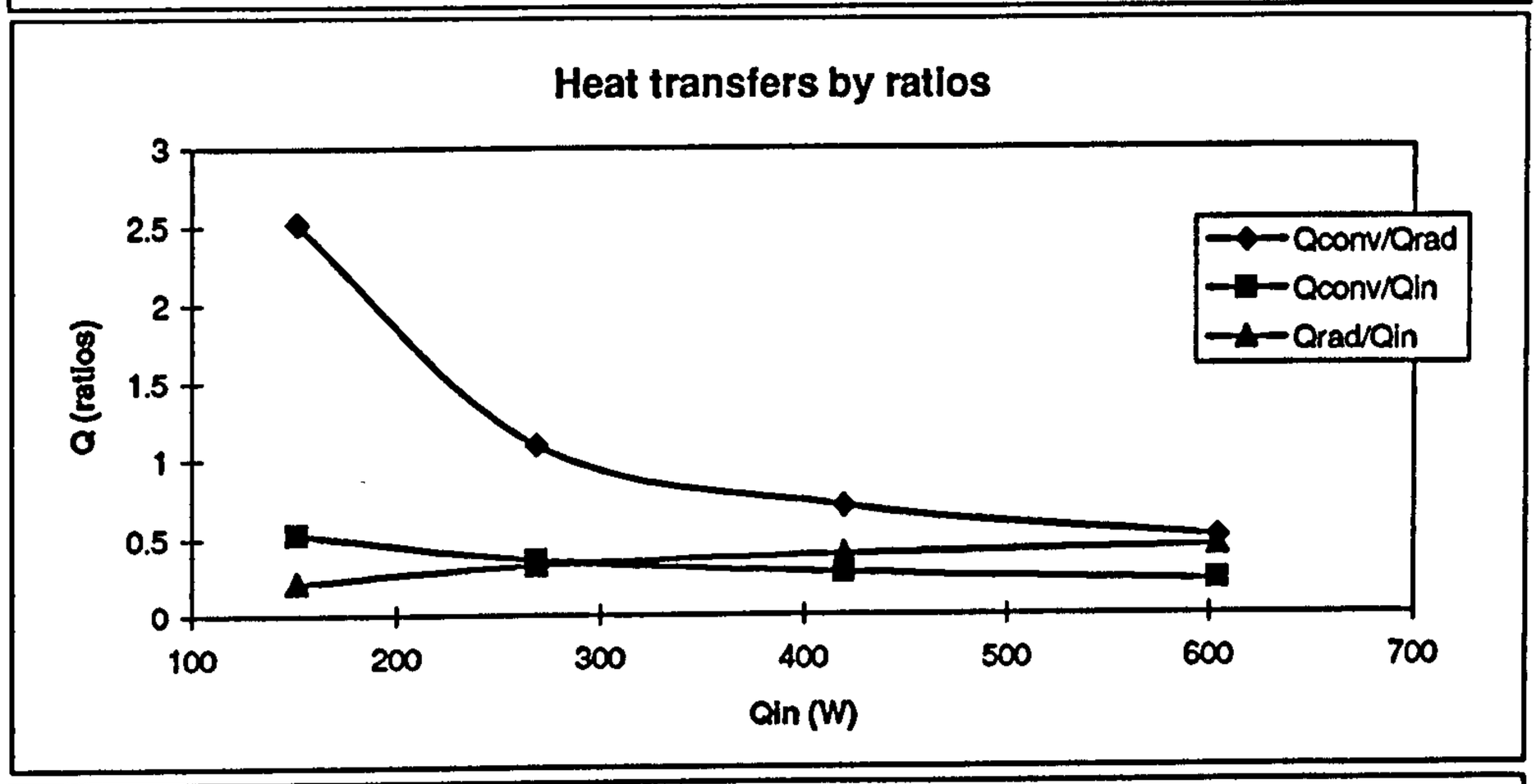
Heat transfers by ratios
Q (ratios)
3
2.5
2
1.5
1
0.5
0
100
200
300
400
500
600
700
Qin (W)
Qconv/Qrad
Qconv/Qin
Qrad/Qin

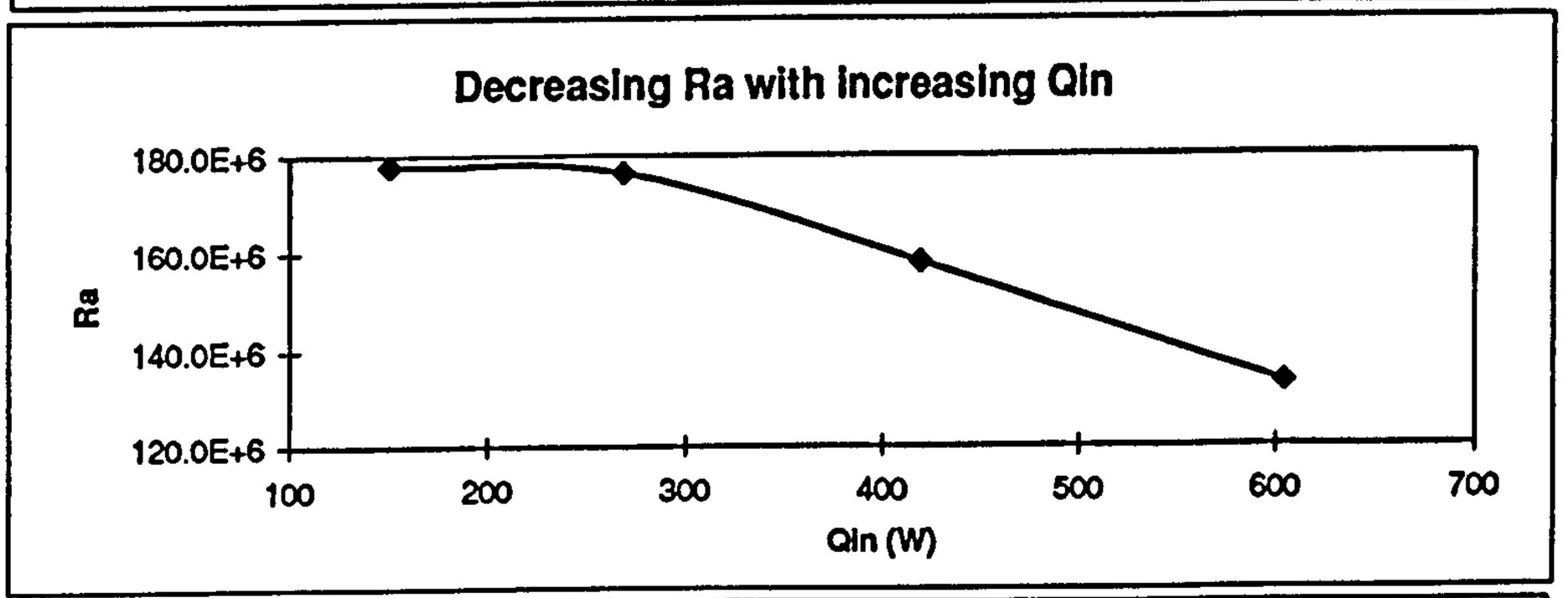
Decreasing Ra with increasing Qin
Ra
180.0E+6
160.0E+6
140.0E+6
120.0E+6
100
200
300
400
500
600
700
Qin (W)

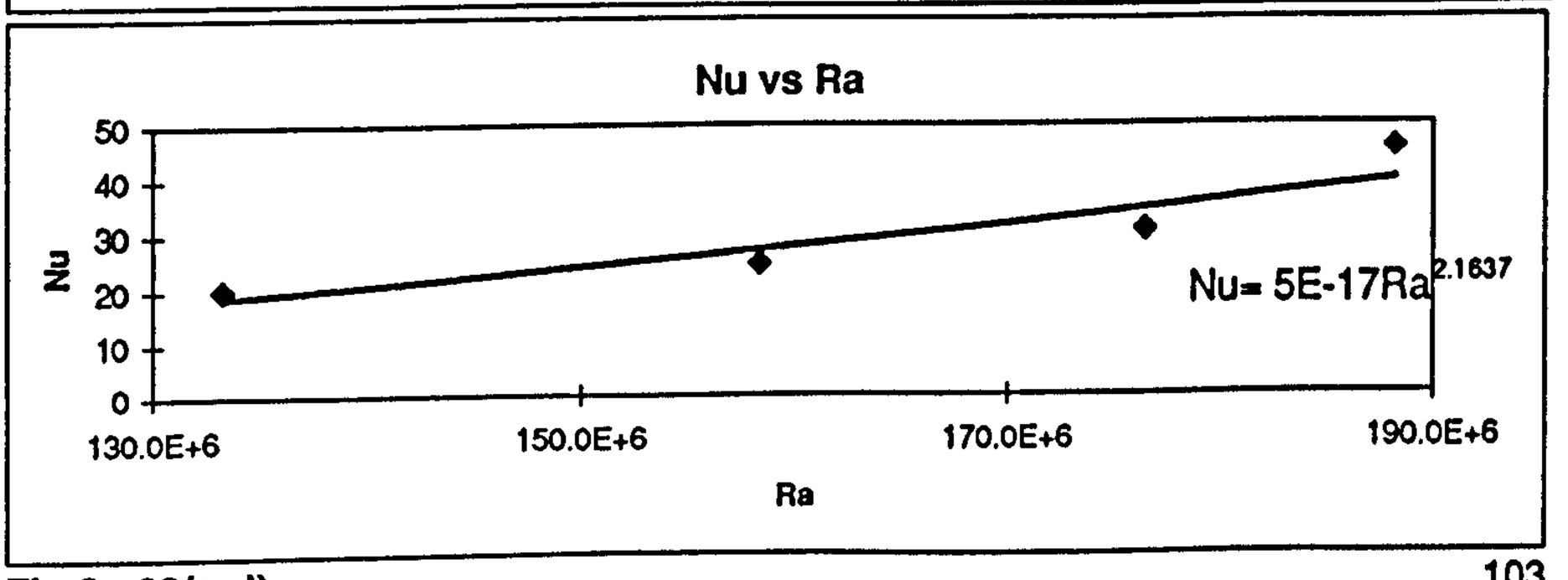
Nu vs Ra
Nu
50
40
30
20
10
0
130.0E+6
150.0E+6
170.0E+6
190.0E+6
Ra
Nu= 5E-17Ra2.1637

Fig 3 - 20(a-d)

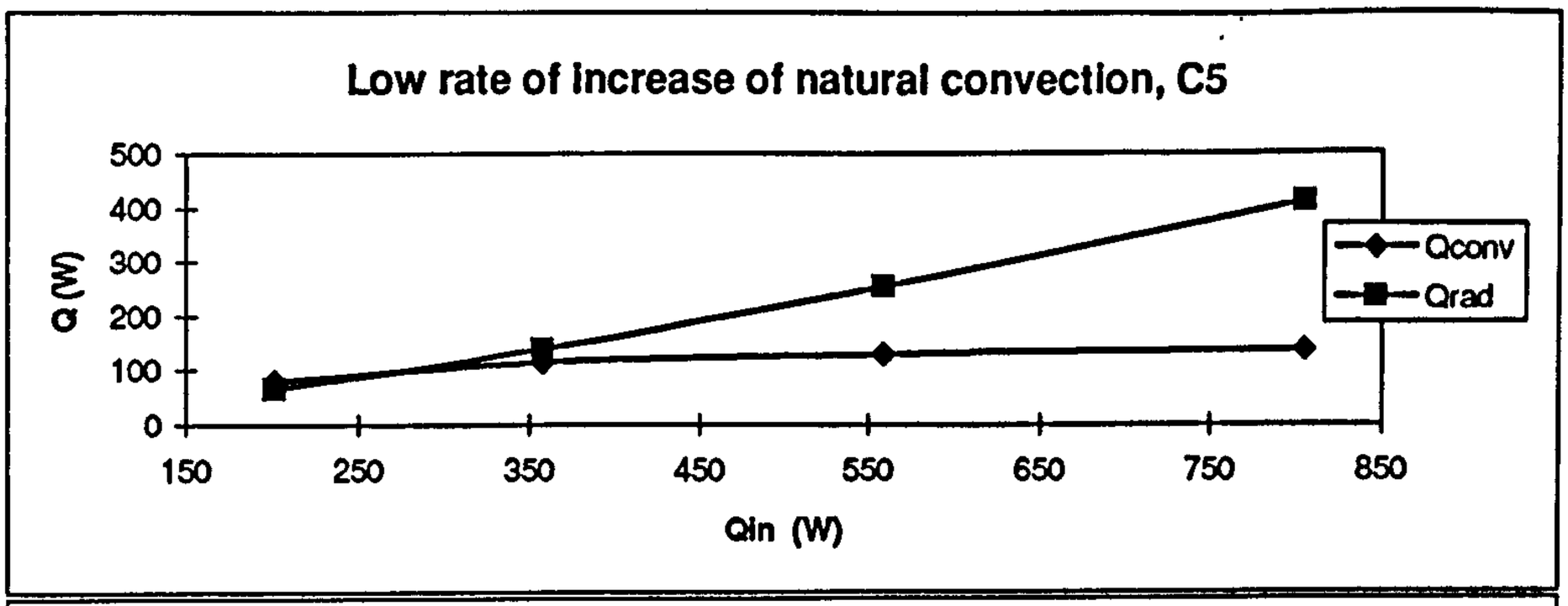
Low rate of increase of natural convection, C5
Q (W)
500
400
300
200
100
0
150
250
350
450
550
650
750
850
Qin (W)
Qconv
Qrad

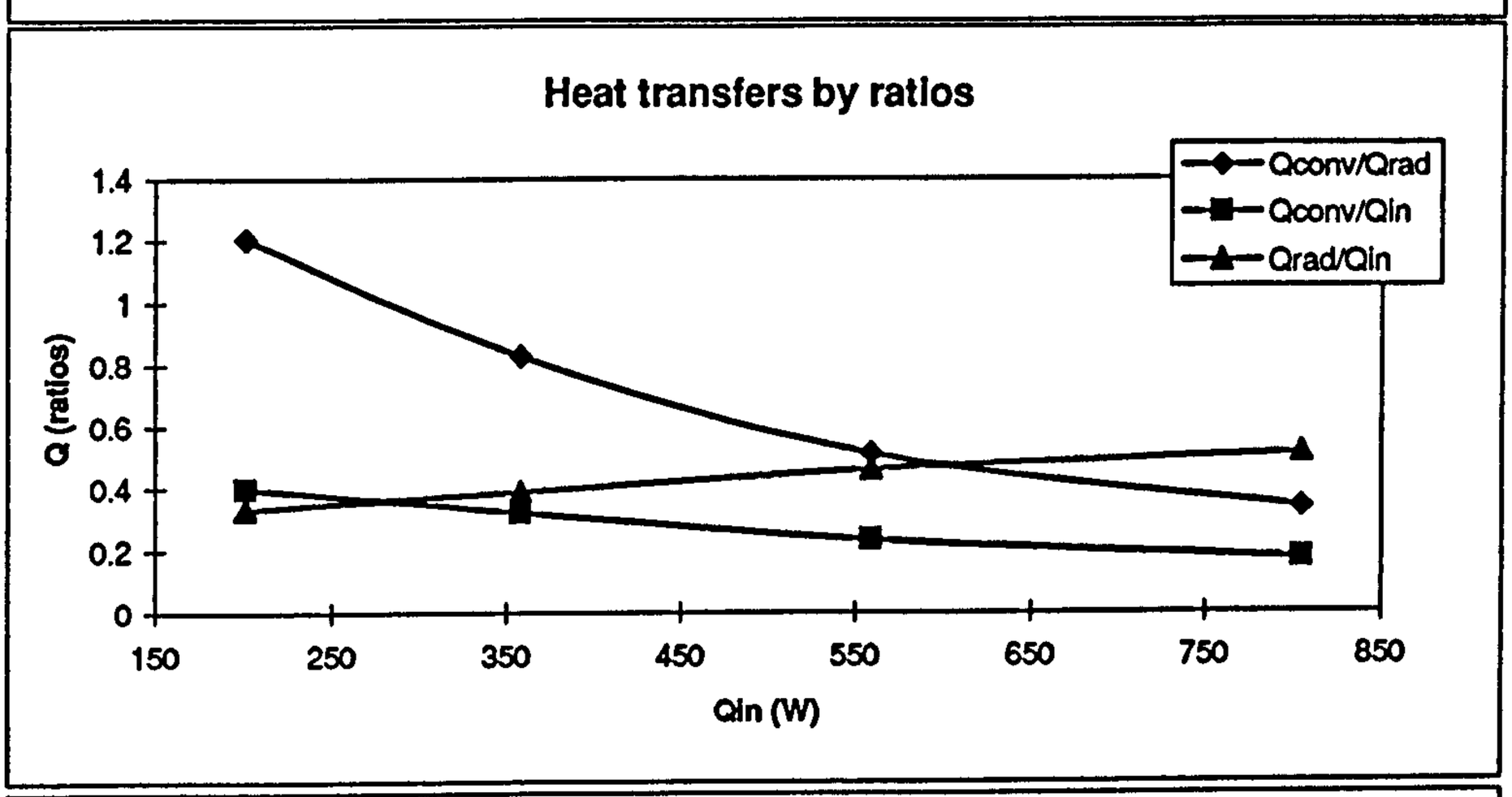
Heat transfers by ratios
Q (ratios)
1.4
1.2
1
0.8
0.6
0.4
0.2
0
150
250
350
450
550
650
750
850
Qin (W)
Qconv/Qrad
Qconv/Qin
Qrad/Qin

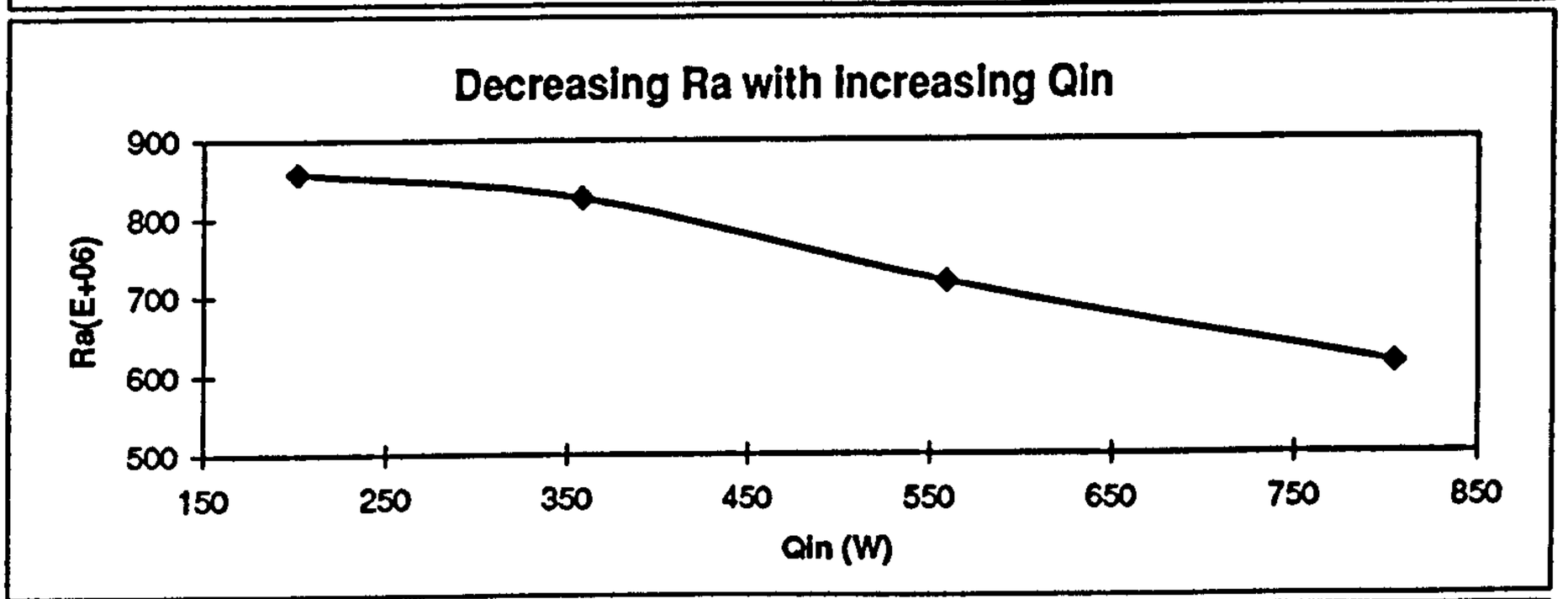
Decreasing Ra with increasing Qin
Ra(E+06)
900
800
700
600
500
150
250
350
450
550
650
750
850
Qin (W)

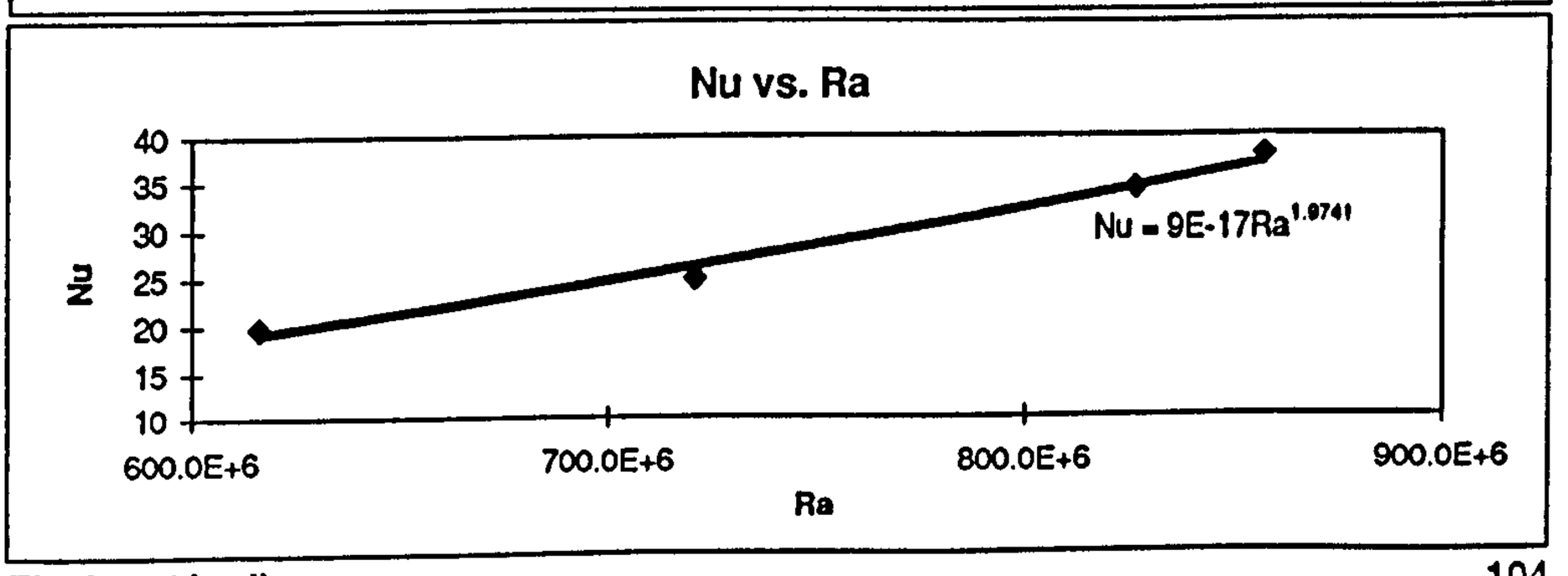
Nu vs. Ra
Nu
40
35
30
25
20
15
10
600.0E+6
700.0E+6
800.0E+6
900.0E+6
Ra
Nu = 9E-17Ra^1.9741

Fig 3 - 21(a-d)

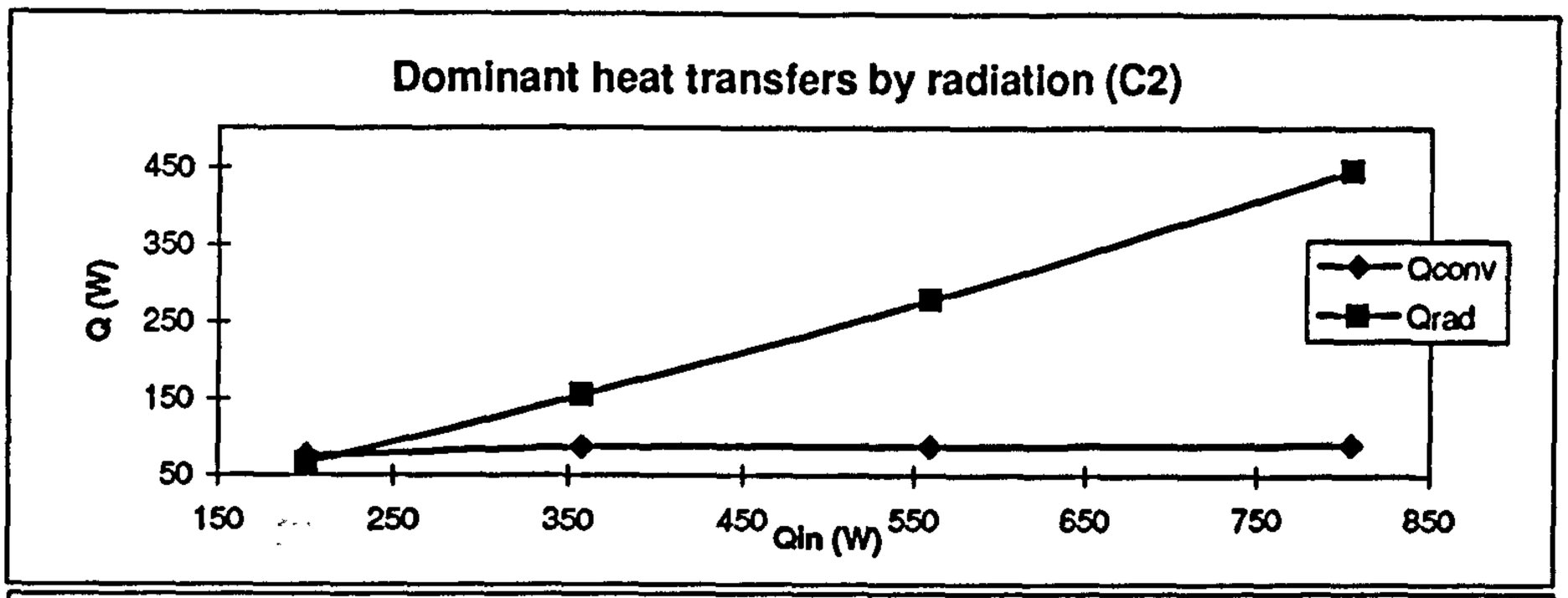
Dominant heat transfers by radiation (C2)
Q (W)
450
350
250
150
50
150
250
350
450
550
650
750
850
Qin (W)
Qconv
Qrad

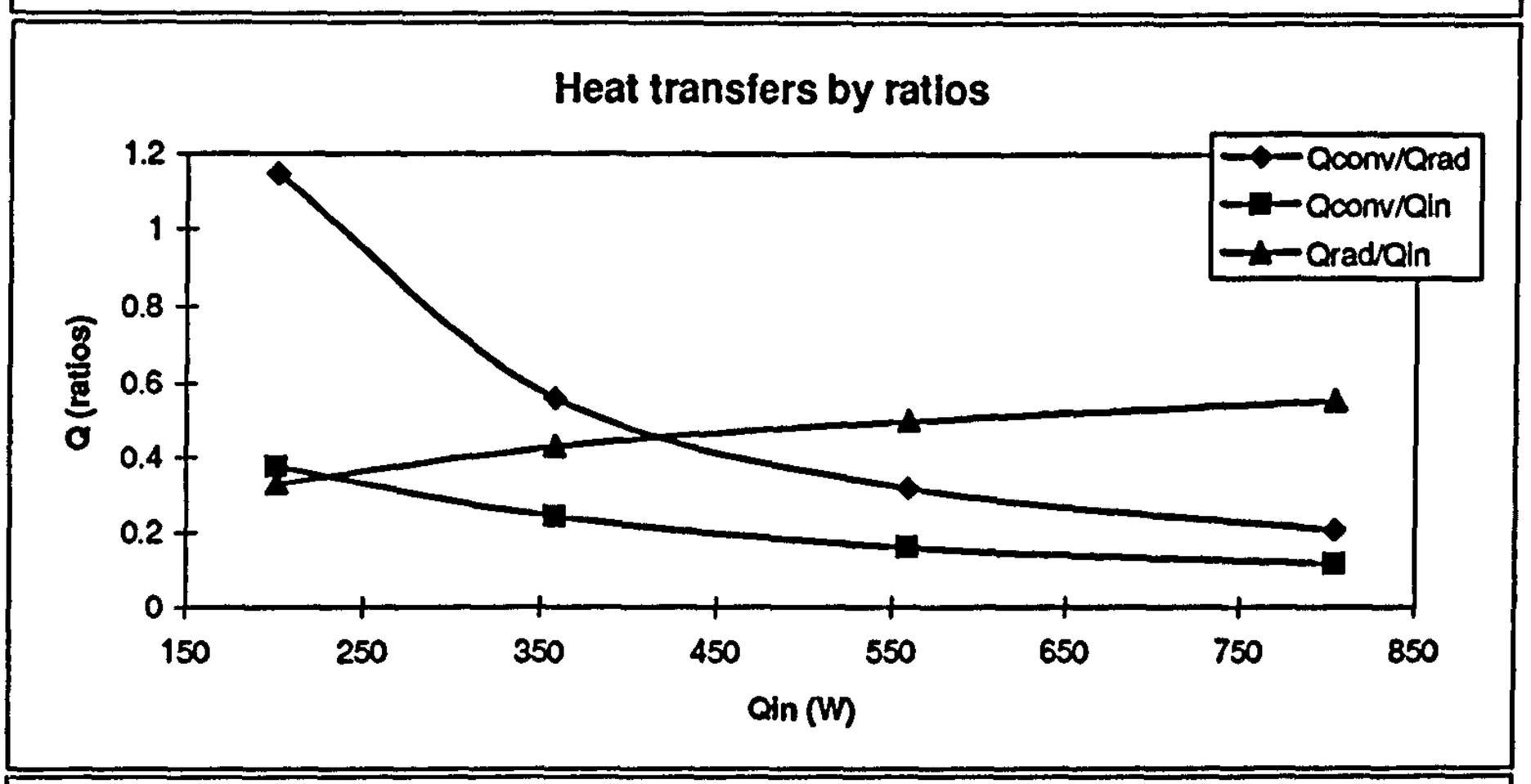
Heat transfers by ratios
Q (ratios)
1.2
1
0.8
0.6
0.4
0.2
0
150
250
350
450
550
650
750
850
Qin (W)
Qconv/Qrad
Qconv/Qin
Qrad/Qin

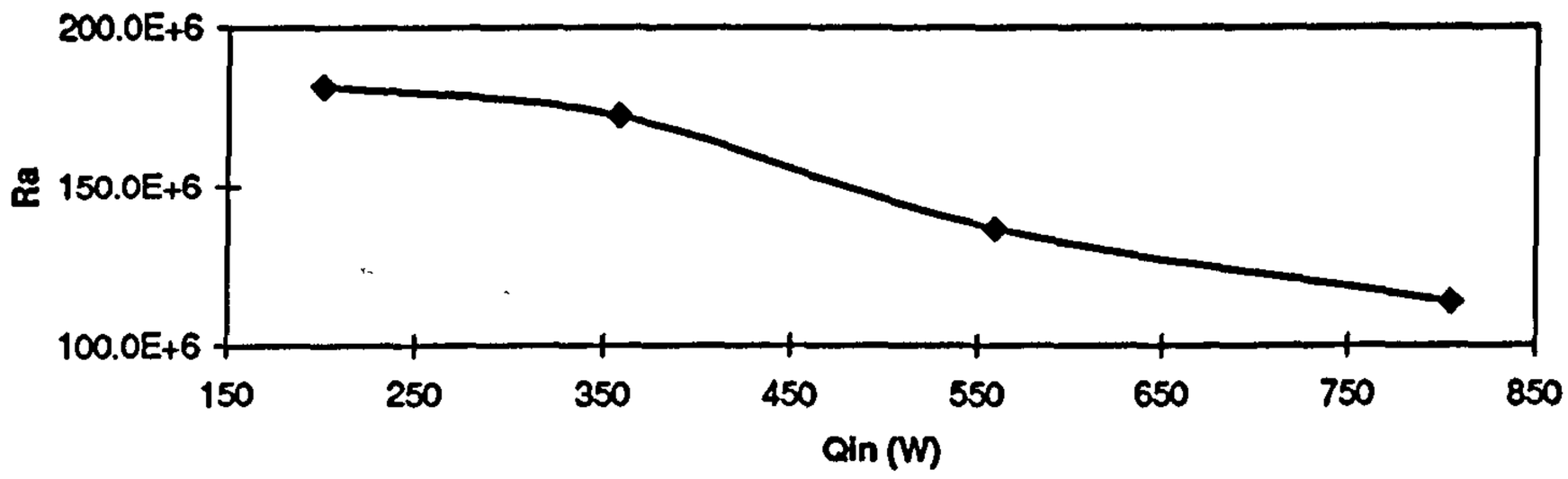
Decreasing Ra with increasing Qin
Ra
200.0E+6
150.0E+6
100.0E+6
150
250
350
450
550
650
750
850
Qin (W)

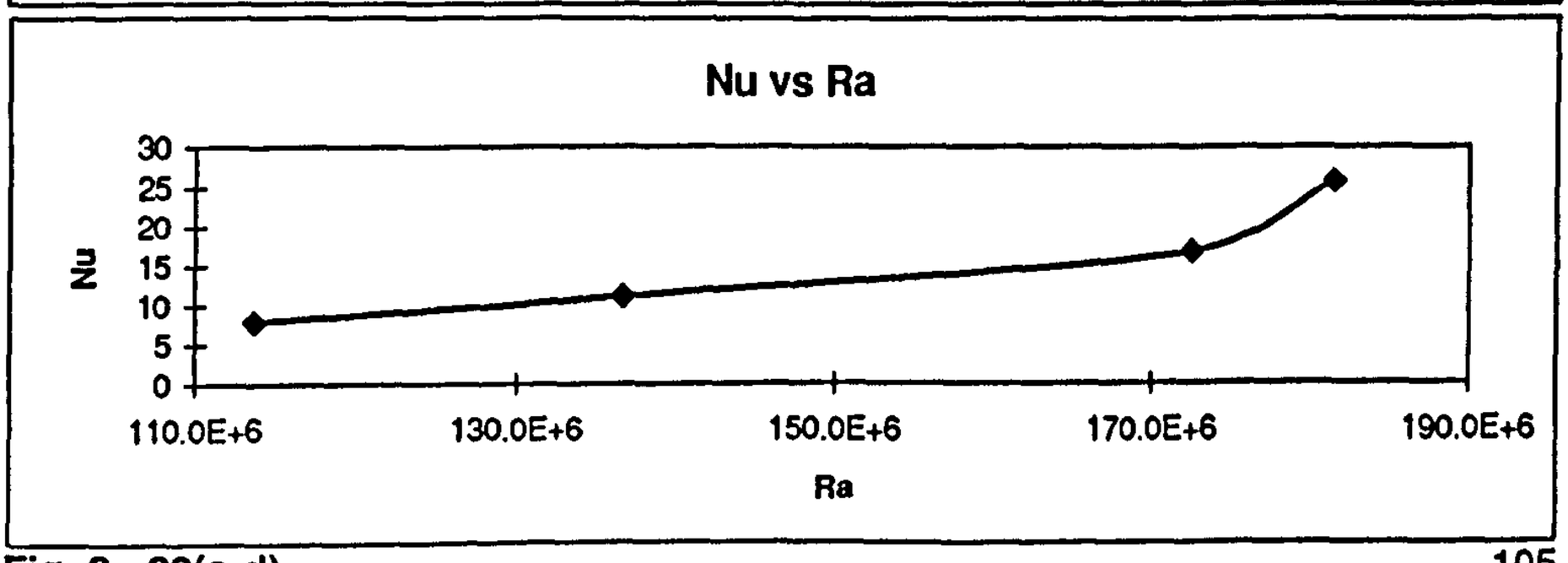
Nu vs Ra
Nu
30
25
20
15
10
5
0
110.0E+6
130.0E+6
150.0E+6
170.0E+6
190.0E+6
Ra

Fig. 3 - 22(a-d)

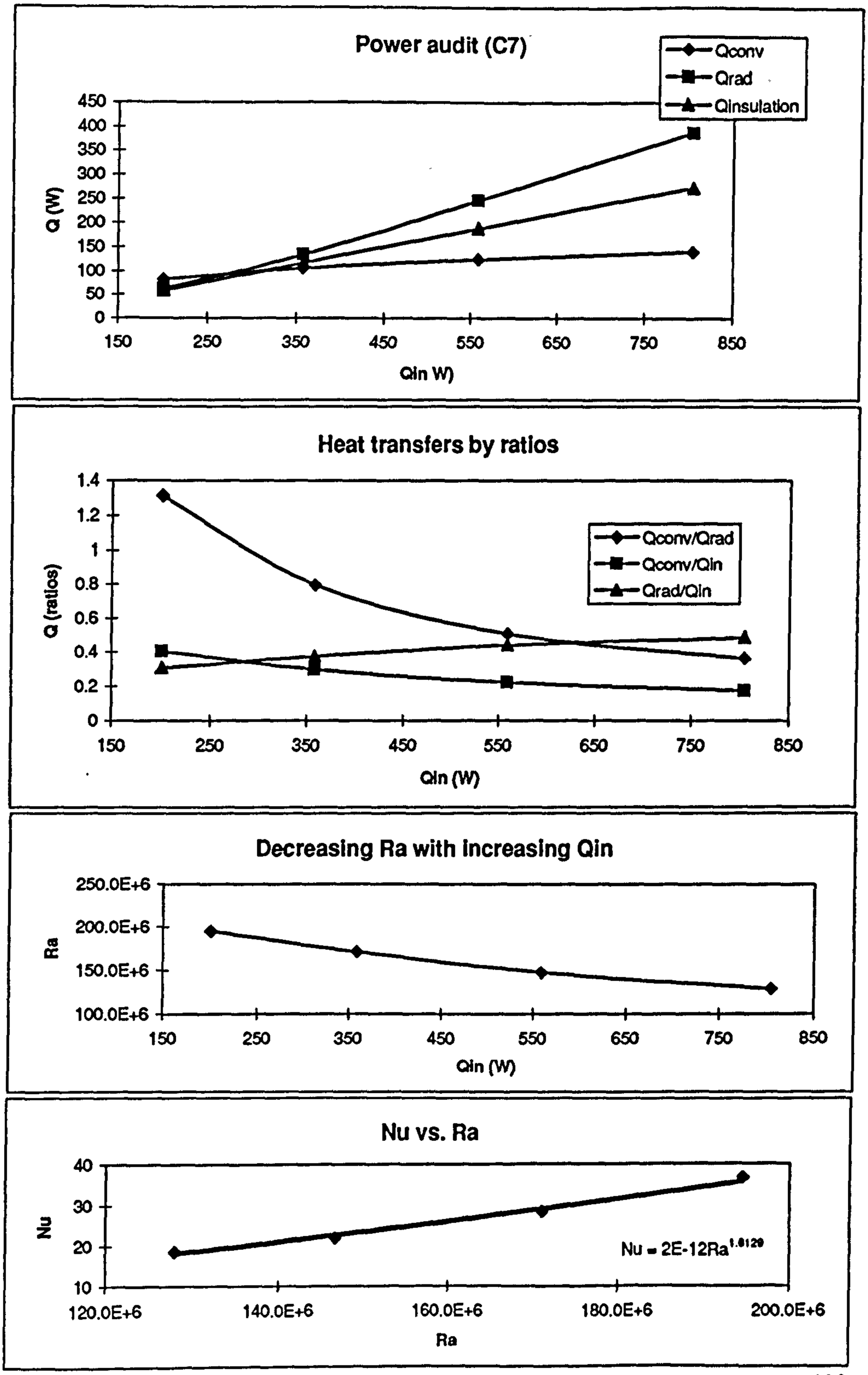
Power audit (C7)
Qconv
Qrad
Qinsulation
Q (W)
450
400
350
300
250
200
150
100
50
0
150
250
350
450
550
650
750
850
Qin W)
Heat transfers by ratios
Qconv/Qrad
Qconv/Qin
Qrad/Qin
Q (ratios)
1.4
1.2
1
0.8
0.6
0.4
0.2
0
150
250
350
450
550
650
750
850
Qin (W)
Decreasing Ra with increasing Qin
Ra
250.0E+6
200.0E+6
150.0E+6
100.0E+6
150
250
350
450
550
650
750
850
Qin (W)
Nu vs. Ra
Nu
40
30
20
10
Nu = 2E-12Ra^1.8129
120.0E+6
140.0E+6
160.0E+6
180.0E+6
200.0E+6
Ra

Fig. 3 - 23(a-d)

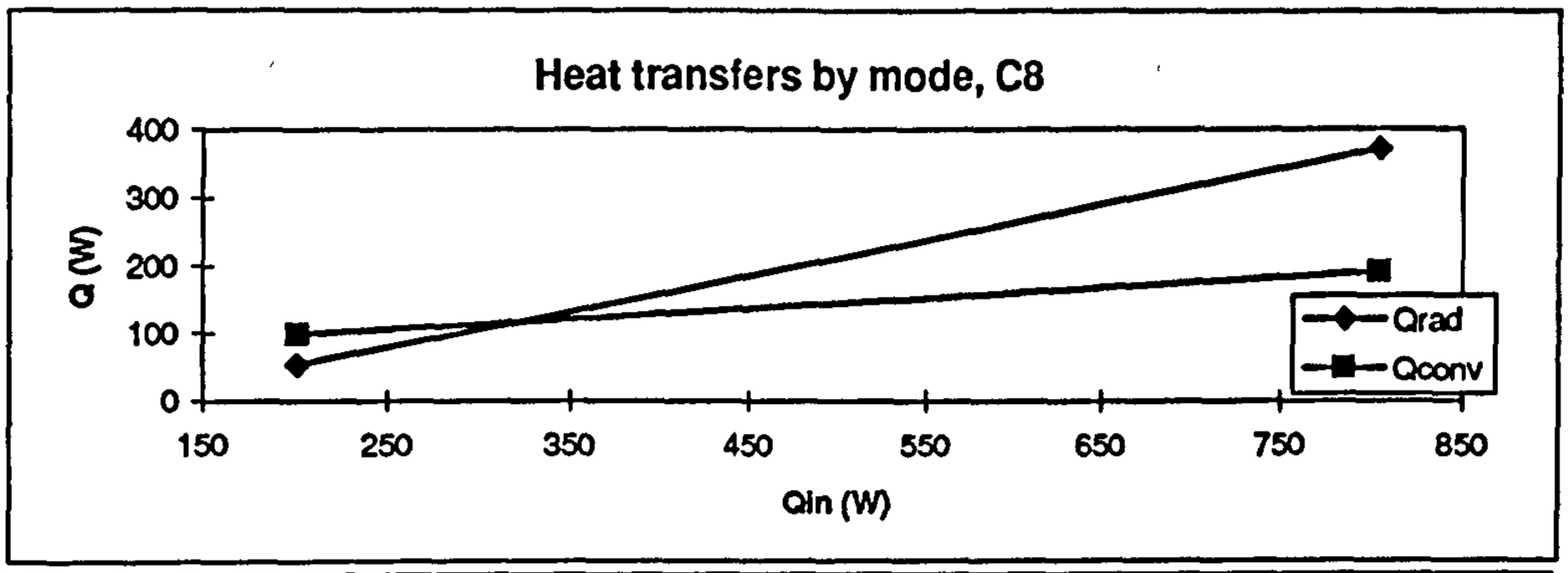
Heat transfers by mode, C8
Q (W)
400
300
200
100
0
150
250
350
450
550
650
750
850
Qin (W)
Qrad
Qconv

Heat transfers by ratios
Q (W)
2
1.8
1.6
1.4
1.2
1
0.8
0.6
0.4
0.2
0
150
250
350
450
550
650
750
850
Qin (W)
Qrad/Qin
Qconv/Qin
Qconv/Qrad

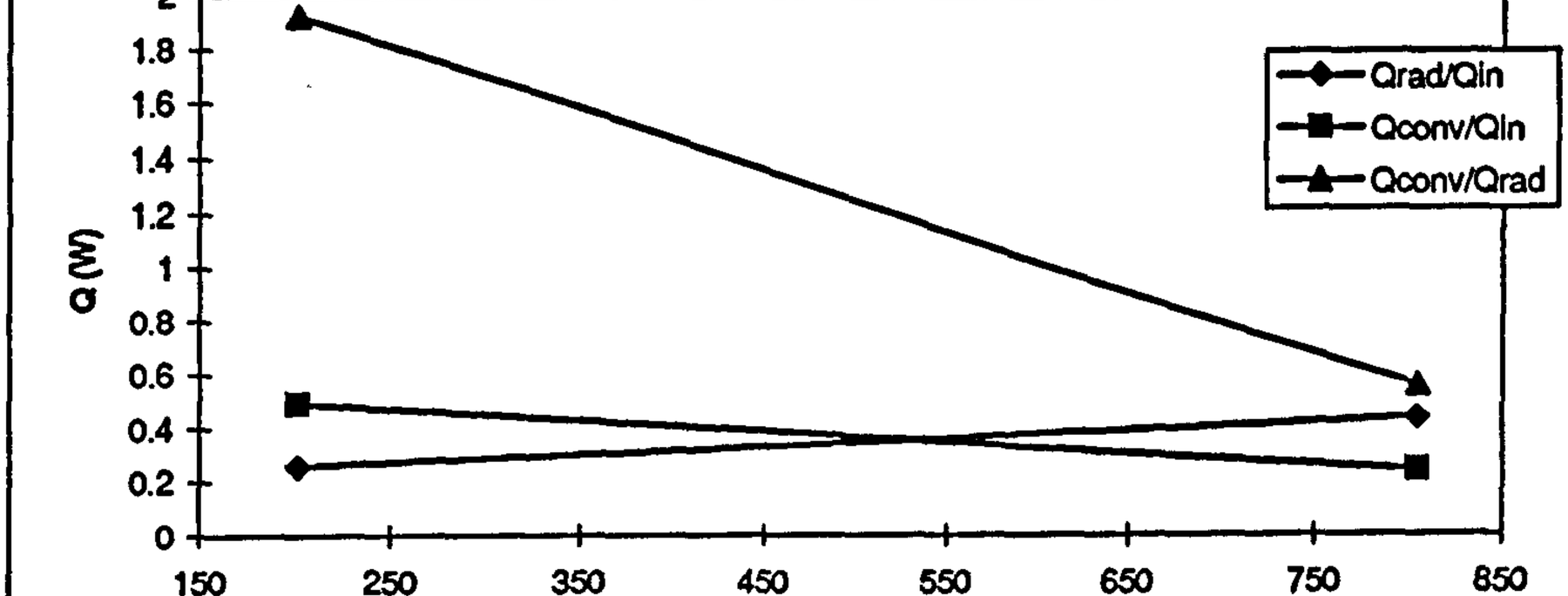
Decreasing Nu with increasing Qin (C8)
Nu
60
50
40
30
20
150
250
350
450
550
650
750
850
Qin (W)

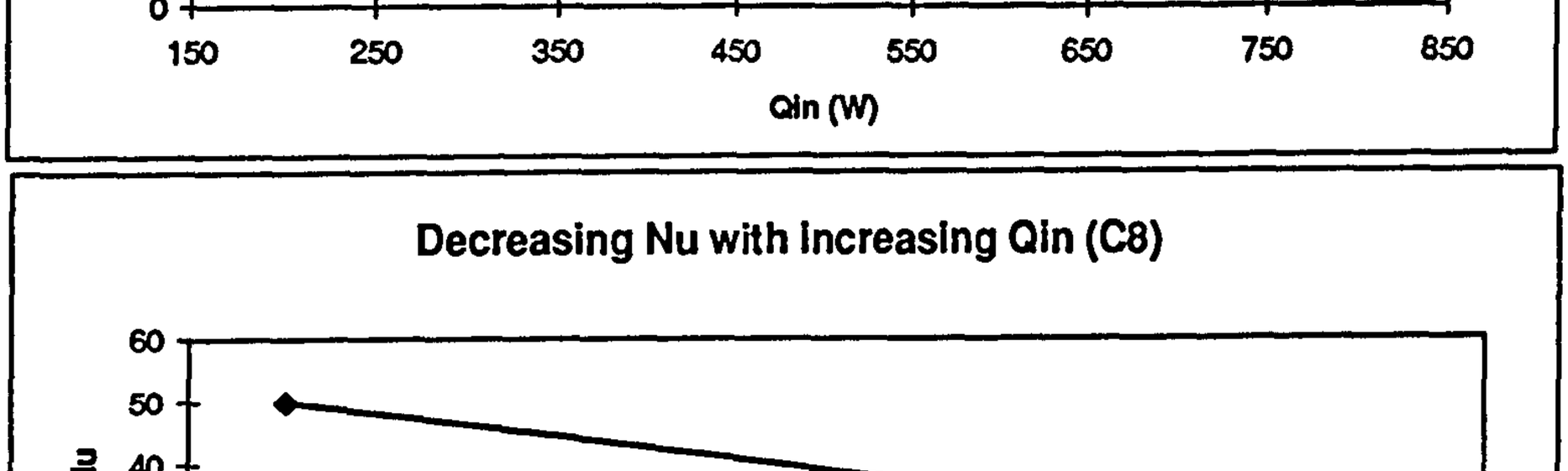
Nu vs. Ra
Nu
60
50
40
30
20
120.0E+6
140.0E+6
160.0E+6
180.0E+6
Ra
Nu = 4E-07Ra - 22.07

Fig. 3 - 24(a-d)

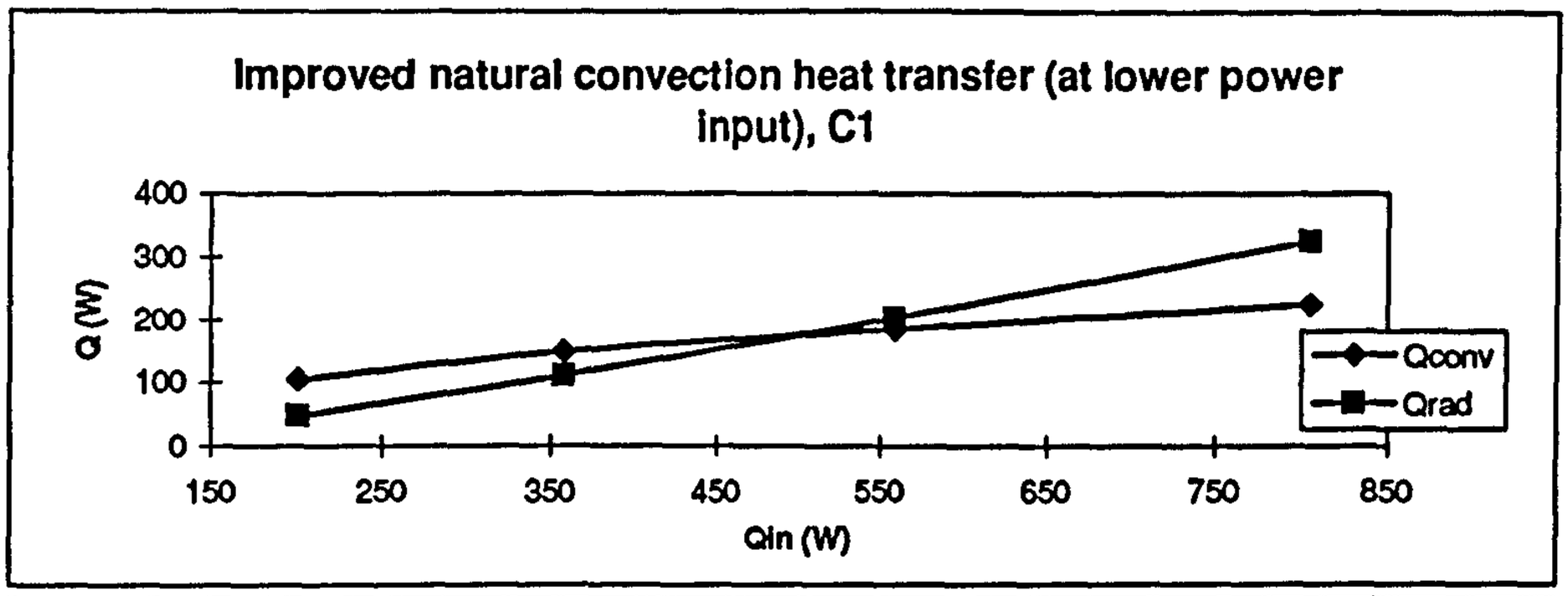
Improved natural convection heat transfer (at lower power input), C1
Q (W)
400
300
200
100
0
150
250
350
450
550
650
750
850
Qin (W)
Qconv
Qrad

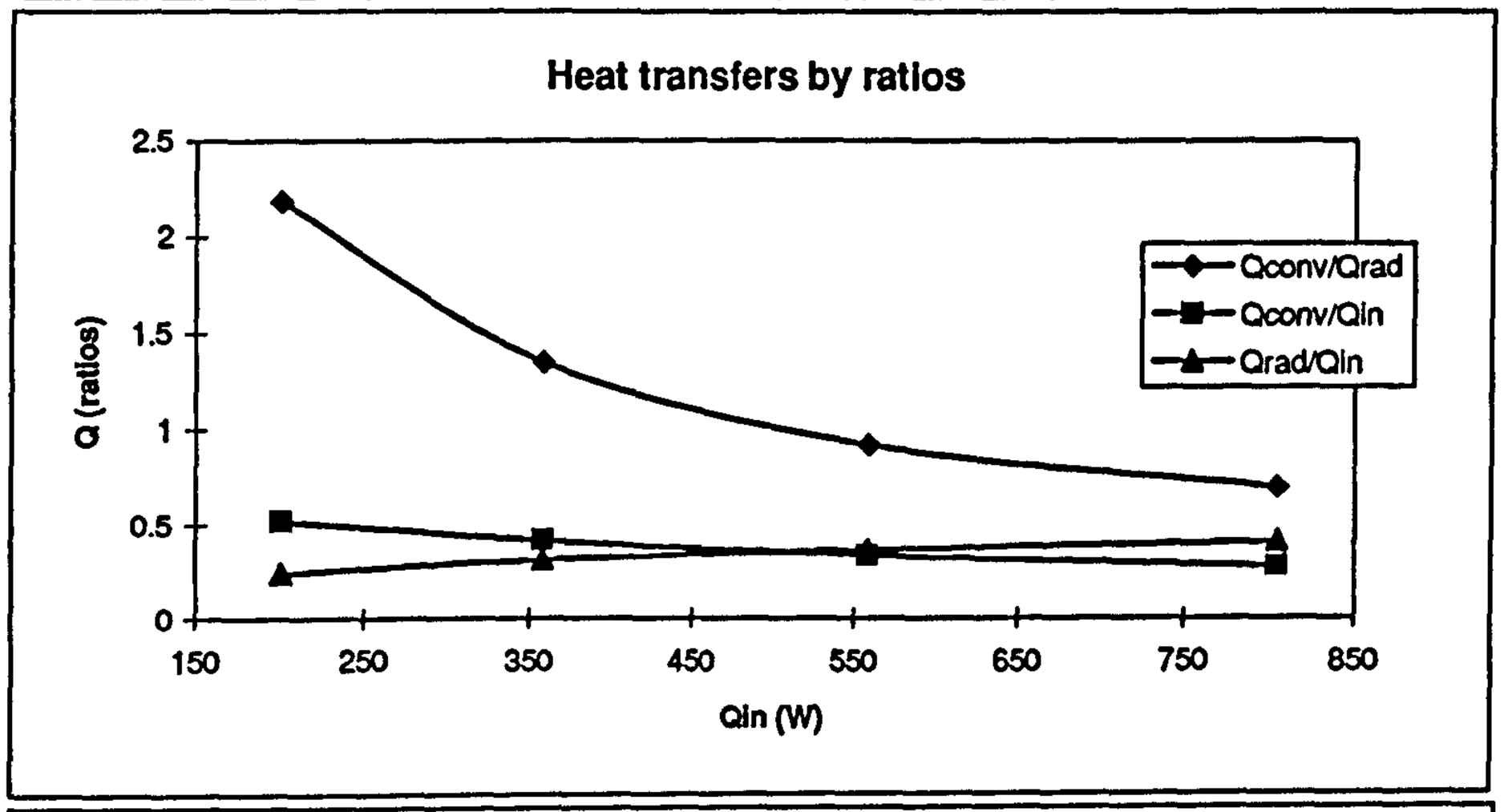
Heat transfers by ratios
Q (ratios)
2.5
2
1.5
1
0.5
0
150
250
350
450
550
650
750
850
Qin (W)
Qconv/Qrad
Qconv/Qin
Qrad/Qin

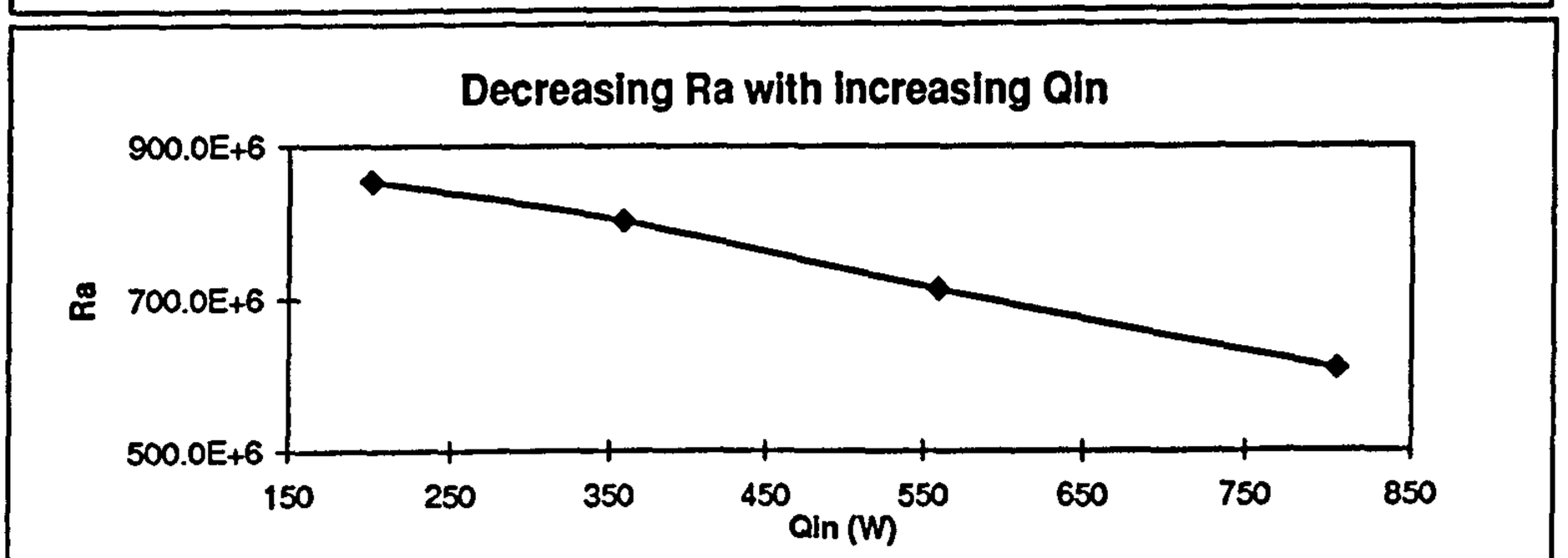
Decreasing Ra with increasing Qin
Ra
900.0E+6
700.0E+6
500.0E+6
150
250
350
450
550
650
750
850
Qin (W)

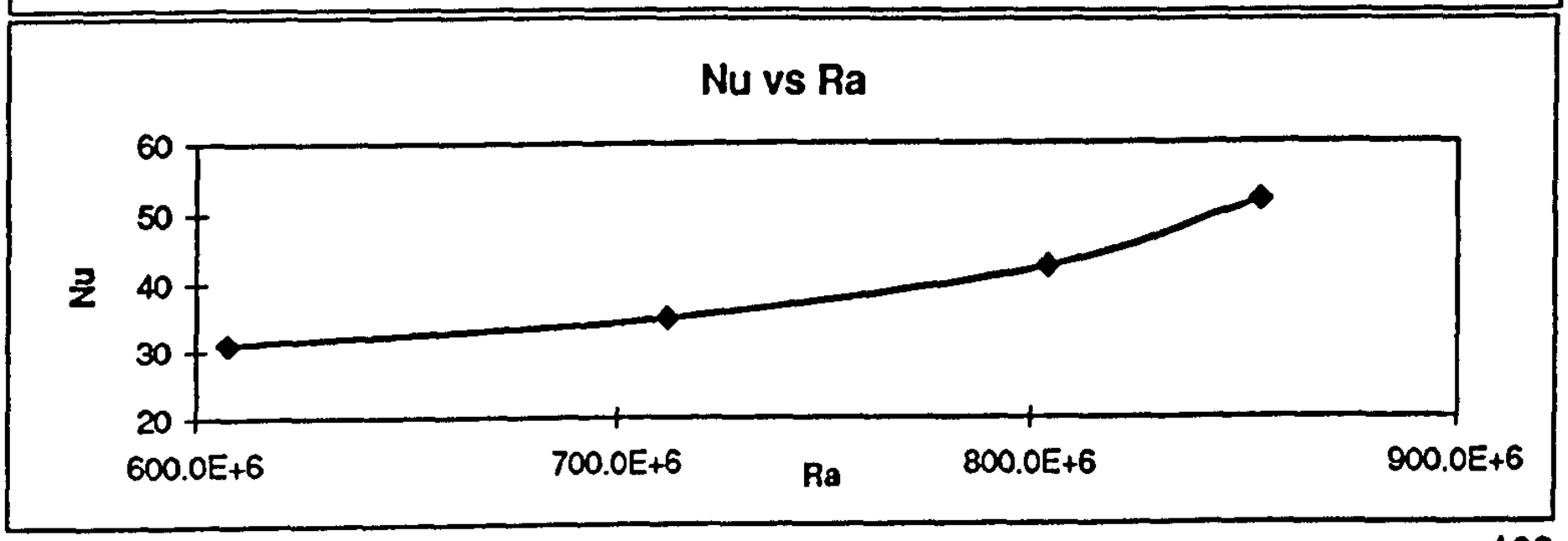
Nu vs Ra
Nu
60
50
40
30
20
600.0E+6
700.0E+6
800.0E+6
900.0E+6
Ra

Fig. 3 - 25(a-d)

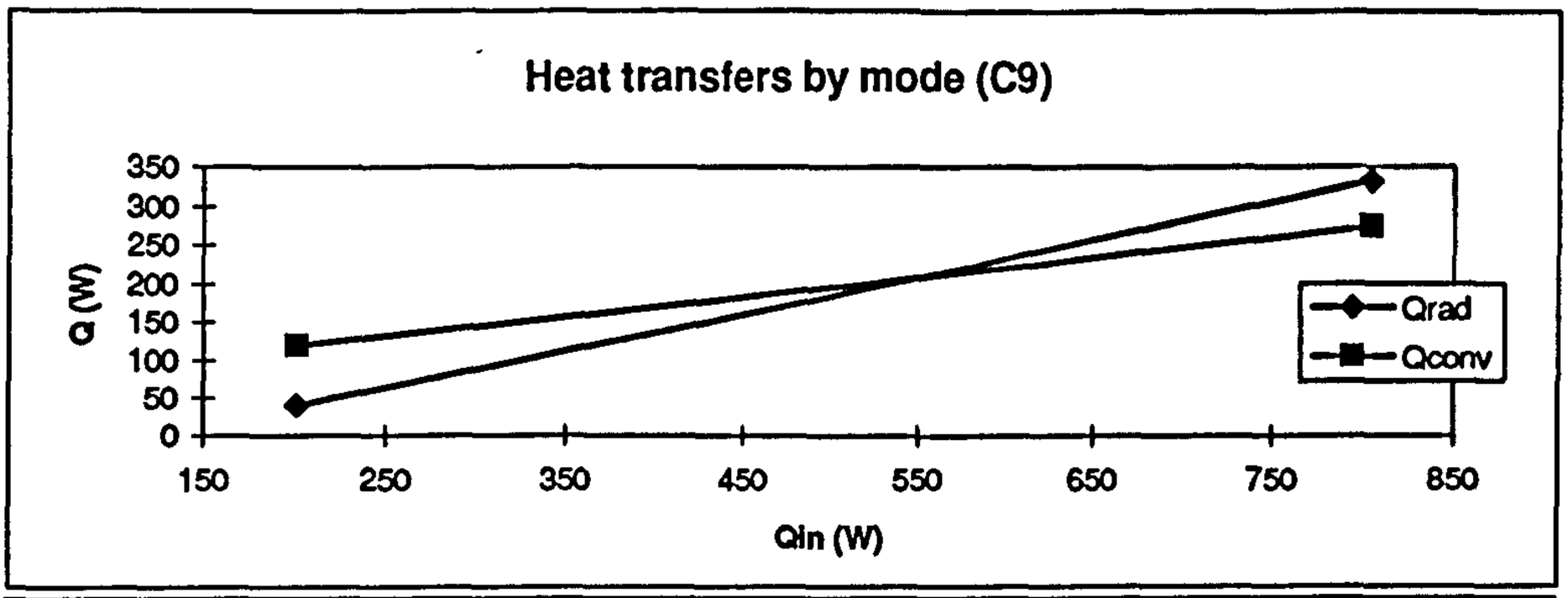
Heat transfers by mode (C9)
Q (W)
350
300
250
200
150
100
50
0
150
250
350
450
550
650
750
850
Qin (W)
Qrad
Qconv

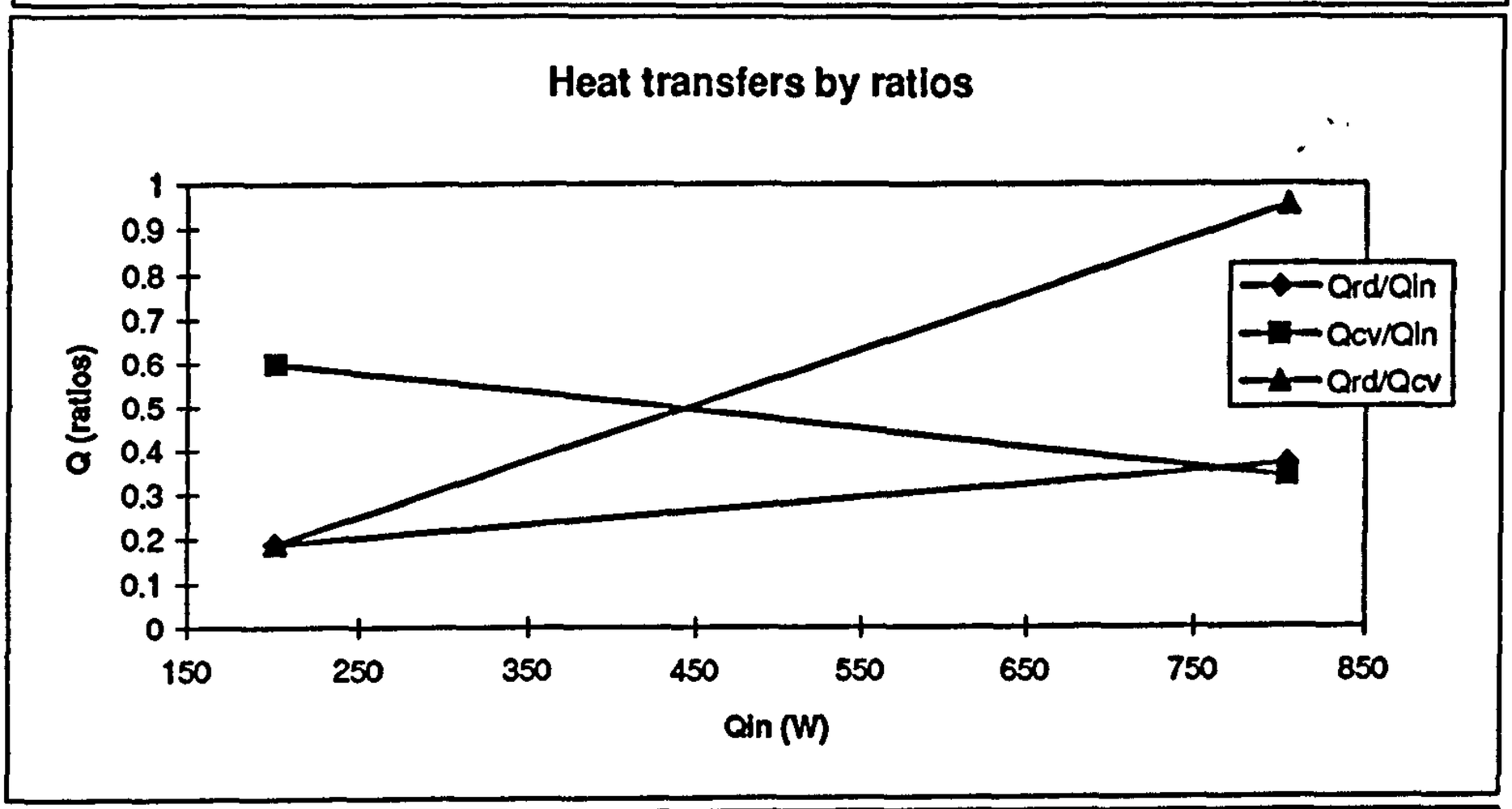
Heat transfers by ratios
Q (ratios)
1
0.9
0.8
0.7
0.6
0.5
0.4
0.3
0.2
0.1
0
150
250
350
450
550
650
750
850
Qin (W)
Qrd/Qin
Qcv/Qin
Qrd/Qcv

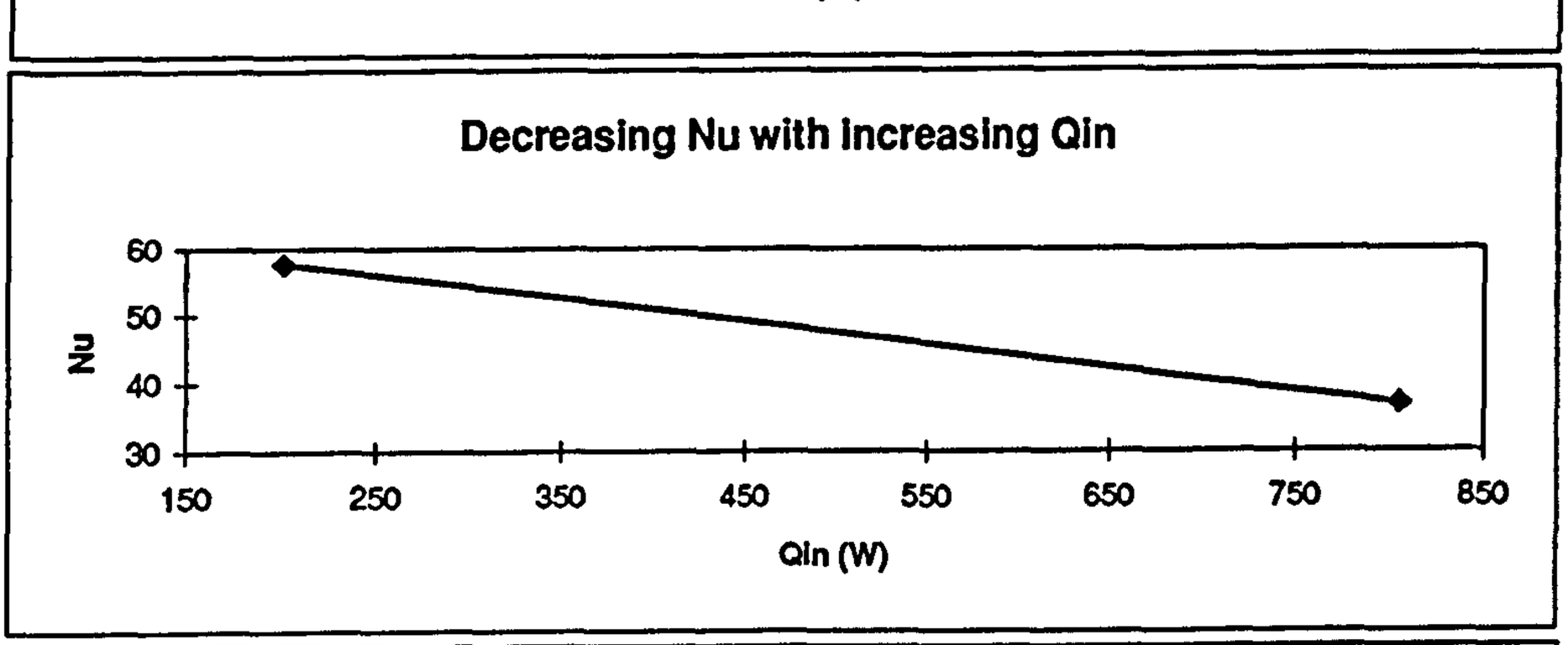
Decreasing Nu with increasing Qin
Nu
60
50
40
30
150
250
350
450
550
650
750
850
Qin (W)

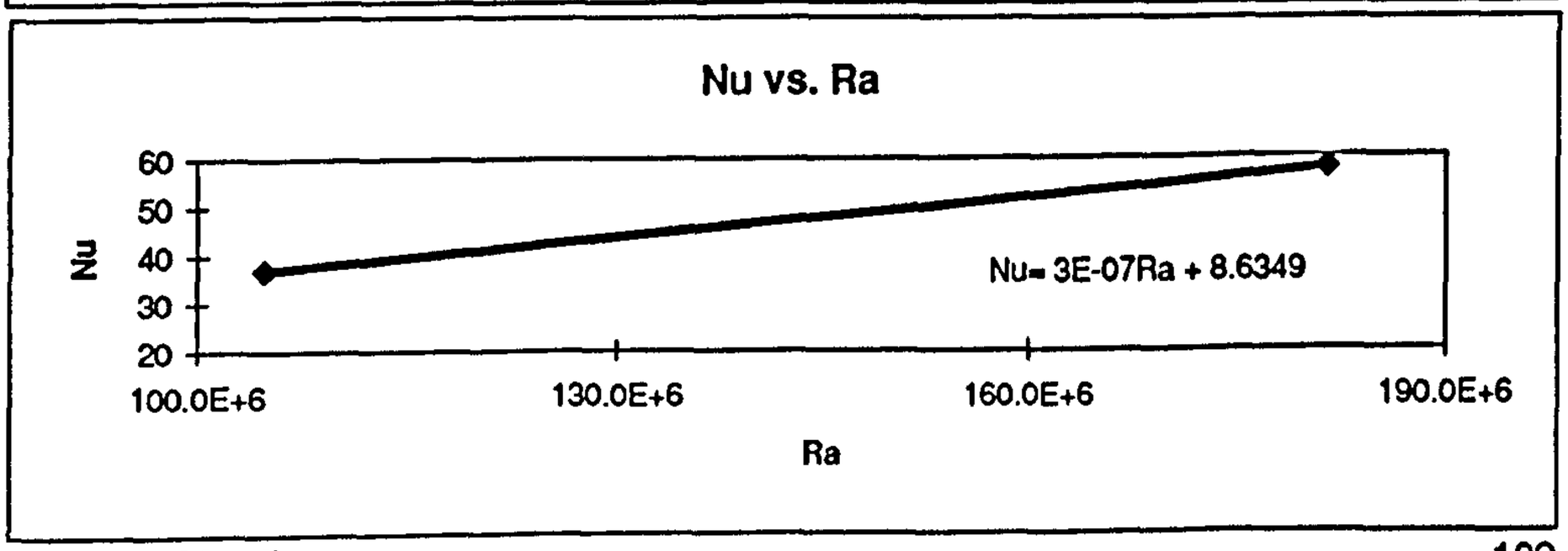
Nu vs. Ra
Nu
60
50
40
30
20
100.0E+6
130.0E+6
160.0E+6
190.0E+6
Ra
Nu= 3E-07Ra + 8.6349

Fig. 3 - 26(a-d)

Fig. 3-27. Interferogram, C9.

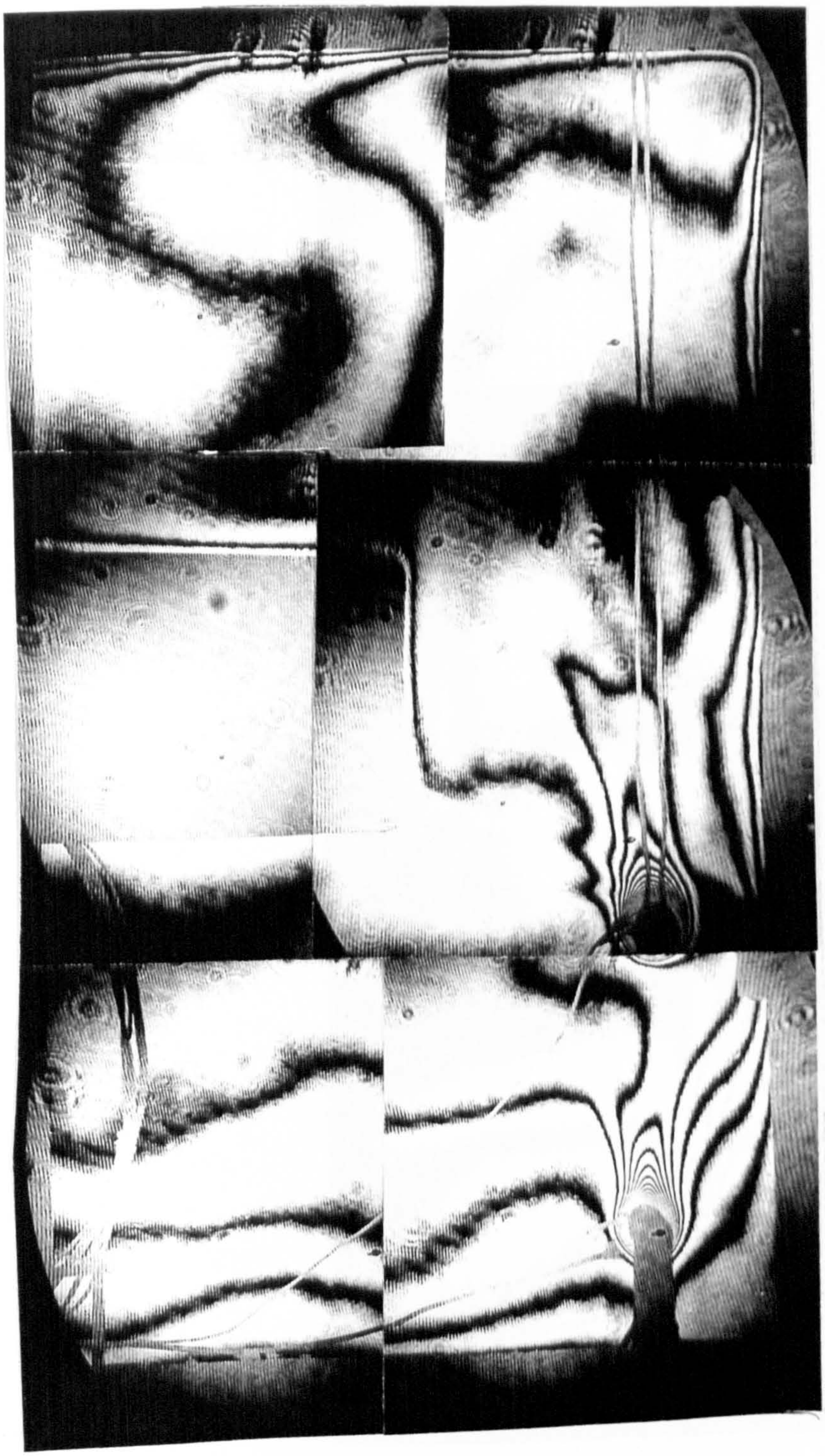

Fig. 3-28.

Interferograms,

raised upper heaters.

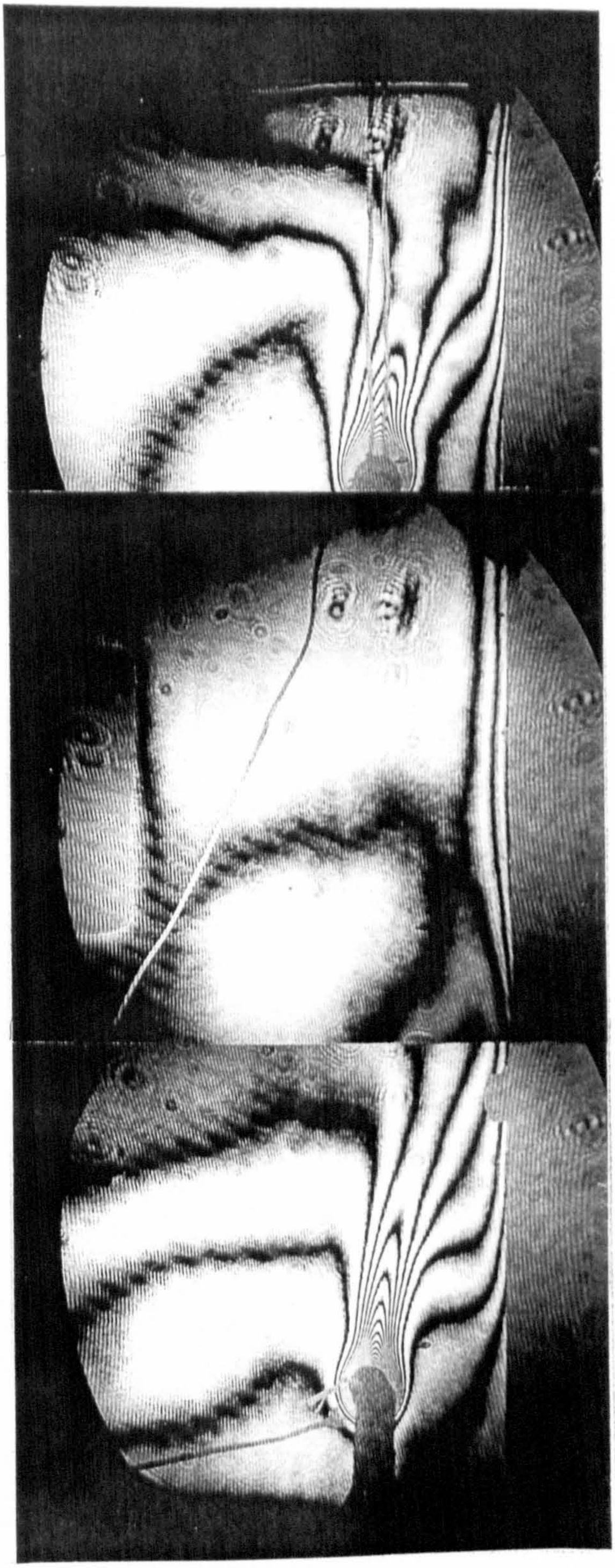

4. NATURAL CONVECTION HEAT TRANSFERS FROM ENCLOSED HEATERS

4.1. INTRODUCTION

The preceding experimental investigation was carried out with the centreline of the heaters tentatively set at about 35mm from the walls (depending upon heater flexure under thermal loading). The greatest convective heat transfers occurred for configurations with either base- or wall-mounted heaters. However, it appears that there may be optimal locations either along the vertical wall or base, which could further improve the natural convective heat transfers.

Rectangular enclosures have an effect on convection from isolated heat sources, but the degree of enhancement achievable has not been explicitly shown to depend upon their positions within the enclosure or on the proximity to adjoining walls.

In order to resolve this issue, an examination of the existing literature was made. The experimental studies carried out utilised a line heat source (cylindrical heater) in a square-sectioned enclosure. The heater was located in various sections of the enclosure and steady-state measurements were carried out to enable an analysis of the convective heat transfers.

4.2. EXISTING LITERATURE

Experimental studies of natural convection heat transfers from horizontal cylinders in free space and close to adjoining walls, have indicated an enhancement or degradation in convective heat transfers depending upon the spacing between the heaters [22-23], between the heater and the wall, or on whether the wall is vertical, or horizontal (above or below) [24-28]. The performance of heaters in free space is often an indication of their behaviour in enclosed spaces. Therefore, a knowledge of heaters and arrays in free space was further examined as a means of anticipating their performance in a square-sectioned enclosure.

4.2.1. Single Cylinder In Free Space

Horizontal single cylinders and wires in free space have been intensively studied culminating in a review by Morgan [26] which contained a comprehensive compilation of correlations. The relevant correlations within the studied Rayleigh number range (10^2-10^{12}) are presented (see Table 4.1).

The characteristic lengths were based on the hot cylinder diameter and the fluid properties measured at the film temperatures T_m=0.5ΔT. It was also reported that repeated experimental studies did not always produce identical experimental data. This is because heat transfer by natural convection was found to be susceptible to environmental (atmospheric) pressure [26].

Table 4.1 Correlations from horizontal cylindrical heaters [26].

Range of Ra		$Nu=c_1Ra^{c2}$	
From	To	c_1	c_2
10^2	10^4	0.85	0.188
10^4	10^7	0.48	0.25
10^7	10^{12}	0.125	0.333

The wide dispersion or specifically the percentage coefficient of variation {=100x(standard deviation/mean)} varied from 3% to 35% for the experimental data, but the extent of the uncertainty was suppressed (5% to 26%) in the correlations. Which means that the established correlating techniques dampen the sensitivity of the

experimental data. Another phenomenon pointed out contradicted Nusselt's postulation [66], based on the differential equation of natural convection, that a temperature loading effect should exist and reduce Nu as ΔT was increased (Ra<10) when Nu was based on the cylinder surface temperature. No such systematic effect was found when Nu was based on the film temperature [26] for a wider range of Ra ($10^{-4} \leq Ra \leq 10^{8}$).

4.2.2. Cylindrical Heater Arrays in Free Space

Eckert and Soehngen [22] observed that if a second hot tubular heater was placed directly above the first in external flow, then Nu for the upper tube was only 87% of the value of the lower tube. If a third, identical heater (d=22.3mm) was then positioned above the second, (see Fig.4-1a) it would have a Nu of only 65% of that of the lowest tube. A subsequent investigation [23] confirmed that when the spacing between the cylinders was small, the heat transfer rate from an upper cylinder or wire in a vertical array decreased with decreasing cylinder spacing because of interference arising from the hot buoyant flow from the preceding cylinders.

For larger spacings, the rate of heat transfer increased with the vertical spacing by up to 30%. This is because the rising buoyant flow had more time to accelerate, and so it entrained more air from the cooler surroundings, thereby reducing the plume temperature of the ensuing mixture before reaching the next heater situated above. However, extremely small wires were used (d=0.127mm) and the average separation high. When the axis of the middle tube in a 3-cylinder vertical array was offset horizontally, its Nu increased from 87% to 103% [22], while that of the uppermost tube was only 86% (see Fig. 4-1b).

Sparrow and Boesneck [24] compared a range of horizontal and vertical offsets with that for no offset using only two horizontal cylinders of 38mm diameter. At the smallest vertical separation distance tested, ($CC_V/d = 2$), horizontal offsetting caused an increase in Nu of up to 27%. Generally, at small vertical separations, Nu was responsive to small horizontal offsets, but did not respond to further offsetting when the offset exceeded the cylinder diameter. At larger vertical separations ($CC_V/d>5$; $CC_h/d>1$), the rate of heat transfer was hardly affected by small horizontal offsets, but became more responsive to larger offsets. However, as the horizontal offset increased beyond a critical value, ($\approx CC_h/d > 2$) depending upon the vertical separation, the effect of the lower cylinder plume became so small, that the Nu ratio results blended to a

general value of just over unity (Nu/Nu_{∞}=1.03, for CC_V=2). For CC_V>4, there was degradation throughout.

4.2.3. Heaters within confining walls

Sparrow and Pfeil [67] studied natural convection heat transfers from a single horizontal cylinder situated within walls which form a vertical channel or shroud. A 38mm cylindrical heater was employed at five interwall spacings, ($1.5<S_W/d<10$), for each of three shroud heights. The cylinder was initially tested in the absence of bounding walls and favourably compared to one of the external flow correlations of Morgan [26] - $Nu=0.480Ra^{0.25}$ (see Table 4.1). This then served as a datum from which to compare the subsequent heat transfers from the partially enclosed heater.

The highest enhancement of heat transfer rates was obtained for the narrowest interwall spacing coupled with the tallest shroud i.e. $S_W/d=1.5$,H/W=20, but the extent of enhancement decreased markedly as the height decreased. Thus for H/W=20, the enhancement was about 40% whereas at H/W=5 it was only 11%. The corresponding correlation at H/W=20,$S_W/d=1.5$ was $Nu=0.892Ra^{0.221}$, for $2x10^4<Ra<2x10^5$.

The effect of confining parallel plates on a single horizontal cylinder was examined by Marsters [68]. Two cylindrical heaters (d=6.35mm and d=3.18mm) were separately examined and the interwall spacing varied by up to 20d. The use of different fluids (air, water, and freon) permitted the analysis across a wide range of Ra. For all the wall spacings greater than 2d, enhancement was confirmed. However, all the data were obtained from a fixed elevation. Also, the effect of the Prandtl number was found to be suppressed in the deduced correlations.

Tokura et al. [25] examined a 3- and a 5-cylinder cylindrical array, (d=28.5mm), in a confined space between parallel plates. The optimum heat enhancement for the 3-cylinder array situated between parallel walls was obtained at a plate-to-plate distance of 3d, with the cylinders being vertically separated by 2d ($Nu/N_{\infty}\cong1.12$,$Ra\cong9x10^4$). This resulted in a gap of one cylinder diameter between the array and each wall (see Fig. 4-2a). The effects of the walls became negligible when the distance between any of the plates and the cylinder array exceeded 6 cylinder diameters. However, due to a large span of the multiple heater assembly, the interferograms could not be analysed

4.2.4. Horizontal Array of Cylindrical Heaters (parallel to one vertical wall).

Using a 3-cylinder array (d=25.4mm), Al-Alusi & Bushnell [27] showed with the aid of flow visualisation that, with only one wall close to the array, the space between the cylinders and the wall acted as a chimney whereby the air particles were at a higher ambient temperature (Fig. 4-2b). The higher temperature zone creates a low density, low pressure, region between the wall and the cylinders of the array, driving the air horizontally towards the wall through the spacing between the cylinders, and upwards along the wall. The maximum enhancement occurred when the vertical cylinder separation was 3d (CC_V=4d). The uppermost heater also had the highest enhancement of 1.2 (CC_V=1.5d).

4.2.5. Wall system interactions

Sparrow and Ansari [28] examined the heat transfer characteristics of a heated, horizontal cylinder which interacted with three types of wall systems: a) a vertical wall situated to the side of the cylinder, (b) a horizontal wall situated beneath the cylinder, and (c) a corner formed by the vertical and horizontal walls (see Fig. 4-3).

For (a) it was confirmed that the presence of a closely-positioned side wall reduces the cylinder Nusselt value in relation to that occurring when there was no wall, but this can be neglected for $CW_h/d > 0.25$. Although low emissivity heaters were employed (ε=0.05) in order to maintain the radiative heat transfers at a low level, the results were still presented in the form of the ratios of the total heat transferred from each heater. This finding agrees with earlier experiments which showed that for an increased gap, the Q/Q_∞ ratio, (proportional to Nu/Nu_∞ ratio) may reach 103% of that in free space.

For (b), the presence of a lower wall reduced Q/Q_∞ to <1.0 throughout ($0.81<Q/Q_\infty<0.97$, for $0.08<CW_V<1.3$). The smallest values of Q/Q_∞ correspond to the closest spacing, but as the spacing was increased, the reduction in heat transfer was only 3→4%. So the lower wall-to-cylinder interactions can be neglected when $CW_V>1.3$. When the heater was positioned in a corner, as in (c), the relative rate of heat transfer (Q/Q_∞) was greatly reduced to as low a value as 0.57, although if the gap ratios (CW_h/d,CW_v/d) exceeded 0.33, then heat ratios of up to 0.95 could be achieved. However, no flow-visualisation was presented to supplement and aid in the analyses.

Table 4.2. Heated Cylinder or Arrays in Free Space

Geometry	Reference	Correlation	Comment
One cylindrical heater, open space	[26]	$Nu=0.480Ra^{0.25}$	$2x10^4<Ra<2x10^7$
5 heaters between parallel walls (d=28.5)	[25]	$Nu=0.58Ra^{0.25}$	Mean of array 15% higher than in open space
3-cylindrical heaters parallel to one wall (d=35.4)	[27]	$Nu=0.571Ra^{0.2}$ $Nu=0.56Ra^{0.2}$ $Nu=0.6Ra^{0.2}$ $Nu=0.65Ra^{0.2}$	one cylinder in free space Nu average for 3 cylinders $CW_h=0.5d;CC_V=1.5d$ $CW_h=0.5d;CC_V=2d$ $CW_h=\infty;CC_V=4d$ For uppermost heater, $Nu/Nu_\infty=1.2$ $CW_h=0.5d;CC_V=1.5d$
corner effect,one cylinder	[28]		Nu≅15% lower

It can now be concluded that the most significant factor which would enhance the rate of convective heat transfer from arrays in free space is the optimum offsetting practicable, which happens to be only about half the heater diameter depending upon the vertical separation (see Fig. 4-1a). When several horizontal, closely-spaced cylindrical heaters were in an array their average convective heat transfer coefficient was less than that of a single heater, whereas when positioned close to one vertical wall, or between parallel vertical walls, it was possible to effect an arrangement that would enhance the convective heat transfers by up to 15%.

It would also appear that the heater diameter is a less important parameter because the results of the 6.35 and 38 mm diameter heaters for optimal convective heat transfers were similar. Conversely, when heaters are in close proximity to a bottom wall, degradation of convective heat transfers has been shown to occur. This is different

from assumed practice in ovens where convection is thought to be enhanced by base-mounted heaters.

Clearly the same results may not necessarily apply to enclosed heaters, because the confining walls may actually direct the recirculating flows towards the base-mounted heaters. Although extensive experimental studies of cylindrical annuli exist in the open literature [13],[29],[33],[37],[69], probably because of their relative simplicity, very few experimental investigations concerning heaters in rectangular enclosures have been presented.

4.2.6. Hot Cylinders in Rectangular Enclosures

Heat transfers from a cylindrical heater to a square-sectioned enclosure was investigated experimentally [33]. The 100x100x635mm enclosure was traversed by the 28mm dia. heater along the vertical line of symmetry. The main aim of the studies was to obtain the position for the least heat transfers for improved optimal location of a district heating pipe in a duct, so the operational ΔT was less than 20K. Using interferometry, the rate of convective heat transfer was found to decrease as the heater was moved away from the middle of the enclosure to the upper horizontal wall, although enhanced heat transfers were found just below the horizontal line of symmetry. However, only the upper central cavity was studied because it coincided with the position of least convective heat transfers.

Heat transfers from two cylindrical heaters, each at a different temperature in a rectangular-sectioned enclosure were investigated experimentally [34]. When the 28mm dia. heaters were positioned one above the other in the 100x125x650mm enclosure, enhanced heat transfers were confirmed when the warmer heater was situated below. The primary objective was to inhibit heat transfers from the cylinders - simulating insulated district heating pipes - to each other, and to the external environment. However, as in [33], a small enclosure was employed and the use of differentially imposed thermal boundary-conditions reduce the applicability of the derived correlations for onward application in the present studies.

Another study of two cylindrical inner bodies one above the other in a rectangular enclosure (see Fig. 4-4a) was presented [43]. The numerical codes were also tested on a heated protrusion on the vertical wall of a rectangular enclosure (see Fig.4-4b), and this was then supplemented by experimental data. The cylindrical streamline results

were presented at Ra=10^4 and Ra=10^6. When the cylinders were close together at the base of the enclosure, there was a small recirculation between them and the adjoining vertical wall. At the higher Ra, there was increased convective activity at the upper horizontal wall and top corners. This was further accentuated when the upper cylinder was moved higher up towards the upper horizontal wall although the small recirculation earlier indicated by the streamlines sandwiched between the cylinders and the vertical walls had disappeared. As the upper cylinder was traversed vertically, the flow initially remained stagnant around the bottom cylinder, the temperature gradients in the vicinity were very small, and conduction was the prevailing mechanism of heat transfer. But as Ra was increased a dramatic increase in Nu occurred, although the rate of increase decreased as Ra approached 10^6.

The experimental and numerical study of three uniform-flux cylinders placed side by side at the base of a rectangular enclosure [47,48] revealed that although the centrally-positioned cylinder was warmest, it also produced the lowest mean convective heat transfers because there was restricted peripheral flow. This significant finding immediately demonstrates that an increase in system temperature does not necessitate a relative increase in the convective heat transfers. While it has been experimentally demonstrated that the heat transfer characteristics of heaters in the vicinity of a wall can be quite different from when operating in free space, a further scrutiny of the literature did not reveal the extent of the difference in heater flow behaviour when totally immersed in an enclosure.

The numerical investigation of Deschamps and Desrayaud [70] concerned a concentrated line heat source in the form of a cylindrical heater situated in a rectangular-sectioned enclosure. Flow velocity and the pattern of the flows appear to have been the main focus of study, and no analysis of the heat transfers occurring were presented. Otherwise, there is a dearth of information regarding heaters in rectangular enclosures.

4.2.7. Cylindrical Annuli

In the studies of eccentric horizontal annuli [33,37,67], when the hotter inner cylinder was traversed towards the outer cylinder, it was established that the position of the minimum or maximum convective heat transfers was a function of the radius ratios. Generally, for a small annular gap, gaseous conduction effects reduce the influence of the eccentricity on convection [33]. As the annular gap increased, the inner cylinder

must be offset vertically upwards by a relatively larger eccentricity in order to minimise convective heat transfers.

In the numerical studies of cylindrical annuli [69], the horizontal variation in eccentricity established a different pattern for the heat transfers, but the convective heat transfers still increased as the periphery of the outer cylinder was approached. However, this was attributed to conduction effects. The erratic variability of convective heat transfers with vertical eccentricity further demonstrate the complications encountered in enclosed spaces even though there are no abrupt profile changes, unlike in rectangular enclosures.

4.3. AIMS

In the earlier (oven) experimental studies (see Chapter 3), the heaters were provisionally set at fixed geometries (35mm) from the enclosure walls. This was partly based on the notion that the further from the enclosure walls, the less intense the radiative heat transfers and insulation heat losses, and partly because of design restrictions. Questions which remained unanswered include the spatial position of the heaters relative to the walls, and the effect when heaters are positioned at the corners. Also, convective flow from bottom heaters suggest that there may be more flow for this configuration than in free space.

The primary objective here is to obtain heat transfer data for various positions of a cylindrical heater in a rectangular enclosure and to obtain an optimum position where the heater can be situated for achieving enhanced natural convection.

4.4. EXPERIMENTAL APPARATUS

Both flow visualisation and interferometric tests were carried out using the 350x350x750mm enclosure utilised previously (see Chapter 3). The enclosure was regarded as the cold surface, being cooled by the surrounding ambient air similar to the techniques of Zhao et al. [48]. Consequently, the maximum power input flux to a cylindrical electric heating-element was limited to 990W/m^2.

The first heat source was a single cylindrical electric heater, 9.5mm dia. with an overall heated length of 590mm. The ratio of the heater diameter to the enclosure length was only 1:35. Radiative heat transfer is inherently three-dimensional and to reduce any 3-D effect would necessitate conducting the study at low power inputs corresponding to low heater temperatures. Consequently, the study was undertaken within the constraints of the apparatus to exclude high temperature operations. Power was supplied through a variable voltage regulator. The heater power consumption was measured with a calibrated wattmeter.

The second heater was obtained via a 55mm dia. copper pipe which was fabricated as shown, and through which water ($25^0C<T<55^0C$) was circulated (see Fig. 4-5). The black protective paint gave an emissivity of 0.88. The heater vertical position was adjusted by leverage, raising or lowering the inlet and outlet pipes via externally mounted brackets.

4.5. PROCEDURE

The 9.5mm dia. heater was first suspended in free space in the laboratory in order to ascertain its heated length, the amount of conductive loss at the ends, and the trends of the heat transfers as ΔT was altered. To this end, it was instrumented with 10 thermocouples, four of these radially distributed around the periphery at the heater mid-position. The useful heated length was 590mm. The ends were suspended by relatively large electrically insulating sindanyo tubes. The considerably larger diameter of the sindanyo tubes (17mm), and the slightly warped profile of the heaters precluded the use of the MZI for obtaining the heat transfer coefficients directly. Therefore, the convective heat transfers were obtained by subtracting the radiative heat transfers from the total heat input, any other losses being assumed to be via the enclosure.

Flow visualisation tests were carried out for two positions at the base, two at the top, and four at the horizontal mid-position as shown (see Fig. 4-6b). The minimum horizontal spacing S_h was limited to 1.5d due to arrangements for electrical insulation of the heater terminals. However, it was possible to obtain S_h=0 for the larger diameter piping arrangements. Because of the substantial similarity in the flow results of both the 9.5mm and 55mm cylindrical heaters, only that for the 55mm heater at S_h=0 is presented. Additional flow visualisation tests were also carried out for multiple cylindrical heaters in the enclosure.

A vertical probe with seven thermo-junctions (see Fig. 4-6a) was traversed across the enclosure in the x-direction in order to examine the cavity temperature profiles during each preliminary test. Because of symmetry, the probe need only be traversed across half of the enclosure for the centrally-positioned heaters. For the non-symmetrical configurations, both glass end plates were opened in order to re-position the probe on either side of the heater during the traversing process. Appropriate thermal equilibration periods were then necessary for steady-state conditions to be re-established.

The probe was retained for the main tests and this additionally served to indicate the mean air temperatures and when steady-state conditions were achieved. The data obtained when the heater was centrally-positioned was processed for use as the reference datum. Experiments were conducted on both sides of the central sidewall in

order to ascertain the consistency of the cavity results with respect to symmetry. Otherwise, all the other tests were conducted either at the central vertical line, or on one side of the cavity only.

Based on the deductions, interferometric tests .were subsequently carried out for a limited number of configurations, and strictly for the larger cylindrical heater. Tests were carried out for the centre-line symmetry, and with the pipe being progressively moved closer to the vertical wall (S_h=d, S_h=d/2, S_h=d/4). For these, the glass end plates and retaining end flanges were replaced by the narrower, optically-flat glass plates mounted on the wooden jig as described in Chapter 3 (see 3.3.3). The difficult process of aligning the enclosure (sidewall and horizontal walls), and the pipe with the interferometer was then carried out. However, this process was necessarily repeated after each relevant flow visualisation test was completed. The MZI employed produced an ellipse (180mm x150mm) thereby requiring a minimum of 6 photographic frames for one half-symmetry (see 3.3.3).

Further tests were carried out to examine both the air flows and isotherms of two horizontal 55mm diameter heaters in the same enclosure. This was accomplished by varying the horizontal offsets (horizontal cylinder-to-cylinder distances). The vertical spacing between the lowest heater and the lower enclosure horizontal wall was 55mm (i.e. S_V=d) and the gap between the two heaters, also 55mm (see Fig. 4-14(c-e)). Although the heater vertical position was adjusted by raising or lowering the inlet and outlet pipes via externally mounted brackets, this assembly was not sufficiently robust to afford exact alignment with the interferometric beam simultaneously as the enclosure walls. The problem was exacerbated by supply pipe distortions caused by differential expansion when subjected to increased temperatures. However, this would not unduly affect the deductions since no quantitative data were sought from the interferograms.

4.6. DATA REDUCTION

When a heater was located in the upper half of the enclosure, stratification occurred below. Similarly when the heater was located near one of the enclosure's upper corners, or generally in an unsymmetrical position, stratification or very limited convection occurred in the lower portion of the unoccupied position. Hence convective heat transfers occurred in an indeterminate fractional volume of the enclosure.

For a cylinder or pipe exchanging heat within an enclosure, an exchange factor which incorporates the areas and emissivities can be obtained [11]:

$$XCHF_{1\text{-}2}=\frac{1}{\varepsilon_1}+\frac{A_1}{A_2}\left(\frac{1}{\varepsilon_2}-1\right) \qquad (4\text{-}1)$$

where subscript 1 represents the inner object and $F_{1\text{-}2}$ is unity.

Then Q_{rad} is obtained from: $(1/(XCHF_{1\text{-}2})).\sigma.|T_1^4\text{-}T_2^4|$.

Although the heaters were immersed in the enclosure, the environmental ambient air was the heat sink. The heater temperatures were less than 363K, and the glass end plates were correspondingly treated as opaque to long-wave radiation.

The thermal conductivity of the glass was taken as 1.038 $Wm^{-1}k^{-1}$ ($T<100^oC$), which means that the heat losses through the end plates were relatively small for the tested range of temperatures, when compared with the rest of the uninsulated 1.2mm thick MS enclosure ($k=51\ Wm^{-1}K^{-1}$). Therefore the result was assumed to be 2-D, the enclosure surfaces being used as the cold surface. The mean cold surface temperature of the walls were obtained from the arithmetic average of 20 thermocouples.

In presenting the results, it was assumed that the heat transfers with the heater located at the centre-line of the enclosure (at zero eccentricity), were subjected to the least wall interference. The Nusselt number at this position was designated Nu* (Q^*_{conv} for the corresponding convective heat value). Nu was calculated from $hL/k=\{Q_{conv}/A\Delta T\}L/k$, where L, the characteristic length was taken as the perimeter of the heater (0.0298). It was initially necessary to investigate the use of either Q or Nu for comparison because Nu incorporated ΔT, where the effects of the variability in

the environmental temperatures were expected to be more pronounced. However, Fig. 4-9a subsequently confirms that the trends were similar and the differences marginal between both sets of ratios. The deviations of Q_{conv}/Q^*_{conv} from Nu/Nu* were +5.0% and -7.1%, and it is seen that the use of the Nu/Nu* relation subtly accentuates the comparative changes in the experimental data, thereby easing the analyses. This contradicts Morgan's observations [26] where the correlations dampened the fluctuations in the experimental data.

The use of the external (free space) heat transfer correlations was found to give a less exacting comparison, although the supplementary experiment enabled the level of accuracy of the correlations to be established.

The experiments involving the flow visualisation were conducted at $Ra=9.1x10^4$ while the heat transfer experiments were conducted at two other power inputs. The variation in the value of Ra for the different heater positions were negligible for identical power input, thus giving two average values for Ra (i.e. $7.5x10^4$, and $1.1x10^5$). Therefore, the numerator and denominator of Nu/Nu*, recorded at an identical power input were regarded to be at similar Ra. A deviation of Nu/Nu* (or Q_{conv}/Q^*_{conv}) from unity immediately provides a comparative measure of enhancement or otherwise with respect to the heater location.

4.7. RESULTS

4.7.1. Flow Visualisation and Convection Heat Transfers

The heater location is referenced in non-dimensionalised X-Y co-ordinates, where X=x/350, Y=y/350 (0<X<1, 0<Y<1). The flows associated with each heater configuration are shown (see Fig. 4-7(a-f)) but because of the complications and significant differences in flow direction, strength and overall patterns, they are analysed separately. There was very little change in the value of Ra at the different locations, so the flow visualisations have been analysed at conditions for $Ra=9.1x10^4$, (T_H59.3°C).

4.7.1.1. Flow visualisaton: vertical traverse heater position - Centre: X=0.5,Y=0.5

The heated stream described two vortices. The descending flows along the vertical walls progressively weakened as branches drifted towards the middle of the enclosure (see Fig. 4-7b). The first set of branches contributed to the recirculating loop at each upper quadrant. The branches below the centre-line (Y=0.5) turned back sharply upwards and then horizontally, joining the earlier branches to converge on the heater. For a similar enclosure fitted with a relatively large prismatic heater, Oosthuizen and Paul [41] predicted streamlines which were unicellular but with the stationary cores located at the upper quadrants which are quite different from the present data. In addition, the descending flows were reported to separate about midway from the vertical wall whereas the present results show quite clearly a weak flow continued to descend along the vertical wall (flow penetration) until looping back upwards just before touching the lower horizontal wall.

The single interferogram composed from six photographs of the 55mm dia. pipe (see Fig. 4-17, and Fig.4-14a) is similar to that obtained by Shilston [33] (28mm dia. in a smaller 100x100x635 enclosure which allowed a single photographic exposure), with flow penetration downwards along the cold vertical wall. This agreement, in spite of the distortion introduced by concatenation, indicates that for the central position only, the enlarged enclosure would not unduly influence the flow characteristics of a single heated source. Therefore, incorporating the aspect ratio derived from a single enclosure into any deduced correlations would not significantly improve its accuracy.

The main inflows approached the heater virtually horizontally, from both sides, with an initial impetus driven by the cavity flow, but a stationary, oval-shaped cell was formed below the heater. This indicated a pocket of zero convective flow. Pockets of such reduced or zero activity signify a reduction in the mass of fluid participating in convection. Therefore, an arrangement where a line heat source, centrally-positioned and exhibiting identical flows, would not provide optimal convective heat transfers within the enclosure. Above the heater, the rising stream which entrained more air from both sides, was seen to oscillate where it met the upper quadrant recirculation (see 01 in Fig. 4-7b).

The numerical results of Oosthuizen and Paul [41] resembled more closely the study of a cylindrical annulus of zero eccentricity [69] than a rectangular enclosed heater where more flow penetration along the cold wall would be indicated.

4.7.1.2. Flow visualisaton: vertical traverse heater position - Base: X=0.5,Y=0.1(S_y/d=3)

The heater inflow remained horizontal but converged upon the heater just above its horizontal centre-line (see Fig. 4-7c). There was no visible smoke around the base of the heater, which implied that a degradation in natural convective heat transfers would occur. This was partially inferred in the FEM and interferometric studies of Larson et. al. [42] where the streamlines failed to touch the base of the cylindrical heater in the rectangular enclosure. The stagnation layer around the base of the heater would be associated with transferring heat purely by conduction. However, a higher proportion of the lower heater surface was still reached in [41] than observed from the smoke patterns in the present experimental studies.

4.7.1.3. Flow visualisaton: vertical traverse heater position, Top: (X=0.5,Y=0.9 (S_y/d=3)

The heater inflow was similar to that of the centrally-positioned heater (X=0.5,Y=0.5). But just below the heater, a portion of the inflow split, symmetrically flowing downwards, and forming large, progressively weakening counter-rotating flows throughout the remaining expanse of the enclosure volume (see Fig. 4-7a). At low temperatures as in the present studies, the effect of the heater plume would be to transfer heat to the upper surface, but at higher temperatures as in ovens, the plume would be contacting a higher temperature upper surface (because of heater proximity),

thereby cooling it and attenuating the temperature profile as it travelled across the upper surface. This temperature modification should result in a more uniform irradiance from the wall to an inner body. The lower flows were very weak, although their effects were visible throughout the lower volume, decreasing in intensity progressively towards the base of the enclosure. Although the oval shaped stationary cell, observed below the centrally-positioned heater (see Fig. 4-7b) was not repeated in this arrangement, the weakness of the flows confirm that locating heaters along the upper horizontal wall cannot improve natural convection. However, it could reduce the temperature gradient across the crown.

4.7.1.4. Heat transfers - centre-line vertical traverse: base to crown (X=0.5, 0.1≤Y≤0.9).

The corresponding relationship between the heat transfers and the vertical distance are presented in Fig. 4-9b ($Ra=7.5x10^4$) and Fig. 4-10a ($Ra=1.1x10^5$). Referring to the former, the value of Nu/Nu* was first seen to rise from 0.725 at the base to a maximum of 1.24 at Y=0.24. The value was then reduced to unity at the centre of the enclosure, and further lowered to 0.79 as the heater approached the upper horizontal surface. Somewhat similar non-linear trends have also been observed in cylindrical annuli [33, 69], and in vertical pipe traverses in square ducts [33]. The reduction in the convective heat transfers could be attributed to the reduced air contact with the heater at the extreme positions due to interference by the proximity of the horizontal walls, while the highest heat transfers (just below the centre of the cavity at Y=0.25) would be as a result of improved air flow into the heater from all directions.

It should be recalled from the flow visualisation (see Fig. 4-7b) that a stagnant cell existed below the heater, interpreted as a non participating mass of air, and therefore, not an optimal convective flow pattern. This partially explains why the heat transfers were higher at Y=0.25, than at Y=0.5 where axi-symmetry should have ensured the most optimal flow convergence on the heater. The other explanation is that the two main recirculating vortices created at the upper quadrants somehow interfered with flow convergence on the heater. As the heater elevation was increased, it came increasingly under the adverse influence of the recirculating vortices, such that copious inflow towards the heater was suppressed.

However, at the higher Ra (see Fig. 4-10a), the heat transfers followed a different pattern. The Nu/Nu* values rose less steeply from a low value of 0.495 to the

maximum value of unity at Y=0.5, before being reduced to a value of 0.68 at the extreme position near the crown. But the rate of decline in the upper quarter was lower than at the lower value of Ra as conduction effects improved the rates of convective heat transfers. It can be inferred from this that conduction effects became more and more significant as the temperature difference increased. Another trend noticed was that the peak enhancement in convective heat transfers shifted upwards as Ra increased, from Y=0.24 at $Ra=7.5x10^4$ to Y=0.5 at $Ra=1.1x10^5$. This is clearly depicted in Fig. 4-13d.

The variation in the value of Nu/Nu* of the 9.5 mm diameter line heat-source with elevation was curve-fitted with a 4th-degree polynomial ($R^2=1$) to yield:

$Nu/Nu^* = -35Y^4 + 76.4Y^3 - 57Y^2 + 17Y - 0.47$; $Ra=7.5x10^4$; $0.1<Y<0.9$, and
$Nu/Nu^* = 9.7Y^4 - 16.7Y^3 + 6.4Y^2 + 1.1Y + 0.34$; $Ra=1.1x10^5$; $0.1<Y<0.9$.

4.7.1.5. Flow visualisaton: vertical wall traverse, X=0.94,Y=0.5(S_h/d=1.5)

The flow from the heater created a single recirculating vortex which was largely bound by the horizontal centre-line (see Fig. 4-7e). The inflows (to the heater) passed under the heater, and rose between it and the vertical wall. In so doing, the combined stream was heated and expanded as it rose, giving rise to a chimney effect in the enclosure. The flow rate was considerably higher than at any other location and no cells or quadrant recirculation were formed along the vertical wall. Also, no stratified pockets were noticed in this configuration.

4.7.1.6. Flow visualisaton: vertical wall traverse: Base(corner): X=0.94,Y=0.1;S_h/d=1.5,S_v/d=3.0

The flow from the heater rose vertically without any perceptible deflection, where it entrained more air from the cavity space. The lower left corner was not quite stratified, being slowly driven by the heater in-flow, which was virtually horizontal. Because the flow was not seen to completely surround the cylindrical heater, and there was apparently little or no flow acceleration, it was presumed from the flow visualisation that locating heaters at the base corner would produce reduced natural convection ($Ra\sim9.1x10^4$).

4.7.1.7. Flow visualisaton: vertical wall traverse: upper(corner): X=0.94,Y=0.95;S_h/d=1.5,S_v/d=3.0

The main flow activity was concentrated mostly in the upper half of the cavity, with the most vigorous portion of the flow forming a recirculating crescent-shaped cell at the upper left hand quadrant (see Fig. 4-7d). A secondary, counter-rotating weak flow, the centre of which was below the cavity centre-line, was attributed to the bifurcation of the descending flow from the cold vertical wall.

A very small, rapidly-rotating (clockwise) cell was formed at the top right hand corner adjacent to the heater (see 02 in Fig. 4-7d). The high degree of inactivity in the lower space was indicative of lower convective heat transfers. Also the tiny, rapidly-rotating cell at the top corner suggested wasteful convection because thermal energy was required to drive the cell, which was transferring heat to the enclosure corner rather than to the main stream flow which, otherwise would have been beneficial to an inner body or cold wall.

4.7.1.8. Heat transfers - sidewall vertical traverse:
base to crown (X=0.94, 0.1<Y<0.9).

The corresponding relationship between the heat transfers and the vertical traverse along a vertical wall are presented in Fig. 4-9d ($Ra=7.5x10^4$) and Fig. 4-10c ($Ra=1.1x10^5$). Referring to the former, the value of Nu/Nu* was found to vary haphazardly, firstly from an enhancement of 1.3 at the base, to a degradation of 0.85 at Y=0.2, then rising again to a maximum of 1.4 at Y=0.5. The enhancement at the base corner is in conflict with the observations of a partially enclosed heater located at a corner, [28], where the values of the heat ratios fell to as low a value as 0.57 ($Ra=2x10^4$, S_h/d=1/12) or to 0.80 ($Ra=2x10^5$,S_h/d=2/3), still below unity.

At the higher elevation, the flow visualisation indicated improved air flows, principally rising between the heater and the vertical wall, similar to the chimney effect described by Al-Alusi and Bushnell [27] in their free space studies of horizontal array of heaters (also see section 4.7.1.5). The enhancement at Y=0.5 could be similarly attributed to the aforementioned improved air flows resulting from the chimney effect, whereby the rising, heated air stream created a zone of low pressure between the heater and the vertical sidewall. The improved air flows would dominate any conduction effects attributed to the proximity of the heater to the enclosure walls.

This finding is very significant for lower temperature inner bodies such as in totally enclosed, intrinsically safe electrical and electronic modules. Certain positions along the sidewall should be exploited for unvented enclosures.

The reduction in the value of Nu/Nu* above and below this position would be a combination of the growing influence of the horizontal walls as well as a probable adverse influence of the cavity vortices in inhibiting air inflows to the heater. The values of Nu/Nu* were then found to rise again at the extremities, near the horizontal walls. These could be attributed to double conduction effects - conduction influence from the two mutually perpendicular walls, the proximity of the heater to the walls promoting increased heat transfers by gaseous conduction, which offset, somewhat, the reduction in natural convection. At the higher value of Ra however, there was virtually no increase as the heater approached the horizontal walls. This was unexpected, but it should be recalled that the heater utilised was a high emissivity heater. Therefore, the increasing temperature would cause a higher value of radiative heat-transfers, thus resulting in a lower proportion of convection, ultimately leading to lower values of h and Nu. Also, for separation distances greater than the heater diameter, Sparrow and Ansari [28] reported that the value of Q/Q* (~Nu/Nu*) was found to decrease as Ra increased which agrees with the trends in this study.

4.7.1.9. Flow visualisation: Additional central horizontal traverses.

Further tests were performed in order to investigate the vertical wall interactions, in particular its role in the formation of the eddies in the upper quadrants. The heater was traversed from the centre of the enclosure (X=0.5,Y=0.5) horizontally towards one of the vertical walls (see Fig. 4-8(a-f)). For greater clarity, Fig. 4-7a and Fig. 4-7e have been reproduced as Fig. 4-8a and Fig. 4-8e respectively.

As the heater was gradually moved from the centre of the cavity, specifically to X=0.7; Y=0.5, the convective activity (in the decreasing upper right hand space) was seen to gradually intensify (see 01 in Fig. 4-8b). Simultaneously, rolling vortices or eddies were noticed along the upper horizontal wall for the left hand zone, where the flow descended. Although the flow at the base was generally weak and haphazard, the active upper right recirculating flow appeared to drive its adjacent lower flow where a somewhat increased flow was noticed flowing towards the heater.

With a further traverse towards the wall, at X=0.88 (S_h/d=4, ≅40mm), the recirculating vortex in the upper right hand corner had become smaller and much more vigorous (see 02 in Fig. 4-8c). But a triangular stratified cell was centrally positioned to the left of the heater. Increased flow was noticed at the underside of the heater, with an increasing preference to flow between the heater and the vertical wall. The heated rising flow was seen to oscillate horizontally (see 03 in Fig. 4-8c).

At X=0.9 (S_h/d=3, ≅30mm), the recirculating vortex in the upper right hand corner had disappeared (see Fig. 4-8d), and the flow resembled that at X=0.95 described earlier (see Fig. 4-7e and 4-8e). However, the larger gap which resulted from the deflected heated flow was occupied by a very small rapidly-rotating clockwise cell as shown (see 04 in Fig. 4-8d). The upper corner was also occupied by another rapidly-rotating cell (see 05 in Fig. 4-8d). A stratified pattern was also positioned below the horizontal centre-line but appeared to be smaller than for X=0.9, indicating improved convective capacity.

4.7.1.10. Heat transfers - traverses in the horizontal direction:

Between the central and sidewall vertical traverses, the heater was also traversed vertically at X=0.25, (X=0.75), providing further data points for analysing the wall-to-wall traverses at the base (Y=0.1), at Y=0.25, 0.5, 0.75, and at the crown (Y=0.9). The vertical symmetry permitted the reproduction of the traverses at X=0.06 and at X=0.25 as X=0.94 and X=0.75 respectively. The traverses across the base and the crown will be referred to as horizontal wall traverses and are discussed in the following sub-section. The traverses at Y=0.25, 0.5 and 0.75 are referred to as vertical wall traverses and are discussed in 4.7.1.10.2.

4.7.1.10.1. Heat transfers - traverses across the base and crown

These refer to traverses across the base and the crown (see Figs. 4-12a and 4-12e for $Ra=7.5x10^4$). Each figure corresponds to a vertical clearance S_v of 0.030m (30mm), and a minimum horizontal clearance at the corners S_h=0.015m. The increased values of Nu/Nu* at the corners have earlier been attributed to a double conduction effect. But the values increased slightly, as the heater was traversed from the sidewall towards the middle of the enclosure. The rise in convection was attributed to this slight increase. However, the values steeply declined again as the middle of the enclosure

was approached. Therefore, the absence of a second wall has not been compensated for by the exposure of the heater to a presumed higher flow. At the higher value of Ra, (see Figs. 4-11a and 4-11e for $Ra=1.1x10^5$) similar profile was maintained, but a reduction in the heat transfers occurred throughout the traverse. The reduction of Nu/Nu* (at the base) was most severe at the centre (Nu/Nu*=0.495 - the lowest value in this study), but it rose to 0.588 at the corners. Since the results of Sparrow and Ansari [28] for bottom wall interactions in open space showed a reduction of only 3-4% in the range ($2x10^4<Ra<2x10^5$), the present results affirm that enclosure convective heat-transfer degradation for the base configuration would be more severe than that for open space.

At the crown, the values of Nu/Nu* at the corners were higher than at the centre of the enclosure, but still below unity throughout (see Fig. 4-12e for $Ra=7.5x10^4$, and Fig. 4-11e for $Ra=1.1x10^5$). The double conduction effect is again partly responsible for the increases at the corners as well as the increased convective activity at the corners (see Fig. 4-7d) which are now seen to have a less adverse effect on the natural convection heat transfers than inferred from the flow visualisation.

4.7.1.10.2. Heat transfers - traverses between sidewalls;
Y=0.25, 0.5 and 0.75 ($0.06\leq X\leq 0.94$)

The three cases considered were with the heater horizontally traversed at Y=0.25, 0.50 and at 0.75, and are presented respectively in Figs. 4-12(b-d) for $Ra=7.5x10^4$. Each case followed similar patterns, the values of Nu/Nu* decreasing as the gaps between the heaters and the walls increased reaching a minima at X=0.25, (X=0.75). It could be recalled that a vigorous vortex developed when the heater was in an eccentric position (see Fig. 4-8(b,c)). It is postulated that this vortex suppressed the upward air flow around the heater, and as the eccentricity increased this adverse influence would increase, further interfering with copious flow around the heater; additionally, the presence of stationary cells had been associated with a reduction in the mass of fluid actively participating in the convective heat transfers; hence the reduction in the values of Nu/Nu* as the heater eccentricity increased. The heat transfer increases nearest to the walls have been explained previously, either as conduction effects (at Y=0.25 and Y=0.75) or the chimney effect (at Y=0.5). At the higher value of Ra, the profiles of Nu/Nu* were maintained although their values indicated a reduction in the heat transfers throughout.

It can be further postulated that the smaller, faster vortex of the non-symmetrical flow was subjected to more wall drag and consequently, to a lower corresponding velocity than if the configuration had been symmetrical. So that if the heater were to be brought closer to the vertical wall until the faster upper quadrant vortex disappears (i.e. S_h << 30mm), then an optimal convective enhancement would be achieved.

In the literature, the increase in heat transfers with heater proximity has been explained differently in tests conducted for eccentric cylindrical annuli by Zagromov and Lyalikov [71], Kuehn and Goldstein [37] and Cho et al. [69], where conduction effects were held responsible (analytically, and therefore numerically) for the increases in heat ratios, irrespective of where the heater was nearly touching. Sparrow and Ansari attributed the observed increase (1-3% , $S_h/d>4/3$) to possible supplementary buoyancy induced by the sidewall.

However, it is demonstrated here experimentally that while a heater in close proximity to the base (and to the crown) may be subjected to conduction effects because of restricted air flows, it is a chimney effect which must be responsible for increases in convective heat transfers at the middle region of the vertical walls of a rectangular enclosure. Furthermore, the chimney effect must be driven by the thermal energy from the heater, since the high conductivity metallic wall utilised in this study could not contribute sufficient supplementary buoyancy because its temperature rise was relatively negligible.

4.7.1.11. Flow visualisation, heater position - abut sidewall, S_h=0 (for Y=0.5, Y=0.4 and Y=0.7), Ra=$2.7x10^7$

The first analysis at S_h=0 refers to the flow patterns from the cylindrical pipe heater (d=55mm), which touched the vertical wall at Y=0.5.

The main flow activity was in the upper half of the cavity, with the lower half virtually stationary. It was also noted that the direct air flow contact with the heater occurred in only about a third of the heater periphery; the sluggish air flow which contacted the heater base was an indication of dominant gaseous conduction. So, apart from the sidewall or substrate conduction effect, the convective component, whenever the heater abuts the vertical wall, should always be less than for any other position in the horizontal traverse. A small, rapidly-rotating recirculating cell (07 in Fig. 4-8f), similar to that for the smaller diameter heater (05 in Fig. 4-8d), was re-established at the upper

quadrant as well as two other tiny cells, sandwiched between the heater and the vertical wall (08 and 09 in Fig. 4-8f). The lower heater cell (09) was stationary while the upper heater cell (08) indicated rapid rotation. The upward flow around the periphery of the cylindrical heater appeared to travel with reduced velocity than when the smaller (9.5mm dia.) heater was used. However, the value of Ra for the larger heater was higher for the same temperature difference because of the larger characteristic lengths.

The photographs for Y=0.4, and for Y=0.7 clearly show the transient progress of the smoke flow paths (see Fig. 4-15(a-d) and Fig. 4-16(a-d) respectively; and the complementary schematic dimensions, Fig. 4-14(a,b)). No localised flow existed around the supply pipes, which were heavily insulated. The rolling vortices across the crown were faintly visible. Fig. 4-15d also shows the smoke penetrating right to the base at the opposite vertical wall. It was noticed that a considerable difference existed from the benchmark numerical solution [18] for a flush-mounted heater, where a wall-mounted plate heater produced uniformly unicellular streamlines. While the unicellular core was located at about the middle of the enclosure, the corresponding core in the present study was located much higher up at the middle of the upper quadrant.

Fig. 4-16(b-d) show the effect of introducing smoke at the upper part of the cavity (Y=0.7). Some mixing was eventually achieved, although a dichotomous cavity of both clear and smoky space, fenced by a planar partition in line with the heater, was still visible. Fig.4-16a shows the introduction of smoke from below, where mixing was achieved more rapidly. This can be attributed to the additional buoyancy acquired, and the longer vertical distance travelled by the smoke particles when introduced into the cavity.

4.7.2. Interferograms of sidewall interactions

Interferograms for the enclosed 55mm dia. pipe clearly show that moving the pipe closer to the sidewall reduced the rate of rise of the enclosure sidewall temperatures (see Fig. 4-18(a-c)). Fig. 4-18a shows two fringes parallel to the vertical wall. At this stage, there was negligible deflection of the plume from the vertical towards the sidewall, because the rarefied gap between the plume, the sidewall, and the upper horizontal wall would be occupied by the rapidly-rotating, rectangular-shaped

recirculation which was earlier observed in the smaller heater flow visualisation at X=0.88 (see Fig. 4-8c).

As the pipe was moved closer (S_h/d=1/2≅27mm), the visible fringe width along the sidewall had been reduced to a half (see Fig. 4-18b), indicating that the rising flow was sweeping and influencing the sidewall vertical temperature profile directly opposite the heater. This temperature rise was 1.5fringes x 0.789°C/fringe=1.2°C (see Appendix A). This action was seen to shift the peak sidewall temperature well above the heater centre-line. Therefore, for the purposes of data acquisition, the exact point of temperature measurement along the vertical sidewall should be above the centre-line, and not on the closest approach of the cylindrical heater, as was assumed [28] in the experimental data acquisition.

At the closest distance to the sidewall (S_h/d=1/4≅14mm), the fringe had disappeared altogether (see Fig. 4-18c). Ordinarily, the sidewall should have become much more warmer in response to the proximity of the heater as discussed by Sparrow and Ansari [28] due to increased radiative heat transfers. However, the high conductivity wall utilised in this study responded rapidly to the environmental thermal conditions. Therefore, it could not have produced appreciable supplementary buoyancy.

It was shown in the flow visualisation and the corresponding heat transfer analyses (see 4.7.1.8) that the imbalance in the upper vortices inhibited convection from the heaters. It was also shown that when the heater was so close to the wall that the vortices disappeared, increased convective heat transfers should occur. For the centred horizontal traverse, it can be recalled that heat transfer data were obtained at 3 discrete positions (X=0.5, 0.75 and 0.94) using the 9.5mm diameter heater. Between X=0.75 and X=0.94, it was expected that a gradual rise in the heat losses from the larger cylindrical heater would occur, to be exhibited as increasing fringe density around the cylindrical heater. However, the reducing fringe density for the 55mm diameter pipe (see the interferograms Fig. 4-18(b and c)) as the wall-to-heater spacing was being reduced, indicated further reduction in the convective heat transfers. This suggests that the value of Nu continued to fall as the heater approached the vertical wall and that the optimal position for convective heat transfers had not yet been reached.

Since the interferograms (see Fig. 4-18(b,c)) show that the heater plume was deflected towards the wall, this would indicate that the quadrant recirculation (see 02 in Fig. 4-8c) had already been replaced by the smaller, rapidly-rotating cell just above the heater

(see 04 in Fig. 4-8d). The presence of the small cell, however, indicated that increased flow around the heater could not occur. Still, it could be stated at this stage that larger cylindrical heaters would require smaller heater-to-wall offsets before improved or optimal convection heat transfers could be achieved.

At the minimum gap between the heater and the wall, the larger heater plume centre-line would be S_h+d/2 (S_h+27.5), whereas the plume for the smaller diameter heater would only be at S_h+4.75 from the wall. It is, therefore, possible to achieve zero cell formation for the smaller diameter heater. Conversely, as a cylindrical heater gets larger, the enhancement of natural convection heat transfers becomes impracticable (i.e. recirculating vortices or cells would always be formed for relatively large heaters, such as the 55mm diameter heater employed for the interferograms). However, if the spacing becomes too small, conduction effects would prevail and eventually, a recirculation would develop at the lower portion of the heater and the adjacent vertical wall, signifying further reduction in convective flows, because the spacing between the heater and the vertical wall had become too narrow for the expanding, heated air.

Another point to note concerns similarity. The value of Ra ($Ra=2.7x10^6$; $\Delta T=7.6K$; $T=299.1K$) was much greater than that for the smaller diameter heater ($Ra=7.5x10^4$; $\Delta T=34.0K$; $T=52.0$). However, the density difference that could be generated by the smaller diameter heater at the lower Ra would be much higher than that for the larger heater ($\Delta T \propto 1/\Delta\rho$). It is now seen that the powerful influence ΔT would not be adequately emphasised by the dimensionless parameter. Therefore, similarity must take into account the increased influence of the density ratios between the narrow gap and the cavity.

It was revealed in the literature that for one cylindrical heater situated between two confining walls or shrouds, the extent of convective heat enhancement decreased rapidly as the shroud height decreased [67]. The basic principle behind the chimney effect relies on a physical separation of the heated fluid from an environment. In the situation considered here, the physical separation provided by the small diameter heater and the vertical wall is very small indeed which immediately exposes the generated plume to the enclosure environment, and therefore is limited to a finite pressure differential. A larger cylindrical profile would be expected to provide a larger separation, and, consequently exhibit larger improved effect. However, it has now been shown that this is not so, and that a smaller gap would be necessary for a possible

chimney effect to occur. Therefore, the density difference is a more powerful parameter than the geometrical profile.

For the 9.5mm dia heater, however, the criterion for optimal convection heat transfers when positioned along the sidewall is $S_h/d \leq 15/9.5$, or $S_h/d \leq 1.5$ in a 0.35x0.35 enclosure (for Y=0.5, Ra≅10^5; or Y=0.25, Ra≅$7.5x10^4$). The optimal offset for the larger diameter was not determined but, as it did not occur at $S_h/d = d/4 = 14mm$, then the optimal offset $S_h/d << d/4$. Another implication of this finding is that industrial ovens which utilise large fire tubes could not take advantage of a chimney effect. It is recommended that other cylindrical heater diameters be investigated in order to obtain a relationship between optimal convection, heater diameter, heater horizontal spacing from the vertical wall, and height along a vertical sidewall of an enclosure.

4.7.3. Flow and interferometric observations of multiple heaters in an enclosure

The studies were extended to augment the primary objectives by observing interferograms of two horizontal cylindrical heaters in an enclosure. Alignment problems, exacerbated by the differential expansions of the inlet and outlet heater pipes used in heater elevation adjustment, were overcome and simplified by using optical techniques which expanded the laser output, and consequently magnified any misalignment between the heater, the enclosure walls and the laser beam (see Appendix A). However, the hot fluid flow through the heaters could not be sufficiently balanced.

Six photographs were required to obtain half of a vertical symmetry. However, the inherent oscillation of the fringes, coupled with the differentially applied heat flux to the heaters reduced the useful applicability of the merged photographs for data analyses. Therefore, only those embracing both cylinder's plumes in a single exposure have been shown (see Fig. 4-19a,b). The wall and cylinder-to-cylinder offsets are as shown in the complementary schematic figure (see Fig. 4-14c,d).

For the vertically aligned configuration (see Fig. 4-19a), the lower plume was seen to be deflected towards the sidewall, while the upper (combined) plume was deflected towards the enclosure cavity. When the upper heater was moved closer to the sidewall ($S_{h,\text{upper heater}}$=d/4), (see Fig. 4-19b) the lower plume was still deflected but a recirculation could be deduced, from the pattern of the interferograms, between the upper heater, the sidewall, and the lower heater, suggesting that convection for the

staggered flow would be lower than for the vertically-aligned (S_h=d/2). Therefore, the gap for the upper heater should be wider in order to accommodate the higher volume of flow.

Arrays of enclosed horizontal fire tubes or electric heaters along a vertical wall should be similarly arranged. This finding could also be extended, by implication, to non-enclosed systems, such as refrigeration condenser tube arrays. The convective heat losses should benefit if the array were to be slightly inclined, with the lower tube being nearest the wall and offset by only 1.5d.

Flow visualisation studies carried out for the same heaters, but at more generous offsets (see Fig. 4-20), showed that when the cylinder-to-cylinder separation equalled their diameters , (CW_h=d, CC_h=d, CC_v=2d, see Fig. 4-14e) the lower plume oscillated, alternately rising along either side of the upper heater. This sweeping oscillating flow as depicted in the photographs (see Figs. 4-20a,b) was visually concluded to be extremely beneficial to convective flows. However, it was also noted that the lower heater was swept at only half of its circumference, on the same side as the offset upper heater. This may ultimately result in poorer convective heat flow from enclosed multiple heaters if the enclosing sheath is not of a high thermal conductivity.

To enable a comprehensive quantitative evaluation of any interferograms, it is recommended that the heat flux applied to each heater be equal and uniform, which may be obtained via specially designed electric heating.

4.8. DISCUSSION

4.8.1. Discussion of experimental techniques and recommendations

1. The heat transfer data were obtained using the 9.5mm dia. heater only. It was assumed that there was negligible circumferential variation in the temperature. This was plausible because of the small diameter [25], and that the high thermal conductivity of the sheath would enable surface temperature uniformity to be achieved. However, the uncertainty in circumferential variation of the Nusselt number would be very high for the larger diameter heater [33], so that the use of interferometry for the larger 55mm dia. heater would be a prerequisite for enhanced quantitative analyses. The MZI would also enable a detailed comparison of the Nusselt numbers at various horizontal positions.

2. Photographic recording of the flow (smoke) visualisation was not possible with the smaller diameter heater because the glare from the lighting produced a dazzling effect which could not be suppressed by the filter on the camera. Therefore, it is imperative that the enclosure be incorporated with an aperture at mid-length to introduce the lighting.

3. The alignment of the larger diameter heaters for interferometry was particularly difficult because the horizontal wall, the vertical wall, the upper heater and the lower heater must be aligned simultaneously with the working beam. A specially designed bracket and vernier adjusting mechanism would be necessary if the relatively heavy, fluid-filled large heaters were to be analysed.

4. The 9.5mm dia. electric heater employed warped slightly under thermal loading. Although this did not unduly affect the experimental results, the use of any interferometry would be compromised because the heater was not straight along its axial length. Therefore, additional recommendations would include specially designed heaters which would remain rigid under thermal loading.

It is similarly recommended that the larger diameter heaters be constructed of electrically wound, hollow tubes which would be lighter, and would additionally afford the measurement of surface temperatures by passing thermocouple wires through their

bores. The uniformity of temperature along its length could also be ensured by differential electrical winding.

5. The cross-sectional aspect ratio of the heater dia. to the enclosure width was very low (9.5:350 ~ 1:37) so that the influence of the 3-D radiation from the heaters could not be determined exactly. The use of a longer rig would reduce this 3-D effect.

4.8.2. Conclusions

At the higher $Ra=1.1x10^5$, the horizontal walls cause reduction in convection throughout whereas the vertical walls may enhance convection provided that the heater is located about half-way up at Y=0.5. As Ra was decreased to $Ra=7.5x10^4$, there was substantial improvement in the convective heat transfers, and it was possible to obtain some enhancement at the lower corners.

The combined data are shown in Fig. 4-13(a-d). The main findings are that:

(a) The optimal peripheral distance of a cylindrical heater from a vertical wall of an enclosure is $S_h/d=1.6$, for $0.25<Y<0.5$.

(b) As the temperature difference rises, or as the value of Ra in an enclosure rises ($Ra>7.5x10^4$), the degree of possible convective enhancement from wall-mounted heaters must diminish. Also, for the centred vertical traverse, the optimal position for convective heat transfers shifts vertically upwards ($0.25<Y<0.5$) as Ra increases $7.5x10^4<Ra<1.1x10^5$, and,

(c) a localised chimney effect, which enhances natural convection heat transfer, exists in an enclosed space when a heat source is in close proximity to a vertical wall and the full effect does not occur until the recirculation at the upper quadrant is minimised.

Fig. 4-1 Effect of offset on vertically stacked horizontal cylinders in free space

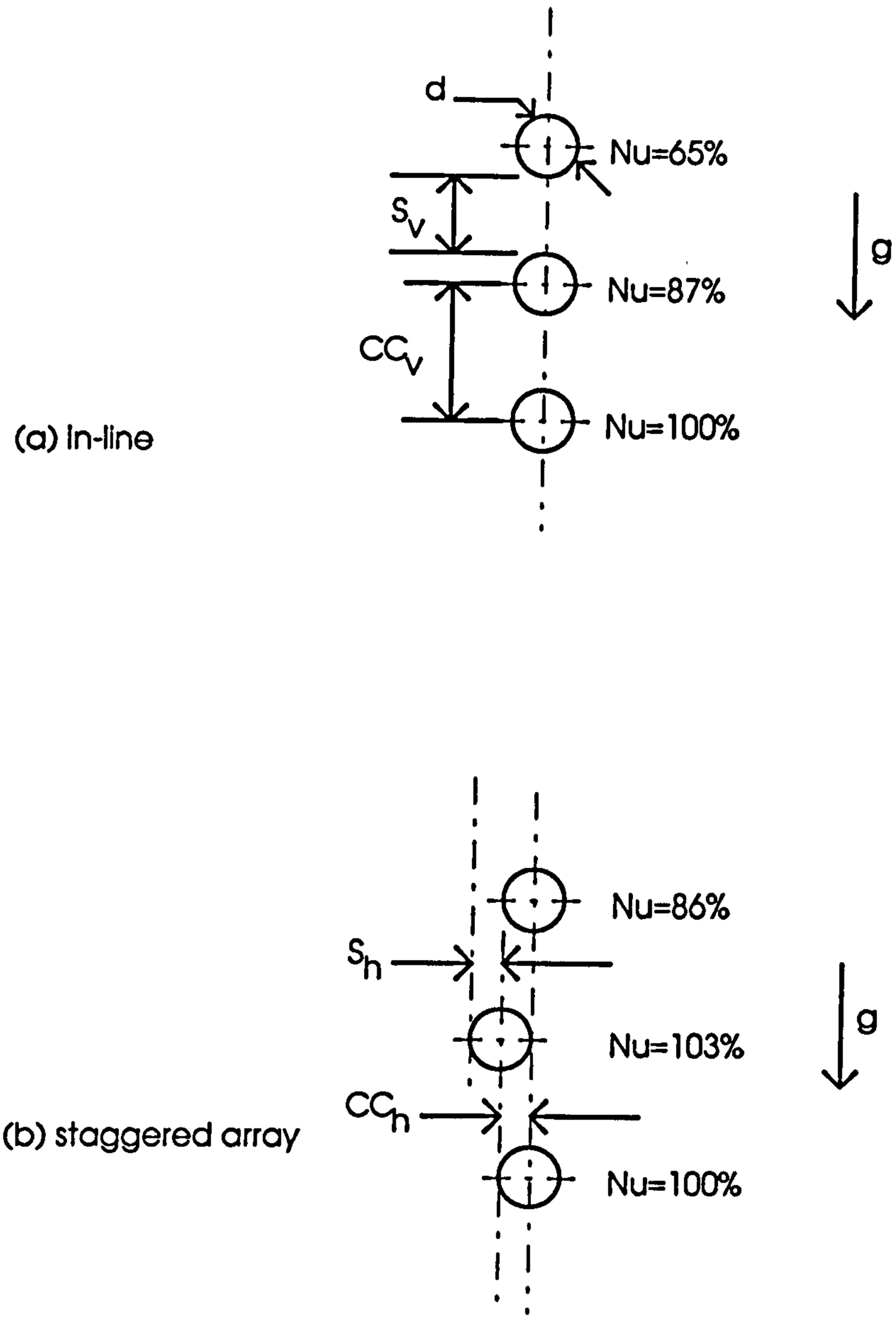

CC - cylinder centre-to-centre spacing

S - peripheral surface-to-surface separation

Fig.4-2 Interactions of cylindrical arrays with vertical walls

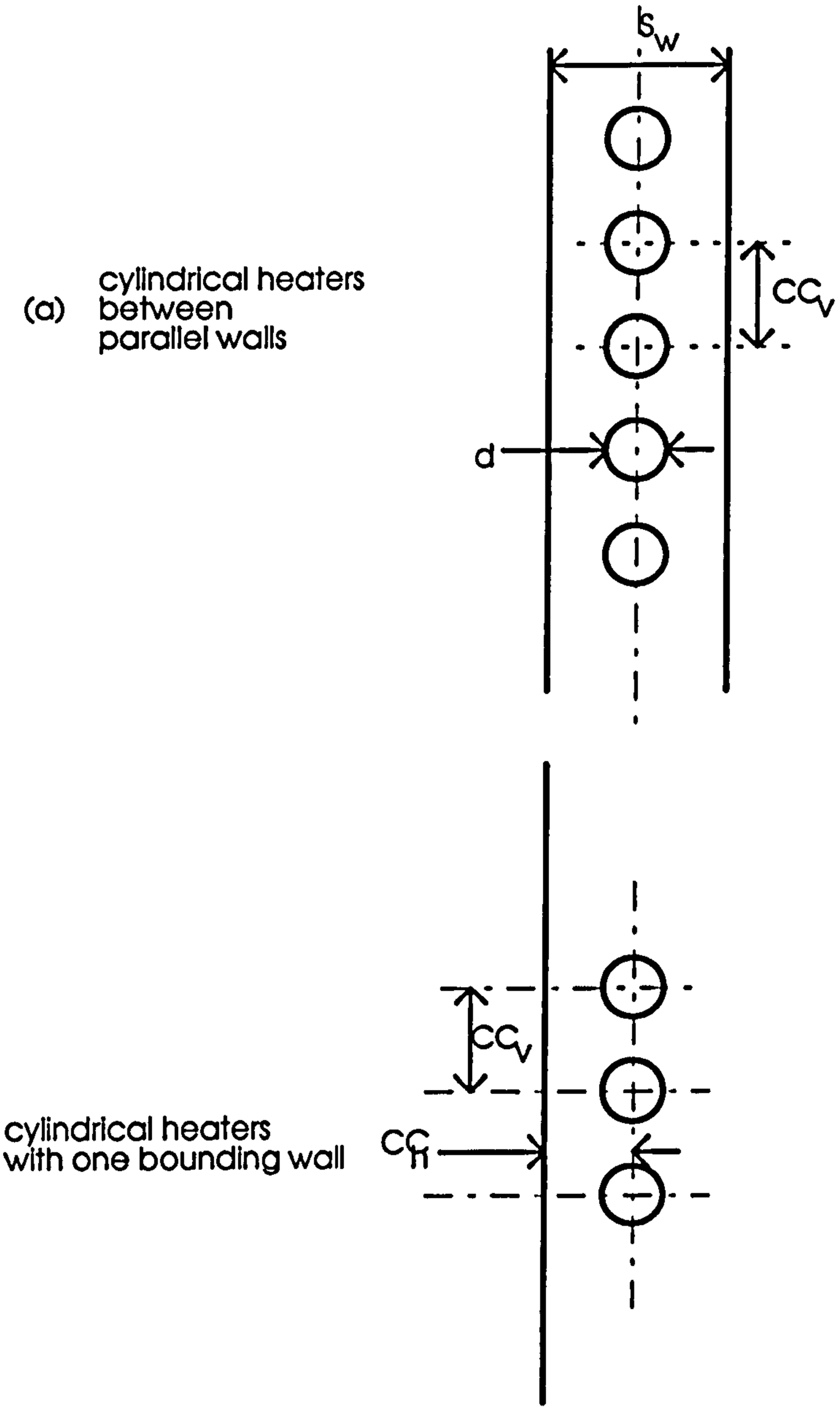

(a) cylindrical heaters between parallel walls

(b) cylindrical heaters with one bounding wall

Fig.4-3 Heater interactions with wall configurations

(a) vertical wall interactions

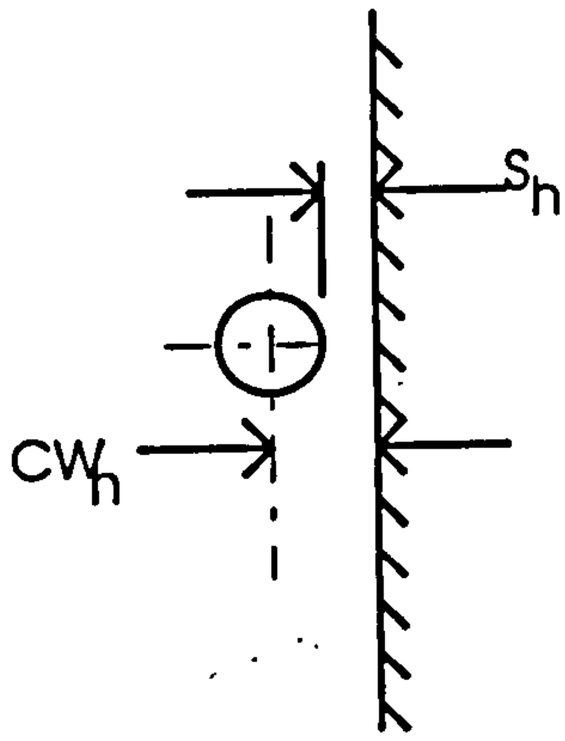

(b) lower horizontal wall interactions

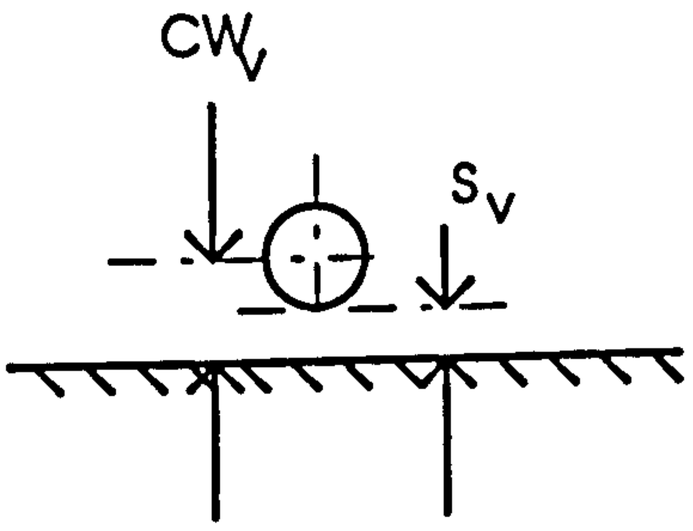

(c) lower corner interactions

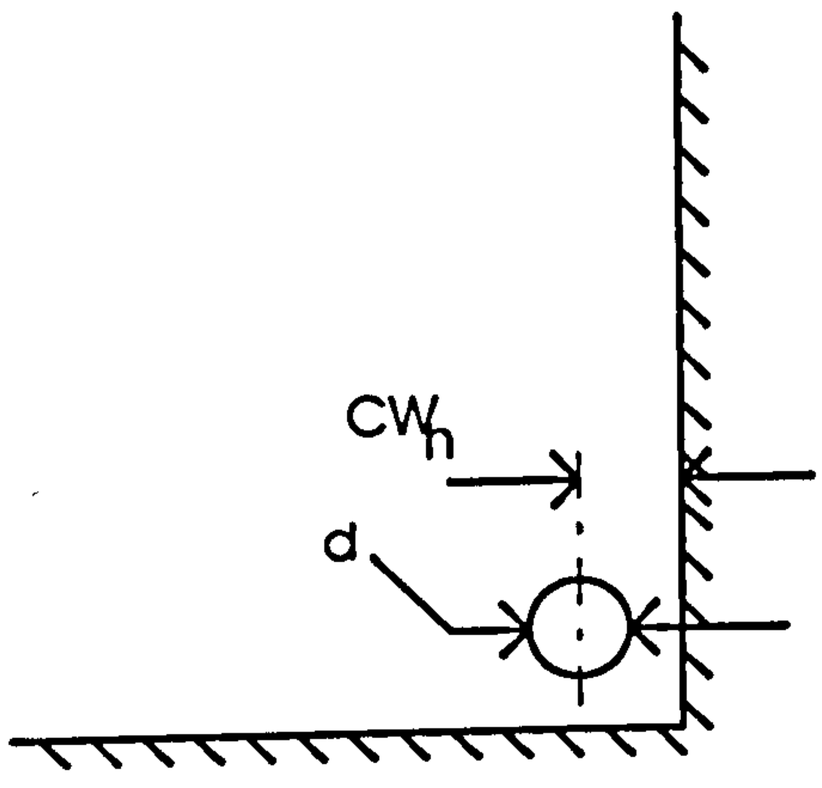

Fig.4-4 Cylindrical and rectangular heaters in a rectangular enclosure

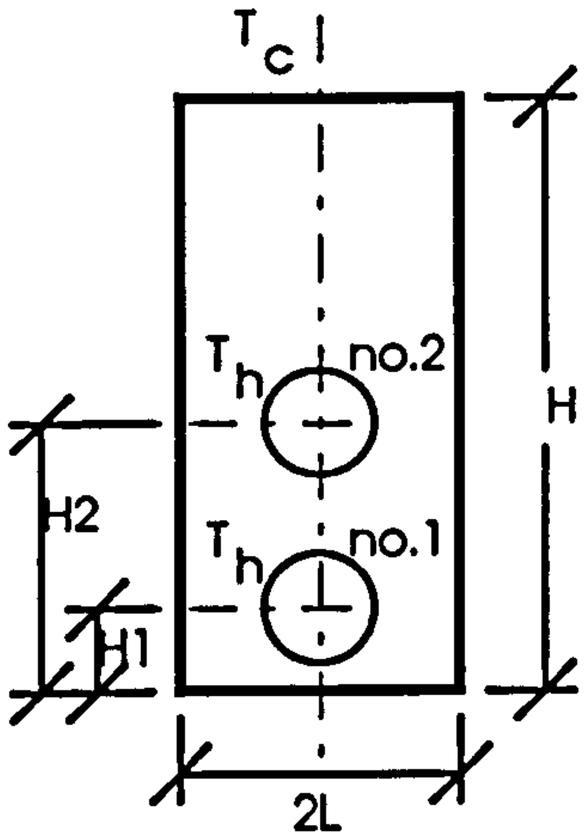

(a) Enclosure with horizontal circular cylinders - H2 variable

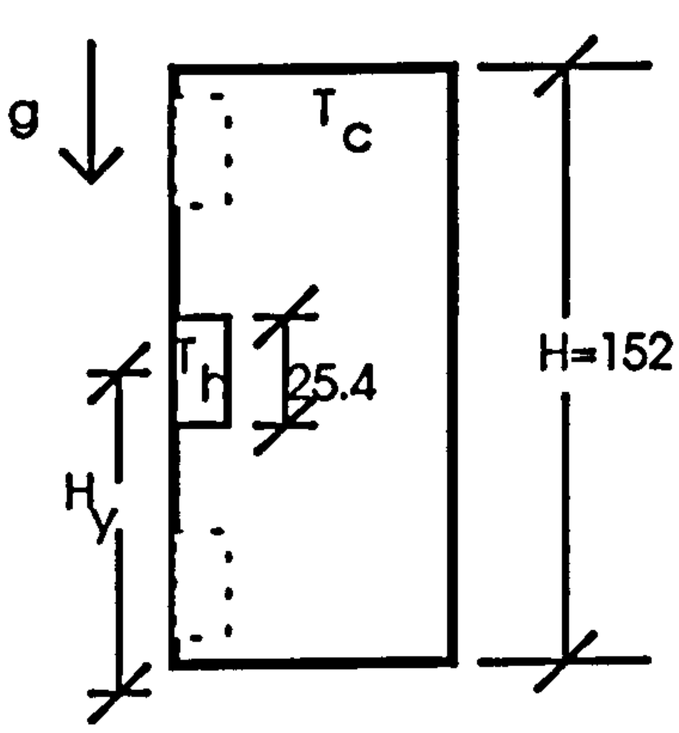

(b) Heated protrusion

Heater Locations
Top Hy=114
Middle Hy=76
Bottom Hy=38

Fig. 4-5 Heated pipe arrangement

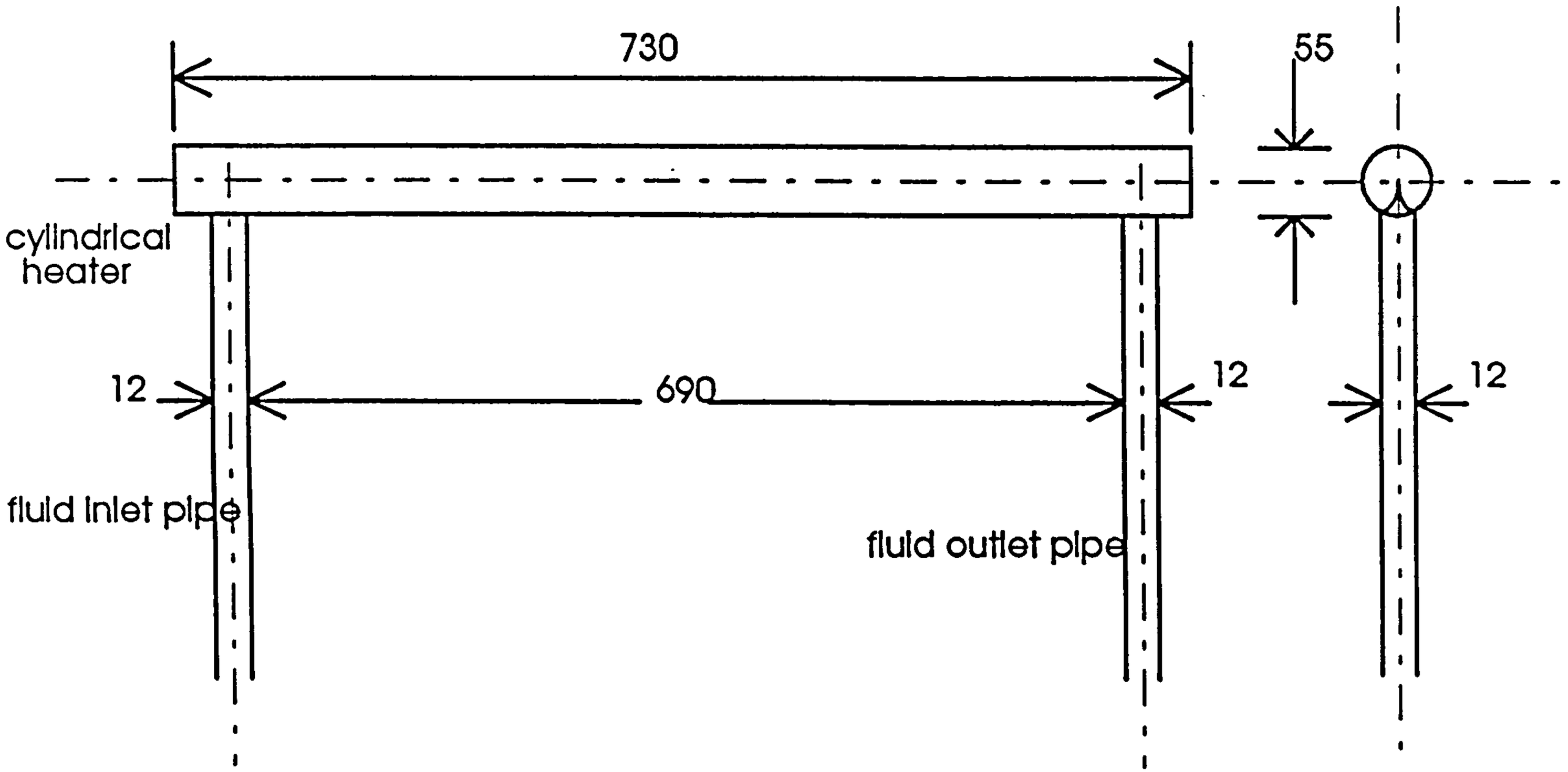

Fig.4-6 Enclosed heater, data acquisition positions

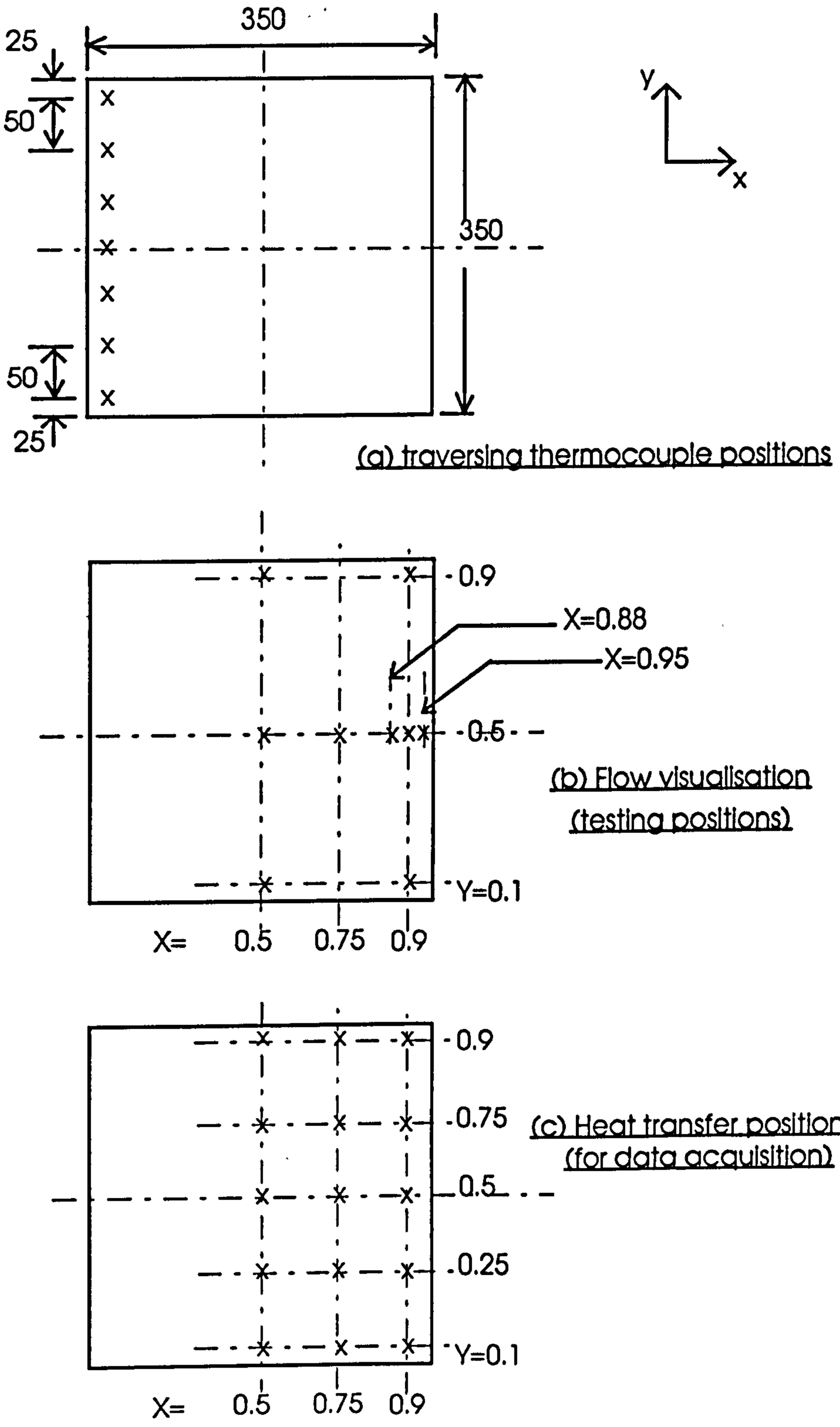

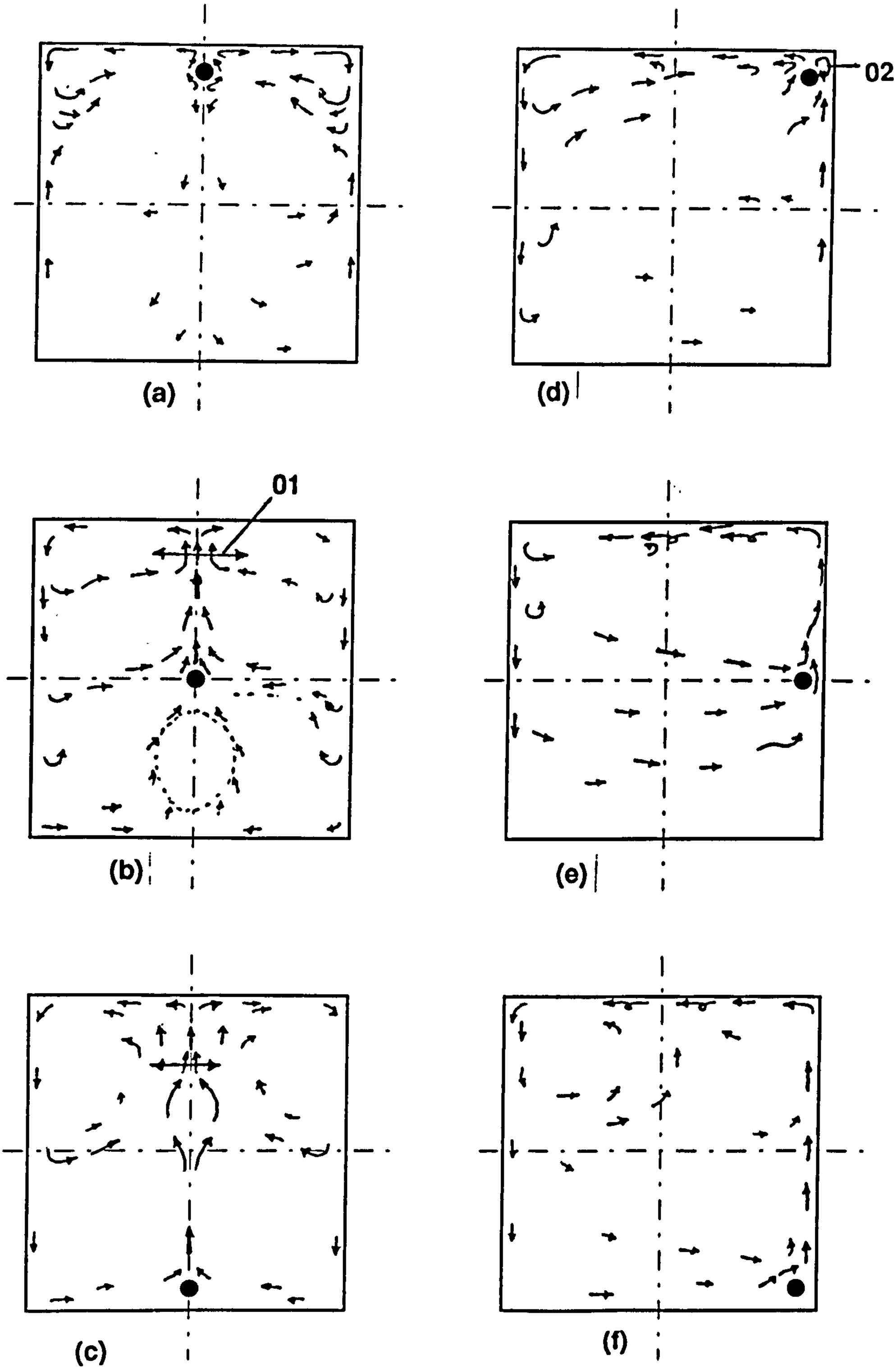

Fig. 4-7 (a-f). Flow visualisation with different heater positions

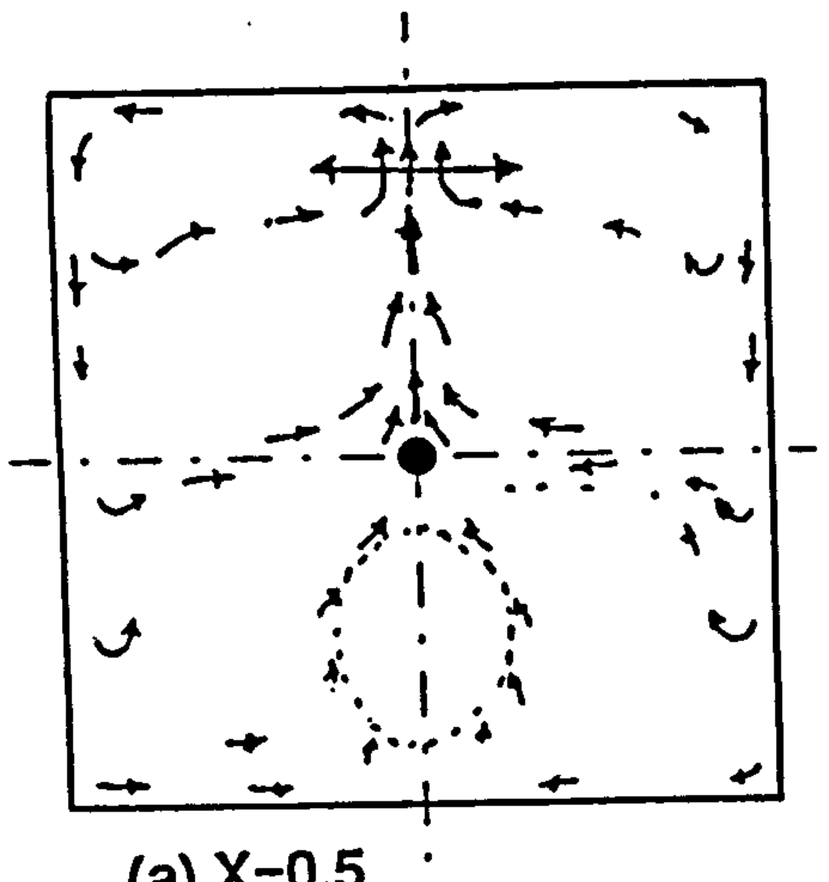

(a) X=0.5

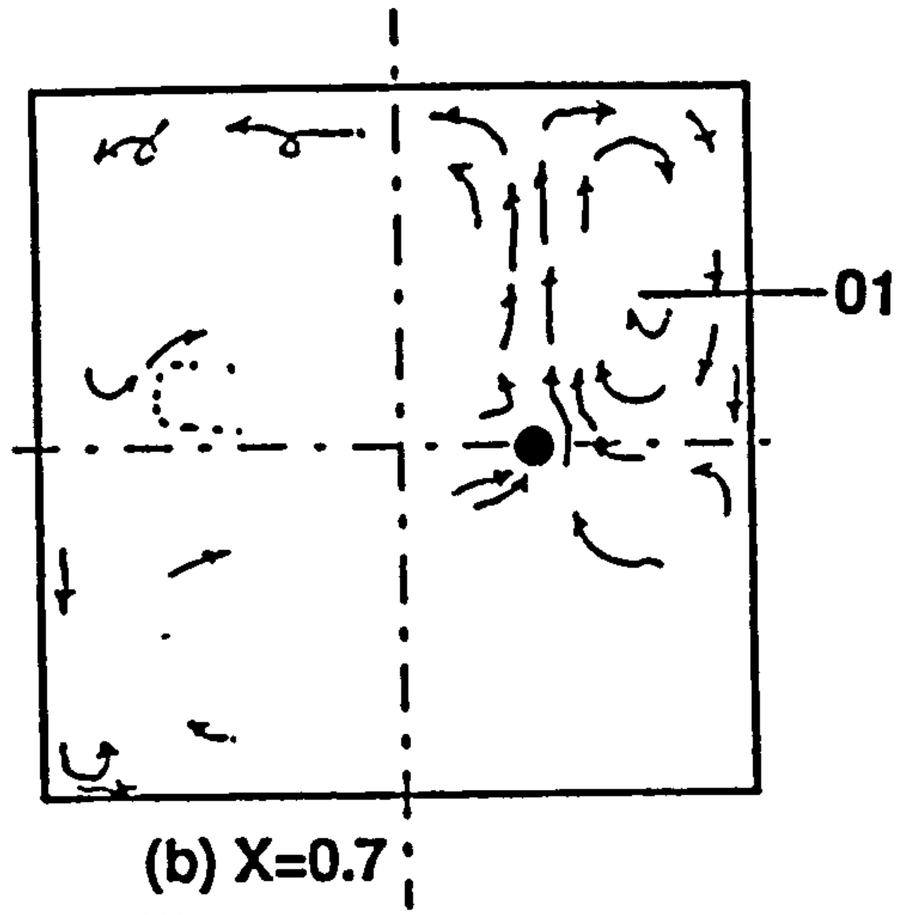

(b) X=0.7

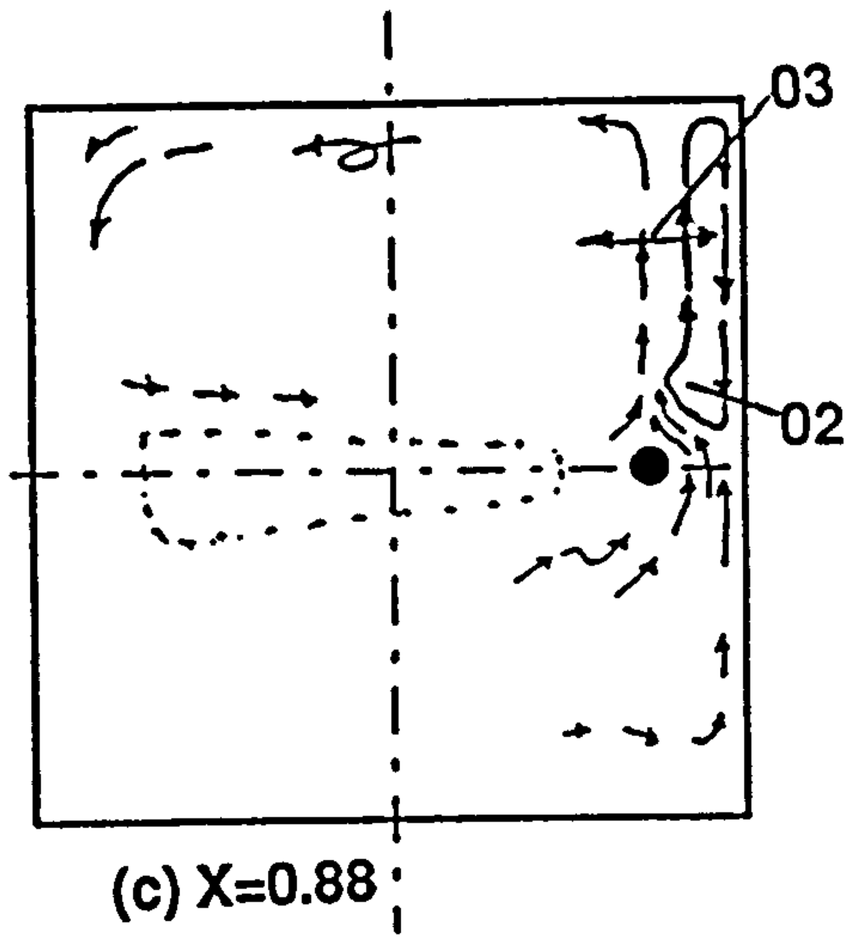

(c) X=0.88

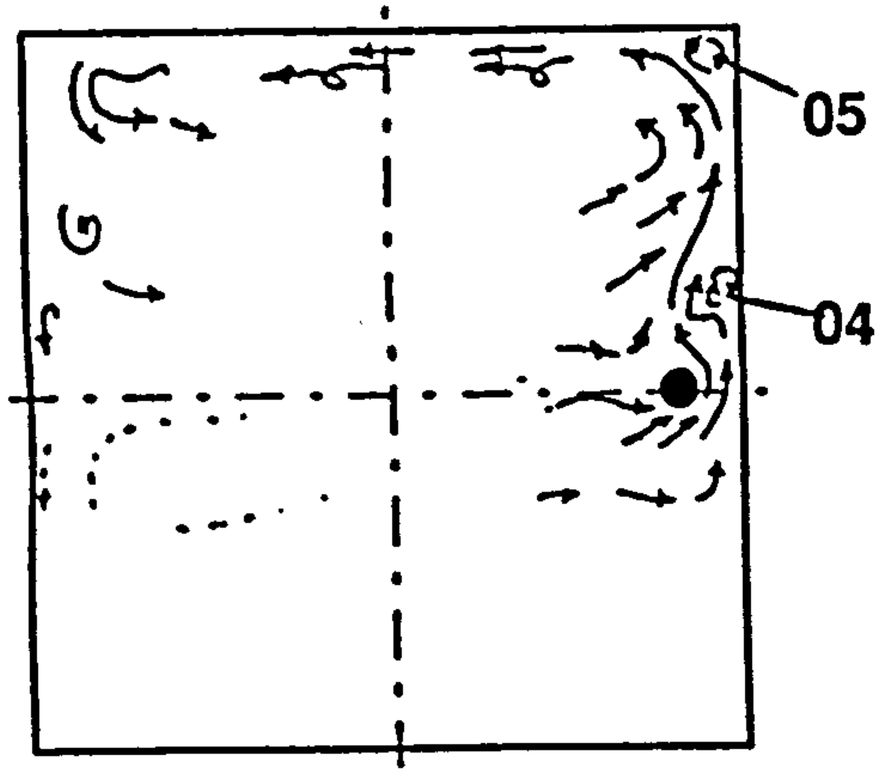

(d) X=0.9

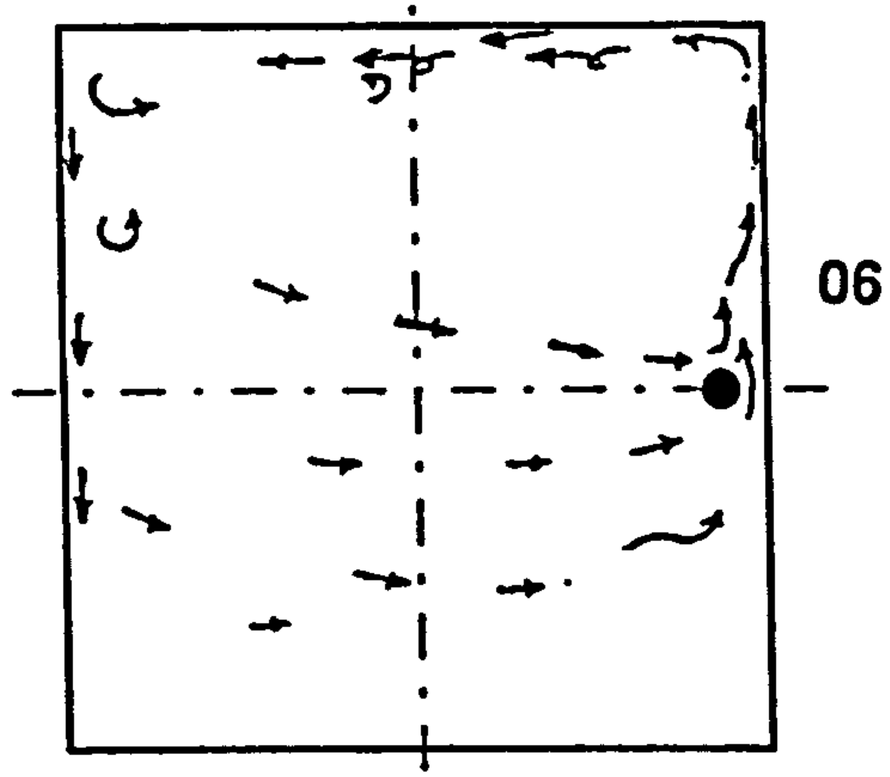

(e) X=0.95

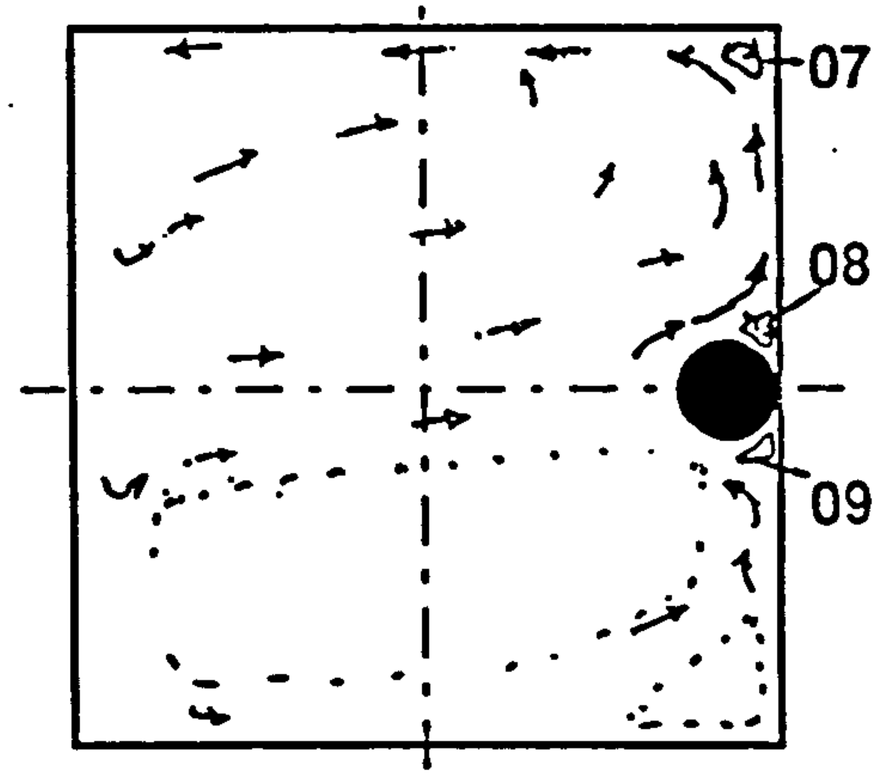

(f) S_h=0

Fig.4-8 (a-f). Alteration of flow patterns with central horizontal traverse

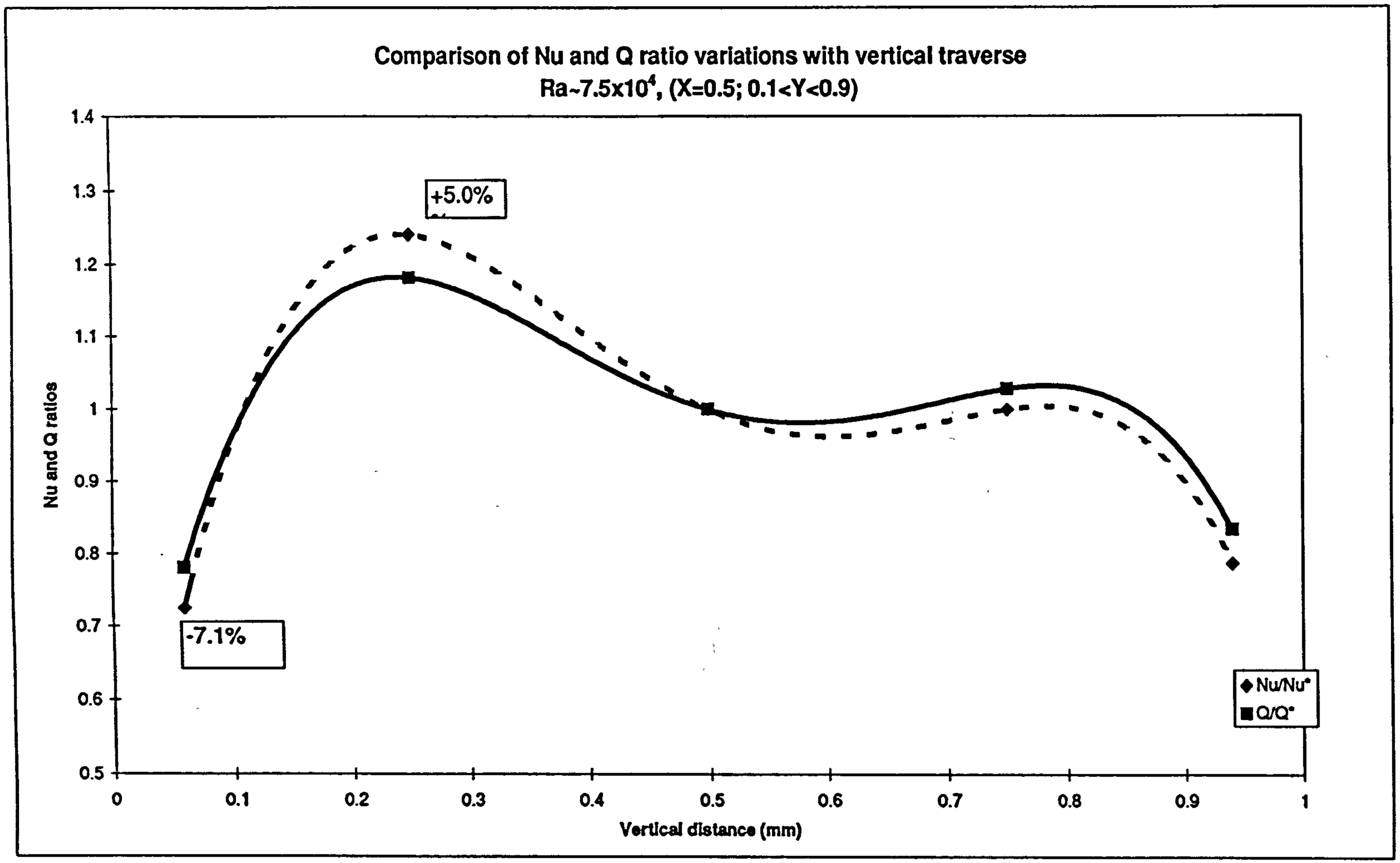
Comparison of Nu and Q ratio variations with vertical traverse
Ra~7.5x10^4, (X=0.5; 0.1<Y<0.9)
Nu and Q ratios
Vertical distance (mm)
+5.0%
-7.1%
Nu/Nu*
Q/Q*
1.4
1.3
1.2
1.1
1
0.9
0.8
0.7
0.6
0.5
0
0.1
0.2
0.3
0.4
0.5
0.6
0.7
0.8
0.9
1

Fig. 4-9a

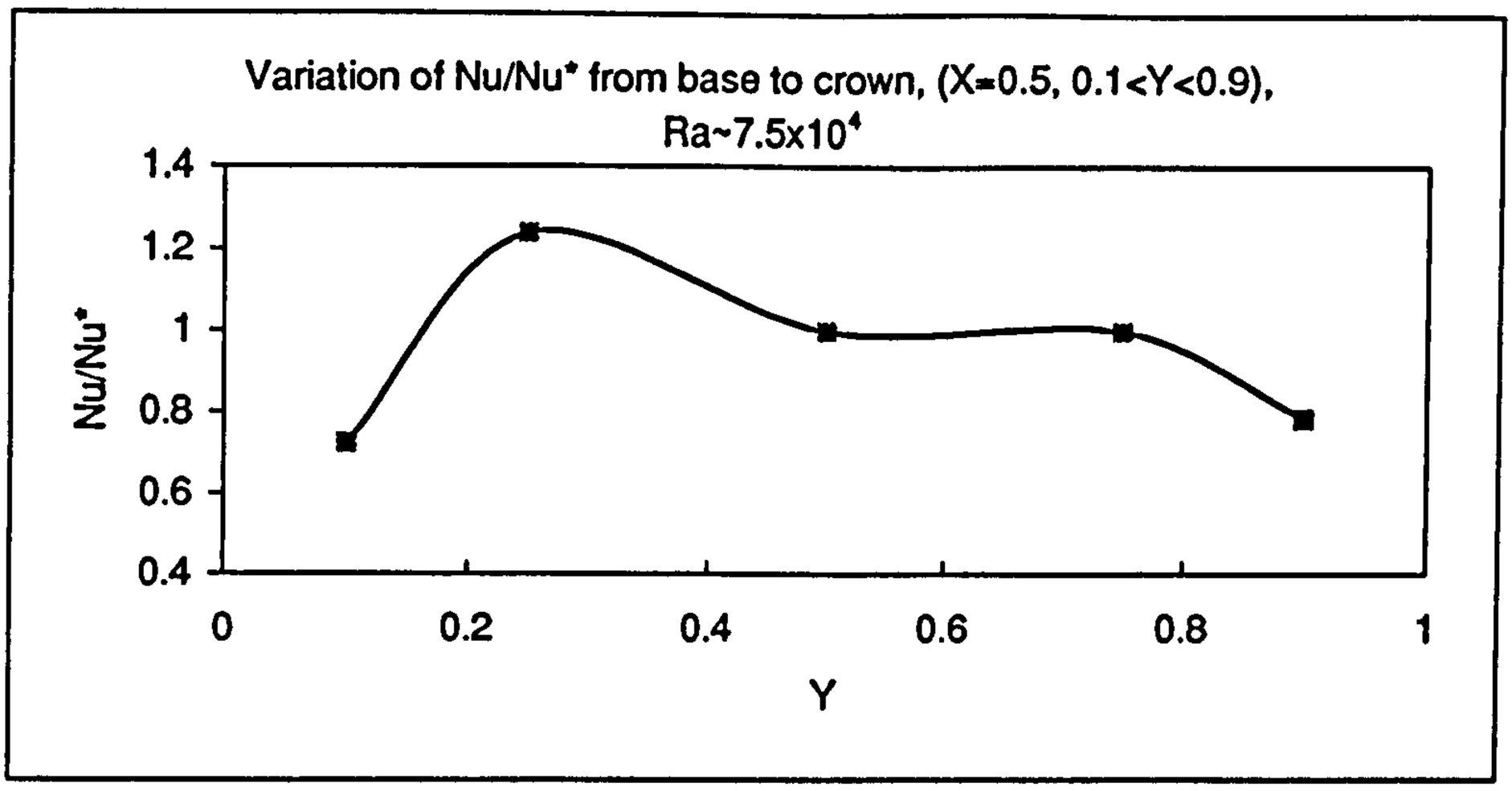
Variation of Nu/Nu* from base to crown, (X=0.5, 0.1<Y<0.9),
Ra~7.5x10⁴
Nu/Nu*
1.4
1.2
1
0.8
0.6
0.4
0
0.2
0.4
0.6
0.8
1
Y

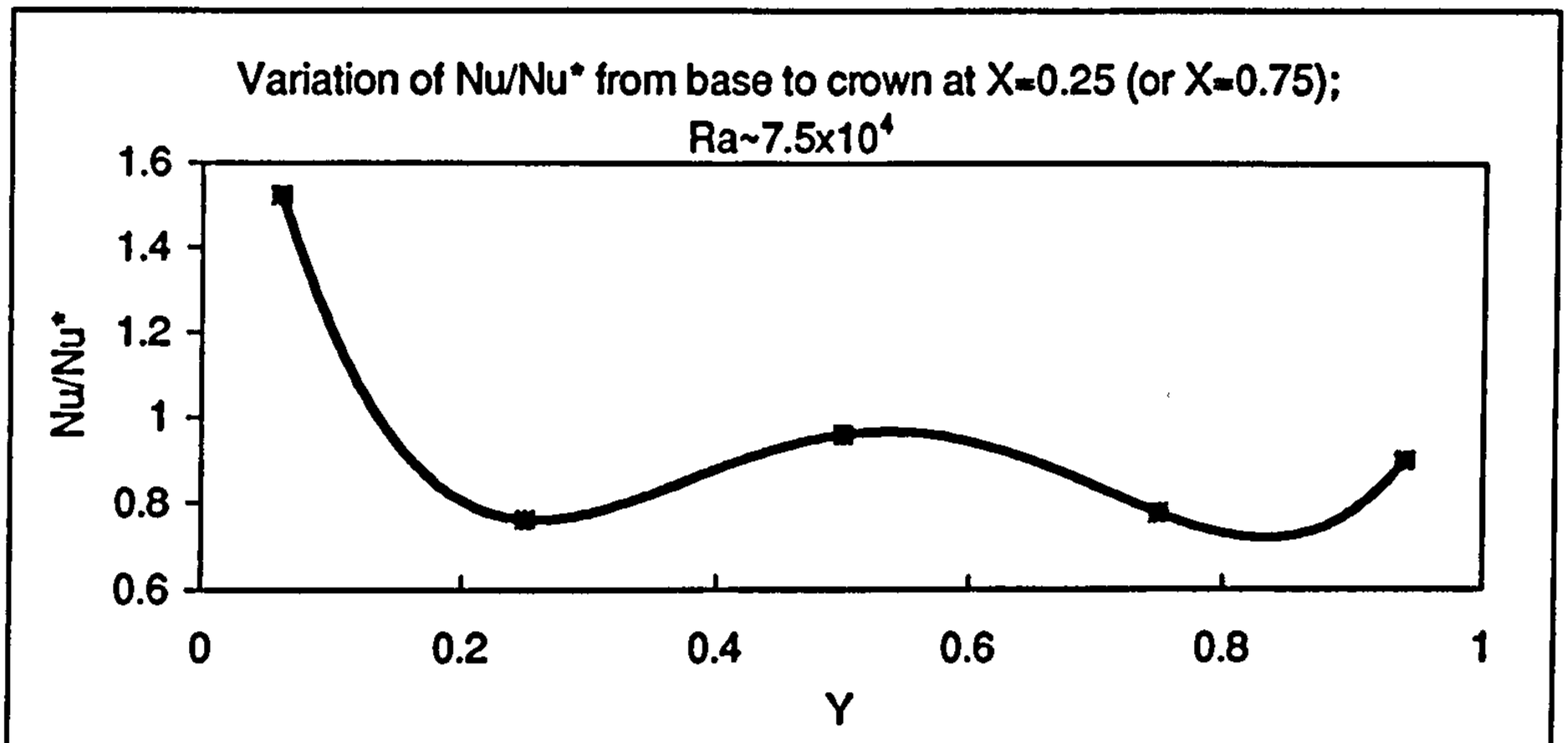
Variation of Nu/Nu* from base to crown at X=0.25 (or X=0.75);
Ra~7.5x10⁴
Nu/Nu*
1.6
1.4
1.2
1
0.8
0.6
0
0.2
0.4
0.6
0.8
1
Y

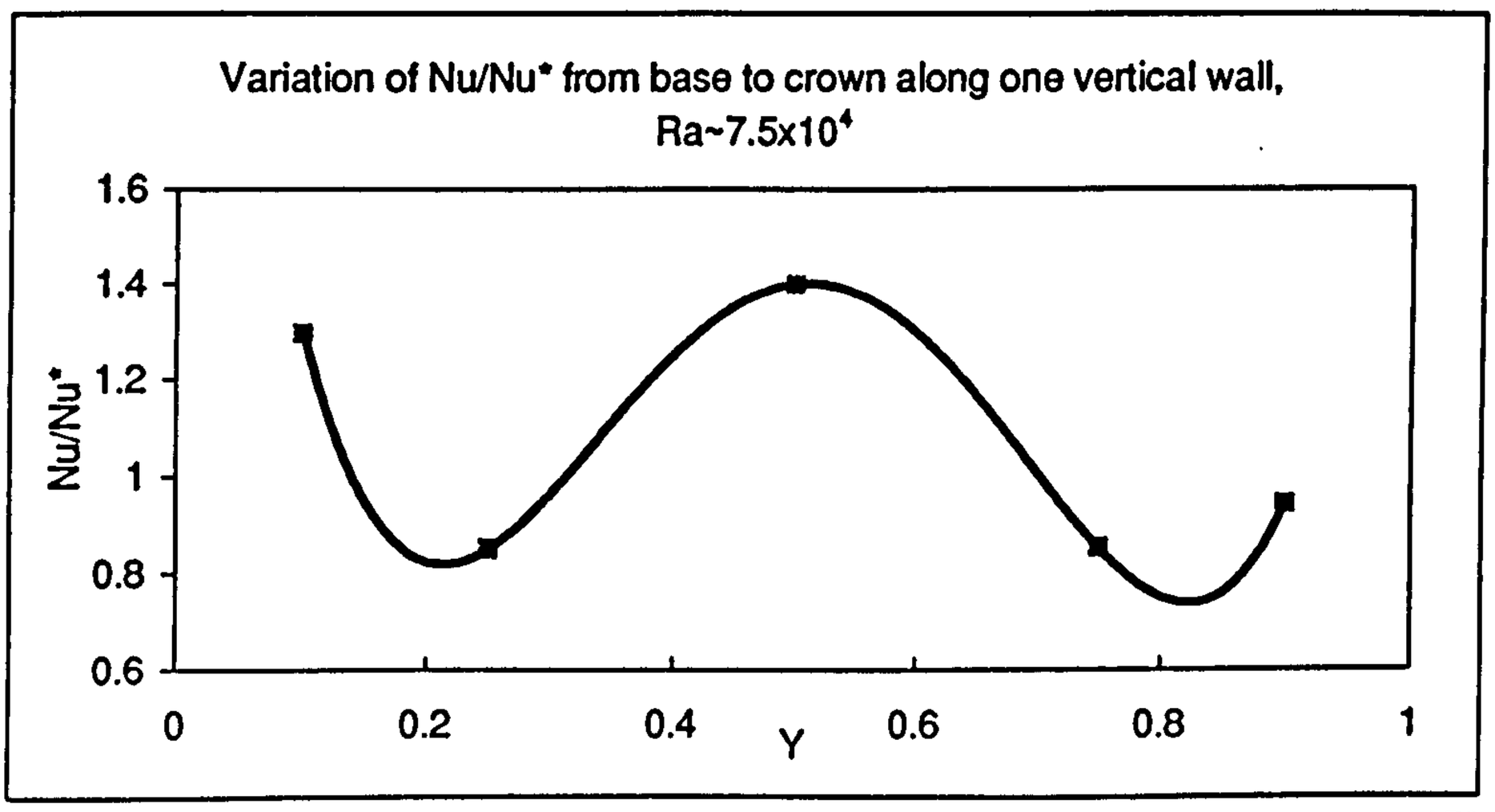
Variation of Nu/Nu* from base to crown along one vertical wall,
Ra~7.5x10⁴
Nu/Nu*
1.6
1.4
1.2
1
0.8
0.6
0
0.2
0.4
Y
0.6
0.8
1

Fig. 4-9(b-d)

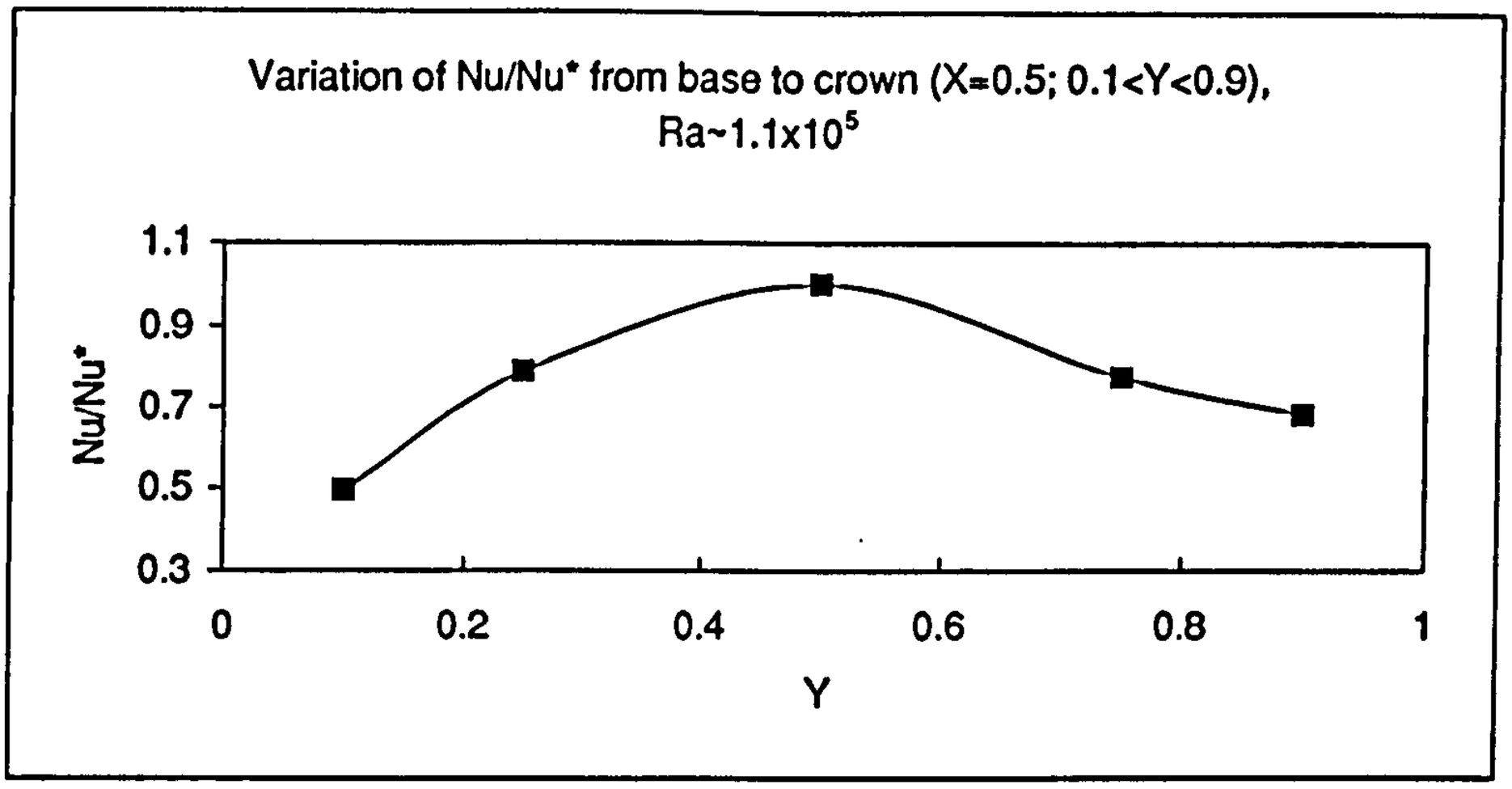
Variation of Nu/Nu* from base to crown (X=0.5; 0.1<Y<0.9),
Ra~1.1x10^5
Nu/Nu*
1.1
0.9
0.7
0.5
0.3
0
0.2
0.4
0.6
0.8
1
Y

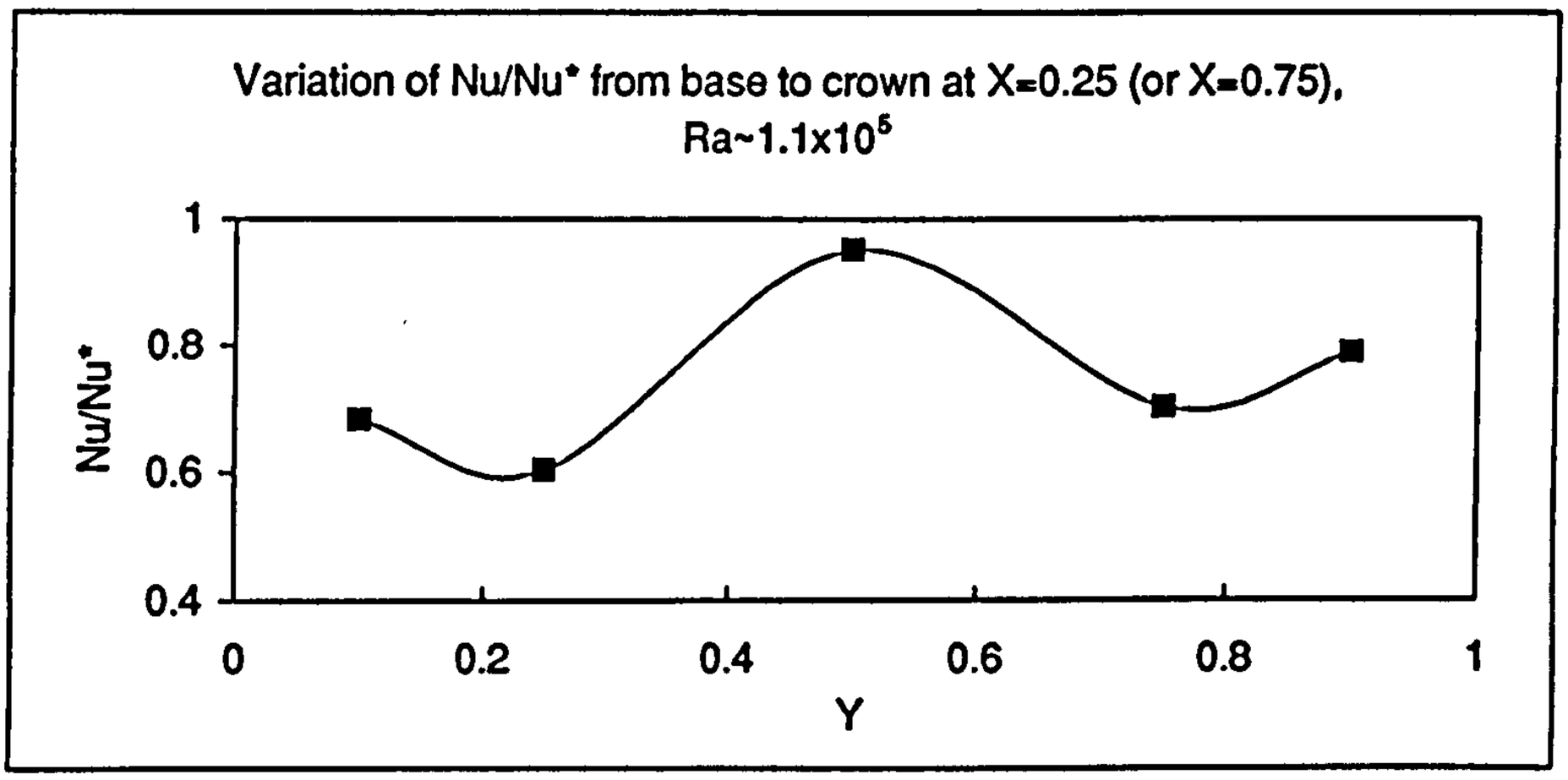
Variation of Nu/Nu* from base to crown at X=0.25 (or X=0.75),
Ra~1.1x10^5
Nu/Nu*
1
0.8
0.6
0.4
0
0.2
0.4
0.6
0.8
1
Y

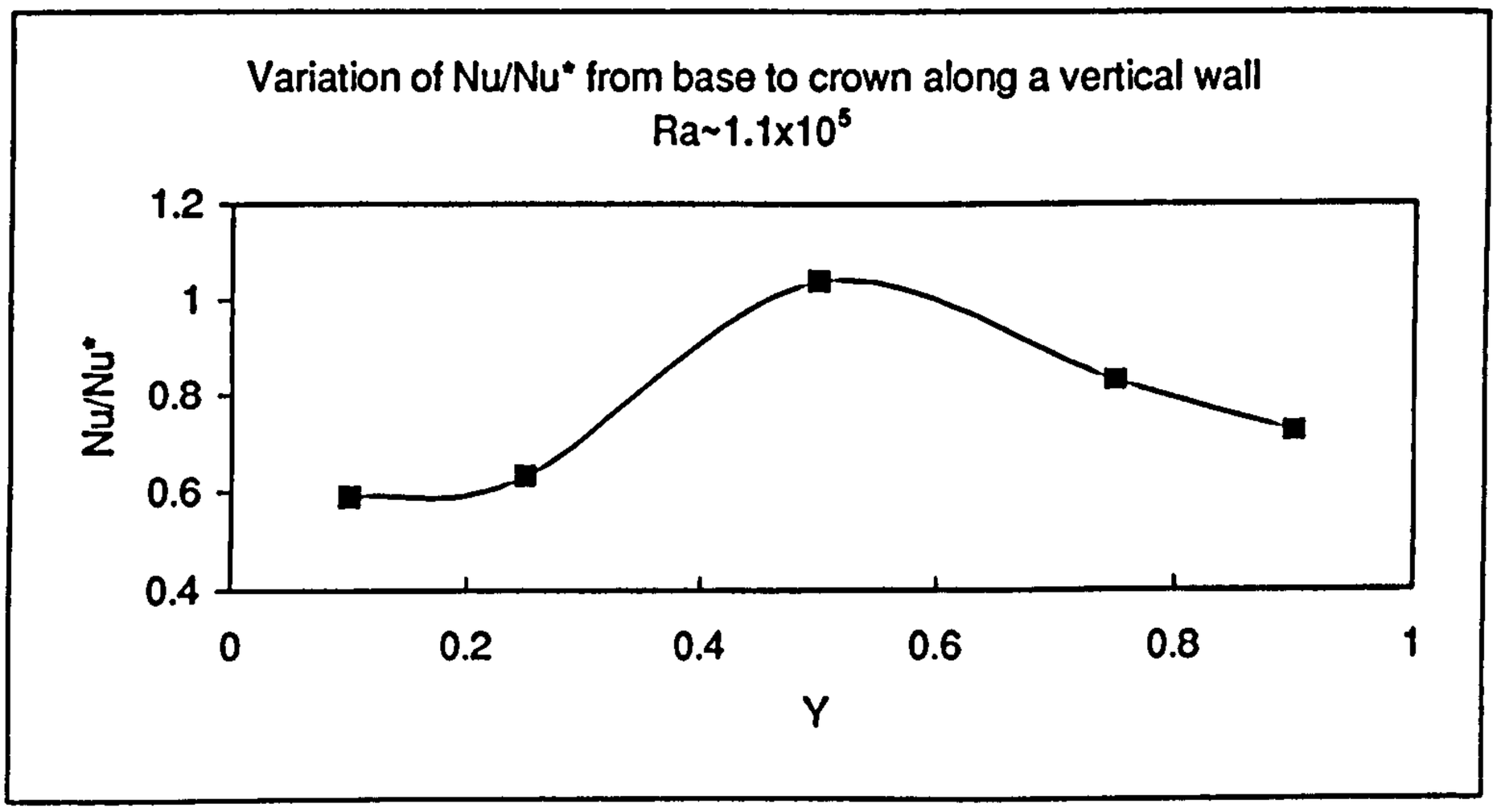
Variation of Nu/Nu* from base to crown along a vertical wall
Ra~1.1x10^5
Nu/Nu*
1.2
1
0.8
0.6
0.4
0
0.2
0.4
0.6
0.8
1
Y

Fig. 4-10(a-c)

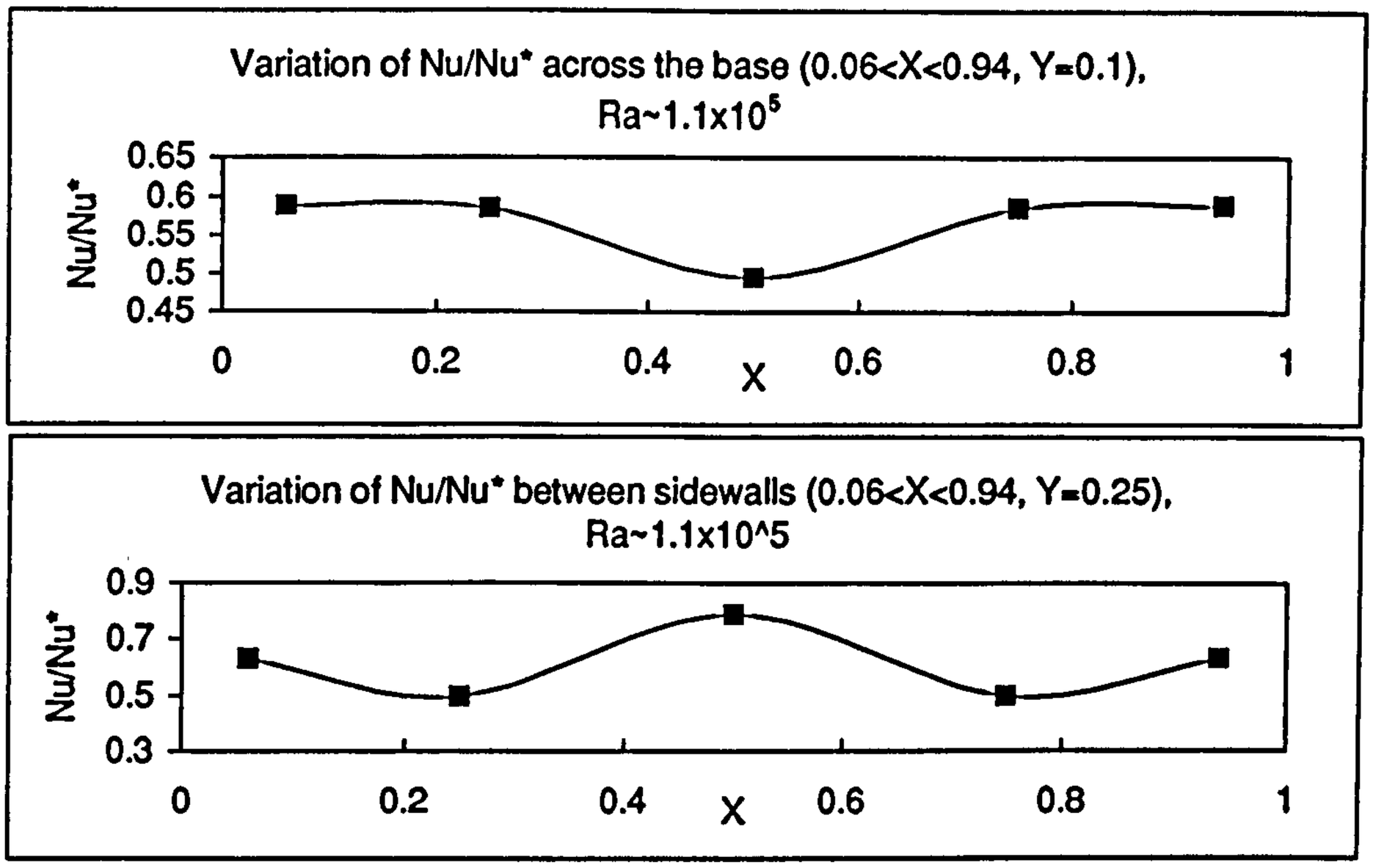
Variation of Nu/Nu* across the base (0.06<X<0.94, Y=0.1),
Ra~1.1x10^5
Nu/Nu*
0.65
0.6
0.55
0.5
0.45
0
0.2
0.4
X
0.6
0.8
1

Variation of Nu/Nu* between sidewalls (0.06<X<0.94, Y=0.25),
Ra~1.1x10^5
Nu/Nu*
0.9
0.7
0.5
0.3
0
0.2
0.4
X
0.6
0.8
1

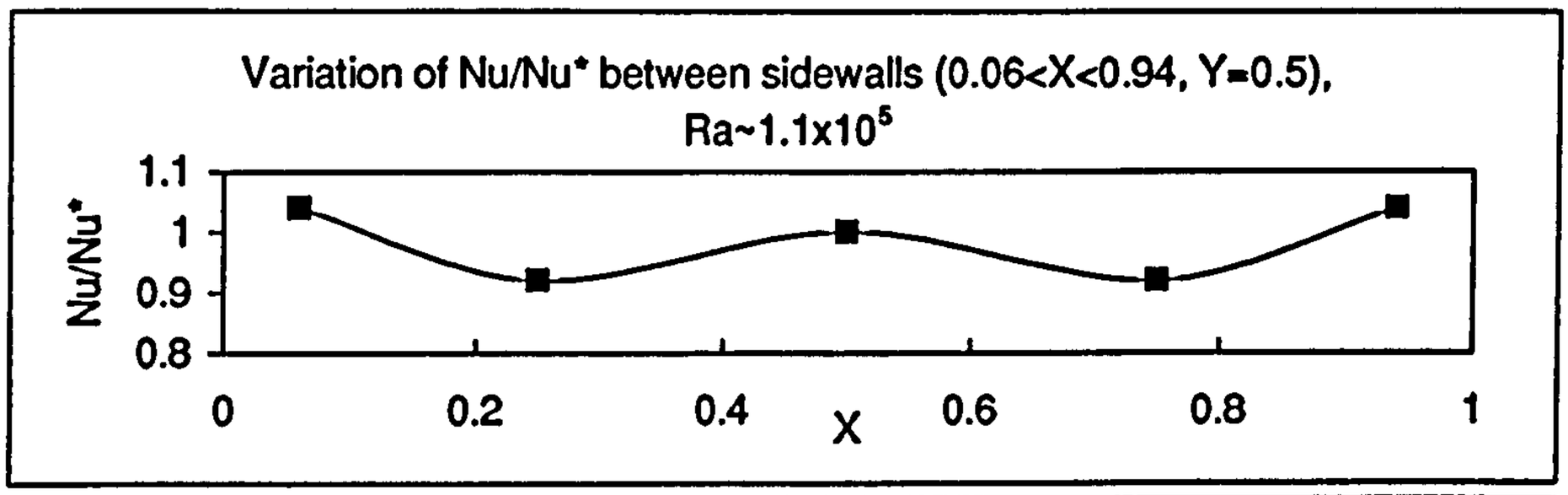
Variation of Nu/Nu* between sidewalls (0.06<X<0.94, Y=0.5),
Ra~1.1x10^5
Nu/Nu*
1.1
1
0.9
0.8
0
0.2
0.4
X
0.6
0.8
1

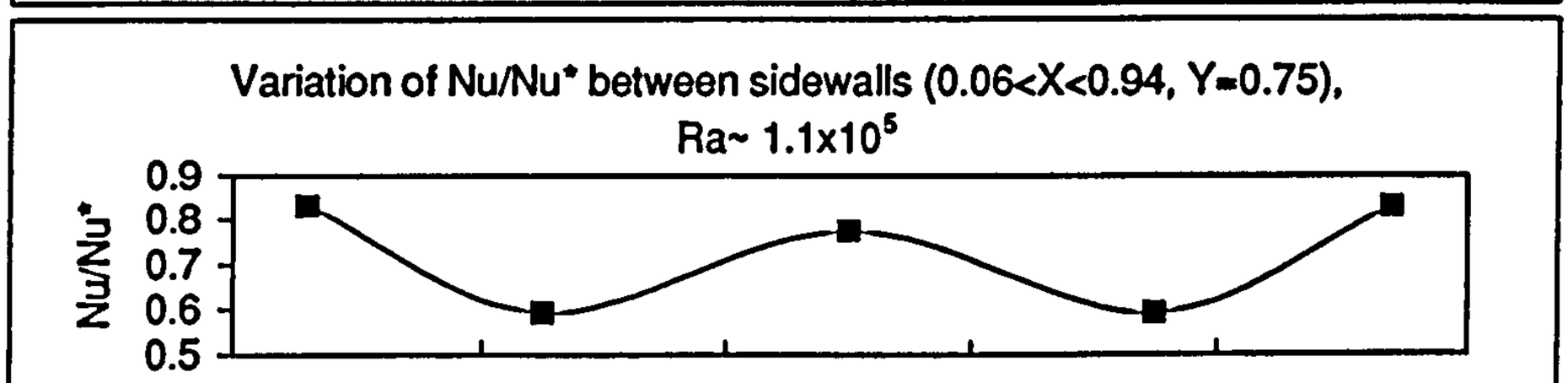
Variation of Nu/Nu* between sidewalls (0.06<X<0.94, Y=0.75),
Ra~ 1.1x10^5
Nu/Nu*
0.9
0.8
0.7
0.6
0.5
0
0.2
0.4
X
0.6
0.8
1

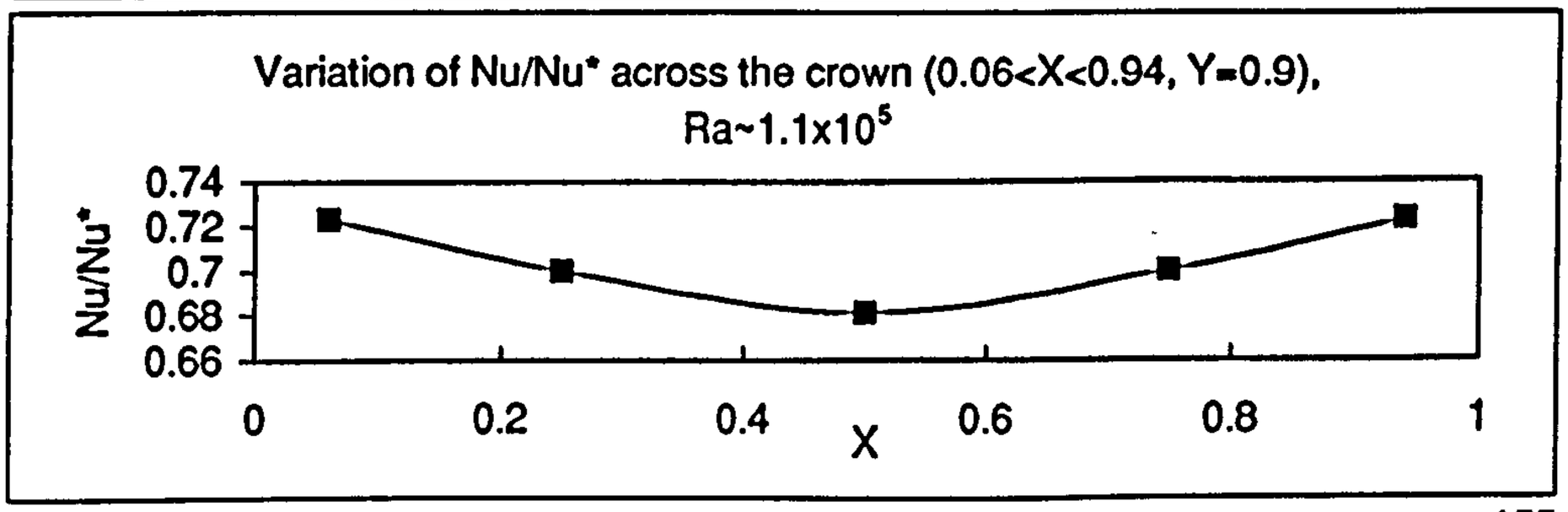
Variation of Nu/Nu* across the crown (0.06<X<0.94, Y=0.9),
Ra~1.1x10^5
Nu/Nu*
0.74
0.72
0.7
0.68
0.66
0
0.2
0.4
X
0.6
0.8
1

Fig. 4-11

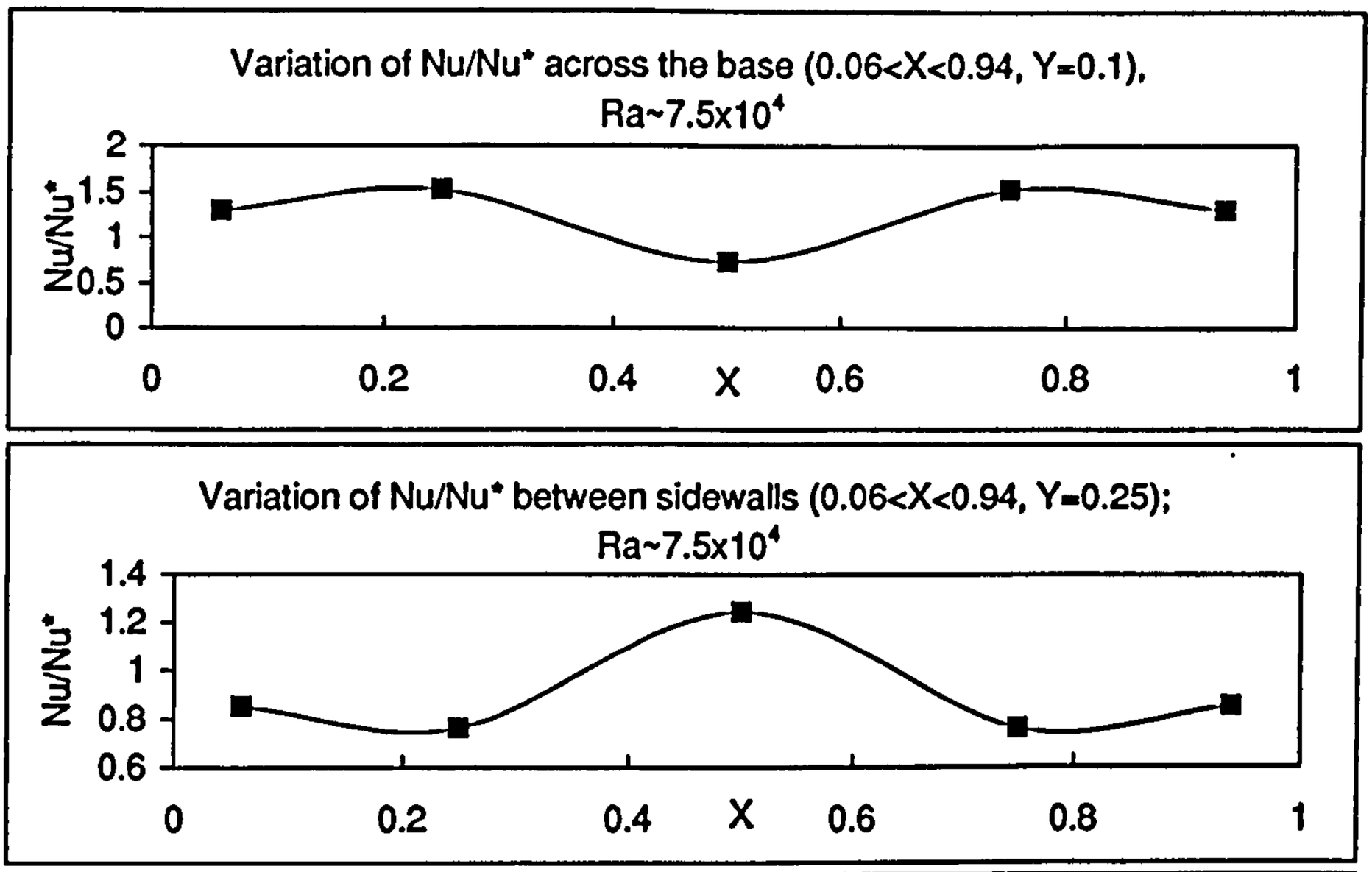
Variation of Nu/Nu* across the base (0.06<X<0.94, Y=0.1),
Ra~7.5x10^4
Nu/Nu*
2
1.5
1
0.5
0
0
0.2
0.4
X
0.6
0.8
1

Variation of Nu/Nu* between sidewalls (0.06<X<0.94, Y=0.25);
Ra~7.5x10^4
Nu/Nu*
1.4
1.2
1
0.8
0.6
0
0.2
0.4
X
0.6
0.8
1

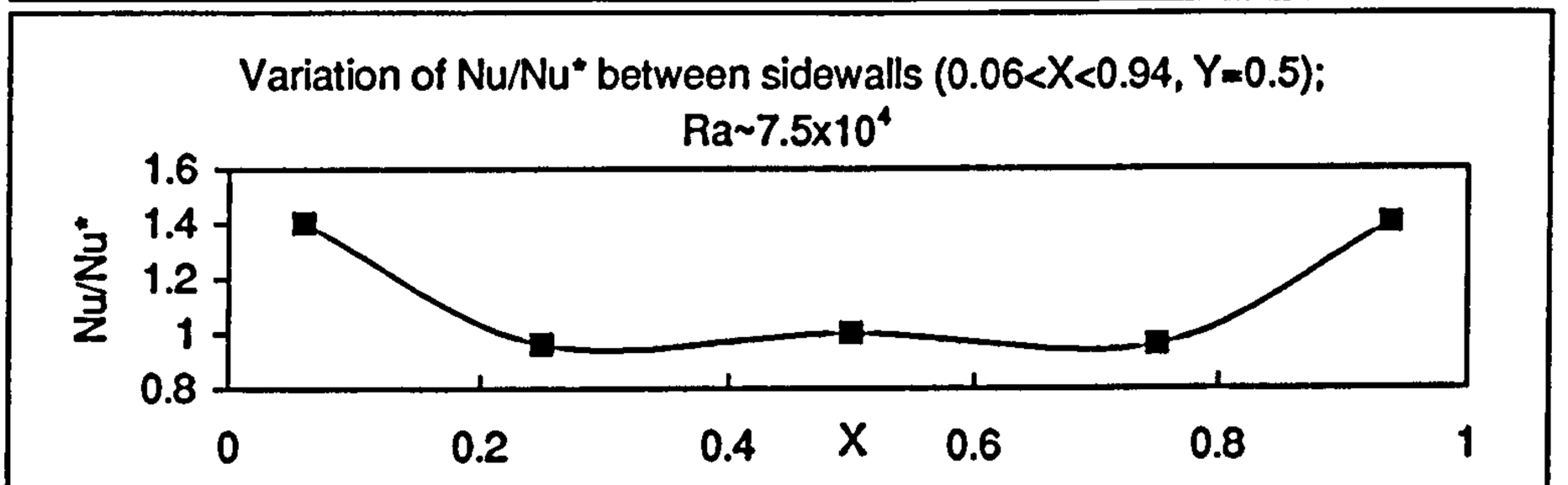
Variation of Nu/Nu* between sidewalls (0.06<X<0.94, Y=0.5);
Ra~7.5x10^4
Nu/Nu*
1.6
1.4
1.2
1
0.8
0
0.2
0.4
X
0.6
0.8
1

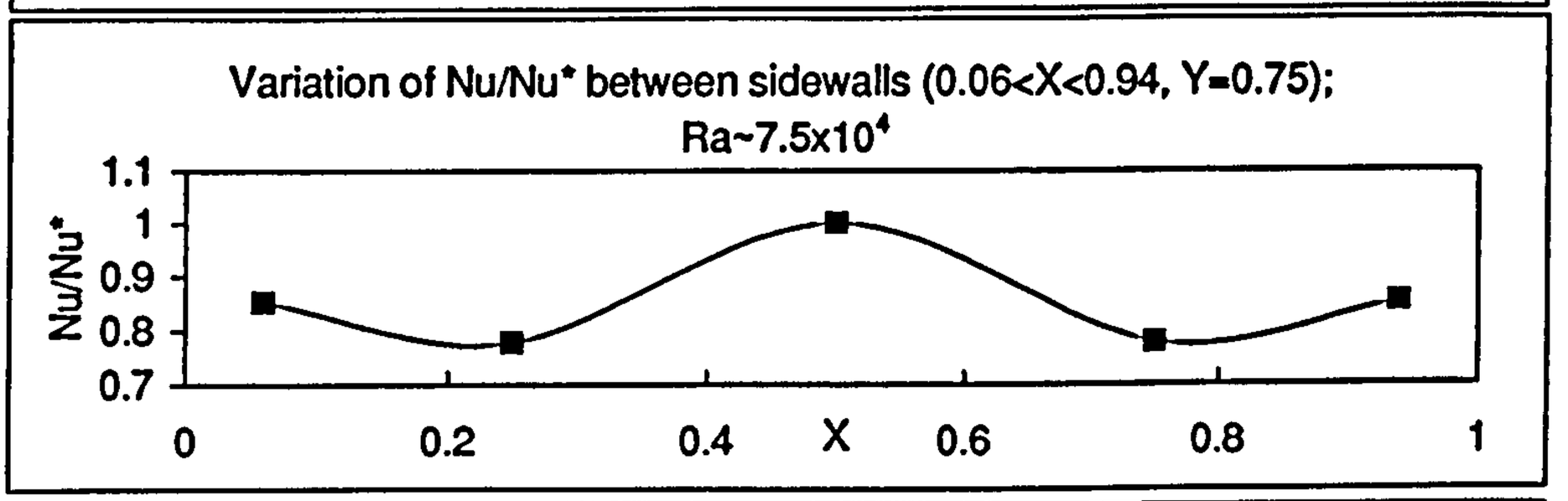
Variation of Nu/Nu* between sidewalls (0.06<X<0.94, Y=0.75);
Ra~7.5x10^4
Nu/Nu*
1.1
1
0.9
0.8
0.7
0
0.2
0.4
X
0.6
0.8
1

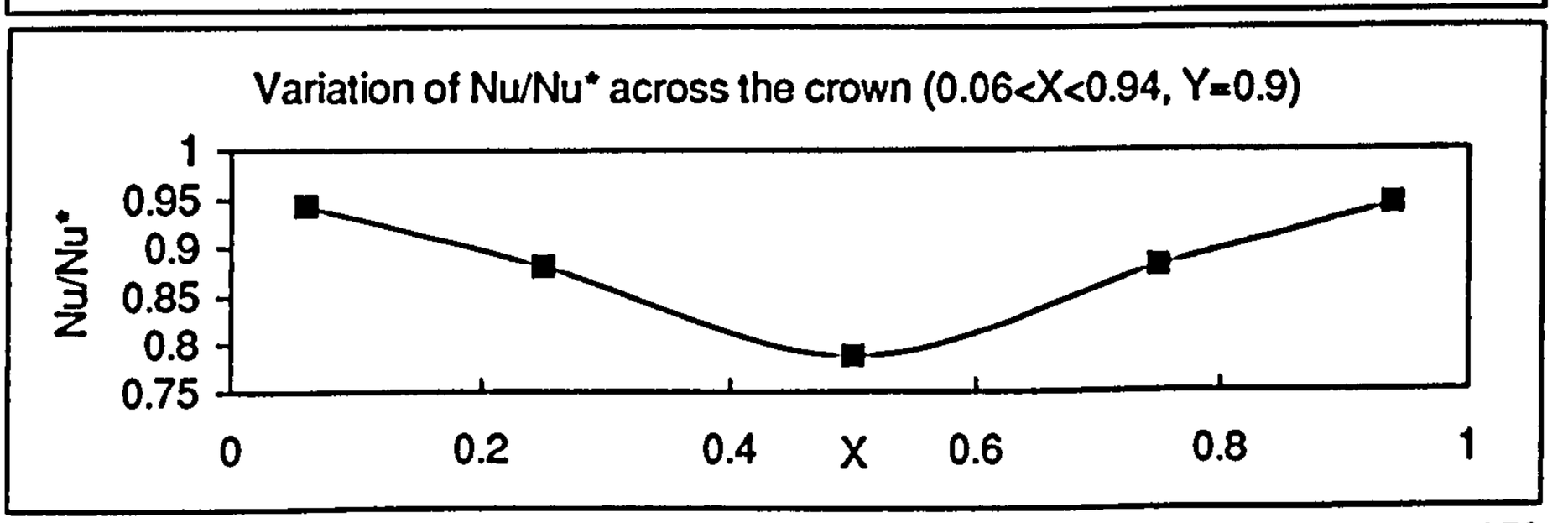
Variation of Nu/Nu* across the crown (0.06<X<0.94, Y=0.9)
Nu/Nu*
1
0.95
0.9
0.85
0.8
0.75
0
0.2
0.4
X
0.6
0.8
1

Fig. 4-12

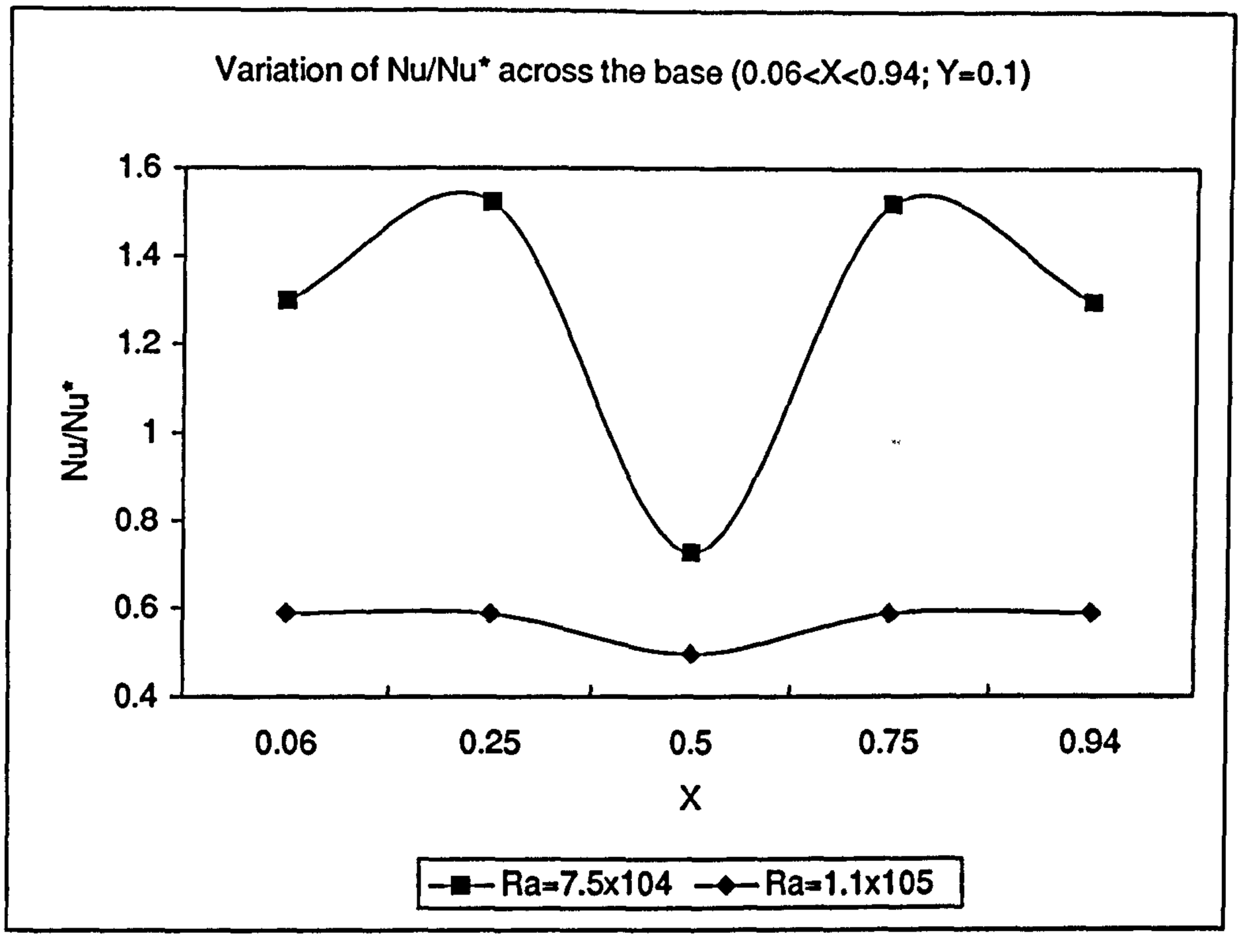
Variation of Nu/Nu* across the base (0.06<X<0.94; Y=0.1)
Nu/Nu*
1.6
1.4
1.2
1
0.8
0.6
0.4
0.06
0.25
0.5
0.75
0.94
X
Ra=7.5x104
Ra=1.1x105

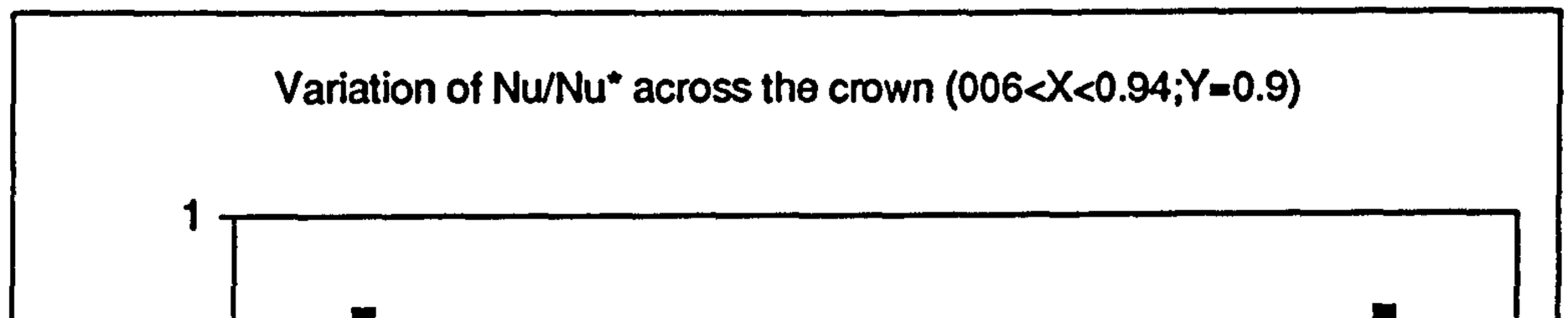
Variation of Nu/Nu* across the crown (006<X<0.94;Y=0.9)
Nu/Nu*
1
0.9
0.8
0.7
0.6
0.06
0.25
0.5
0.75
0.94
X
Ra=7.5x104
Ra=1.1x105

Fig. 4-13(a,b)

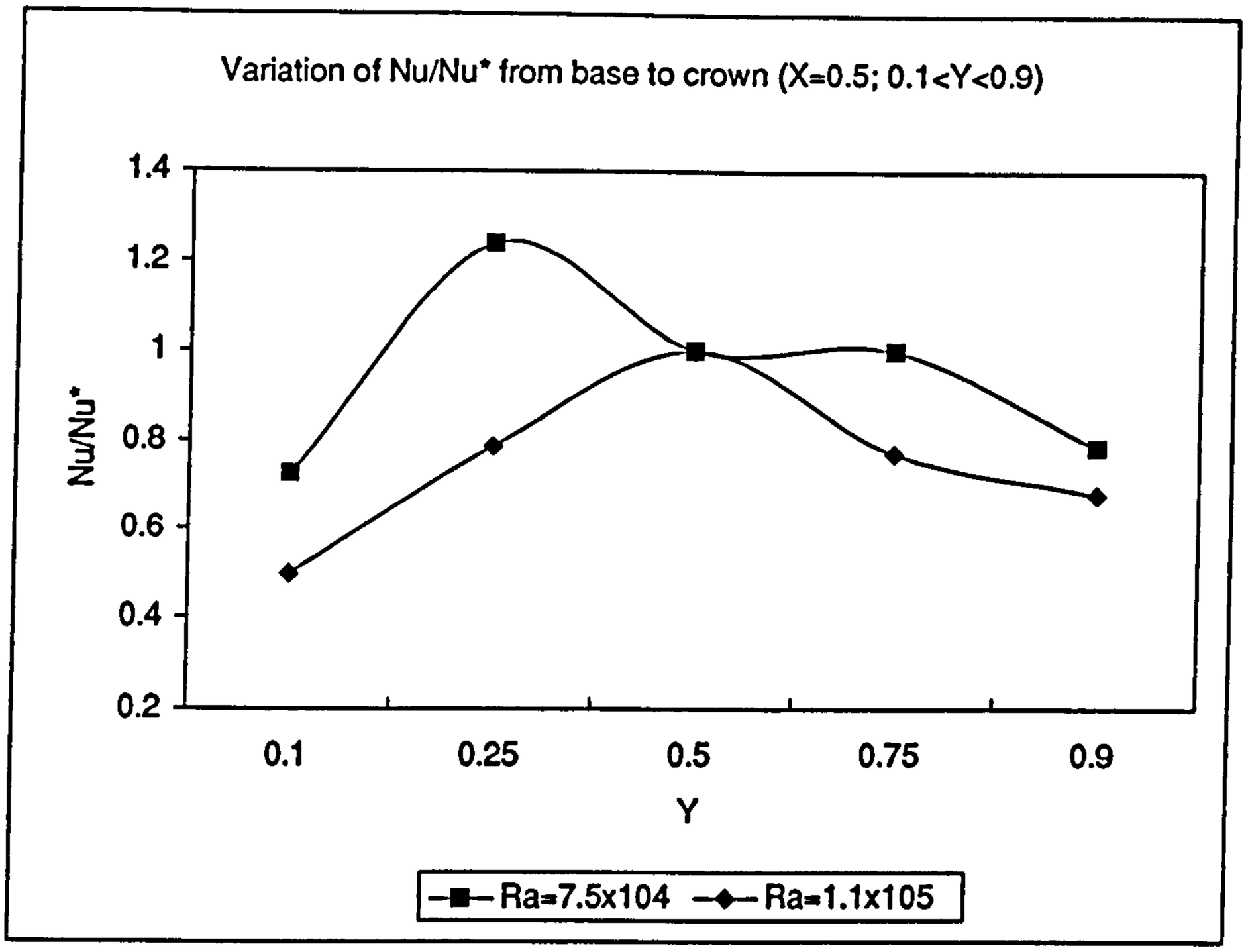
Variation of Nu/Nu* from base to crown (X=0.5; 0.1<Y<0.9)
Nu/Nu*
1.4
1.2
1
0.8
0.6
0.4
0.2
0.1
0.25
0.5
0.75
0.9
Y
Ra=7.5x104
Ra=1.1x105

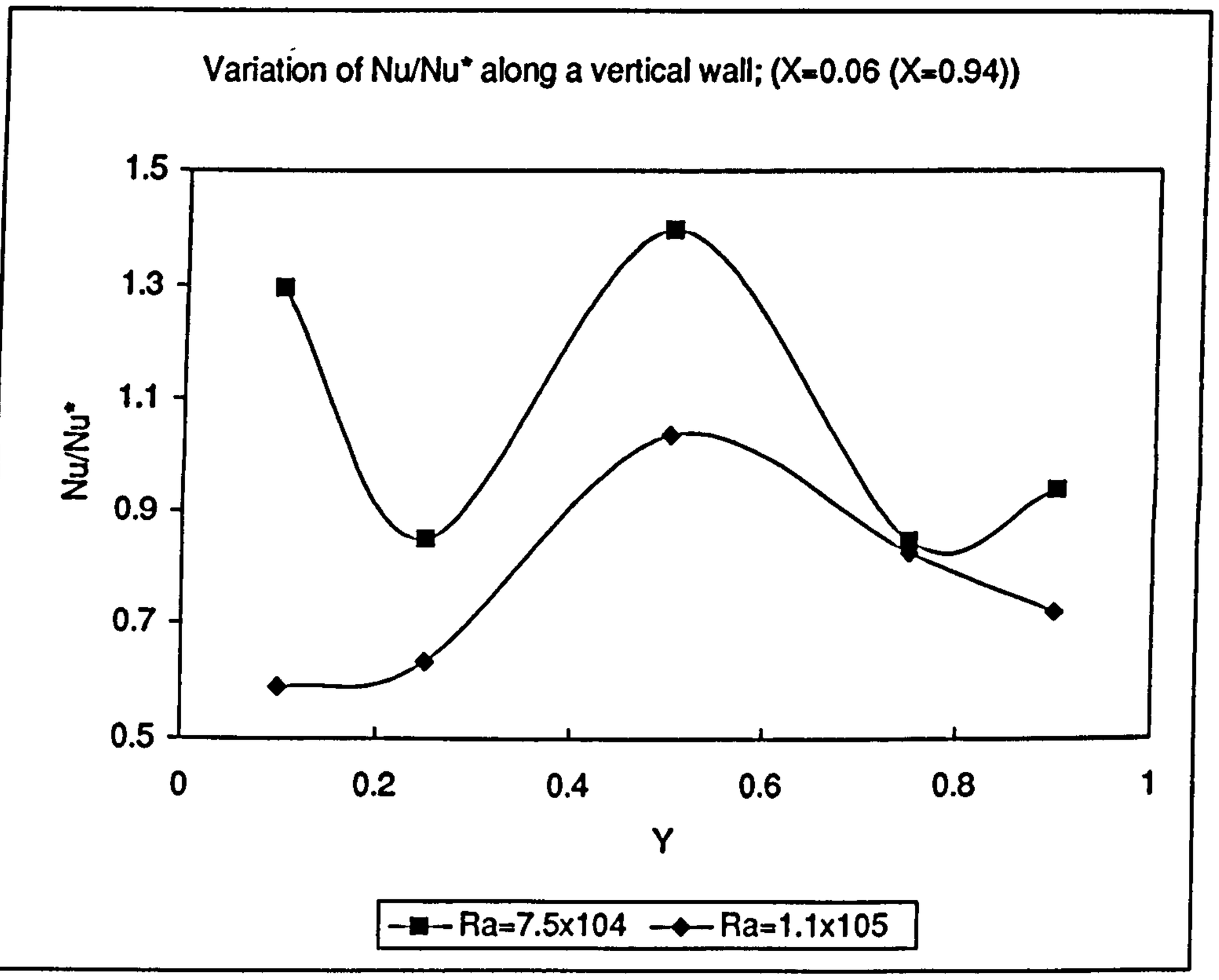
Variation of Nu/Nu* along a vertical wall; (X=0.06 (X=0.94))
Nu/Nu*
1.5
1.3
1.1
0.9
0.7
0.5
0
0.2
0.4
0.6
0.8
1
Y
Ra=7.5x104
Ra=1.1x105

Fig. 4-13(c,d)

Fig.4-14a Dimensions for Fig.4-15

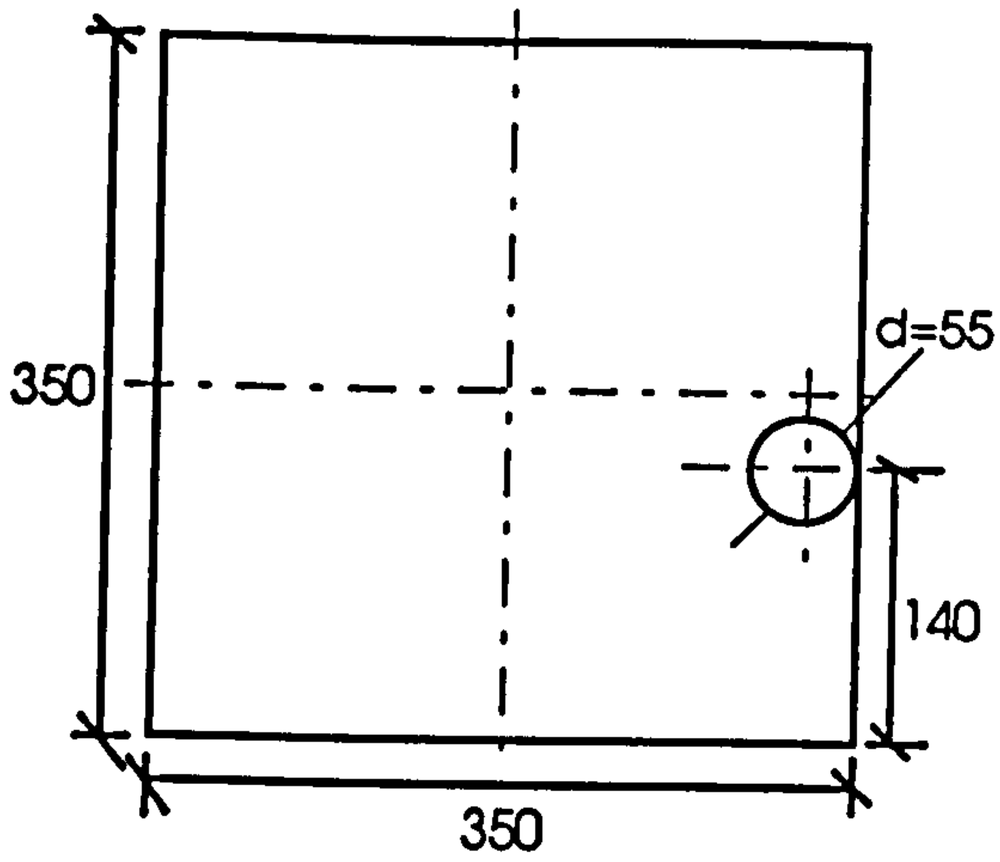

Fig. 4-14b Dimensions for Fig.4-16

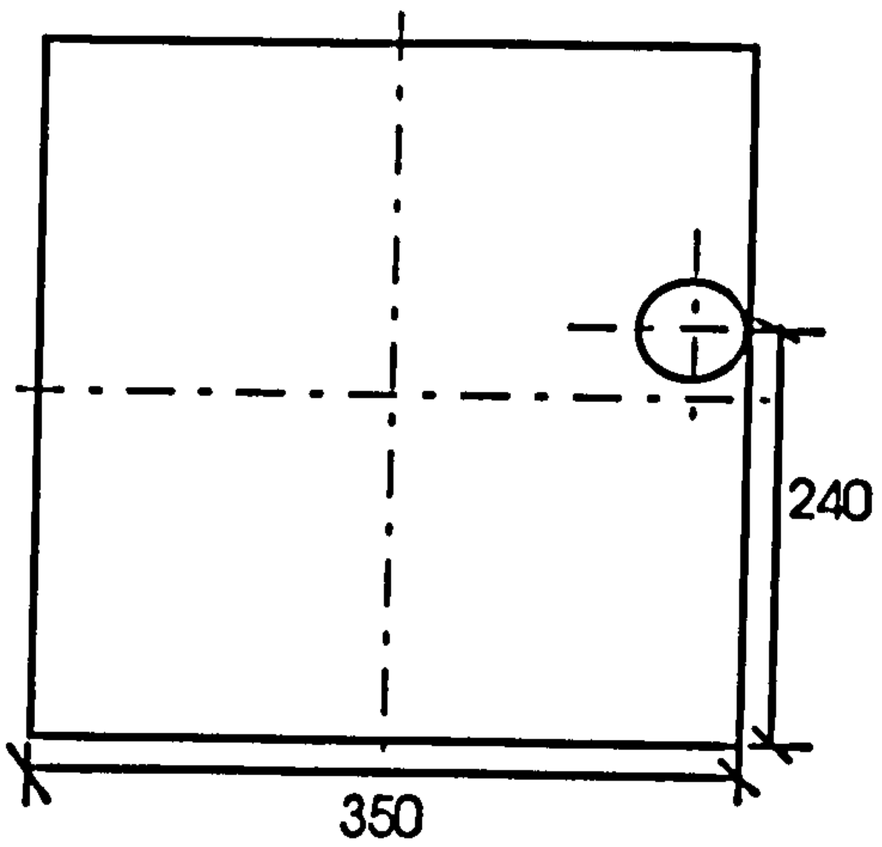

Fig. 4-14c,d Dimensions for Fig.4-19

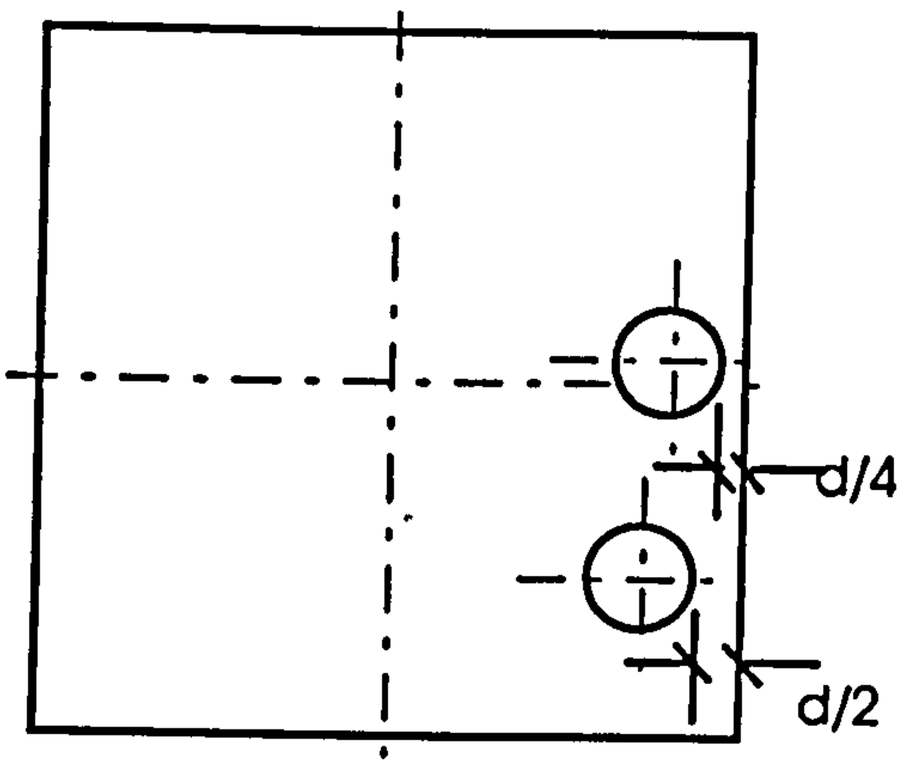

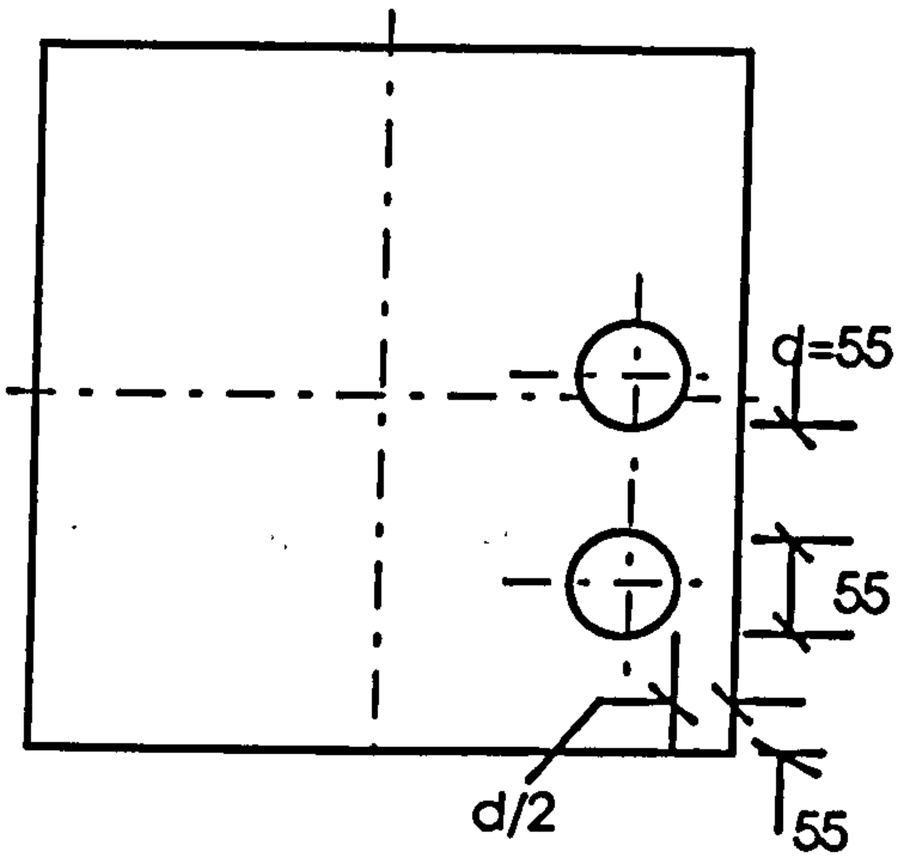

Fig. 4-14e Dimensions for Fig.4-19

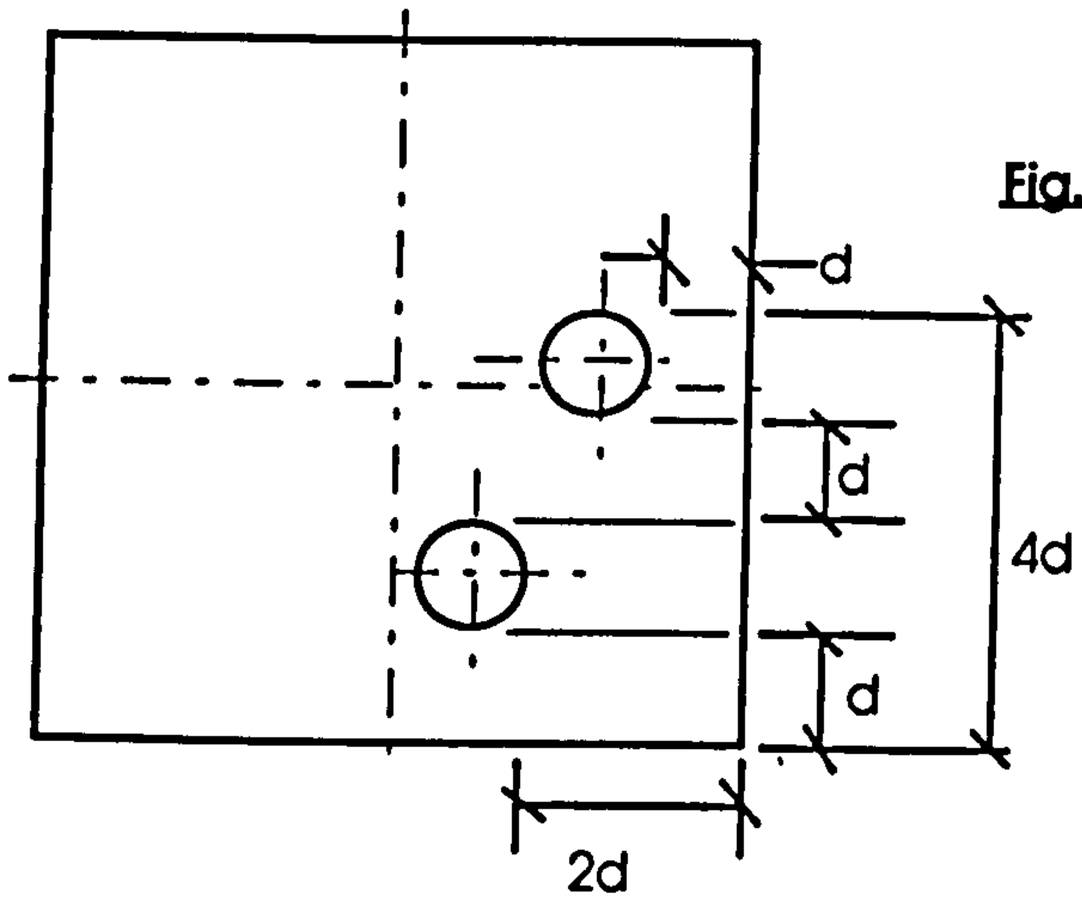

Fig. 4-15. Flow visualisation, y=140

a

b

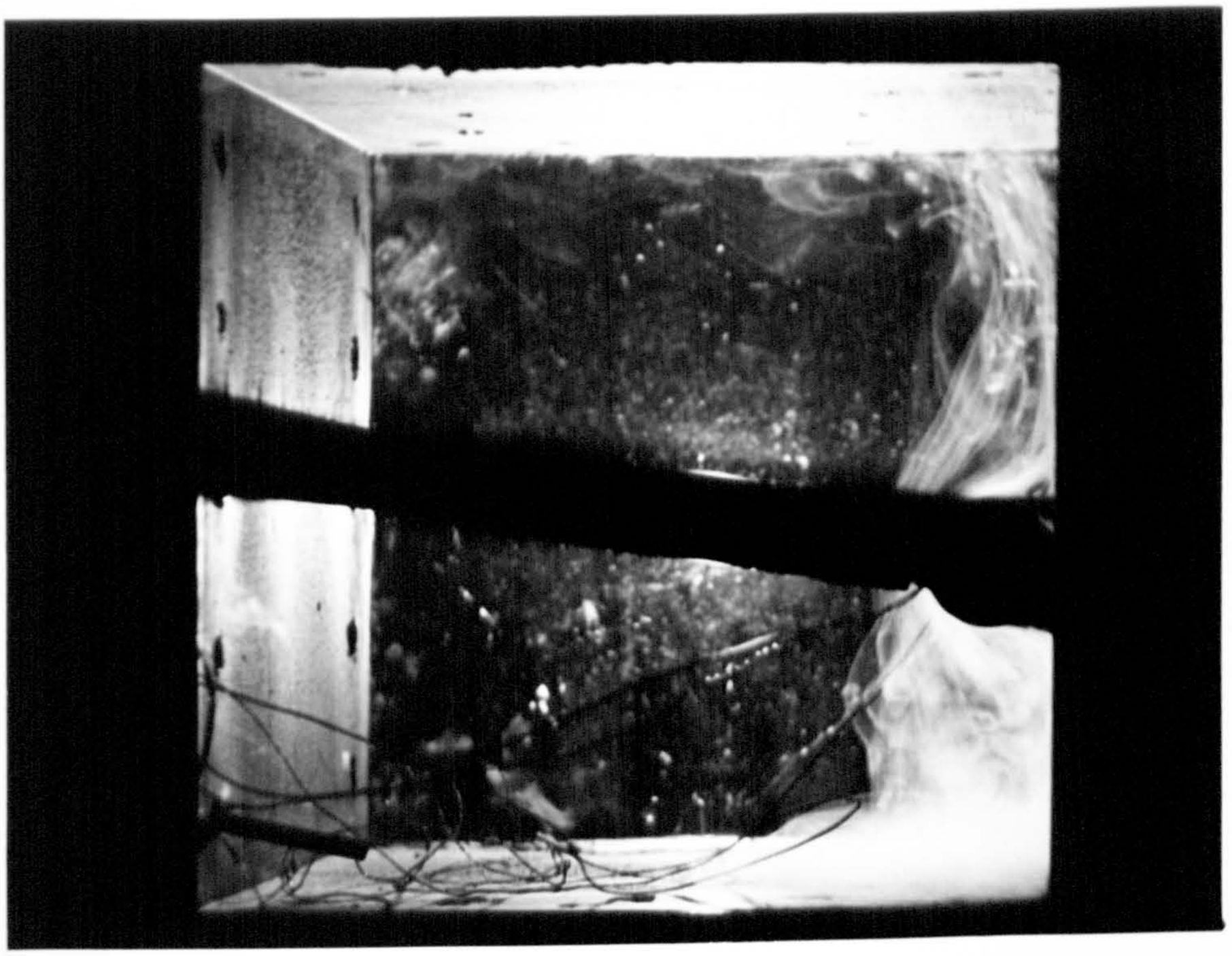

Fig. 4-15. Flow visualisation, y=140

c

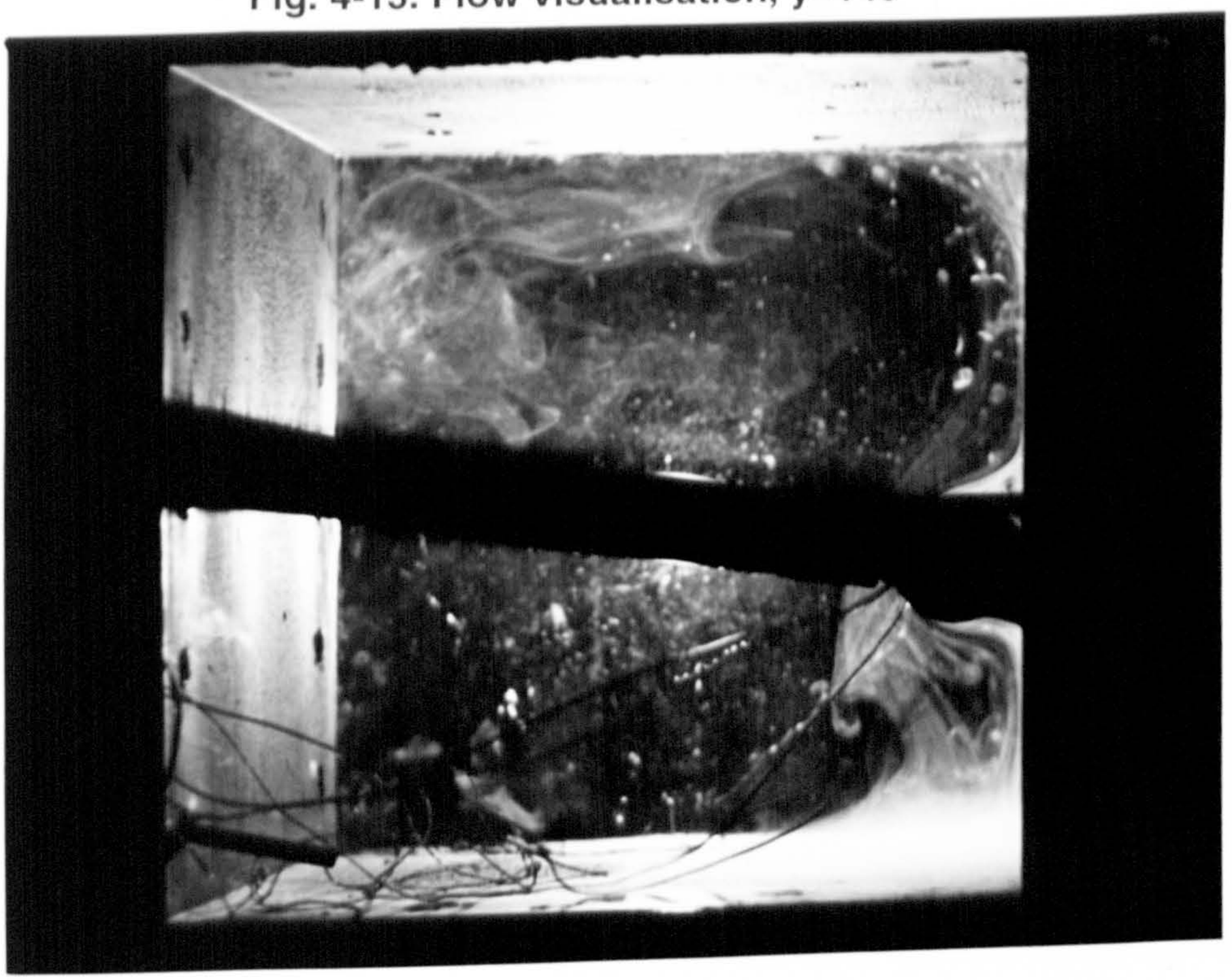

d

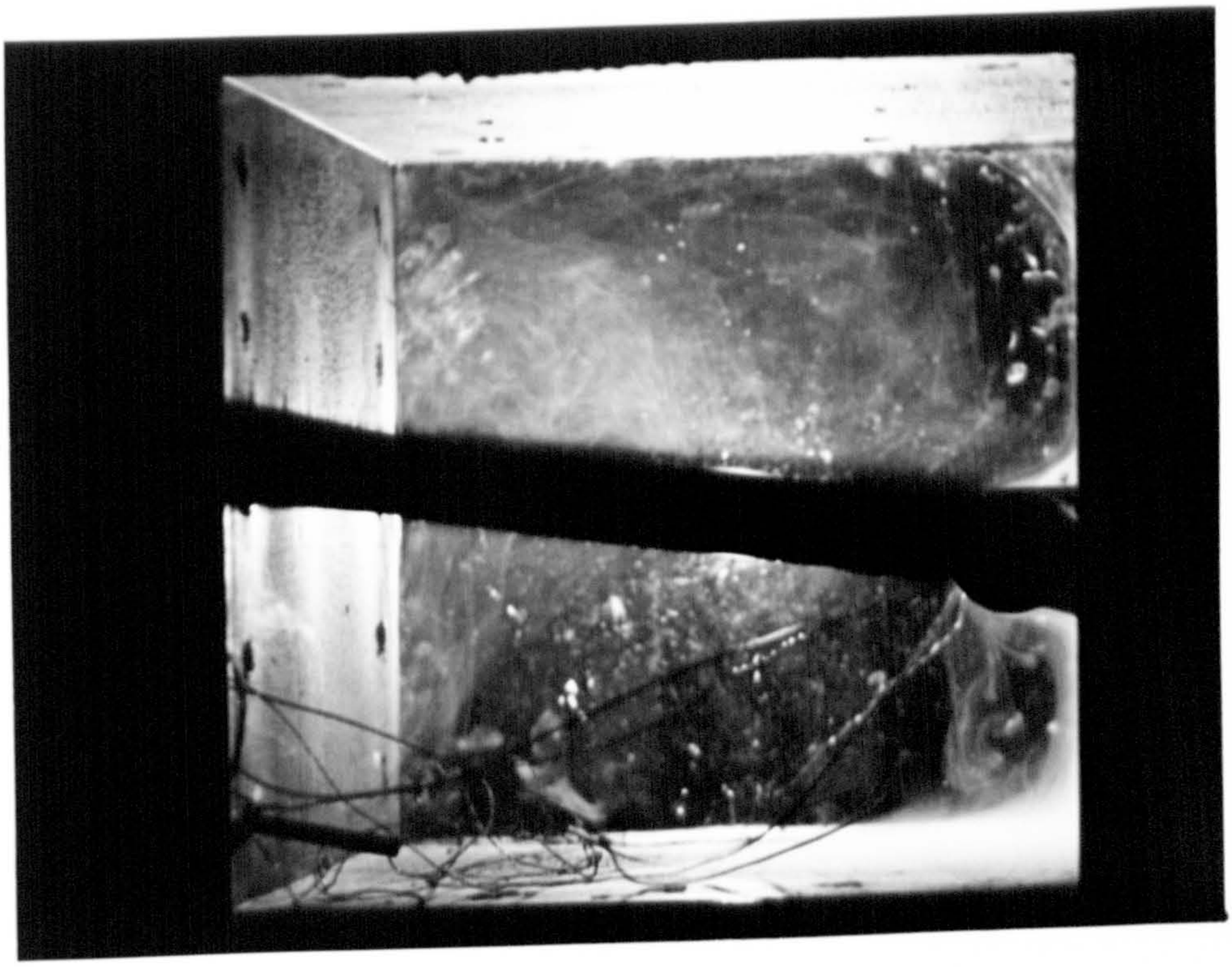

Fig. 4-16a. Smoke introduced from below, y=240

Fig. 4-16b. Smoke introduced from above, y=240

Fig. 4-16c &d. Flow visualisation, eventually mixed

Fig. 4-17
Centrally-positioned Enclosed Heater

$Ra=1.64x10^7$

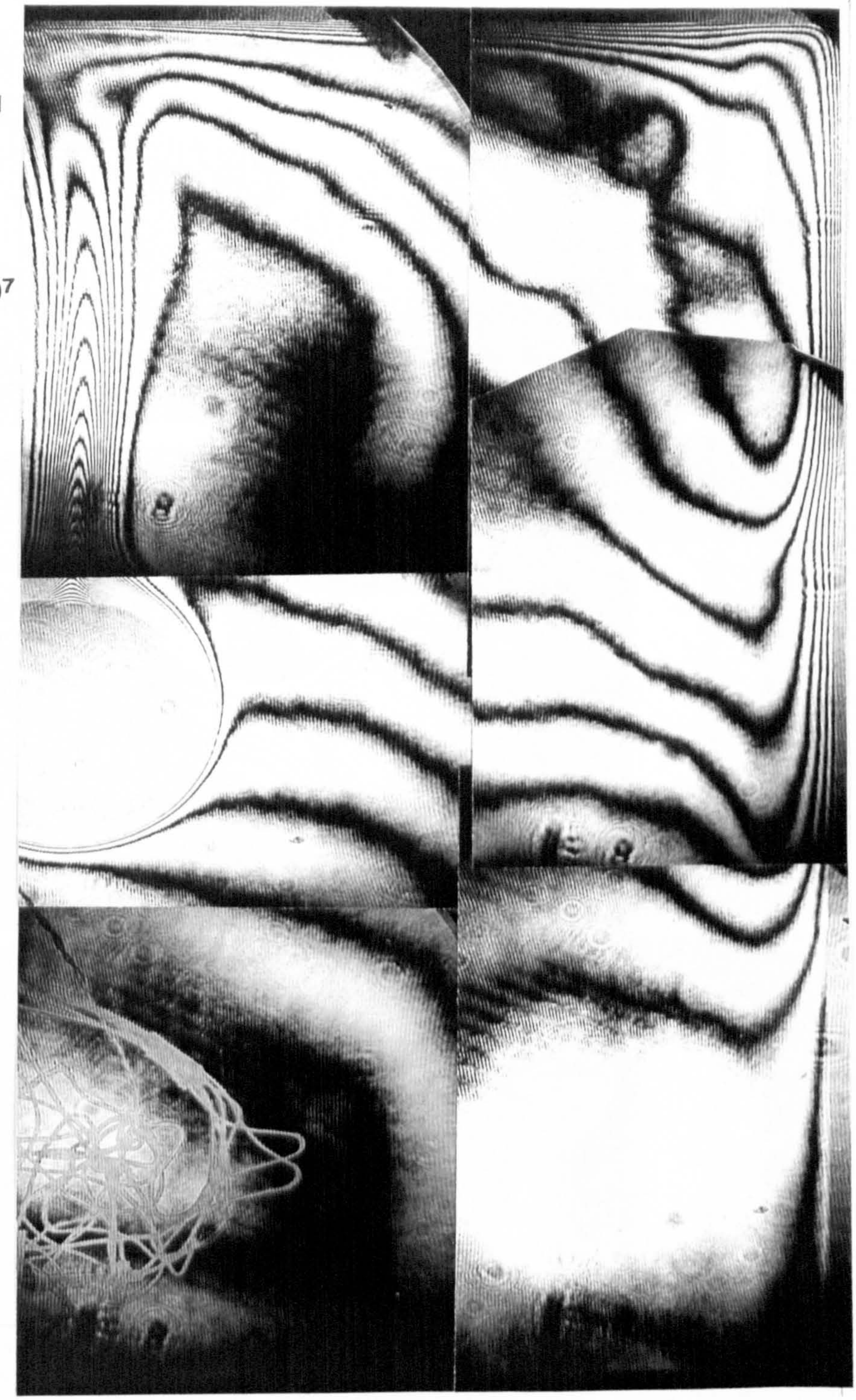

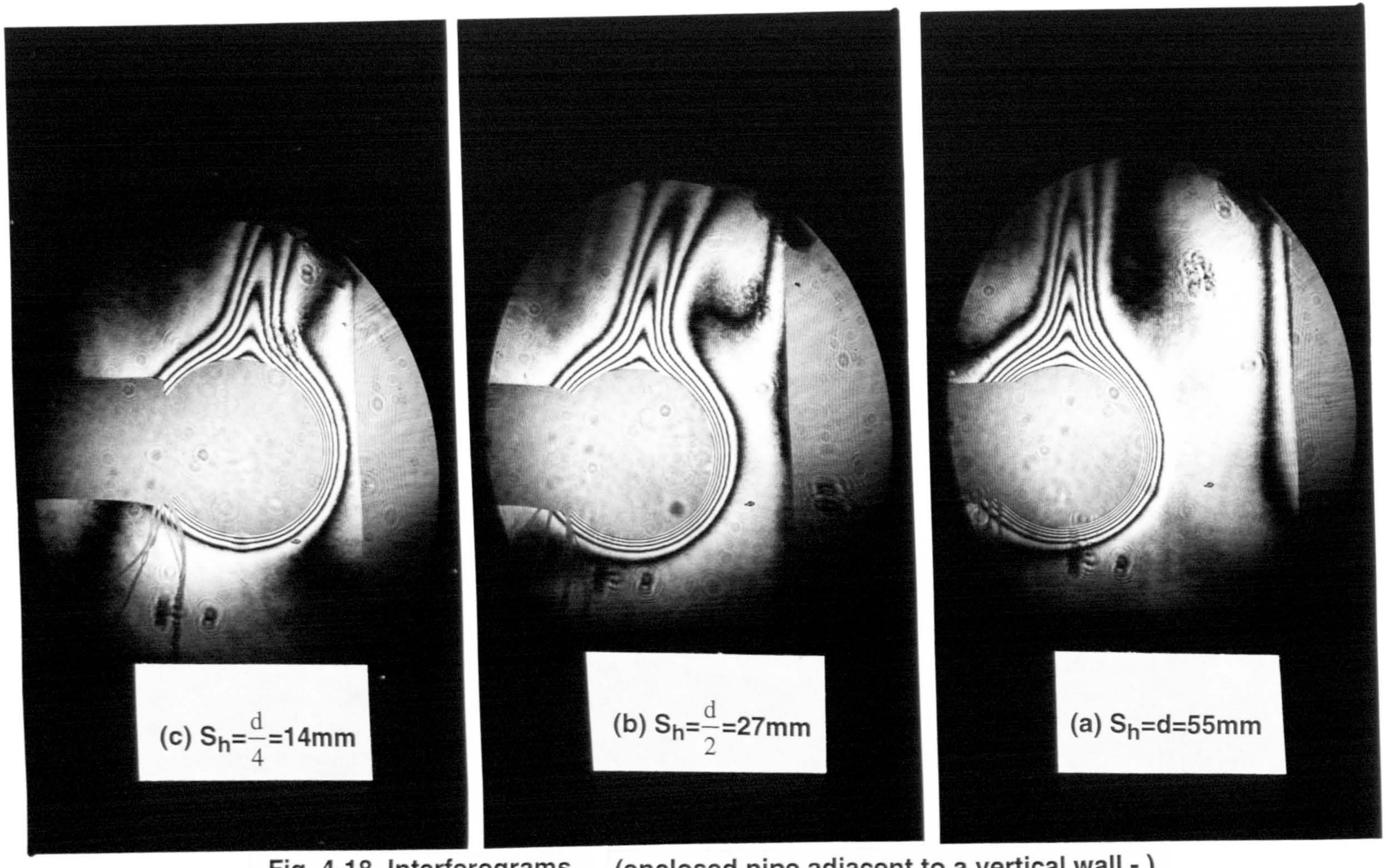

Fig. 4-18. Interferograms (enclosed pipe adjacent to a vertical wall -)

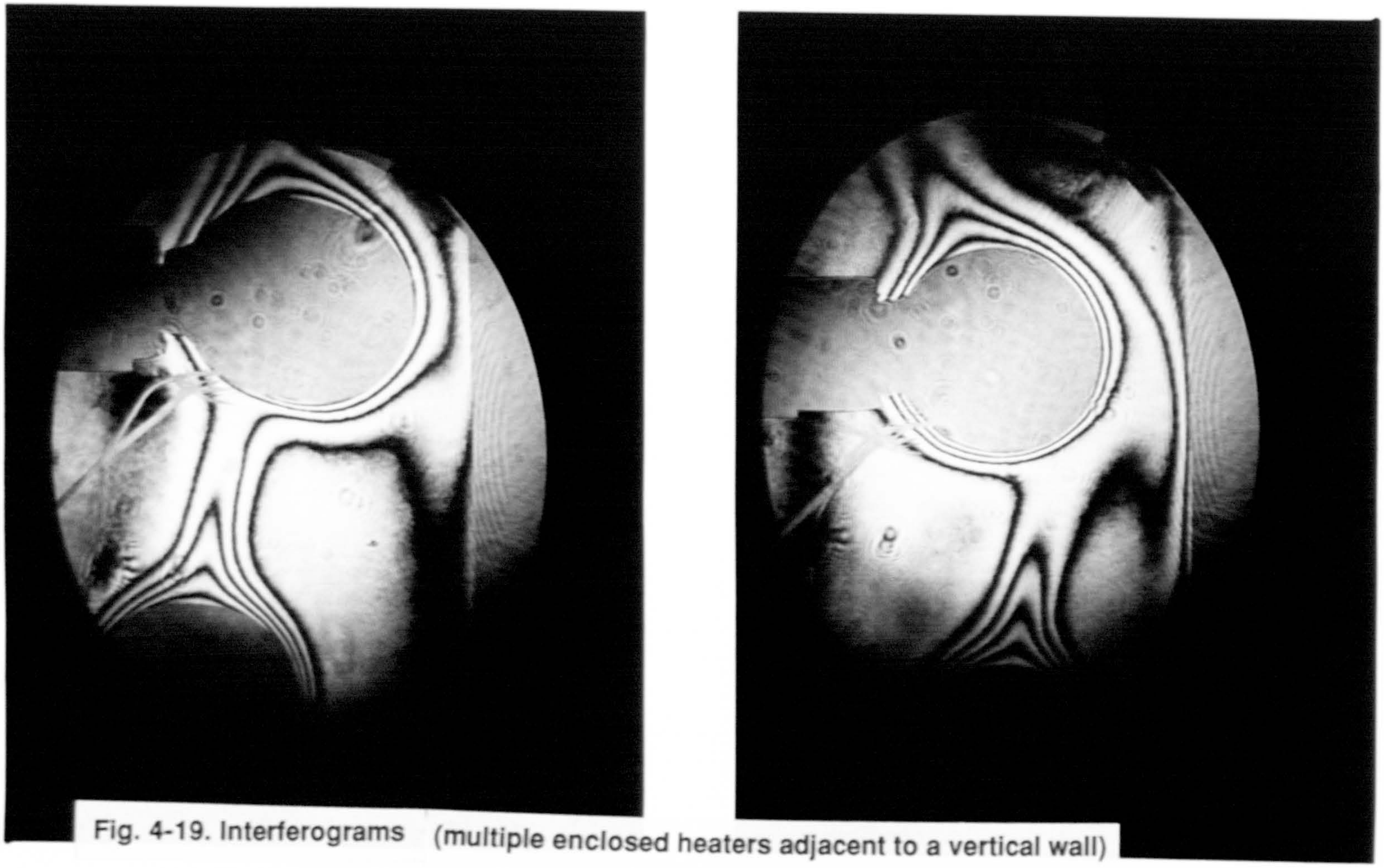

Fig. 4-19. Interferograms (multiple enclosed heaters adjacent to a vertical wall)

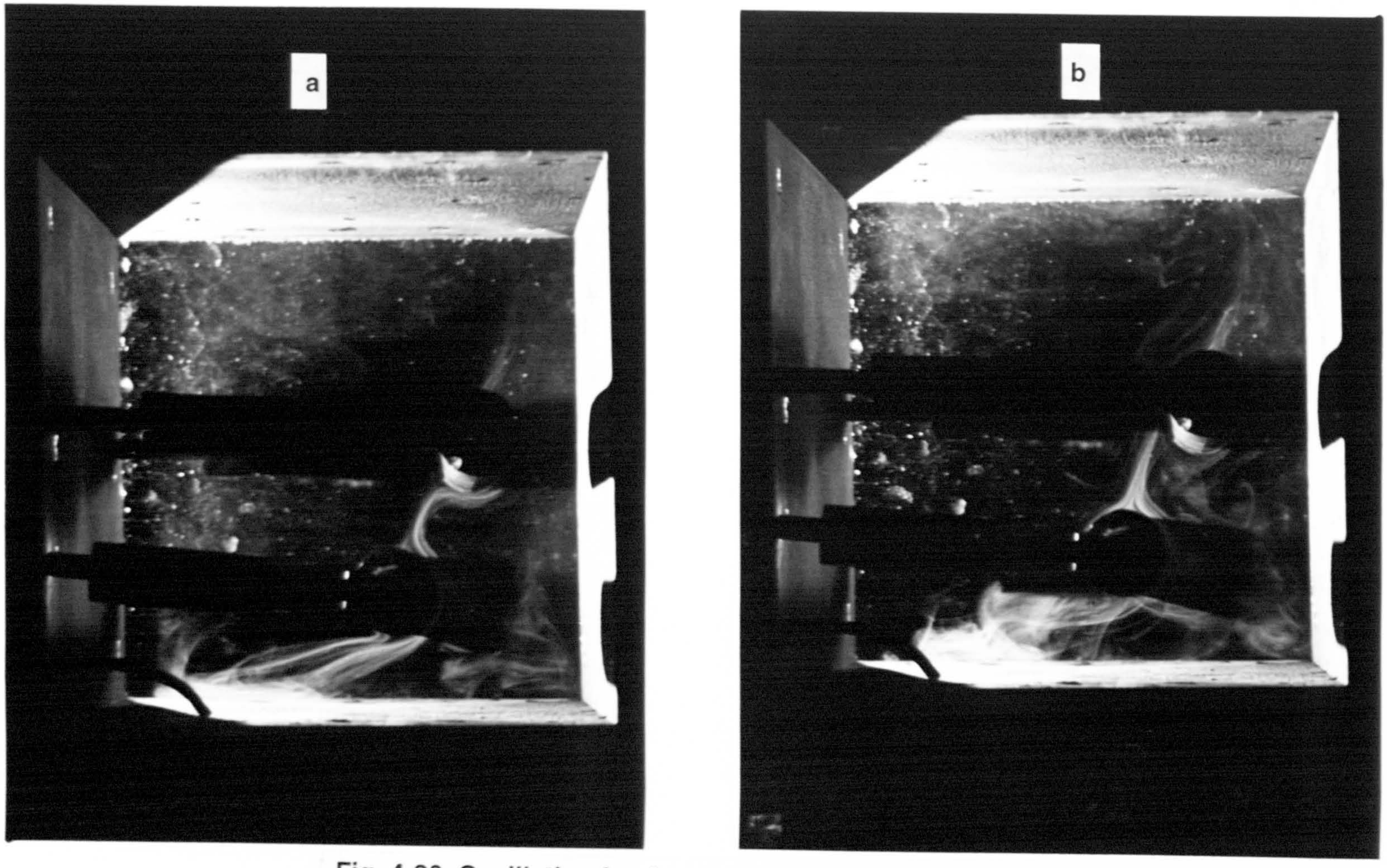

Fig. 4-20. Oscillating impingement (at CC_V=CC_h=d=55mm)

5. DESIGN OF A RECTANGULAR-SECTIONED VACUUM TUNNEL OVEN

5. DESIGN OF A RECTANGULAR-SECTIONED VACUUM TUNNEL OVEN

5.1 INTRODUCTION

One of the aims of the foregoing investigations was to quantify the convective heat transfers. This was achieved by analysing the radiation heat transfer to the inner body and calculating the heat loss through the insulation; these were then subtracted from the measured heat input to obtain the heat transfer to the inner body by convection. Several errors were taken into account in the analyses of the data including uncertainty in the measurement of the emissivity of the enclosure walls and the glass end covers, the need to average the raw thermometric data to obtain zonal heat transfers, and a further assumption of negligible reflectance from the black-painted enclosure.

It was easily deduced that the errors and uncertainty in the convection values would be cumulative (see Appendix C). For very low values of the evaluated convective heat transfers, the ratio of uncertainty to the calculated convective heat transfer would easily exceed 100%.

To reduce these associated errors, an interferometric technique of evaluating the thermal profile was considered. For small temperature differences, interferometry is a proven accurate method of obtaining the heat transfer values [56]. However, apart from the financial constraints of obtaining a large (420x420mm), high temperature optically flat glass window, the temperature differences anticipated would be too large for a meaningful quantitative evaluation of the ensuing interferograms because of high fringe density.

If a highly-polished material such as aluminium were to be employed, a reduction in the radiative heat transfers would result in an increase in the evaluated convective heat transfers, and consequently be subjected to a lower uncertainty ratio. But the loss of strength at elevated temperatures, as would be encountered during experimental work when considerable heat inputs are applied, the inherent porosity of aluminium and anticipated difficulties in fabrication were the principal reasons for discarding this concept. The final approved option was to design a rig for evacuation so that the convective heat transfers would be suppressed [72]. This would require either inserting the entire 1.5m long vessel into a dedicated vacuum chamber, or designing the enclosure rig to be capable of withstanding vacuum operation. A 2-D analysis would also necessitate the use of a long rig in order to reduce end effects.

5.2. DESIGN CONCEPTS

5.2.1 Length of the Enclosure

A provisional length greater than 1.5m was chosen with a cross-sectional dimension of 0.350 x 0.350m. This would give an empty enclosure working aspect-ratio (length/height) of 4.5:1, and, if fitted with the inner body, a subsequent length/annular gap aspect ratio of 17:1. Consequently, the enclosure would improve the validity of the experimental data for 2-D analyses because end effects would be suppressed. However, the increased length precludes the use of the available Mach-Zehnder interferometer at the lower temperature range. Therefore, a traversing thermocouple was developed in conjunction with dedicated wall-attached thermocouples.

5.2.2. Vacuum chamber design

5.2.2.1. Optimal pressure vessel design considerations

Pressure (or vacuum) chambers are preferably spherical as this is the most economical shape for resisting pressures. The next preferred shape is cylindrical, but the critical (hoop) stresses are doubled for this relatively simple alteration. However, the minimum dimensions of a dedicated vacuum chamber would be very large(0.8m dia x 2.3m long). Moreover, as the experimental rig to be manoeuvred into the chamber would have appendages such as heat exchange pipe work and data acquisition probes, the final dimensions of the dedicated vacuum chamber would be much too large for the available working space. The accepted option was therefore to design the rig to cope with evacuation thereby eliminating the requirement for a dedicated, large cylindrical vacuum chamber.

5.2.2.2. Governing criteria and analyses

A procedure for designing rectangular vessels subject to internal pressure is available from ASME Boiler and Pressure Vessel Code [73] derived from Faupel [74]. For vessels subject to external pressure, the stresses are reversed, but an additional factor for consideration is buckling of the plate elements. Therefore the minimum plate thickness was first ascertained before invoking the appropriate section of the Code to

verify that the stresses are within safe limits. Further stresses introduced by providing supports for the inner body were subsequently calculated.

The governing criteria for the design of parallelepiped pressure vessels are principally the ratio of the length of each wall to its breadth and the ratio of the deflection to the plate thickness [75]. This necessitates considerably thicker plates than if spherical or cylindrical shapes had been feasible.

5.2.3. Materials considerations

The use of mild steel (MS) was considered because of the lower initial first cost both in materials and in fabrication. However, an additional statutory constraint in the use of mild steel for pressure (or vacuum) vessels is a minimum corrosion thickness [76], especially where the working life has not yet been determined. The overall weight of the rig including a correspondingly long inner body would have exceeded 300kg! This exposed further problems in local handling within the laboratory, the large concentration of heating power required to raise its temperature to steady state conditions, and an overall higher degree of uncertainty as to the extent of the influence of wall thickness on the wall temperature profile.

5.3. ENCLOSURE

The adopted design concept entailed the use of low carbon stainless steel (SS), because of its greater resistance to corrosion. The major constraint here was the probability of distortion caused by welding a relatively long SS rig, but this was overcome by the fabrication techniques through the use of suitable jigs, fixtures, and by appropriate heat treatment in a furnace [77].

A schematic view of the enclosure rig is shown in Fig. 5-1. The 1700mm long, square-sectioned enclosure, 350x350mm, was fabricated from 6.35mm thick SS. Three threaded reinforcing members or stiffeners, with through slots, were welded on each of the four walls for the insertion of heating-elements and for subsequent flow visualisation equipment. Other SS stiffeners were welded at the far ends of each vertical wall for supporting the inner body piping. The slotted openings provided by the threaded stiffeners were then covered by cheaper, MS bolt-on supporting plates for either the heating-elements, the inner body, or the flow visualisation equipment. These

features ensured that the rig could be used for several types of heater and inner body configurations without requiring costly alterations.

The wall stresses were further reduced by incorporating stiffeners (or reinforcing members) about mid-way between the heating-element and flow visualisation stiffeners [78]. These arrangements enabled the overall length-to-breadth ratio of the wall dimensions to be reduced from 5:1 to 1:1 for optimal flat plate stress calculations.

A SS I-section was fabricated and welded on to the enclosure base, at both ends, to serve as foot stands directly in line with the inner body support carriers pads. A SS angle-section was fabricated and welded to the corresponding upper horizontal wall onto which the end cover supports could be bolted.

The layout of the enclosure is shown in Fig. E-2 (see Appendix E), which includes construction details as well as the methods of attachment of the I-section foot and end plate supports. The method of fabrication and attachment of the pads for the inner body, heaters, and flow visualisation are depicted in Fig. E-3. The all-round welded construction of the stiffeners or pad supports justified the assumption that a stress discontinuity would exist between adjacent plate elements.

The enclosure ends were provided with 420x420mm MS cover plates, of 10mm thickness. To carry each end cover plate, channel sections were bolted on to the SS stand and angle sections. The upper and lower channel sections were additionally linked together by vertical angle bars. The channels and angle bars were designed with M6 tapped holes so that the end cover plates could be screwed tightly against the enclosure. This permitted the edge conditions of the cover plate to be treated as fixed-fixed. The 10 mm thickness therefore provided a generous factor of safety (3.8). The MS supports for the inner body, were provided with oval openings (40x35), to allow for sufficient length (up to 8mm), to accommodate any differential expansion between the SS enclosure and the MS inner body. Other calculations involved are provided in Appendix E.

5.4. INNER BODY

The rectangular-sectioned inner body to be employed in the vacuum tunnel should withstand the inner fluid circulating pressure in addition to the pressure (external to it) under evacuation. Therefore, the calculation procedure to determine the strength requirements for the walls, similar to that employed for the vacuum tunnel oven, now incorporated an additional uniformly-distributed (pressure) load of $1x10^5$ Nm^{-2} applied to the inside of the surfaces (i.e. the inner body plates were designed to withstand a pressure of 1.7(+15%)+1.0=3.0bar).

The inner body, was designed for isothermal operation along its length using water (mixed with a corrosion inhibitor) as the circulating fluid. The inlet and outlet pipes within the inner body chamber each had 8 holes of progressively larger diameters (8-10mm) along the inner body length, through which water was respectively supplied and discharged. Both pairs of inlet, and outlet pipes, obtained from double strength steel pipes (33mm o.d, 6.5mm thickness), were used to support the weight of the inner body via the enclosure supporting/carrier plates. This sideways supporting arrangement was preferred to base support, because it would create less localised flow. Each pair of pipes was connected together with welded flanges, so that the weight of the inner body was equally distributed between each pair. The hydraulic and structural strength requirements of the inner body end plates and the inner body walls necessitated the use of 10mm and 6mm thick MS plates respectively.

The cooling circuit was designed to follow a tortuous route around baffles before exiting through the two outlet pipes (see Fig.5-2, and Fig. E-4). This method of internal circulation has been shown (Chapter 3) to be very effective in eliminating stagnant hot spots along the corners and ends. The holes of 8-10 mm diameter equispaced at 150mm centres, were drilled and staggered along the top of each of the inlet pipes within the chamber, so as to provide uniform-temperature fluid entry along the length of the inner body. The increase in diameter was necessitated from calculations involving losses due to fluid friction [79]. Similarly, complementary holes (7mm diameter) were drilled along the top of the exit pipes (see Fig.5-2). These additionally served as an auto-vent piping system.

Another novel feature was the incorporation of a cylindrical void space within the channel baffle which reduced the cooling fluid volume by some 25%. Consequently,

the operational weight of the inner body assembly was reduced as well as the overall capacity of the fluid circuit.

To reduce or prevent any local air circulation at the ends of the inner body when installed in the enclosure, a compressed fibre sheet (170x145x5mm) was glued to each end, so that these blocks nearly abutted the MS enclosure end plates. The enclosure supports for the inner body pipes were accurately drilled (±0.5mm) so that precise adjustment of the inner body inside the enclosure could be achieved by horizontal movement, in order to achieve concentricity.

5.5. HEATING-ELEMENTS

An improved design was necessary for the 1400mm long heating-elements, in order to accommodate the differential expansion, which was estimated to be up to 20mm during start-up conditions. In the conventional method employed earlier, both ends of the electric heating-elements were bent through a radius of 90^{o} so that the end terminals which protruded through the enclosure were exposed to the cooler atmospheric surroundings. Previous experience showed that when both ends are thus fixed, there is a tendency for the heating-elements to bow out in order to compensate for the ensuing differential expansion between the heaters and the enclosure. While the strain put on the sheath may be acceptable for a 500mm long heater, it would not be tolerable in this instance because the envisaged increased gap resulting from the flexure due to the differential expansion between the 1400mm long heater and the enclosure walls would substantially alter the radiative view factors. As the heater diameter in this case is also larger (9.5mm versus 7.9mm) without an increase in sheath wall thickness, the ensuing deformation may also result in complete heater failure.

The heaters were therefore designed to be fully immersed within the enclosure test rig (see Fig.5-3). Because their terminals would be exposed to temperatures in excess of 250^{o}C, the commonly used end seals (epoxy resin or silicone rubber) were replaced with ceramic beads [80] which would withstand temperatures in excess of 600^{o}C. As this does not fully isolate the hygroscopic MgO insulant from the atmosphere, a short period of supplying electrical power for drying out (and reducing electrical leakages through the sheath, to the measuring thermocouples), would be required each time a heater is commissioned.

The photograph (see Fig. 5-5a) shows the partly assembled enclosure, lifted on to the wheeled stand and with one of the end plates supported and held in place by bolts through the channel sections. The end view (see Fig. 5-5b) shows the installed inner body and its supporting arrangement. The photograph clearly shows that the double strength twin pipes would equally share the inner body load through the welded-on flange. Fig. 5-5b also shows two horizontally positioned heaters along the sidewalls supported at the ends by MS brackets via electrically insulating sindanyo tubes.

5.6. SEALING ARRANGEMENTS

Compressed fibre jointings were used between the pads and the corresponding enclosure surfaces. Sets of layers of woven asbestos cloth were provided between the enclosure's milled ends and the 420x420mm MS cover plates. Each set was made up of four layers, the middle layers having narrow openings for the electrical power supply leads (see Fig.5-4a). Similar joints were improvised for one of the central vertical MS pads through which the thermocouple leads were passed. When these improvised joints were pressed by either the pad or the MS end plates, an acceptable air tight seal was achieved.

Frequent access was required to manipulate the enclosure cover plates and pads, either to alter the heating-element configuration, the flow visualisation perspex pads, or to prepare the rig for vacuum operation. Therefore, for insulating the enclosure, Rockwool (k_{max}=0.06) was chosen because of its greater structural pliability over Micropore (k=0.036). However, two layers were required in order to keep the heat losses to a minimum. The outer surface of the insulation was further covered in reflective aluminium foil to minimise radiative heat losses.

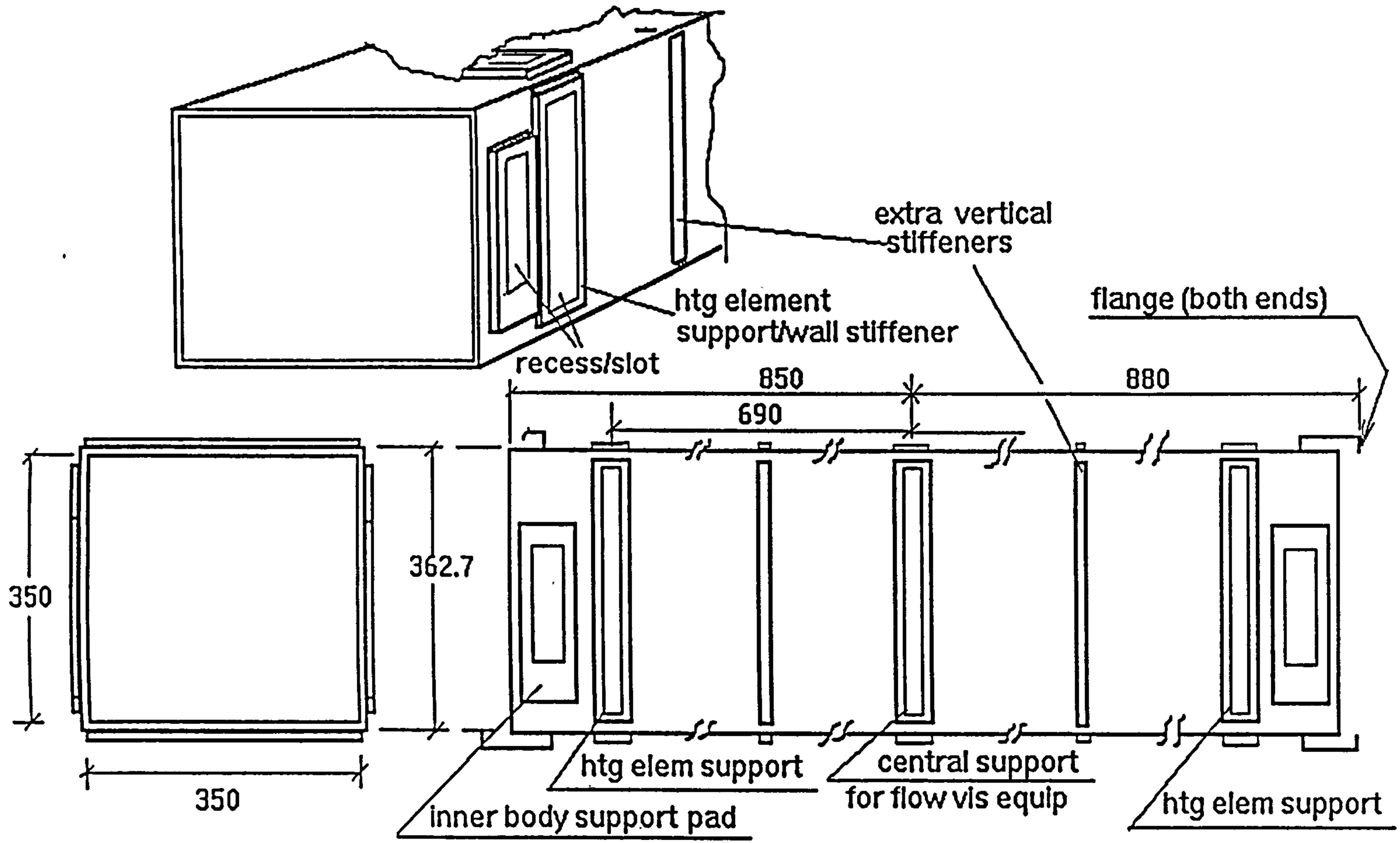

Fig. 5-1 Vacuum enclosure

Fig. 5-2 Inner body (inlet end)

Inner body
(water flow arrangement)

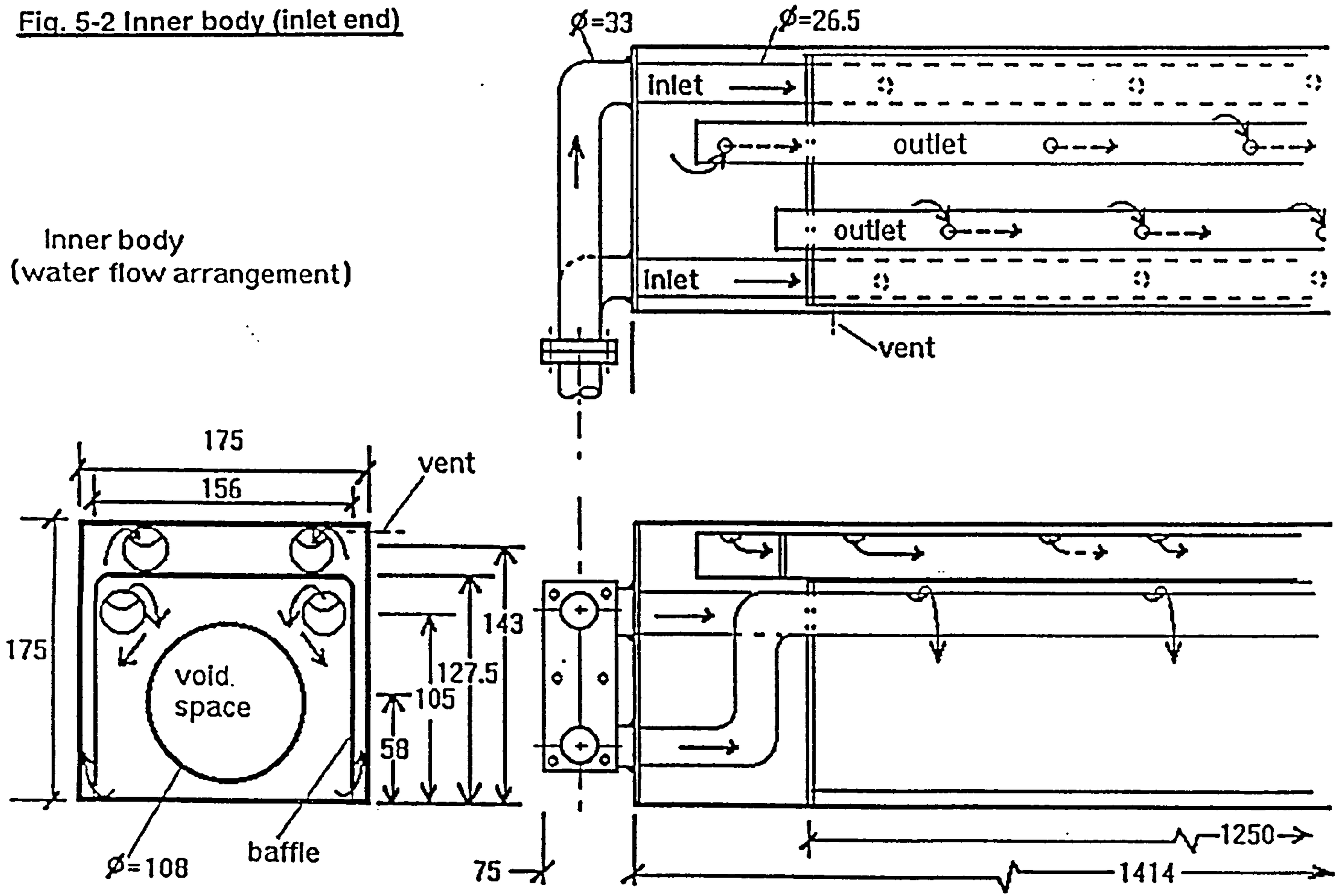

Fig. 5-3 Heating element

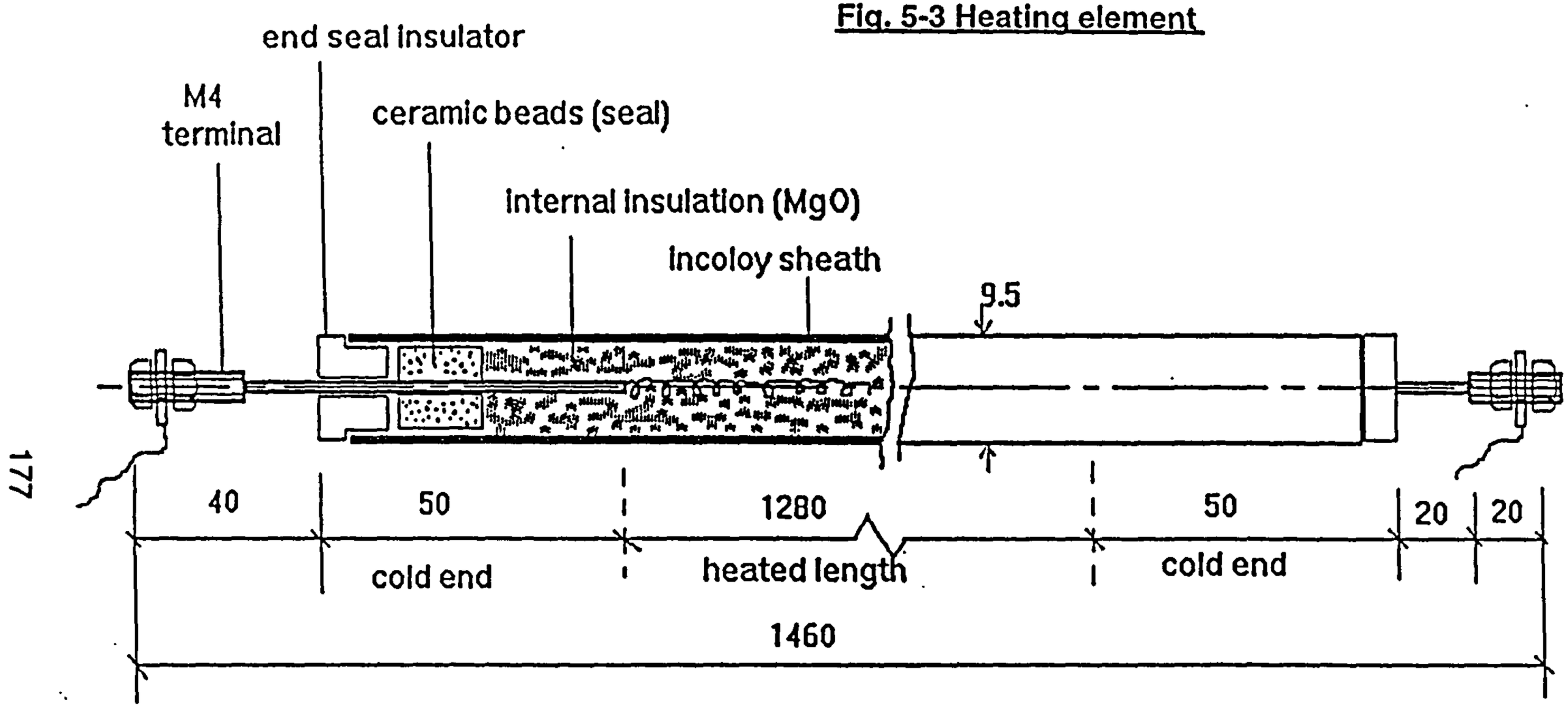

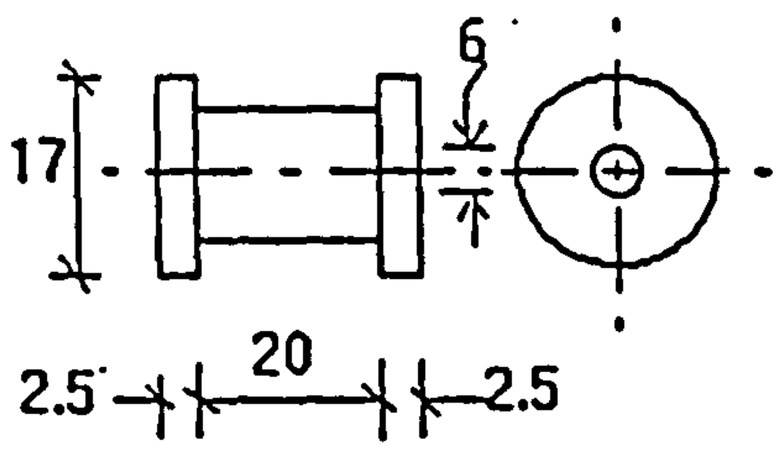

syndanyo end support

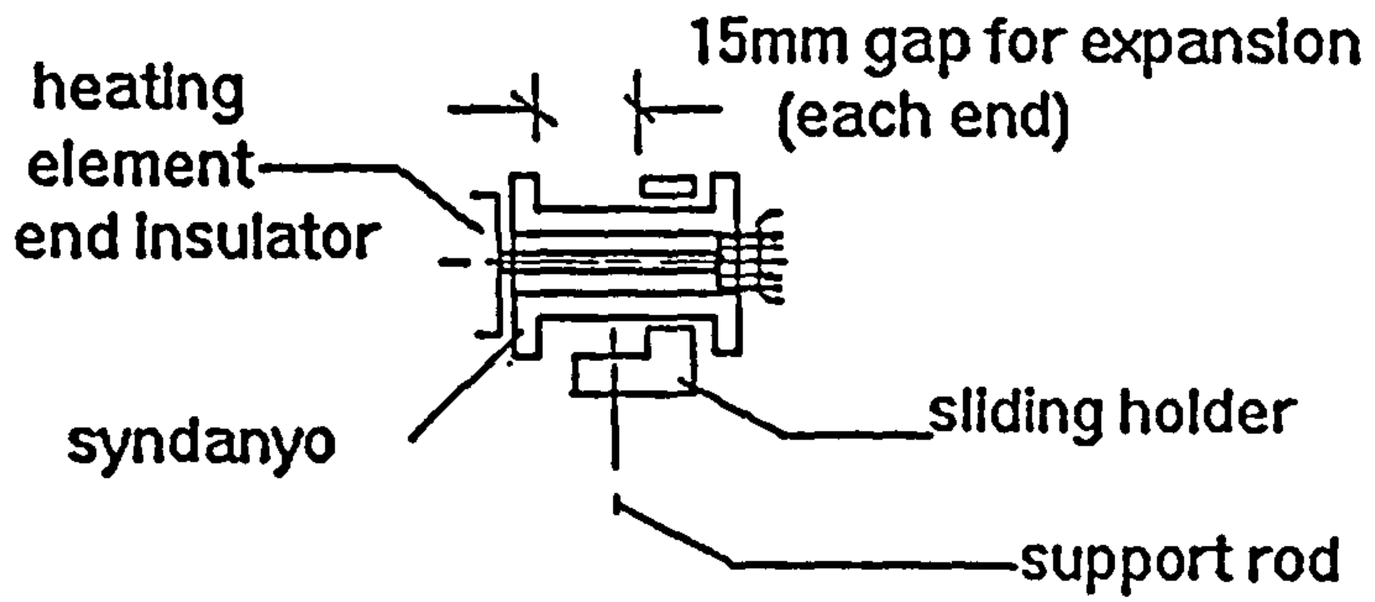

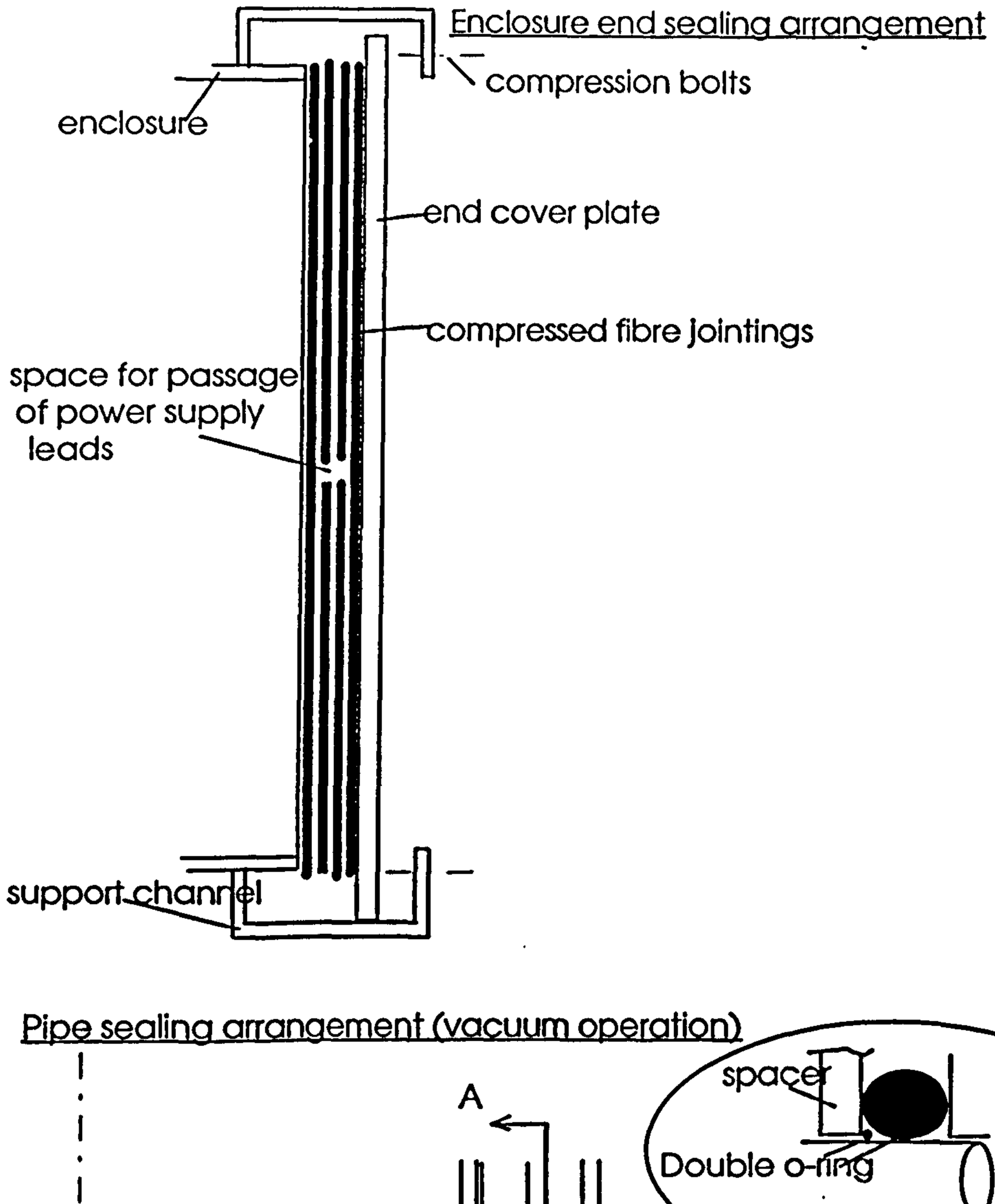

Fig. 5-4 SEALING ARRANGEMENTS

Fig. 5-5a Rectangular Vacuum Enclosure

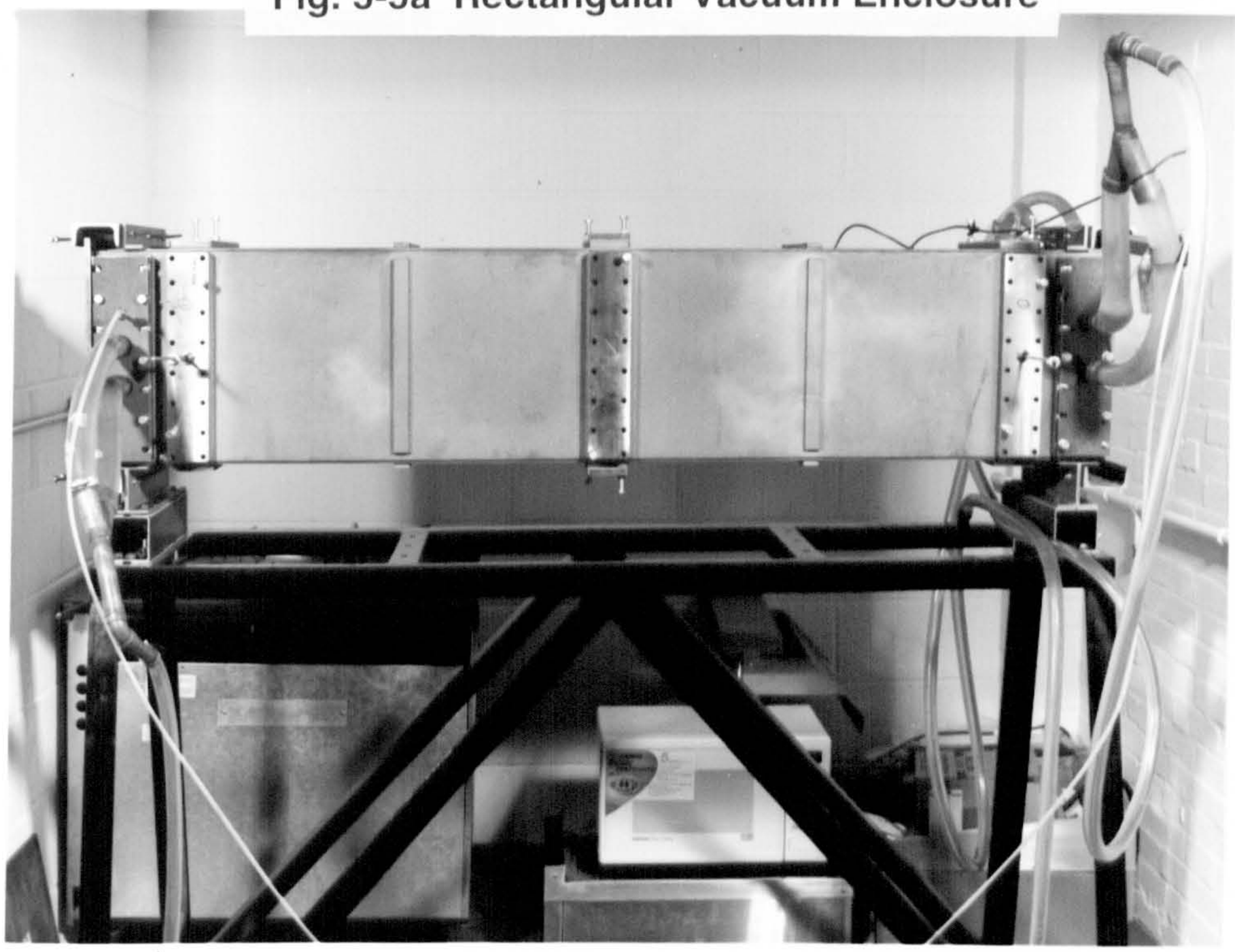

Fig. 5-5b Oven with fluid-cooled inner body

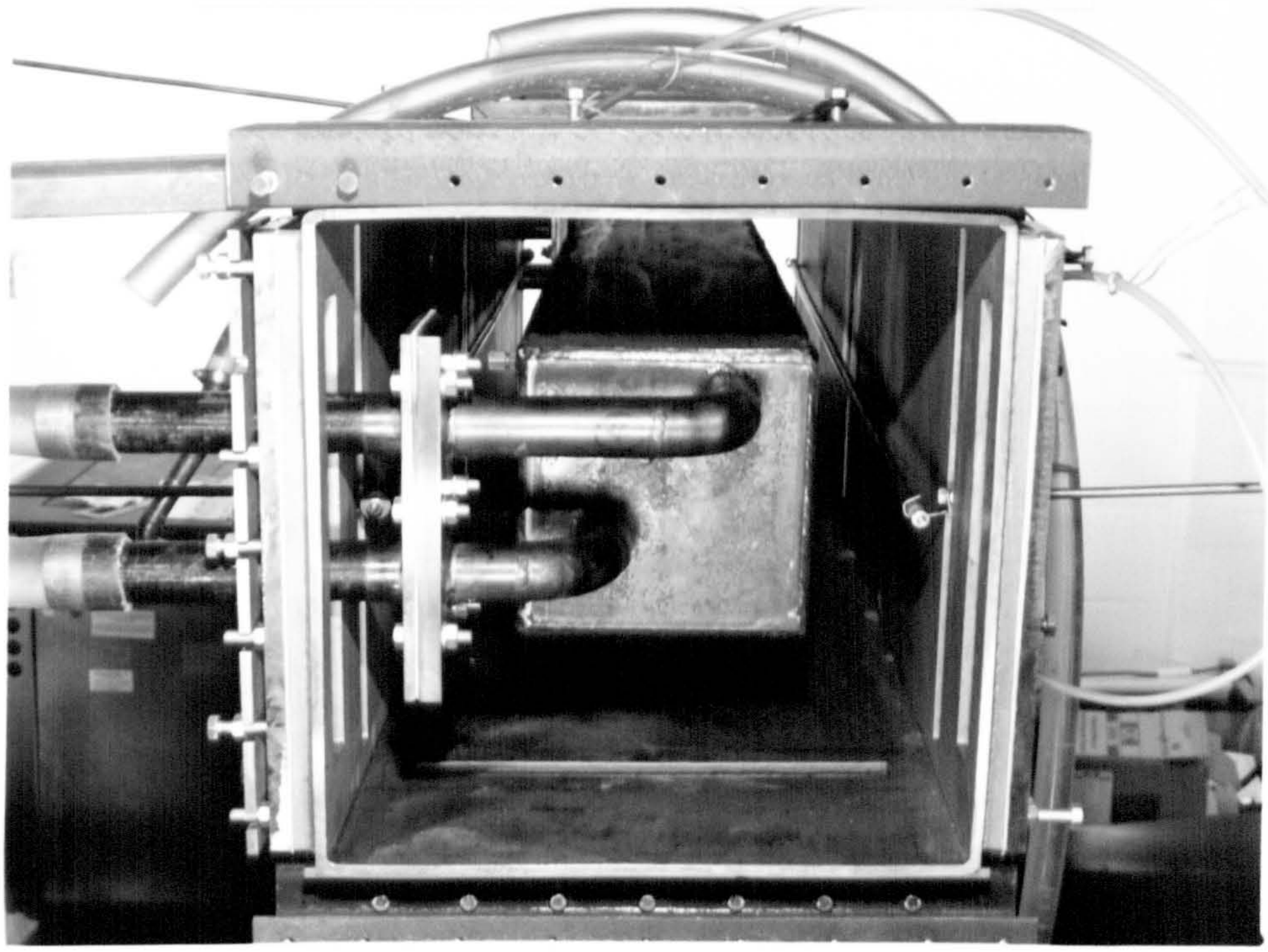

6. CONVECTIVE CONFIGURATIONS IN A TUNNEL OVEN

6.1 INTRODUCTION

In order to reduce the errors and uncertainties inherent in the previous analyses, another technique of obtaining the convective component of the heat transfers was adopted. This was to evacuate the enclosure. The ensuing heat transfers to the inner body would be by radiation, so the difference between the heat input under atmospheric pressure and that under vacuum would be that transferred by convection. The primary objectives in this phase of the study were then to:

(a) obtain an enhanced and more accurate convective component of the heat transfers to an inner body using a varied arrangement of protruding heating-elements in an enclosure;

(b) quantify the proportions of convective and radiative heating to an inner body for each heating configuration;

(c) quantify the net radiative heat transfers to the individual sidewalls of the inner body.

(d) use an evacuation procedure to validate the convective component of the heat transfers.

(e) examine the influence of the differences in wall temperature profiles between the atmospheric and evacuated tests.

6.2. RIG ASSEMBLY AND EXPERIMENTAL PROCEDURE

The apparatus used was previously described in Chapter 5 and assembled as shown (see Fig. 6-1 and 6-2). The enclosure was mounted on a 1.2m high wheeled stand with a lower platform upon which the wattmeters and the variacs were mounted. The inner body was lifted and inserted into the enclosure, and supported at its approximate working height with wooden blocks. Joints were then positioned before the connecting piping flanges were bolted to the inner body pipe flanges. The inner body wooden supports were then removed and the concentricity with the enclosure ascertained. Flexible hoses with isolating valves were then connected between the inner body and the thermocirculator. The vents were similarly connected.

6.2.1. Power supply and instrumentation

Type T thermocouples of 0.2mm diameter were used for the water circuit. Type K thermocouples of 0.2mm diameter were employed on the heaters, walls and air spaces. A Fluke 2201A datalogger was used to record the output from the type K thermocouples, a multimeter for the water turbine flowmeter, and a Newport TC2 datalogger for the type T thermocouples. Regulated power at 235 ±0.01% volts, was supplied via variable transformers, and through individually dedicated wattmeters to each of the heaters (see Fig.6-2).

6.2.2. The heat exchange circuit

The chiller circuit (see Fig.6-3) consists of a refrigeration unit with a built-in process pump which delivered cooling fluid to the inner body at 1.7bar. The chiller temperature control system was always maintained at $\pm 0.75^{0}C$ of the fluid circulating temperature ($48^{0}C$). Preliminary tests were carried out to investigate the isothermality of the inner body, the uniformity of the heating-elements' surface temperatures, the outputs of the thermo-junctions, the variation of wall emissivities with temperature, and the effectiveness of the insulation.

The room within the laboratory in which the experiment was carried out was equipped with a dedicated air supply and exhaust system which allowed precise control of the local thermal environment.

6.2.3. Convective heater arrangements

The heater configurations investigated utilised earlier findings from both the literature and from the deductions in Chapters 3 and 4. The configurations (see Fig.6-4), each consisted of four sheathed electrical heating-elements. The preliminary tests utilised C20 (see Fig. 6-4a), similar to C2 (see Chapter 3), with axi-symmetrical heating arrangements. However, the horizontal offset was lower, being only 15mm measured from the cylinder periphery for a presumed maximum benefit from the chimney effect (see Chapter 4), while the vertical offset from the horizontal walls was 30mm to promote air inflow at the base [28].

The main tests were carried out with C91, C92 and C93 (see Fig. 6-4(b-d)). A larger number of configurations were initially tested in the flow visualisation (see section 6.4.1) and they were all variants of the convective C9 as deduced from Chapter 3. Generally, the heaters were positioned in the lower half of the cavity for maximum convection. The heaters for C91 were positioned along the vertical walls (see Fig. 6-4b) and the vertical centre-to-centre distance between them was 140mm. This distance was assumed to be important for the lower plume to entrain and mix with the surrounding cavity air before contacting the upper heater. The vertical distance between the centre-line of the heaters in C92 (see Fig. 6-4c) was only 40mm (i.e. 4d) which was the distance obtained for maximum convective heat transfers [27] for the vertically-stacked, horizontal cylindrical arrays along a vertical wall. It is also similar to C9 studied in Chapter 3. Some baking products including rolls, pizzas and oven bottom bread benefit from improved base heating [81]. Therefore, a configuration was created by locating the lower heaters much nearer the middle of the enclosure (see Fig. 6-4d). This configuration would have been designated C92-135, but the upper heater could be traversed inwards to form a series of base heating arrangements in its own right; hence it was designated C93.

6.2.4. Data Acquisition

Initially, five thermocouples were positioned on each of the inner body walls. However, preliminary data analysis showed the need for more data points in order to increase accuracy when assessing axial temperature variations. A total of 20 data points were consequently found to be sufficient. Three of these were installed on the centre-line top surface in the x-direction, and the rest positioned on each wall in the z-direction, along the length. Similarly, the number of thermocouples on the enclosure

internal surfaces was increased (see Fig. 6-5a), in order to improve accuracy when calculating the zonal radiative heat transfers because of the temperature gradient in the z-direction.

Each heater was separately tested up to its maximum design voltage of 240V. The power input was varied up to 60% of installed power (2200W of a possible 3000W), using configuration C20 and no significant errors were observed in the thermocouple outputs. 140 temperature data-points were recorded for each configuration, 81 of these exclusively for air space temperatures.

Measurements of the air temperatures inside the enclosure were carried out for both horizontal and vertical profiles. Each thermocouple head was spot-welded to give head diameters of less than 0.5mm, and not shielded. Initially, three thermocouples were installed on the traversing probe, two for the upper and lower spaces and the third for the vertical space adjacent to the inner body. However the traversing process was very time consuming and was found to lead to erratic results in certain planes. This was attributed to the unsteady nature of the air flows. Subsequently a total of 20 thermocouples were installed on the rack (see Fig.6-6), traversed and recorded at only six discrete positions, to give 81 data points {(3x20 (air space) + 3x7 (close to the wall), (see Fig. 6-7). A bracket was calibrated in-situ to locate precisely the traversing rack (see Fig. 6-8) at each of the selected data points.

6.2.5. Flow Visualisation

To examine the flow patterns, three of the four MS plates at the middle of the enclosure were replaced by perspex plates. A hole was drilled through the remaining MS plate at the centre-line base which then accommodated a smoke-conducting pipe. A powerful projector lamp (250W) was focused through the 20mm slit covered by one of the vertical perspex panels. As the upper and lower corners were not illuminated by the projector lamp, two 100W lamps mounted in front of parabolic reflectors were directed through the opposite perspex side wall. By illuminating only the central portion of the rig in the x-y plane which provided a light sheet of 20mm thickness, optical irregularities such as curvature and three-dimensional taper were eliminated.

Smoke tracers were obtained from ventilation smoke tubes, with the aid of aspirators, and guided to the base of the enclosure through a combination of flexible and rigid smoke-conducting pipes. Smoke was injected to the enclosure as soon as the heater

temperatures approached steady states (≅6minutes). This was necessary in order to avoid prolonged exposure of the perspex panels to high temperatures. The smoke patterns were recorded schematically, and also by a camera and video recording system.

6.2.6. Experimental procedure for vacuum operation

The major difference between the apparatus used for the atmospheric tests and that for vacuum tests is the incorporation of the evacuation pumping system. Other modifications and additional equipment are given below.

6.2.6.1. Operational Requirements

The layout of the evacuation system is shown in Fig.6-9. It has been shown [70] that within the environmental pressure range $10<p<100$ torr, the convective flow is suppressed. The task then is to estimate the heat transfers by gaseous conduction, the rest being dissipated by radiation and by extraneous losses through the insulation and the rig (solid) conduction. To be absolutely certain that the convective flow was at a minimum, the vacuum tests were performed at the lower end of the range (i.e. where $p_{(enclosure)}<12$ torr), and a stable evacuated environment of less than 5 torr was actually achieved. Therefore, it was only necessary to use a two-stage vacuum rotary mechanical pump which enabled the $0.202m^3$ system to be evacuated down to <10torr. For verification three gauges were used as shown in Fig. 6-9, the working gauge being that of 50-0 mbar

6.2.6.2 Sealing for vacuum operation

Extra sealing arrangements were necessary for vacuum operations. The oval openings in the piping supports were sealed by two o-rings separated by MS washers, and pressed together by the outer pads (see Fig.5-4b). Additional sealing was provided on the outer sealing arrangement by a smaller o-ring which formed a double o-ring system as shown in Fig. 5-4b. The woven joints for the machined enclosure ends and the covers were replaced by flat universal jointings. Therefore power was supplied to each heater via vacuum leadthroughs, so for each of the four heaters, two leadthroughs were installed. Vacuum leadthroughs were also utilised for passing the thermocouples through the vacuum enclosure by fabricating an adaptor housing for the upper (horizontal) central MS pad.

6.2.6.3. The use of iterative procedure for heat flux

The thermal boundary-conditions required for the evacuated enclosure should ideally be the same as that for the atmospheric tests (i.e. heater, enclosure walls and inner body temperatures). As soon as steady-state conditions were reached in the atmospheric tests, the various readings were taken, and evacuation commenced by starting the double-stage rotary vacuum pump. Pumping down from atmospheric to 20 torr took less than 2.5 minutes. But at the same time, a rapid rise in heater temperatures was observed (see Fig.6-10), symptomatic of air flow suppression within the enclosure.

In order to achieve the heater thermal boundary-conditions, it was necessary to reduce the power input to each heater and it is this difference which accounts for the convective component of the heat transfers. While the inner body temperature could be satisfactorily controlled, it was not possible to precisely adjust the enclosure wall temperature profiles to the original boundary-conditions; these being a function of the asymmetrically-positioned concentrated heat source temperatures, and the convective flow directions.

When vacuum conditions were somewhat steady, the heater power input was lowered to try to regain the original temperatures. But this, in turn, affected the vacuum upon which the heater temperatures ultimately depended. And because of the additional complication of radiative heat exchange between the enclosure walls and the heaters, and between the heaters themselves, a difficult and intricate iterative adjustment procedure was necessary in order to achieve the original atmospheric heater temperatures with reasonable precision. This period was typically followed by up to 1.5 hours before a satisfactory steady-state condition was achieved.

6.3. DATA REDUCTION AND CALCULATIONS

In experimental work involving pure natural convection heat transfers in enclosures, several methods have been employed to measure the heat transfer modes. It can be sufficient to employ apparatus that was designed with highly-polished reflective surfaces (or to use reflective paint or aluminium foil on the surfaces) in order to minimise radiative heat transfers in the cavity. As the temperature difference between the hot and cold surfaces becomes larger, the proportion of radiation that can be eliminated by these methods becomes too large, so a comprehensive radiative analysis must be employed in order to obtain the appropriate proportions of the heat transfer modes.

If the convective heat transfer is eliminated by evacuating the enclosure, the heat transfer to the inner body will be by thermal radiation. But as the vacuum tests could be carried out at low power inputs only due to the high temperature limitation (120^0C) of some of the sealing materials, it was still necessary to be able to obtain comparable estimates at higher power inputs, from which a more accurate radiative component could be extrapolated.

In the course of this investigation therefore, a secondary means of verifying the heat transfers was necessarily adopted by numerically modelling the steady-state radiative heat transfers. Moreover, the proportion of radiation received by the inner body upper and lower walls, as well as its side walls was estimated separately.

6.3.1. Radiation Heat Transfer Modelling

In chapter 3, the enclosure walls were each divided into only three main zones, each parallel to the inner body walls. It was then possible to obtain the view factors by simply employing the "crossed-strings" method. The wall temperature profiles exhibited steep gradients, which must have introduced further errors in obtaining the radiative heat exchanges since for each zone, only one temperature was assumed for the entire length of the cavity. It was also noted that as the temperature of the enclosure increased, the proportion of the radiative heat transfers also increased so that when used to obtain the convective component of heat transfers, any errors in the radiative term would have been seriously magnified in the convective heat transfer coefficients.

6.3.1.1. Calculation of the radiation view factors

Therefore, the long enclosure walls and the end plates were divided into a total of 118 zones (see Fig. 6-5a), each zone characterised by the near uniformity of its temperature. Although this would enable a much more accurate analysis of the radiative heat received by the walls of the inner body, this would be at the expense of calculating several view factors.

The problem with view factors is not that they are inherently difficult to compute, but that the calculation time increases exponentially with the number of surfaces involved. In calculations involving j surfaces, there are j^2 view factors. When view factor algebra is employed, this only reduces it to j(j-1)/2 [82], or for a 60-node model, there will be a minimum of 1770 computations.

To facilitate obtaining view factors, several general purpose programs already exist - COIL [14], VIEW [83], GRAY[84], SHAPEFACTOR [85], FACET [86]. But the generation of inputs into these can be generally cumbersome. They also include several features not required including shadowing and transient effects, which makes them too large and too slow running for the present purposes. Additionally, many are not supported, so becoming proficient in their use requires considerable time.

The common numerical methods used are based on either the double area integration (AI), a variation of the double line or contour integration (LI), or the finite element analyses. When the surface is not approximated by the diffuse relationship, the Monte Carlo technique (essentially a form of statistical ray tracing technique), is employed such as in MONTE [87], but the accuracy may not be readily determined.

However, the view factors need only be calculated once for the same geometry. Some of the available analytically-derived formulae for planar geometries were found to contain some errors which made them unusable particularly when the inclination between the surfaces exceeded certain angles. Therefore, in the course of this investigation, the computer-intensive AI method was initially employed, until appropriate analytically-derived, error-free formulae were obtained. The main methods used to obtain the view factors, are briefly documented (see Appendix F).

Some zones see more than one side of the inner body, and although a total of 250 enclosure zones were required, symmetry permitted the calculation of only 29 view

factors as parallel or perpendicular planes from the enclosure to the inner body. However, for each heater a total of between 28 and 36 view factors were necessary (depending upon heater asymmetry) from any one of the heaters to three or four of the enclosure walls (for one reflection).

6.3.1.2. The Radiation Exchange Factor

The earlier calculations took advantage of the properties of the enclosure and inner body surfaces which were painted black, so that the cavity reflections could be ignored. However, the present rig was treated as heat exchange between grey surfaces, because of the relatively low emissivity of the enclosure. Hence, the respective reflectivities of the exchanging surfaces were incorporated in the formulation.

Using configuration 20 as an example, with the heaters located along the centre-line of each enclosure wall, it can be seen (see Fig.6-11) that the enclosure wall will receive direct radiation from the heater, a fraction of which is reflected depending upon the magnitude of the emissivity. The 9.5mm diameter cylindrical heater was located at only S_V=1.5d, and treated as a parallel flat strip 10mm wide. This gives an exact (3-D) view factor of 0.99669 for the heater to the enclosure wall, but only a view factor of 0.75556 for the heater to the corresponding inner body wall. So, for a power output of, say 550W, considering that each view factor refers to the heater hemisphere, or 50% of the 550W (275W), then a higher portion of the power output first goes directly to the backwall than to the inner body, and a large proportion of that (ρ=1-0.42), is then available for re-radiation within the enclosure.

Therefore, to obtain improved accuracy the principle of radiation exchange factor analysis was employed which accounts for the enclosure wall, the heating-elements, and the inner body not being thermally black. The analysis as employed in this context assumed that heat exchange occurred only between any two surfaces considered (e.g. heater-to-zone-to-heater, or zone-to-IB-to-zone) as moderated by the view factor. Consequently, other forms of multiple reflections, and shadowing (e.g. when the enclosure was partially obstructed by a heater) were ignored.

The incident radiation or irradiation from the cooler surface is then subtracted from the total radiation leaving the surface, the radiosity, to obtain the net radiative heat exchange between the two surfaces. The exchange factor incorporates the emissivities,

areas, and the view factor of the participating surfaces. The direct heat exchange between a heater, A and a zone, Z, can then be written as:

$$Q_{HA\text{-}Z} = \frac{\sigma\left(T_{HA}^{\,4} - T_Z^{\,4}\right)}{\frac{1-\epsilon_H}{\epsilon_H A_H} + \frac{1}{A_H F_{H\text{-}Z}} + \frac{1-\epsilon_Z}{\epsilon_Z A_Z}} \qquad (6\text{-}1)$$

where the denominator is the exchange factor XCHF, between the heater and the enclosure zone (H-Z). The use of the exchange factor can be seen to increase the overall radiative heat exchange. When the emissivity was taken as a constant (0.42 in this study) the increase was 103.3%. For the net exchange between the zone and an inner body wall, equation 6-1 becomes:

$$Q_{Z\text{-}IB} = \left(\frac{\sigma}{XCHF_{(Z\text{-}IB)}}\right) * \left(T_Z^{\,4} - T_{IB}^{\,4}\right) + \left(1-\varepsilon_Z\right)\left(\frac{\sigma}{XCHF_{(H\text{-}Z)}}\right) * \left(T_H^{\,4} - T_Z^{\,4}\right) \quad (6\text{-}2)$$

6.3.1.3. Computer radiative modelling

Equations (6-1 and 6-2) were used to calculate the heat exchanges from either the heater, or the enclosure walls to the inner body. The detailed calculations were carried out by developing several subroutines, which included subroutines to expand the area, view factor and temperature data into full arrays to take advantage of symmetry, and then to combine them into an input file.

The input data comprised:

1. Inner body constants (RYVC9jjj.DTA):
   Emissivity, temperature, area (of one wall).
2. Enclosure constant:
   Emissivity.
3. Heater constants:
   Emissivity, area.
4. Enclosure zonal parameters:
   Three arrays for temperature, TEMP(280), AREA(280), and view factors 'zone-to-inner body' VFZN(280).
5. The view factor of the heaters to the enclosure walls
   Dynamic input from array (VFHZ(120)) which was expanded from the individual 'heater-to-zone' view factor array.

The heat exchange between a heater and a zone, QXHZ, was calculated using a function subroutine FNQXHZ. The heat exchange between a zone and one inner body wall was calculated. For each of the 120 zones per heater considered (reflection from the MS end plates were ignored), the reflected heat exchange between a zone and the heater was calculated, and added to the emitted heat exchange.

The foregoing appeared in another function subroutine FNQZIB as:

$$FNQZIB(j) = \frac{\sigma}{XCHF_{Z\text{-}IB}}\left(T_j^4 - T_{IB}^4\right) + (1-\varepsilon) * FNQXHZ(j) \qquad (6.3)$$

A simple summation thereby results in the net heat exchange to the inner body. The irradiance received by each wall of the inner body could also be calculated separately. For centrally positioned heaters, only one view factor was possible to the inner body. When a heater can view more than one side of the inner body, two view factors would be used such as for C92 or C93 heaters. The direct heat exchange between the heaters and the inner body were then calculated and added to the summation for determining the total Q_{rad}.

The foregoing algorithm enables individual net heat gains by the inner body top, sidewalls, and base to be calculated simultaneously. The flowchart is listed in Table 6.1.

6.3.2. Experimentally derived Radiation.

If the oven enclosure is evacuated down to 10^{-3} torr or less, the gaseous conduction and convection processes are completely eliminated (see Fig.6-12), and heat exchange with the inner body takes place by thermal radiation only. However, the capacity of the existing vacuum pump and limitations of the rig meant that such complete evacuation of the $0.21m^3$ annular space and connecting piping could not be achieved.

The major operational constraints were the expected outgassing by the various sealing components and the dissolved gases and moisture from the metallic surfaces.

Table 6.1. FLOW CHART TUNNEL OVEN INCLUDING ONE REFLECTION

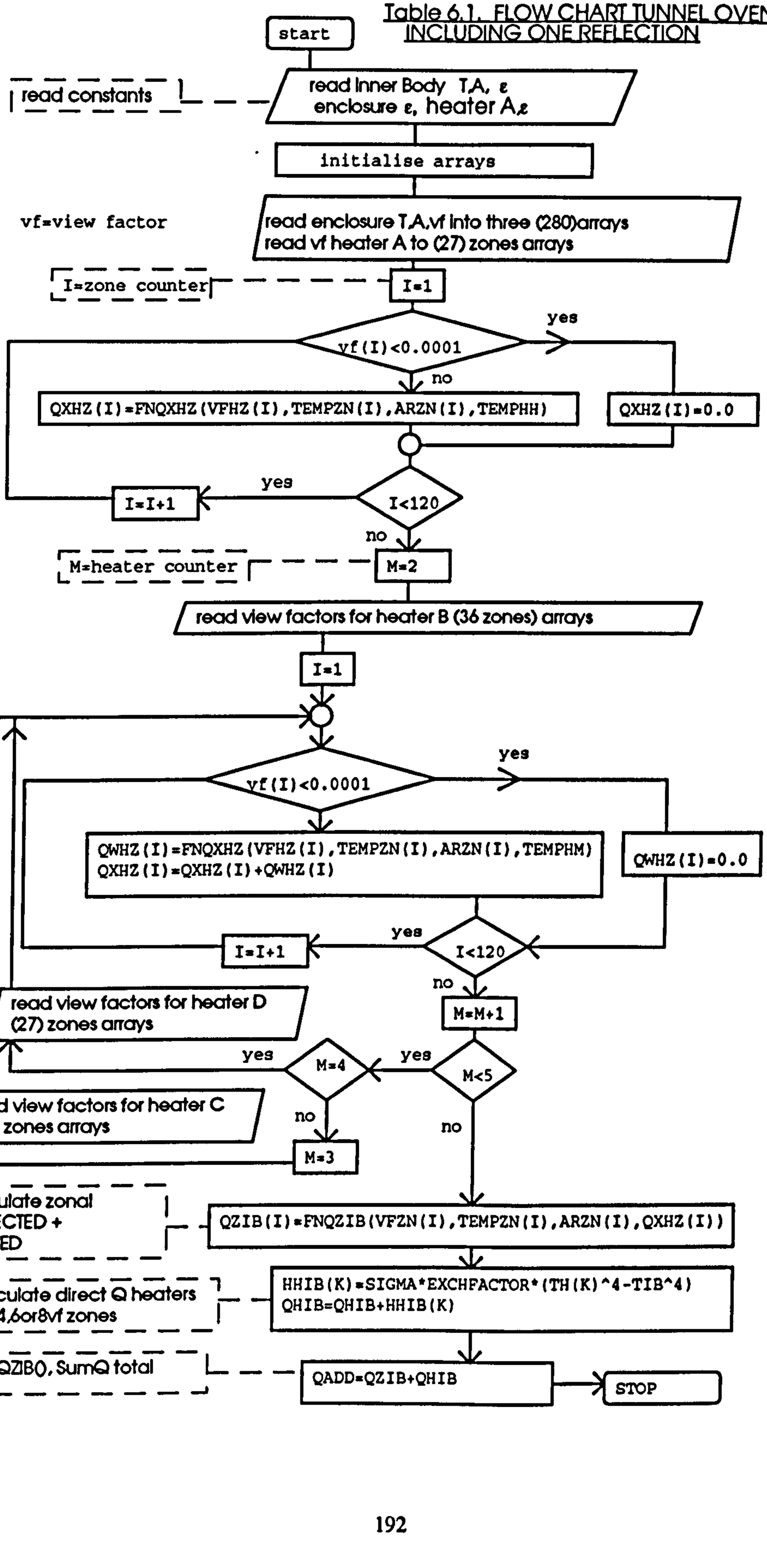

Between 10 and 10^{-2} torr, some heat transfer would now take place by gaseous conduction, in addition to that by thermal radiation. If the pressure were reduced to 10^{-3} torr the mean free path of the air molecules would be comparable to the minimum annular dimensions of the experimental rig (88mm), and the air molecules would collide more frequently with the walls than with each other. For the attained pressure of just over 4 torr, the mean free path was still only about 0.05mm [88]. As such, the molecules were still densely packed with respect to the dimensions of the experimental rig, so that heat transfer by gaseous conduction would still be by intermolecular collisions [89], i.e. there should be no temperature jump at the wall [6]. Consequently, there would be no marked difference in the behaviour of the gas when compared with that at atmospheric pressure. The range of thermal conductivity applicable is therefore $0.0262<k<0.0466$, $(300<T<600)$ [63].

6.3.3. Approximation of gaseous conduction:

The gaseous conduction was approximated by calculating separately the heat transfer by conduction from the enclosing walls to the inner body walls, and that from the heaters to the innerbody walls. Uniform wall and heater temperatures were assumed in order to obtain a single ΔT for each system. The use of shape factors [11] gave the required approximation for wall-to-IB conduction. Each heater was treated as a flat strip from which heat was conducted to an opposing flat strip. The total heat transfer by gaseous conduction (heater to inner body wall) averaged 3%.

6.3.4. Extraneous Losses

The main losses occurred through the insulation. The losses through the enclosure stand were negligible (<0.01%). The losses are graphically depicted (see Fig. 6-21b).

6.3.5. Extrapolation for Qrad

The trend of the radiative heat transfers obtained through the vacuum experiments were first noted in order to choose an appropriate type of curve fitting for onward extrapolation to a higher power input, where temperature limitation prohibited further experiments. Either a straight line (C92) or a quartic fit (C91 & C93) was used to simulate the trend. The convective heat transfers were then obtained by subtracting the derived radiative transfers and the extraneous losses from the total power input.

6.4. RESULTS AND DISCUSSION

6.4.1. Flow Visualisation

Flow visualisation was conducted at only a low power input, (300W) for each configuration and before overall steady state conditions could be attained, in order to prevent damage to the specially adapted perspex windows. The smoke patterns were recorded using a 35mm Praktica camera, and also video-taped via a CCD camera connected to a video recorder. Because of rapid dispersion of smoke for these highly convective transient flow conditions, recordings were also carried out schematically.

A large number of configurations were examined with a view to selecting some of these for detailed analyses. These were variants of the convective C9 as deduced from Chapter 3. Consequently, all the tested configurations were mounted at or below the middle horizontal centre-line. Four of the tests were grouped under C91, two under C92, and one as C93. In each case, two of the heating-elements could be traversed inwards, outwards, or vertically, while the other set (the pivotal heaters), would be stationary. The variants under C91 were named C91-j where j was the horizontal offset (in mm) of one of the lower heaters from the vertical wall (see Fig. 6-4a). Similarly for C92, the configurations were C92-15 and C92-45. 15mm was the minimum offset, so C91-15 and C92-15 were simply designated C91 and C92 respectively. C93 was designed so that the pivotal heater was the lower heater at x=135 (also x=215), so that the upper heater could be traversed as15<x<150 (also 335<x<200). In this case, the configuration with the upper heater at x=45 would have been designated C93-45. However, the rapid increase in the calculated view factors easily indicated that there would be a rapid rise in the radiative heat transfers and that the best convective configuration would be C93. Consequently, no variants of C93 have been presented (see Fig. 6-4d). Therefore, the first descriptions refer to C91, C92 and C93 (see Fig. 6-4(a-d)) with the other configurations (see Fig. 6-4(e-h)), subsequently presented.

All the observed flow patterns were actively buoyant (see Fig. 6-13, 6-14).

6.4.1.1. C91

The following descriptions refer to Fig. 6-13a. The rising lower heater plume, which entrained air from the inboard flows, passed close to the upper heater and its plume, squeezed between the heater and the enclosure wall, as depicted in the photograph (see

Fig. 6-15a). This action suggested that the upper heaters would be contributing significantly to convective heat transfers. More significantly, the sweeping movement of the cooler air would reduce the effect of the concentrated irradiance from the heater on the adjacent vertical wall, thus possibly reducing losses through insulation.

The upper heater received air from both the lower heater plume and a portion of the descending recirculation. The recirculation was seen to limit the convective contribution by the lower heater. The other portion of the recirculation which flowed closer to the inner body descended to fill the lower space and subsequently flowed slowly towards the lower heater. Because this lower flow did not follow the inner body base surface profile exactly, separating well before the centre-line, it was concluded that its contribution to convection was limited.

6.4.1.2. C92

The upper quadrant flow patterns were similar to those of C91, but the upper recirculation cells were more pronounced (see Fig. 6-13b and the photographs Fig. 6-15e,f). This resulted in the permanent deflection of the rising plumes towards the centre-line, which served to cause the upper flows to follow the inner body top surface profile more closely.

Although the lower heater was subsequently slightly offset (0.5d) from the upper heater centre-line in a temporary test, its rising plume was still deflected towards the enclosure wall, and did not immediately mix with the upper heater plume until well upstream. This is clearly depicted in Fig. 6-15f where a stable stream was seen to rise between the lower heater and the wall, and past the upper heater, apparently without any entrainment. The temporary offset was as a result of the deduction from the interferometric observations of two enclosed heaters in the proximity of a vertical wall (see Chapter 4, and Fig. 4-19). The flow at the base did not quite follow the inner body base profile, being more inclined to drift back towards the rising plume from the lower heaters as clearly depicted in the photograph, (see Fig. 6-15(e,f)), from where it would be entrained.

6.4.1.3. C93

Again the upper section was similar to those of C91 and C92. However, the lower air flows were more complicated due to the demand for air by the lower heaters (see Fig.

6-13c). The rising air plumes from the lower heaters vertically approached the inner body and split into two, the inboard flows forming local closed-loop recirculations. The outboard flows contacted the main recirculations which descended via the inner body sidewalls. The ensuing mixture oscillated and was seen to alternately contribute to the air supply to both heaters. These are shown in the accompanying photograph (see Fig. 6-15h). Essentially, only about half of the available convective flows from the lower heaters contributed to the main stream flows, the other half being apparently restricted to the respective inboard position of the inner body base. Because of the observed sluggishness of the inboard recirculating loops, it was concluded that its contribution to convection would be more pronounced in reducing local radiative heat concentration at the base of the inner body.

6.4.1.4. Other flow configurations

These tests refer to Fig. 6-14a-d.

Starting with C91-135, (see Fig. 6-14a) the lower heater behaved somewhat like that of C93, whereby inboard recirculating flows were created. The bulk of the complementary outboard flows joined the descending flows from the inner body to form the inflows to the upper heaters. This shows clearly in the photograph (see Fig. 6-15d). Inflows to the lower heaters appeared limited, and because of rapid smoke dispersion, it can only be conjectured that limited outboard recirculating flows existed at the lower quadrants. Although, the base of the inner body was seen to benefit from more convection than C91, it is obvious that it would also be subjected to increased radiation because of its proximity to the base-mounted heaters.

Next, to be considered is C91-90 (see Fig. 6-14b and Fig. 6-15c), where the lower heaters were virtually in line with the vertical walls of the inner body. The inboard recirculating flows were larger and descended right to the base, and can be seen to pass much closer to the lower heaters. When considered in conjunction with the weak recirculating flow at the lower quadrant, convective heat extraction from the lower heaters was actually seen to improve.

The third variant C91-45, appeared to have the counter-rotating recirculating flows at the lower heater opposing each other, which somehow seemed to prevent copious flows around the lower part of the heater (see Fig. 6-14c). But the rising plume was

seen to oscillate and swing thus imposing a fanning action as it approached the upper heater. A clear space below the inner body (see Fig. 6-15b) indicated no convection.

It appears therefore that if the lower heaters were to be traversed horizontally from the vertical wall, convective flows generated would first decrease (to a minimum around S_h=45), and then increase. There may then be an optimum offsetting along the path. However, the configuration selected for further experimentation was C91.

The other test carried out was for C92-90 where the lower heaters were virtually in line with the inner body vertical walls as in C91-90. The first half of the rising flow from the lower heater was seen to create inboard flows (see Fig. 6-14d and the photograph, Fig. 6-15g), which exchanged heat with the base of the inner body, while the other half was seen to mix and oscillate with the descending flow via the inner body. This variant was seen to create more convection to the inner body base, but the extent to which its flows interfered with the upper heater convection of C92 could not be determined.

Because of transient effects, the results from the flow visualisation could only be regarded as a rough guide as to the possible enhancement or otherwise of convection. Overall, the main convective activity appeared to be centred around the upper wall-mounted heaters, which created localised flows in addition to receiving buoyant flows from the lower heaters. Based on the flow visualisation, C91, C92 and C93 were subsequently selected for detailed thermal analyses.

6.4.2. Wall Temperature Profiles

6.4.2.1.Temperature Profile of the Inner Body

Recorded temperature variations along the length of the inner body were small (the inner body was virtually isothermal). No significant differences were recorded in the temperature profiles of the inner body irrespective of the heating-element configurations (see Fig. 6-15) in spite of the larger thermal mass.

6.4.2.2. Enclosure temperature profile

The distribution of the wall temperatures was initially examined in the preliminary experiments (C20), and subsequently used to determine the optimal positions of the

thermocouples and the zonal areas for calculating the radiative heat transfers. The thermocouples were fixed to the inside walls by reflective aluminium tape, in order to reduce radiative heating of the thermo-junctions. This method was preferred to using a cement-based compound, which because of excessive protrusion would cause the thermocouple to be unduly influenced by convective flows and consequently indicate lower wall temperatures.

The wall temperature profiles varied according to the configuration employed and were a reflection of the proximity of each heating-element to the walls.

The crown temperature profile for C20 (see Fig. 6-16a) showed a significant portion where the temperature was uniform. From the sidewall temperature profile of C92, the lower portion ($y<100$mm) recorded higher temperatures than the upper section ($y>250$mm) (see Fig.6-16d). This indicated that the base of the inner body will receive significantly higher radiative heat transfers from the sidewalls than the top. However, although the heating-elements were generally in the lower portion of the enclosure, the variations were not as pronounced as earlier observed (see Chapter 3). It can also be seen from a consideration of the temperature profiles for C20 and C91 (see Fig. 6-16b,c) that the z-direction isothermality of the central portion of the enclosure did not depend upon the heating arrangements.

It was also noted that the crown (see Fig. 6-16a), and the base (see Fig. 6-16e) showed a slightly higher range of isothermality within the middle portion of the enclosure ($350<z<1350$mm) than the sidewalls ($550<z<1150$mm), (see Fig. 6-16d). This can be partly attributed to the reduced view factors from the heaters to the enclosure ends, which reduced the radiative heat transfers. As the power input was increased, with a corresponding increase in the heating-element temperature, a larger temperature difference existed between the interior of the enclosure and the ends (see Fig. 6-16e). Additionally, the proportion of convection to radiation reduced, thereby reducing the attenuating effect of air flows at the higher power input. Any local 3-D recirculation at the ends would also be reduced, thereby accentuating the temperature difference between the central areas between the heaters and the enclosure ends.

However, the surface temperatures can be seen to be sufficiently uniform in the range $500<z<1200$mm, so that any annular air space data within these limits can be confidently treated as two-dimensional.

6.4.3. Air Space Temperatures

The three convective configurations (C91, C92 and C93) have been studied in some detail, with data being recorded across at least three positions parallel to the respective walls (horizontal or vertical) of the annulus. This allowed a comprehensive analysis of each set of data with respect to air temperature variations across the spans.

6.4.3.1. Vertical air space temperature profiles (y-axis)

The vertical air space is restricted to the gap provided between the inner body and the enclosure, providing an annular width for data acquisition of 87.5mm minimum. The requirement for increased data points was necessitated by the complicated air flows associated with this type of enclosure with inner body configurations (C9, Chapter 3), because the central gaps accommodate both the rising buoyant air and the returning air at different temperatures. The process of obtaining more data points was achieved by rotating the thermocouple rack in the horizontal (x) direction and taking readings at four spatial intervals, at zero mm., (i.e. nearest to the vertical enclosure wall), then at 30, 55, and 85mm. By traversing in the vertical direction (at only 3 discrete, calibrated positions on the bracket), it was possible to obtain eleven vertical data ranges (at y=25, 55, 85, 115, 145, 175, 205, 235, 265, 295, and 325mm).

The vertical annular air temperature profiles for all the configurations at 2200W and at discrete horizontal distances are shown in Figs. 6-17(a-d). The flatness of all the temperature profiles (i.e. the small temperature differences between the upper and lower enclosure spaces) confirm that all the configurations studied achieved good convection. Therefore, it was logical to conclude that there was no stratification across all the power input ranges. C93 profiles were least steep, and the highest average profile reduction was shown by C92. The region adjacent to the inner body showed the steepest temperature gradient indicating the zone with the highest convective heat transfers.

Nearest the inner body at x=85mm and within the vertical range $85<y<265$ (see Fig. 6-17d), the rate of convective heat transfers should be indicated by the steepness of the curves, assuming that the air flow was parallel to the inner body vertical sidewall, and the radiative heat flux as recorded by the thermo-junctions was minimal. For instance, if recirculating currents exist somewhere along that inner body wall, then the flatness

or steepness of the curves will not necessarily indicate the rate of convective heat dissipation.

For this distance (nearest the inner body, x=85mm), C91 and C92 exhibited the steepest drop in the temperature profiles. But the mean temperatures of C92 was also the highest, which suggests that its convective heat transfers to the sidewalls would be the most efficient for this zone. C93 was virtually flat, and was actually seen to be slightly increased around y=85mm, probably due to the rising flow from the lower heater as observed from the flow visualisation (see Fig. 6-13c). Close to the enclosure walls (x≅0mm), the air temperatures were seen to be quite similar, except for C92, which recorded significantly higher temperatures because of the closely spaced heaters. At the core of the annulus as indicated by the individual configurations (see Fig. 6-17e-g), the profiles were virtually flat but dropped sharply near the inner body (x=85). This was most marked for C92. At the lower power input (see Fig. 6-17h-j) the profiles of C92 (Fig. 6-17i) were remarkably similar to that produced at the higher power input (see Fig. 6-17f). However, some discrepancy noted for C91 and C93 indicate that the flow path would be significantly altered as the power input was increased.

6.4.3.2. Upper air space temperature profiles (x-axis)

Data were recorded for the span of the enclosure 0<x<350mm, and at three heights, y = 325, 295, and 265mm, the latter being parallel and nearest to the top of the inner body (see Figs. 6-18(a-c)).

At y=265mm, the portion of the data nearest to the inner body was within 85<x<265mm. C91 had the average warmest temperatures in this zone, with C93 the lowest. This is as expected because C91 had the most elevated heating-element. All configurations showed a dip in the temperature profiles at the centre-line which is also as expected, being exposed to the least direct influence of the heating-elements in this zone. The lowest average temperature was consistently produced by C93. Similar results were observed for y=295, where again, the lowest average temperature was produced by C93. At the uppermost level (y=325), C93 consistently achieved the least temperatures at all data points. However the most useful profile is considered to be the section nearest to the inner body (y=265). Here, steep gradients were provided by both C91 and C92 indicating higher convective heat transfers to the inner body top.

At the lower power inputs (see Figs. 6-18d-f), the profiles were somewhat similar (to those at 2200W) except nearest the inner body where the drop in C92 profile was less noticeable, whereas for C91 there was a pronounced reduction. The discrepancy in the temperature profiles of C92 is indicative of altered flow patterns at increased power inputs. At the lower power input, C93 again appeared to be the least effective with respect to convective heat transfers.

The patterns shown in Figs. 6-18(g-i) 2200W, and 6-18(j-l) 530W, are for each configuration's temperature profiles across the upper annular space at different heights. The profiles clearly demonstrate here again that heat is convected mainly in the region of the wall boundaries, and virtually no transfers occur far from the inner body (at the core) as indicated by the absence of gradients (85<y<265). At 530W, C93 again appears to be the least effective.

6.4.3.3. Lower air space temperature profiles (x-axis)

Data were recorded across the span of the enclosure similar to that for the upper annular space, but for y=85mm, 55mm, and 25mm (see Figs. 6-19a-c). The data recorded at y=85mm and for 85mm<x<265mm represented the measurements nearest to the inner body. The presence of heaters in this zone was mirrored in the output of the thermo-junctions. C92 recorded the highest temperatures towards the extreme enclosure walls while C93 showed two peaks below the inner body approximately corresponding to the location of the lower heaters. The mean temperature of C93 was also the highest whereas that of C91 was lowest. Coupled with its steepness, C93 can be assumed to be the most effective in convective heat dissipation in this region. The profiles are also shown individually for each configuration at different elevations (see Fig. 6-19g-i). The similarity of the profiles at the lower power input (see Fig. 6-19j-l) suggest that there would be no significant alteration in flow patterns as the power input was altered.

6.4.4. Steepness of temperature profiles and flow tenacity around the inner body

The above analyses were summarised by adopting a transitional technique which translated the analysis of the individual configurations into something more quantitative by assigning arbitrarily simple units, which visually mirror the convective effectiveness of each heating arrangement.

For instance, the steepness of the temperature profile along the inner body suggests the rate at which the air flows lose heat, or in other words the rate at which convective heat is transferred to the inner body. So the largest unit, 3 would be assigned to the configuration which showed the steepest profile, while a value of one would be assigned to that with the flattest profile.

Similarly, when air flows appeared to be wrapped around the inner body as observed from the flow visualisation, high values would be assigned.

Table 6.2. Simple thermal profile weighting:

Configuration	Upper inner body y=265	Vertical 85<y<265	Lower inner body y=85	
	steepness, temperature weighting			Convective value
C91	2,3	3,1	2,1	12
C92	3,2	2,3	1,2	13
C93	1,1	1,2	3,3	11

Table 6.3. Flow visualisation weighting

Configuration	Upper inner body y=265	Vertical 85<y<265	Lower inner body y=85	
	visual air speed, and,proximity of air flow to inner body (weighting)			Flow value
C91	2,3	3,1	2,1	12
C92	3,2	2,3	1,2	13
C93	1,1	1,2	3,3	11

Adding gives C91=24, C92=26, and C93=22.

These initial analyses therefore suggest that the convective heat transfers to the inner body would be in the descending order of C92, C91, and C93. This simple approach in

analysis, though largely subjective through the flow speed analyses, can reinforce any assertions deduced in the analyses. However, further limitations as to the adoption of this method would be the difficulty in ascertaining the positive or negative contribution of the complicated vortices to the heat transfers.

6.4.5 Discussion of the experimental techniques

6.4.5.1. Evacuation

The atmospheric tests were first performed up to the required power input of 2200W. The rig was then cooled, and reassembled with the appropriate jointings, leadthroughs and seals. Power was then supplied until steady state conditions were attained, the various heater and wall temperature data compared with that of the previous runs, and then evacuation applied. Reduction from atmospheric pressure was initially very time consuming.

However, after the initial purge period which lasted six hours, the rig subsequently responded very rapidly to evacuation, and reduction to 300 torr from 760 torr was repeatedly achieved very rapidly (< 55s from 755torr). For C92 only and at 520W, it was kept constant at this pressure (i.e. 300 torr) while the rates of increase in the heater temperatures were noted. Subsequent reduction to 25 torr suggested that most of the convective activity had already ceased by 300 torr. This is similar to observations made by Brooks [58], where interferometric tests were performed at 317, 92, and 10 torr on an enclosed cavity. It was found that limited convection occurred at 317 torr, but had virtually ceased by 92 torr; at 10 torr, no convection was indicated by the interferogram.

It can be recommended therefore, that for particularly difficult evacuation tests, data gathered at as high as 50 torr could be regarded as being independent of convective flows, although gaseous conduction heat transfers would still need to be considered.

6.4.5.2. Pressure measurements

Because the operating pressures were above 3 torr, the Pirani gauge was found not to be necessary, except at the commissioning (purging) stage when the pressures dropped below 0.5 torr.

6.4.5.3. Changes in the enclosure surface temperature profiles

With no hot air movements under evacuation, there would be no convective heat transfers to the enclosure crown. The ensuing changes to the temperature profiles of the crown are shown (see Fig. 6-20a), where the crown temperatures were lower under evacuation, than when atmospheric tests were carried out. This clearly demonstrates that for base-mounted or lower sidewall-mounted ovens, the main heat transfers to the upper cavity is by convection.

To accomplish this, the air must first of all be heated; then it must achieve sufficient buoyancy to reach the cooler crown, where a considerable proportion of the heat would be lost. The descending air is consequently cooler, thereby keeping the heater at a lower temperature than would otherwise be for radiative configurations. Also, the initial contribution of convection to the heat transfers to the inner body is reduced because of this initial heat losses to the crown before the air descends to the inner body.

This experimental evidence permits the explanation of why more prolonged preheat would always be necessary for convective configurations.

At the middle of the enclosure sidewall (y=185mm), the temperature profile along the length of the enclosure (z-axis) was also lower (see Fig. 6-20b). But at the lower portion of the sidewall (y=15mm) in the vicinity of the heating-elements, the z-axis temperature profile was higher under evacuation than when under atmospheric tests (see Fig. 6-20c). As there was no cooler air movement to sweep over the enclosure surface, the central portion (z~850mm) recorded higher temperatures after receiving direct radiation from the heaters, and reduced temperatures at the ends (z<200mm), because of the lower view factors.

It can be seen quite clearly (see Fig. 6-20d) that convection reduced the temperature profile gradient along the vertical wall, the profile being relatively flat, when compared with the evacuated temperature profile. A uniform wall temperature would radiate more uniformly, that is, there would be less concentrated irradiance to an inner object.

This again demonstrates that convection redistributes heat energy, thereby improving temperature uniformity of heated objects.

For the limited range of power input and temperatures studied, it was found that the overall arithmetic mean enclosure surface temperatures under evacuation were nearly equal to those for atmospheric studies. This is because for enclosure areas in close proximity to the heaters, the wall temperatures were significantly higher under atmospheric pressure, but for zones far from the heaters, the mean temperatures were lower under evacuation (see Fig. 6-20(a-d)), and much more so for the upper horizontal surface. The percentage difference between the mean wall temperatures was only 6.5% so that the heat losses via the insulation under atmospheric tests were utilised with only minimal numerical alterations.

6.4.5.4. Inner body temperature variation:

Only a small adjustment was made to the thermocirculator temperature controller in order to keep the external inner body surface at the same temperature as observed in the atmospheric tests. The anticipated changes in the inner body temperature difference between the inlet and outlet streams did not materialise because the thermo-junctions were not sensitive enough to indicate any subtle changes which might have occurred. It was concluded that the thermocirculator compensated for any such changes by reduced cycling. Therefore, it was assumed that the heat transfers to the inner body under evacuation were equal to those under atmospheric pressure.

6.4.5.5. The various problems associated with this technique are:

a) The initial pumping down period was lengthy, which was then supplemented by a further period to attain steady-state conditions.

b) Achievement of sustained pressures of less than 10^{-1} torr was time consuming and, for this assembled rig, ultimately impracticable.

c) The temperature profiles of the enclosure walls would alter, which in turn, would alter the radiative heat transfers to the inner body, and also the heat losses through insulation and the inner body. However, if the boundary-conditions remain as at atmospheric tests, the convection component of the heat transfers is simply the reduction in the heat input obtained under vacuum conditions. Since the radiative computations are not required to derive the convective component of the heat transfers, this method can easily be seen to be subject to much less uncertainty, and consequently more accurate, even though the radiation heat transfer profile may alter.

d) The enclosure, the inner body and the other inner components must be designed to withstand vacuum ($-1x10^5 Nm^{-2}$). This required a structurally robust apparatus constructed of materials with different thermal properties and thickness from the usual oven materials of mild steel or aluminium; the cost in resources must therefore include design expertise, raw materials, fabrication techniques, special data acquisition and control equipment and heating-elements.

e) Expensive seals were required to achieve evacuation in a reasonably short period of time.

f) To obtain the convective component of the heat transfers, the heater temperatures at evacuation were maintained at the same level as those obtained under atmospheric pressures; the intricate iterative procedure for this was time consuming (see section 6.2.5.3), because the enclosure surface temperatures were also changing and re-radiating towards the heaters, which simultaneously affected the heater temperatures again and the vacuum level, thereby making the iteration procedure complicated; a precision heating-element temperature control circuit would improve the operational procedure substantially.

g) Extrapolation of the vacuum data was required in order to obtain the results at elevated temperatures beyond the conditions where the components exceeded their operational limits.

6.4.6. Difference between Modelled and Vacuum Qrad

An underestimation of the radiative heat transfers was anticipated not only because only one heater reflection was computed, but because no reflections from the end plates were incorporated due to their high emissivity. If the percentage difference between the modelled and that obtained by evacuation was linear, then one could possibly suspect that the wrong value of a constant, such as the emissivity (in the heat exchange factor) was responsible for the difference.

The error initially calculated was very large (48%) when the evacuated data was used as the basis. Therefore, a rescrutiny of the experimental data was undertaken to ascertain the source of discrepancy.

The AI method of obtaining view factors normally overestimates by greater than 2% for parallel planes (>8% for perpendicular planes) [90], depending upon the fineness of the interval. An inherently optimal step size of 2 was utilised in the AI algorithm which gave a mean error of 1.8%. However, as analytically derived formulae were employed, the view factors were treated as being subject only to very low errors. Using the reciprocity relationship ($A_1F_{12}=A_2F_{21}$), the error in the total view factors (from all the enclosure surfaces to all the inner body surfaces) was obtained from:

$$F_{IB-enclosure} = \frac{1}{A_{(IB)}} \sum_{j=1}^{n} \left(F_{j-IB} A_j \right)_{(enclosure)} \qquad (6\text{-}3)$$

which should have been equal to unity because the inner body could not see itself. The final error obtained in this way was only 1.2% when compared with unity. This was also treated as a linear constant. A comparison of the analytically-derived formula with the AI method showed that the slight negative error originated from the view factors obtained from the perpendicular planes. The error was traced to the manner in which zero or negative logarithmic solutions of the analytically derived view factor formulae were numerically trapped as zeros.

The variation of emissivity of the SS enclosure with temperature ($0.65<\varepsilon<0.67$, $673K<T<873K$ [91]) was considered to be too low to be a major source of computational error. The measured emissivity utilised for the sandblasted enclosure was 0.42 and was similarly assumed not to vary with increased temperature. Even then, a variation of the emissivity was verified to cause only an approximately linear variation in the exchange factor. Therefore, a non-linear variable, such as the temperature, which was an independent quartic variable, would be suspected.

Noting that under evacuation, the power input to the heating-elements was reduced to achieve the original temperature readings of the heater thermo-junctions, heat transfers would then take place by radiation and gaseous conduction only. If the heat losses via the insulation were identical to that lost under atmospheric pressure, then the difference between the heat input under evacuation and that under atmospheric pressure would be attributed to heat transfer by convection. The only variation here would be to obtain and add the heat transfer under gaseous conduction (subsequently found to be less than 3%) to obtain the true value of Q_{conv}. However, a slight reduction (~6.5%) in the heat losses through the insulation was detected when a numerical, mean temperature averaging technique was undertaken thus:

$$T_2 = \frac{1}{A_{enclosure}} \sum_{j=1}^{n} (T_j A_j) \qquad (6\text{-}4)$$

where j is the zone number. This reduction in Q_{insul} shows that if the losses through the insulant was assumed to be negligible, then the value of Q_{rad} obtained would be considerably lower. This principally accounted for the discrepancy between the modelled Q_{rad}, and that obtained via evacuation. Unfortunately, this does not altogether eliminate the dependency of Qrad on thermometric accuracy, particularly if extrapolation is necessary. However, it is to be noted that the bulk of the convective component of the heat transfers is still the difference between the atmospheric and evacuated Q_{rad} and infinitely more reliable. The heat balance now becomes:

$$Qrad_{(evacuation)} = \{Qin - Qinsulation - Qgaseous\ conduction\}_{(evacuation)} \qquad (6.5)$$

$$Qconv = Qin_{(atmospheric)} - Qin_{(evacuation)} + Qgaseous\ conduction \qquad (6.6)$$

So long as the losses via the insulation and the power input could be accurately obtained, this method would still give a very reliable result. The maximum error obtained was then well within the span of the uncertainty for the lower temperature range. Another advantage of this technique is that the evacuated data reproducibility is guaranteed to virtual-zero percent variance, depending upon the consistency of the external thermal boundary-conditions. This is because, the effect of the variability of environmental pressure on natural convection heat transfers is eliminated.

For extrapolation, a historical trend in Q_{conv} was not available. Therefore, it was not feasible to obtain an acceptable extrapolation for the range where inherent thermal limitations in equipment prevented the acquisition of experimental data. The alternative method adopted was to extrapolate the heat loss via the insulation using a least squares linear fit, and that of the radiative heat transfer under evacuation extrapolated using a power fit. The type of curve fitting chosen resulted from the main variable in each equation, which was the temperature. Although the thermal conductivity of the insulant increased slightly in the range tested, the error introduced by using a linear fit for the losses via the insulation was considered negligible. This more accurate analysis revealed the initial source of error, as the mean wall temperature which was some 6.5% lower under evacuation.

The heat transfer by radiation is graphically shown in Fig. 6-21a, and losses via the insulation in Fig. 6-21b. From the data (see Tables 6.4 and 6.5), and as subsequently graphically indicated, (see Figs. 6-21c), the computations overestimated the radiative

heat transfers at the lower power inputs by up to 14%. However, as the power input was increased, the error rapidly diminished to become a slight underestimation beyond a power input of 960W. This was partly attributed to the extrapolation technique employed which was considered to be subjective. However, the trend of the experimental data as well as known analytical variables constrained the choice of regression.

To trace other sources of error, it was established, by numerically varying the emissivity ($0.3<\varepsilon<0.7$) for a constant surface area and temperature, that a variation of emissivity would only cause an approximately linear variation in the exchange factor, and a corresponding linear variation in the calculated radiation heat exchange. Therefore, it was concluded that, for the atmospheric tests, the temperature indications would be one source of error. One recommendation would be to utilise a larger number of zones in order to obtain more exact surface temperatures under atmospheric pressure, and then validating with evacuation.

To obtain the actual values from the tabulated data, the percentage differences were subsequently applied to the values calculated for the inner body surfaces. C20, which was tested essentially to validate the integrity of the apparatus, was not included in the convective vacuum studies (see Table 6.5). The data in Table 6.5 were taken from the highest power input, which is similar to actual oven conditions at higher temperatures. The data here were very close to that obtained under atmospheric conditions, which also validated the radiation model but only at these higher power inputs.

Table 6.4. Modelled (Atmospheric) Qrad at 2200W (units in Watts)

configuration	C20	C91	C92	C93
heater-to-zone	711	956	1164	1091
enclosure zone to inner body (radiosity)	1127	840.4	845	850
heaters, direct to inner body	512	369	282	384
QRAD to inner body top	459	216	195	173
QRAD to inner body side(x2)	(713)	(724)	(628)	(552)
QRAD to inner body base	295	234	276	476
Sum QRAD to inner body	1638	1210	1127	1234
QLOSS (insulation)	231	194	184	203
QCONV	331	796	889	763

Table 6.5. Qrad by Evacuation (at 2200W)

configuration	C91	C92	C93
heater-to-zone	955.4	1164	1087
enclosure zone to inner body	864	845	847
heaters, direct to inner body	369	282	383
QRAD to inner body top	222	189	172
QRAD to inner body side(x2)	(744)	(604)	(550)
QRAD to inner body base	240	267	474
Sum QRAD to inner body	1209	1126	1251
QLOSS (insulation)	186	196	182
QCONV	805	879	767

6.4.7. Inner body radiative heat distributions

Only the heat distribution by radiation to the various walls of the inner body could be assessed with respect to the heat input, since the convective heat distribution to the individual inner body walls and its attenuating effect could not be separately determined.

The ratios of the radiative heat received between the base and that received by the top of the inner body were virtually constant throughout the power input range (see Fig. 6-21d). The heaters were all mounted at the lower portion of the enclosure. Therefore, it was expected that the base of the inner body would receive more radiation than the top. This was certainly true for C93 and, to some extent C92. But for C91, the top received the same amount as the base giving a ratio of about unity (see Fig.6-21d). This was attributed to the enclosure crown temperatures, which gained sufficient heat from both the mid-mounted heaters and the convective flow thereby offsetting the absence of a crown-mounted heater.

The sidewalls were also subjected to considerable radiative heat transfers, being highest for C91. The respective ratios to the inner body sidewalls were also uniformly maintained throughout the power input range (see Fig.6-21d).

6.4.8. Heat transfer analyses of the configurations

The trends of the heat transfers are depicted in Figs. 6-22 to 6-25. Ra for all the configurations were decreased as the power input increased. The view factors of the heating configuration of C92 was the lowest and it was expected that it would also produce the lowest radiative heat transfers. Since the heater temperatures were also lower due to the improved air flows as observed in the flow visualisation (see Fig. 6-13), its calculated radiative heat transfers were consequently the lowest. This is clearly depicted in Fig. 6-25b where the radiative heat transfer trends for C91 and C93 were also shown to be virtually identical.

The domination of the convective heat transfers for C92 was also shown to extend up to an input of 1520W before radiation became the major source of heat transfers to the

inner body (see Fig. 6-23b). For C91 and C93 however, radiation was dominant at an earlier stage (960W) of the power input (see Fig. 6-22b and 6-24d).

6.5. DISCUSSION

Because of the high thermal conductivity of the inner body, it was impossible to detect the local influence of the convective flows on the inner body temperatures.

Table 6.6. Correlations obtained:

Configuration	Correlation	Limits
C91	$Nu=0.287\ Ra^{0.251}$	$8.5x10^7<Ra<14x10^7$
C92	$Nu=7.109\ Ra^{0.0743}$	$17.5x10^7<Ra<42x10^7$
C93	$Nu=1.145\ Ra^{0.174}$	$8.5x10^7<Ra<10.2x10^7$

	$Nu=c_1Ra+c_2$			$\frac{Qconv}{Qin}=(c_4)(q_{in})^{c5}$			$Q_{conv}=c_6Ln(Q_{in})+c_7$		
	c_1	c_2	R^2	c_4	c_5	R^2	c_6	c_7	R^2
C91	7E-08	+22.4		3.7	-0.21	0.99	376	-2115	0.98
C92	8E-09	27.8	0.91	3.13	-0.19	0.95	404	-2272	0.98
C93	5E-08	23		4.76	-0.24	0.95	355	-1980	0.99

The correlations obtained from the previous investigation of C9 (see chapter 3) using a least squares linear fit (Nu = -2E-05Ra +0.68) was seen to be numerically different from those of the present investigations (see Table 6.6). Aside from the differences in enclosure depth and the opaque end plates, which improved the acceptability of C92 data as 2-D, the inner body dimensions utilised for C9 was not wholly symmetrical, being rectangular within a square enclosure. The inner body surface area of C92 was also larger and cooler, thus accounting for the much lower air space temperatures. The smaller annular gap as well as the aforementioned differences ensure that the correlations would significantly differ, as previously observed, from enclosure convection heat transfer characteristics.

The correlation obtained for C91 surprisingly conformed to the trend of universal correlations. This may be due to the flow patterns which was the most symmetrical for the upper and lower portion of the cavity, as well as the improved change in wall temperature with elevation.

It was expected that C91 would have a comparative value of convection to C92. However, as the upper heating-elements had large view factors (with respect to the inner body sidewalls), C91 also produced higher direct radiation. Being an enclosed system, the convective component was consequently lower. The same argument applies to C93 because of the proximity of its lower heating-elements to the base of the inner body. A visual examination could then be used to predict the convective effectiveness of heating-element arrangements with respect to the radiation view factors.

The use of standard Nusselt numbers and Rayleigh numbers may lead to quite misleading interpretations as indicated by the range of correlations. The convective flows were not evenly distributed within the enclosure because of pronounced upper cavity vortices, whereas correlations generally tend to represent uniform heat transfer distributions.

Referring to Fig. 6-25b, it can be seen quite clearly that the trend of the convective to radiative heat ratios is instantly indicative of the heat transfer characteristics of the system, with C92 demonstrating significant convective advantages. Although C91 indicated a universal correlation when compared with the other two configurations, the limits imposed should be rigorously observed if these were to be incorporated into design guidelines.

At the oven air temperatures (≈130^{o}C), 40% of the heat transfers for C92 was by natural convection, while it was 36.6% and 34.9% for C91 and C93 respectively.

Fig. 6-1. Layout and instrumentation

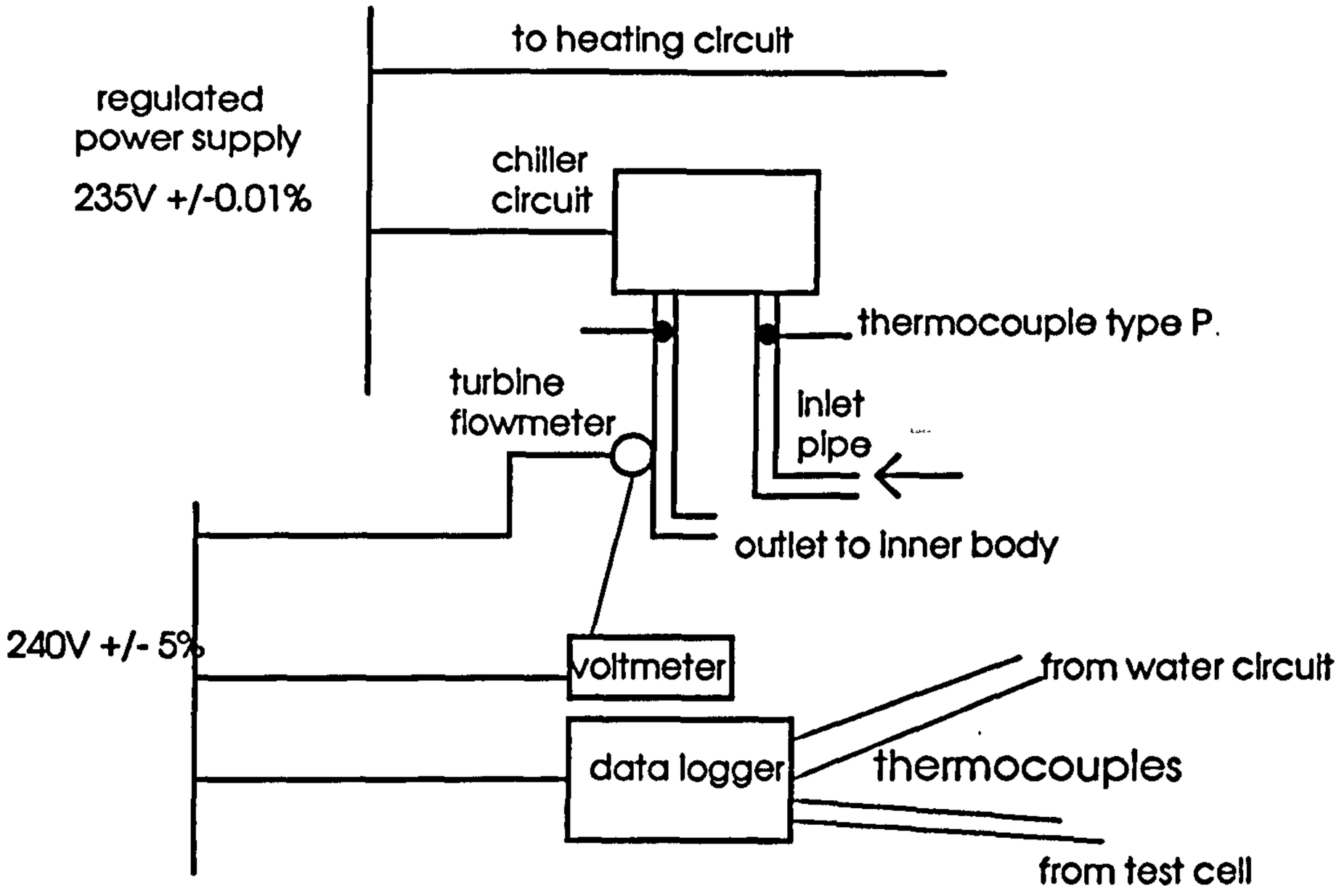

Fig. 6-2. Heating circuit power supply

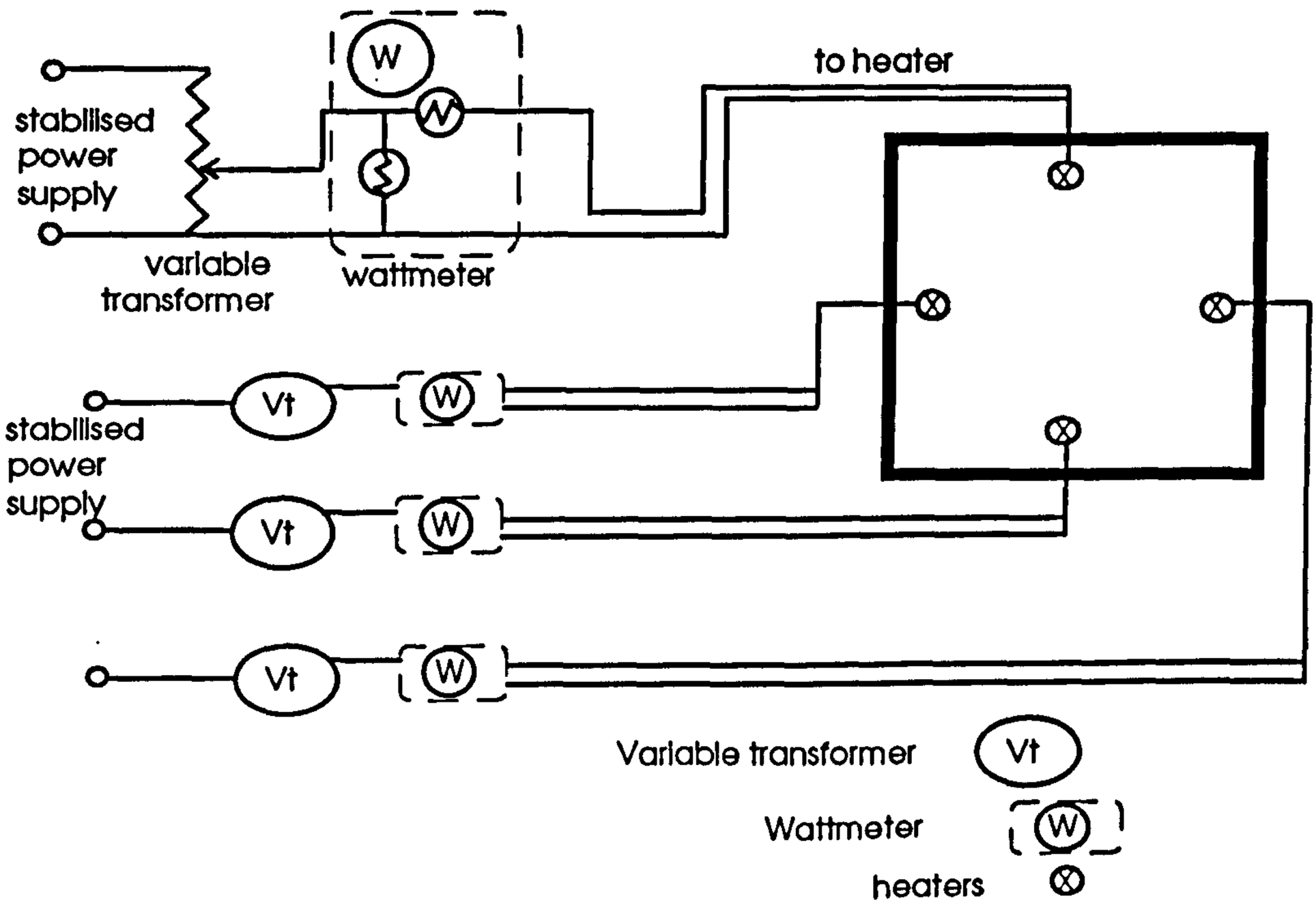

Fig. 6-3 The chiller circuit

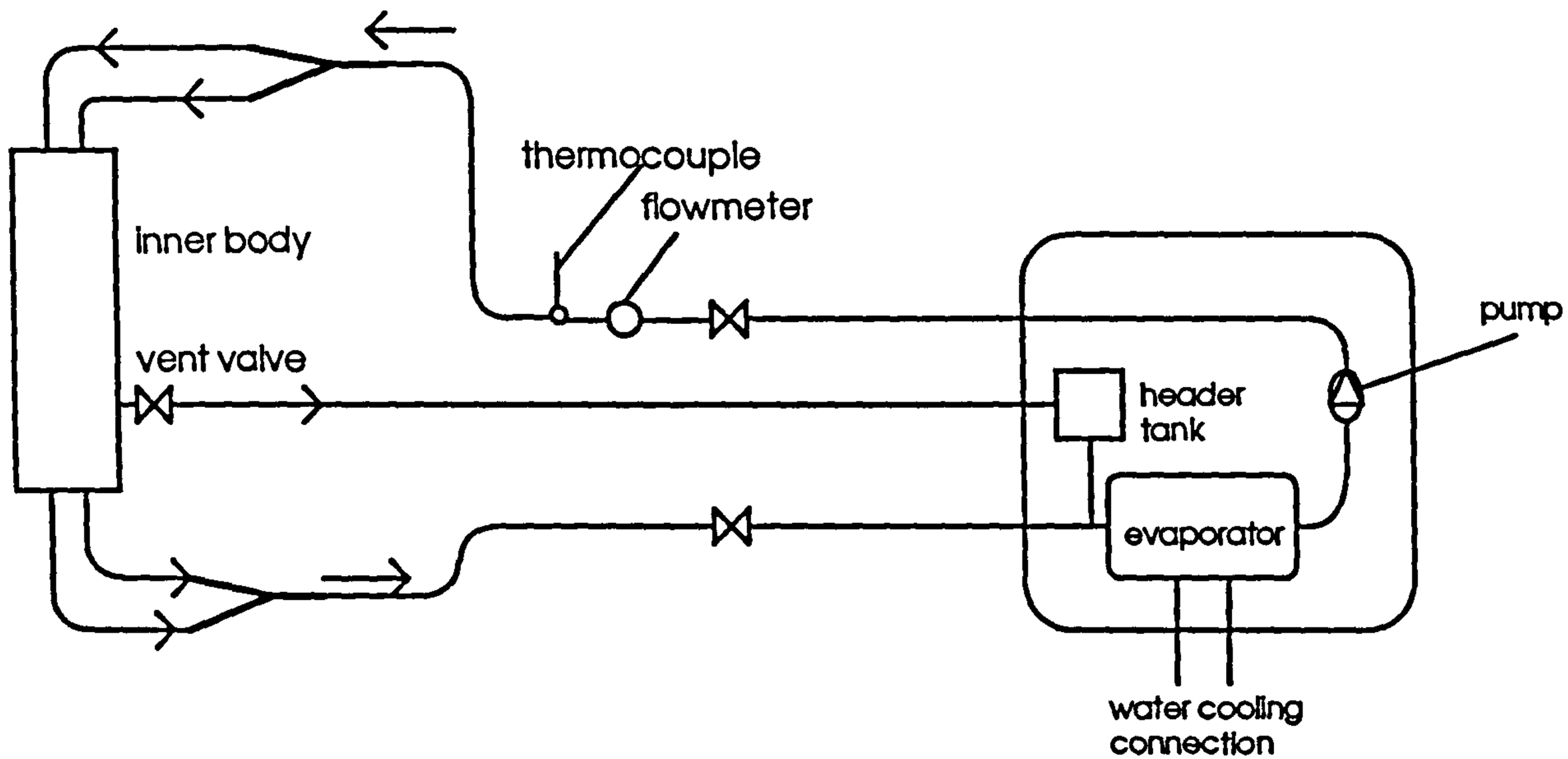

Fig. 6-4(a-d) Heater Configurations

(a) C20

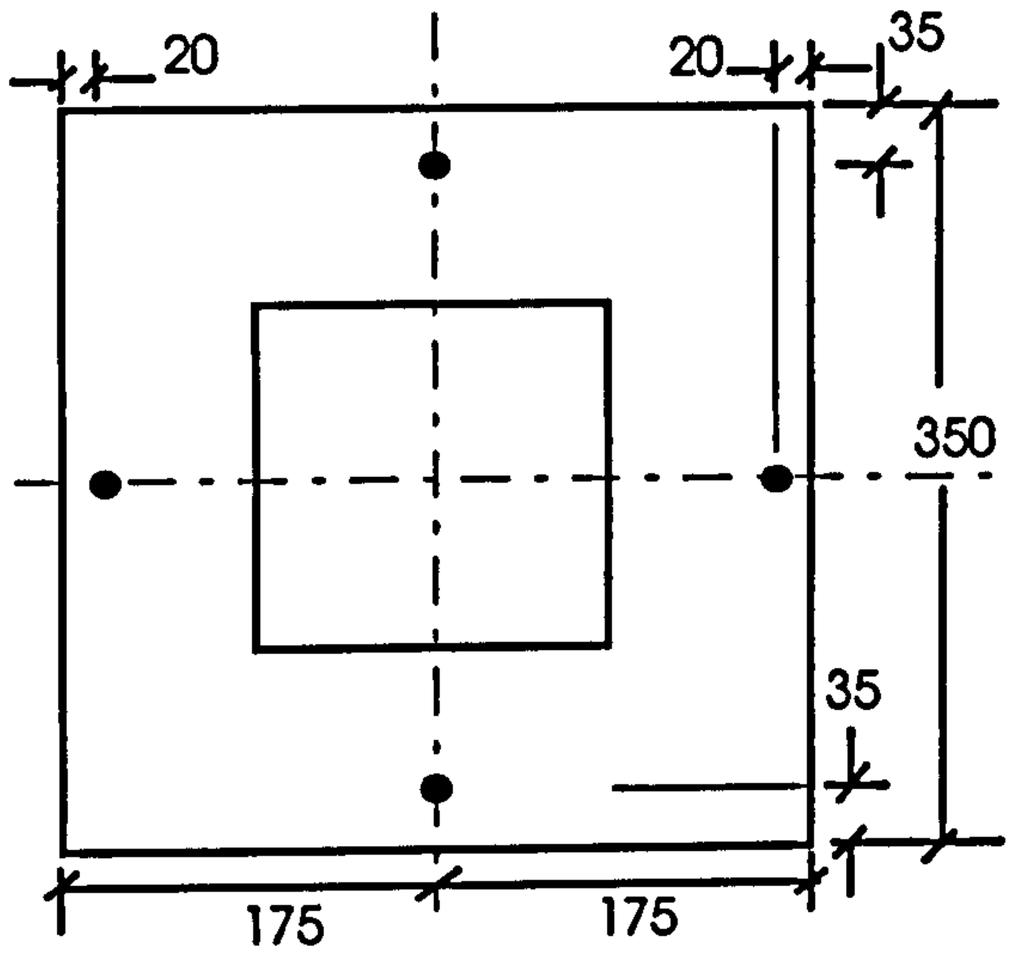

(b) C91

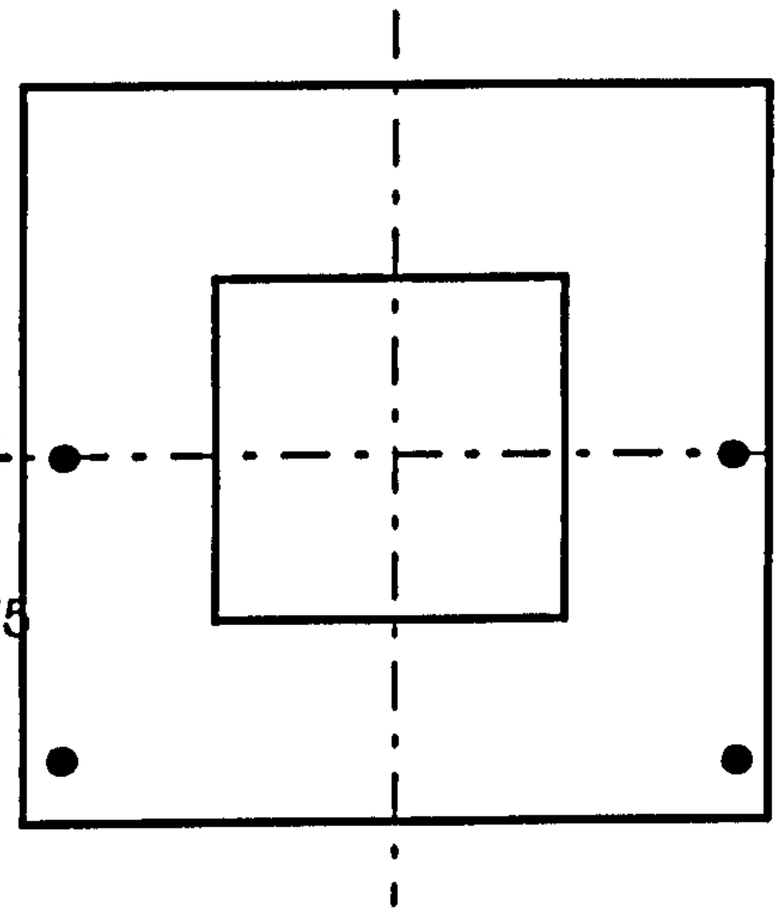

(c) C92

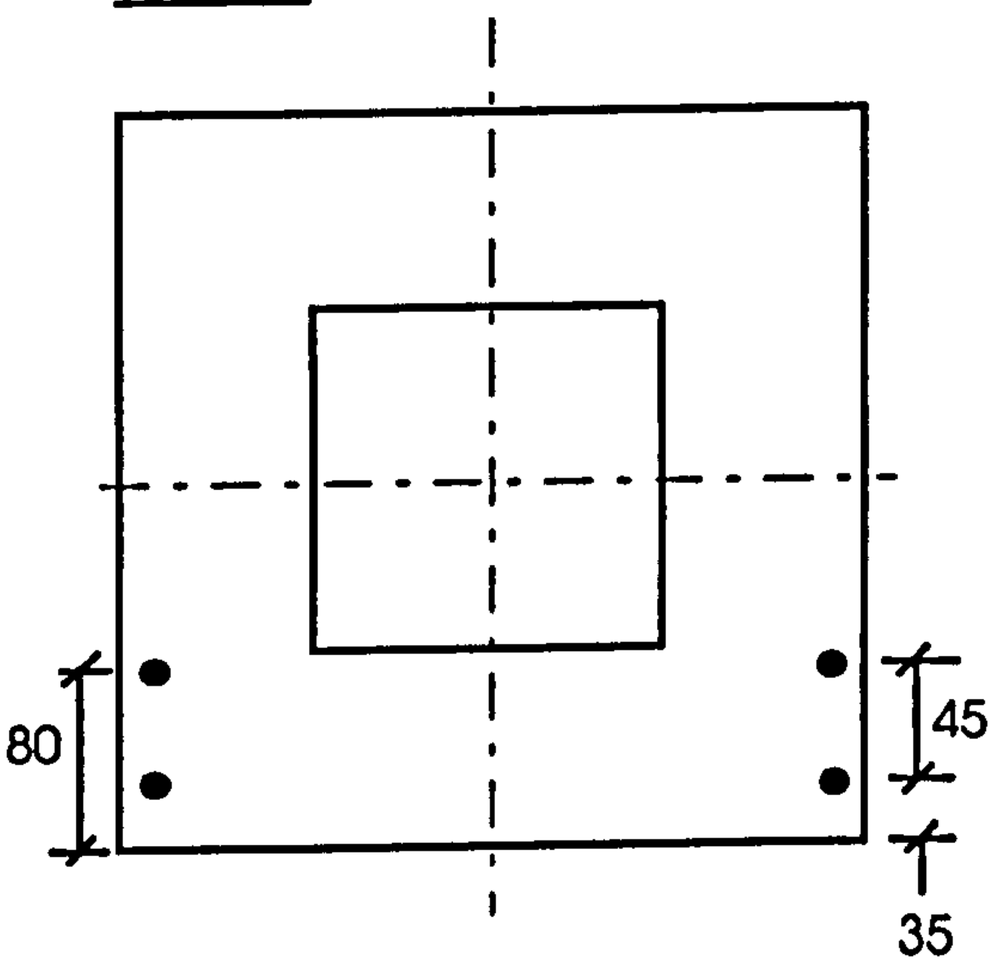

(d) C93

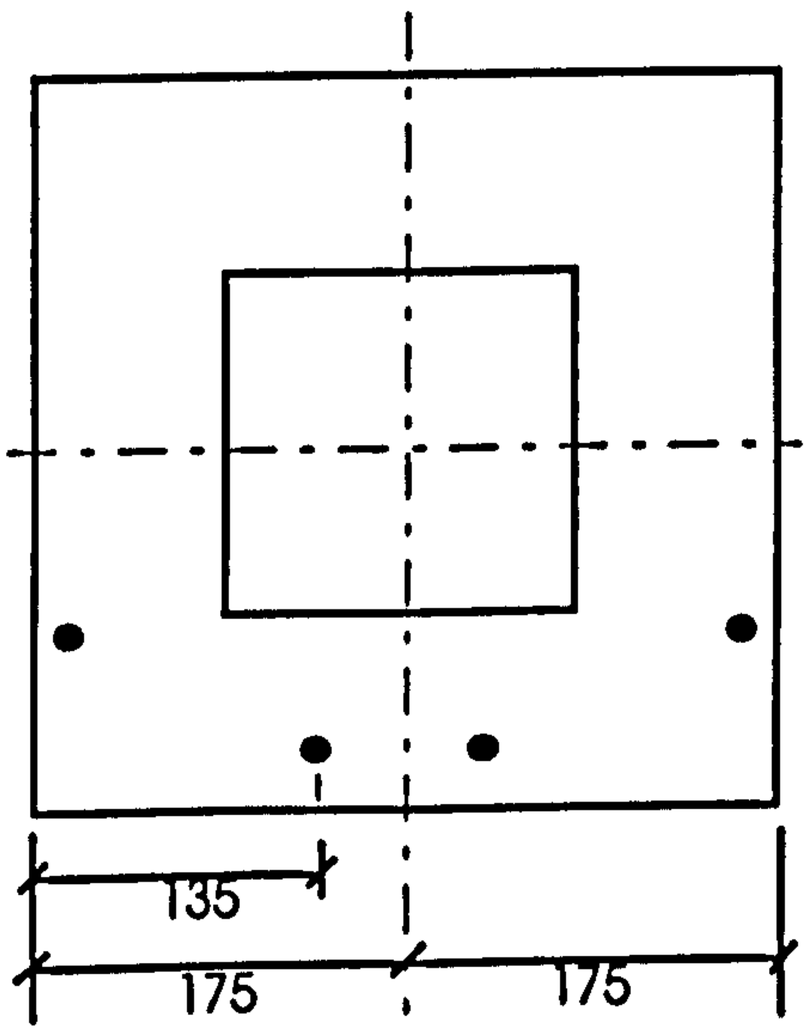

Fig. 6-4(e-h) Heater Configurations

(e) C91-135

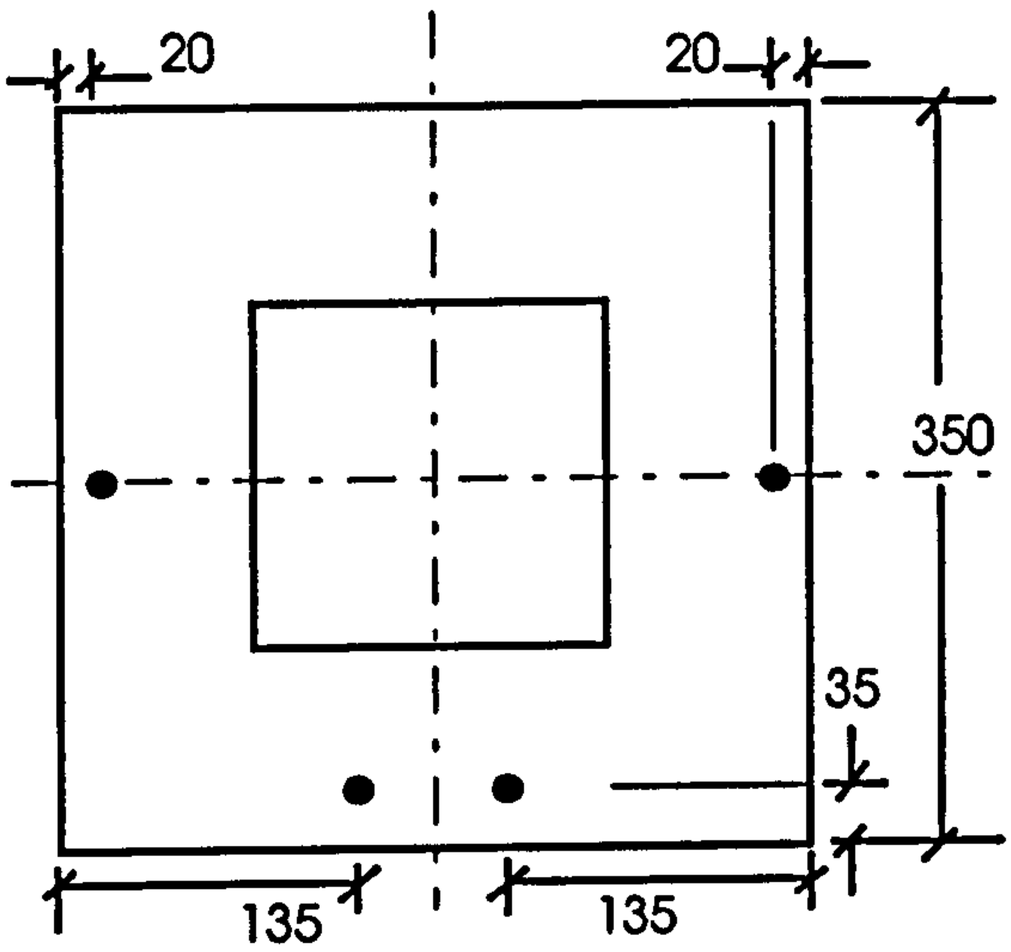

(f) C91-90

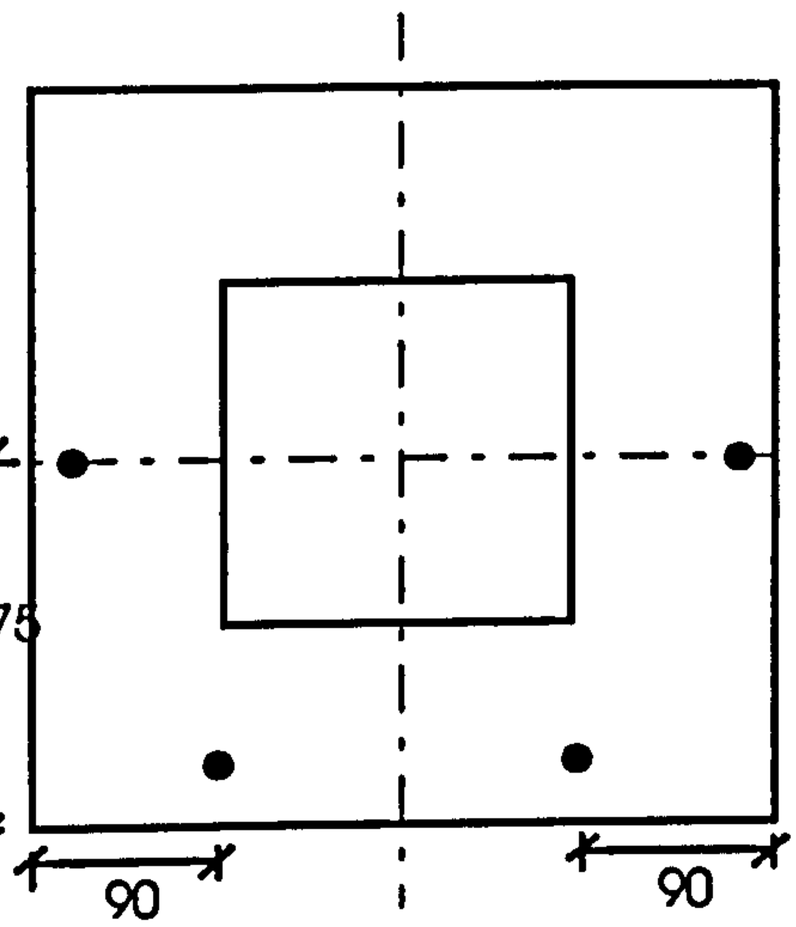

(g) C91-45

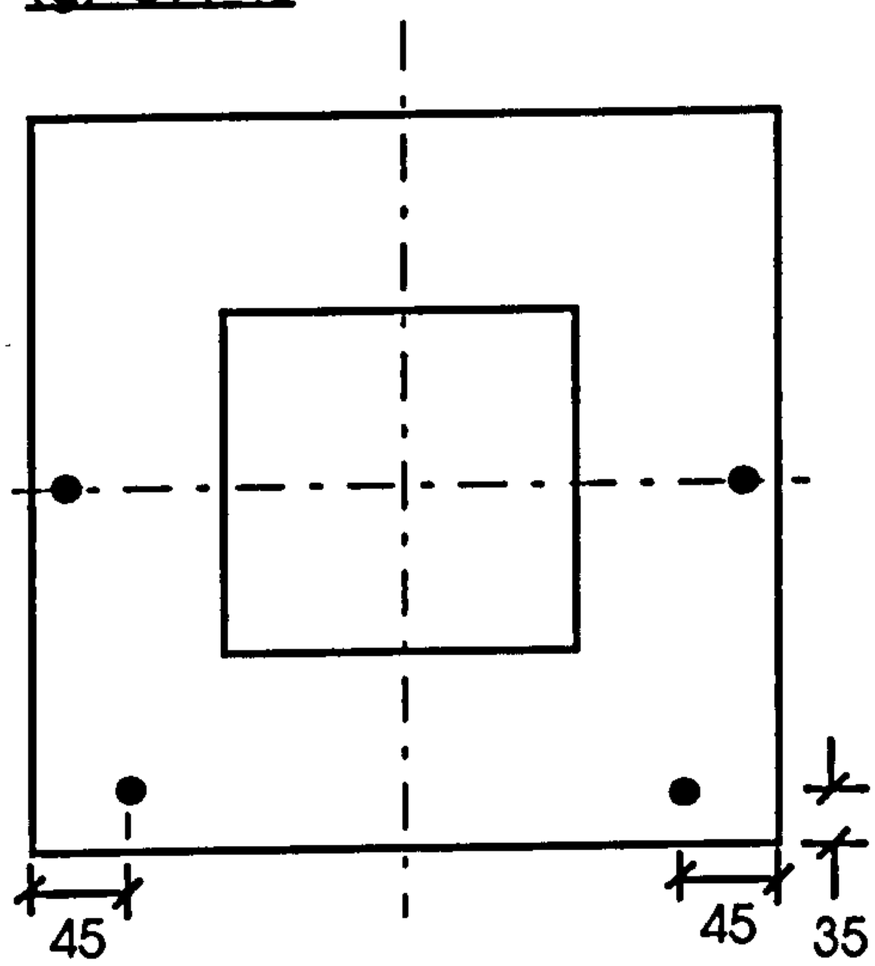

(h) C92-90

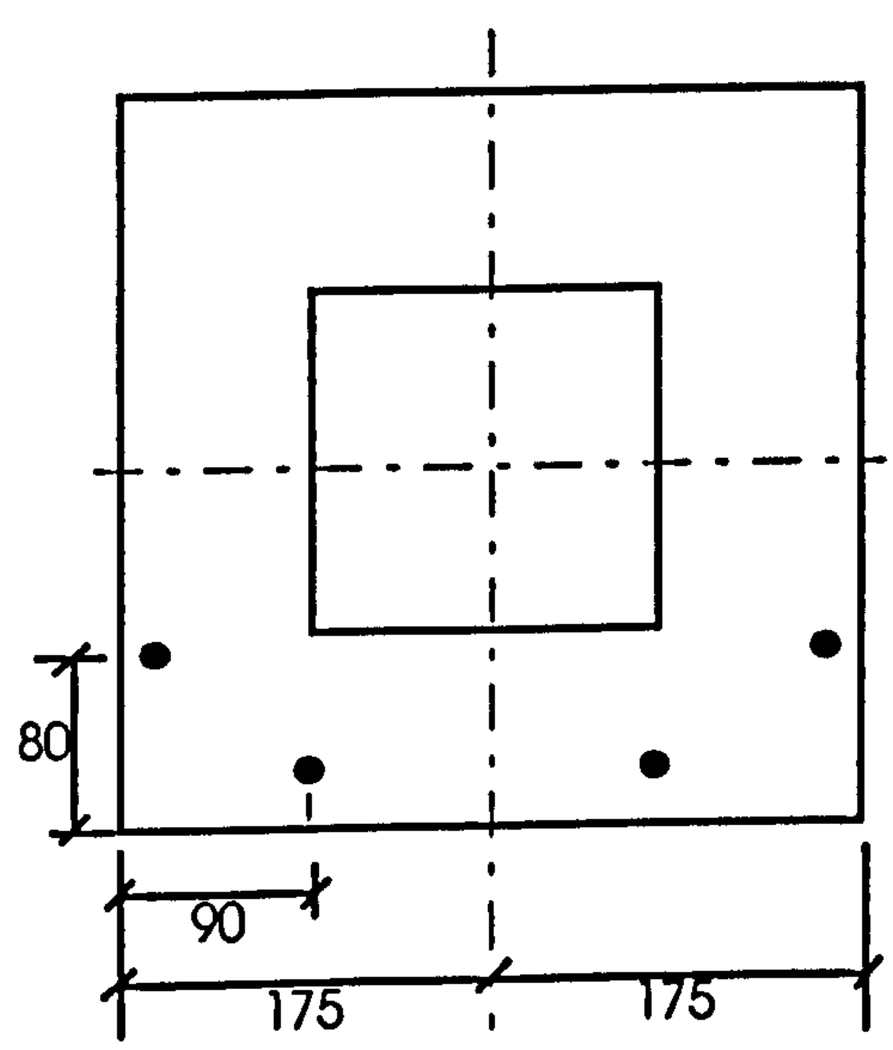

Fig. 6-5 Enclosure surface data points and zoning

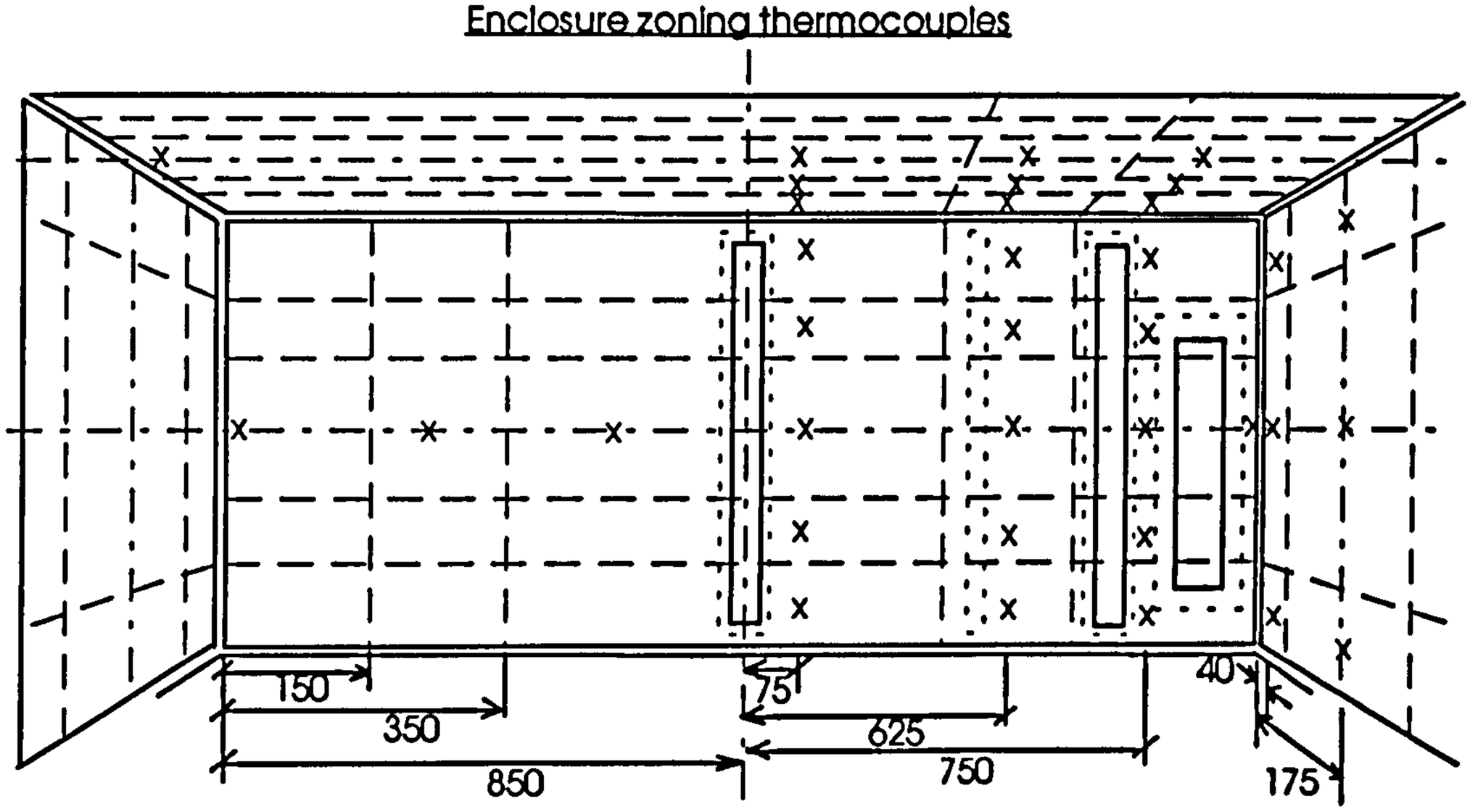

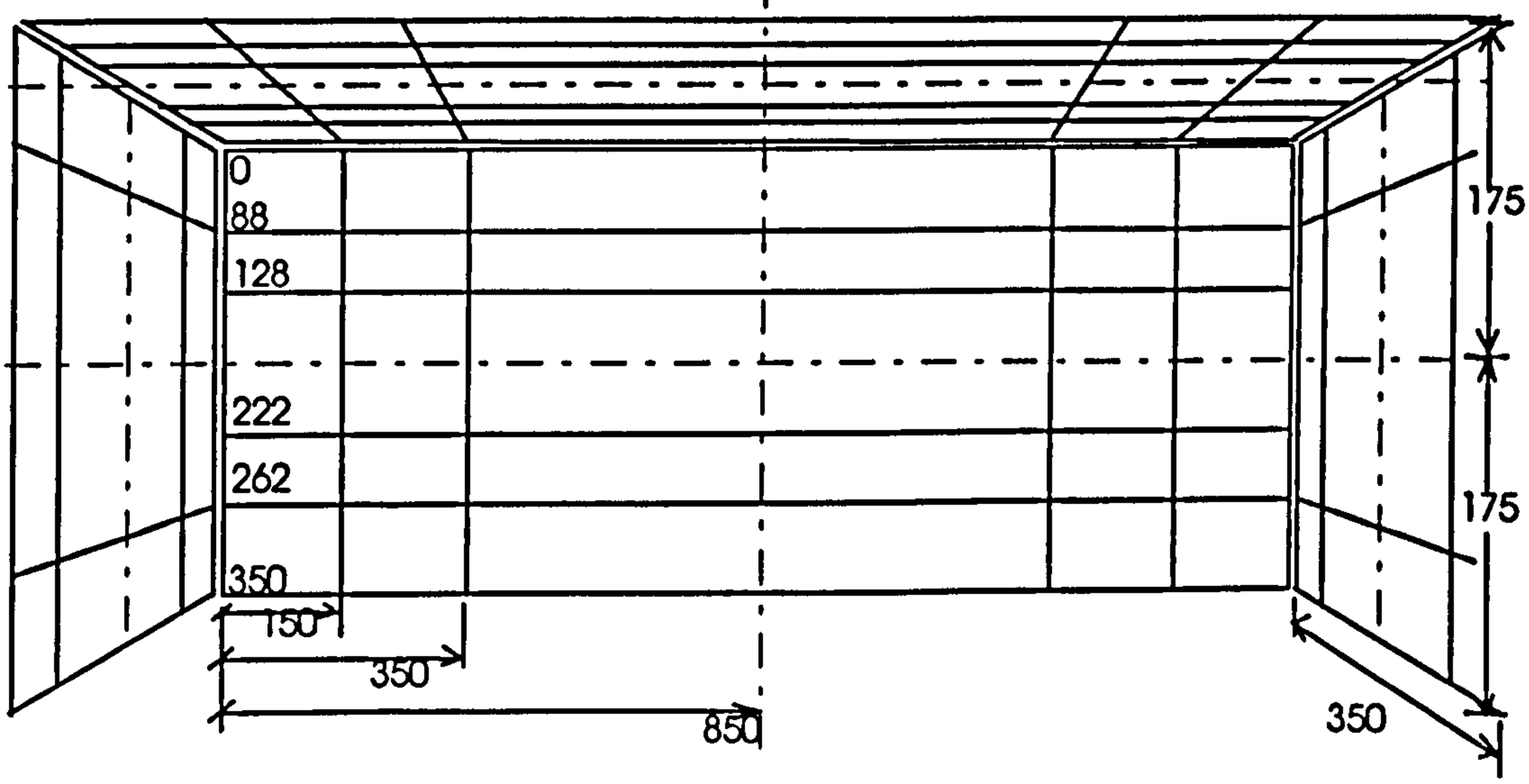

Fig. 6-6 Thermocouple rack

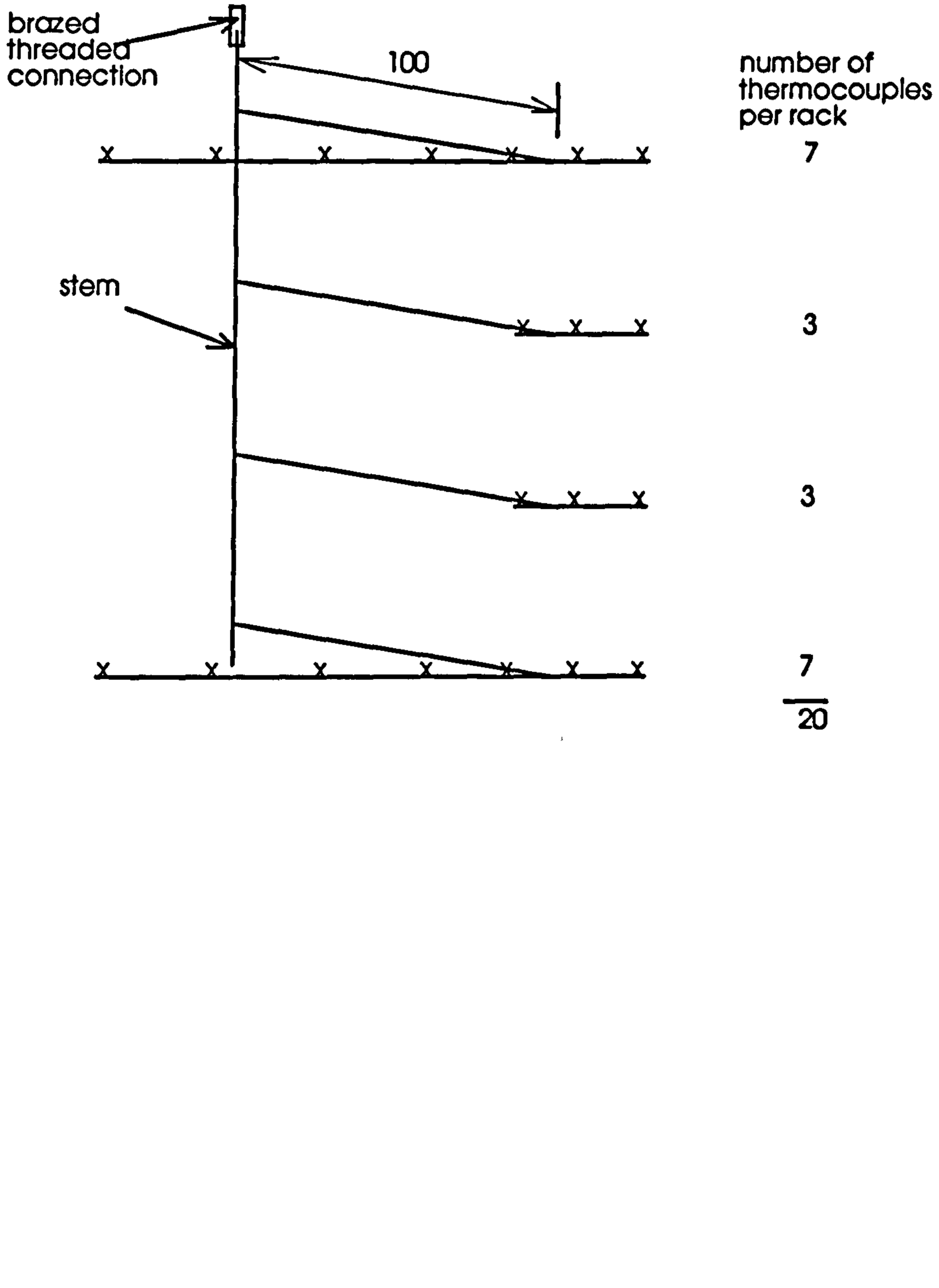

Fig. 6-7 Air space data points

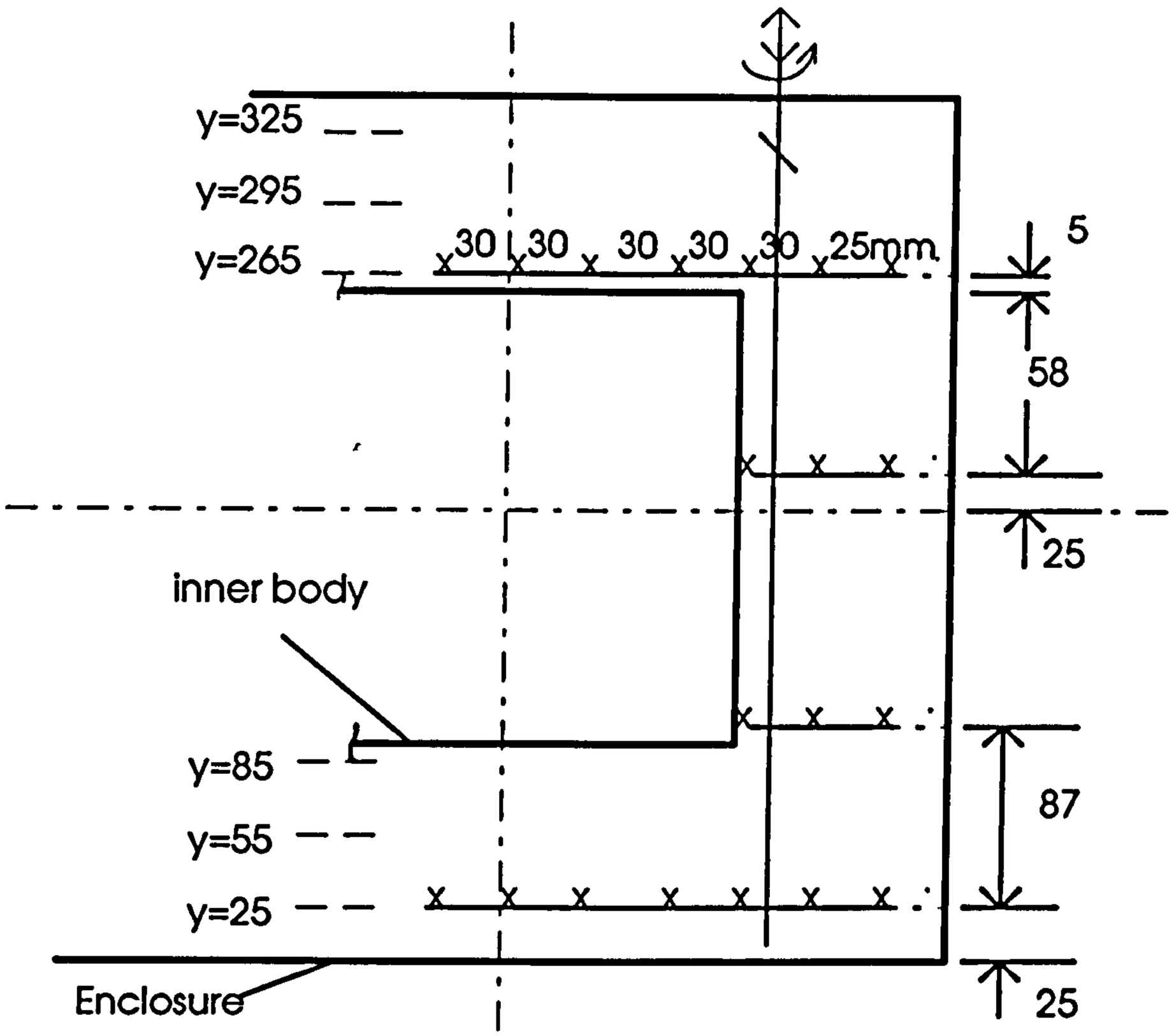

Fig. 6-8 Operating and sealing arrangements for traversing thermocouples

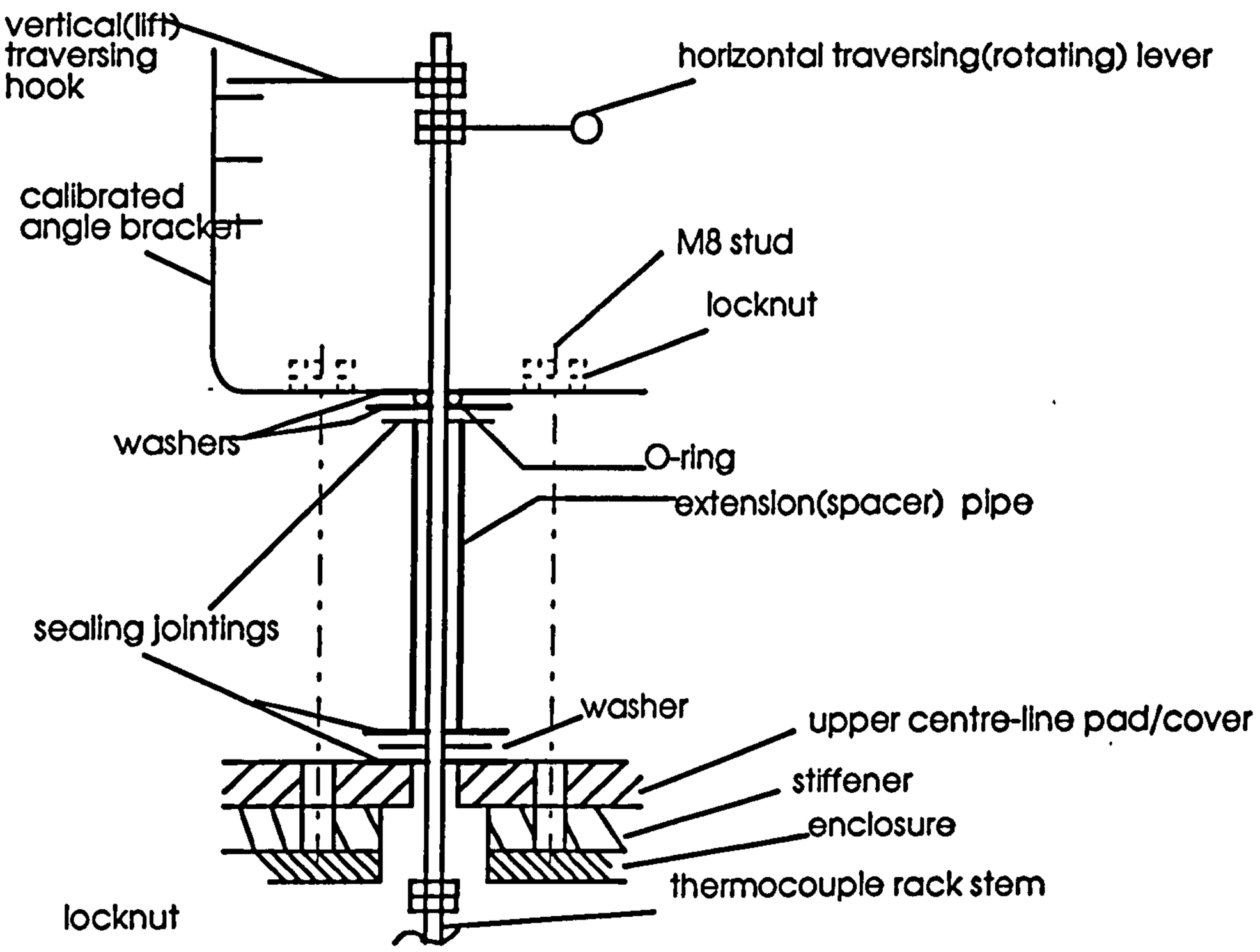

Fig. 6-9 Layout of the oven evacuation system

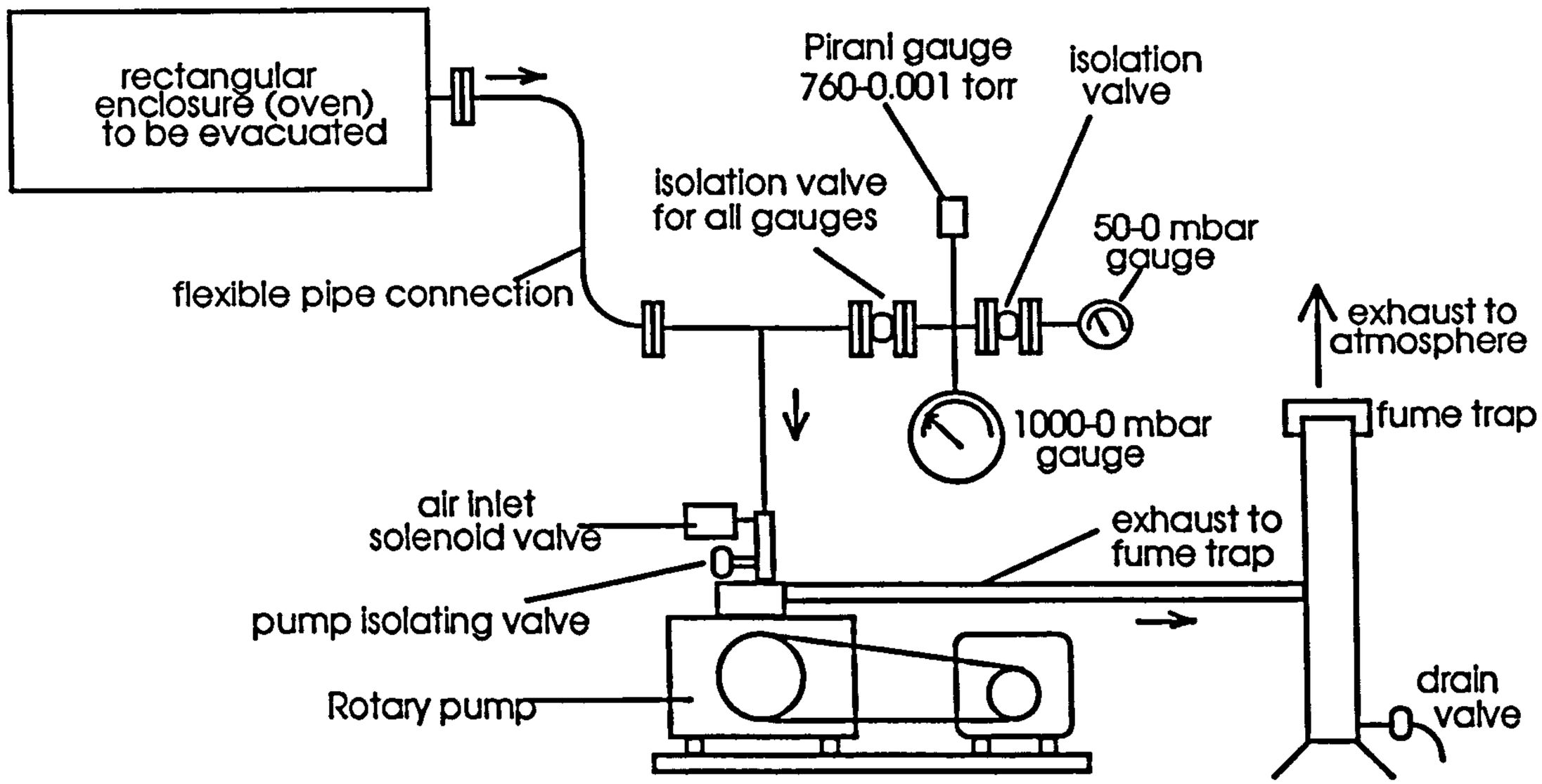

Fig.6-10

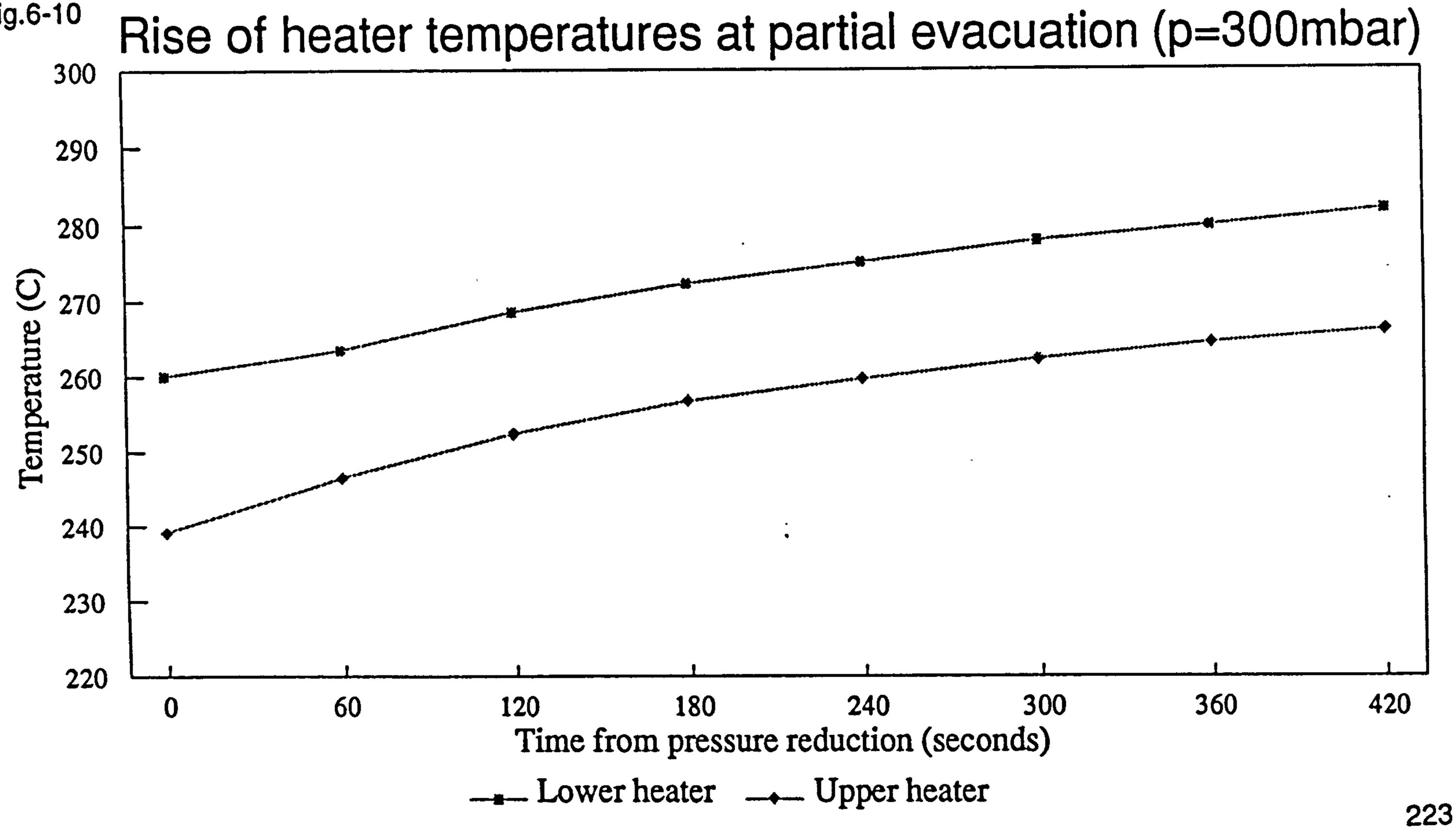
Rise of heater temperatures at partial evacuation (p=300mbar)
Temperature (C)
300
290
280
270
260
250
240
230
220
0
60
120
180
240
300
360
420
Time from pressure reduction (seconds)
Lower heater
Upper heater

Fig. 6-11 View factors from centrally positioned heaters

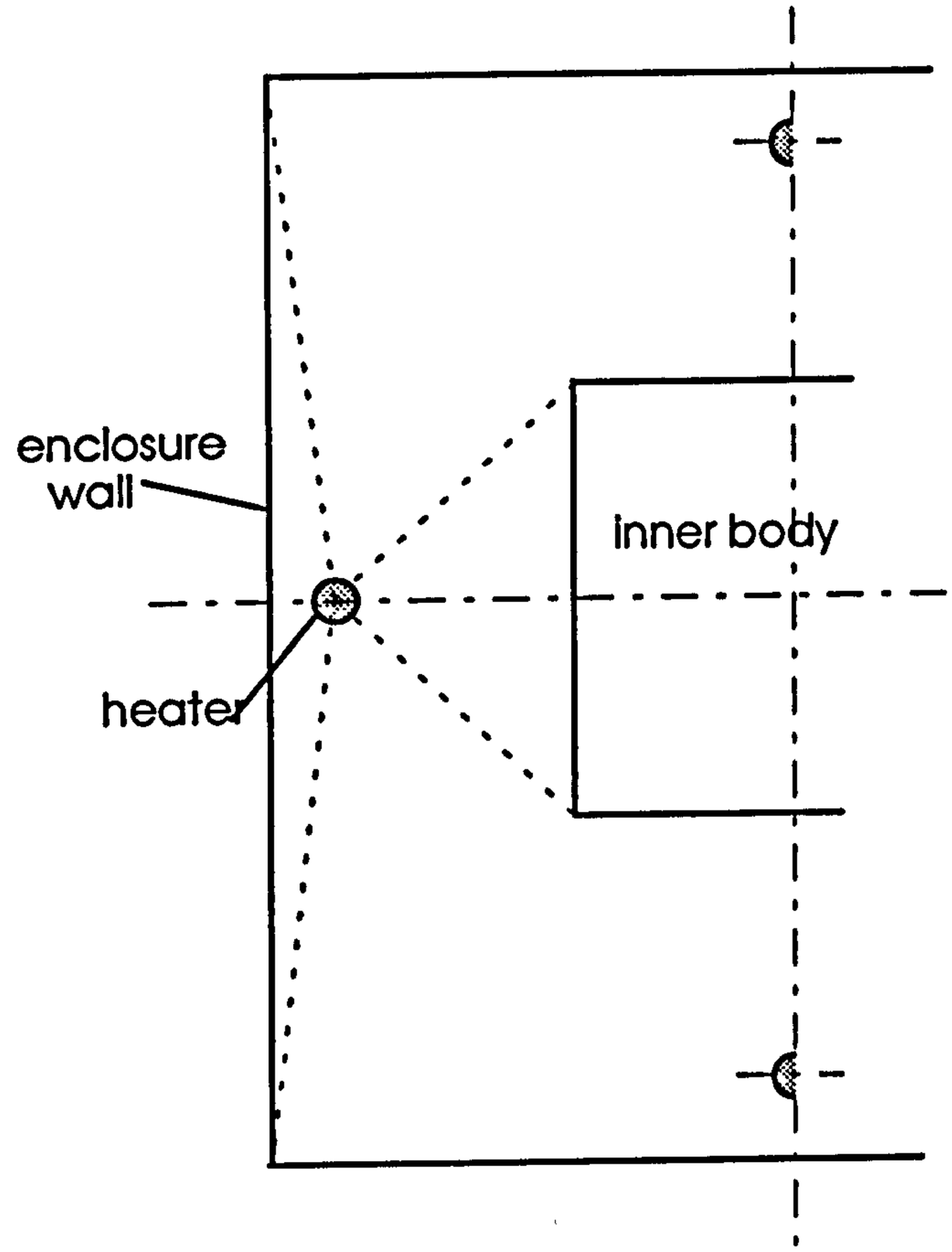

Rate of convective heat loss from a heated body in an evacuated enclosure [Edwards R.M., 1968]

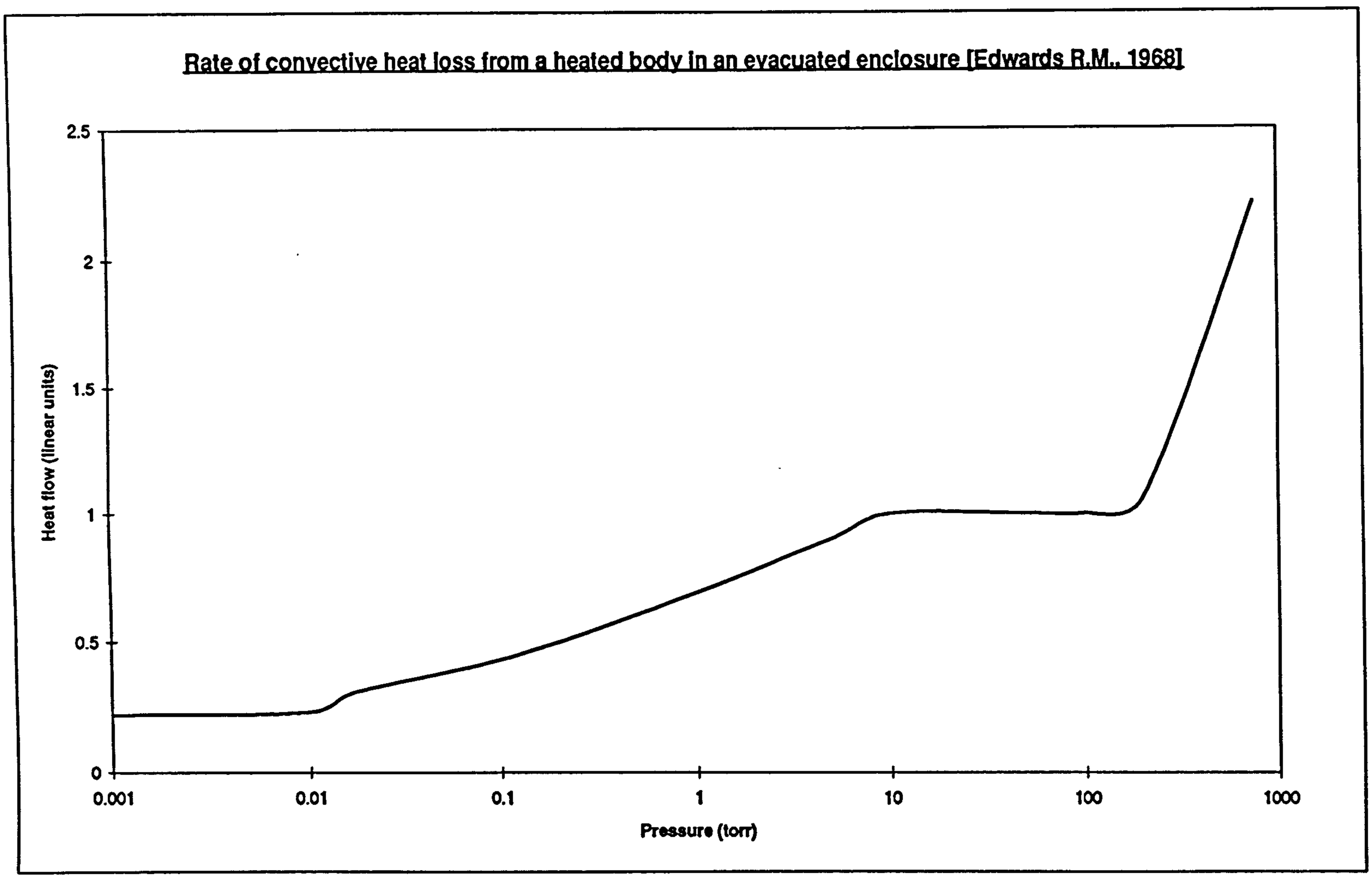

Fig. 6-12

Fig. 6-13 Flow visualisation

(a) C91

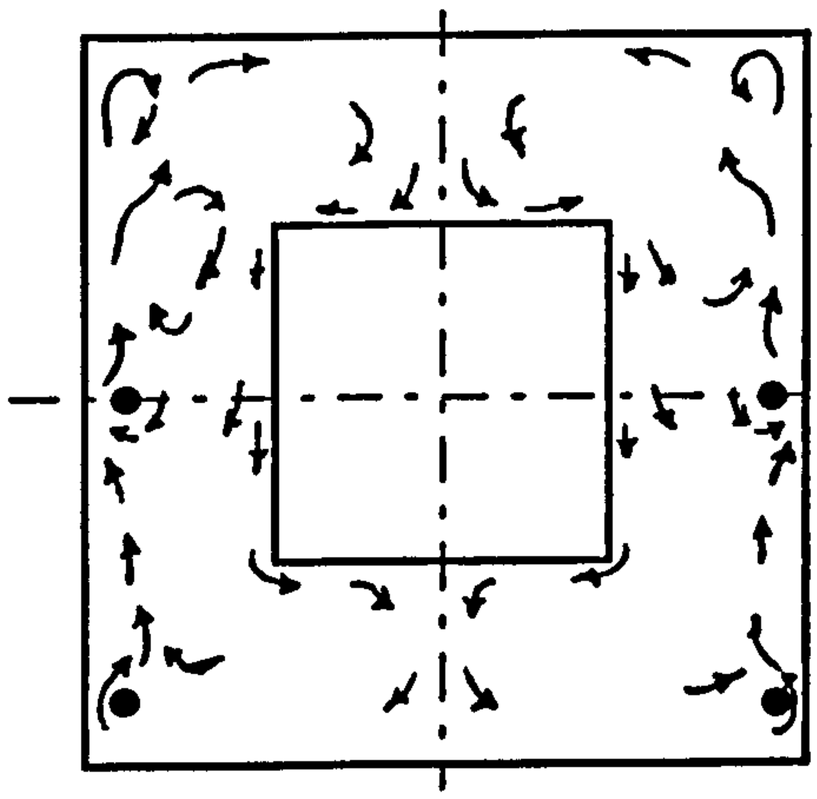

(b) C92

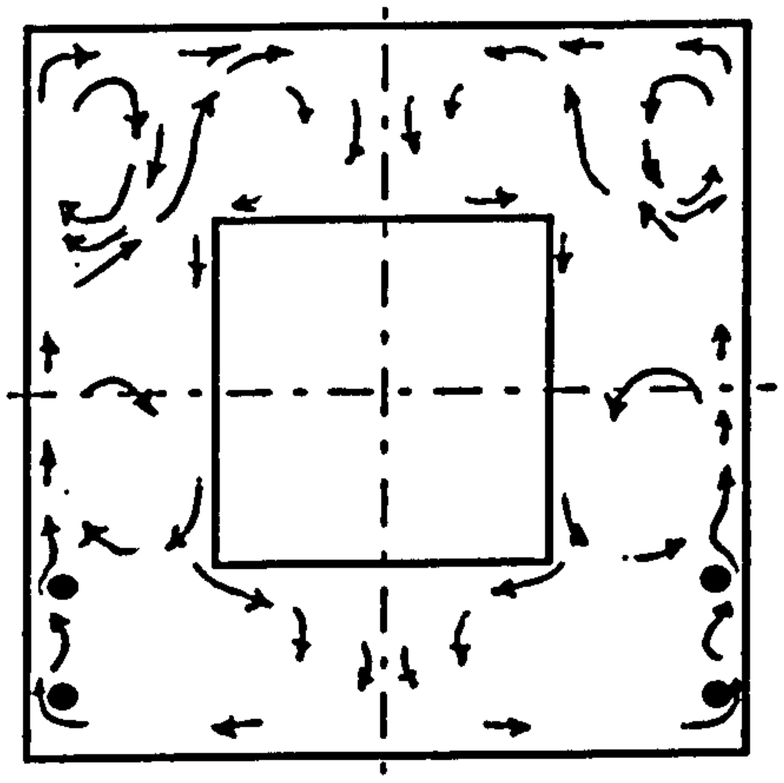

(c) C93

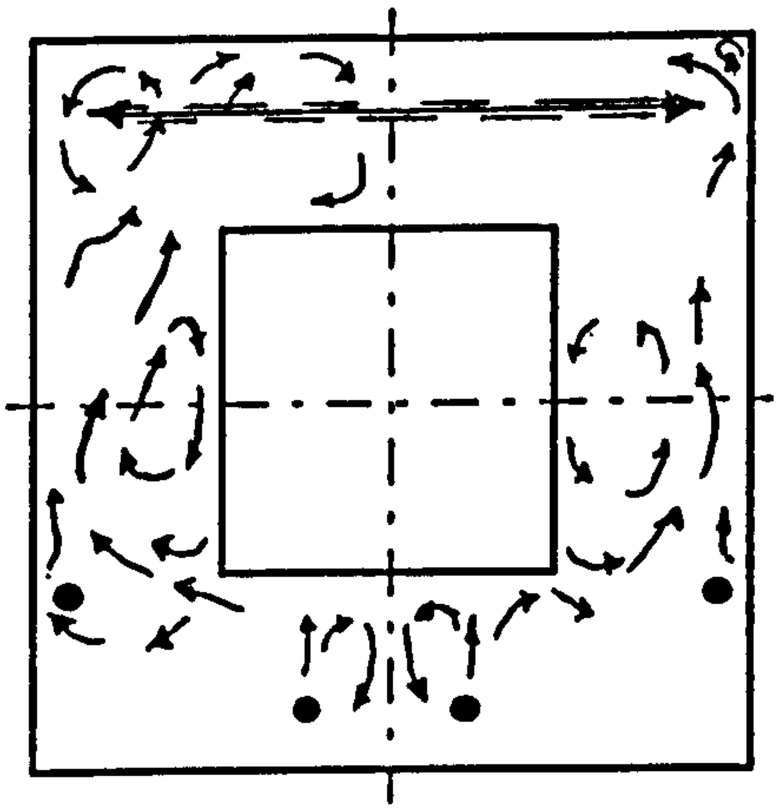

Fig. 6-14 Flow visualisation

(a) C91-135

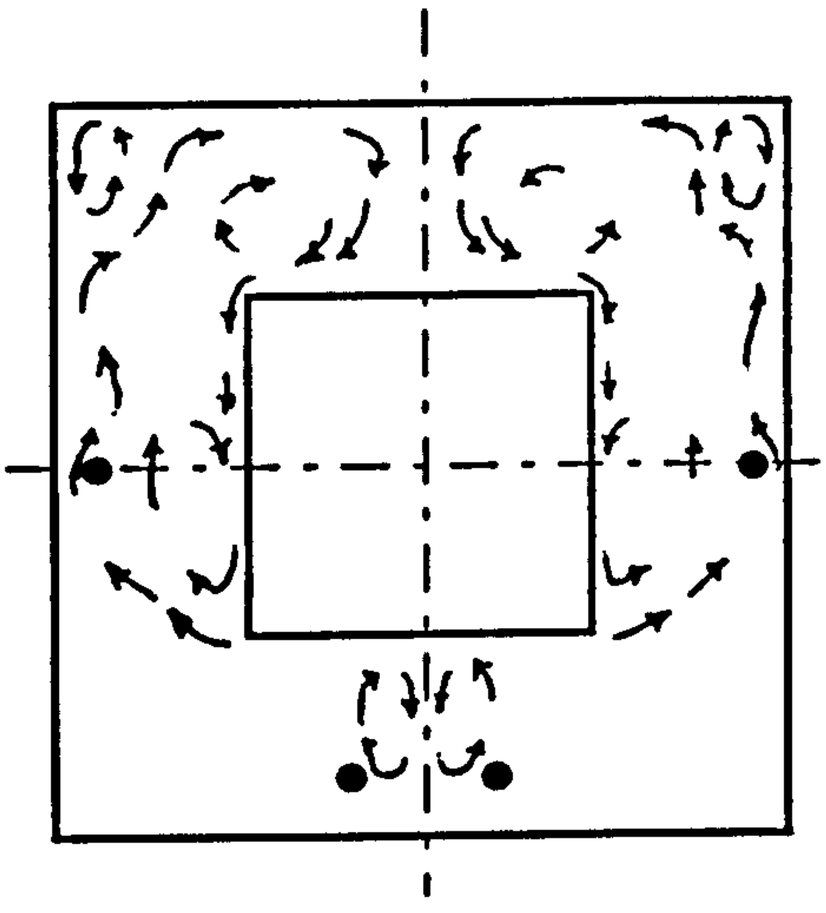

(b) C91-90

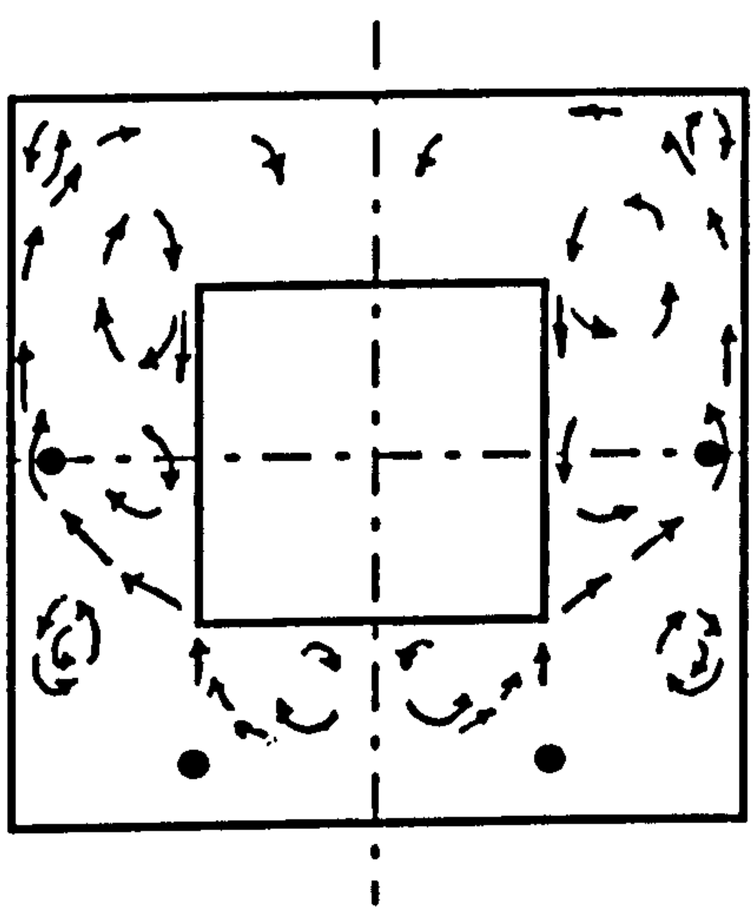

(c) C91-45

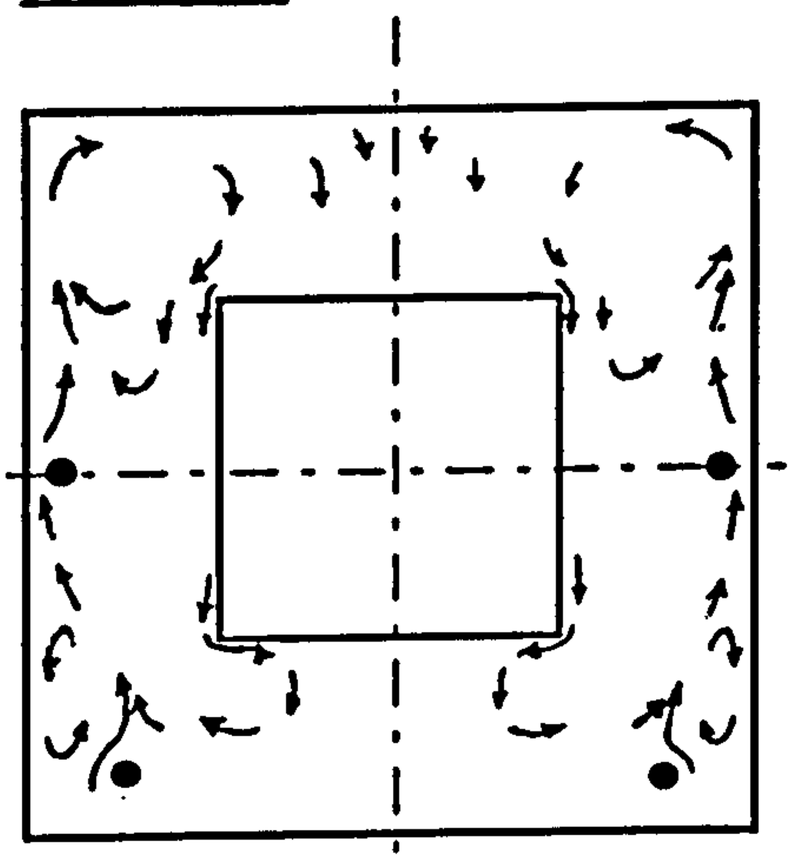

(d) C92-90

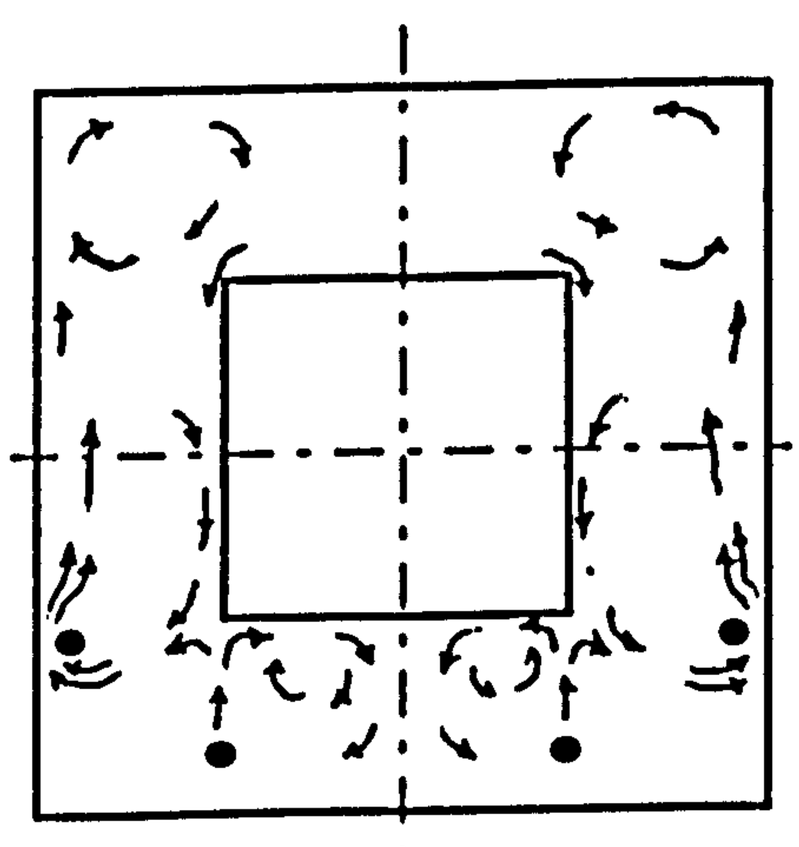

C91

Fig.6-15a

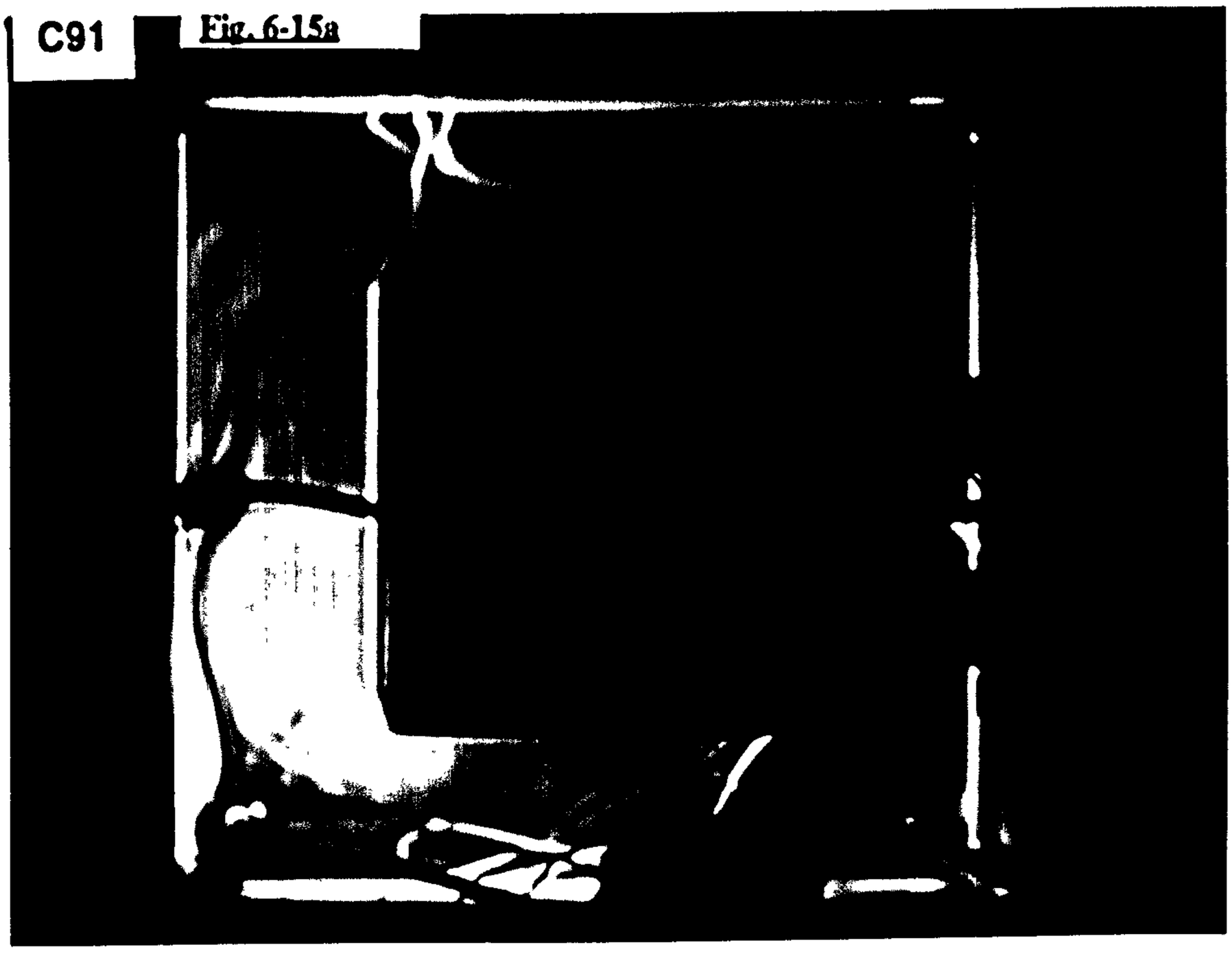

C91-45

Fig.6-15b

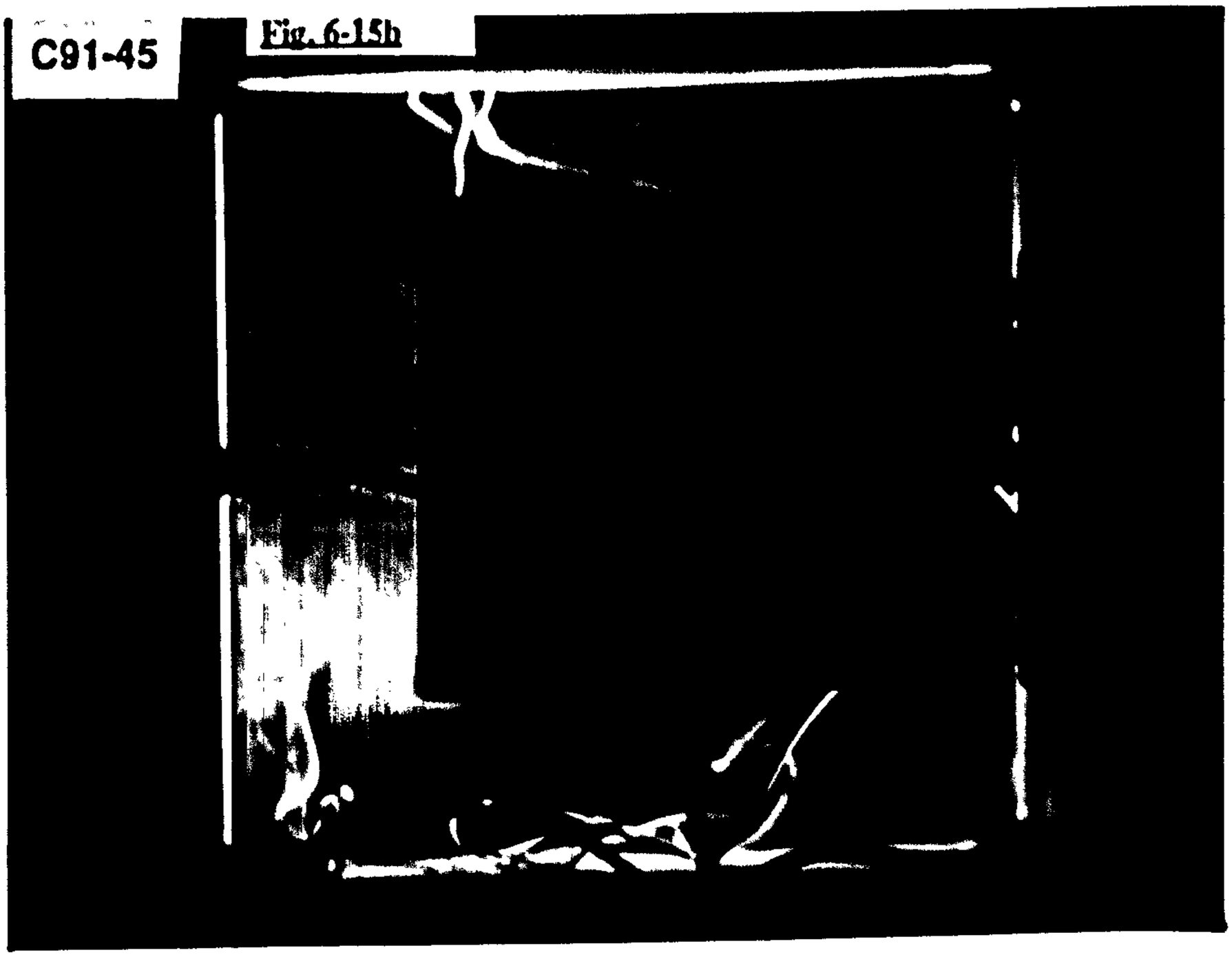

C91-90

Fig. 6-15c

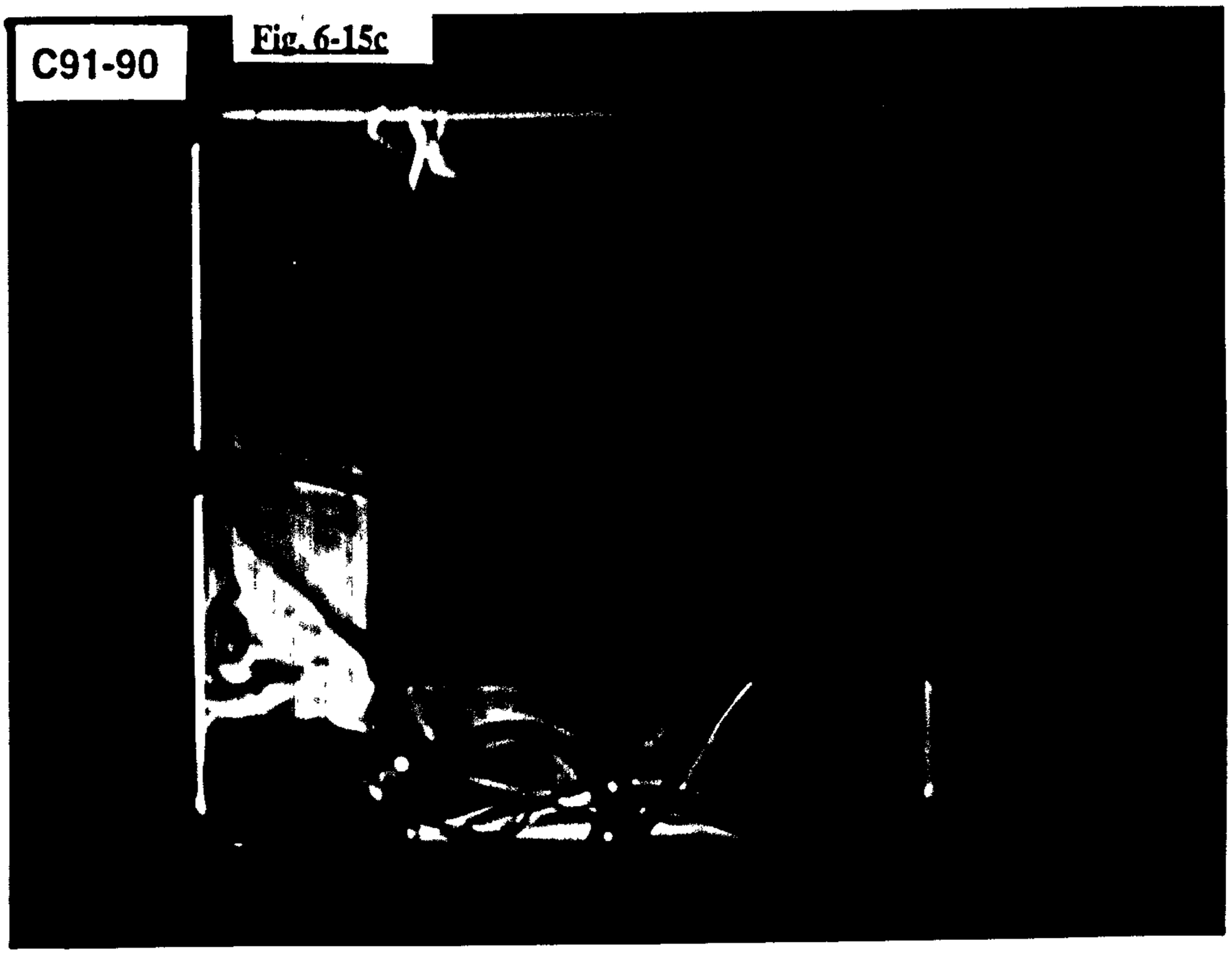

C91-135

Fig. 6-15d

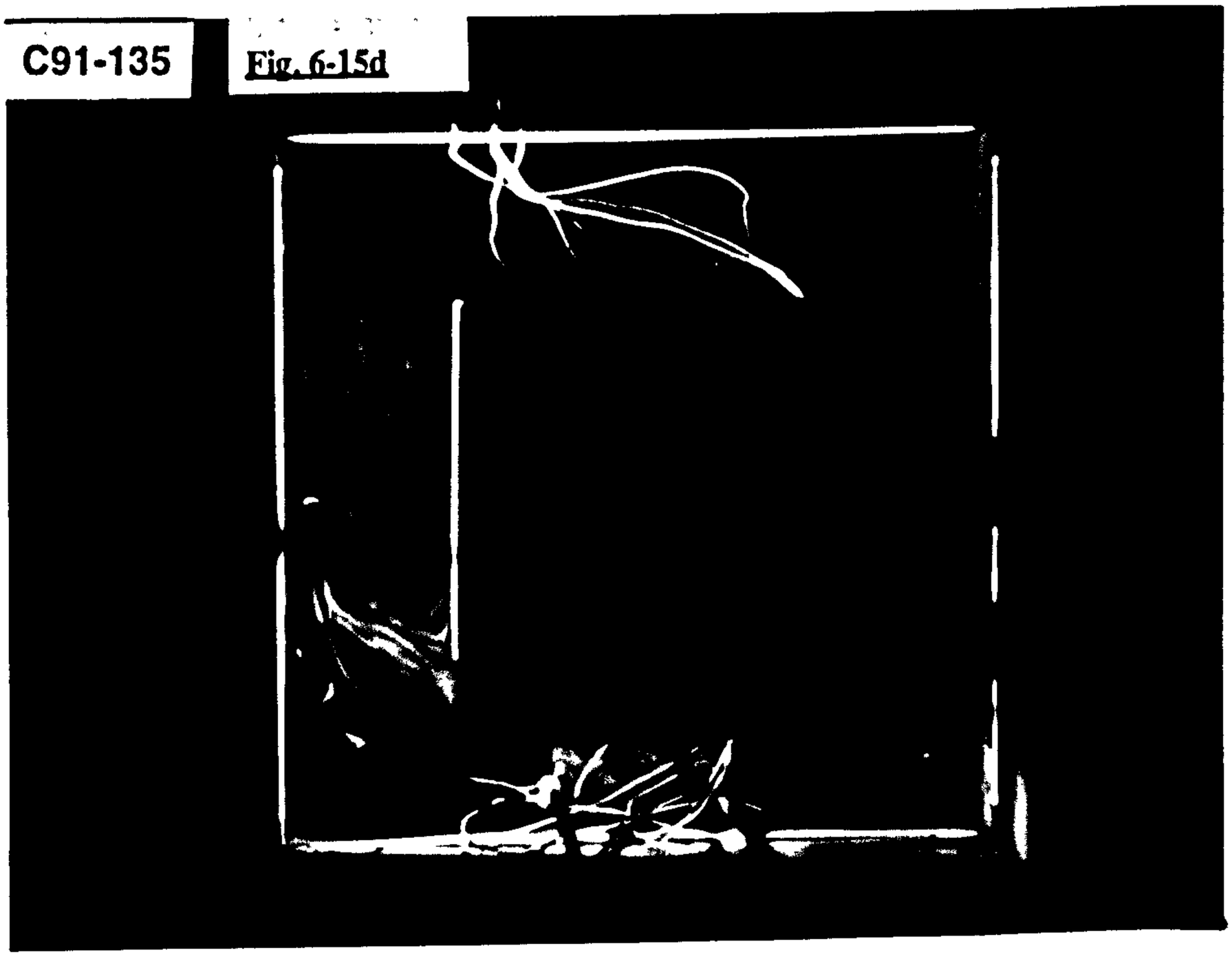

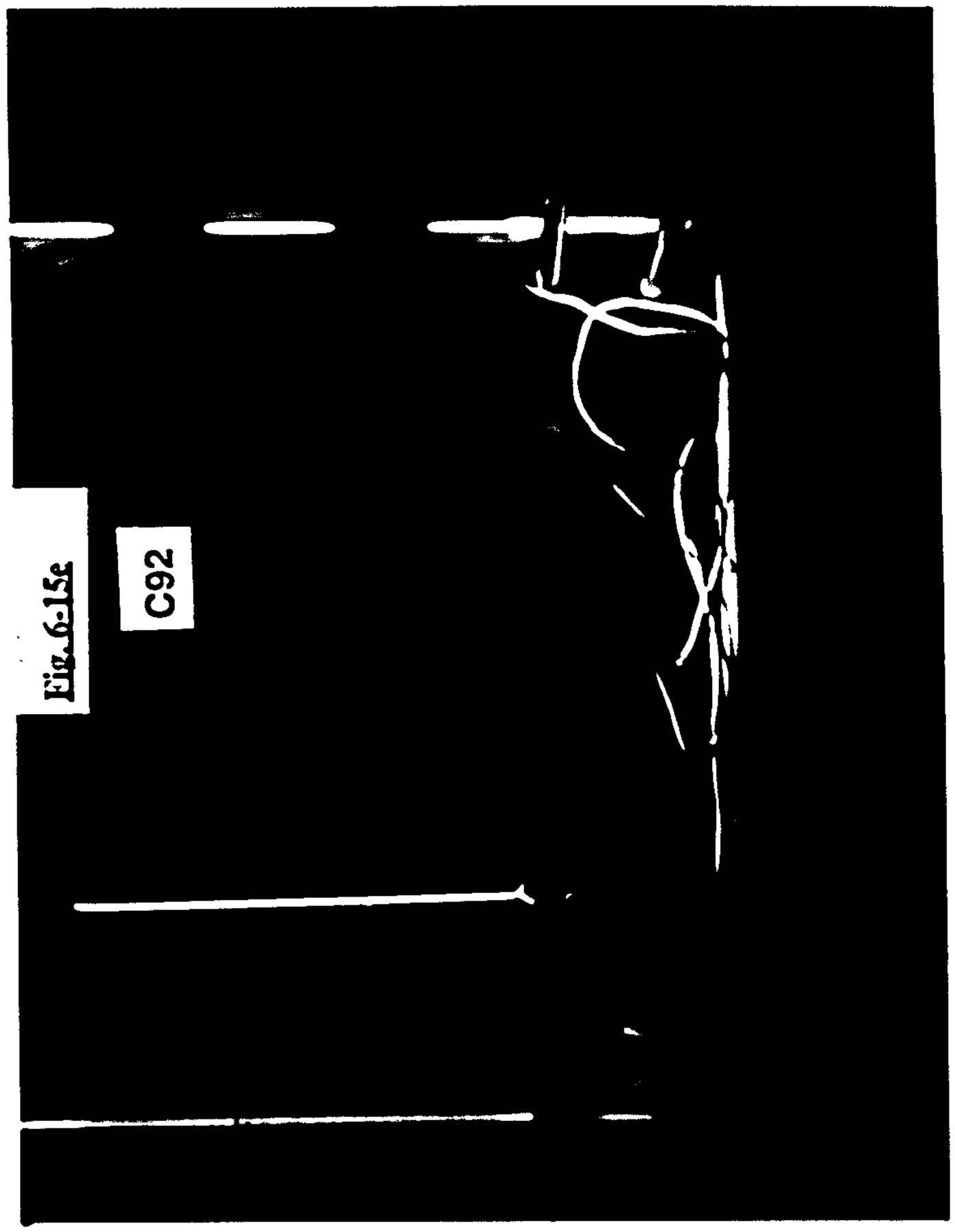

Fig.6-15e

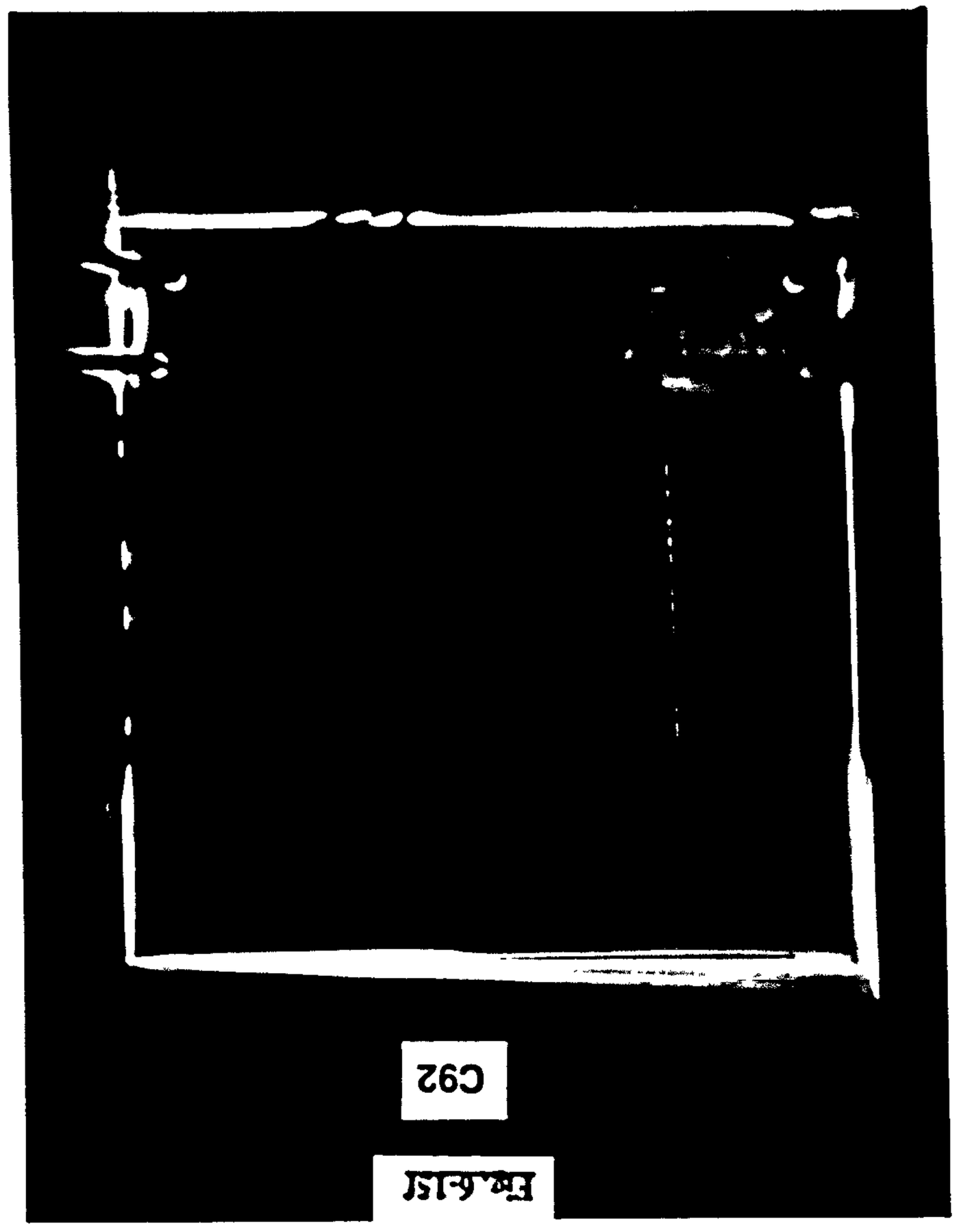

Fig.6-15f

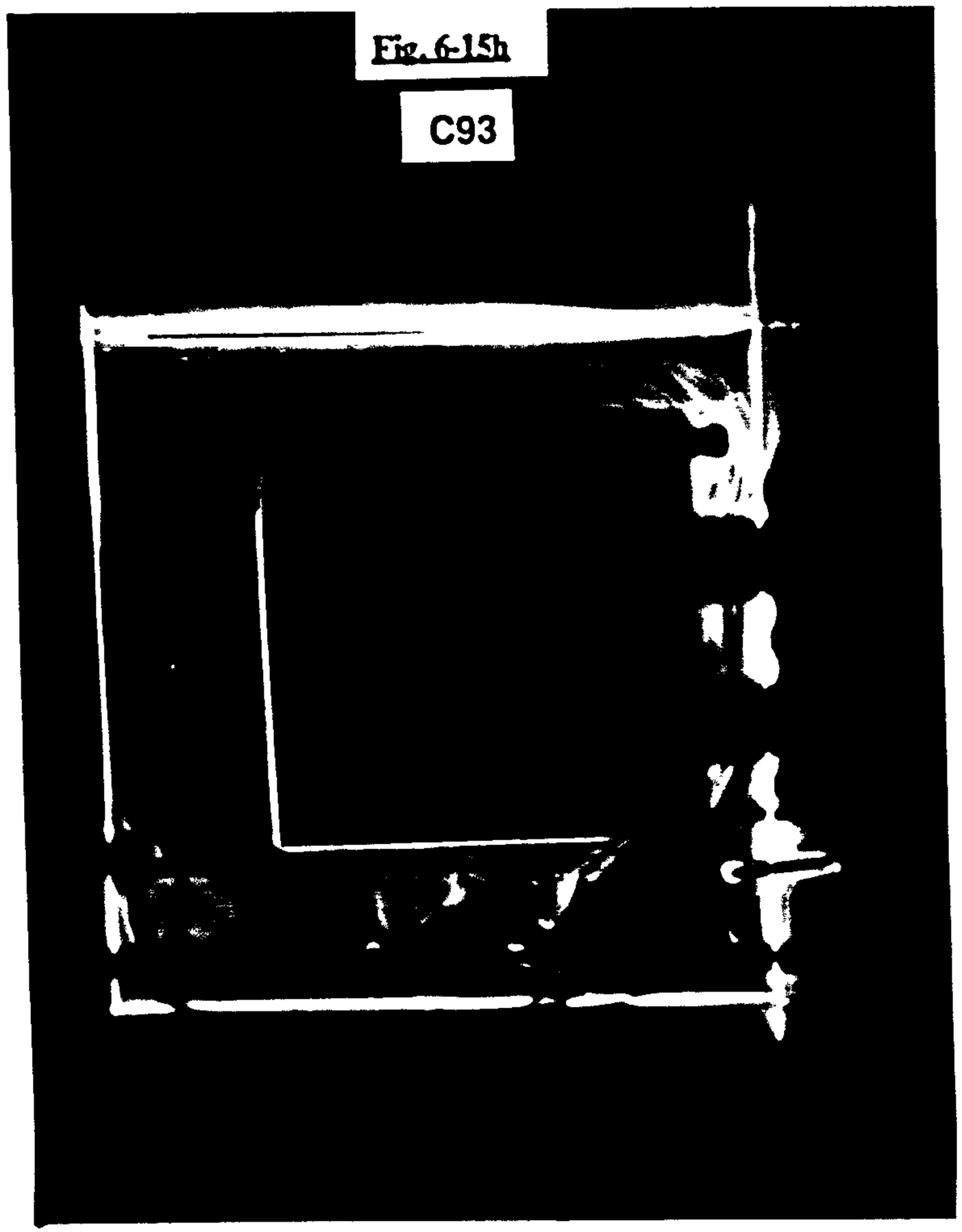
Fig.6-15h
C93

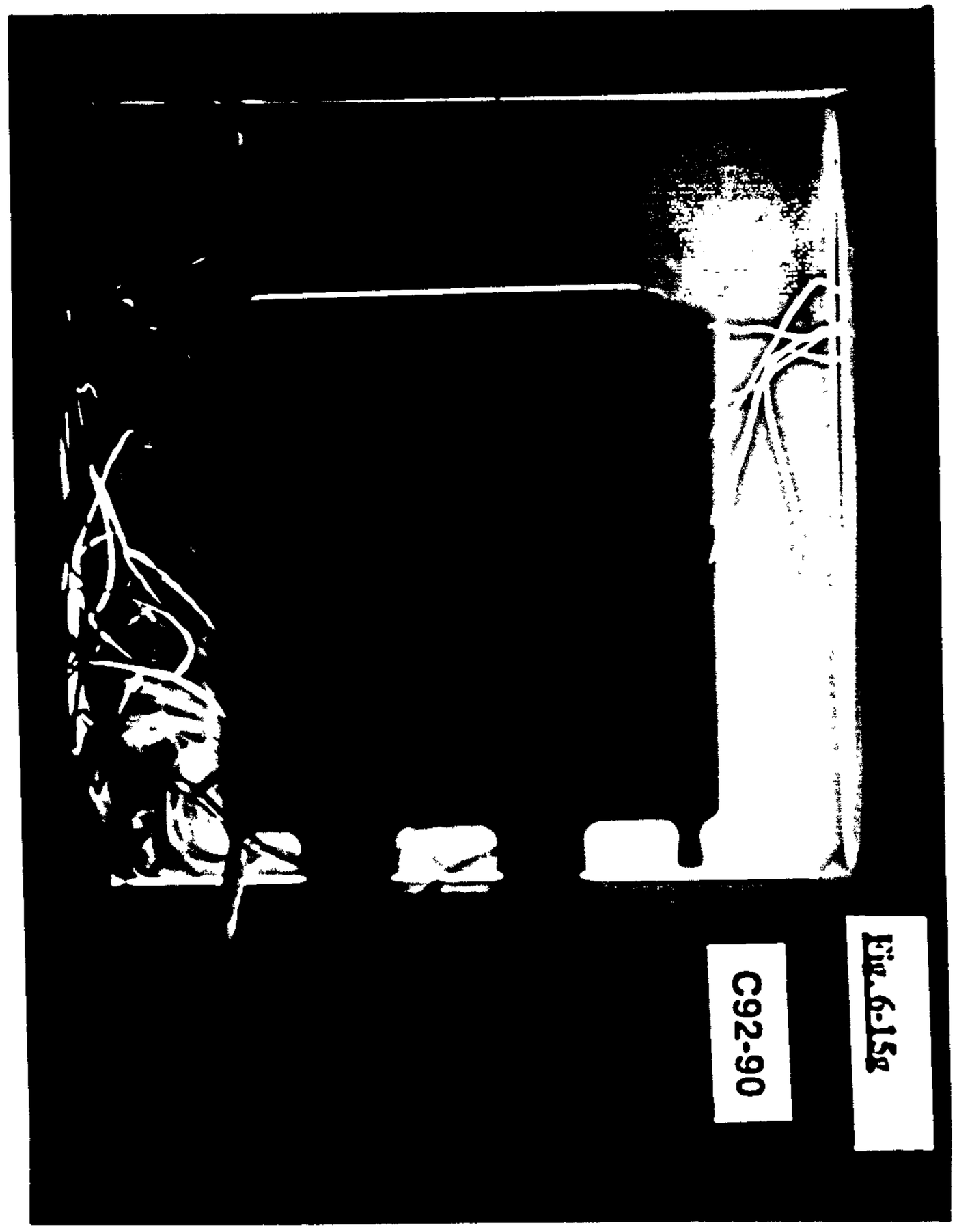
Fig.6-15g
C92-90

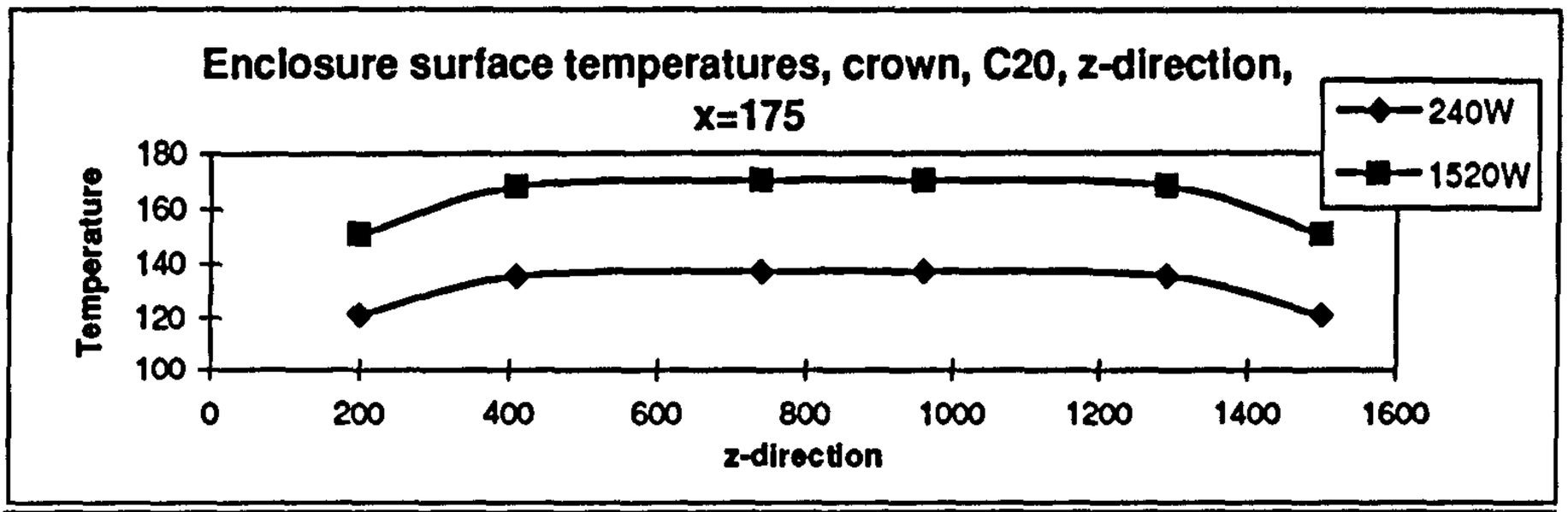
Enclosure surface temperatures, crown, C20, z-direction, x=175
Temperature
180
160
140
120
100
0
200
400
600
800
1000
1200
1400
1600
z-direction
240W
1520W

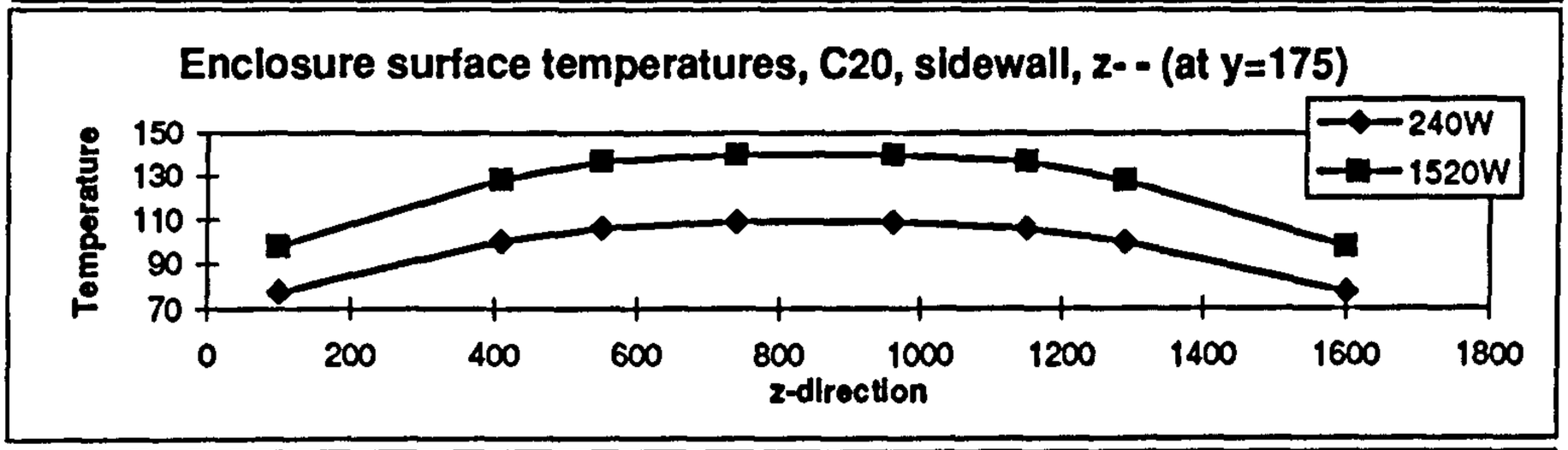
Enclosure surface temperatures, C20, sidewall, z- - (at y=175)
Temperature
150
130
110
90
70
0
200
400
600
800
1000
1200
1400
1600
1800
z-direction
240W
1520W

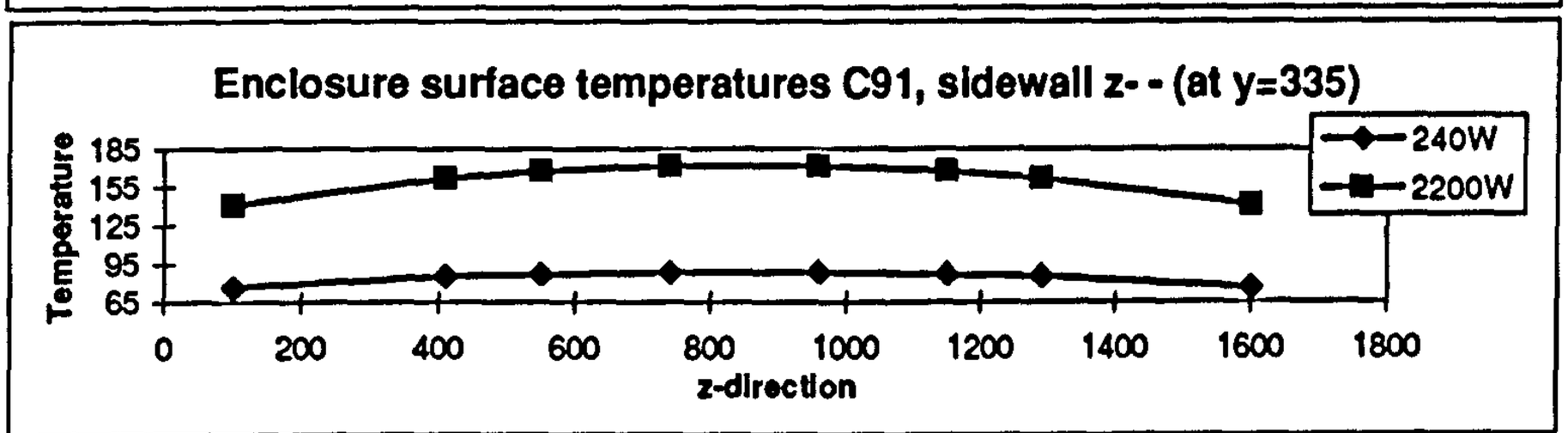
Enclosure surface temperatures C91, sidewall z- - (at y=335)
Temperature
185
155
125
95
65
0
200
400
600
800
1000
1200
1400
1600
1800
z-direction
240W
2200W

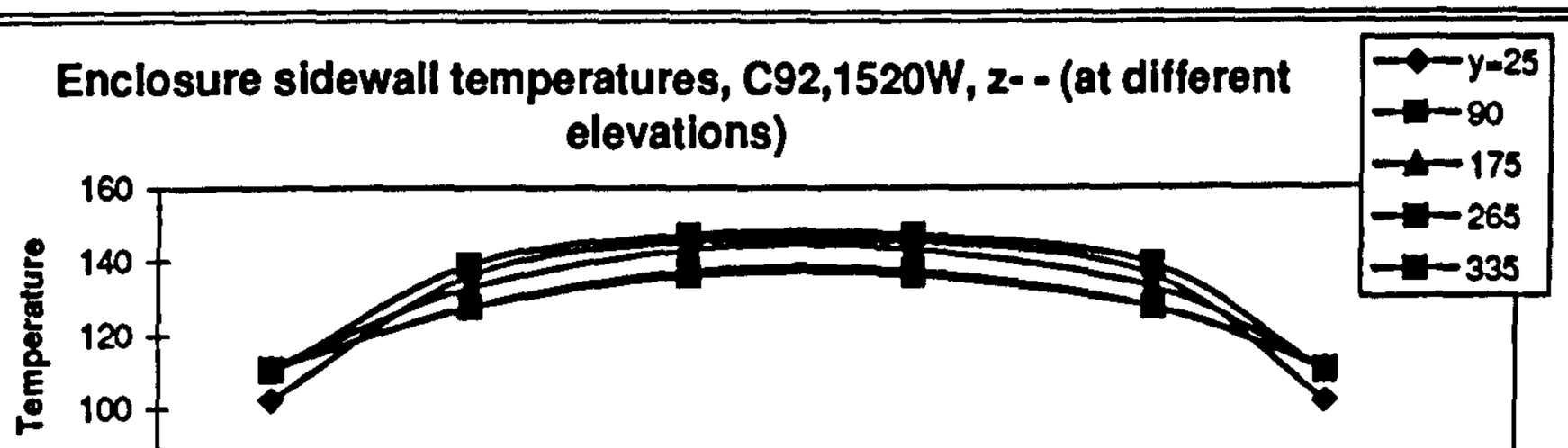
Enclosure sidewall temperatures, C92,1520W, z- - (at different elevations)
Temperature
160
140
120
100
80
0
200
400
600
800
1000
1200
1400
1600
1800
z-direction
y=25
90
175
265
335

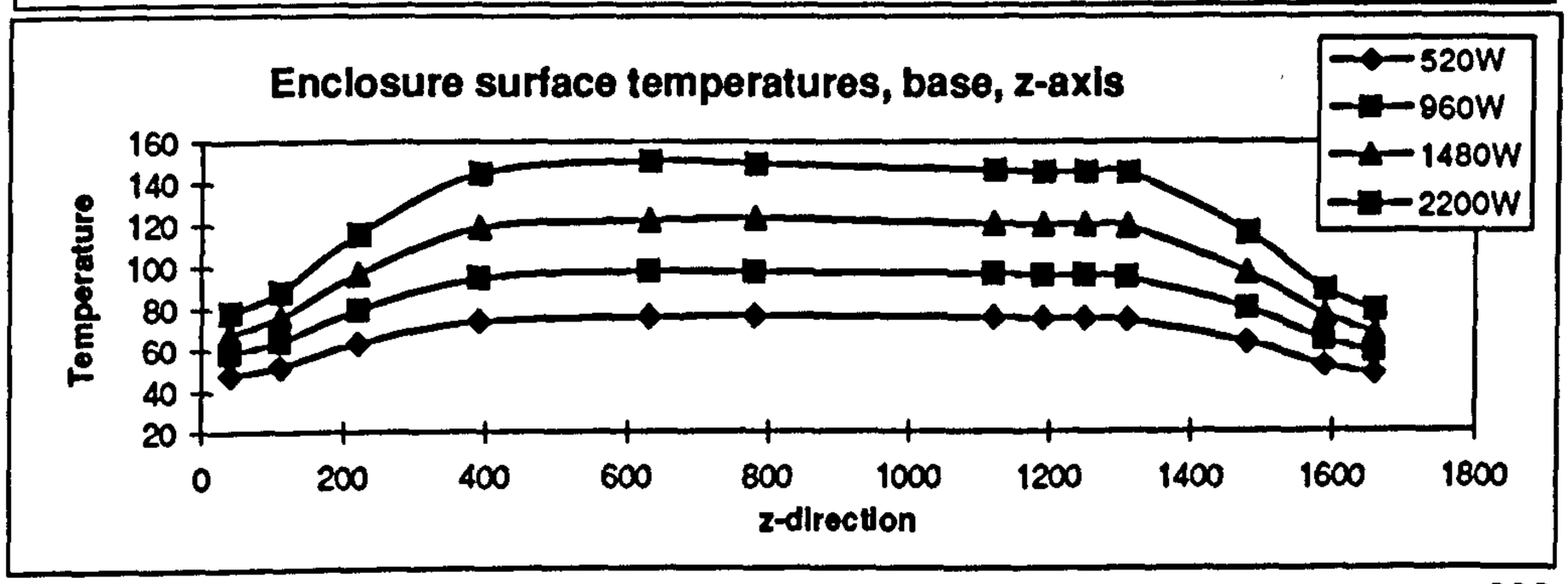
Enclosure surface temperatures, base, z-axis
Temperature
160
140
120
100
80
60
40
20
0
200
400
600
800
1000
1200
1400
1600
1800
z-direction
520W
960W
1480W
2200W

Fig. 6-16(a-e)

Fig. 6-17(a-d)

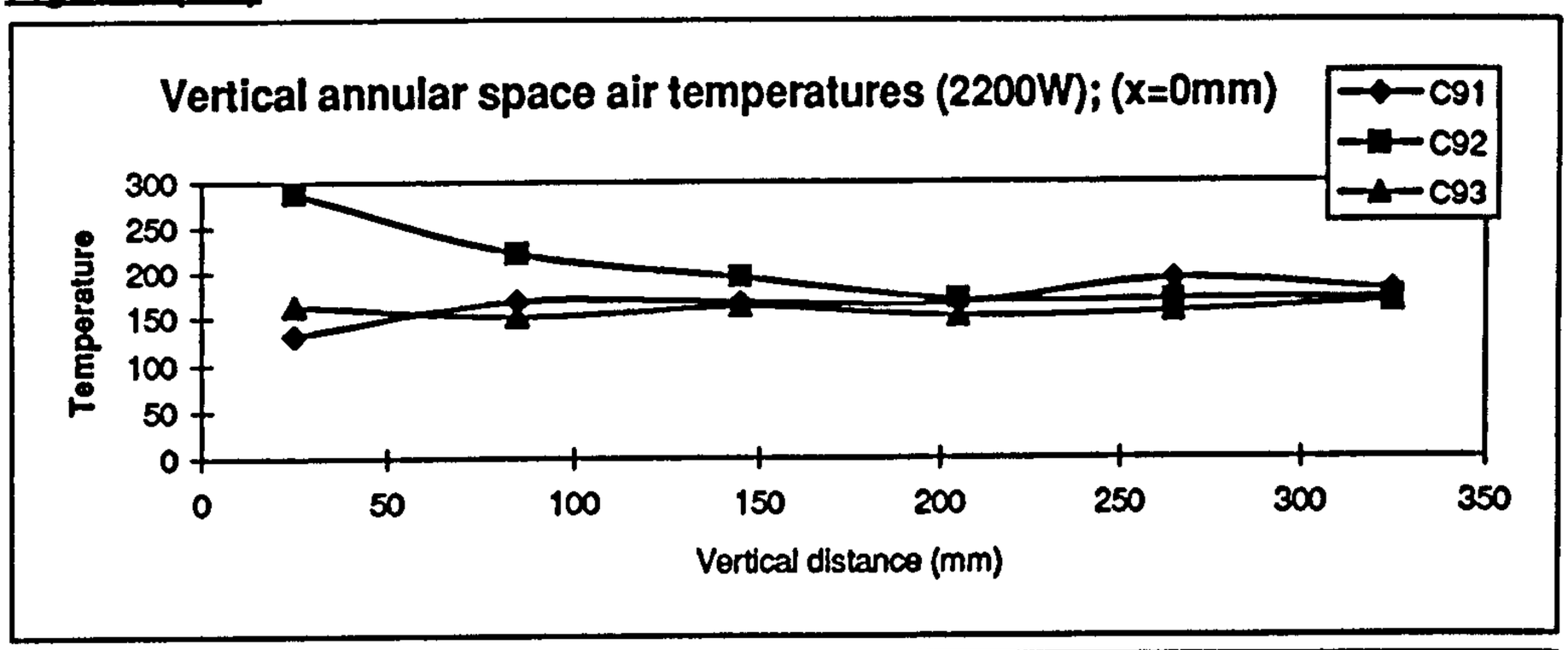
Vertical annular space air temperatures (2200W); (x=0mm)
C91
C92
C93
Temperature
300
250
200
150
100
50
0
0
50
100
150
200
250
300
350
Vertical distance (mm)

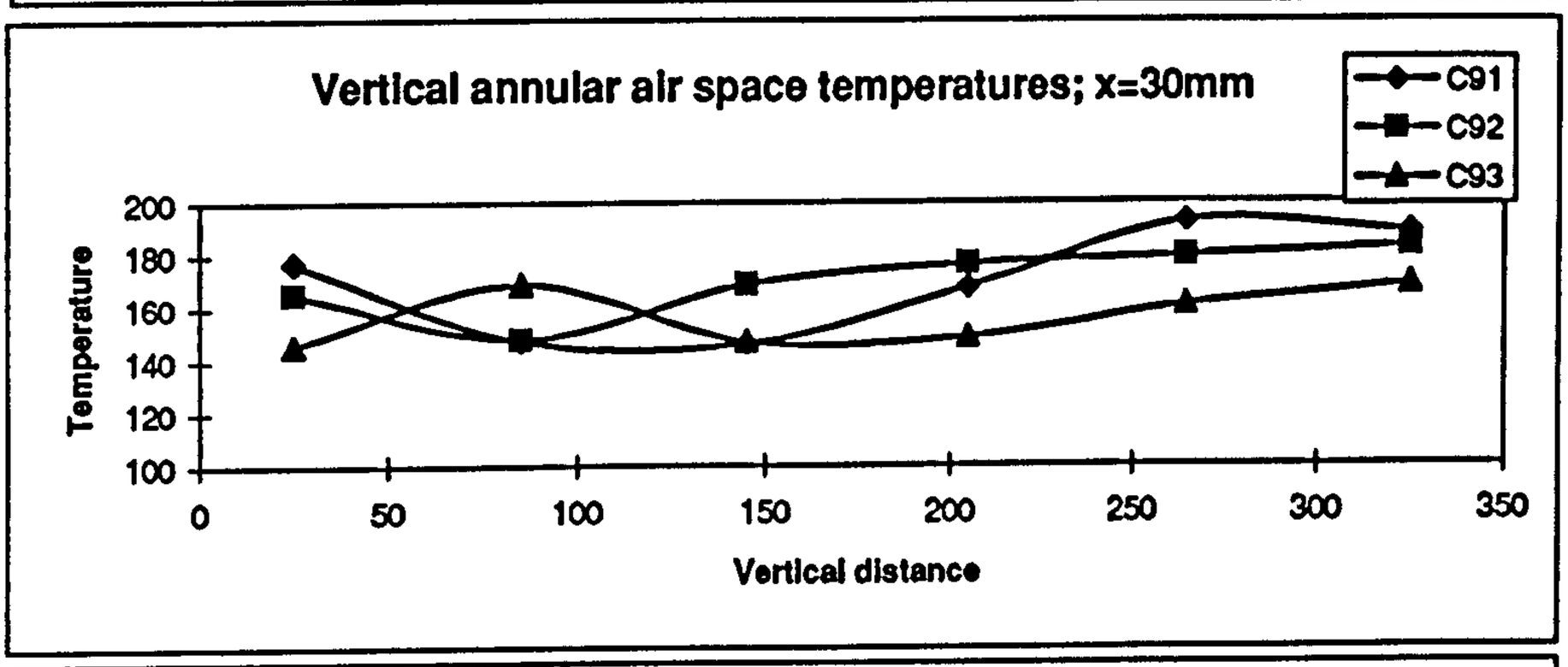
Vertical annular air space temperatures; x=30mm
C91
C92
C93
Temperature
200
180
160
140
120
100
0
50
100
150
200
250
300
350
Vertical distance

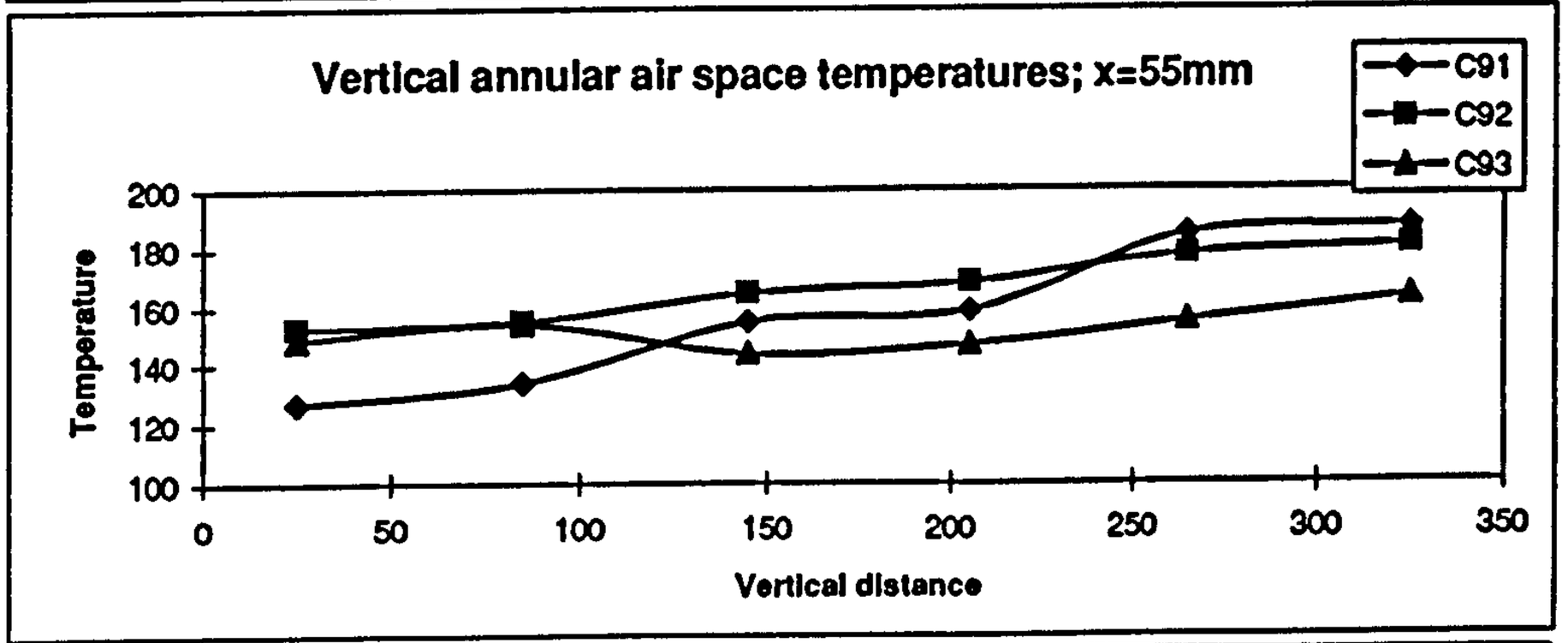
Vertical annular air space temperatures; x=55mm
C91
C92
C93
Temperature
200
180
160
140
120
100
0
50
100
150
200
250
300
350
Vertical distance

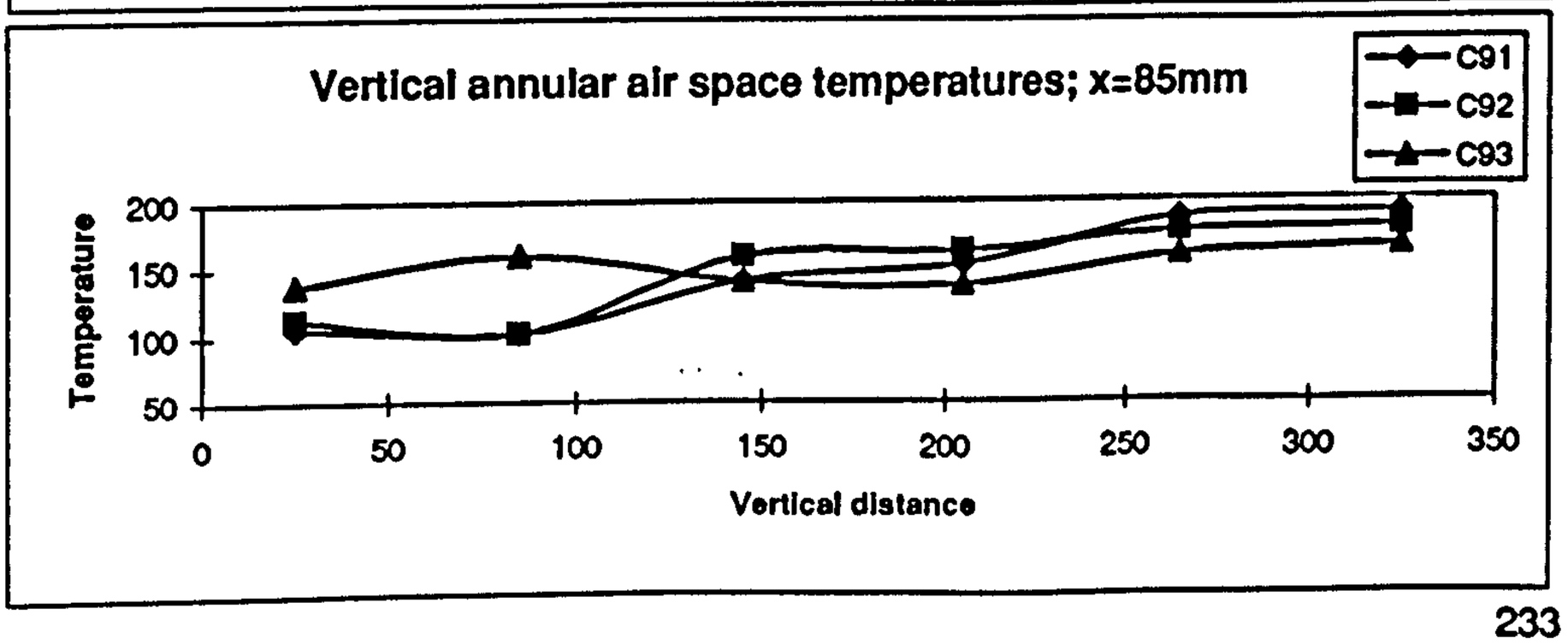
Vertical annular air space temperatures; x=85mm
C91
C92
C93
Temperature
200
150
100
50
0
50
100
150
200
250
300
350
Vertical distance

Fig. 6-17(e-g)

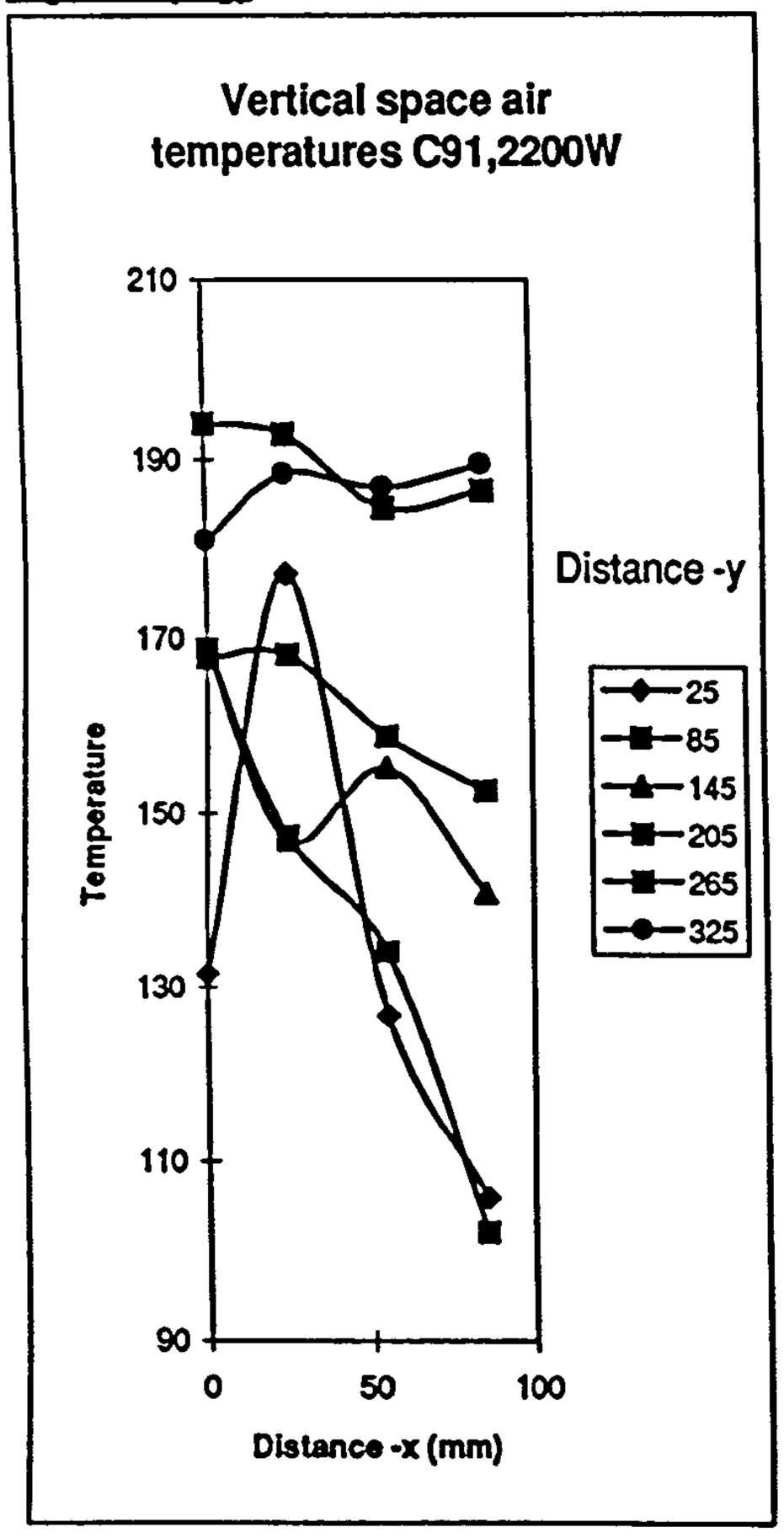
Vertical space air temperatures C91,2200W
210
190
170
150
130
110
90
0
50
100
Temperature
Distance -x (mm)
Distance -y
25
85
145
205
265
325

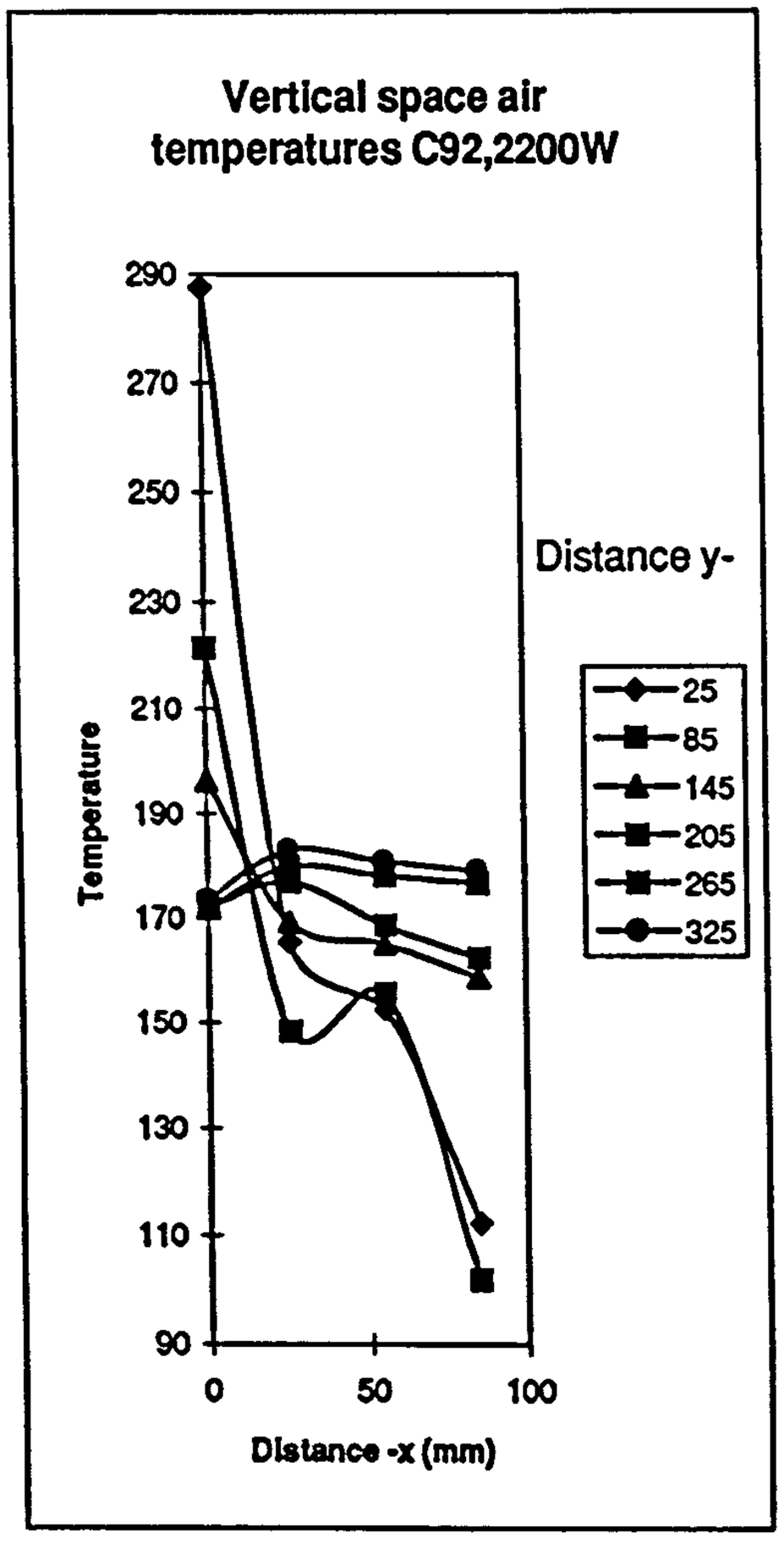
Vertical space air temperatures C92,2200W
290
270
250
230
210
190
170
150
130
110
90
0
50
100
Temperature
Distance -x (mm)
Distance y-
25
85
145
205
265
325

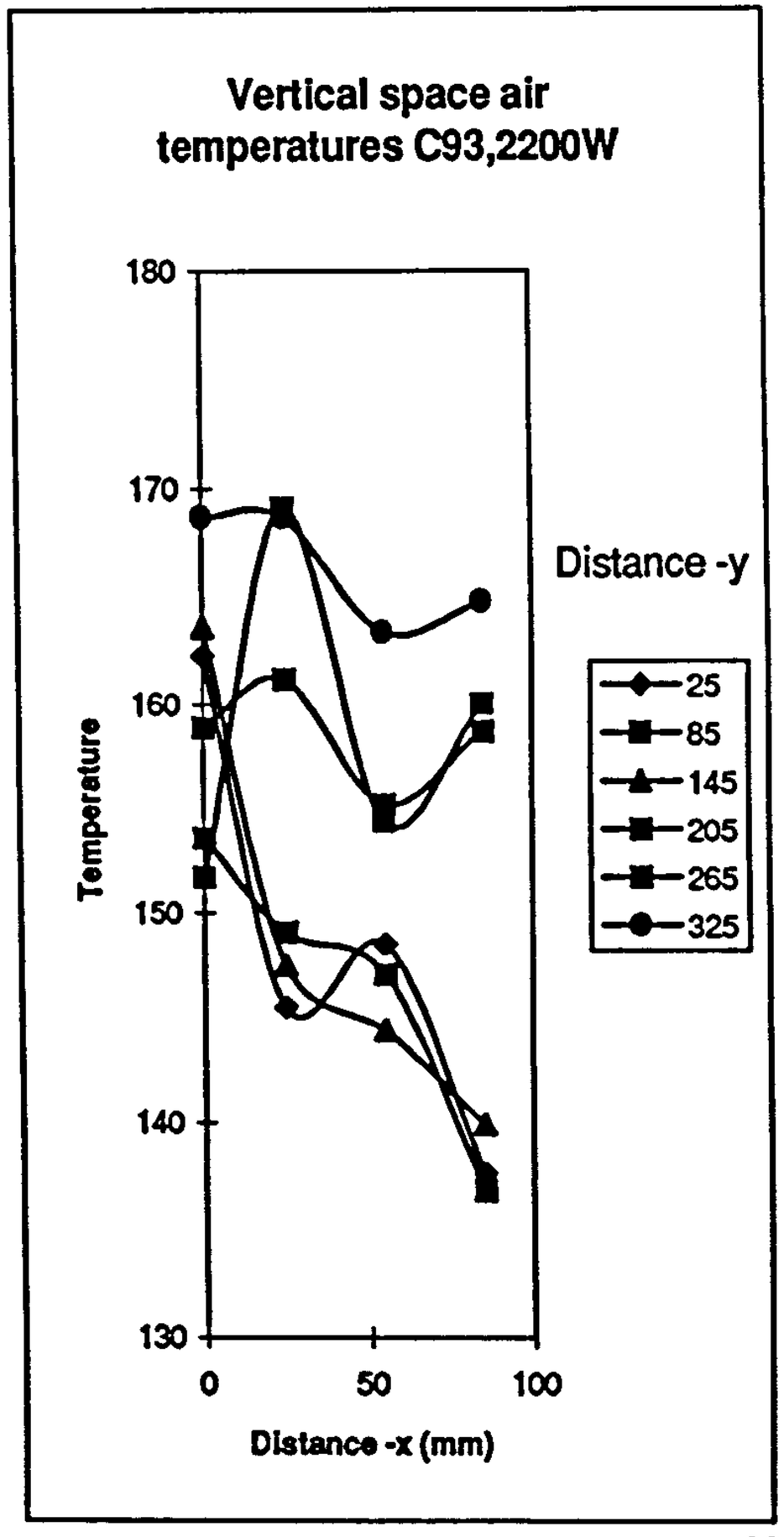
Vertical space air temperatures C93,2200W
180
170
160
150
140
130
0
50
100
Temperature
Distance -x (mm)
Distance -y
25
85
145
205
265
325

Fig. 6-17(h-j)

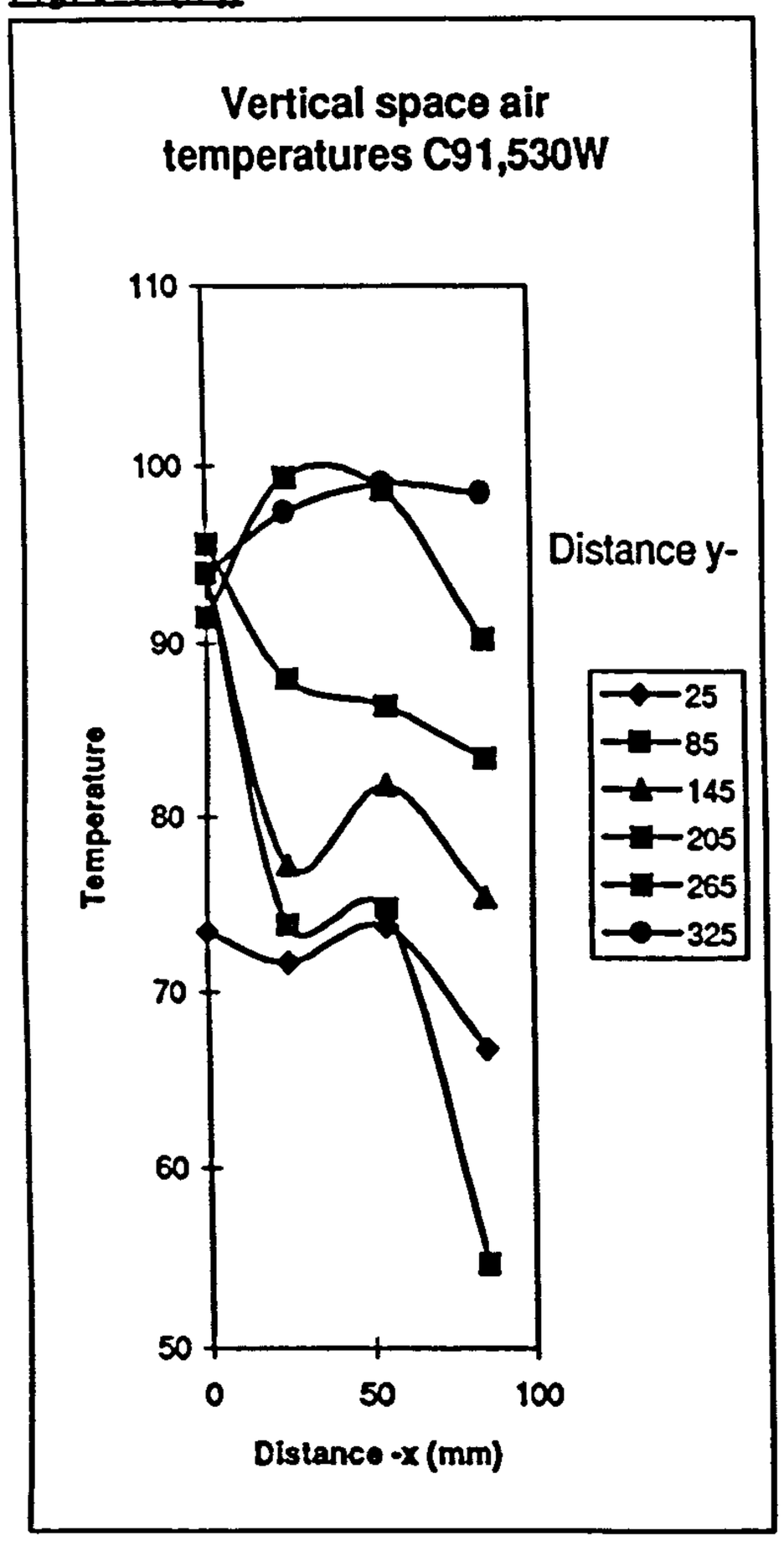
Vertical space air temperatures C91,530W
110
100
90
80
70
60
50
Temperature
0
50
100
Distance -x (mm)
Distance y-
25
85
145
205
265
325

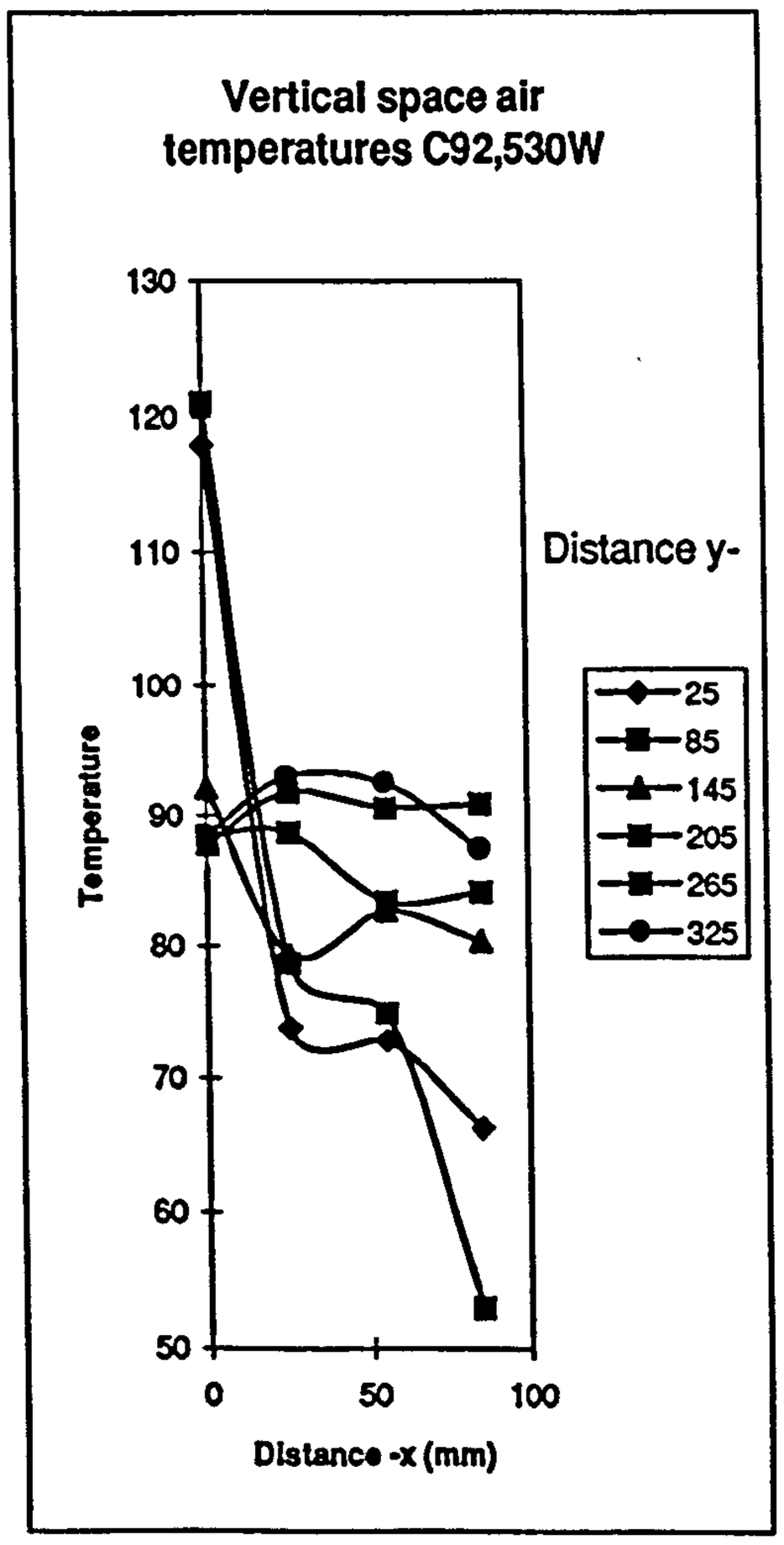
Vertical space air temperatures C92,530W
130
120
110
100
90
80
70
60
50
Temperature
0
50
100
Distance -x (mm)
Distance y-
25
85
145
205
265
325

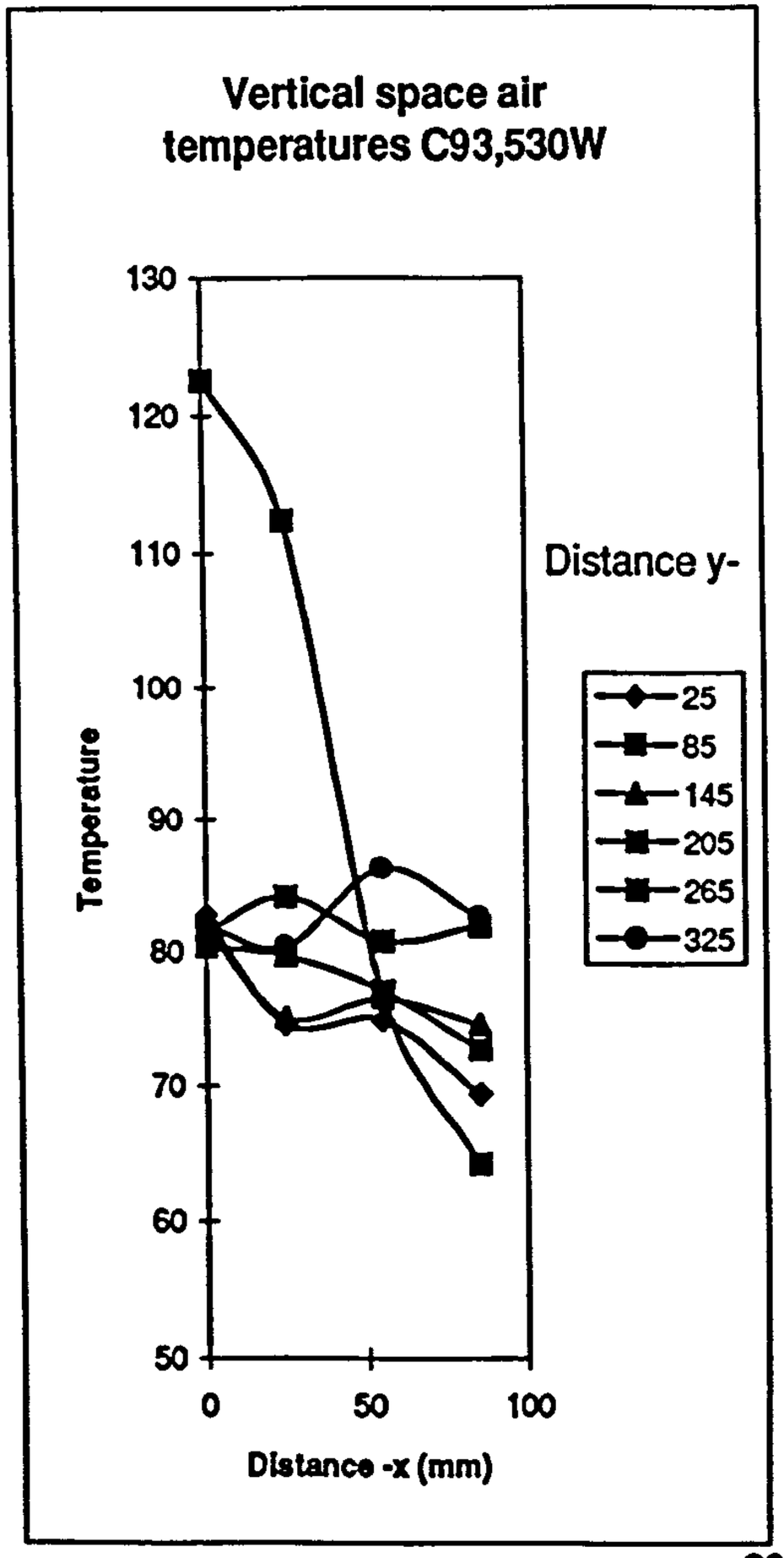
Vertical space air temperatures C93,530W
130
120
110
100
90
80
70
60
50
Temperature
0
50
100
Distance -x (mm)
Distance y-
25
85
145
205
265
325

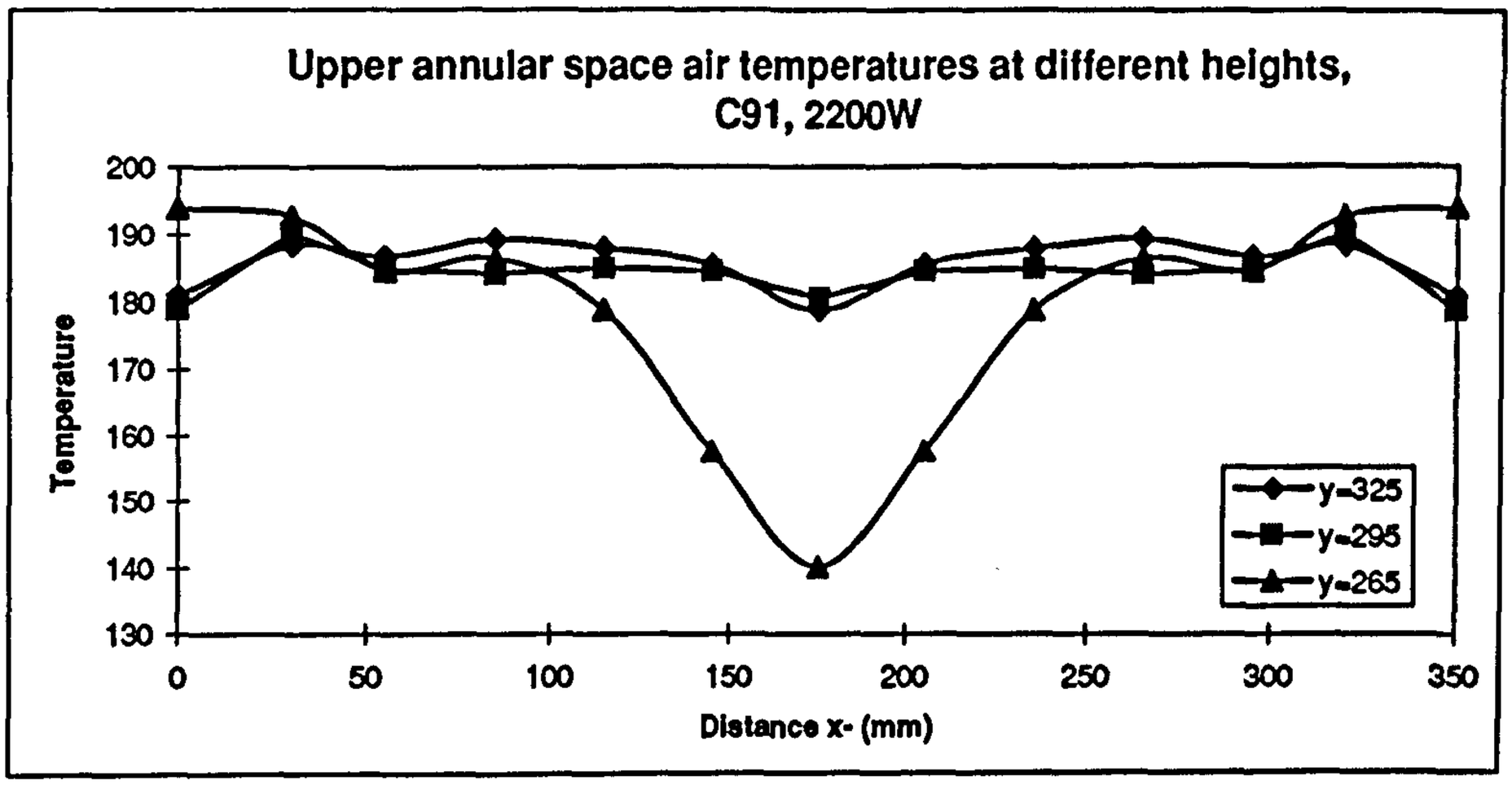
Upper annular space air temperatures at different heights,
C91, 2200W
Temperature
200
190
180
170
160
150
140
130
0
50
100
150
200
250
300
350
Distance x- (mm)
y-325
y-295
y-265

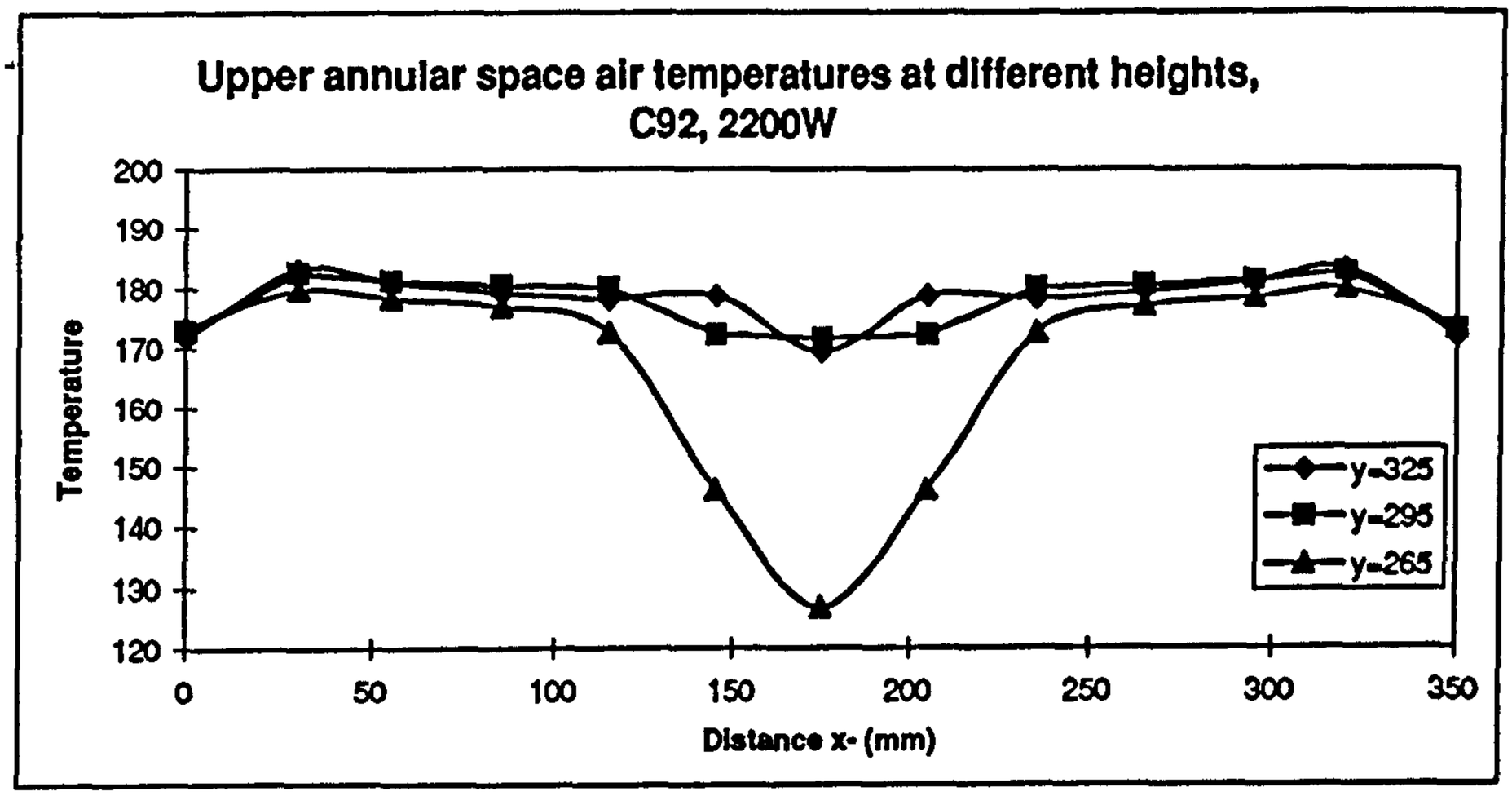
Upper annular space air temperatures at different heights,
C92, 2200W
Temperature
200
190
180
170
160
150
140
130
120
0
50
100
150
200
250
300
350
Distance x- (mm)
y-325
y-295
y-265

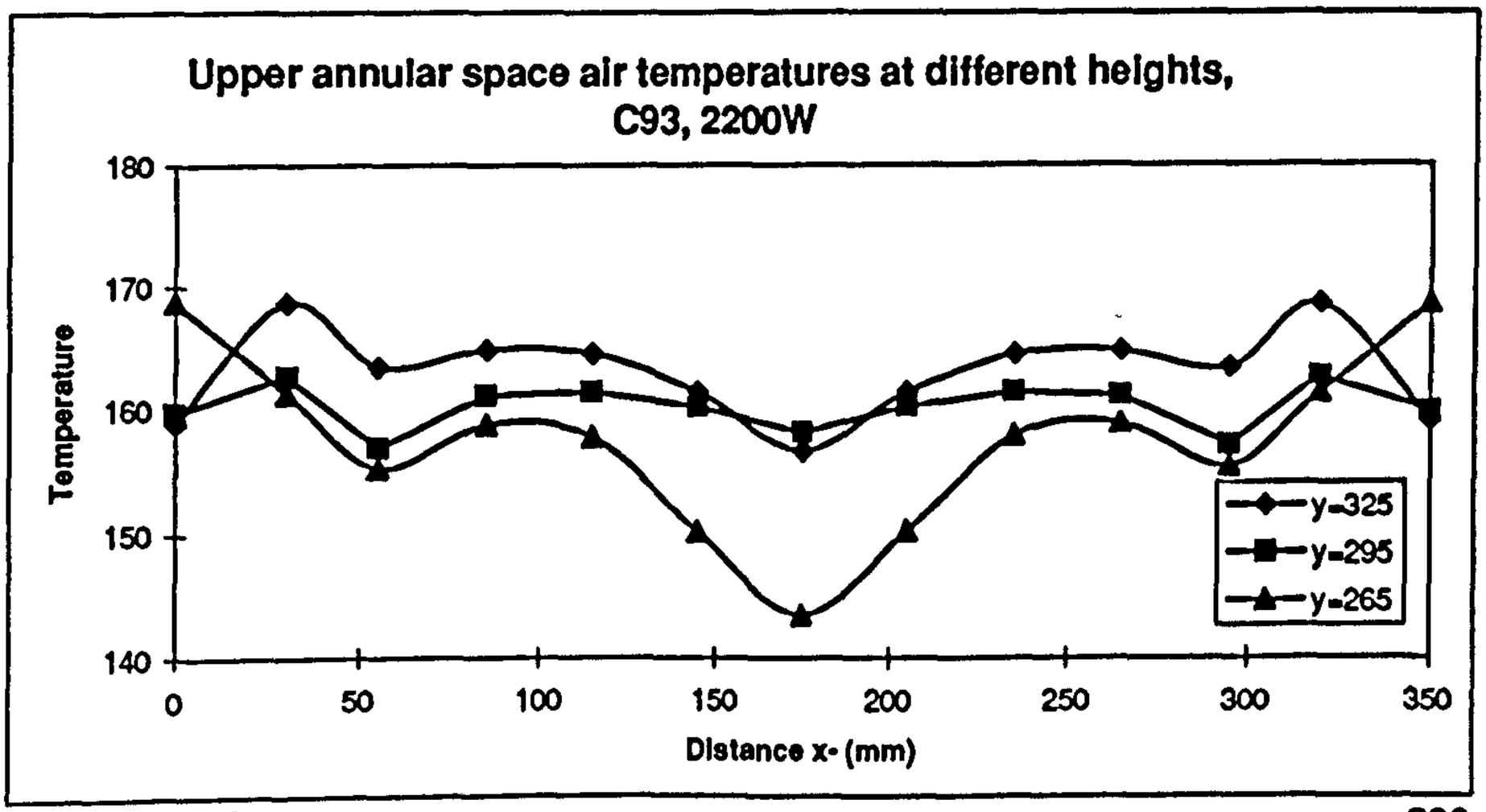
Upper annular space air temperatures at different heights,
C93, 2200W
Temperature
180
170
160
150
140
0
50
100
150
200
250
300
350
Distance x- (mm)
y-325
y-295
y-265

Fig. 6-18(a-c)

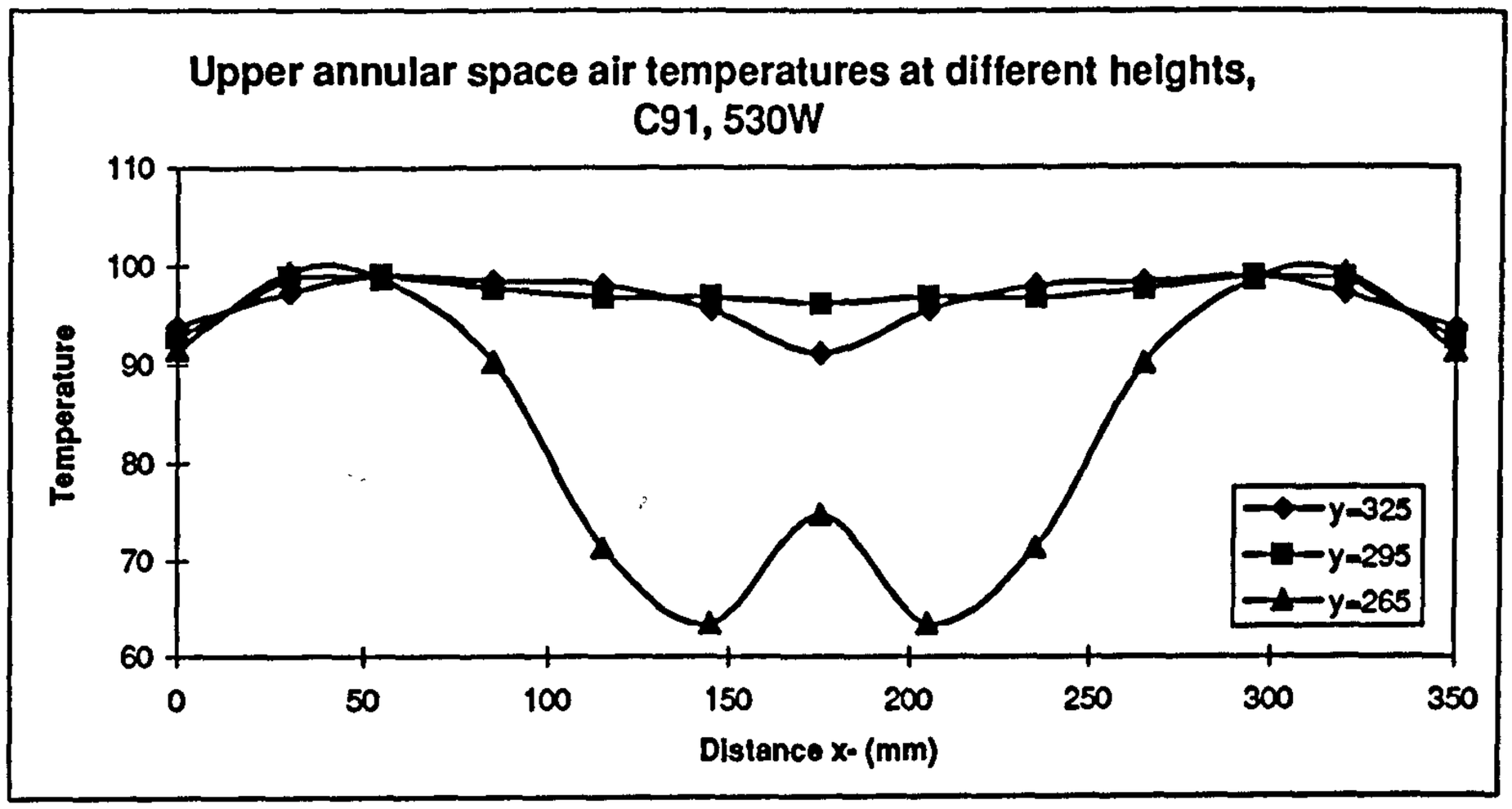
Upper annular space air temperatures at different heights,
C91, 530W
Temperature
110
100
90
80
70
60
0
50
100
150
200
250
300
350
Distance x- (mm)
y=325
y=295
y=265

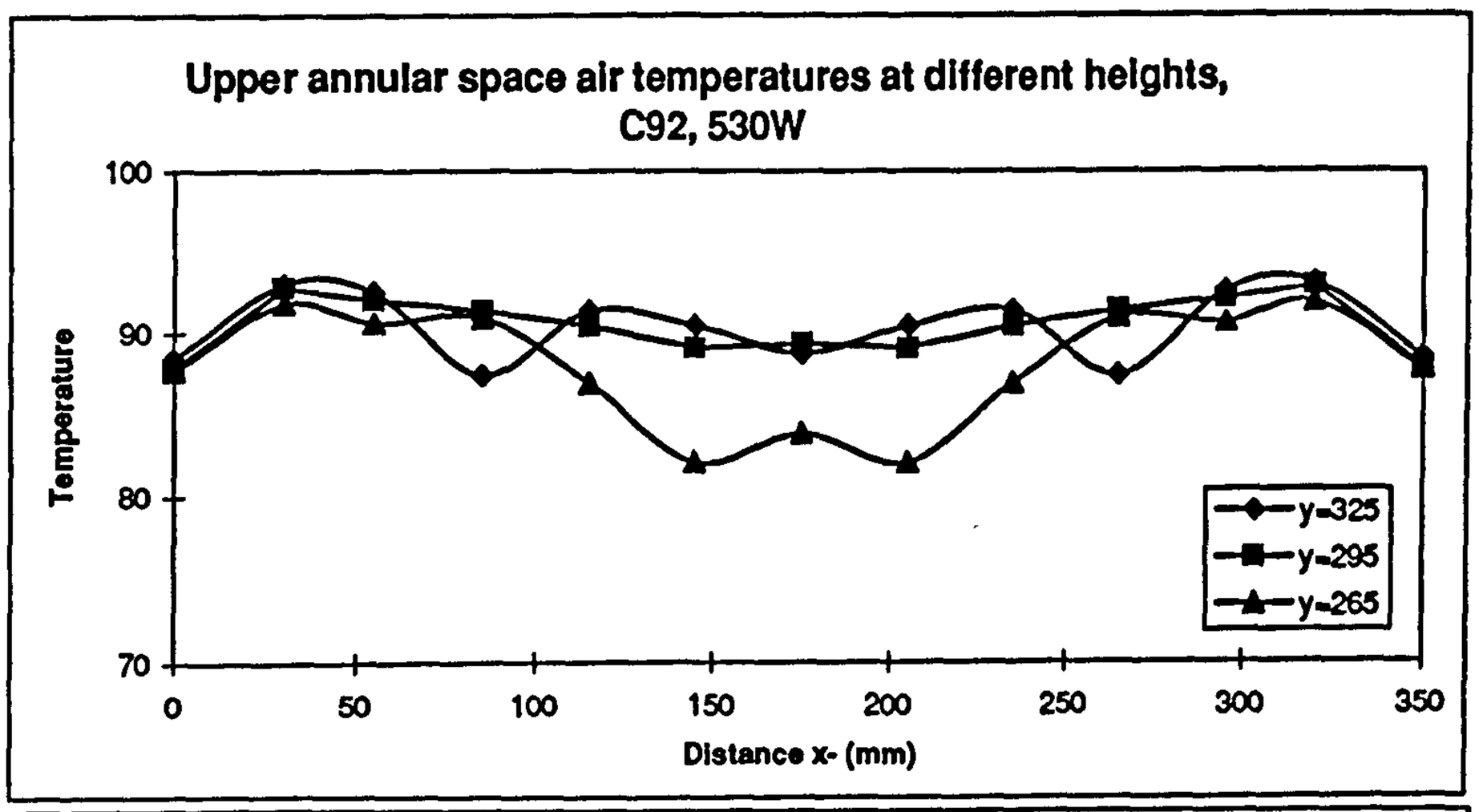
Upper annular space air temperatures at different heights,
C92, 530W
Temperature
100
90
80
70
0
50
100
150
200
250
300
350
Distance x- (mm)
y=325
y=295
y=265

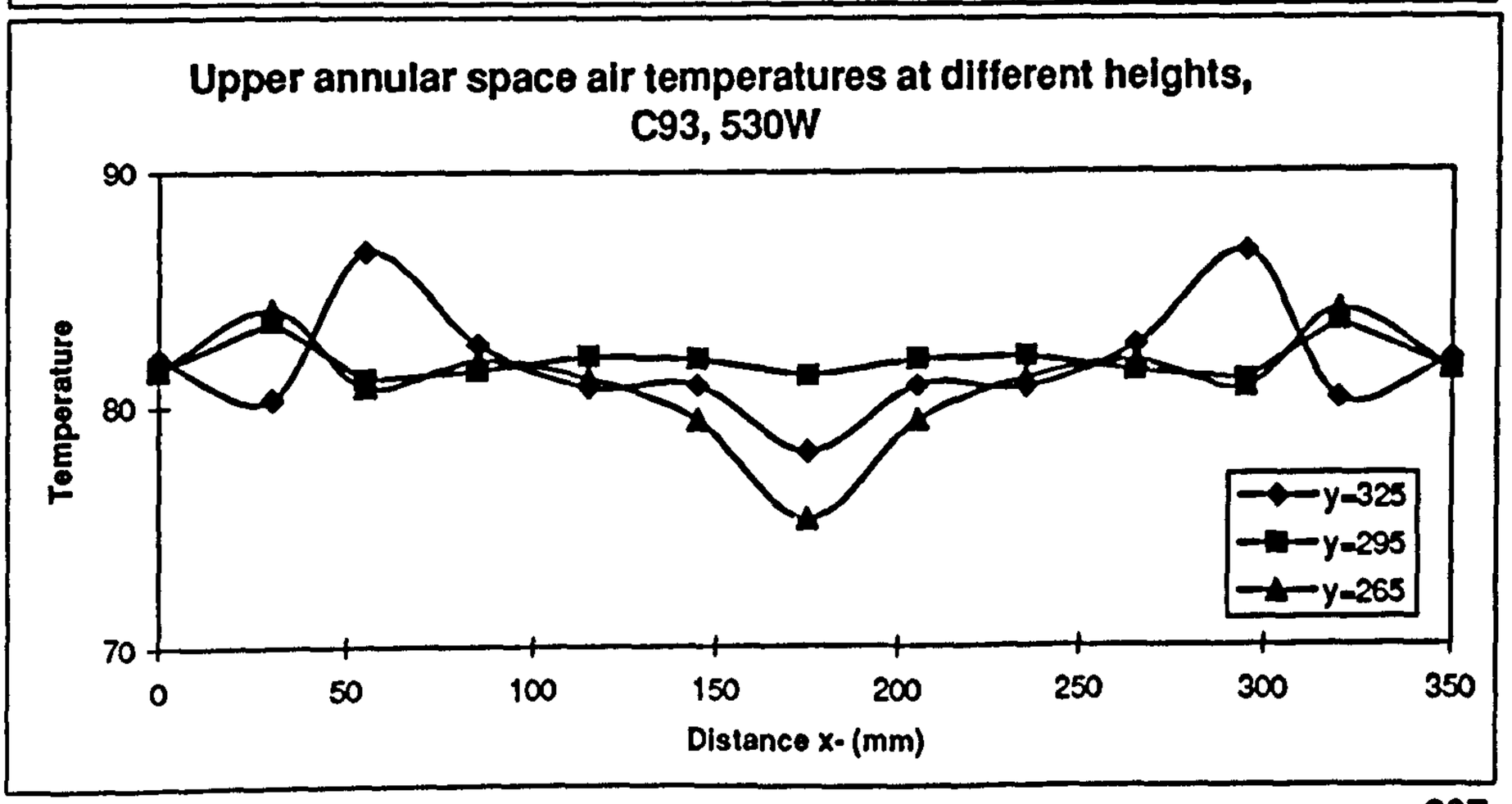
Upper annular space air temperatures at different heights,
C93, 530W
Temperature
90
80
70
0
50
100
150
200
250
300
350
Distance x- (mm)
y=325
y=295
y=265

Fig. 6-18(d-f)

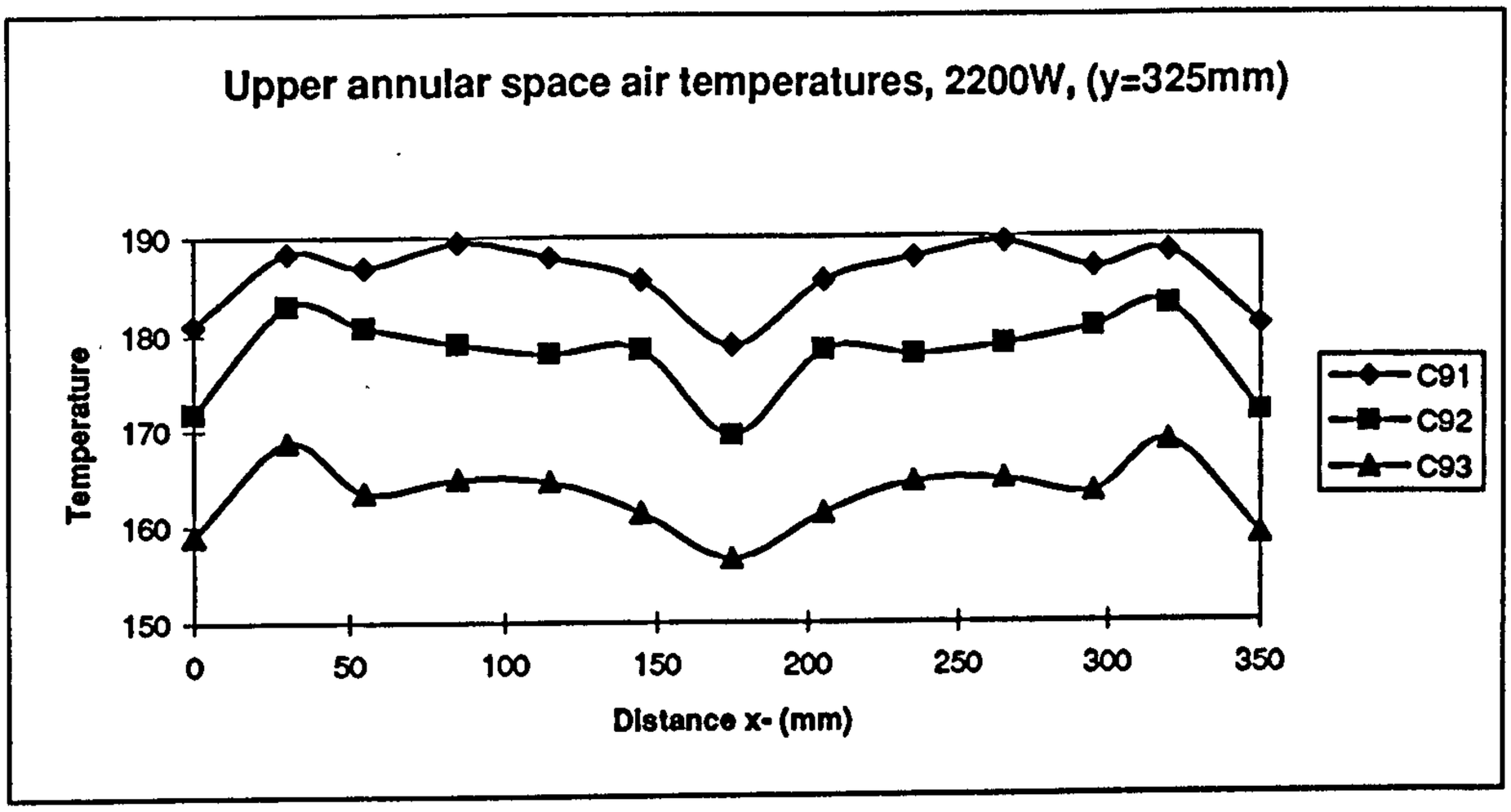
Upper annular space air temperatures, 2200W, (y=325mm)
Temperature
190
180
170
160
150
0
50
100
150
200
250
300
350
Distance x- (mm)
C91
C92
C93

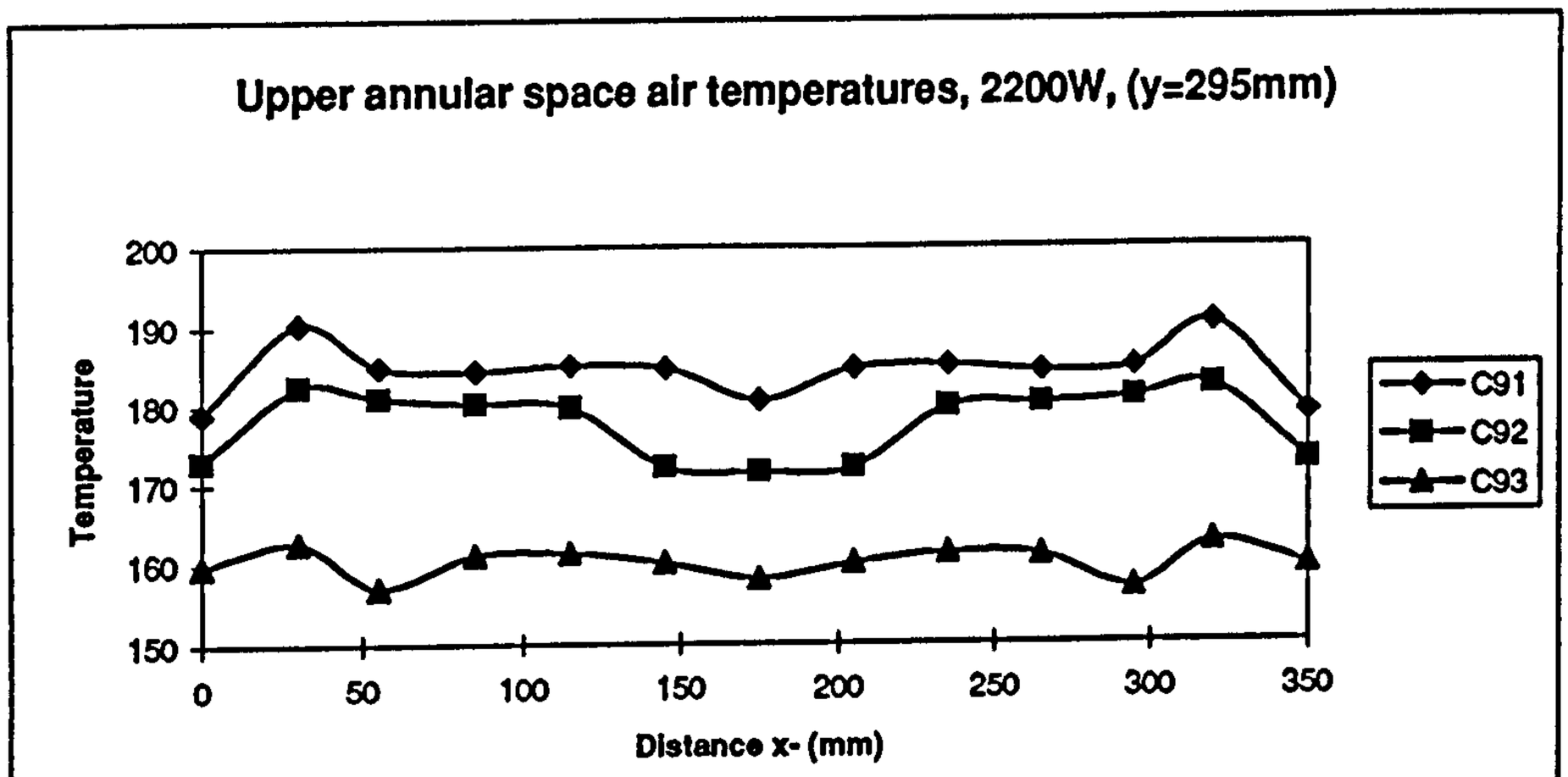
Upper annular space air temperatures, 2200W, (y=295mm)
Temperature
200
190
180
170
160
150
0
50
100
150
200
250
300
350
Distance x- (mm)
C91
C92
C93

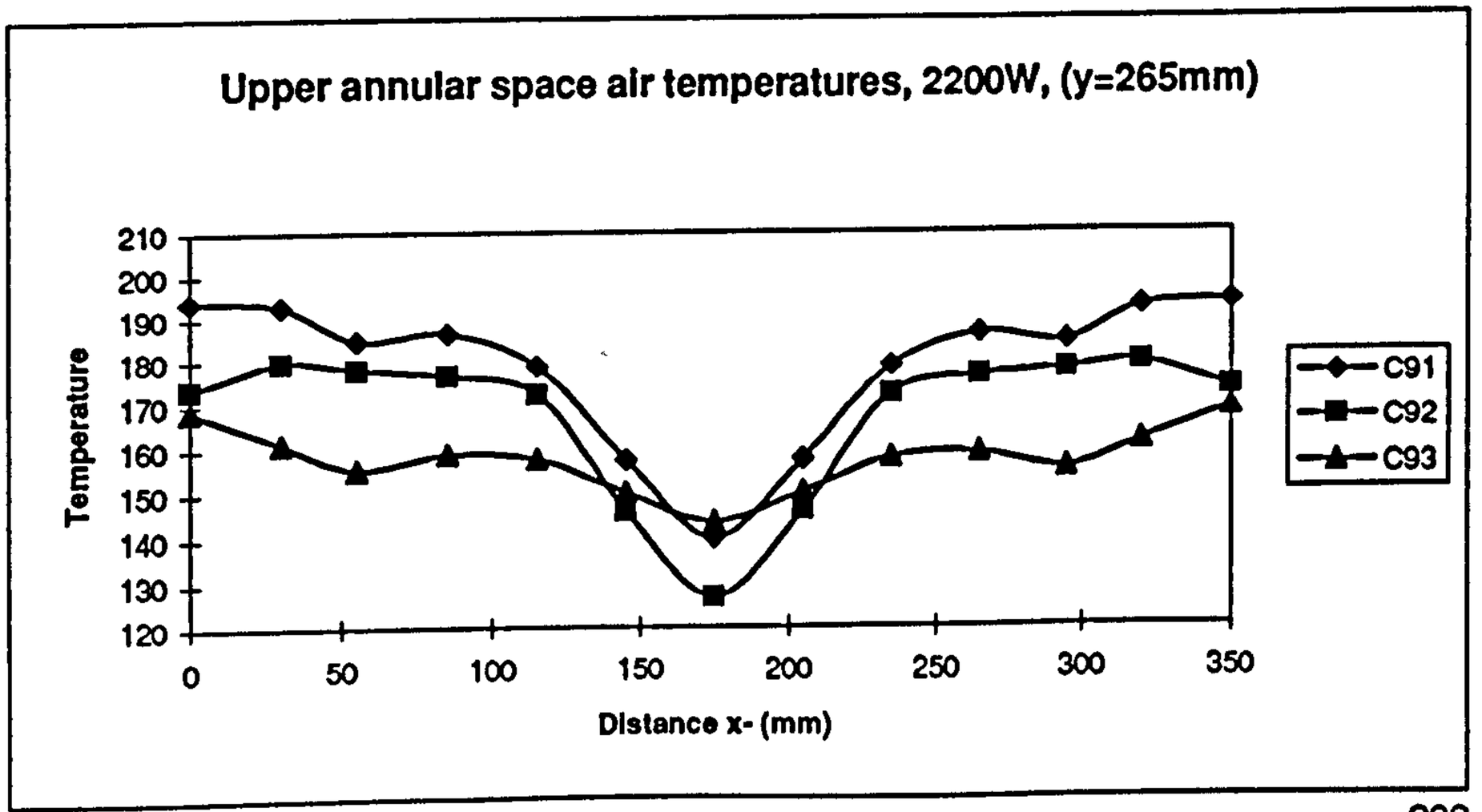
Upper annular space air temperatures, 2200W, (y=265mm)
Temperature
210
200
190
180
170
160
150
140
130
120
0
50
100
150
200
250
300
350
Distance x- (mm)
C91
C92
C93

Fig. 6-18(g-i)

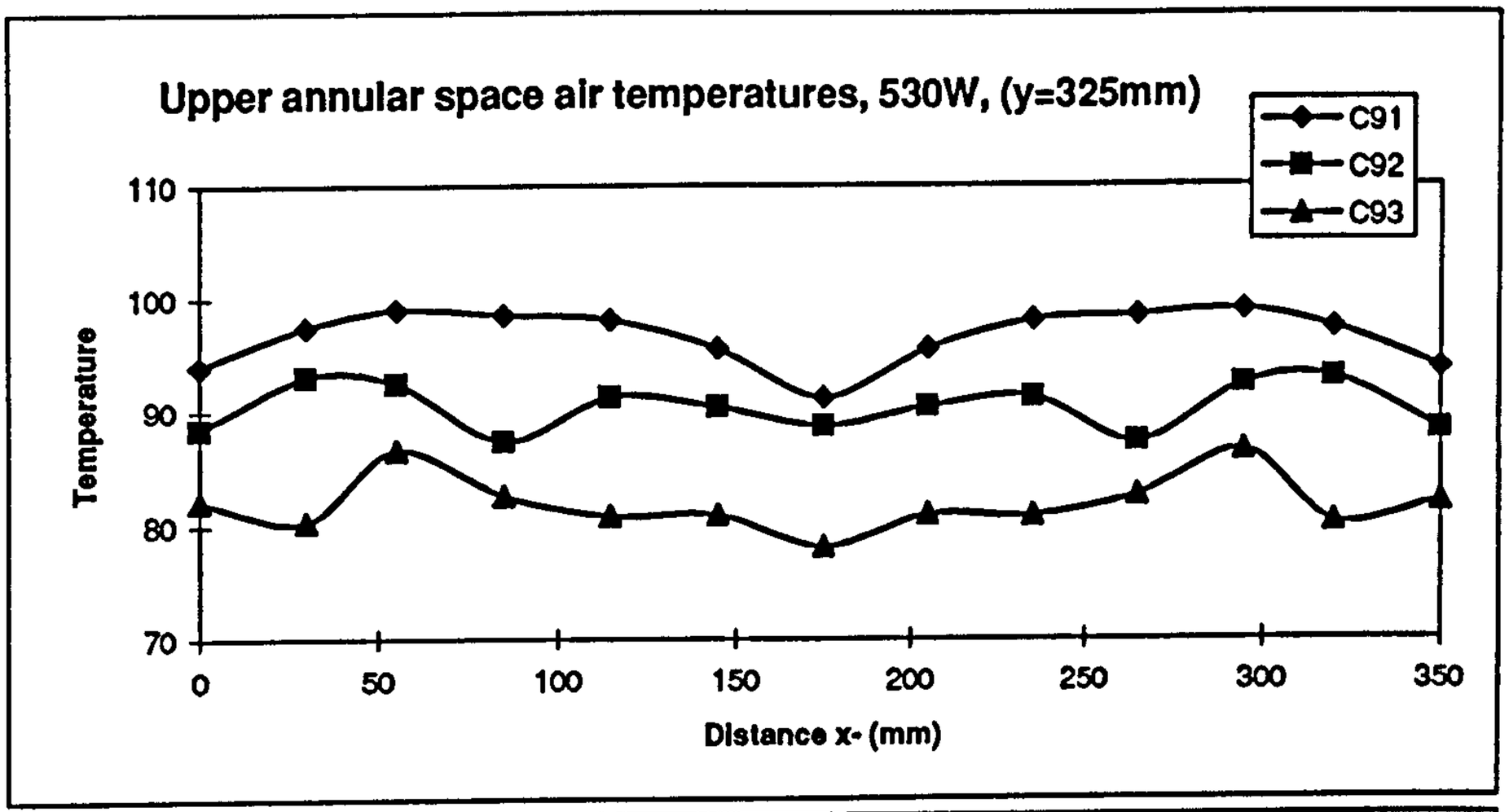
Upper annular space air temperatures, 530W, (y=325mm)
C91
C92
C93
Temperature
110
100
90
80
70
0
50
100
150
200
250
300
350
Distance x- (mm)

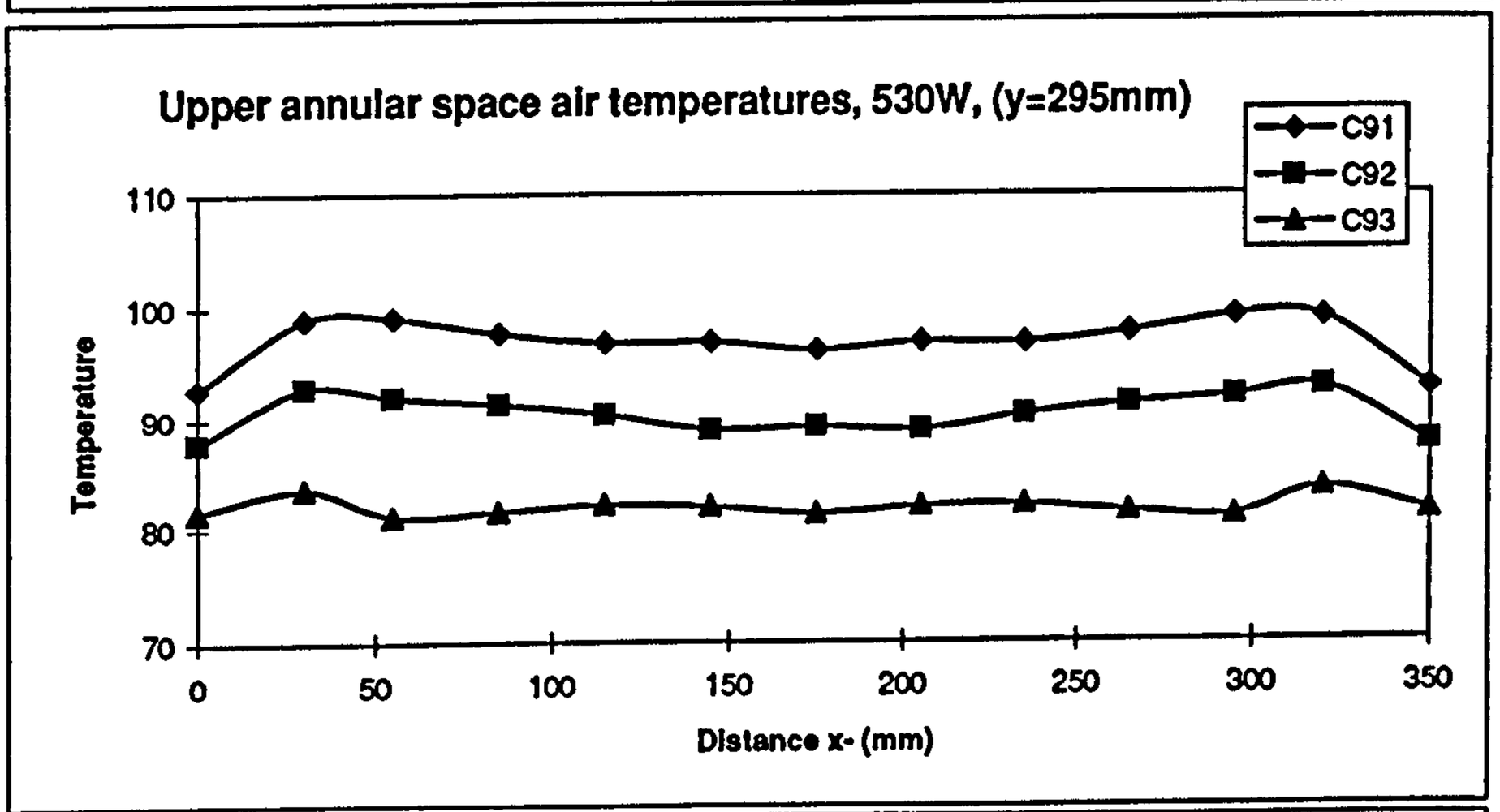
Upper annular space air temperatures, 530W, (y=295mm)
C91
C92
C93
Temperature
110
100
90
80
70
0
50
100
150
200
250
300
350
Distance x- (mm)

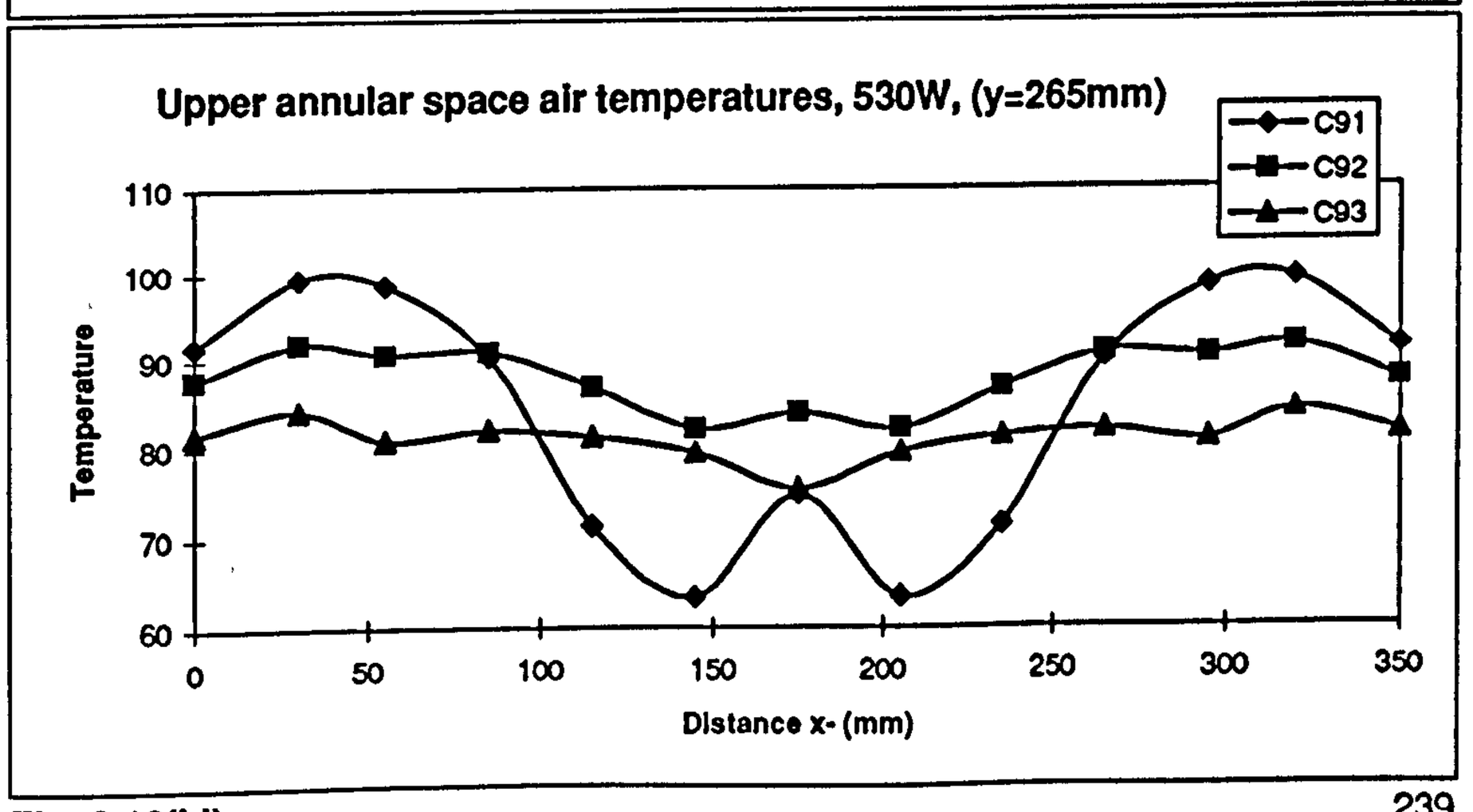
Upper annular space air temperatures, 530W, (y=265mm)
C91
C92
C93
Temperature
110
100
90
80
70
60
0
50
100
150
200
250
300
350
Distance x- (mm)

Fig. 6-18(j-l)

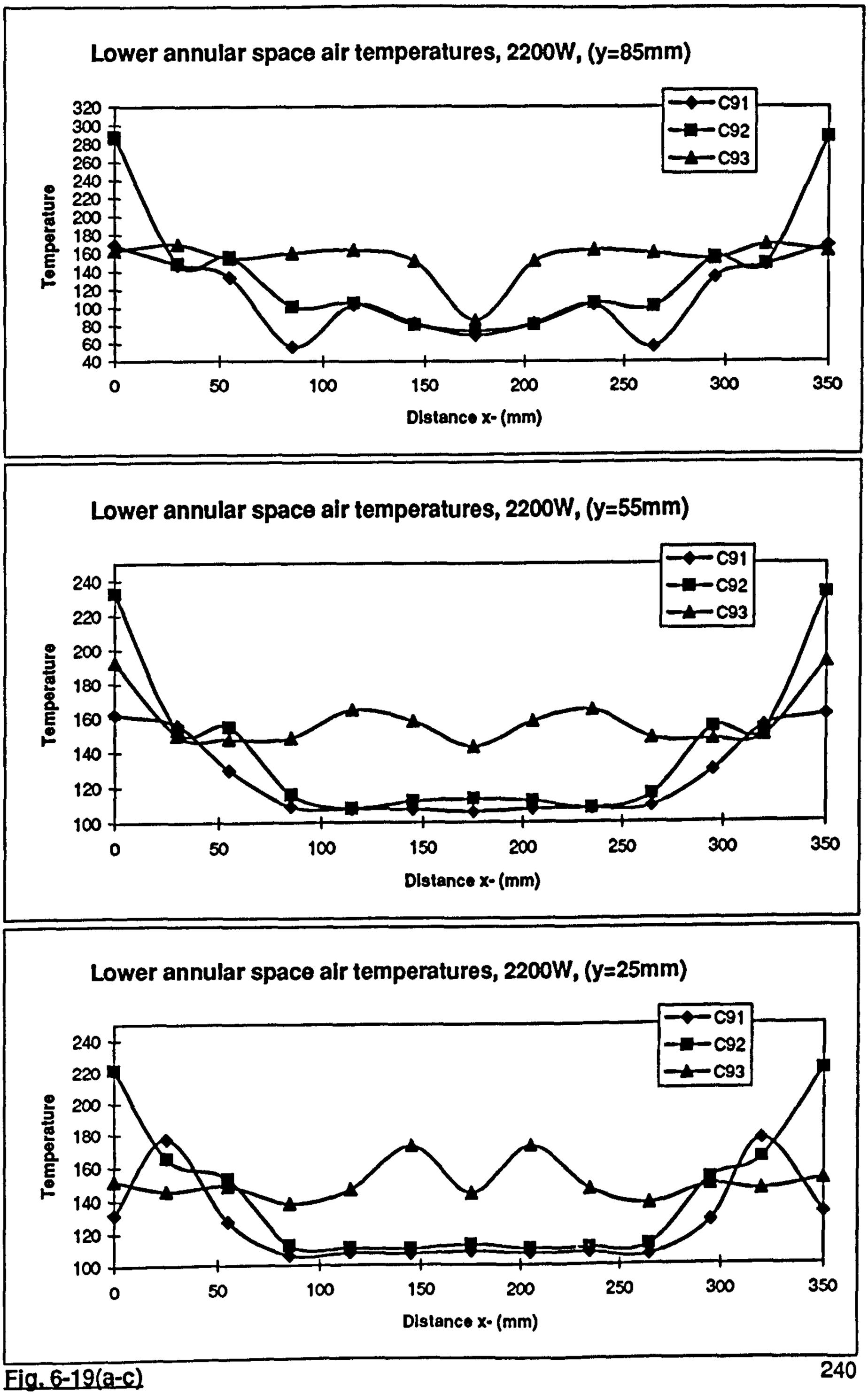
Lower annular space air temperatures, 2200W, (y=85mm)
C91
C92
C93
Temperature
320
300
280
260
240
220
200
180
160
140
120
100
80
60
40
0
50
100
150
200
250
300
350
Distance x- (mm)
Lower annular space air temperatures, 2200W, (y=55mm)
C91
C92
C93
Temperature
240
220
200
180
160
140
120
100
0
50
100
150
200
250
300
350
Distance x- (mm)
Lower annular space air temperatures, 2200W, (y=25mm)
C91
C92
C93
Temperature
240
220
200
180
160
140
120
100
0
50
100
150
200
250
300
350
Distance x- (mm)

Fig. 6-19(a-c)

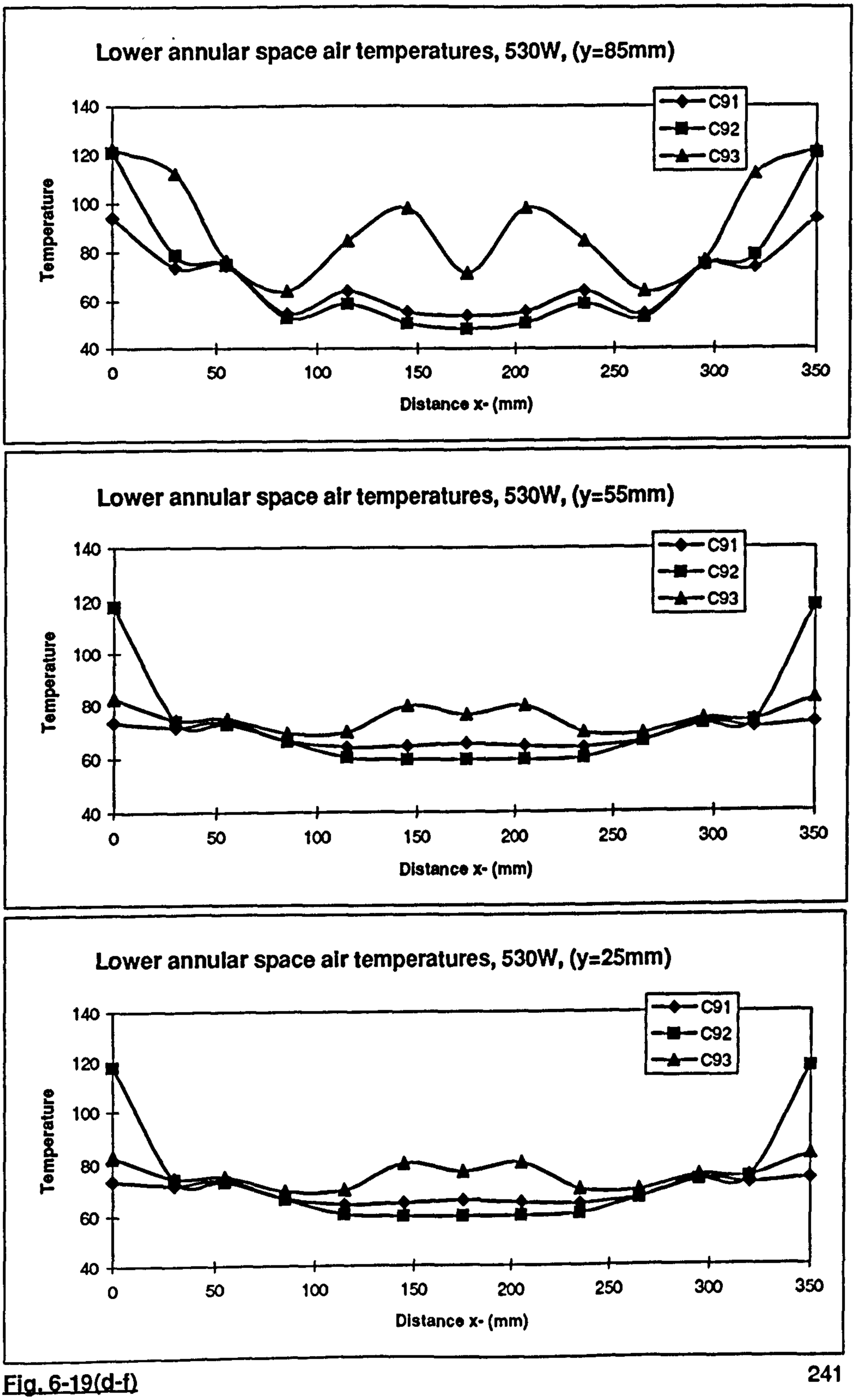
Lower annular space air temperatures, 530W, (y=85mm)
C91
C92
C93
Temperature
140
120
100
80
60
40
0
50
100
150
200
250
300
350
Distance x- (mm)
Lower annular space air temperatures, 530W, (y=55mm)
C91
C92
C93
Temperature
140
120
100
80
60
40
0
50
100
150
200
250
300
350
Distance x- (mm)
Lower annular space air temperatures, 530W, (y=25mm)
C91
C92
C93
Temperature
140
120
100
80
60
40
0
50
100
150
200
250
300
350
Distance x- (mm)

Fig. 6-19(d-f)

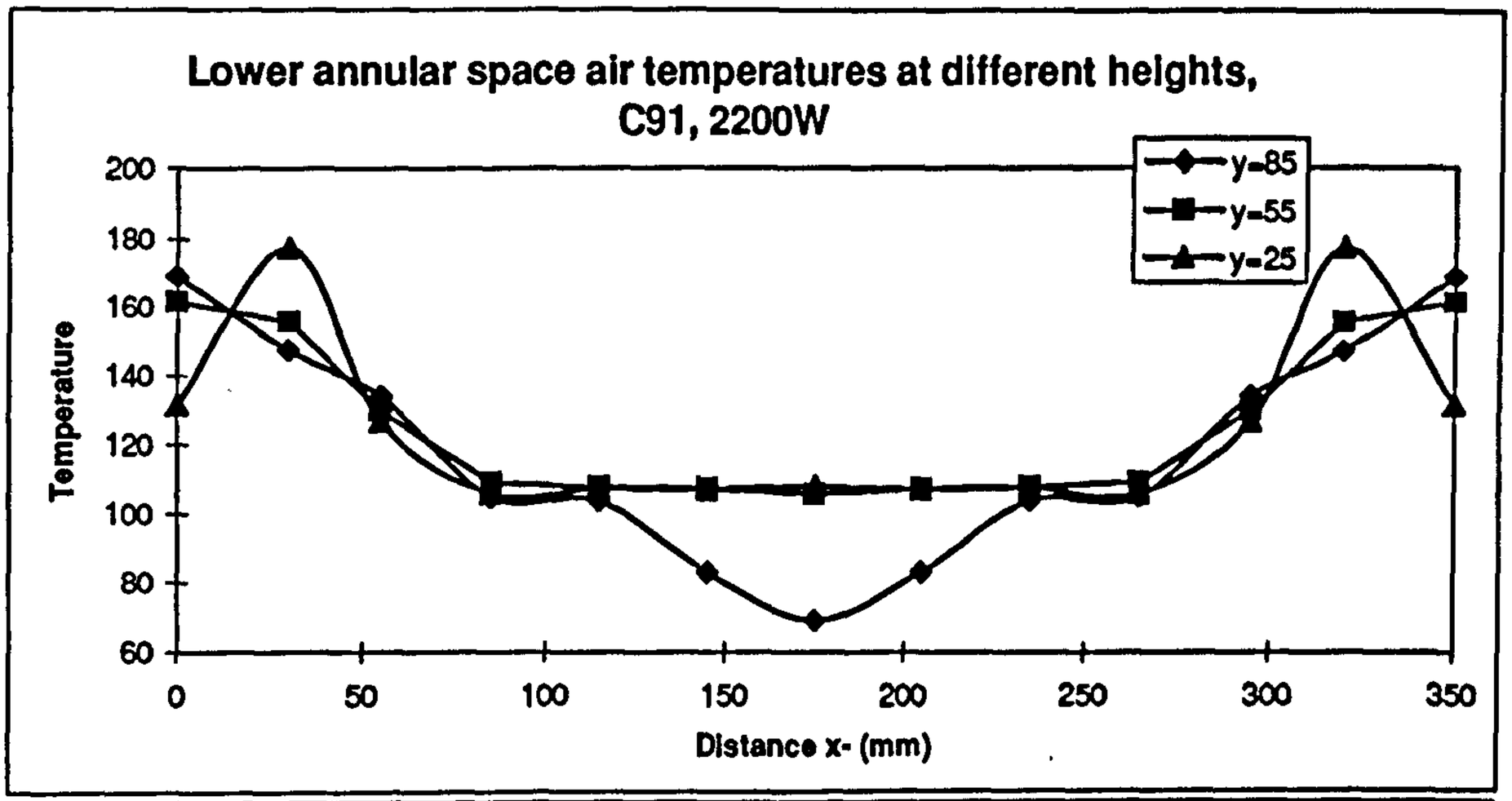
Lower annular space air temperatures at different heights,
C91, 2200W
y-85
y-55
y-25
Temperature
200
180
160
140
120
100
80
60
0
50
100
150
200
250
300
350
Distance x- (mm)

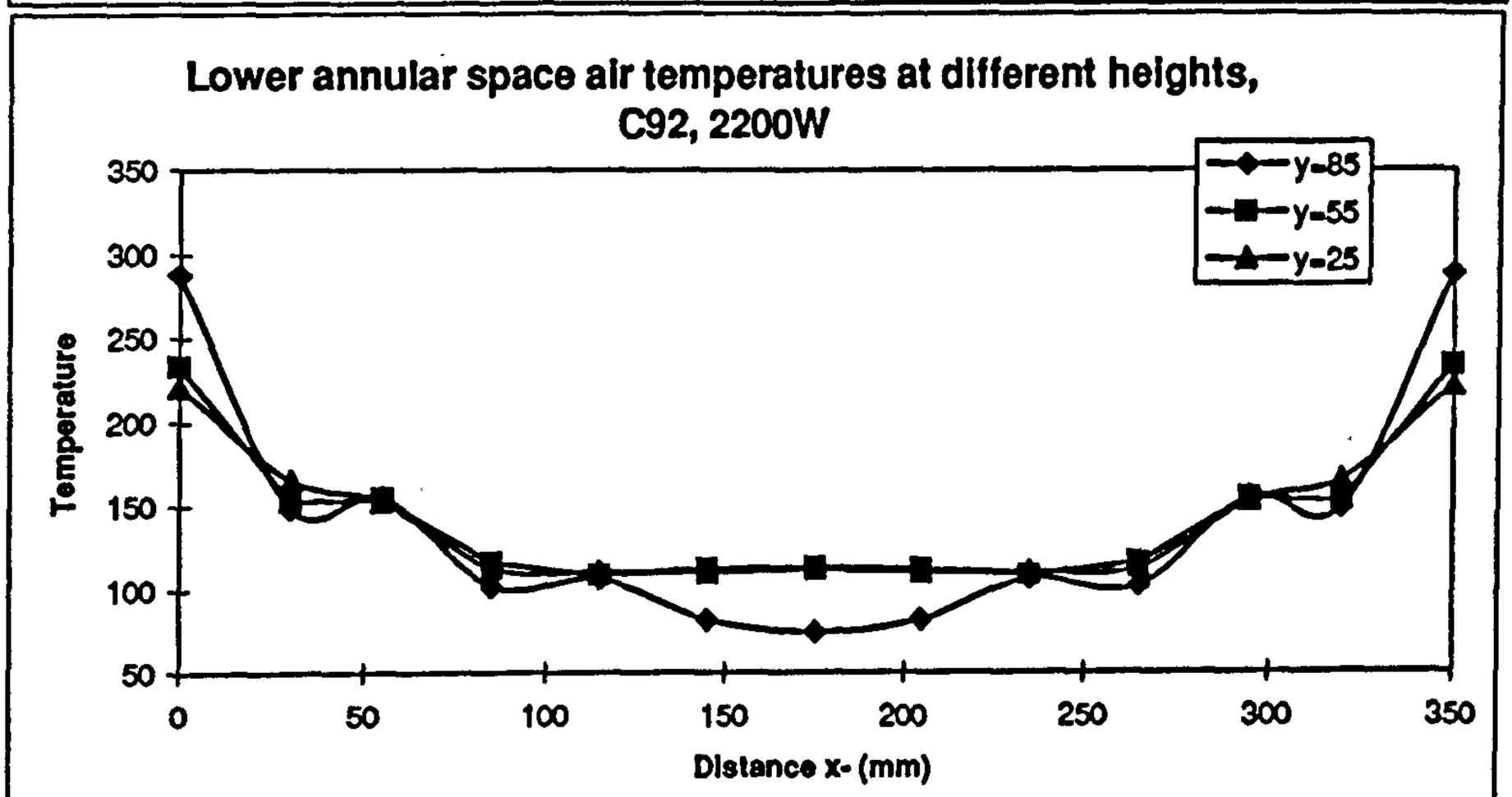
Lower annular space air temperatures at different heights,
C92, 2200W
y-85
y-55
y-25
Temperature
350
300
250
200
150
100
50
0
50
100
150
200
250
300
350
Distance x- (mm)

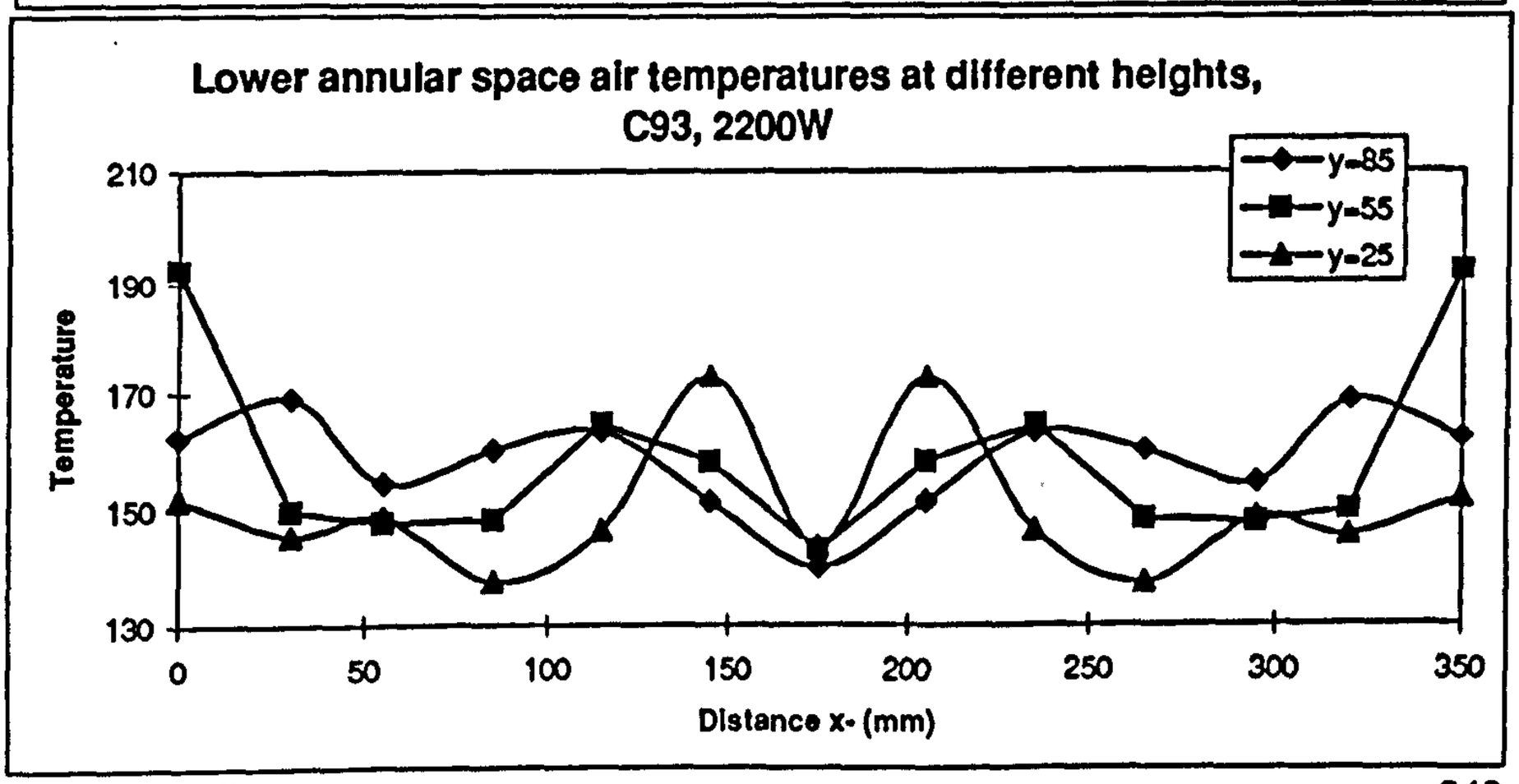
Lower annular space air temperatures at different heights,
C93, 2200W
y-85
y-55
y-25
Temperature
210
190
170
150
130
0
50
100
150
200
250
300
350
Distance x- (mm)

Fig. 6-19(g-i)

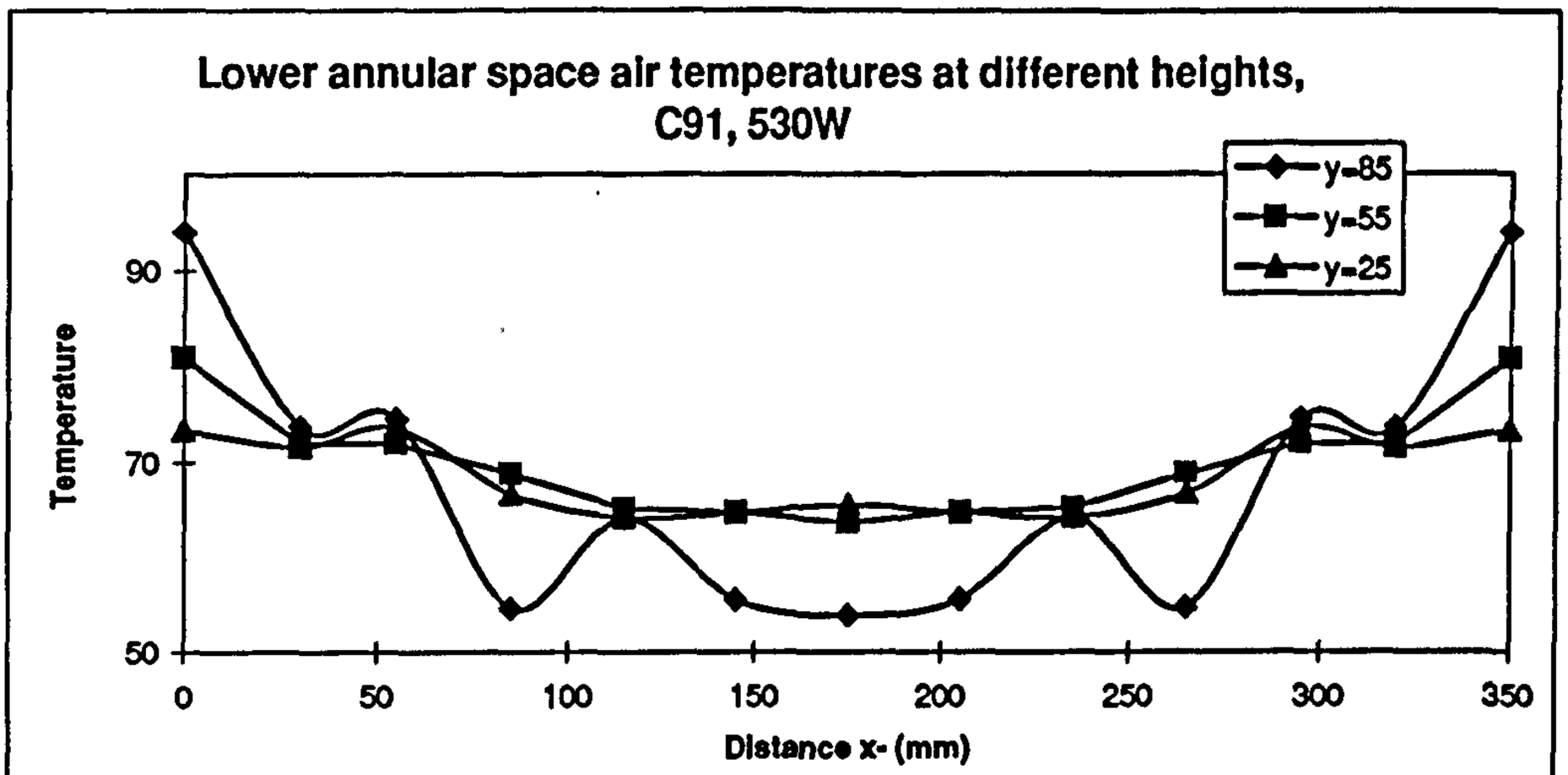
Lower annular space air temperatures at different heights,
C91, 530W
y-85
y-55
y-25
Temperature
90
70
50
0
50
100
150
200
250
300
350
Distance x- (mm)

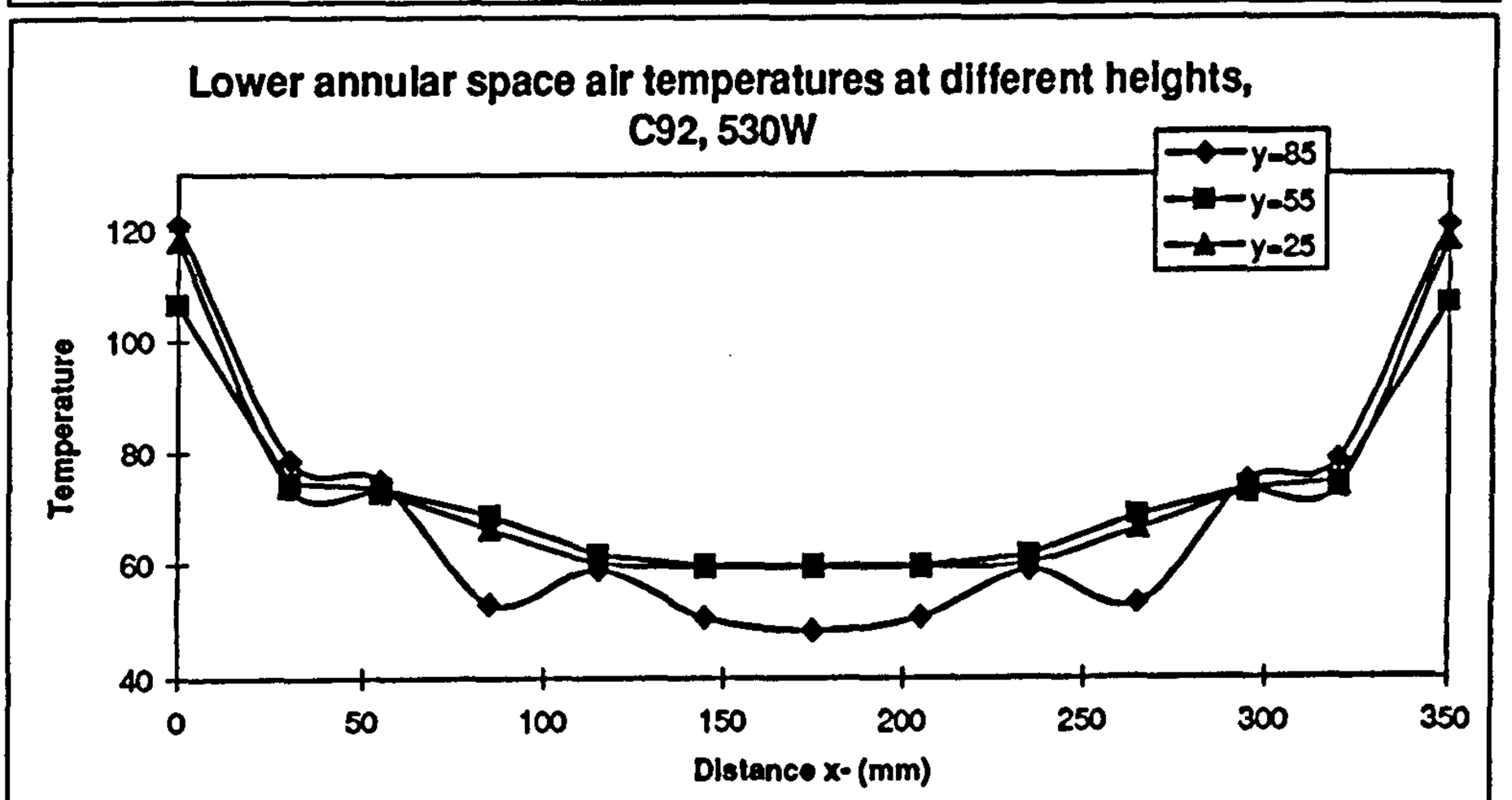
Lower annular space air temperatures at different heights,
C92, 530W
y-85
y-55
y-25
Temperature
120
100
80
60
40
0
50
100
150
200
250
300
350
Distance x- (mm)

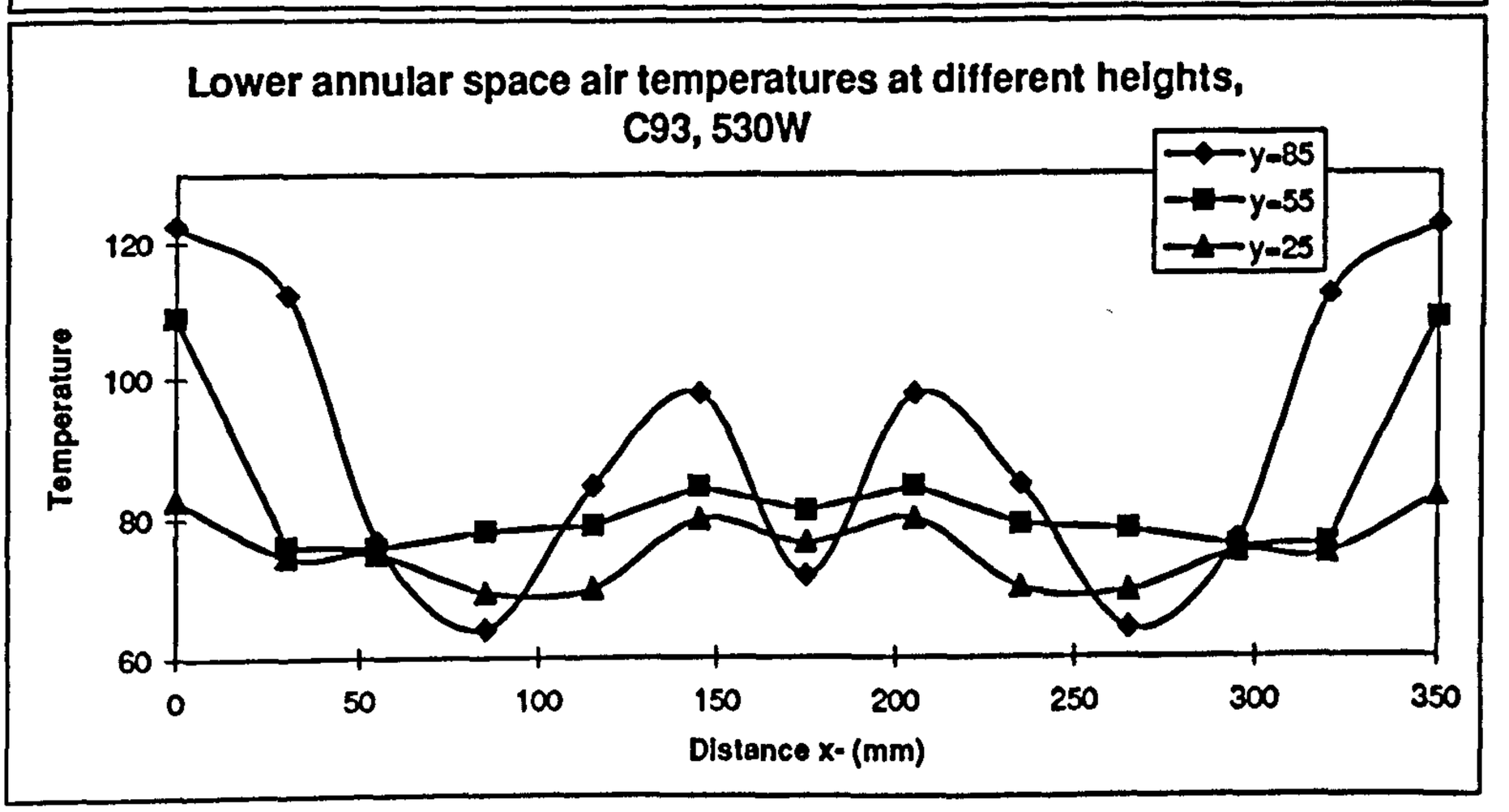
Lower annular space air temperatures at different heights,
C93, 530W
y-85
y-55
y-25
Temperature
120
100
80
60
0
50
100
150
200
250
300
350
Distance x- (mm)

Fig. 6-19(j-l)

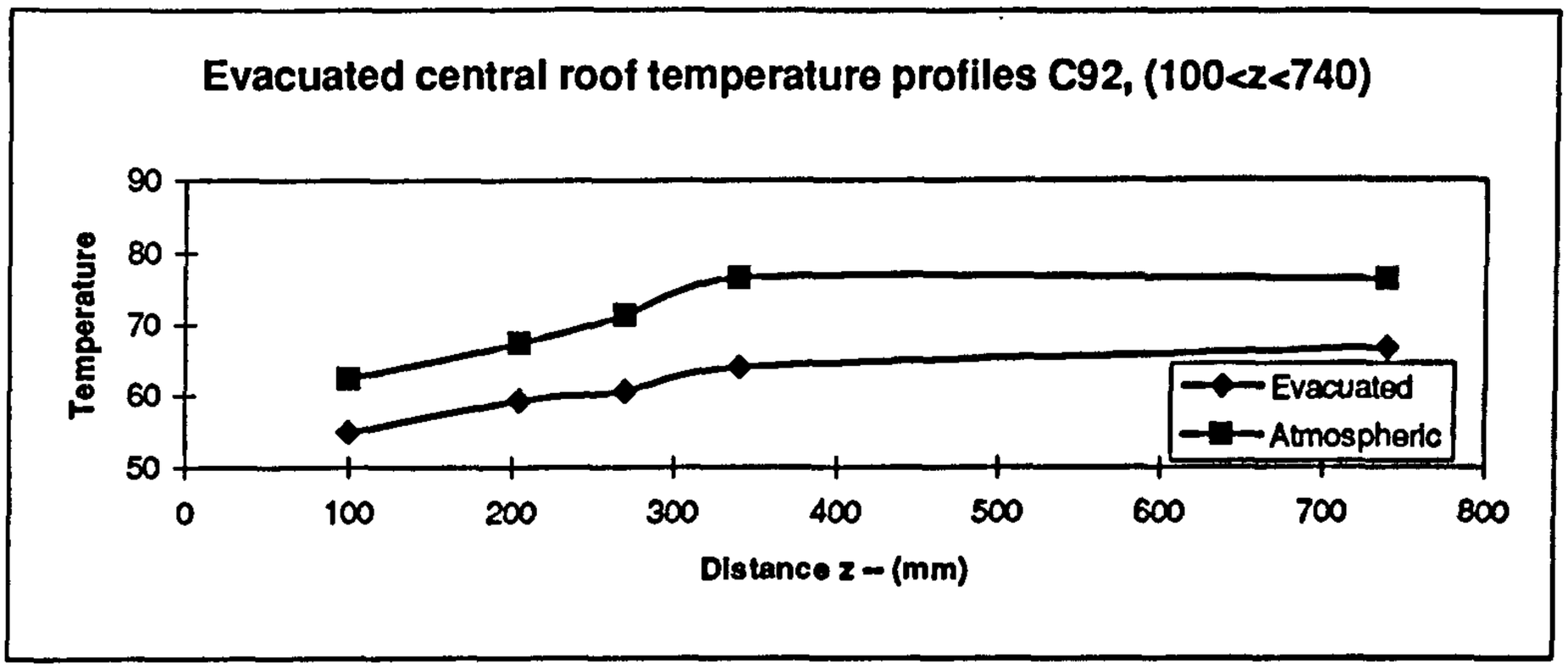
Evacuated central roof temperature profiles C92, (100<z<740)
Temperature
90
80
70
60
50
0
100
200
300
400
500
600
700
800
Distance z -- (mm)
Evacuated
Atmospheric

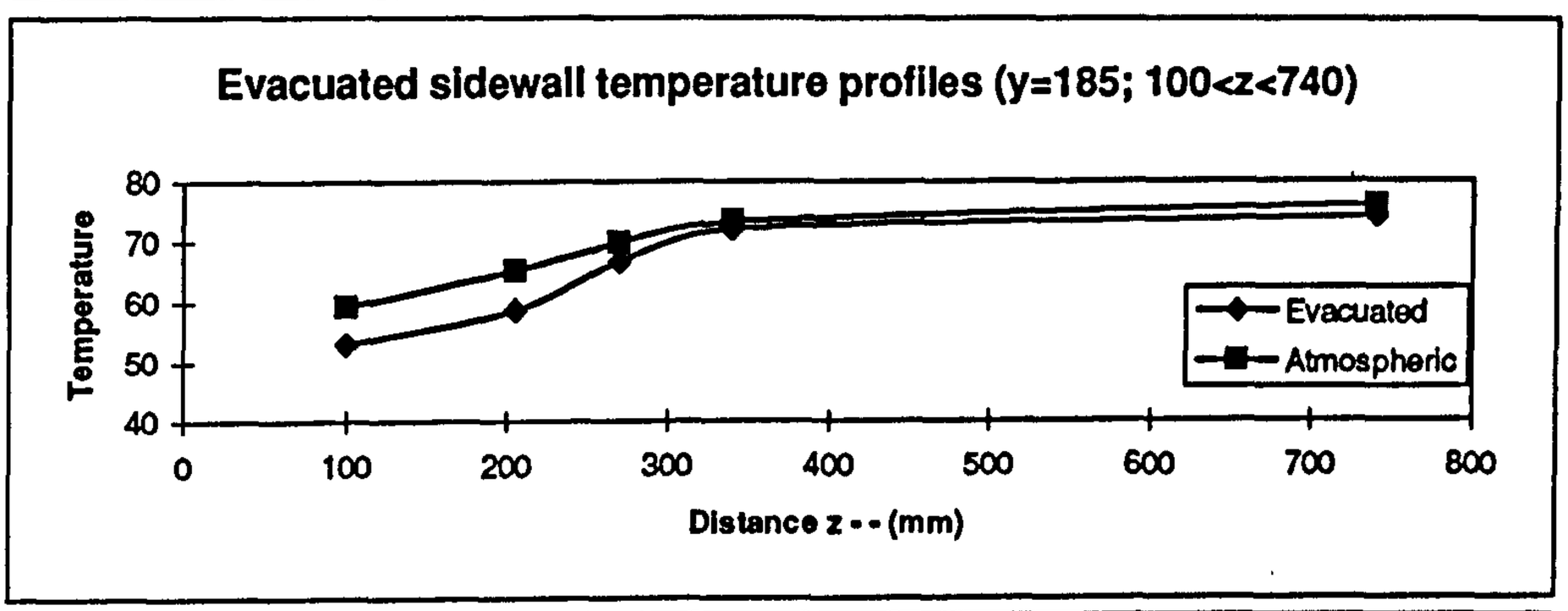
Evacuated sidewall temperature profiles (y=185; 100<z<740)
Temperature
80
70
60
50
40
0
100
200
300
400
500
600
700
800
Distance z -- (mm)
Evacuated
Atmospheric

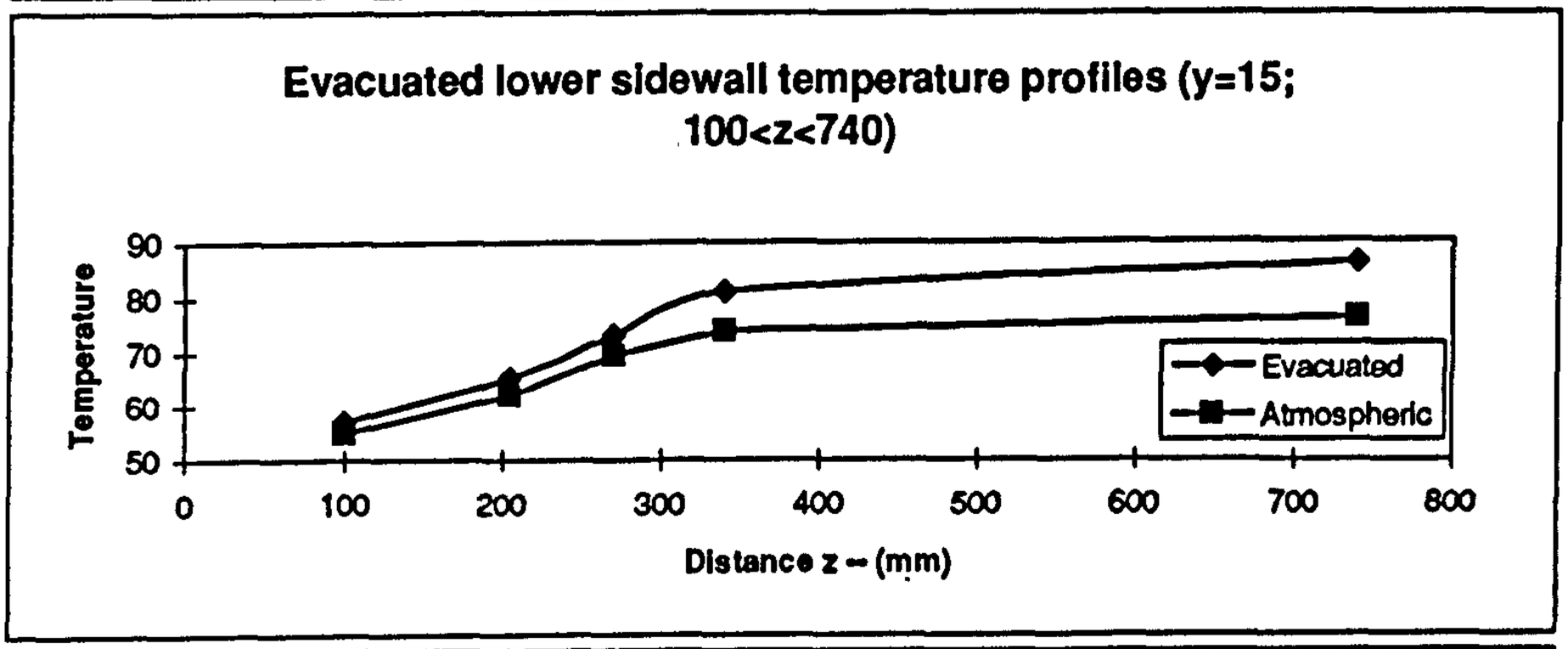
Evacuated lower sidewall temperature profiles (y=15;
100<z<740)
Temperature
90
80
70
60
50
0
100
200
300
400
500
600
700
800
Distance z -- (mm)
Evacuated
Atmospheric

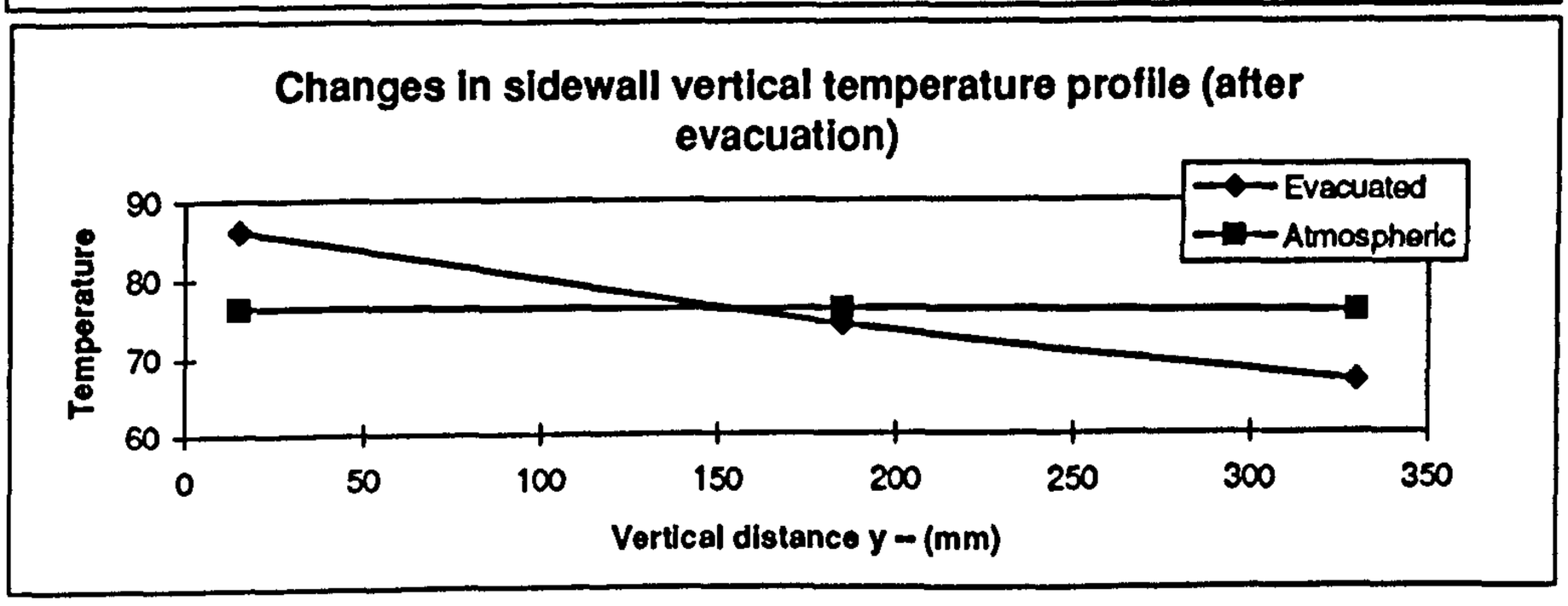
Changes in sidewall vertical temperature profile (after
evacuation)
Temperature
90
80
70
60
0
50
100
150
200
250
300
350
Vertical distance y -- (mm)
Evacuated
Atmospheric

Fig. 6-20(a-d)

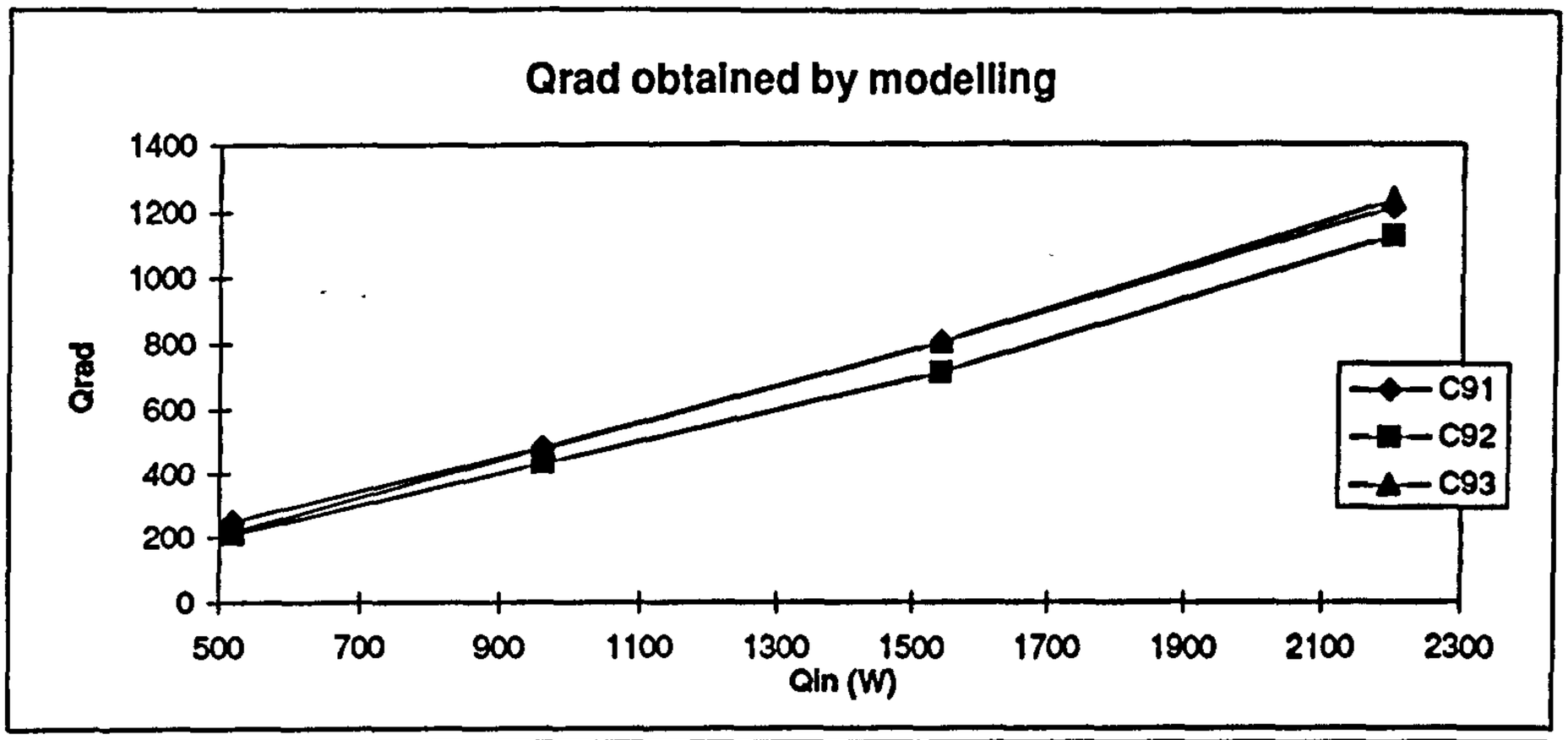
Qrad obtained by modelling
Qrad
1400
1200
1000
800
600
400
200
0
500
700
900
1100
1300
1500
1700
1900
2100
2300
Qin (W)
C91
C92
C93

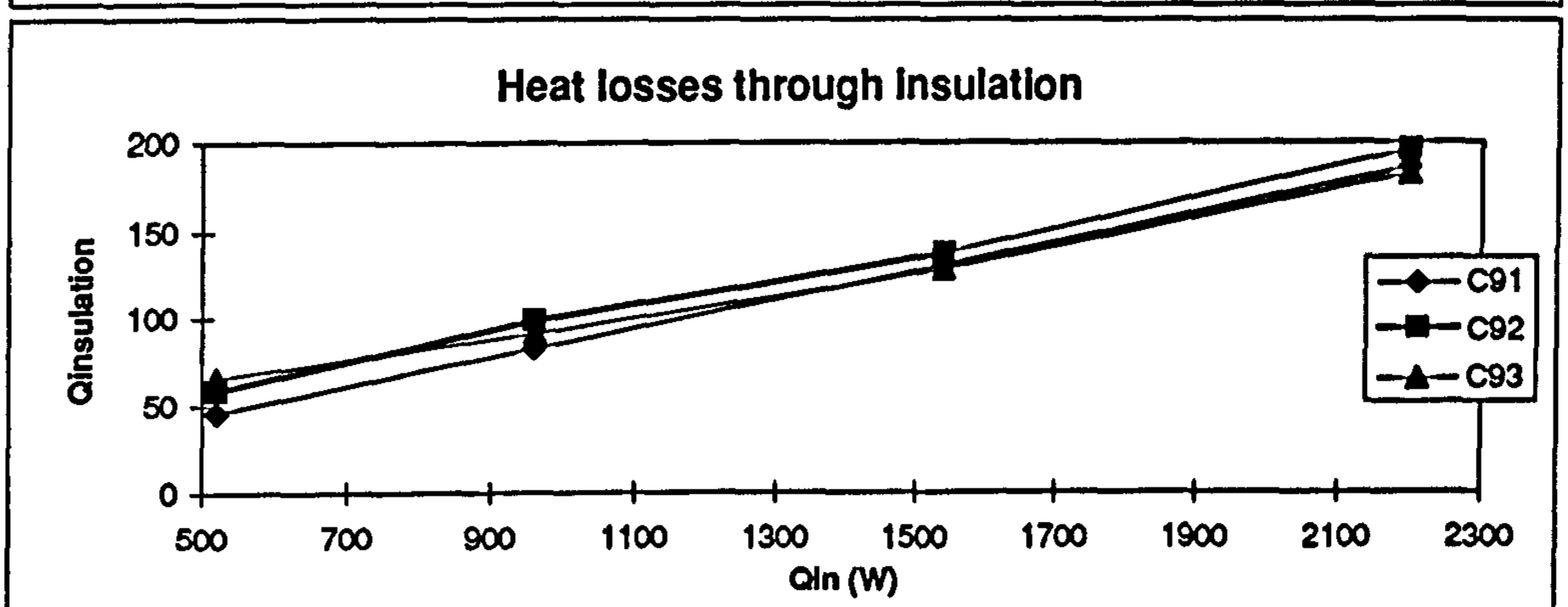
Heat losses through insulation
Qinsulation
200
150
100
50
0
500
700
900
1100
1300
1500
1700
1900
2100
2300
Qin (W)
C91
C92
C93

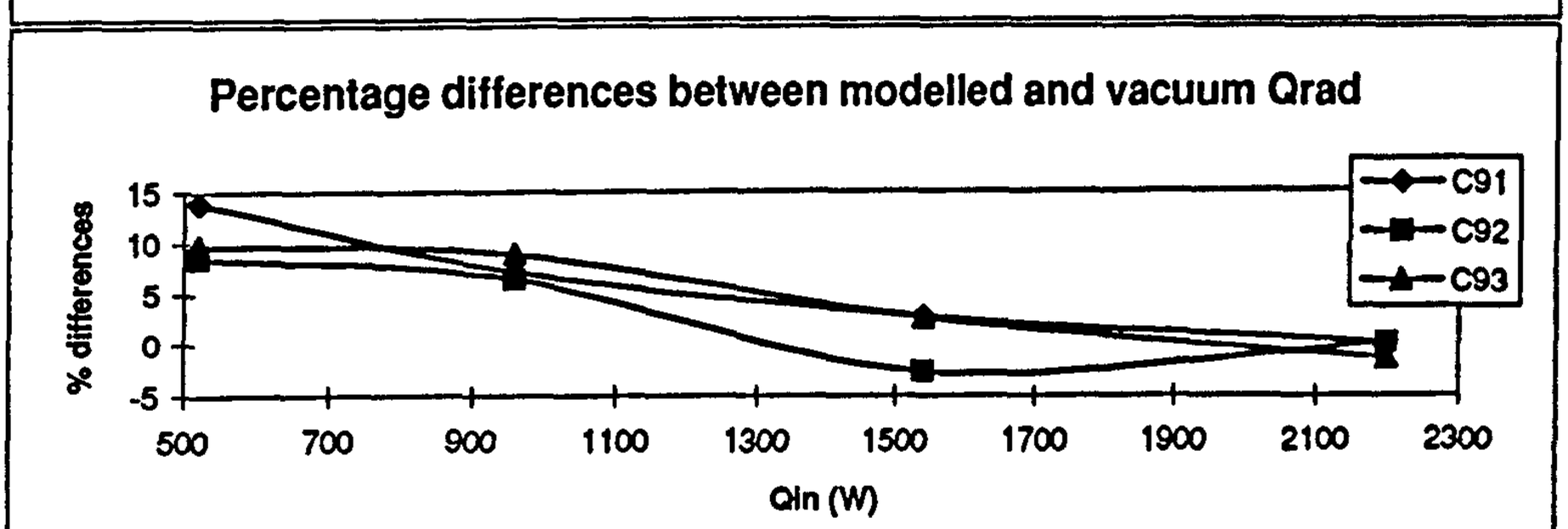
Percentage differences between modelled and vacuum Qrad
% differences
15
10
5
0
-5
500
700
900
1100
1300
1500
1700
1900
2100
2300
Qin (W)
C91
C92
C93

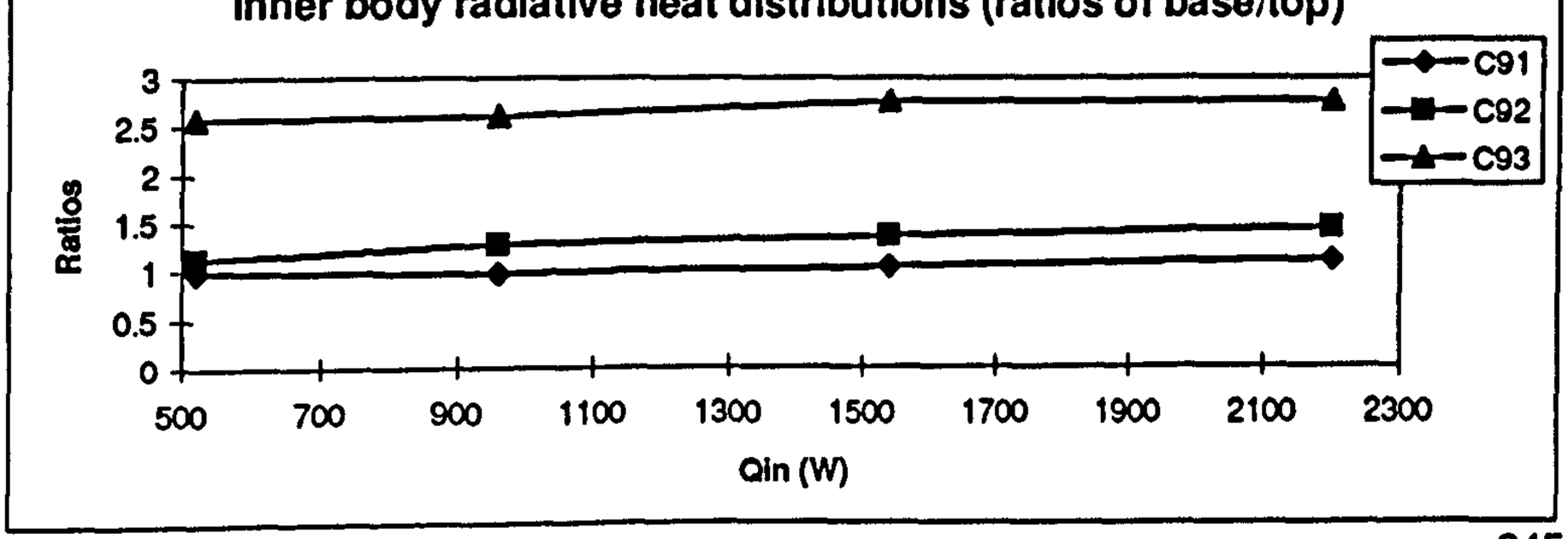
Inner body radiative heat distributions (ratios of base/top)
Ratios
3
2.5
2
1.5
1
0.5
0
500
700
900
1100
1300
1500
1700
1900
2100
2300
Qin (W)
C91
C92
C93

Fig. 6-21(a-d)

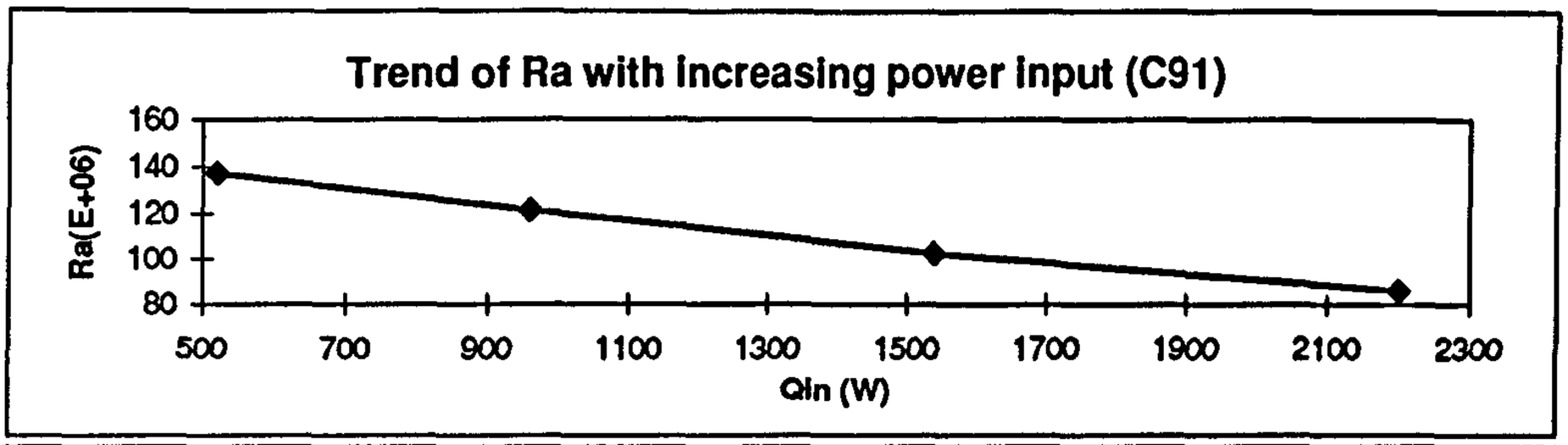
Trend of Ra with increasing power input (C91)
Ra(E+06)
160
140
120
100
80
500
700
900
1100
1300
1500
1700
1900
2100
2300
Qin (W)

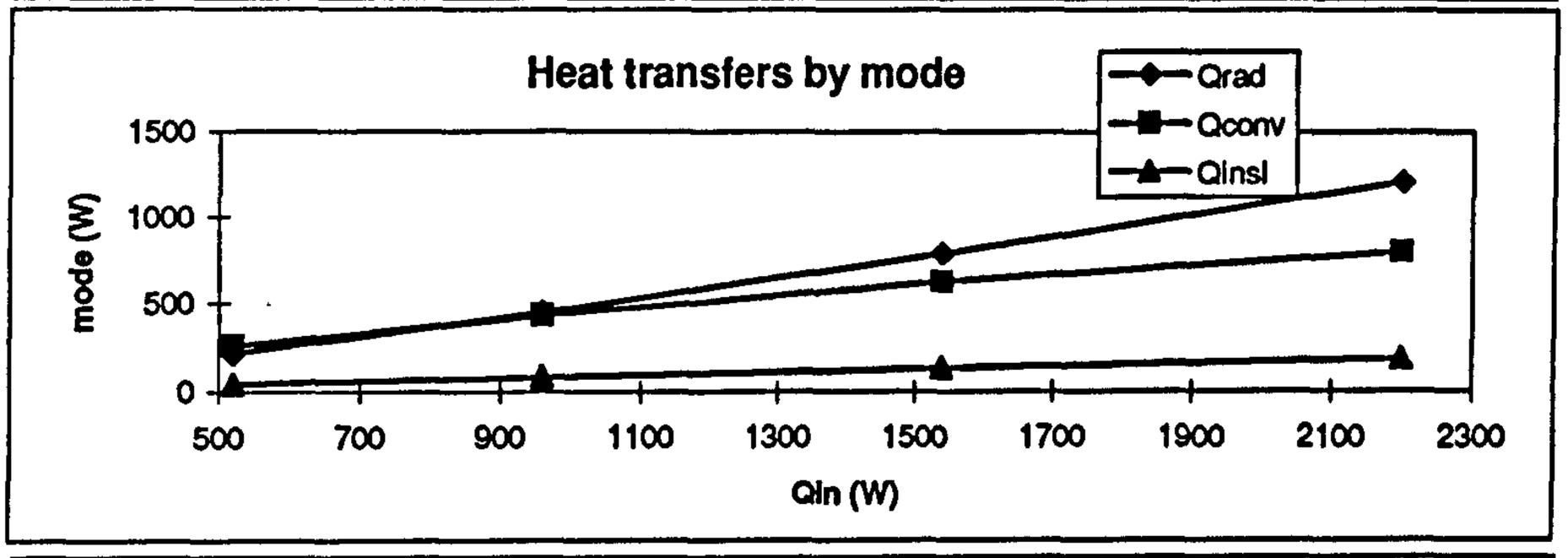
Heat transfers by mode
Qrad
Qconv
Qinsl
mode (W)
1500
1000
500
0
500
700
900
1100
1300
1500
1700
1900
2100
2300
Qin (W)

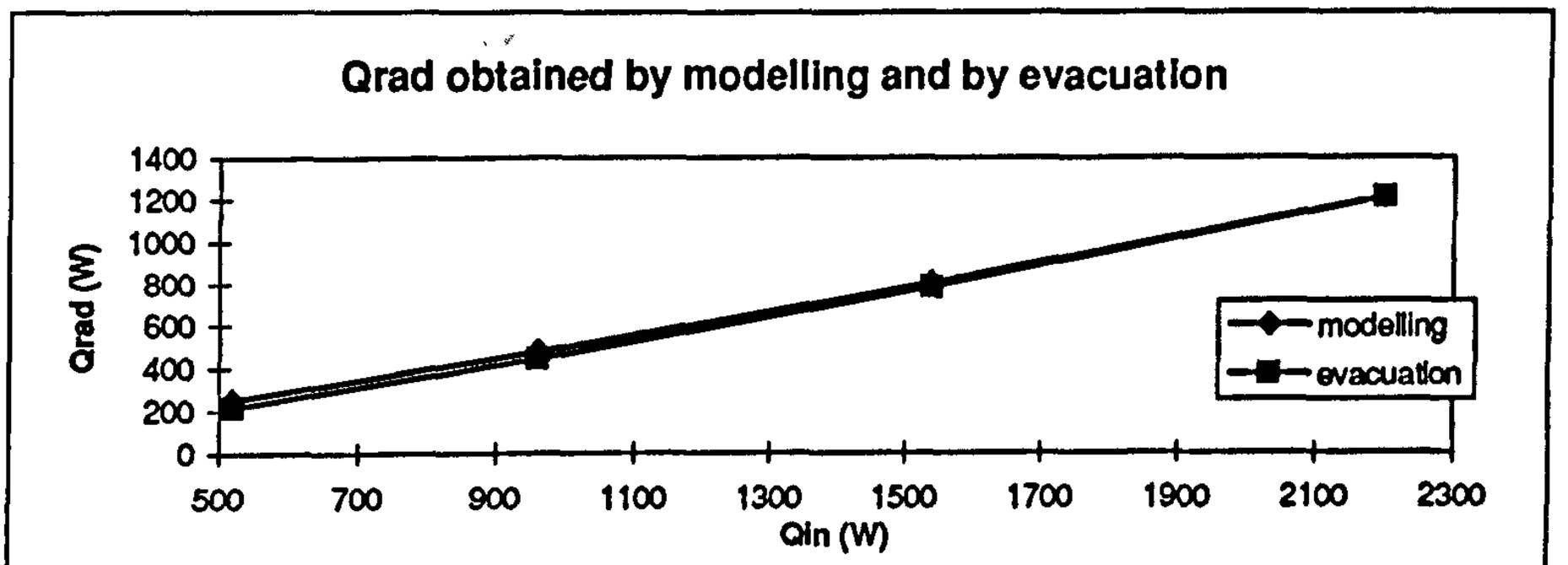
Qrad obtained by modelling and by evacuation
Qrad (W)
1400
1200
1000
800
600
400
200
0
500
700
900
1100
1300
1500
1700
1900
2100
2300
Qin (W)
modelling
evacuation

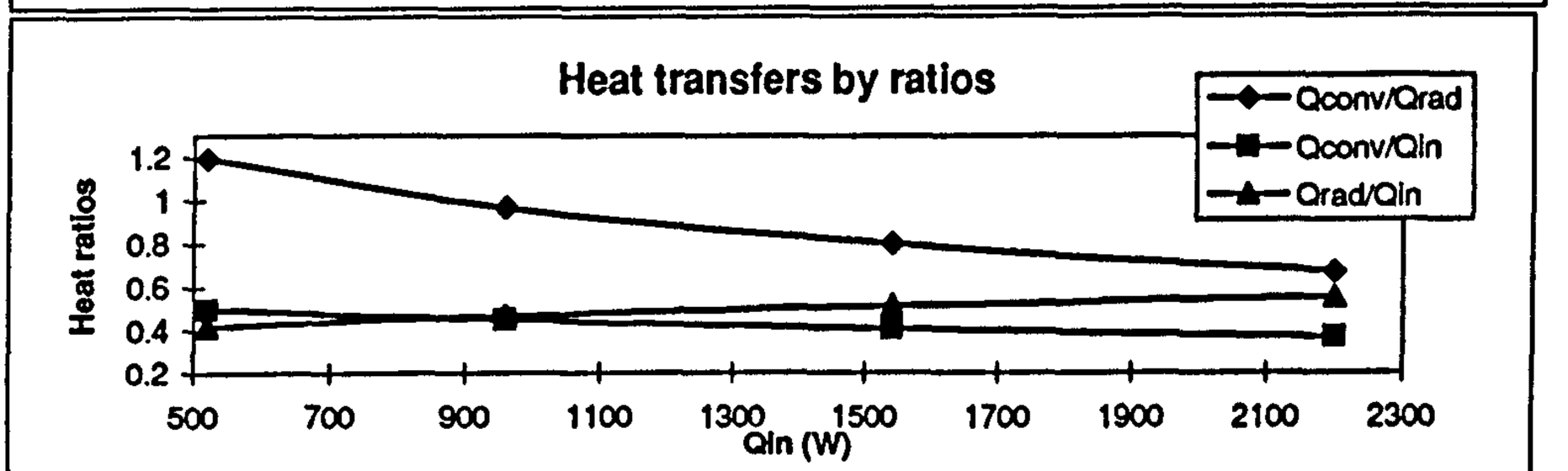
Heat transfers by ratios
Heat ratios
1.2
1
0.8
0.6
0.4
0.2
500
700
900
1100
1300
1500
1700
1900
2100
2300
Qin (W)
Qconv/Qrad
Qconv/Qin
Qrad/Qin

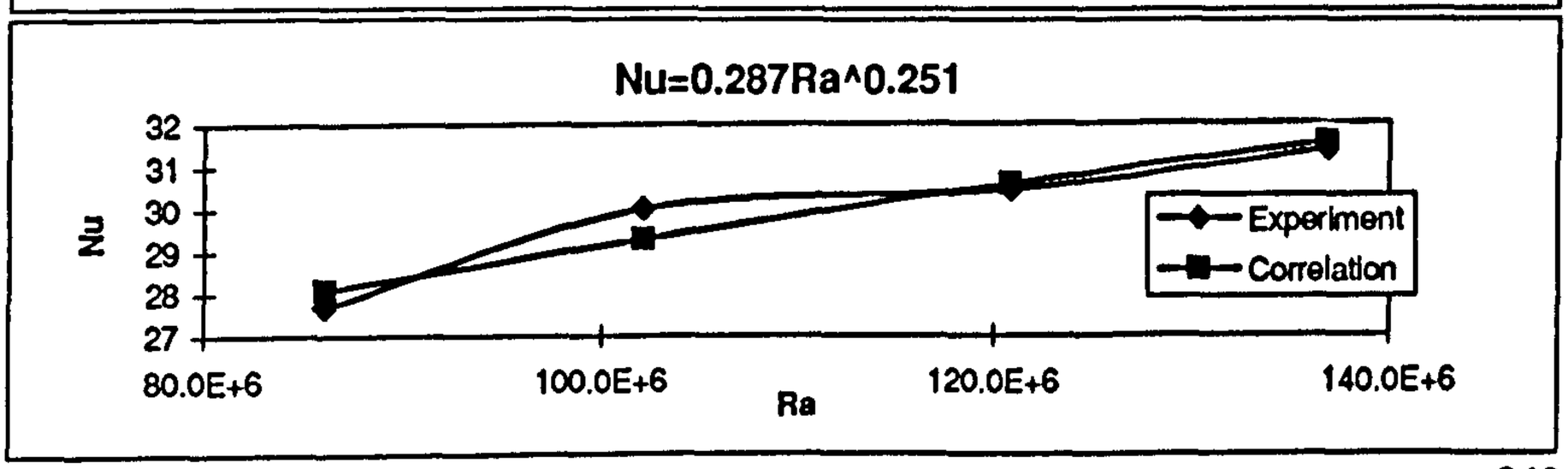
Nu=0.287Ra^0.251
Nu
32
31
30
29
28
27
80.0E+6
100.0E+6
120.0E+6
140.0E+6
Ra
Experiment
Correlation

Fig. 6-22(a-e)

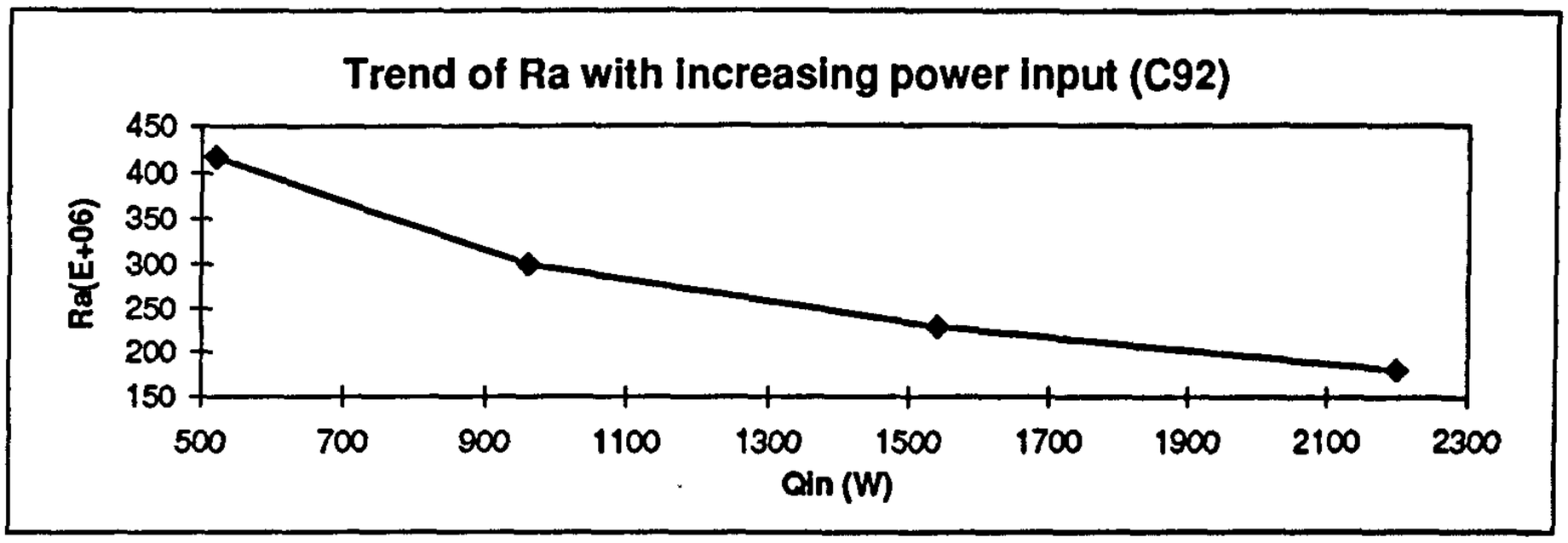
Trend of Ra with increasing power input (C92)
Ra(E+06)
450
400
350
300
250
200
150
500
700
900
1100
1300
1500
1700
1900
2100
2300
Qin (W)

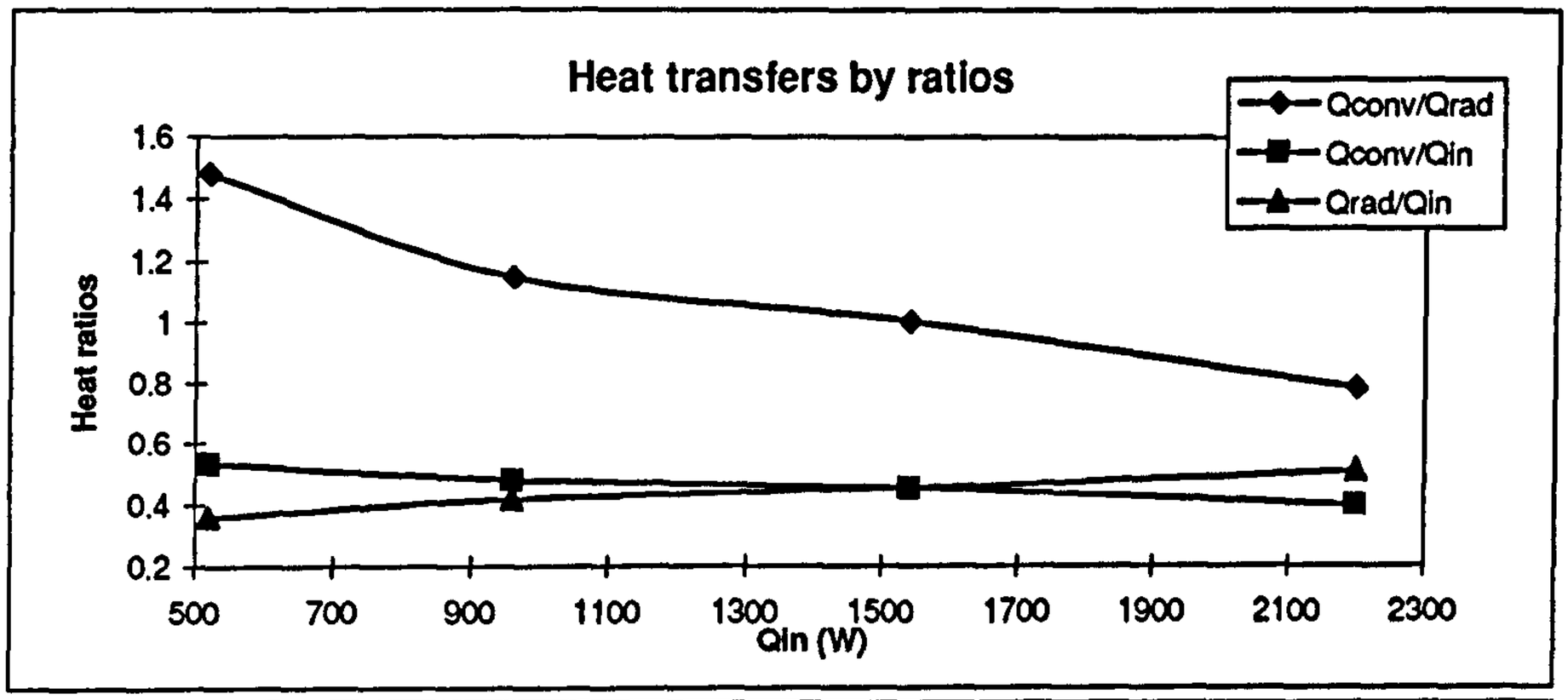
Heat transfers by ratios
Qconv/Qrad
Qconv/Qin
Qrad/Qin
Heat ratios
1.6
1.4
1.2
1
0.8
0.6
0.4
0.2
500
700
900
1100
1300
1500
1700
1900
2100
2300
Qin (W)

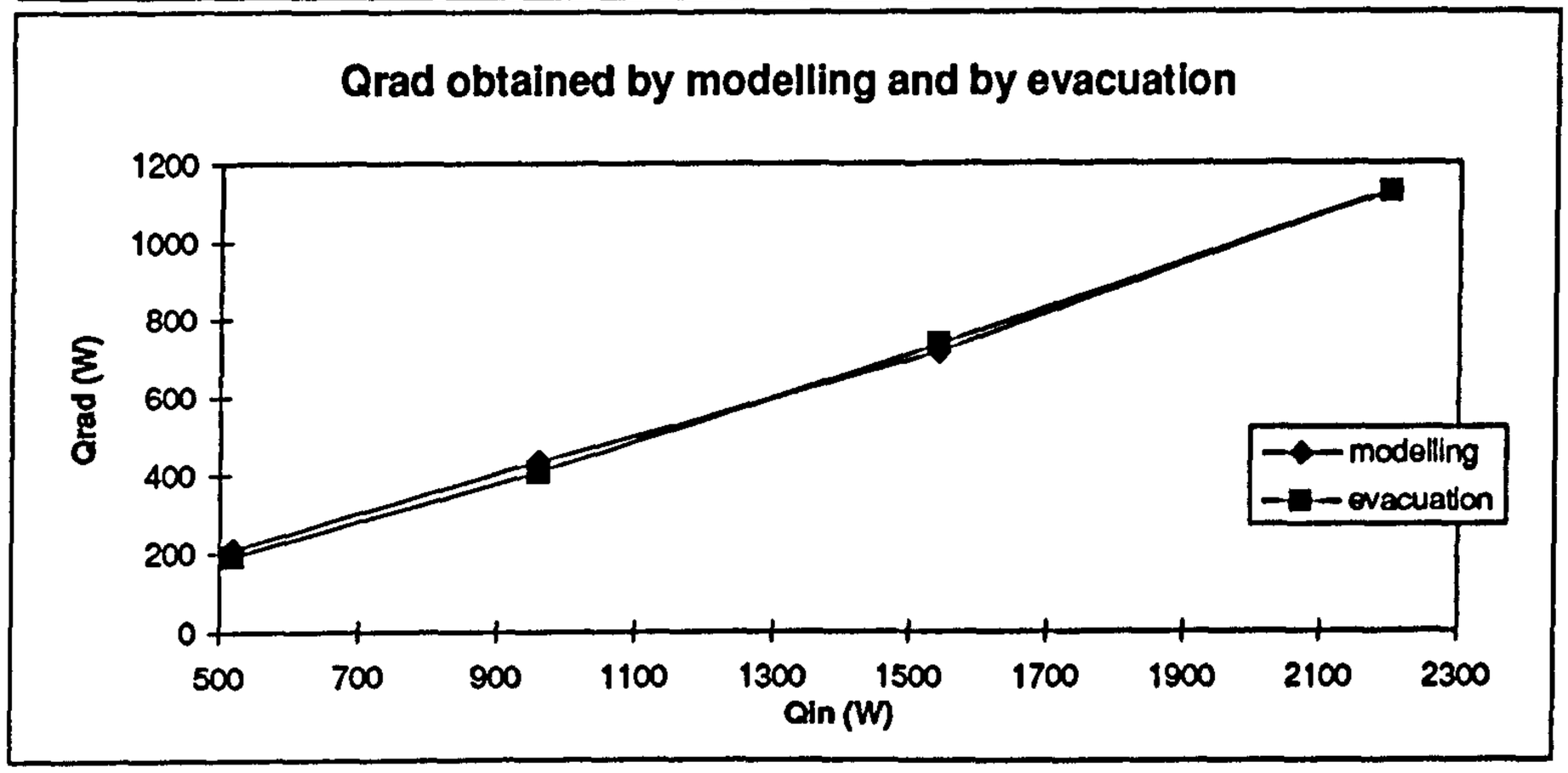
Qrad obtained by modelling and by evacuation
Qrad (W)
1200
1000
800
600
400
200
0
500
700
900
1100
1300
1500
1700
1900
2100
2300
Qin (W)
modelling
evacuation

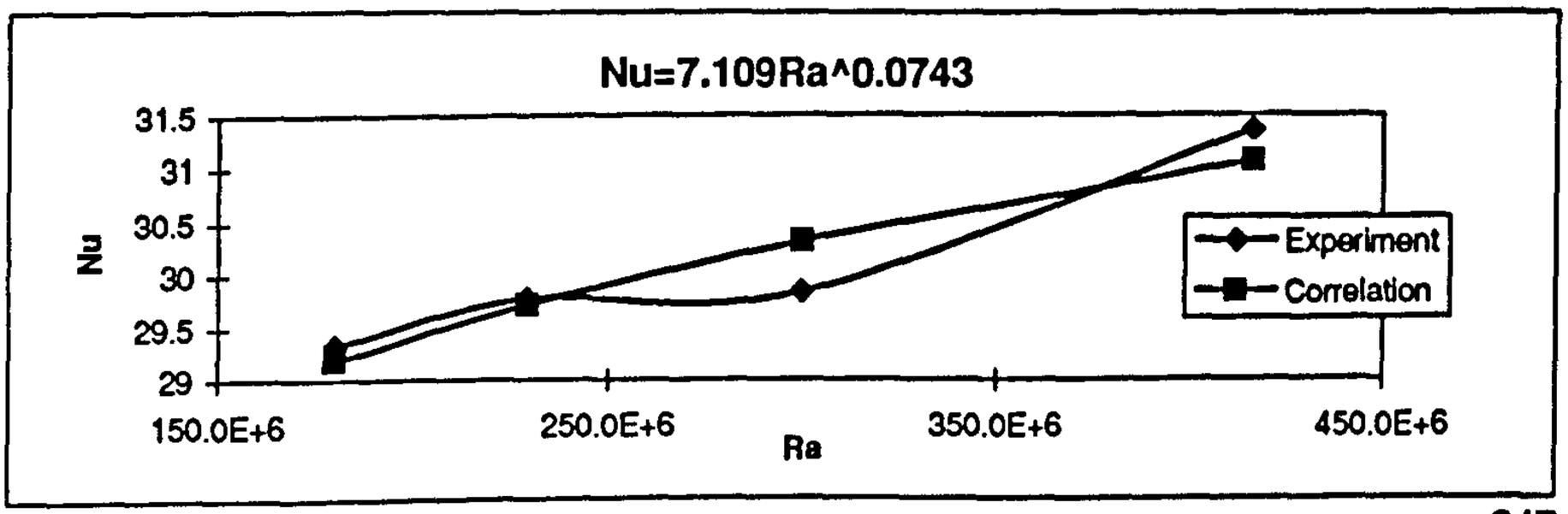
Nu=7.109Ra^0.0743
Nu
31.5
31
30.5
30
29.5
29
150.0E+6
250.0E+6
350.0E+6
450.0E+6
Ra
Experiment
Correlation

Fig. 6-23(a-d)

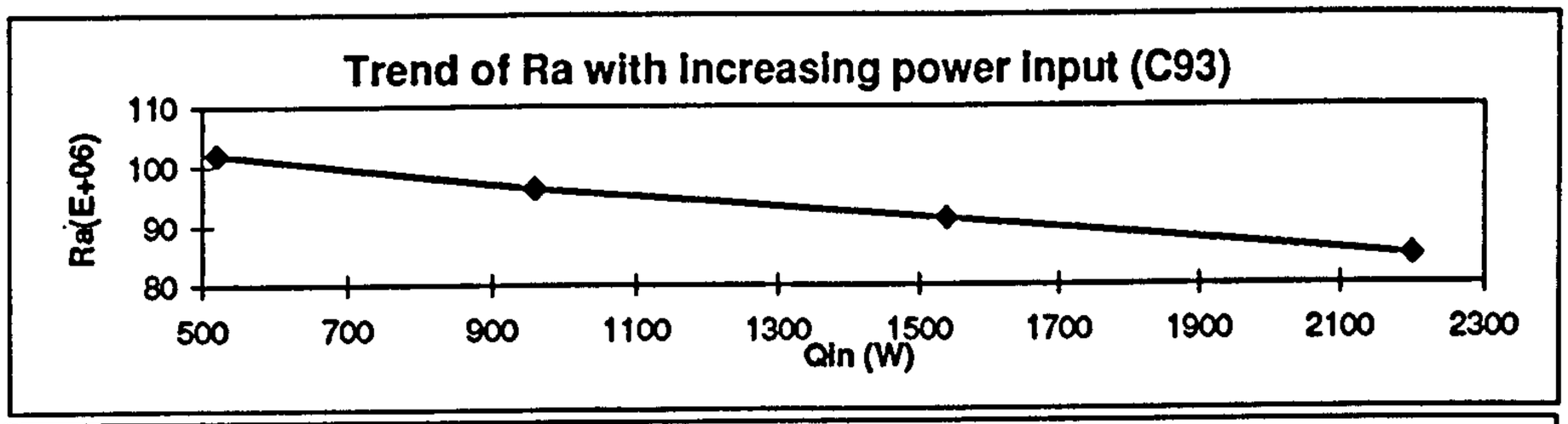
Trend of Ra with increasing power input (C93)
Ra(E+06)
110
100
90
80
500
700
900
1100
1300
1500
1700
1900
2100
2300
Qin (W)

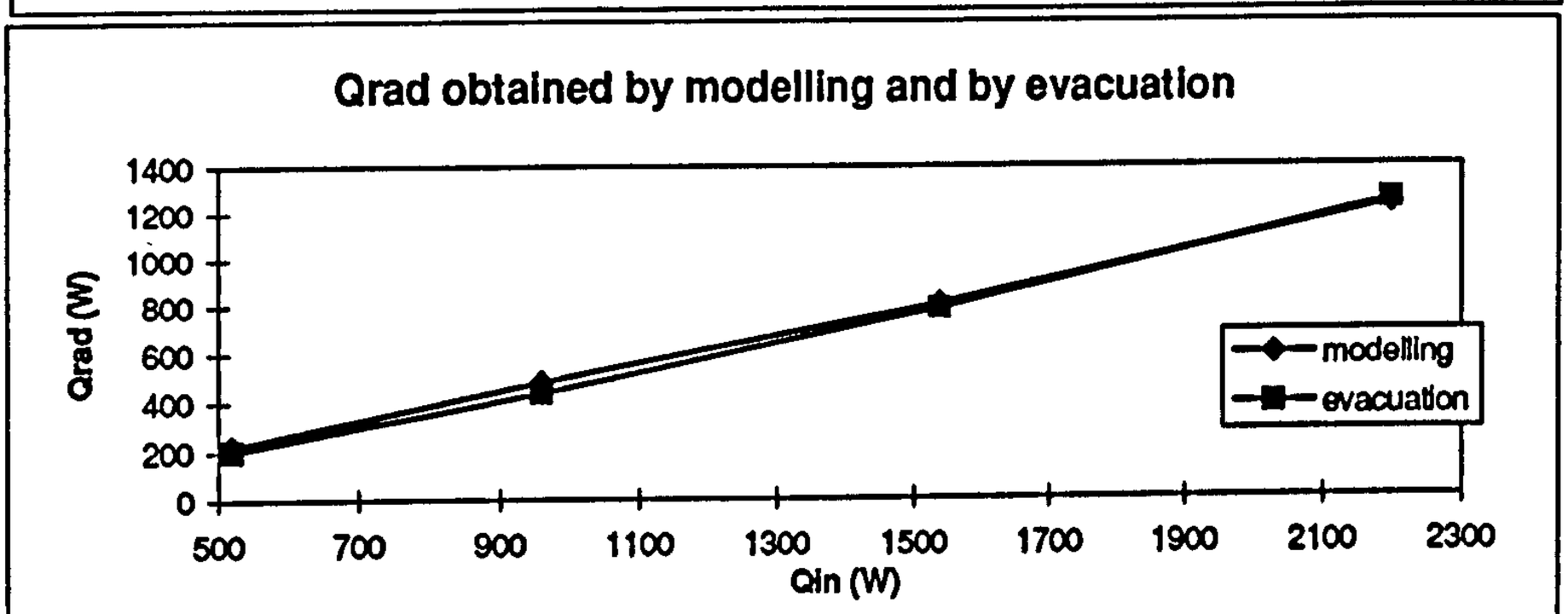
Qrad obtained by modelling and by evacuation
Qrad (W)
1400
1200
1000
800
600
400
200
0
500
700
900
1100
1300
1500
1700
1900
2100
2300
Qin (W)
modelling
evacuation

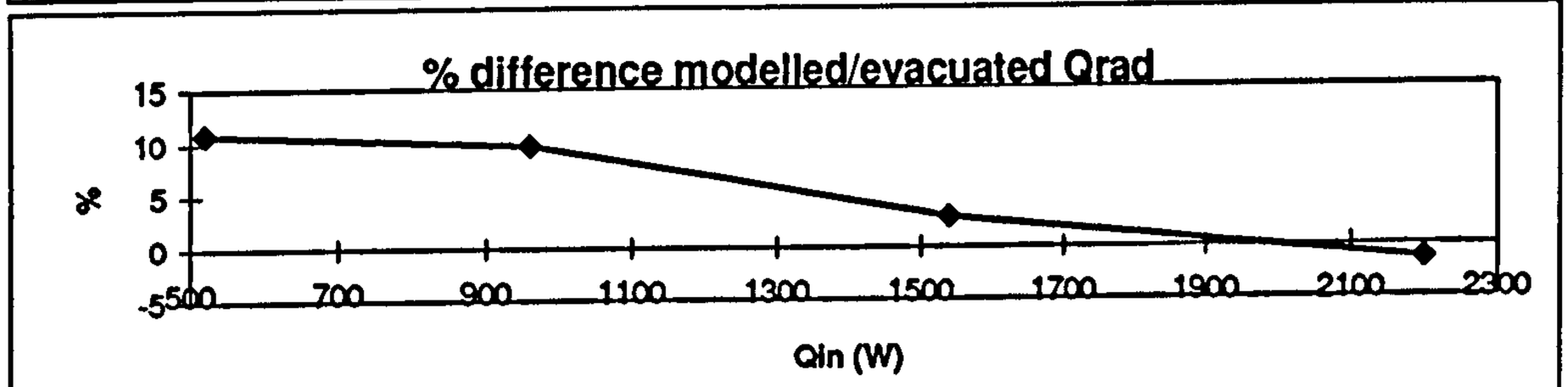
% difference modelled/evacuated Qrad
%
15
10
5
0
-5
500
700
900
1100
1300
1500
1700
1900
2100
2300
Qin (W)

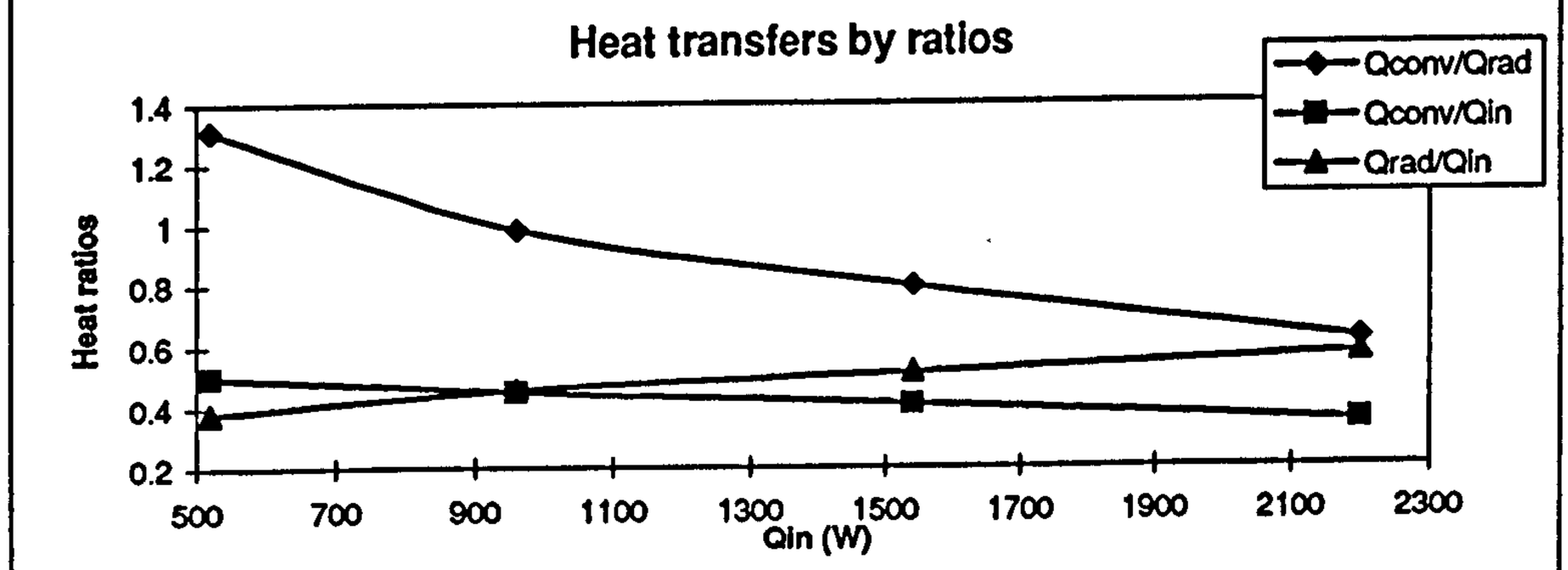
Heat transfers by ratios
Heat ratios
1.4
1.2
1
0.8
0.6
0.4
0.2
500
700
900
1100
1300
1500
1700
1900
2100
2300
Qin (W)
Qconv/Qrad
Qconv/Qin
Qrad/Qin

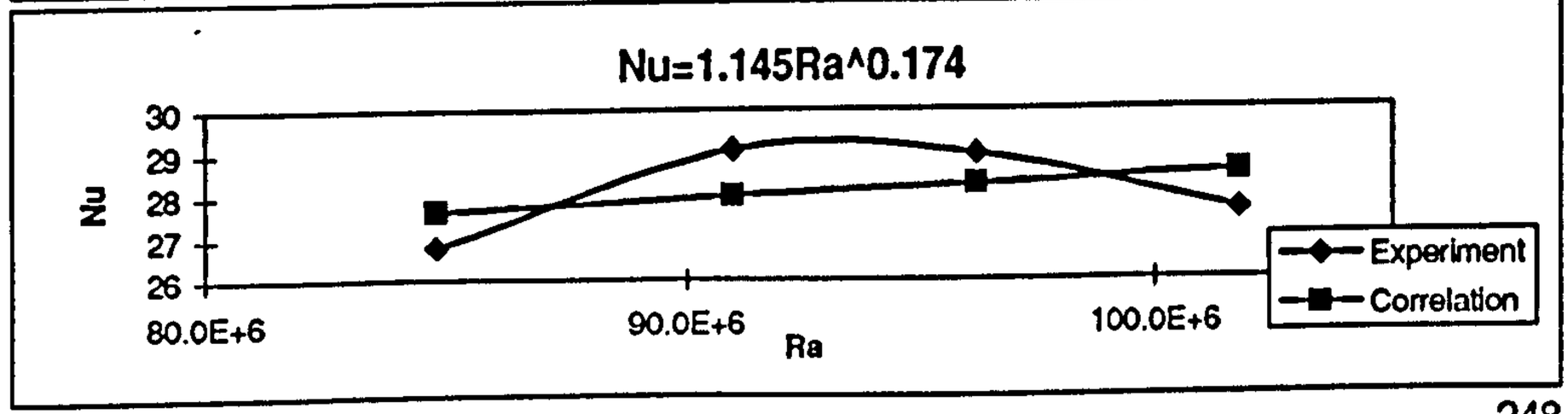
Nu=1.145Ra^0.174
Nu
30
29
28
27
26
80.0E+6
90.0E+6
100.0E+6
Ra
Experiment
Correlation

Fig. 6-24(a-e)

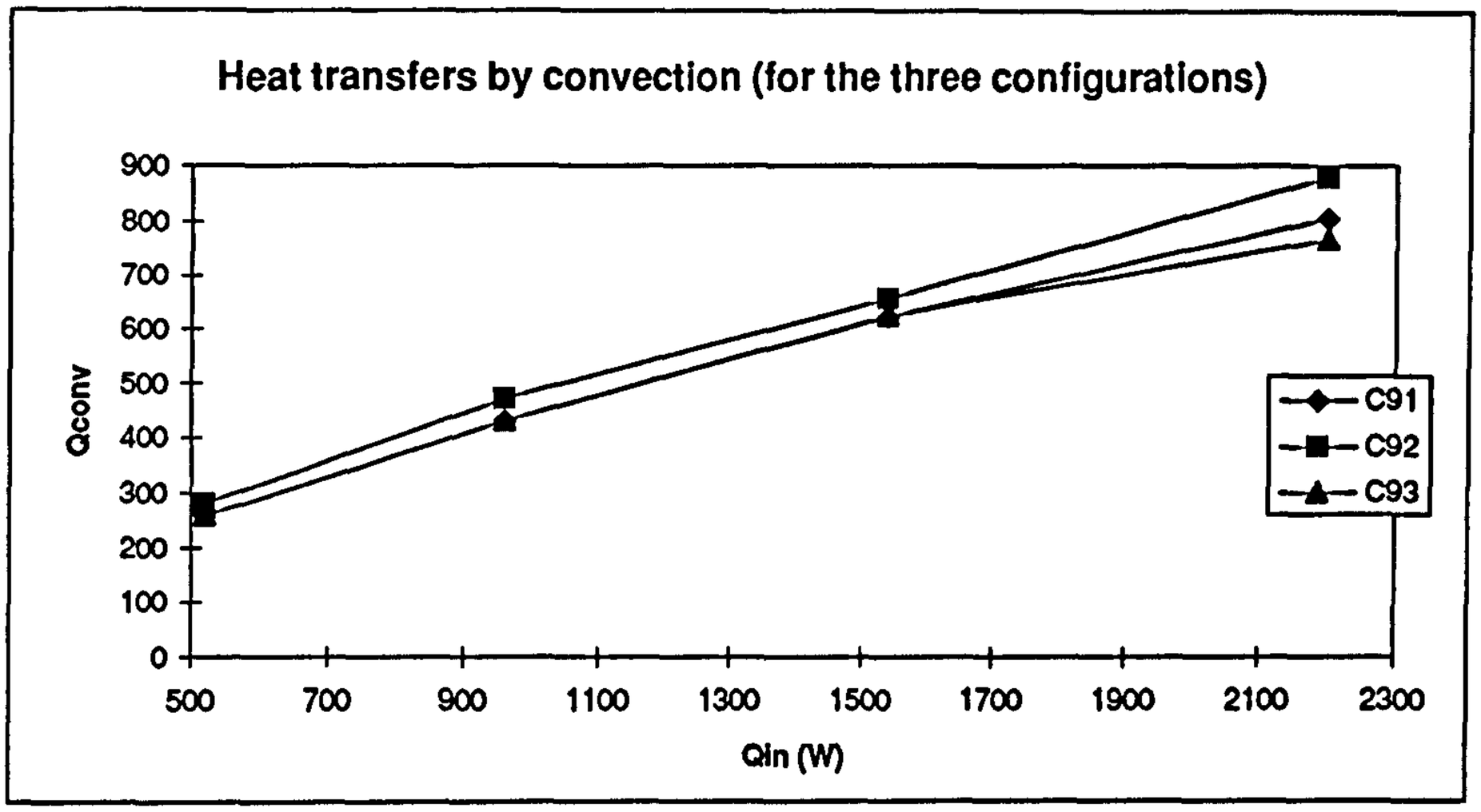
Heat transfers by convection (for the three configurations)
Qconv
900
800
700
600
500
400
300
200
100
0
500
700
900
1100
1300
1500
1700
1900
2100
2300
Qin (W)
C91
C92
C93

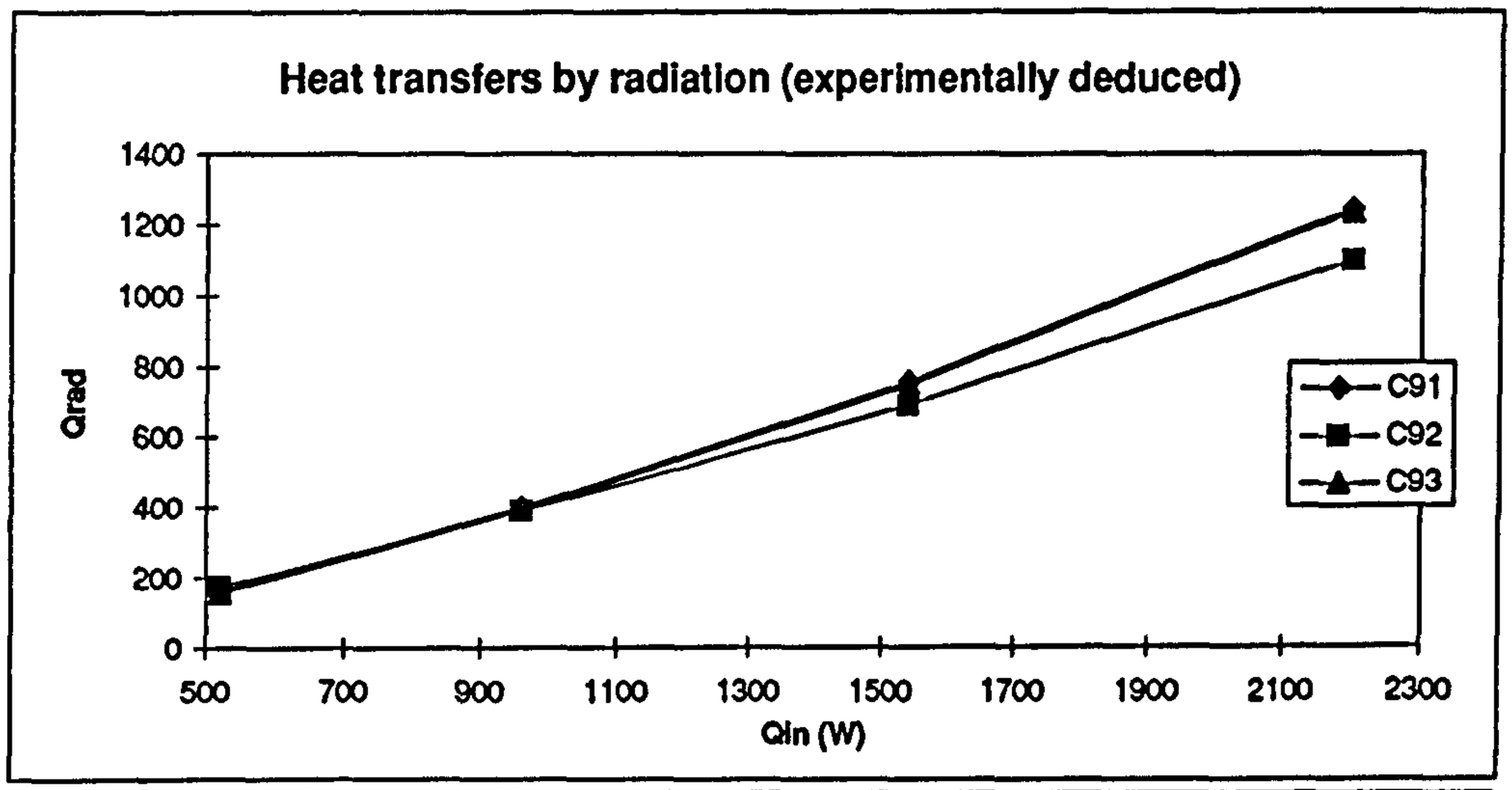
Heat transfers by radiation (experimentally deduced)
Qrad
1400
1200
1000
800
600
400
200
0
500
700
900
1100
1300
1500
1700
1900
2100
2300
Qin (W)
C91
C92
C93

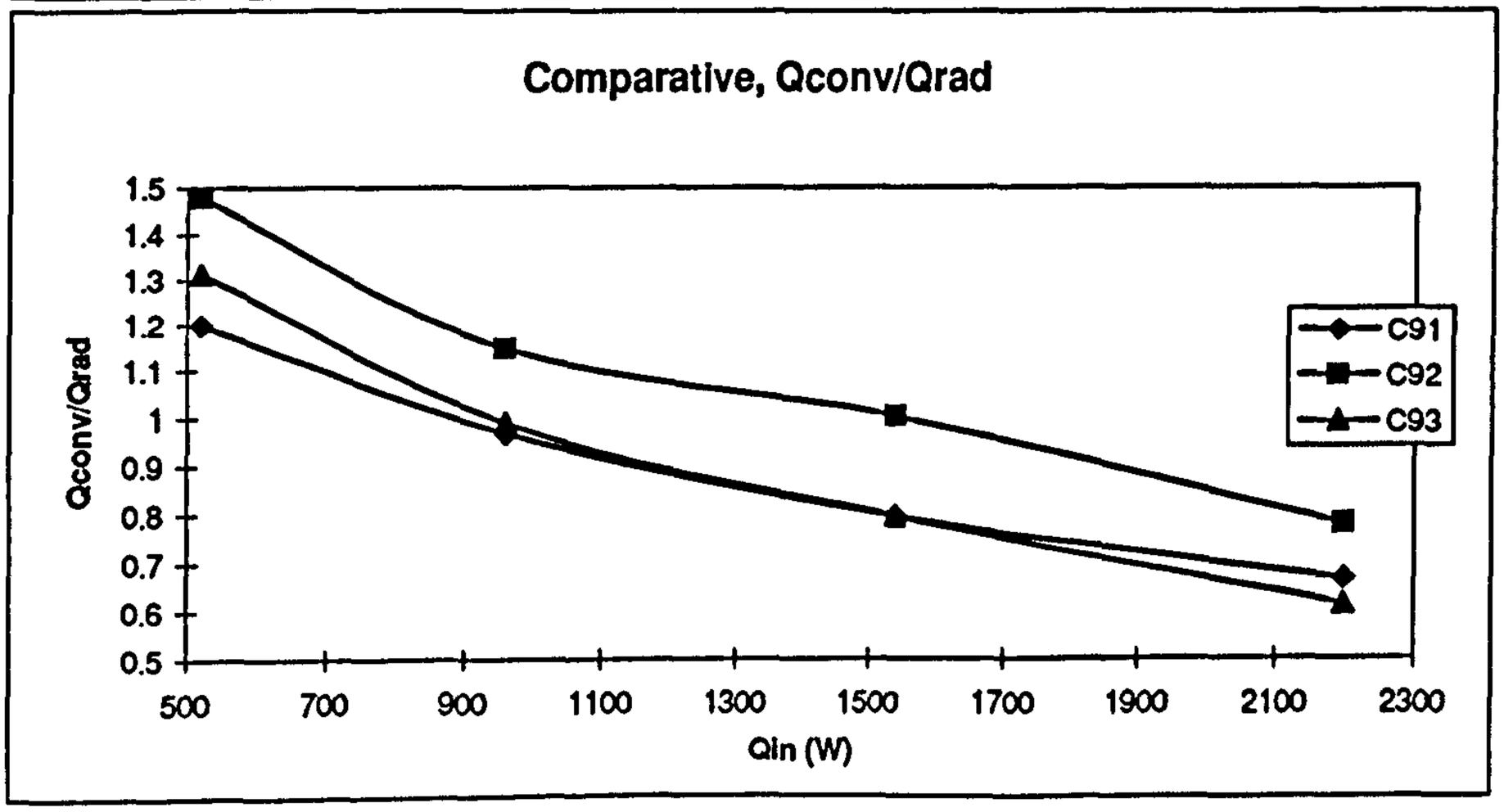
Comparative, Qconv/Qrad
Qconv/Qrad
1.5
1.4
1.3
1.2
1.1
1
0.9
0.8
0.7
0.6
0.5
500
700
900
1100
1300
1500
1700
1900
2100
2300
Qin (W)
C91
C92
C93

Fig. 6-25(a-c)

7. DISCUSSION

7.1. DISCUSSION OF THE EXPERIMENTAL TECHNIQUES

Two experimental techniques were employed to determine the convective component of the total heat transfers - a thermometric and an evacuation method. Interferometry was also employed and although no quantitative analyses were utilised from the results, the interferograms provided a unique insight into heater-wall proximity behaviour. The experimental studies also provided an opportunity to examine the benefits which accrued from the use of either method. The use of a long 2-D rig permitted the extensive flow visualisation studies to be undertaken which provided a sound basis upon which to identify certain heat transfer problems. The problems or benefits associated with the experimental studies are now considered in turn.

7.1.1. Flow visualisation

The flow visualisation technique (see Chapter 3), utilised smoke generated by passing air through a tubular bed of chemical granules. The use of high temperature glass windows allowed smoke data acquisition at elevated temperatures. Because of rapid smoke dispersion however, the flow was presented schematically. A similar flow visualisation technique was employed for the enclosed heater (see Chapter 4).

However, the positioning of the camera in the shadow cast by the inner body (pipe and piping system) was more critical, because the shadow projected was smaller than that obtained via the inner body of Chapter 3. Consequently, for the line heat source (9.5mm dia. electric heater), the use of the camera was not practicable. Hence, the related flow visualisation was also presented schematically.

For the vacuum rig, the availability of dedicated flow visualisation apertures eliminated these photographic restrictions. Although the dedicated apertures improved the quality of the video recordings, the use of perspex, however, reduced the operating temperatures at which the flow visualisations could be conducted satisfactorily. Consequently, any convective effect that the hot enclosure walls might have added to the flow was generally absent. Therefore, it is recommended that higher temperature (pyrex glass) windows be utilised in order to achieve flow visualisation at a much higher temperature.

7.1.2. An improved adjustment procedure for the MZI

An existing problem tackled in the course of this investigation was to enable the operation of the MZI in an infinite fringe mode. This mode greatly simplifies the evaluation of the ensuing interferograms. In spite of the use of the dedicated adjusting procedure available, it was still impossible to operate it in this mode. This problem was solved by developing an improved adjustment procedure, which was validated in the course of this investigation (see Appendix A).

7.1.3. Deducing the convective heat transfers by evacuation

The convective heat transfer was obtained by taking the difference between the meter reading at atmospheric pressure and at evacuation and adding the very small proportion by gaseous conduction. This process is inherently less erroneous because it omits the process of zoning and associated radiation heat transfer calculations which were subjected to cumulative uncertainties. More important is the fact that data gathered under vacuum would be the same irrespective of the atmospheric pressure and would be consistently more reliable and reproducible.

In this study, a square-sectioned enclosure, 350x350x1700mm was designed and the capability to operate under vacuum was validated.

In addition to the design expertise required, the other requirements and problems associated with employing this method for deducing the convective component of the total heat transfers were discussed in section 6.4.5.5.

However, the method offers two main advantages that are unique:

7.1.3.1. The convective component of the heat transfers obtained would be directly obtained and inherently more reliable. The vacuum data would also be universally more consistent.

7.1.3.2. The effectiveness of convection to attenuate the wall temperature profiles could be determined by comparing the profiles under evacuation to the more uniform profiles obtained under atmospheric conditions.

7.2. DISCUSSION OF THE OVERALL RESULTS

7.2.1.

It was concluded that C9 produced the most convection (see Chapter 3). But it was also observed that its time to reach steady-state was longest, whereas for C2, it was the shortest. It is clear, therefore, that convective arrangements would always take much longer to achieve steady-state conditions, and may prove to be the least desirable from the sole consideration of energy efficiency. A thorough explanation for this was provided in Chapter 6 (see 6.4.5.3). However, a desire for temperature uniformity would override this temporal consideration. Also, for prolonged steady-state operation, transient effects may be less significant. The time to reach steady-state conditions was also short for C4. It was also emphasised that the value of Ra (and to a lesser extent, Nu) generally decreased as the power input was increased.

7.2.2.

Before attention could be directed towards the main aim of obtaining improved convective component of the heat transfers, an important issue, that of the optimal position of a heater in a rectangular enclosure had to be resolved. This was carried out in Chapter 4. It was established that at low Ra, the enclosure base corners are ideal locations for hot spots such as electrical components and electronics boards in a totally enclosed, intrinsically safe system. Also as the Ra increased towards $1x10^5$, the proportion of heat losses by natural convection rapidly declined. The design advice suggested an offset (<1.5d) specifically for the 9.5mm diameter horizontal cylindrical heater along the middle or lower region of a vertical wall.

When multiple cylindrical heaters are mounted horizontally, one above the other, adjacent and parallel to a vertical wall, the offset from the wall should be increased progressively with heater elevation, to ensure that the rising heated air from the lower heater in addition to the entrained flow, would be accommodated by the offset between the latter heater and the vertical wall. Arrays of enclosed horizontal fire tubes or electric heaters along a vertical wall should benefit from this concept. The implication for non-enclosed systems, such as refrigeration condenser tube arrays, is that convective heat losses should be enhanced if the array profile were to be slightly inclined, with the lowest tube being nearest the wall, and offset by less than 1.5d.

The large amount of experimental information provided by this phase of the study, could form the basis of improved numerical analyses and methods. Especially important were the variation of convective heat transfers with heater location in an enclosure, and that the flow visualisation alone could be utilised to provide the solution for the optimal location for maximum convective heat transfers of horizontal cylindrical heaters, by noting the position where the upper vortex disappears, as the heater approaches the vertical wall.

7.2.3.

The improved method of obtaining convective flows was carried out in Chapter 6 where C9 was developed to give C91, C92, C93 and their variants. Because the evacuation technique gave the total natural convection heat transfer however, it was still found to be important to quantify the radiative component to each side of the inner body. Therefore, an elaborate radiation modelling was carried out which involved over 412 surface zones and reflections and adjusted via the vacuum data. It was then possible to gain an insight into the differences in heat transfer activities to the inner body between the studied configurations. Each of the configurations was found to have its own merits.

C92 was the most convective and somewhat similar to existing natural convection configurations in cubical ovens. Adding heating-elements along the wall above this arrangement could actually be to the detriment of natural convection as inferred via the interferograms (see Fig. 3-28), where the upper plume was seen to be deflected away from the interior and towards the upper corner. In spite of the insensitivity of the rig to transients, it was still possible to discern that C93 appeared to reach steady-state faster than the other two configurations, and because of its increased base heating, it is also recommended for further developments as well as a variant C91-135. C91 had the most uniform enclosure heating characteristics. This was because the crown of the oven was warmest, thereby contributing to radiative heat transfers to the upper inner body horizontal surface. The capability of C91 to uniform heating merits a further exploration as to further development.

8. CONCLUSIONS AND RECOMMENDATIONS

8.1. CONCLUSIONS

The experimental studies have demonstrated that locating heating-elements in the lower half of the enclosure (C92, see Fig. 8-1) would provide the highest convective heat transfers, as well as improved uniformity of the heated products. However, it is obvious that the design of natural convection heating systems cannot be over-simplified by a general recommendation of a single type of heating arrangement. While heaters mounted on the lower half of the vertical wall of an oven have produced the best convective heat transfers in this study, the type of product to be predominantly heated (whether high conductivity aluminium, or low conductivity foods and plastics), and their arrangement, would determine the most suitable type of heating arrangement, and this could include base-mounted heating systems.

The thermometric technique of obtaining and analysing the convective component of the heat transfers was supplemented by an evacuation technique, which gave the convective component of the heat transfers directly. The evacuation technique was shown to be inherently more accurate than the method utilised for the studies carried out under atmospheric pressure, because it is not prone to the variability in the environmental pressure. The use of multi-zone radiation modelling enabled a fairly high accuracy in data analyses to be achieved, for the experiments carried out at atmospheric pressure.

It was shown that a line heat source in a rectangular-section enclosure would achieve higher convection along the vertical wall than at the middle of the enclosure. It was also shown that the enhancement in the convective heat transfers would only occur if vortices or cells between the heater, the adjacent vertical wall and the upper horizontal wall disappear, as the heater is horizontally traversed towards the vertical wall. For a single, larger cylindrical heater, an enhancement due to a chimney effect cannot occur because the upper vortex or cells would always exist (between the plume and the vertical wall), which interfere with copious flow around the cylinder.

Furthermore, as the heater temperature increases (ΔT and Ra increase), the positions for maximum convective heat transfers shift upwards along the centred vertical (y-z) plane ($0.25<Y<0.5$; $7.5x10^4<Ra<1.1x10^5$; $X=0.5$). Also at low Ra, along the vertical wall, the increase in convection becomes less significant. For optimal convective heat transfers from an enclosed, 9.5mm diameter horizontal cylindrical heater, the heater-to-wall separation should be less than 15mm ($Ra\approx7.5x10^4$). For arrays of vertically-

aligned, horizontal cylindrical heaters situated next to an adjacent vertical wall, the array should be tilted away from the wall, such that the rising, heated fluid from the lower heater, as well as the entrained flow, would be accommodated by the spacing between the downstream heaters and the vertical wall.

8.2. RECOMMENDATIONS

For cylindrical heaters in enclosures, further work should take advantage of interferometry for a detailed analysis of the local heat transfers for an improved accuracy of the Nusselt numbers. Data should be acquired at a larger number of finite steps as a general stepping stone to improved understanding of enclosed heat transfer processes, to determine if there are certain discontinuities in trends, and an encouragement to improved numerical methods. The employment of other enclosures of different aspect ratios could be considered, as well as different sized and multiple heaters along the vertical wall. This would permit the development of related empirical correlations.

The development of ovens is product-led. Therefore, recommendations from the oven studies (see Chapter 3) could include several of the studied configurations for onward development. The developmental process could take advantage of the changes in convection brought about by the alteration in the proximity of the heating-elements to the enclosing walls.

Where base heating is not a priority, C8, which achieved slightly more convection than C7 is recommended for further development. For C7, increased numbers and differential control of the upper heating-elements could be studied, as well as modelling the irradiance on the baking plane, with a view to improving the temperature uniformity of the finished products. However, the study confirmed that C2, with one heater along each of the four enclosure walls, approached steady-state fastest, and although it does not conform to a convective configuration, a further development of this is also recommended from a consideration of efficient energy usage.

Generally, the best natural convection would be obtained from heaters mounted horizontally and offset along the lower half of the vertical walls (C91 and C92). Where base heating is not a priority, C91 is recommended for further investigation because it

combines enhanced convective heat transfers with a rapid start-up to steady-state conditions, as well as improved temperature uniformity of the enclosure.

For increased base heating, the upper heater of C93 could be traversed inwards to create a high heat flux at the base (see Fig. 8-2). In this context, C91-135 which was examined in the flow visualisation, is also recommended for further development.

Further work should also focus on the effect of multiple inner bodies within cubical or conveyorised tunnel ovens on the flow and heat transfer characteristics of the system; the effect of non-louvered radiation shields which form parallel walls locally enclosing wall mounted heaters; the use of staggered, large diameter gas-fired tubes as heat sources; and the effect of generous rounding-off of the upper corners of ovens.

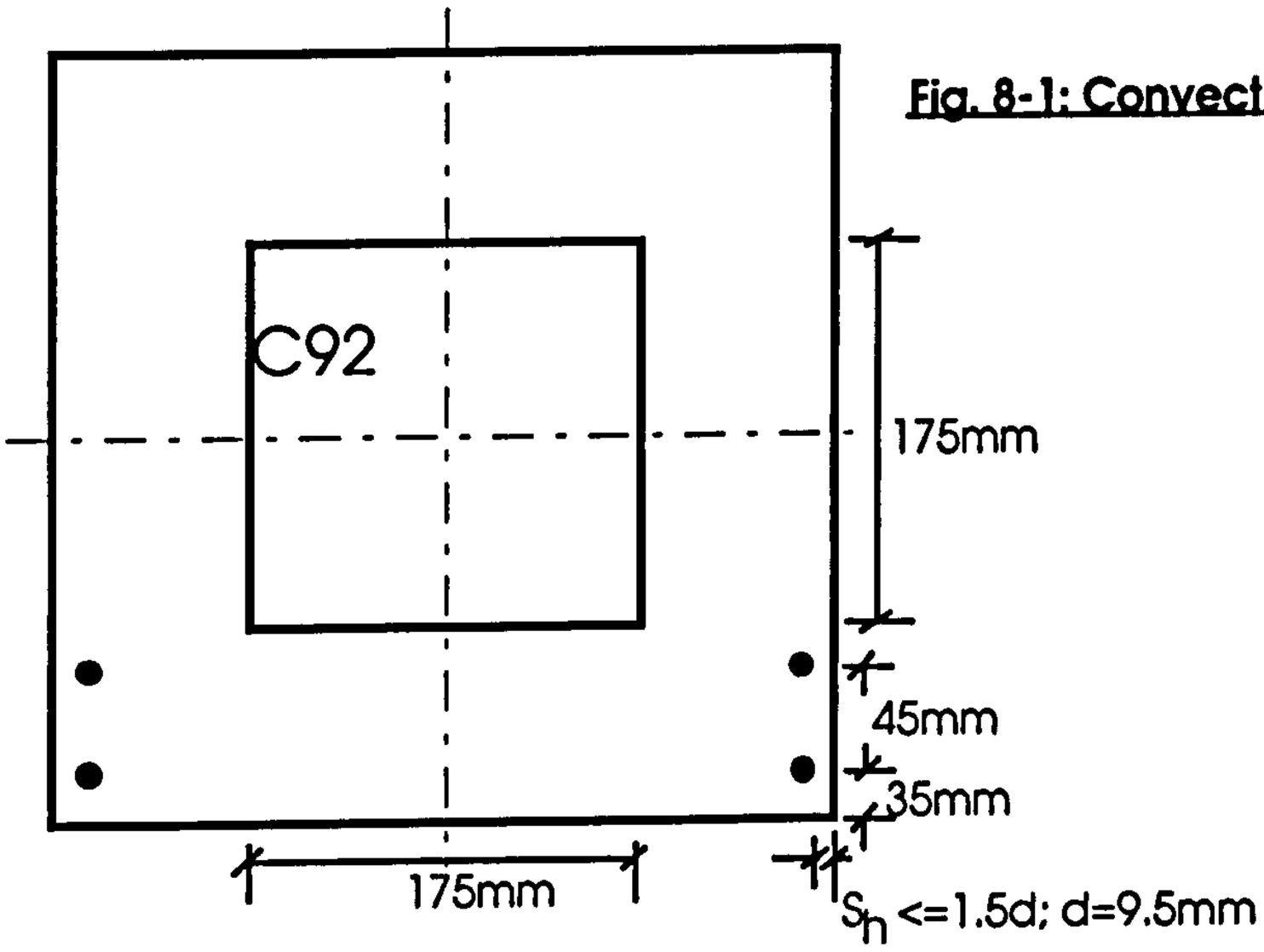

Fig. 8-1: Convective configuration

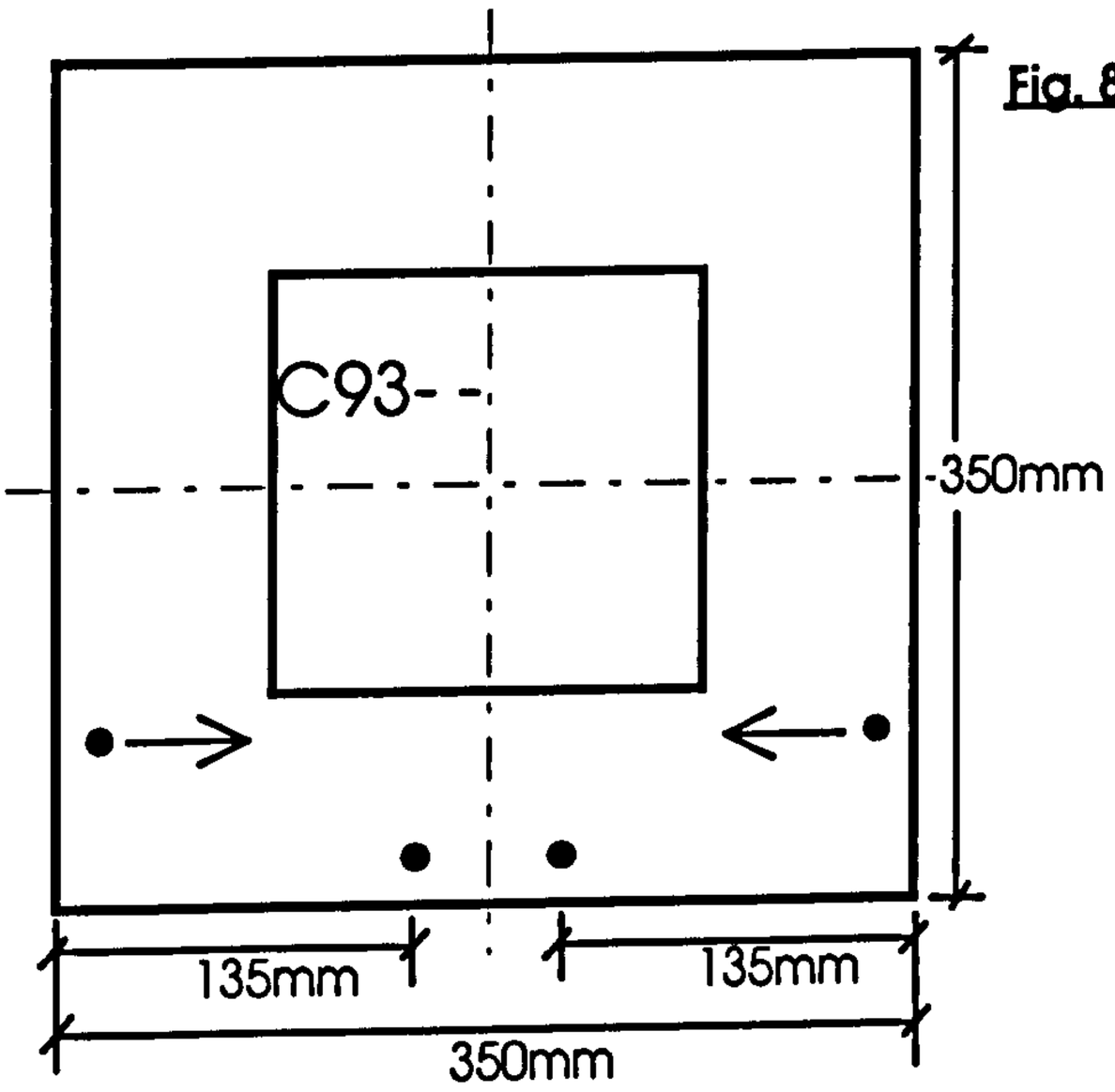

Fig. 8-2: Base-heating/convective configurations

REFERENCES

1. Gebhart B.
Heat Transfer, 2nd Ed., McGraw-Hill, 1971.

2. Prandtl L.
'*Grenzschichten und Widerstand*' ('The movement of fluids with very small friction')
Verhandlungen des III, Internationalen Mathematiker-Kongresses, Heidelberg, pp. 484-491, 1904.

3. Pohlhausen E.
'Der Warmeaustausch zwichen festen Korpern und Flussigkeiten mit kleiner Reibung'
Angewandte Mathematik und Mechanik, Vol. 1, p.115, 1921.

4. Adiutori E.
The New Heat Transfer, Ventuno Press, Cincinnati, USA, 1975

5. Wilkie D.
'Some Doubtful Natural Convection Correlations'
Proc. 9th Int. Heat Transfer Conf., 555-560, 1990.

6. Hottel H.C., Sarofim, A.F.
Radiative Transfer, McGraw-Hill, NY, (1967).

7. Milson A., Kirk D.
Principles of Design and Operation of Catering Equipment, Ellis Horwood, 1980.

8. Kay H.
'Design of Furnaces for Reheating', Metals Technology, Vol.2, Oct. 1975

9. Adams J.A., Rogers D.F.
'Computer-Aided Heat Transfer Analysis', McGraw-Hill NY, 1973

10. Ostrach S.
'Natural Convection in Enclosures'
J.Heat Transfer, Vol. 110, 1175-1190, 1988

11. Holman, J.P.
Heat Transfer, 7th Ed., McGraw Hill, 1990

12. Probert S.D., Brooks R.G., Dixon M.
'Heat Transfer Across Rectangular Cavities'
Chemical Proc. Eng. - (Heat Transfer Survey), 1970

13. Catton I.
'Natural Convection in Enclosures'
Proc. 6th Int. Heat Transfer Conf., Vol. 6, 13-31, 1978

14. Scheitlin G.G., DeWitt D.P.
'Bi-Radiant Oven, A Low Energy Oven System', Vol. III, Part 1.
Oak Ridge National Laboratory, Oak Ridge, Tennessee, Report prepared for US Dept of Energy 1981.

15. Scarisbrick C., Newborough M., Probert S.D.
'Improving the Thermal Performances of Domestic Electric Ovens'.
Applied Energy, Vol.39, 263-300, 1991.

16. Cheung, H
'Energy-Efficient Ovens: An Investigation of Natural Convection Heat Transfers'
MSc. Thesis, School of Mechanical Engineering, Cranfield Institute of Technology, 1991.

17. Hamady F.J., Lloyd J.R., Yang H.Q., Yang K.T.
'Study of Local Natural Convection Heat Transfer in an Inclined Enclosure'
Int. J. Heat and Mass Transfer, Vol.32, 1697-1708, 1989.

18. Chu H.H.-S., Churchill S.W., Patterson C.V.S.
'The Effect of Heater Size, Location, Aspect Ratio, and Boundary Conditions on Two-Dimensional, Laminar, Natural Convection in Rectangular Channels'.
J.Heat Transfer, Vol.98, 194-201, 1976.

19. Turner B.L., Flack R.D.
'The Experimental Measurement of Natural Convection Heat Transfer in Rectangular Enclosures with Concentrated Energy Sources'
J. Heat Transfer, Vol.102, No2, 236-241, 1980.

20. Ho C.J., Chang J.Y.
'A Study of Natural Convection Heat Transfer in a Vertical Rectangular Enclosure with two-dimensional Discrete Heating: Effect of Aspect Ratio'
Int. J. Heat and Mass Transfer, Vol.37, 917-925, 1994.

21. Chen L., Keyhani M., Pitts D.R.
'Convection Heat Transfer Due to Protruded Heat Sources in an Enclosure'
J. Thermophysics and Heat Transfer, Vol. 5, No.2, 1991.

22. Eckert E.R.G., Soehngen E.
'Studies on Heat Tansfer in Laminar Free Convection With the Zehnder-Mach Interferometer'.
Tech. Report No. 5747, USAF AMC, Dayton, Ohio, 1948.

14. Scheitlin G.G., DeWitt D.P.
'Bi-Radiant Oven, A Low Energy Oven System', Vol. III, Part 1.
Oak Ridge National Laboratory, Oak Ridge, Tennessee, Report prepared for US Dept of Energy 1981.

15. Scarisbrick C., Newborough M., Probert S.D.
'Improving the Thermal Performances of Domestic Electric Ovens'.
Applied Energy, Vol.39, 263-300, 1991.

16. Cheung, H.
'Energy-Efficient Ovens: An Investigation of Natural Convection Heat Transfers'
MSc. Thesis, School of Mechanical Engineering, Cranfield Institute of Technology, 1991.

17. Hamady F.J., Lloyd J.R., Yang H.Q., Yang K.T.
'Study of Local Natural Convection Heat Transfer in an Inclined Enclosure'
Int. J. Heat and Mass Transfer, Vol.32, 1697-1708, 1989.

18. Chu H.H.-S., Churchill S.W., Patterson C.V.S.
'The Effect of Heater Size, Location, Aspect Ratio, and Boundary Conditions on Two-Dimensional, Laminar, Natural Convection in Rectangular Channels'.
J.Heat Transfer, Vol.98, 194-201, 1976.

19. Turner B.L., Flack R.D.
'The Experimental Measurement of Natural Convection Heat Transfer in Rectangular Enclosures with Concentrated Energy Sources'
J. Heat Transfer, Vol.102, No2, 236-241, 1980.

20. Ho C.J., Chang J.Y.
'A Study of Natural Convection Heat Transfer in a Vertical Rectangular Enclosure with two-dimensional Discrete Heating: Effect of Aspect Ratio'
Int. J. Heat and Mass Transfer, Vol.37, 917-925, 1994.

21. Chen L., Keyhani M., Pitts D.R.
'Convection Heat Transfer Due to Protruded Heat Sources in an Enclosure'
J. Thermophysics and Heat Transfer, Vol. 5, No.2, 1991.

22. Eckert E.R.G., Soehngen E.
'Studies on Heat Tansfer in Laminar Free Convection With the Zehnder-Mach Interferometer'.
Tech. Report No. 5747, USAF AMC, Dayton, Ohio, 1948.

23. Lieberman J., Gebhart B.
'Interactions in Natural Convection From an Array of Heated Elements, Experimental'.
Int. J. Heat and Mass Transfer, Vol.12, 1385-1396, 1969.

24. Sparrow E.M., Boessneck D.S.
'Effect of Transverse Misalignment on Natural Convection From a Pair of Parallel, Vertically Stacked, Horizontal Cylinders'.
J. Heat Transfer, Vol.105, 241-247, 1983.

25. Tokura I., Saito H., Kishinami K., Muramoto K.
'An Experimental Study of Free Convection Heat Transfer From a Horizontal Cylinder in a Vertical Array Set in Free Space Between Parallel Walls'.
J. Heat Transfer, Vol.105, 102-107, 1983.

26. Morgan V.T.
'The Overall Convective Heat Transfer from Smooth Circlar Cylinders'.
Advances in Heat Transfer, Vol.11, 199-264, 1975, Academic Press, New York.

27. Al-Alusi T.R., Bushnell D.J.
'An Experimental Study of Free Convection Heat Transfer From An Array of Horizontal Cylinders Parallel to a Vertical Wall.'
J. Heat Transfer, Vol. 114, 394-400, 1992.

28. Sparrow E.M., Ansari M.A.
'All-modes Heat Transfer from a Horizontal Cylinder Situated Adjacent to Adiabatic, Partially Enclosing Walls.'
Int. J. Heat and Mass Transfer, Vol. 27, 1855-1864, 1984.

29. Liu,C.Y., Mueller, W.K., and Landis, F.,
'Natural Convection Heat Transfer in Long Horizontal Cylindrical Annuli.'
Int. Developments in Heat Transfer, pt.5, Paper No.117, Boulder, Colorado., 976-984, 1961.

30. Weber N., Powe R.E., Bishop E.H., and Scanlan J.A.
'Heat Transfer by Natural Convection Between Vertically Eccentric Spheres.'
J. Heat Transfer, Vol. 95, 47-52, 1973.

31. Warrington R.O., and Powe R.E.
'The Transfer Of Heat between Bodies and their Enclosures'
Int J. Heat and Mass Transfer, Vol. 28, No.2, 319-330, 1985.

32. Warrington R.O., Crupper G.,
'Natural Convection Heat Transfer Between Cylindrical Tube Bundles and a Cubical Enclosure'
J. Heat Transfer, Vol. 103, 103-107, 1981.

33. Shilston M. J.
'Heat Transfers across air-filled cavities'
PhD Thesis, School of Mechanical Engineering, Cranfield Institute of Technology, 1982.

34. Babus'Haq R., Probert S.D., Shilston M.J., Talati A.
'Design Improvements of District-Heating Pipeline Configurations'
Applied Energy, Vol.17, 77-96, 1984.

35. Warrington R.O., Weaver R.A.
'Natural Convection Heat Transfer Between Arrays of Horizontal Cylinders and Their Enclosure'
Proc. 9th Int. Heat Transfer Conf., Vol. 2, 205-209, 1990.

36. Warrington R.O., Smith S., Powe R.E., and Mussulman R.L.
'Boundary Effects On Natural Convection Heat Transfer For Cylinders And Cubes.'
Int J. Heat and Mass Transfer, Vol.31. No.6, 1322-1325, 1988.

37. Kuehn T.H., Goldstein R.J.
'An Experimental and Theoretical Study of Natural Convection in the Annulus Between Horizontal Concentric Cylinders'.
J. Fluid Mechanics, Vol.74, 695-720,1976.

38. Kumar R.
'Study of Natural Convection in Horizontal Annuli'
Int J. Heat and Mass Transfer, Vol.31, No.6, 1137-1148, 1988.

39. Chang K.S.; Won Y.H.; Cho C.H.
'Patterns of Natural Convection Around a Square Cylinder Placed Concentrically in a Horizontal Circular Cylinder.'
J. Heat Transfer Vol.105, 273-280, 1983.

40. Oosthuizen P.H., Paul J.T.
'Natural Convective Heat Transfer From a Square Element Mounted on the Wall of an Inclined Square Enclosure'.
AIAA 22nd Thermophysics Conference, Honolulu, Hawaii, AIAA-87-1588, 1987.

41. Oosthuizen P.H., Paul J.T.
'Finite Element Study of Natural Convective Heat Transfer From A Prismatic Cylinder in An Enclosure'.
Winter Annual Meeting of ASME, Numerical Methods in Heat Transfer, vol.62, pp 13-21, 1987/88.

42. Larson D.W., Gartling D.K., Schimmel Jr. W.P
'Computational and Experimental Methods for Enclosed Natural Convection'.
Report No. SAND 770645, Sandia Laboratories, Albuquerque, USA, 1977.

43. Lacroix M.
'Natural Convection Heat Transfer Around Two Heated Horizontal Cylinders Inside a Rectangular Cavity Cooled From Above'.
Numerical Heat Transfer, Part A, vol.21, 37-54, 1992.

44. Zhong Z.Y., Yang K.T., Lloyd J.R.
'Variable Property Natural Convection in Tilted Enclosures With Thermal Radiation', in
Numerical Methods in Heat Transfer, Ed.R.Lewis, Volume III, J.Wiley, 1985.

45. deGroh III H.C., Kassemi M.
'Effect of Radiation on Convection in a Top-Heated Enclosure'.
J. of Thermophysics and Heat Transfer, Vol.7, No.4, Oct.-Dec., 1993.

46. Kassemi M., Naraghi M.H.N.
'Analysis of Radiation-Natural Convection Interactions in 1-g and Low-g Environments Using the Discrete Exchange Factor Method'.
Int J. Heat and Mass Transfer, Vol 36, No.17, 4141-4149, 1985.

47. Zhao Z., Poulikakos D., Ren Z.
'Combined Natural Convection and Radiation from Heated Cylinders Inside a Container'.
J. Thermophysics and Heat Transfer, vol.6, No.4, pp 713-720, 1992.

48. Zhao Z., Ren Z., Poulikakos D.
'Heat Transfer in Power Cables Packaged Inside Trays'
J. Heat Transfer, Vol.114, 777-780, 1983.

49. Incropera F.P., DeWitt D.P.
Fundamentals of Heat and Mass Transfer, 3rd Ed., Chichester, Wiley, 1990.

50. Belling & Co. Ltd.
Belling Compact 4 (430N) - Domestic cooker,
Belling & Co. Ltd., Bridge Works, Southbury Road, Enfield, Middlesex.

51. Hines A.J.
Personal Communication, Sept.,1994.
Creda Ltd., Creda Works, Blythe Bridge, Stoke-On-Trent ST11 9LJ.

52. Elliston D.G., Gray W.A., Hibberd D.F., Ho T-Y,
Williams A.
'The Effect of Surface Emissivity on Furnace Performance'
J. Inst. of Energy, Vol. 155, 155-167, Dec. 1987.

53. Hughes N.
'Fan Ovens', BBC2 Food & Drink Programme, 1992.

54. Ozoe,H.; Churchill,S.W.; Okamoto, T.; and Sayama,H.
'Natural convection in doubly inclined rectangular boxes'
Proc. 6th Int. Heat Transfer Conf., Vol. 2, 293-298, 1978.

55. Brown J.
'Ovens - The Heart of the Matter'
Baking Today, Oct. 1985.

56. Hauf W., Grigull U.
'Optical Methods in Heat Transfer' in
Advances in Heat Transfer, Vol.6, 202-366, Plenum Press, NY, USA,
1970.

57. Janikowski H.E.
'Heat Transfer and Flows in air-filled Cavities fitted with Baffles'.
PhD Thesis, School of Mechanical Engineering, Cranfield Institute of
Technology, 1979.

58. Brooks R.G.
'An interferometric Study of Heat Transfer through Gases'
PhD Thesis, University of Wales, 1970.

59. Howell J.R
A Catalog of Radiation Configuration Factors
McGraw-Hill, New York, 1982.

60. King W.J.
'The Basic Laws and Data of Heat Transmission - III, Free Convection,
Mech. Engineering, Vol.54, 347-353, 1932.

61. McAdams
Heat Transmission, 3rd Ed., McGraw-Hill, New York, 1954.

62. Sparrow E.M., Stretton A.J.
'Natural Convection From Variously Oriented Cubes and From Other Bodies of Unity Aspect Ratio.'
Int. J. Heat and Mass Transfer, Vol.28, 741-752, 1985.

63. Rogers G.F.C., Mayhew Y.R.
Thermodynamic and Transport Properties of Fluids, 3rd Ed., 1982.

64. Gray D.D., Giorgini, A.
'The validity of the Boussinesq approximation for liquids and gases'
Int. J. Heat and Mass Transfer, Vol.19, 545-551, 1976.

65. Langerman M.A.
'A non-Boussinesq Integral Method for Laminar Free Convection between Vertical Flat Plates Subject to a Uniform Wall Heat Flux'
Int. J. Heat and Mass Transfer, Vol.36, 3429-3435, 1993.

66. Nusselt W.
'Das Grundgesetz des Warmeuberganges'
Gesundh.-Ing., 38, 77-490, 1915.

67. Sparrow E.M., Pfeil D.R.
'Enhancement of Natural Convection Heat Transfer From A Horizontal Cylinder Due to Vertical Shrouding Surfaces'
J. Heat Transfer, Vol.106, 124-130, 1984.

68. Marsters G.F.
'Natural Convective Heat Transfer From a Horizontal Cylinder in the Presence of Nearby Walls'
The Canadian Journal of Chemical Engineering, Vol. 53, 145-149, 1975.

69. Cho C.H., Chang K.S., Park K.H.
'Numerical Simulation of Natural Convection in Concentric and Eccentric Horizontal Cylindrical Annuli'
J. Heat Transfer, Vol.104, 624-630, 1982.

70. Deschamps V., Desrayaud G.
'Modelling a Horizontal Heat-Flux Cylinder as a Line Source'
J. of Thermophysics and Heat Transfer, Vol.8, No.1, 1994.

71. Zagromov Y.A., Lyalikov A.S.
'Free Convection Heat Transfer in Horizontal Cylindrical Layers with Different Positions of the Heated Element'.
Inzh.-Fiz. Zh., Vol. 10 (5), 577-583, 1966.

72. Edwards R.M.
'Heat Transfer Through Cavity Walls'
M.Sc. Thesis, University of Wales, 1968.

73. ASME Boiler and Pressure Vessel Code, Section VIII, Division I, 1983.

74. Faupel J.H.
'Pressure Vessel of Noncircular Cross Section (Commentary on New Rules for ASME Code)'
J. of Pressure Vessel Technology, ASME, Vol.101, 1979.

75. Timoshenko S.
'Theory of Plates and Shells,' 2Ed., McGraw-Hill, New York, 1959.

76. 'Suggested Good Practice Regarding Corrosion Allowance'
Nonmandatory Appendices, Appendix F, ASME Boiler and Pressure Vessel Code, Section VIII, Division 1, 1992.

77. Taylor Kightley Engineering Co. Ltd., Moulton Park
Industrial Estate, Northampton, 1993.

78. Zeng Z-j., Gao J-j., Gu Q-s.
'The Stess Analysis of Rectangular Pressure Vessels having Thin-walled Reinforcing Members'
Int. J. Pressure Vessel & Piping, Vol. 30, 193-204, 1987.

79. Massey B. S.
Fluid Mechanics, 6th Ed., Van Nostrand Reinhold, London, 1989.

80. Morgan, D
Personal Communication, April 1993.
Elmatic (Cardiff) Ltd., Wentlogg Road, Rumney, Cardiff CF3 8XH.

81. Brown J.
'Travelling Ovens'
Baking Today, Nov. 1985.

82. Siegell R., Howell J.R.
Thermal Radiation Heat Transfer, McGraw-Hill, 1972.

83. Puccinelli E.F.
'View factor computer program user's manual'
Goddard Space Flight Center, Greenbelt, MD; Report X-324-73-272, 1973.

84. Wong R.L.
'Gray - program to calculate gray body radiation heat transfer view factors from black body view factors', University of California, Lawrence Livermore National Laboratory, Report UCID17277, 1976.

85. Emery A.F.
'Instruction manual for the program SHAPEFACTOR'
Sandia National Laboratories, Livermore, CA., Report SAND80-8027
1980.

86. Shapiro A.B.
'FACET - A radiation view factor computer code for axisymmetric 2-D planar, and 3D geometries with shadowing'
University of California, Lawrence Livermore National Laboratory, Report UCID-19887, 1983.

87. Burns P.J.
'MONTE - A two dimensional radiative exchange factor code'
Colorado State University, Ft. Collins, CO.,USA, 1983.

88. Ward L., Bunn J.P.
'Introduction to the Theory and Practice of High Vacuum Technology', Butterworths, London, 1967.

89. Kennard E.H.
Kinetic Theory of Gases, 311-325, 1938.

90. Walton G.N.
'Algorithms for Calculating Radiation View Factors Between Plane Convex Polygons With Obstructions'.
US Dept. of Commerce, National Bureau of Standards, NEL, Gaithersburg, Maryland, USA, 1986.

91. Brandes E.A.; Brooks G.B., Eds.
(Table 17.7, SS shot-blasted)
Smithells Metals Reference Book, 7th Ed., 1992; Butterworth-Heinemann.

92. Gebhart B., Knowles C.P.
'Design and Adjustment of a 20cm Mach-Zehnder Interferometer'.
The Review of Scientific Instruments, Vol.37, No.1, 1965.

93. 'A Guide on Protection of Personnel against Hazards from Laser Radiation'
BSI, Publication, BS4803, 1972.

94. Wilkie D.
'Measurement of Temperature by Mach-Zehnder Interferometry'
Proc. Inst. of Mech. Engrs., Vol. 178, Pt 1, No.17, 1963-64.

95. Feingold A.
'Radiant-interchange Configuration Factors between Various Selected Plane Surfaces'
Proc. Royal Soc. Ser. A, Vol. 292, no.1498, 51-60, 1966.

96. Ray M.S.
Engineering Experimentation
McGraw-Hill Book Company, London, 1988.

97. Kline S.J., McClintock F.A.
'Describing Uncertainties in Single-Sample Experiments'
Mechanical Engineering, 3-8, 1953.

98. Anon
'Electric Infrared Oven Designed for Thermal Efficiency in Curing Operation'.
Industrial Heating, V.45, No.7, 23-24, 1978.

99. British Standards Institution,
BS 5500:1991, Unfired Fusion-Welded Pressure Vessels,
BSI, London, 1991.

100. Young W.C.
Roark's Formulas for Stress and Strain, McGraw-Hill Inc., 1989.

101. Timoshenko S., Woinowski-Krieger S.
Theory of Plates and Shells, 2.Ed., McGraw-Hill Book Co., 1959.

102. Boeke W., Wall L.
'Radiative Exchange Factor in Rectangular Spaces for the determination of Mean Radiant Temperatures'
Building Services Engineer, Vol.43, 244-253, 1976.

103. Gross U., Spindler K., Hahne E.
'Shapefactor-Equations for Radiation Heat Transfer Between Plane Rectangular Surfaces of Arbitrary Position and Size with Parallel Boundaries.'
Letters in Heat and Mass Transfer, Vol.8, 219-227, 1981.

APPENDICES

APPENDIX A

ADJUSTMENT OF THE MZI (and the evaluation of the interferograms)

A.1. Introduction

From time to time it is necessary to reset the drift or loss of alignment caused by vibration, thermal expansion, or inadvertent manipulation of the adjusting devices. The need for an improved adjustment procedure arose because the use of the existing dedicated method [57] still failed to produce the infinite fringe mode. The layout is reproduced in Fig. A-1.

A.2. Modes of operation

The MZI can be used in three different modes:

a The instrument can be adjusted to produce several parallel (or wedge) fringes each having a small finite width and spacing. As temperature gradients are introduced in the test beam, points of equal fringe shift (i.e. isotherms) can be identified.

b When an undistorted interferogram is superposed on a distorted interferogram (to yield moiré fringes), isotherms can be identified by locating lines of equal fringe shift. This mode of operation has the advantage of eliminating the effects of imperfections of the interferometer optical plates, as both the distorted and undistorted fringe patterns suffer equally as a result of any defects

c The fringes can be as widely spaced as possible until only one fringe occupies the entire screen or field of view (nominally infinite fringe spacing). As temperature gradients are introduced in the test beam, the fringe will shift and also become narrower. Several fringes will come into view and each fringe is nominally an isotherm.

A.3. Adjustment

The following adjustment procedure is based largely on the procedure specifically dedicated to the MZI available at Cranfield University [57]. The main variation is the incorporation of the 'cross hairs' method [92].

If the geometric alignment has been carefully set up, then go to the second part - A6, 'The method of cross-hairs', after noting the safety instructions A.4.5 and A.5.5. For standard operations where only a small adjustment is required, it is common to use only the M2 adjusting devices to regain the optimised settings. Basically the initial procedure is to align the laser light source, adjust the four optical plates, insert the pinhole assembly and re-align.

A.4. Initial Preparations

A.4.1.
Obtain a pair of appropriate safety goggles for eye protection.

A.4.2.
Obtain two test templates made from thick cardboard paper and mark them as shown (see Fig. A-2). The offset marking is to allow for parallax effects due to the thickness of the card or template.

A.4.3.
Obtain, on a suitable mobile stand a screen preferably made of graph paper.

A.4.4.
Check to see that each wheel stand is reasonably inflated. Uniform inflation of the wheeled tyres is not critical although it should facilitate the subsequent adjustment of the pinhole filter on the input bench assembly.

A.4.5.

The optical devices are precision-manufactured, costly, and easily damaged. The optical surfaces should, therefore not be touched or otherwise they may require expensive, expert cleaning.

A.5. Geometric alignment

Refer to Fig. A-3, A-4 and A-5.

A.5.1.
On the upright stands, there are facilities for over 20mm of vertical (height) adjustment for each of the four optical devices. Check that all the four optical surfaces are raised to only about halfway up their adjustable mountings (≅6 acme threads), and that M2 is also positioned at about its central position on the vernier translation table.

A.5.2.
Each of the mirrors and beam splitters has two fine vernier rotational adjustment about the horizontal and vertical axes. Using these screws ensure that the optical plate holding faces are initially flat with the gymbal assembly faces.

A.5.3.
Remove the laser pinhole filter assembly (integral with L1) and the collimating lens L2.

A.5.4.
Position one test template to cover M2. The template is positioned such that the continuously drawn diameter is vertical and the offset mark, (if any), on the horizontal and to the left.

A.5.5.

Precaution [93]:

Wear appropriate SAFETY GOGGLES and then, switch on the laser light source.

A.5.6.
The laser gun can be adjusted vertically via its two span supports; a coarse horizontal adjustment is effected by loosening the flange mountings (see Fig. A-4) and manually shifting the bench in the required direction; a finer horizontal-arc adjustment of the gun is effected by a rocking pivot, using the two screws on either side of the pivoted carrier bench.

A.5.7.
Adjust the laser to strike the optical centre of M2 (the appropriate offset point on the card).

Position the second test template over BS1 (on the input side) and adjust the laser to strike its optical centre. Remove the test template over BS1 and check the displacement from the optical centre of M2; if necessary readjust the laser and bench.

Replace the test template over BS1, and check again for centring.

Iterate this procedure to obtain the optical centre of BS1 and M2 simultaneously.

A.5.8.
Remove the test template from BS1 and position it over mirror M1 so that the offset is to the right.

Obtain the optical centre of M1 by rotation of BS1 about its axes; the vertical (height) position of M1 is also adjustable using the upright.

Remove the test template from M1 and position it on BS2 (see Fig.A-5) on the same side as M1 but with the offset now to the left. Obtain the optical centre of BS2 by rotating M1 about its axes; the height of BS2 can be adjusted at this stage. Shift the other test template from mirror M2 to BS2, the offset now to the right.

A.5.9
With both sides of BS2 now covered, adjust M2 by rotation in order to obtain the corresponding optical centre on the M2 side of BS2 without altering the height of BS2. Remove the test templates.

A.5.10.
L2 is positioned on the input bench and the height and orientation easily fixed by directing the faint reflection back along the laser beam. Remove L2.

A.5.11.
The mobile screen is now positioned on the input collimating bench as closely as possible to BS1, and adjusted vertically so that the light strikes somewhere close to its centre of area. This point is marked.

A.5.12.
The pinhole filter assembly is now re-positioned, as close to the laser as practicable.

The assembly consists of a small, convex condensing lens and a tiny aperture. The aperture can be located using vertical and horizontal vernier adjusters, while, on the same table, the lens can be moved axially towards the aperture; additionally the assembly table can be moved normal to the laser by loosening the mounting and sliding along the input bench. This assembly is adjusted so that the aperture is positioned at the focal point (a short distance), of the condensing lens.

A.5.13.
The brightness on the mobile screen (which is not necessarily uniform) can be used as a guide as to the ideal position of the aperture. (Moving the mobile screen along the bench to ascertain laser height parallelism may introduce errors since the earlier use of the pivot bench adjuster screws would have introduced relative inclination to the horizontal).

A.5.14.
L2 is then re-positioned so that the aperture is somewhat at, or near its focal point. Alternatively, the optimal location is obtained by moving L2 along the input bench in the direction of BS1 until the diameter of the illumination on the screen (≅190mm) just becomes constant, (i.e. beam parallelism or collimation is achieved);

It may be necessary to readjust the height of L2 since the bench may no longer be parallel to the light beam. As a guide, L2 will faintly reflect some laser light back towards the aperture and laser gun direction. Rotation of L2 (about the vertical), and some height adjustment, should enable the misalignment to be corrected, by ensuring that the reflection is in line with the laser source.

A.5.15.
The mobile screen is now transferred to the decollimating bench. The decollimating lens L3 is positioned as close to BS2 as practicable.

Because of geometrical approximations in the adjustment procedure, the beams may not have recombined identically at the surface of BS2. In which case two separate tiny dots should be seen at the focal point of L3. Whenever the two foci are coincident, fringes should be produced.

A.6. The method of cross hairs - α [92]

If the focal points are brought together (using M2 or BS2), fringes should be visible on the screen. To obtain fringes of the widest spacing (infinite fringe), the method of cross hairs is employed.

A.6.1.
Position the movable screen on the output (de-collimating) bench between BS2 and the decollimating lens L3.

A.6.2.
A cross hairs is placed on the input collimating bench, between BS1 and L2 (see Fig. A-6). Due to angular misalignment two images of these cross hairs can be observed on the output collimating bench screen. Note how far apart the images are.

A.6.2.1.
Rotate BS2 to bring the two cross hairs images together.

A.6.2.2.
Shift the screen to the two focal points beyond L3 and, using M2, the two focal points are brought together. This will influence the original positions of the cross hairs images.

A.6.2.3.
Re-position the screen between L3 and BS2 and check the proximity of the two cross hairs.

A.6.3.
IF: the cross hairs images are nearer than they were initially,
repeat the process A6.2.1 - 3
until both the images of the cross hairs and the focal points are each coincident simultaneously.

A.6.4.
But if: the cross hairs images are now farther apart than they were initially,
reverse the process:
4.Rotate M2 to bring the two images together

5.Rotate BS2 to bring the focal points together
6.Check the proximity of the cross hairs images by repositioning the screen between L3 and BS2.

A.6.5.
Continue either process until both the images of the cross hairs and the focal points are each coincident simultaneously. At this stage, there should be only one fringe, or at most two fringes covering the entire screen.

The cross hairs method converges rapidly but it requires that the initial geometric alignment be carefully set up.

A.6.6
A further optimising technique by Brooks [58] which can be adopted if more than one fringe is still visible is to traverse M2 (along the path that bisects the included angle between the incident and reflected rays) as follows:

First of all, swing the fringes into the vertical plane by slightly rotating M2 about its horizontal axis. Now, using the horizontal vernier translation devise, traverse M2 inwards (which shortens the reference beam path length) or outwards (lengthens the reference beam path length). The fringes will be seen to rapidly cross the screen, widening or narrowing depending upon the direction of translation; traverse in the direction that provides the wider fringe spacing. M2 is finally rotated about its axes to bring the central fringe into view or to provide the widest possible fringe spacing.

If necessary, the method of cross hairs is re-applied.

For normal operations, it is usually sufficient to use M2 adjusting devices only, to regain the optimised settings.

A.7. Method of alignment of the test cell along the beam

Exact alignment of the test cell with the interferometric beam was found to be difficult. Common methods for alignment include:

(a) the use of cross hairs at each end of the test cell [58] and matching the interferometric image with a previously drawn contour of the cross-section of the test cell on the screen, and

(b) observing spurious fringes caused by diffraction at the wall [56,33].

In this study, the output beam was expanded using a condensing lens of a short focal length (see Fig. A-8). This also magnified any mis-alignment which was then detected on the screen. This optical method was combined with the diffraction method (b) and the alignment of the enclosure and the inner objects with the beam was thus facilitated.

A.8. Evaluation of the interferograms

When the interferometer is set up from the infinite fringe mode (see A.2c), evaluating the subsequently disturbed interferogram is considerably simplified as the fringes are nominally isotherms. Each fringe has shifted by a constant from the initial zero order fringe. The temperature of any section within the interferogram is then obtained by multiplying the ^{o}C/fringe with the number of fringes from the reference wall to the point of interest.

The relationship between fringe shift (ΔN) and the corresponding temperature change (ΔT) has been derived [56,58] and adapted for the present rig as follows:

The number of wavelengths of light, N, along a test section of path length Z is given by:

$$N=Z/(\lambda_o/n) \qquad (A.1)$$

The relationship between the refractive index of a fluid and its density is:

$$\frac{1}{\rho}\left[\frac{n^2-1}{n^2+2}\right]=\text{constant} \qquad (A.2)$$

For a gas, $(n+1)/(n^2+2)$ is nearly constant so that eqn.(2) reduces to

$$(n-1)/\rho=G_1 \qquad (A.3)$$

where G_1 is the Gladstone-Dale constant. Thus, for a change in the refractive index from n_1 to n_2

$$(n_1-n_2)=G_1(\rho_1-\rho_2) \qquad (A.4)$$

Combining eqns (1) and (4)

$$\Delta N=G_1 Z(\rho_1-\rho_2)/\lambda_o \qquad (A.5)$$

Substituting for G_1 from eqn.(2) yields:

$$\Delta N=\frac{(n_1-1)}{\rho_1}\frac{Z}{\lambda_0}(\rho_1-\rho_2) \qquad (A.6)$$

For a gas at constant pressure,

$$\rho_1 T_1=\rho_2 T_2 \qquad (A.7)$$

and eqn.(6) becomes:

$$\Delta N = (n_1-1)\frac{Z}{\lambda_0}\frac{\Delta T}{T_2} \qquad (A.8)$$

where $\Delta T=T_2-T_1$

Rearranging eqn.(8), the relation between fringe shift and temperature change is obtained in terms of a reference temperature and the corresponding refractive index of the gas in the test section. Thus

$$\Delta T = \frac{T_1\Delta N}{\frac{Z}{\lambda_0}(n_1-1)-\Delta N} = \frac{T_c\Delta N}{\frac{Z}{\lambda_0}(n_c-1)-\Delta N} \qquad (A.9)$$

where T_c represents the temperature at the cold surface.

From eqns (2),(3) and (7),

$$\frac{n_1-1}{n_0-1}=\frac{\rho_1}{\rho_o}=\frac{T_0}{T_1};\ \text{so, } n_c-1=(n_0-1)\frac{T_0}{T_c} \qquad \text{(A.10)}$$

where n_c and n_o are the refractive indices at T_c and T_o respectively.
Substituting eqn.(10) into eqn.(9), then:

$$\Delta T=\frac{T_c\Delta N}{\frac{Z}{\lambda_o}(n_o-1)\frac{T_c}{T_h}-\Delta N}=\frac{T_c}{\frac{Z}{\lambda_o}(n_o-1)\frac{T_c}{T_h\Delta N}-1} \qquad \text{(A.11)}$$

For each experimental rig, the value $\left[\frac{Z}{\lambda_o}(n_o-1)\right]$ can be taken as a constant, G_2. Therefore, for a rig length of 0.75 as used in chapter 3:

$Z=0.750m$, $\lambda=632.8\times10^{-9}$, $n_o-1=0.2936\times10^{-3}$, then $G_2=347.98$

For $\Delta N=1$, and the cold wall surface temperature $T_o=273K$,

$$\Delta T=T_h-273=\frac{273}{347.98\left(\frac{273}{T_h}\right)-1}$$

whence $T_h=273.789$ or $\Delta T=0.789^oC$/fringe shift (at $T_o=273$).
Similarly, for $\Delta N=2$ fringes, $T_h=1.587K$, and for $\Delta N=3$ fringes, $T_h=2.394K$ (at $T_o=273K$). So it is easily seen that the relationship between the value of temperature per fringe shift and the number of fringes is not linear.
Generally, $T_h^2-T_cG_3T_h+T_c^2G_3=0$, where $G_3=G_2/\Delta N$.
So for $T_C=20^oC=293K$, and $\Delta N=10$ fringes, then $G_3=34.8$, $T_CG_3=10193.2$, $T_C^2=85849$ and T_h can be obtained from:

$$T_h=0.5\left\{+(T_cG_3)\pm\sqrt{(T_cG_3)^2-4T_c^2G_3}\right\} \qquad \text{(A.12)}$$

i.e. $T_h=301.9K$
Sources of error [94, 56, 58] could include:

(a) measurement of fringes
(b) proximity of fringes to solid boundaries
(c) poorly processed photographs
(d) poor definition of fringes adjacent to solid walls
(e) vibration
(f) end effects, and
(g) refraction

It must also be noted that any adjustment error for the infinite fringe is additively superimposed on the interferogram, i.e. if more than one fringe occupies the screen. This error, which is equivalent to higher temperature readings than would exist in the test cell, is suppressed if the number of fringes is large [56].

Fig. A-1 Layout of the Mach-Zehnder Interferometer

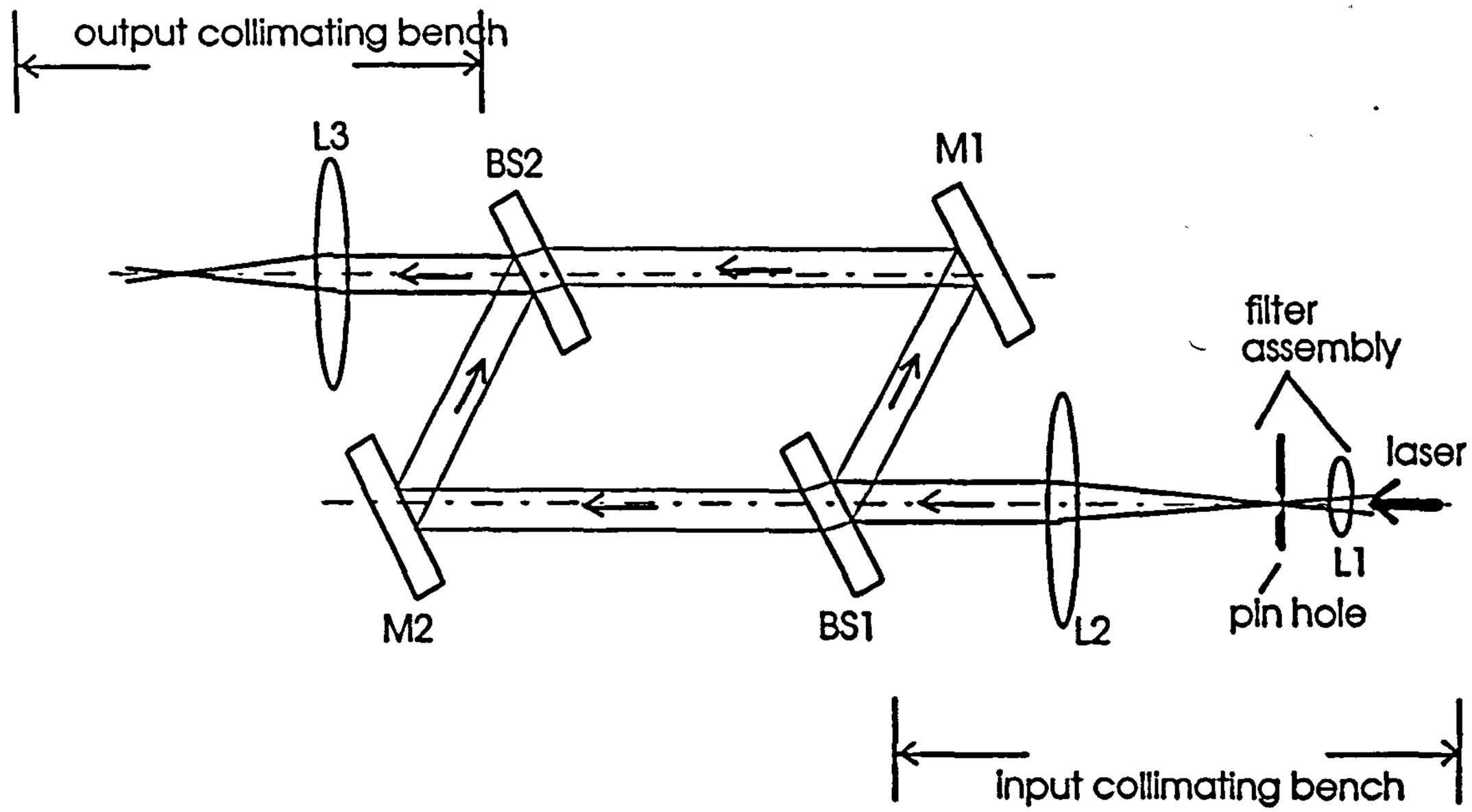

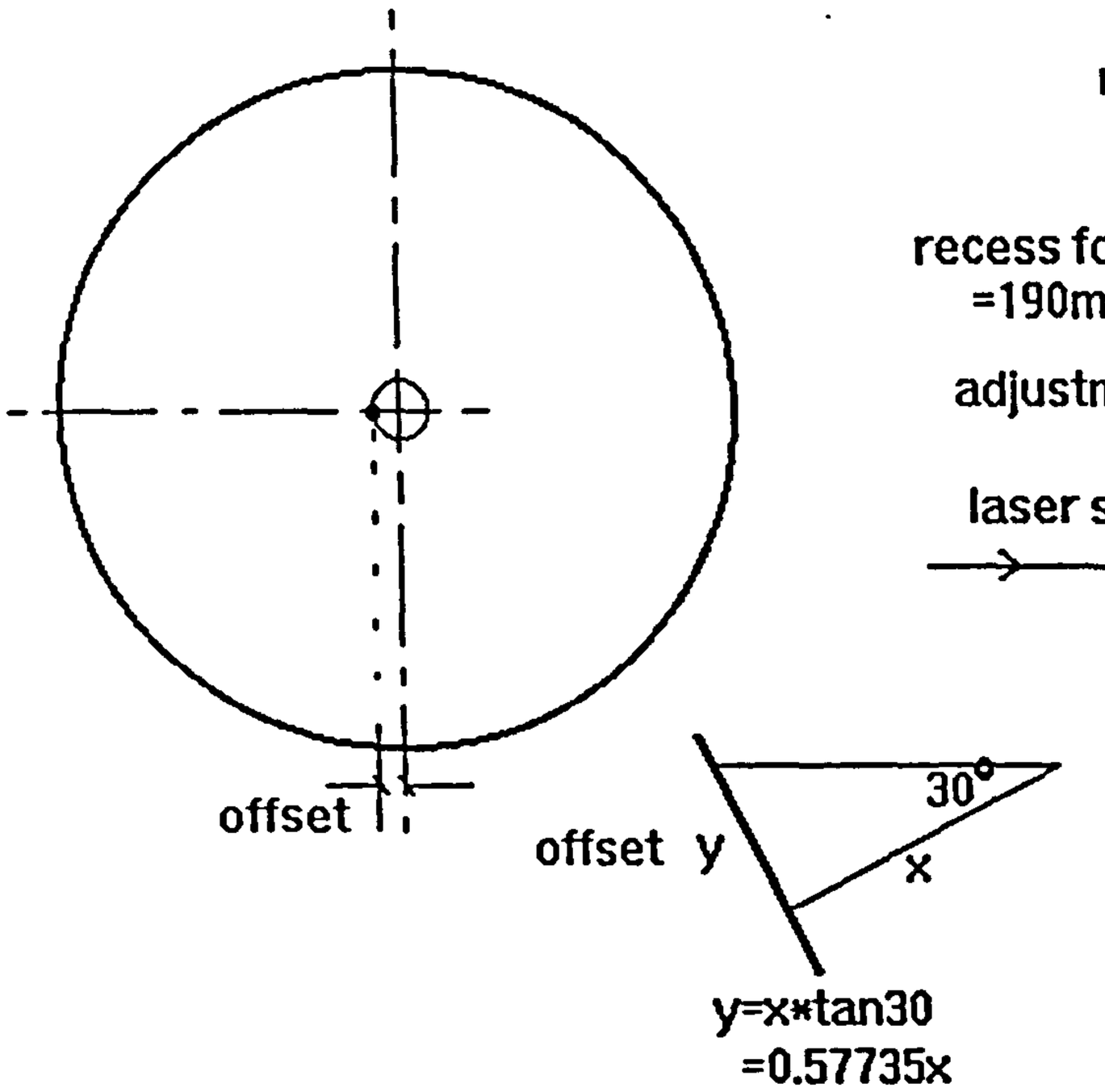

CARD FOR OPTICAL ALIGNMENT

e.g. If card is of 3mm thickness
and is right up against the optical surface,
then the offset is only 0.57735*3=1.732mm

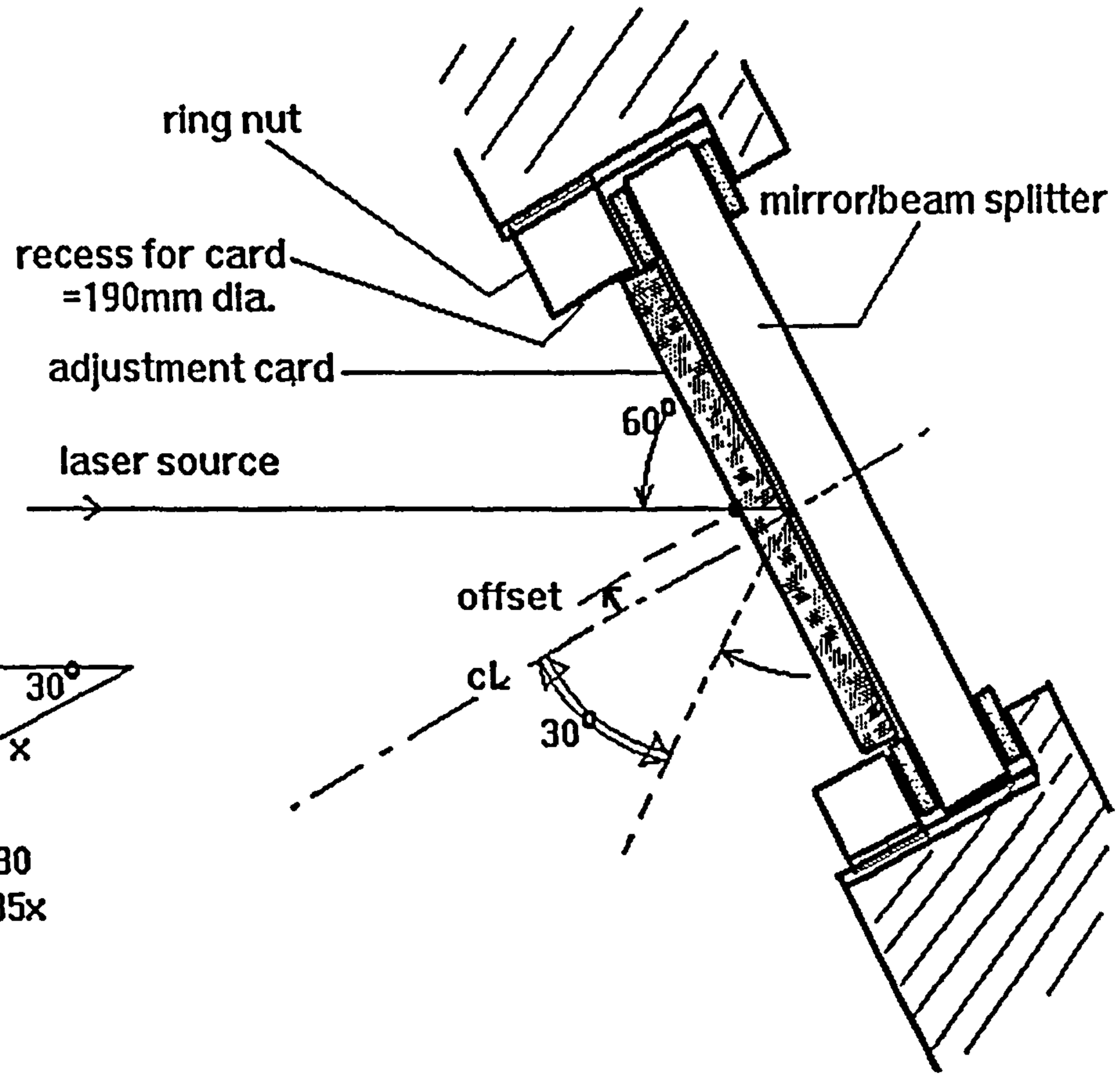

POSITION OF CARD ON
OPTICAL SURFACE

Fig. A-2

Fig. A-3 Reference and Working Beams recombine Identically

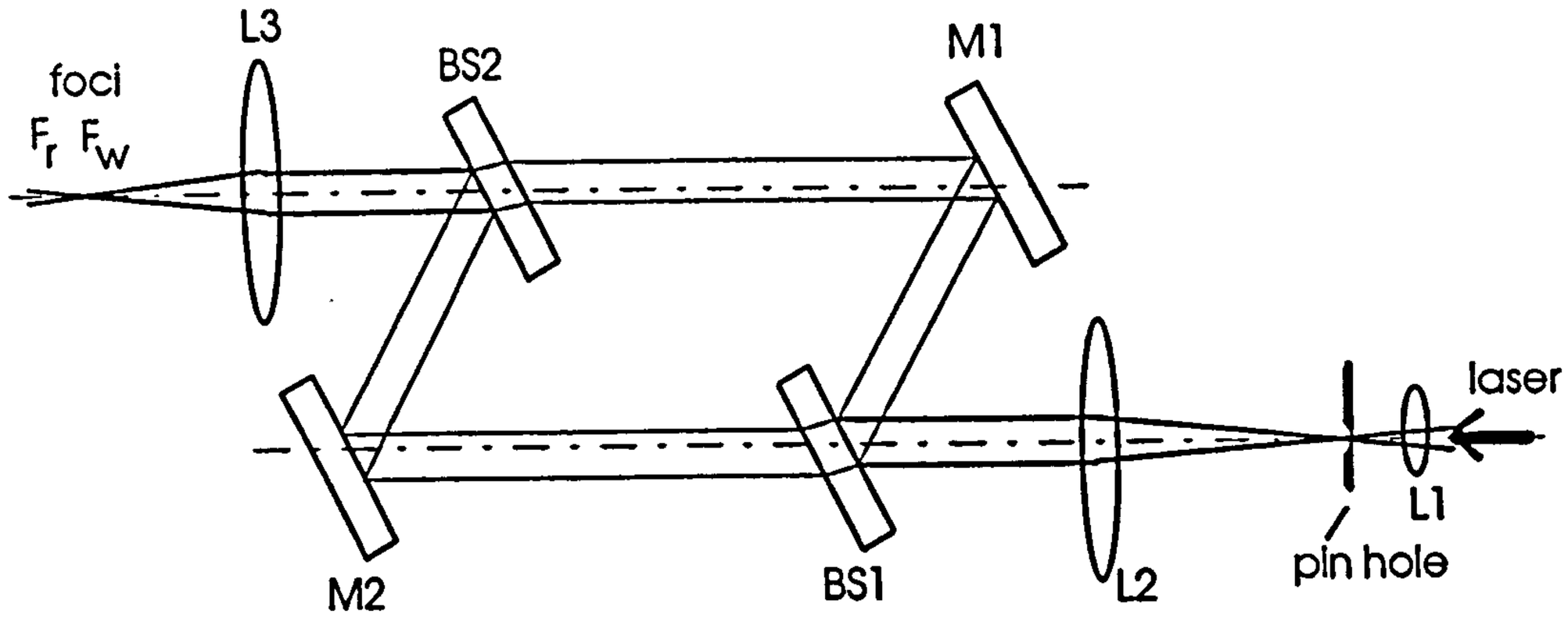

Fig. A-4 Input collimating bench adjusting aids

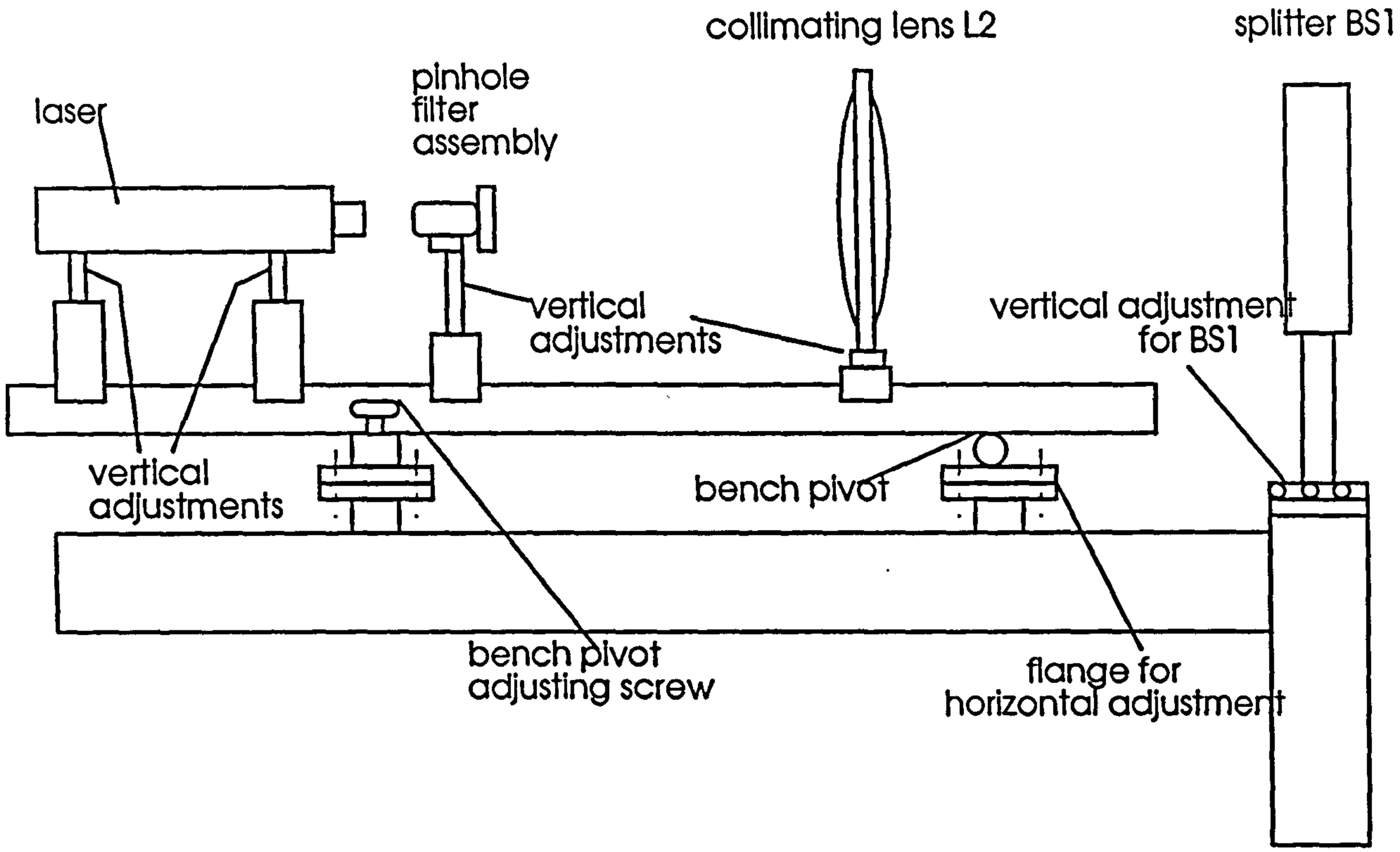

Fig. A-5 Output bench adjusting aids and

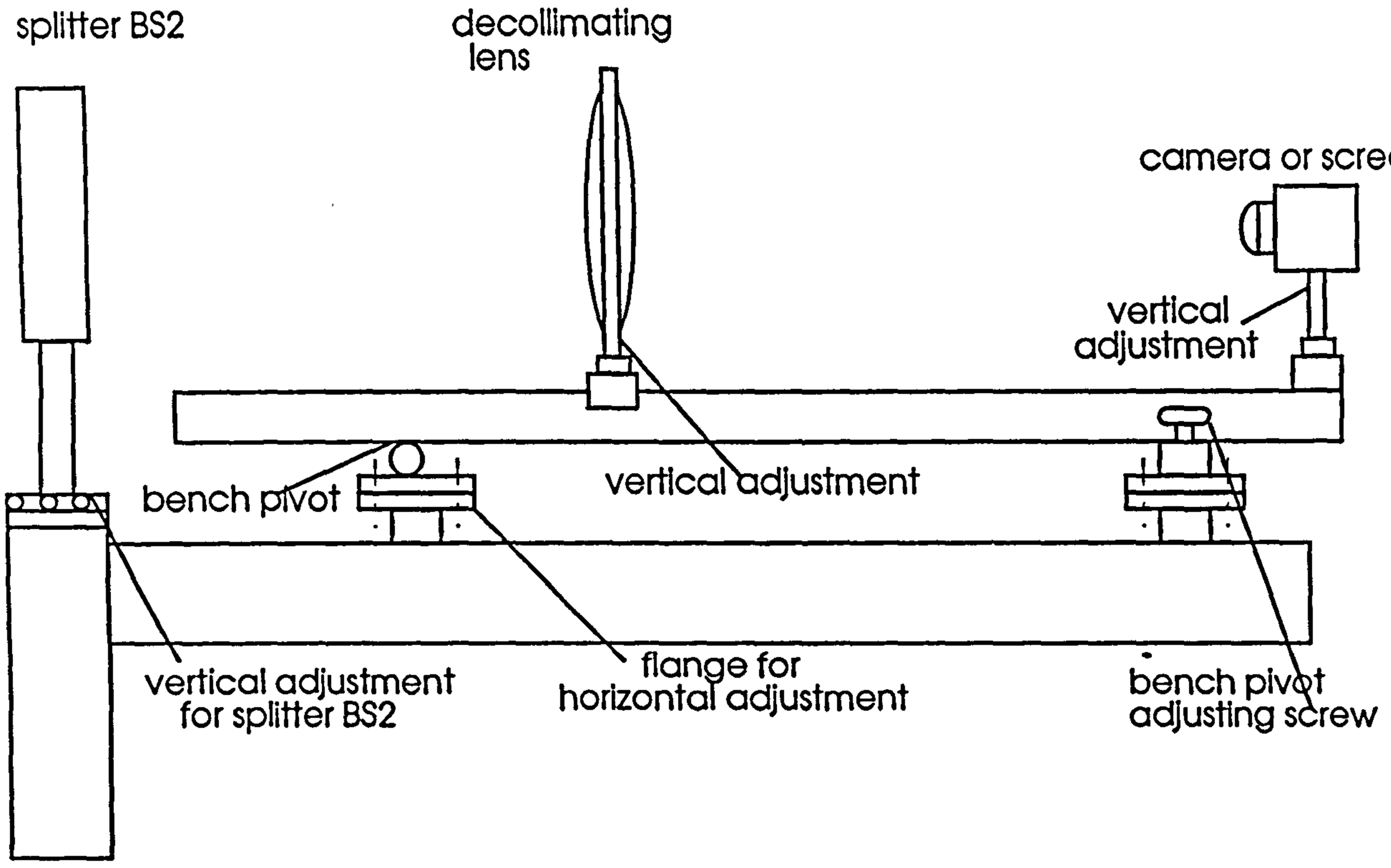

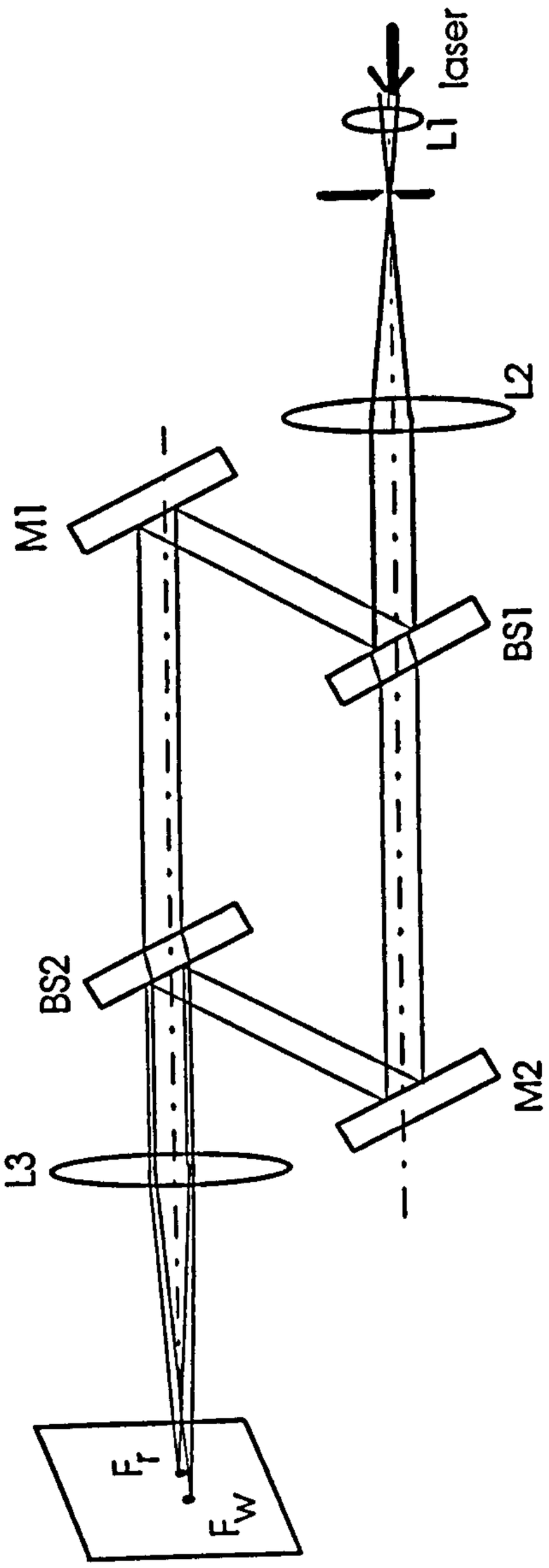

Fig. A-6 Misalignment - Separate Focus (for reference and working beams)

Fig. A-7 Adjustment using cross hairs

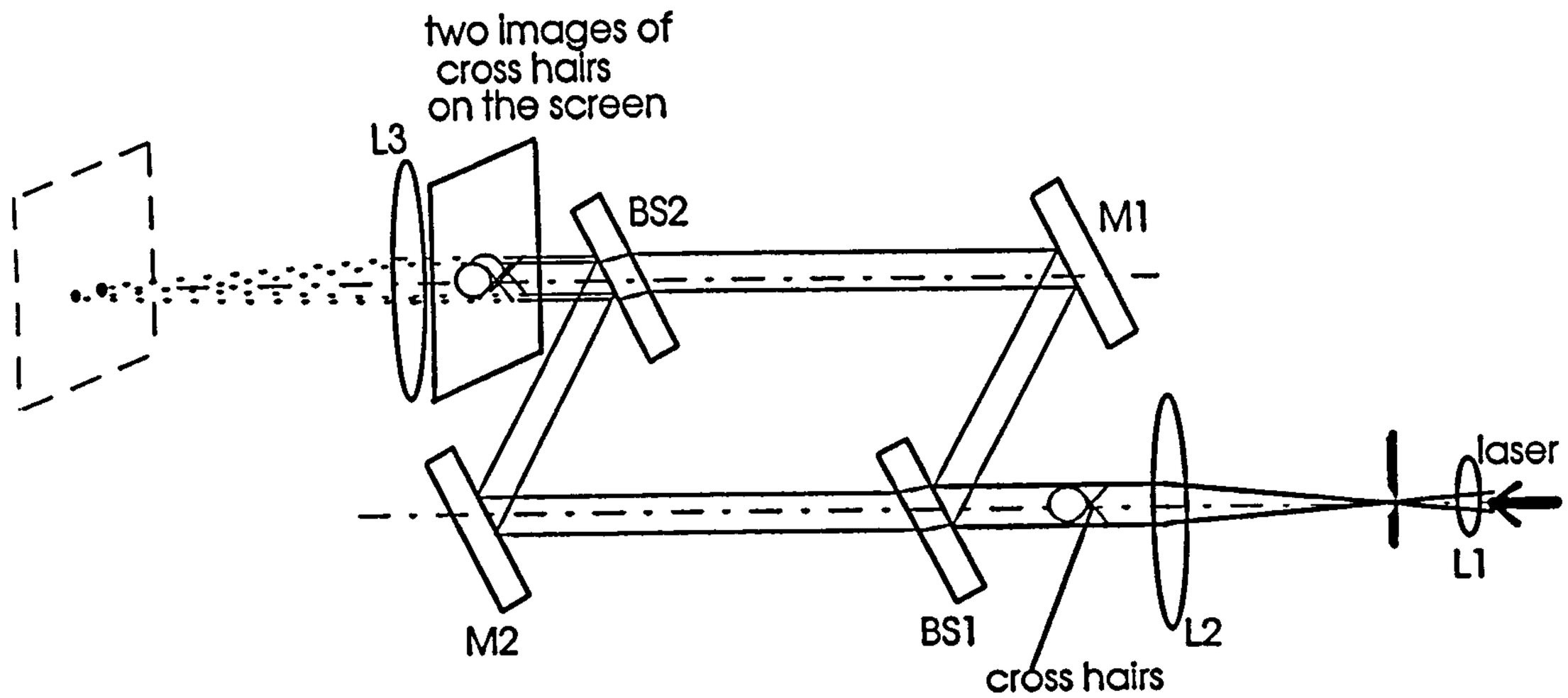

Fig. A-8 Beam expanding system (to facilitate test rig alignment)

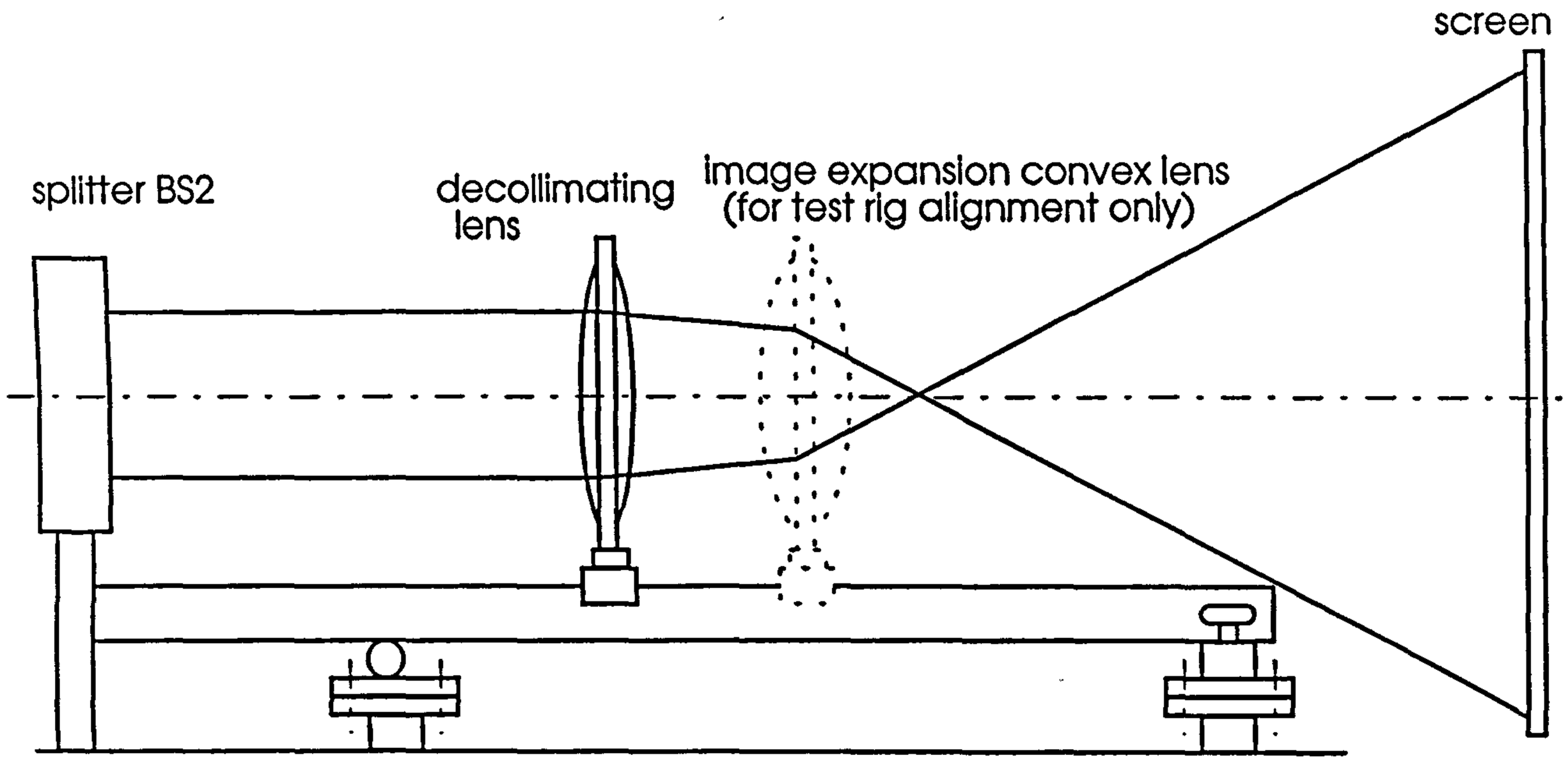

APPENDIX B - VIEW FACTOR CALCULATIONS.

B.1. Introduction

In order to calculate the radiative heat transfers in Chapter 3, it was necessary to determine the view factors. Integrating the view factor equation has been shown to be numerically tedious. Therefore, the use of established view factors were considered but the method of crossed strings was finally adopted.

B.2 Error Propagation from Published Data

From the view factors which already exist in the open literature [6],[58] in graphical or tabulated format, other view factors of similar geometries could be deduced by view factor algebra. By making suitable approximations, other view factors such as from the cylindrical heating elements to the planar inner body, can be obtained. However, several of the documented view factors formulae were seriously in error particularly those involving non-planar surfaces.

The accuracy that could possibly be obtained is also limited because many tables are only obtainable for six-figure accuracy (or graphs read only to a best of 2-figures), which easily lead to large inaccuracies when view factor algebra is employed because of error propagation.

Error propagation from the use of view factor algebra, to deduce related configurations, had also been established by Feingold [95]. The view factors employed are therefore calculated using the crossed strings or related methods.

B.3. Data for Exchange Areas

Fig. B-2a shows the heating elements in all the possible arrangements. The enclosure surfaces were named such that the total upper surface was denoted by P, the sides by Q and S, and the base by R. The corresponding inner body surfaces are similarly denoted. Surface P to J (P-J) was treated as parallel planes, to obtain a view factor of 0.30. It is also seen that a portion of surface P, (QP) would also see surface J (see Fig. B-2b). This, and similar exchange areas were treated as non-intersecting perpendicular planes which yielded a view factor of 0.122 each.

The heater strip was treated as a flat surface, 8mm wide and exchanging with the upper surface as shown (see Fig. B-2c). When a heater could see more than one inner body surface, such as when located at the enclosure corners, it was treated as either a perpendicular, or parallel surface to the appropriate inner body surface, resulting in two view factors.

The view factors employed are shown in Table B.1.

Fig. B-1 View factor calculations

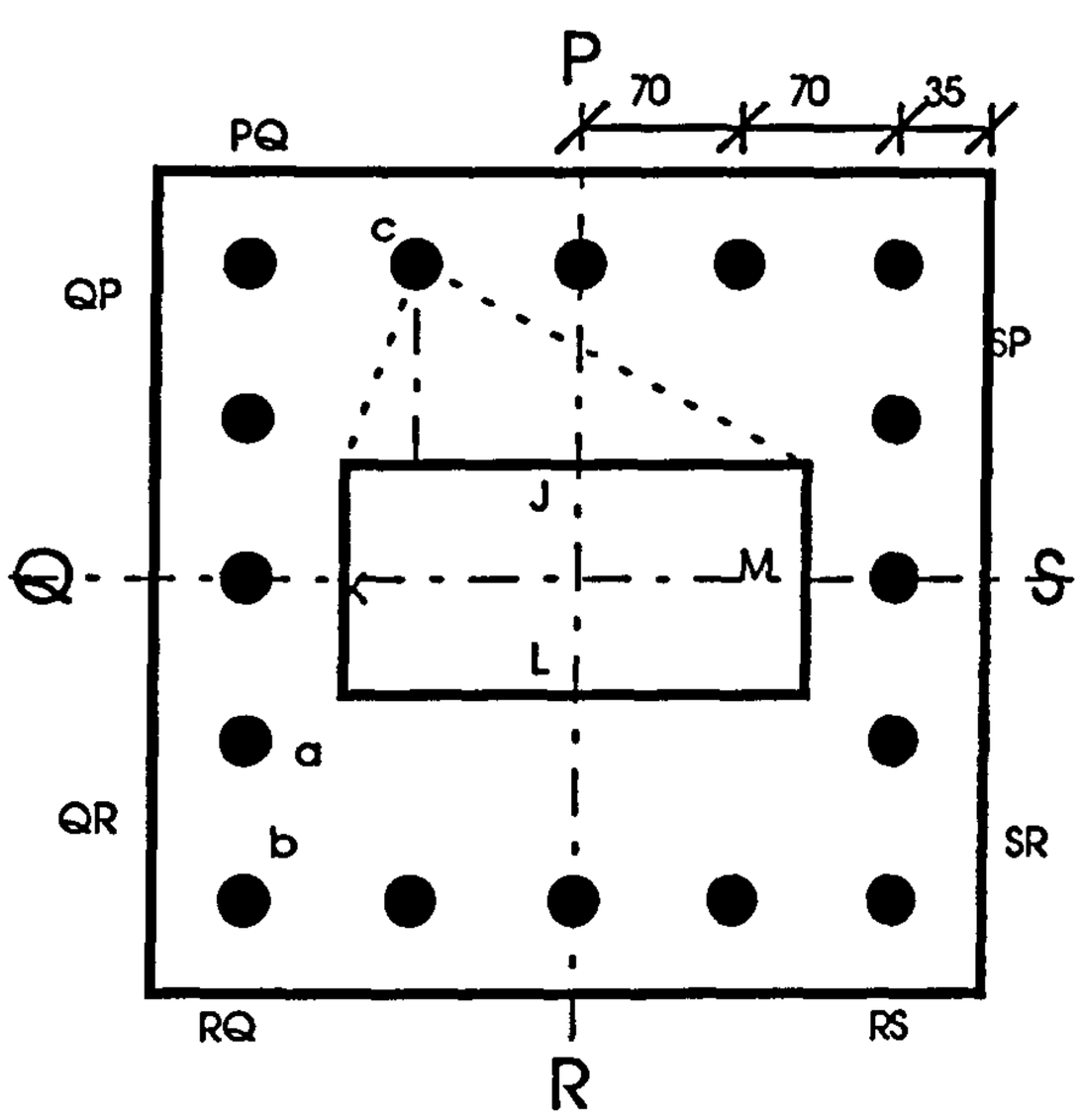

(a)

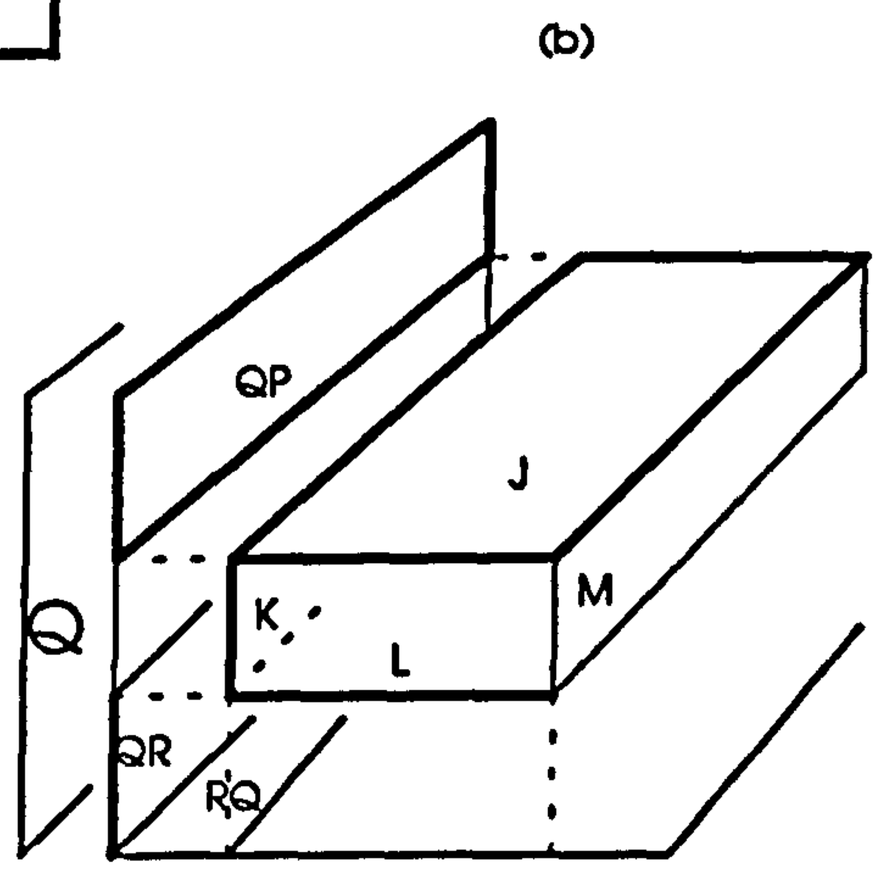

(b)

Examples: View factors (from - to)

QP-J=Perpendicular planes
(=SP-J, =QR-L, =SR-L, =0.122)

Q-K=Parallel planes (=S-M,=0.175)

Heater b, parallel plane to K (=0.114)

Heater b, perpendicular plane to L
(=0.18)

Heater c, parallel plane to J (=0.393)

(c)

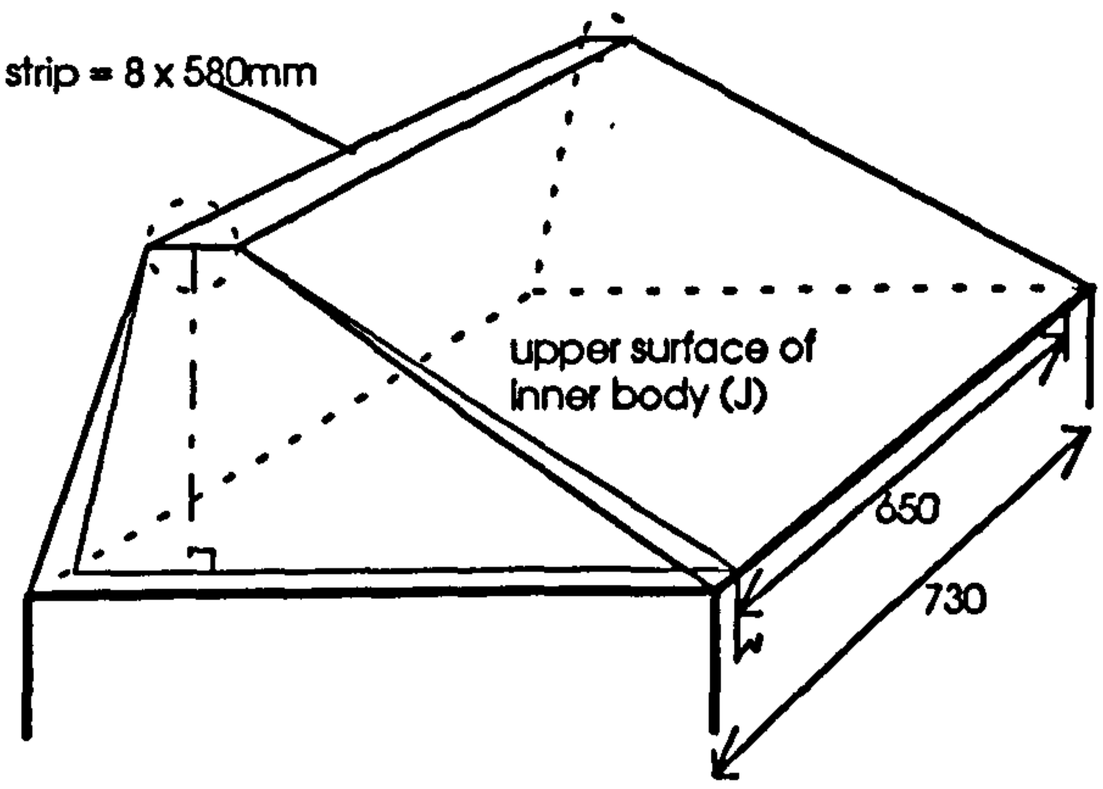

Table B.1. View factors from enclosure and heating elements to the inner body, zoned as shown (see Fig.B.1)

top	area..1		emissiv..1	emissiv..2
P-J	0.3	0.245	0.85	0.7
QP-J	0.12217	0.098	0.85	0.7
SP-J	0.12217	0.098	0.85	0.7
base				
R-L	0.3	0.245	0.85	0.7
QR-L	0.12217	0.098	0.85	0.7
SR-L	0.12217	0.098	0.85	0.7
sides				
Q-K	0.17514	0.245	0.85	0.7
PQ-K	0.0516	0.0665	0.85	0.7
RQ-K	0.0516	0.0665	0.85	0.7
S-M	0.17514	0.245	0.85	0.7
PS-M	0.0516	0.0665	0.85	0.7
RS-M	0.0516	0.0665	0.85	0.7
Heater examples				
top centre	0.5464762	0.0073	0.9	0.7
top left	0.3933856	0.0073	0.9	0.7
side centre	0.4499757	0.0073	0.9	0.7
a-L	0.103	0.0073	0.9	0.7
a-M	0.16236685	0.0073	0.9	0.7
b-K	0.114	0.0073	0.9	0.7
b-L	0.18050505	0.0073	0.9	0.7

APPENDIX C

UNCERTAINTY ANALYSIS

C.1. Introduction

Errors noted during the experimental work were corrected before the data were recorded and utilised. Such corrections were necessary for example when poor thermojunction contacts were suspected, or unrealistic readings were observed from damaged thermojunctions.

Errors which occurred in the experimental studies due to uncertainty in the accuracy of the instrumentation, or to the data associated with equipment or materials employed must be accounted for. Similarly, other errors such as those derived for use in the formulae (such as the view factors) must also be accounted for, except when error-free, analytically derived formulae were employed. The relevant uncertainty was determined either by simple derivatives, or by the root-mean-square method.

C.2. Uncertainty in the convective heat transfers

The uncertainty from the experimental data was determined as follows:
In the experimental analyses Qconv to the inner body was obtained from:

$$Qconv = Qin - Qrad - Qinsul \qquad (C.1)$$

The uncertainty in Qconv was obtained by considering individual errors. Qin was read directly from the wattmeters which was supplied with the calibration data and was utilised here as ±2% for each reading.

From $Qinsul = (k/t)A\Delta T$, the area A and the insulation thickness t were treated as constants. Although the thermal conductivity k for Rockwool varied with temperature, its value as obtained from the supply data contained no uncertainty and was similarly treated as a constant thus:

$$Q_{insul} = c_3\theta_i \qquad (C.2)$$

Therefore, the uncertainty in Qinsul (i.e. δQ_{insul}), which was directly proportional to the uncertainty in the calibrated temperature values (see Table C.1), was analysed as follows:

$$\delta Q_{insul} = \theta_i\, \delta c_3 + c_3\, \delta\theta_i = c_3\, \delta\theta_i \qquad (C.3)$$

$$\text{so, } \delta Q_{insul}/Q_{insul} = \delta\theta_i/\theta_i \qquad (C.4)$$

where $\delta\theta_i$ and θ_i are in ^oC.

Table C.1. Uncertainty in thermocouple outputs

Temperature range (^oC)	Uncertainty (± ^oC)
0 - 400	3
400 - 1100	0.75

The derivation of the formula $Qrad=\varepsilon A\sigma FT^4$, makes various assumptions and approximations as discussed by Siegell and Howell [82]. Even then it is well established as a calculation tool so that σ can be treated as a constant. Therefore, only three variables were considered - the emissivity, view factor and temperature, the rest being lumped together in a constant, c_4.

Hence $Qrad = c_4\,\varepsilon\,FT^4$ (C.5)

and $\frac{\partial Qrad}{\partial \varepsilon} = c_4 FT^4$; $\frac{\partial Qrad}{\partial T} = 4c_4\varepsilon FT^3$ and $\frac{\partial Qrad}{\partial F} = c_4\varepsilon T^4$

It was pointed out [96] that when an uncertainty is to be obtained from differences of variables whose values are numerically close, the uncertainty could be very large. If the net Qrad is taken as the nominal Qrad, then equation (C.5) and its derivatives become:

$Qrad = c_4\,\varepsilon\,F(T_1^4 - T_2^4)$, $\frac{\partial Qrad}{\partial \varepsilon} = c_4 F\left(T_1^4 - T_2^4\right)$, etc., but it was not essential to work out this for all the individual zones because the relative differences in the temperature values at the respective measured points were marginal. However, it is to be noted that a 0.5°C error in the measurement of T_1 when T_1=273K would result in a 0.7% error in the quartic temperature term, whereas at T_1=473K, only a 0.4% error would occur. That is at lower temperatures, any measurement errors are inherently magnified. This is in addition to lower errors being specified for thermojunctions at elevated temperatures. If U_{rad} represents the uncertainty in Qrad, and U_ε, U_F and U_T the uncertainties in the independent variables, then the uncertainty, adapted from Kline and McClintock [97] is:

$$U_{rad} = \pm\sqrt{\left(\frac{\partial Qrad}{\partial \varepsilon}U_\varepsilon\right)^2 + \left(\frac{\partial Qrad}{\partial F}U_F\right)^2 + \left(\frac{\partial Qrad}{\partial T}U_T\right)^2} \qquad (C.6)$$

The error in the temperature measurements involving the radiation and insulation terms varied with increasing temperature. It was consequently found convenient to plot a curve of temperature against uncertainty at convenient thermometric values (see Tables C.2 and C.3, and Fig. C-1 and C-2), from where other values of uncertainty could be obtained at corresponding temperatures.

The emissometer employed was calibrated by taking the emissivities for a standard low emissivity reflective plate and that for a high emissivity plate. The ensuing linear graph of emissivity versus voltage was utilised for the measured emissivity of the experimental apparatus. A mean emissivity of 0.42 was obtained after averaging the data obtained from several zones of the enclosure surfaces. However, the uncertainty in emissivity obtained through the calibration data was ±0.01 and this was applied without any adjustment.

Now, the view factor from a totally enclosed object to its enclosure is unity. Therefore, the uncertainty in the view factor was derived from the reciprocity relations $A_2F_{21}=A_1F_{12}$, noting that F_{12} does not include F_{11} where the enclosure partially sees itself. By summing up the total zonal exchange areas, and comparing with unity, the error in the view factor was obtained as 0.062 (6.2%) for the values utilised in chapter 3. This also fixed the value of F as unity in the uncertainty analysis.

Table C.2. Uncertainty in Qinsul

$U_T(^oC)=\delta\theta_i$	$\Delta T=\theta_i$ (^oC)	k	$U/Q=\delta\theta_i/\theta_i$
3	250	0.079	0.012
3	200	0.066	0.015
3	150	0.055	0.02
3	100	0.045	0.03
3	50	0.038	0.06
3	10	0.033	0.3

Table C.3. Uncertainty in Qrad

T(K)	U_T	U_{rad}	Q_{rad}	U_{rad}/Q_{rad}
873	0.75	958.7	13832.1	0.06931
773	0.75	589.5	8502.6	0.06933
673	0.75	338.9	4885.3	0.06937
573	3	185.7	2567.2	0.0723
473	3	87.9	1192	0.0737
373	3	35.2	461	0.0763
323	3	20.4	259	0.0786
298	3	15.1	187.8	0.0801

The maximum uncertainty is simply obtained from:

$$U_{conv}=\frac{\delta Q_{in}\pm\delta Q_{rad}\pm\delta Q_{insul}}{Q_{conv}} \qquad \text{(C.7)}$$

noting that the maximum uncertainty is obtained by adding the uncertainty to Qin, while those of Qrad and Qinsul were subtracted from them. It is easily seen here that for small values of Qconv, the uncertainty would be very large. Other values were substituted from the appropriate temperatures at the same Qin as follows:

For a particular value of Qin, the uncertainty in Qrad was obtained from the graph (see Fig. C-1) at the mean temperature used to evaluate that Qrad. Similarly, the uncertainty in Qinsul was read from the graph (see Fig. C-2) at the corresponding temperature obtained from the test data. Because the uncertainty in Qinsul decreased with temperature increase, the uncertainty read using ΔT for Qinsul was marginally higher than if the wall temperature data had been used. For configuration 1, when Qin was 201W at ±1.5% (±2%

for C91-3), δQrad at 411.8K was read from Fig. C-2 as 0.08, and δQinsul at 46.8^{o}C read from Fig. C-3 as 0.09.

When an uncertainty is to be obtained from differences of variables whose values are numerically close, it has been found that the uncertainty would be very magnified. This would apply for both Qrad and Qin, but because Qinsul was generally much lower than either Qin or Qrad, the uncertainty in Qinsul would have only a marginal effect on the overall uncertainty. Conversely, when the numbers used to obtain Qconv are numerically close to Qin, so that Qconv was very small, the uncertainty in Qconv would be extremely large as aforementioned and as obtained in this study. The uncertainty was also magnified when ratios of numerically different numbers were considered.

Table C.4. Uncertainties (%) in the heat transfers by convection (Chapter 3).

Input(W)	C1	C6	C8	C9
201	7.3	6.75	8.3	5.7
805	17.7	23.6	21.5	13.70

Table C.5. Uncertainties (%) in the heat transfers by convection (Chapter 6).

Power input (W)	C91	C92	C93
520	10	10.65	9.92
960	12.25	11.54	12.12
1540	14.39	12.23	14.24
2200	18	13.69	17.8

Now, the power measurements for the evacuated studies were taken from the same instrument without switching it off, which leads to the assumption that the difference taken would be subject to zero error. This is the basis for reasoning that the propagation in uncertainty would be very much reduced. Therefore, the uncertainty for the evacuation studies, in addition to not embracing the individual uncertainties from over 450 zones, would be much lower than that for the atmospheric modelling calculations.

C.3. Uncertainty for Q ratios

When ratios are utilised to present the analysis, the uncertainties were not neutralised as would be intuitively anticipated either for Qconv/Q*conv or for Qrad/Qin and Qconv/Qin. Thus for $\psi = Q_p/Q_s$, adopting the benchmark root-mean-square method [97], and substituting for $\partial\psi/\partial Q_p$ and $\partial\psi/\partial Q_s$, equation C.5 can now be re-written:

$$U_{\left(\frac{Q_p}{Q_s}\right)} = \pm\sqrt{\left(\frac{1}{Q_s}\right)^2 \delta Q_p^{\,2} + \left(-\frac{Q_p}{Q_s^{\,2}}\right)^2 \delta Q_s^{\,2}} \qquad \text{(C.8)}$$

where δQ_p and δQ_s represent the uncertainties in the numerator and denominator respectively, and $U_{\left(\frac{Q_p}{Q_s}\right)}$ the overall uncertainty in the arbitrary ratio ψ. It can now be seen that although a larger denominator would contribute to a lower uncertainty, it really is the individual uncertainties that are the influencing parameters.

Table C.6. Uncertainties (%) in the Q/Q ratios by convection (Chapter 4)

Input (W)	Sidewall (Y=0.5))	Base (Central)
4.92	17.0	24.8
11.52	10.7	20.0

Equation C.8 shows the cumulative effect of the uncertainties. The uncertainties in Qconv/Q*conv (see Table C.6) also reflect the important influence of the individual uncertainties. The ratios calculated for the base mounted configurations with higher individual uncertainties recorded higher overall uncertainties in spite of having lower values in the denominators than the sidewall mounted heat ratios.

Fig. C-1 Variation in uncertainty for Qinsul with increasing temperature

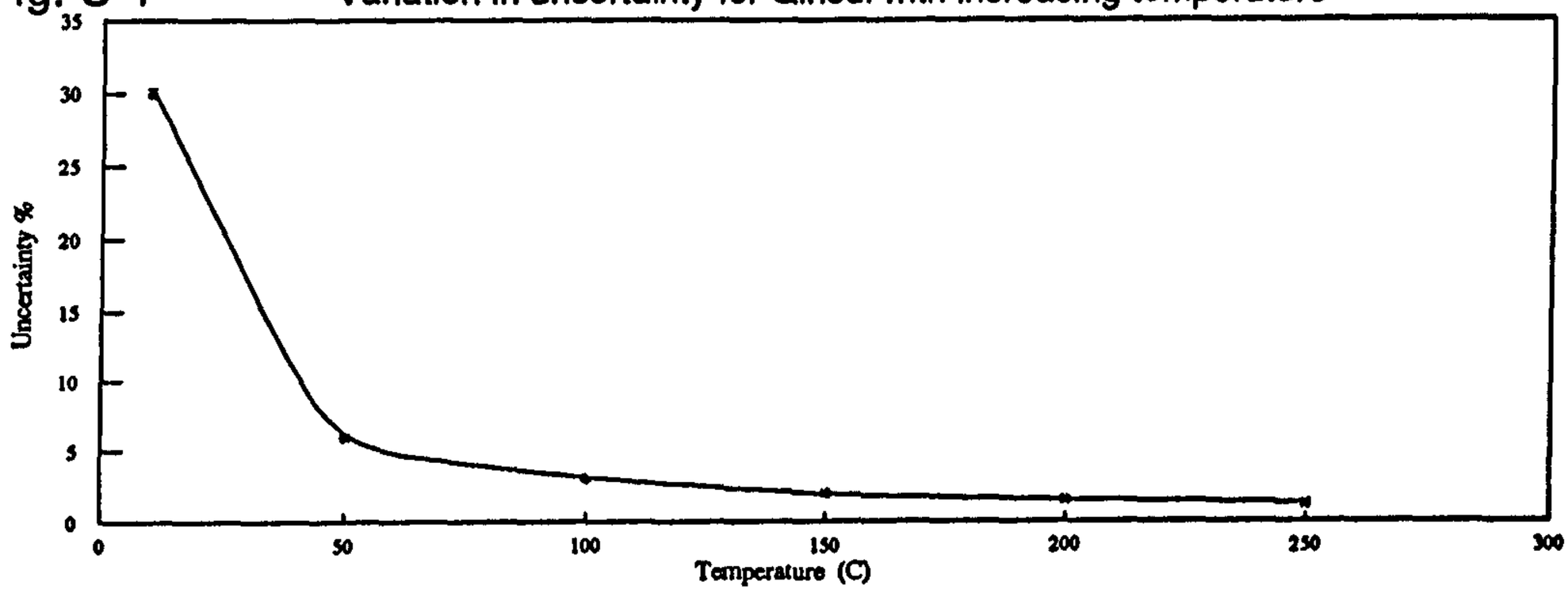

Fig. C-2 Variation in uncertainty for Qrad with increasing temperature

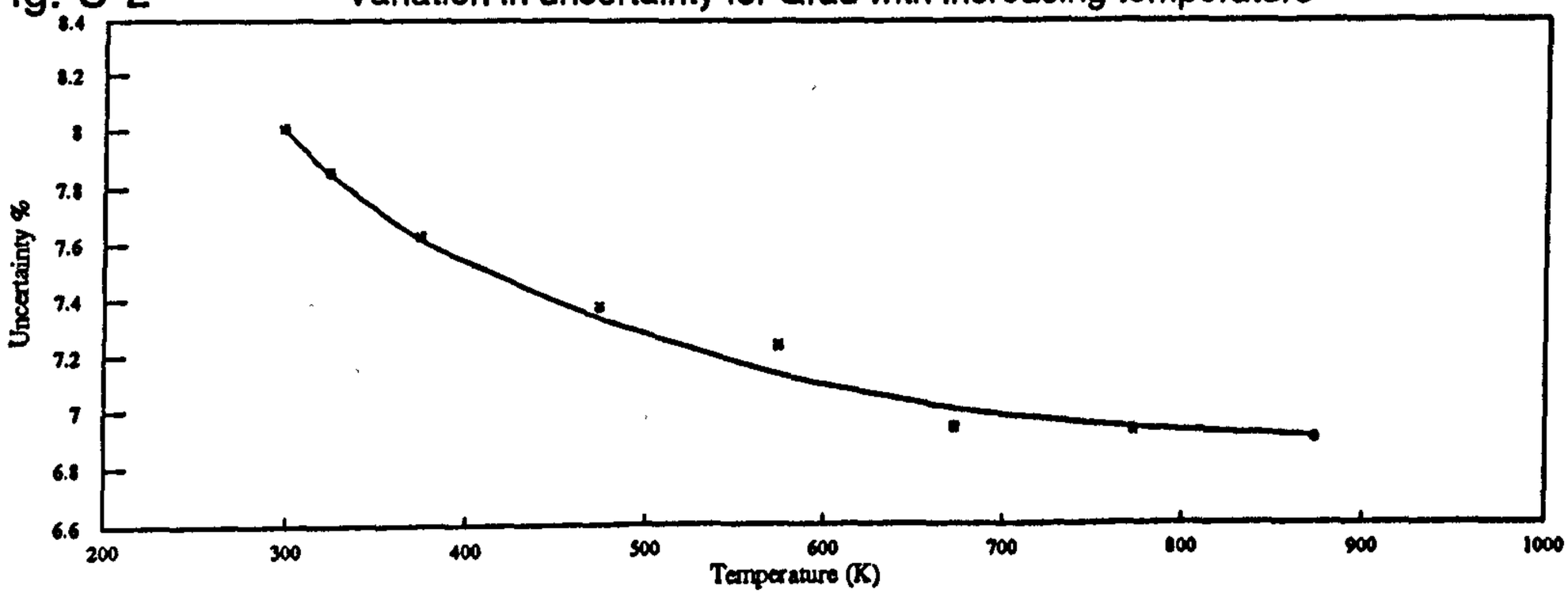

APPENDIX D

INFLUENCE OF HIGH TEMPERATURES ON NATURAL CONVECTION HEAT TRANSFERS (for enclosed systems)

The total heat flux to an inner body is represented by:

$$q = q_{conv} + q_{rad} \qquad (D.1)$$

The air adjacent to a heated vertical wall will rise by natural convection. Experience suggests that the higher the temperature difference between the vertical wall and the ambient, the more vigorous the convective flow would be. Intuition consequently suggests also that the convective heat transfer would correspondingly increase.

The cause of flow by natural convection is attributed to the temperature gradient, which sets up density gradients in the air. The resultant buoyancy force is in opposition to the gravitational force. This sets up free convection currents. The analysis is well established [11] to give:

$$Nu = hL/k = c_1\left(\frac{\rho^2 g\beta\Delta T L^3}{\mu^2} x \frac{\mu c_p}{k}\right)^{c_2} = c_1(Gr\ Pr)^{C2} \qquad (D.2)$$

where Gr is the measure of the vigour of the flow (i.e. the ratio of the buoyancy forces to the viscous forces), while Pr indicates the thermometric conductivity.

As the temperature rises, the thermal conductivity of air rises which at first suggests that microscopic or molecular conduction would increase the convective heat transfers. But the increase in temperature also causes a reduction in the density of the air; so the mass of air in direct contact with the hot surface is also reduced. From D.1, the effect of the reduced density term (within the numerator in the Rayleigh number) can now be seen to be additive to that of the increased thermal conductivity (in the denominator).

An examination of air properties [63] at 300K and at 1100K shows, for a unit ΔT and L, a 350-fold decrease occurs in the buoyancy term. Simultaneously, the 4th power dependence on the temperature variable would have caused a 40-fold increase in the radiative term (e.g. 1100^4-1099^4:3254-3244).

Fig.D-1 depicts the increase of the thermal conductivity, Fig. D-2 the decrease of air density, while Fig. D-3 that of the reduction of Ra with increased temperatures. These confirm that as the air temperature is increased, the convective component of total heat flux must decrease, and at elevated temperatures e.g. as encountered in some high temperature ovens (700K) and furnaces (1050K), the influence of natural convection is virtually suppressed by the inherent characteristics of air properties so that thermal energy transfer will be achieved principally by radiation.

Therefore this limitation should always be borne in mind when convection, particularly natural convection is expected to play an important part in enclosure heat transfer designs.

For this reason, forced convection ovens and furnaces tend to use very high rates of air circulation at elevated temperatures because convective heat transfer is often reduced to less than half of its start-up value [8]. Because reflective (low emissivity) loads would be heated by radiation less rapidly than high emissivity loads, convection would be advantageous over radiation heat transfer. It so happens that the light metallic alloys are generally of low emissivity and require heating to relatively low temperatures where convection and temperature uniformity are indispensable characteristics. This is in contrast to the higher emissivity heavier metals which require heating to higher temperatures (>1000K) and radiation is employed.

However, the foregoing knowledge appears not to have been implemented in the specification and use of infra-red curing ovens for beverage can tops whereby can seals are cured at 226^{o}C by roof-mounted infrared quartz tubes [96]. It is highly recommended that convective ovens should still be adopted for reflective or low emissivity loads rather than radiation ovens.

Fig. D-1

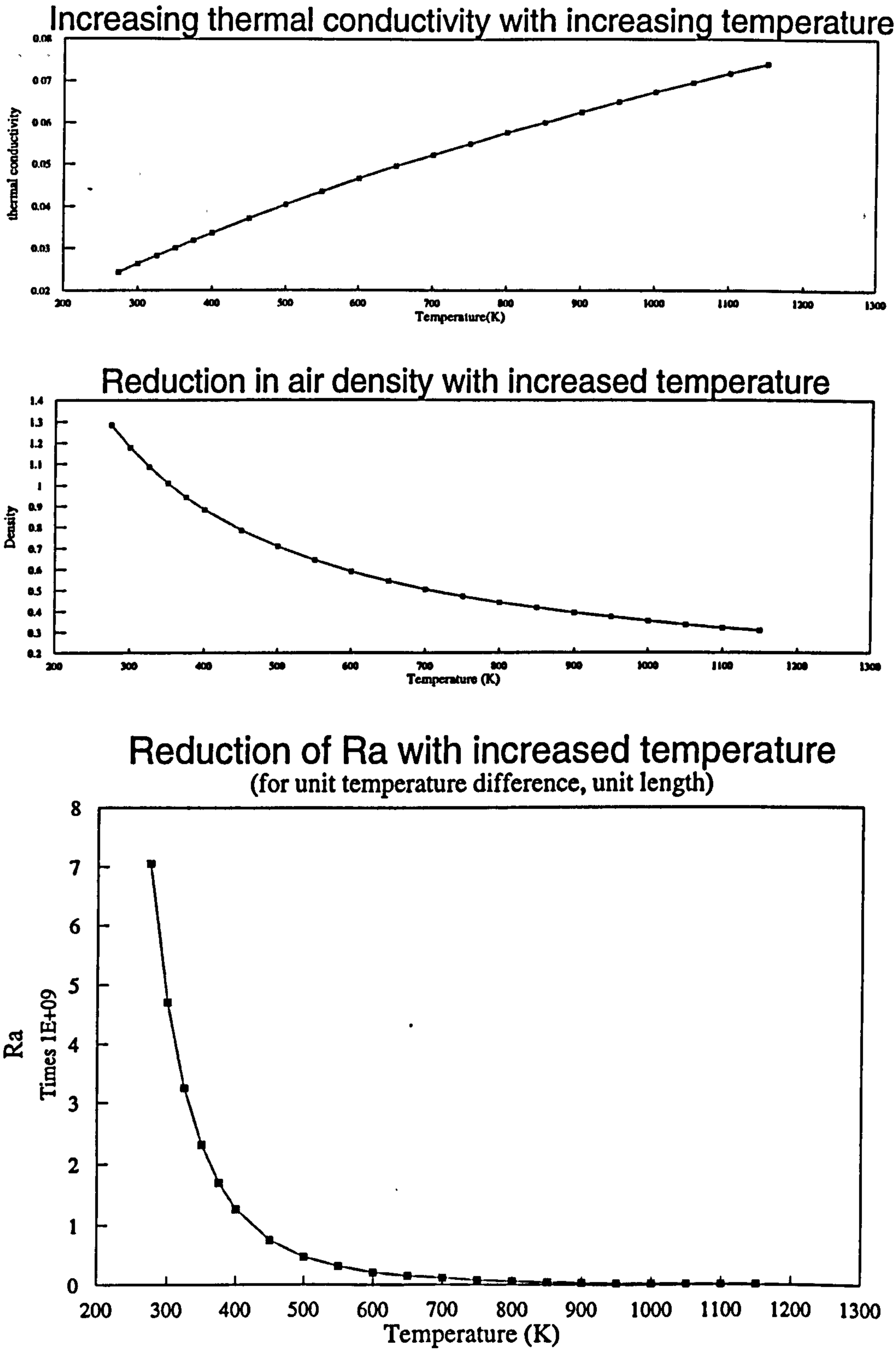
Increasing thermal conductivity with increasing temperature
thermal conductivity
0.08
0.07
0.06
0.05
0.04
0.03
0.02
200
300
400
500
600
700
800
900
1000
1100
1200
1300
Temperature(K)
Reduction in air density with increased temperature
Density
1.4
1.3
1.2
1.1
1
0.9
0.8
0.7
0.6
0.5
0.4
0.3
0.2
200
300
400
500
600
700
800
900
1000
1100
1200
1300
Temperature (K)
Reduction of Ra with increased temperature
(for unit temperature difference, unit length)
Ra
Times 1E+09
8
7
6
5
4
3
2
1
0
200
300
400
500
600
700
800
900
1000
1100
1200
1300
Temperature (K)

APPENDIX E

THE DESIGN OF RECTANGULAR VACUUM/PRESSURE VESSELS

E.1. INTRODUCTION

The ASME Boiler and Pressure Vessel Code VIII D1 [73] provides design guidance for rectangular pressure vessels subject to internal pressure. The formulas, which are also obtainable from Faupel [74], are for internal pressure, but they will apply to cases of external pressure by reversing the stresses and the pressure. While the use of Codes and Standards simplify the testing required, promote more uniformity of design and the cost of validity of the products, the present design problems have not been adequately covered. Design stress limitations were obtained from BS5500 [99]. Hydraulic calculations for the inner body were simplified by utilising the friction factor concept for turbulent flow [79].

E.2 DESIGN OF VACUUM VESSEL OF RECTANGULAR CROSS-SECTION

E.2.1. Introduction

A square-sectioned vessel was designed by welding together 4 SS 304L plates (1700x356), using fillet welds. The fabrication procedure required that the connecting fillet weld could be deposited on only the exterior of the corners, because the interior of the enclosure was too long to allow control of the welding process. The resulting triangular-shaped corner rather than the rigid, square-edge shape as published [73] (see Fig. E-1), required improved stress calculations. Therefore, extra effort was devoted to front-end design calculations in order to optimise the resources. The corners were still considered as rigid, so that the central plate deflection δ, the bending moment, M and the direct stresses ζ, were calculated using tabulated data from flat plate stress analyses [100].

E.2.2. Procedure

The design procedure adopted was as follows:-The minimum plate thickness was calculated and checked for buckling; then the stresses at the fixed (corner) edges were calculated. 3D (Mohr's circle) method was utilised to obtain the maximum principal stresses of the highly stressed parts.

E.2.3. Calculations:

E.2.3.1. Sidewall plate thickness

The required plate thickness was calculated from the tabulated data presented in [101] and derived from [100] - rectangular plates with clamped

edges carrying uniformly distributed loads. For plate dimensions y and z, where z is the shorter side, the maximum deflection, δ, takes place at the centre of the plate:

$$\delta_{max} = \alpha \frac{pz^4}{Ew^3} \qquad \text{(E.1)}$$

but the maximum direct stress occur at the centre of the longer edge:

$$G_{max(centre\ of\ long\ edge)} = -\frac{\beta_1 pz^2}{w^2} \qquad \text{(E.2)}$$

and the direct stress at the plate centroid is given by:

$$\Gamma_{(platecentre)} = \frac{\beta_2 pz^2}{w^2} \qquad \text{(E.3)}$$

where α, β_1 and β_2 are given in Table E.1., p is the uniform pressure ($1.1x10^5 Nm^{-2}$), w is the plate thickness, and $E=200GNm^{-2}$.
It can be noticed from Table E.1 (for constant $\nu=0.3$) that when $y/z > 2.0$, the effect of the restraining edges on the stiffness of the plate diminishes, and this necessitated checking for instability because of the axial (end plate pressure) load.

Table E.1. Constants for uniformly loaded rectangular plates (clamped edges $\nu=0.3$).

y/z	1.00	1.2	1.4	1.6	1.8	2.0	∞
α	0.0138	0.0188	0.0226	0.0251	0.0267	0.0277	0.0284
β_1	0.3078	0.3834	0.4356	0.4680	0.4872	0.4974	0.5
β_2	0.1386	0.1794	0.2094	0.2286	0.2406	0.2472	0.25

By using reinforcing members, the dimensions to be considered were reduced from 0.35x1.7m to 0.35x0.31m giving the ratio y/z=1.13. To obtain the optimal thickness (for $\delta_{max} \leq t/2$), the main values used as input are in Table E.2.

Table E.2 Calculation of optimal thickness

Thickness, w mm (inches)	y/z (350/310)	α	δ_{max} ($x10^{-3}$)	w/δ	is w>2δ
7.938(5/16")	1.13	0.017	7.516	242	Y
6.35(1/4")	1.13	0.017	14.68	17	Y
4.763(3/16")	1.13	0.017	34.8	5.39	Y
3.175(1/8")	1.13	0.017	117.4	1.06	N

Although the minimum plate thickness was obtained as 4.763mm, 6.35mm thick plates were selected to reduce the value of M required for restraint at the edges.

E.2.3.2. Stresses at the Corners

The direct stresses ζ_x and ζ_y were obtained using equation (E.2). To ζ_y was

Table E.3. Input values for stress calculations

	SI	Imperial
p	$1.1x10^5$	15.965
b	0.31	12.2
w	0.00635	0.25
E	$200x10^9$	$29.028x10^5$
δ_{max}	0.33	0.011
M	17Nm (=55.4Nm/m)	

Table E.4. Calculated stresses

p	$1.1x10^5$	$1.0x10^5$
$\zeta_{(max.long\ edge)}=\zeta_x=\zeta_y$	$93.5x10^6$	82.4
$\zeta_{(max.centre)}$	$40.22x10^6$	36.6
$\zeta_{(end\ plate\ thrust)}$ x2=ζ_z	$-4.19x10^6$	-3.77

added the stresses from the mass of the vertical plate and the pressure forces as shown (see Table E.3). For the lower corner, these were subtracted from ζ_y. The SS plates were available in imperial sizes. Table E.4 shows the stresses obtainable at 1.1 x 10^5 and at maximum vacuum ($1.0x10^5$). The latter were used in subsequent calculations following the design advice from Sec.3.2.3 of BS5500 (vacuum vessels - relaxation of design pressure) [99]. Although the stress caused by atmospheric pressure on the end plate was only $3.77x10^6$ compressive, it introduced a third dimension into the stress calculations. The shear stress Γ was estimated by considering the fillet weld as a non-prismatic, wedge-shaped section not subject to twisting. The value obtained was added to that produced by the mass of the plates and the pressure forces to obtain $\Gamma = 4.32x10^6$. The principal stresses were then obtained thus:

$$\zeta_1 \text{ and } \zeta_2 = \frac{1}{2}(\zeta_x+\zeta_y)\pm\frac{1}{2}\sqrt{(\zeta_x-\zeta_y)^2+4\Gamma_{xy}^2}$$

where $\zeta_x = 93.15x10^6$, $\zeta_y = 84.15x10^6$, $\Gamma = 4.32x10^6$.
Using ζ_z (= $-3.77x10^6$)as a principal stress, a 3-D Mohr's stress analysis subsequently yielded:
$\zeta_1 = 94.89x10^6$, $\zeta_2 = 82.4x10^6$, $\zeta_3 = -4.2x10^6$ and $\Gamma_{max} = 49.55x10^6$.

Only a very small section of the plate edge centres would be subjected to these stresses. From the material supply inspection certificate (BS 304S11 TYPE 304L), the tensile stress was given as 596 MNm^{-2}, and the yield stress 313 MNm^{-2}. The design Code (ASME) limits the stresses to 2/3rd the yield stress or, for SS, to 0.9 of the design stress at the operating temperature, whichever is the lower.

The layout of the enclosure is shown in Fig. E-2. It includes construction details and methods of attachment of the I-section foot and end plate channel supports. The end view shows the drilled position of attachment of the channel-section end plate supports. The method of fabrication of the pads for the inner body, heaters, and flow visualisation are depicted in Fig. E-3. The all-round welded construction permitted the assumption that a stress discontinuity would exist between adjacent plate elements.

E.2.3.3. Operational limitations

Data from BS5500 (Table 2.3c) [99] gave the design stress for both 304S11 and 304S61. The latter data aligns closely with the stress data of 304S11 TYPE 304L supplied and it shows that the maximum stress (99.1MNm^{-2} under vacuum) would be accommodated at plate temperatures up to 400^{0}C (90% of 127MNm^{-2}). This is the absolute design limit (fos = 1) under vacuum for the enclosure. Therefore, the maximum recommended wall temperature for fos=1.5 under vacuum is 200^{0}C. It is to be noted that under vacuum, the wall nearest to the heater would register temperatures approaching that of the heater. Therefore, the heater temperature under full vacuum should be continuously monitored and kept not higher than 300^{0}C, based upon the experimental data (see Fig. 6-10, Chapter 6).

E.2.3.4. Stresses at the inner body support pads

The stress induced on the enclosure walls by the inner body were found to be very low, but as an example, the operational mass of the inner body to be carried by the two pads was 125kg. The reinforcing members of the enclosure were assumed to provide a discontinuity from the effects of the external pressure force; that is, at the extreme ends of the enclosure vertical wall, in the region occupied by the inner body support pads, stresses set up as a result of the external pressure would be negligible. Also, by providing the stands for the enclosure in line with the position of the inner body support pads, it ensured that there would be no twist of the welds. Therefore, only the weld area of the pads, and the weld area within that area of the vertical enclosure walls were considered in the stress calculations. Hence, the enclosure vertical plate weld area=0.1x0.004x2, to resist 9.81x125/2, gave Γ=0.697MNm^{-2}.

E.2.4. Enclosure end plates

Provision was made at the enclosure base supports whereby channel sections were bolted to carry the end plates. Two L-section SS brackets were welded externally across the roof (x-direction) at both ends to which the upper channel sections were bolted. Each channel section was provided with threaded holes through which M6 bolts were screwed to keep the end plates tightly sealed against the milled faces of the vacuum enclosure. This arrangement should ensure that the end plate edges could be treated as

fixed-fixed. However, there was uncertainty as to how uniformly tight the plates could be under various operational conditions. Therefore, the plate edges were treated as free-free and the thickness obtained using the deflection procedure as for the enclosure plates. (see Table E.5). Although the lowest calculated size was 6mm, the generous thickness arrived at (10mm) was as a result of safety and corrosion thickness considerations because MS plates were specified.

Table E.5 Calculation of optimal thickness for enclosure end plates

x/y	1.00		Thickness, w mm (inches)	δ_{max}	w/δ	is w>2δ	ζ_{max} x10^6
α	0.0443		10 (0.39")	0.366	27.3	Y	48
β_1	0.0479		8 (0.315")	0.714	11.2	Y	75
β_2	0.0479		6(0.236")	1.69	3.54	Y *	133
			4(0.157")	5.7	0.7	N	

E.3. DESIGN OF INNER VESSEL OF RECTANGULAR CROSS-SECTION

E.3.1. Introduction

The inner body dimensions were specified as 175x175x1400. The length of 1400mm, which was considerably shorter than the enclosure length was chosen so that the enclosure would accommodate the inner body support pipes, which also acted as cooling fluid inlet and outlet pipes.

The inner body was fabricated by welding together 4 MS plates to form a square-sectioned hollow inner body. The design procedure for calculating the optimal wall thickness was similar to that utilised for the vacuum enclosure. The specification also included a requirement for isothermal operation. In order to remove the heat input, it was designed for regulated fluid circulation. A baffle was incorporated which directed the fluid flow as shown (see Fig.5-2), to sweep a substantial internal surface area of the inner body.

The head losses due to friction and the expected increased power input required the specification of a more powerful thermocirculator. Therefore, the inner body walls should withstand an internal pump pressure of 1.8 bar and the vacuum enclosure pressure of -1x10^5Nm^{-2}, i.e. it was designed to withstand an internal pressure of 3 bar. Easier control of the welding for the MS plates permitted the corners to be welded with increased angular weld deposits and penetration.

Although some innovative features (chiefly the void space and the baffle) reduced the operational mass of the inner body, the calculations were still based upon a fully loaded mass (see E.3.3).

E.3.2. Inner body wall thickness

Each inner body plate dimension was 175x1400mm, and end plates 165x165. For the inner body sidewalls, the full ratio (1400/175) was utilised in calculating the required plate thickness, because there were no reinforcing members. Although the minimum optimal thickness was 4mm, subsequent stress calculations dictated the use of 6mm thick wall plates (see Table E.7). In the design process, bolted end plates were originally considered so that safety and corrosion inspection of the interior could be carried out. However, fabrication constraints necessitated welding the end plates on to the four walls. Consequently, a short operational lifetime was anticipated because of the inability to carry out internal inspection of the MS inner body.

Table E.6 Calculation of optimal thickness(pressure) for inner body walls

y/z	1400/175≈ ∞
α	0.0284
β_1	0.5
β_2	0.25

Thickness, w mm (inches)	δ_{max}	w/δ	is w>2δ
8 (0.315")	0.086	93.2	Y
6 (0.236")	0.203	29.48	Y
4 (0.157")	0.687	5.82	Y
2 (0.079")	5.49	0.364	N

In addition to withstanding a total pressure of 3bar, axial tension due to pressure, and upper surface compression (lower surface tension) were considered because the end plates had to carry the mass of the operational inner body. This resulted in selecting 6mm thick plates.

Table E.7. Results of the stress calculations($x10^6$)

thickness	4mm	6mm	8mm
ζ_{max}	238.3	105.9	59.6
$\zeta_{centre\ plate}$	110.2	48.9	27.6
δ	0.461	0.137	0.058
$\zeta_{(mass)}$		2.81	

It can be seen that the maximum stress is less than 110MNm^{-2} under vacuum. The yield stress of 275 gives a fos of 2.5. Other calculations involved the torsional effect of the inlet and outlet pipes used to suspend the inner body.

E.3.3. Fluid flow circuit design

It was necessary to consider the differential pressure caused by the extended surface area swept by the process (cooling) fluid before the specification of the thermocirculator. Although the fluid utilised was a mixture of anti-freeze and water, only the properties for the latter were considered. Two inlet pipes

and two outlet pipes were found to be necessary to reduce the pressure drop across the inner body to less than 0.7bar.

To admit fluid into the inner body chamber, 16 equidistant holes, 8 on each inlet pipe were drilled. The hole diameters (8mm) were derived by considering the total pipes csa, dividing by 16, and deducing the required drill diameter. The inlet pipe csa was (2 off): $2 \times 0.021^2\pi/4=7.0E\text{-}04$; for 16 holes, each csa $= 7.0E\text{-}04/16=4.37E\text{-}05$. Thus the minimum drill diameter $= \sqrt{(4A/\pi)}=0.0078m$ (7.8mm). The outlet pipes were similarly drilled. However, a slightly fewer number of holes were required because of the reduction in flow resulting from friction losses upstream.

A baffle was incorporated to first of all deflect the fluid downwards, and then upwards to flow closely along the vertical wall (see Fig. 5-2), the gap between the baffle and the vertical walls being only 10mm. The flow directions are also shown in the enlarged section through B-B (see Fig. E-4). Although the baffle ensured good flow contact with the vertical walls, the flow contact area considered in calculating the head loss due to friction was consequently increased.

An empty pipe (102mm dia.) was installed within the baffle chamber as a void space. The perspective drawing (see Fig. E-5) shows the strengthening required for the end baffle plates, as well as two 2mm air vent holes on the baffle necessary only during the initial filling stages. The main advantages of the void space were to reduce the overall operational mass of the inner body as well as to reduce the overall capacity of the fluid circuit. Following from these, an added benefit would be the reduced heating-up period required for the inner body.

However, because the internal spaces could not be inspected, the inner body stresses were still based on the total flooded mass. To complete the void space, the pipe was sealed at both ends with flat plates, the thickness calculated as in E.3.2, but using formulae for flat plates and diaphragms [101].

The outlet pipe holes were offset from the inlet pipe arrangement, but a 15th hole was made slightly larger (10mm), to compensate for the reduced number of holes. The path length of fluid and the presumed flow contact area were calculated using half the internal pipe length, the downward flow, the upward flow and the approaches to the pipes thus:

$L=\text{perimeter}=(1400/2+150+175+175/2)\times10^{-3}m=1.113m.$

The swept area = csa(in) + half inner body area + csa(out)= $0.246m^2$. But the area used to calculate the velocity is the minimum csa, taken to be that of the pipe. Therefore, using the data for the 31 litres/min thermocirulator, the mean velocity v = Volume flow/csa = 5.1667E-04/(2x3.497E-04) = 0.739m/s, the

Reynolds number (ρ_{water} at 50°C) = 2.8x10^4, below the turbulent range and giving the friction factor f = 0.012 [79]. The head loss due to friction through the pipes was consequently low. The loss through the 31 holes was:

$$h_f = \frac{4fL}{d}\frac{v^2}{2g} = \frac{4*0.012*31*0.003}{31*0.008} * \frac{0.739^2}{2*9.81} = 5.1E\text{-}04m$$

and similarly through the pipes, 0.24m, i.e. the overall Δp=1000*9.81*0.24 = 2.35kNm^{-2}, (<1.24% of working pressure of 1.9bar). This low pressure loss was practicable because of the large system flow diameter.

It was necessary to ensure that the mass of the inner body was equally and uniformly carried by the support (inlet and outlet) pipes. This was achieved by welding them together on a common flange. A mating flange with two corresponding pipes was utilised which passed from the inside of the enclosure through the enclosure support pads, and outside from where the flexible hoses were connected. The MS supports for the inner body, were provided with oval openings (42x35), to accommodate any differential expansion (8mm maximum for a differential temperature of 200°C) between the SS enclosure and the MS inner body. Fig. 5-4b also shows the assembled inner body arrangement but with the vacuum seals in place.

The assembled rig end view is shown in the photographs (see Fig. 5-5b) and it is to be noted that the inner welds of the enclosure were built up only at the 8 corners and for short distances (20mm each) due to the aforementioned difficulty in weld controls.

E.3.4. The heater capacity

The empty enclosure mass, including the MS end plates was 160kg. With a mean C_p of 500 Jkg^{-1}K^{-1}, it would require a heat input of 80 kJK^{-1}. The lumped capacitance method [11] was suitable for the present purpose, the Biot number being less than 0.1 (Bi=4x10^{-3}). The enclosure wall thickness was doubled and assumed immersed into an infinite space at 200°C with convective boundary conditions. The time taken for the interior (adiabatic) node to reach 199°C was calculated as 6.4 hours. Thus the required heat rate would be 80000x200/(6.4x3600)=695W.

This pertains to only one hemispherical half of the csa of a cylindrical heater because the other half would be radiating to the inner body. So then, two heaters along the entire length of the enclosure must each have a minimum capacity of 700W for steady-state conditions. To achieve the initial radiative or convective boundary conditions, noting that the inner body would remain at only 50°C, and that the interior node would actually be in contact with a non-adiabatic boundary (insulant thickness=100mm), the heater capacity was similarly deduced and specified as 2000W.

The heaters were suspended via their terminals using 25mm long electrically insulating sindanyo bushes and via MS brackets.

Fig. E-1 Welding arrangement at the corners

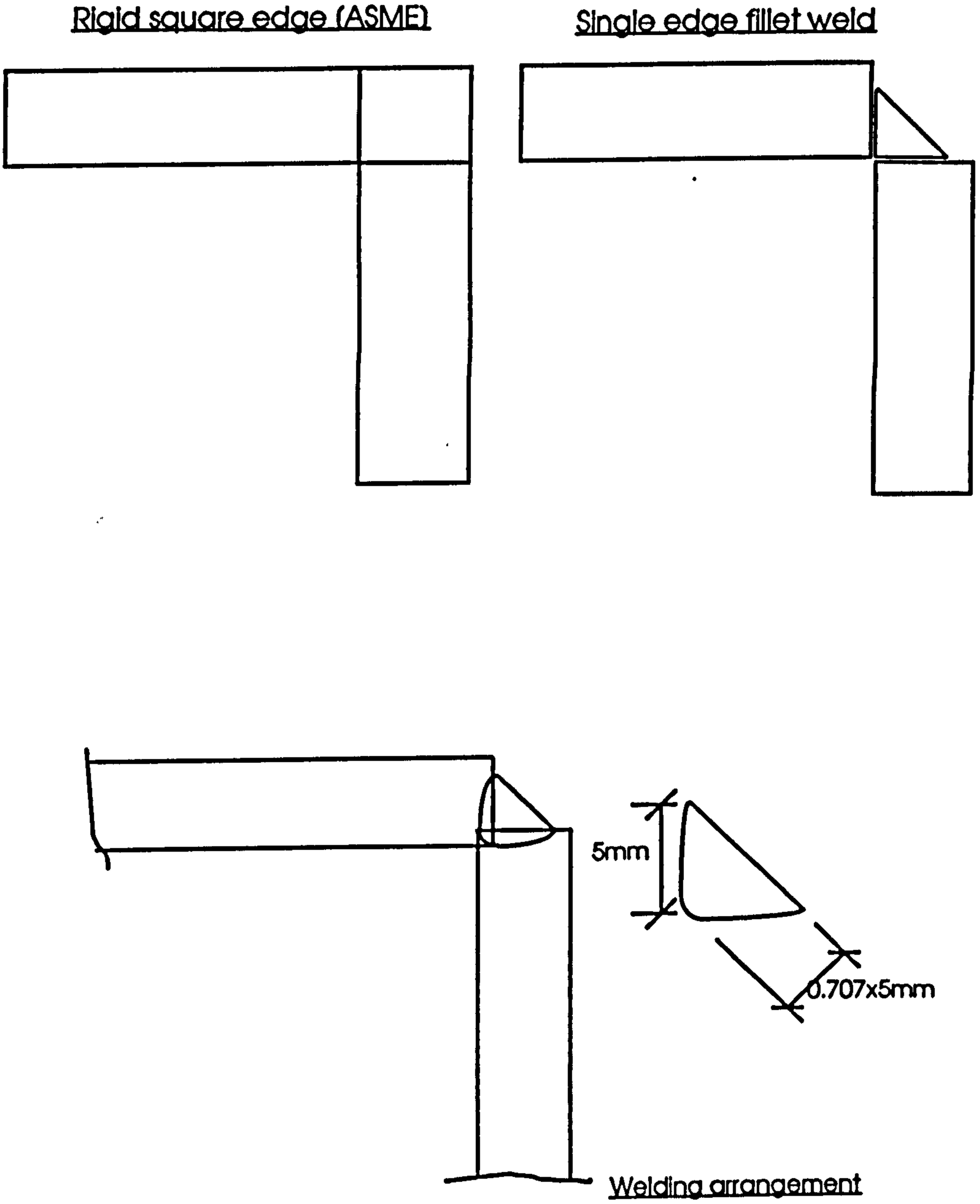

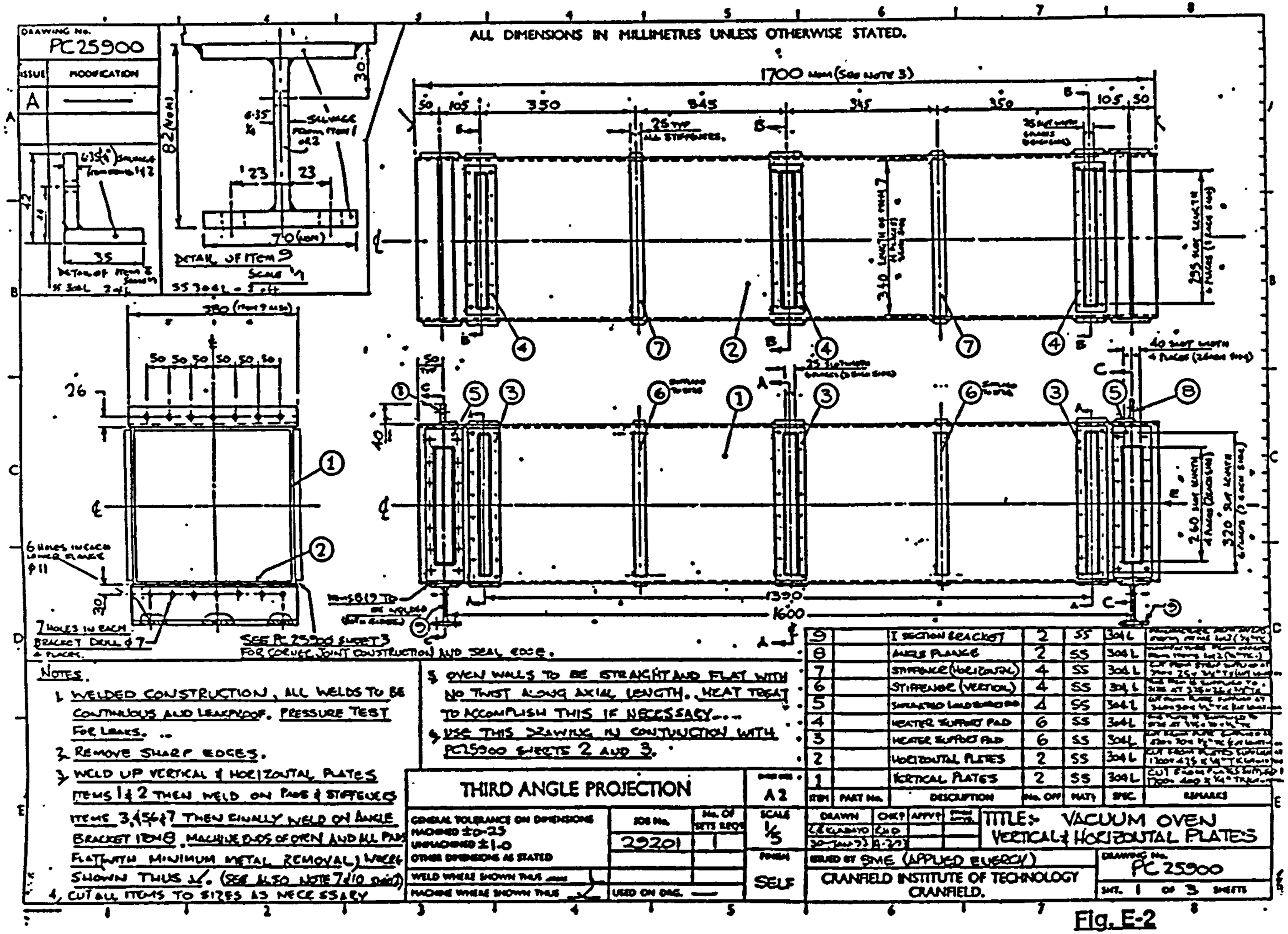

NOTES.

1. WELDED CONSTRUCTION, ALL WELDS TO BE CONTINUOUS AND LEAKPROOF. PRESSURE TEST FOR LEAKS.
2. REMOVE SHARP EDGES.
3. WELD UP VERTICAL & HORIZONTAL PLATES ITEMS 1 & 2 THEN WELD ON PADS & STIFFENERS ITEMS 3, 4, 5 & 7 THEN FINALLY WELD ON ANGLE BRACKET ITEM 8. MACHINE ENDS OF OVEN AND ALL PADS FLAT WITH MINIMUM METAL REMOVAL) WHERE SHOWN THUS ✓. (SEE ALSO NOTE 7 AND 10 SHEET)
4. CUT ALL ITEMS TO SIZES AS NECESSARY
5. OVEN WALLS TO BE STRAIGHT AND FLAT WITH NO TWIST ALONG AXIAL LENGTH. HEAT TREAT TO ACCOMPLISH THIS IF NECESSARY.
6. USE THIS DRAWING IN CONJUNCTION WITH PC25900 SHEETS 2 AND 3.

ITEM	PART No.	DESCRIPTION	No. OFF	MATL	SPEC.	REMARKS
9		I SECTION BRACKET	2	SS	304L	
8		ANGLE FLANGE	2	SS	304L	
7		STIFFENER (HORIZONTAL)	4	SS	304L	
6		STIFFENER (VERTICAL)	4	SS	304L	
5		SHEATHED HEATER ELEMENT	4	SS	304L	
4		HEATER SUPPORT PAD	6	SS	304L	
3		HEATER SUPPORT PAD	6	SS	304L	
2		HORIZONTAL PLATES	2	SS	304L	
1		VERTICAL PLATES	2	SS	304L	

THIRD ANGLE PROJECTION

DRAWING SIZE A2

GENERAL TOLERANCE ON DIMENSIONS
MACHINED ±0.25
UNMACHINED ±1.0
OTHER DIMENSIONS AS STATED
WELD WHERE SHOWN THUS
MACHINE WHERE SHOWN THUS

JOB No. 29201

NO. OF SETS REQ'D 1

USED ON DRG. —

SCALE 1/5

FINISH SELF

DRAWN	CHK'D	APP'D	ISSUED
C.E. GUARAYO	C.H.D		
30 JAN 73	8.2.73		

TITLE: VACUUM OVEN VERTICAL & HORIZONTAL PLATES

ISSUED BY SIME (APPLIED ELEROY)

CRANFIELD INSTITUTE OF TECHNOLOGY CRANFIELD.

DRAWING No. PC25900

SHT. 1 OF 3 SHEETS

Fig. E-2

ALL DIMENSIONS IN MILLIMETRES UNLESS OTHERWISE STATED.

DRAWING No. PC25900

ISSUE	MODIFICATION
A	—

DETAIL of WELDED PAD ITEM 3 (6 PLACES)
(HEATER SUPPORTS ON VERTICAL PLATES)

DETAIL of WELDED PAD ITEM 4 (6 PLACES)
(HEATER SUPPORTS ON HORIZONTAL PLATES)

DETAIL of WELDED PAD ITEM 5 (4 PLACES)
(SIMULATED LOAD WATER PIPE SUPPORT VERTICAL PLATES)

NOTES CONTINUED

7. FACES SHOWN ✓ TO BE MACHINED FLAT WITH MINIMUM METAL REMOVAL AFTER WELDING PADS ITEMS 3, 4 & 5 TO RESPECTIVE ITEMS 1 & 2 (THIS DRG ONLY)
8. USE THIS DRAWING IN CONJUNCTION WITH PC 25900 SHEETS 1 & 3.
9. REMOVE SHARP EDGES.
10. WELD ALL PADS FULLY ON OUTER AND INNER EDGES AS SHOWN

THIRD ANGLE PROJECTION

GENERAL TOLERANCE ON DIMENSIONS
MACHINED ± 0.5
UNMACHINED ± 1
OTHER DIMENSIONS AS STATED
WELD WHERE SHOWN THUS
MACHINE WHERE SHOWN THUS ✓

JOB No. 25201 — No. OF SHEETS 3

USED ON DRG. —

DRAWN SIZE A2 — SCALE ½ — FINISH SELF

SEE PC 25900 SHEET 1 FOR PARTS LIST.

ITEM	PART No.	DESCRIPTION	No. OFF	MATL	SPEC	REMARKS

DRAWN — CHK'D — APP'D

TITLE:- VACUUM OVEN WELDED PADS

ISSUED BY SMB (APPLIED ENERGY)
CRANFIELD INSTITUTE OF TECHNOLOGY CRANFIELD.

DRAWING No. PC25900
SHT. 2 OF 3 SHEETS

Fig. E-3

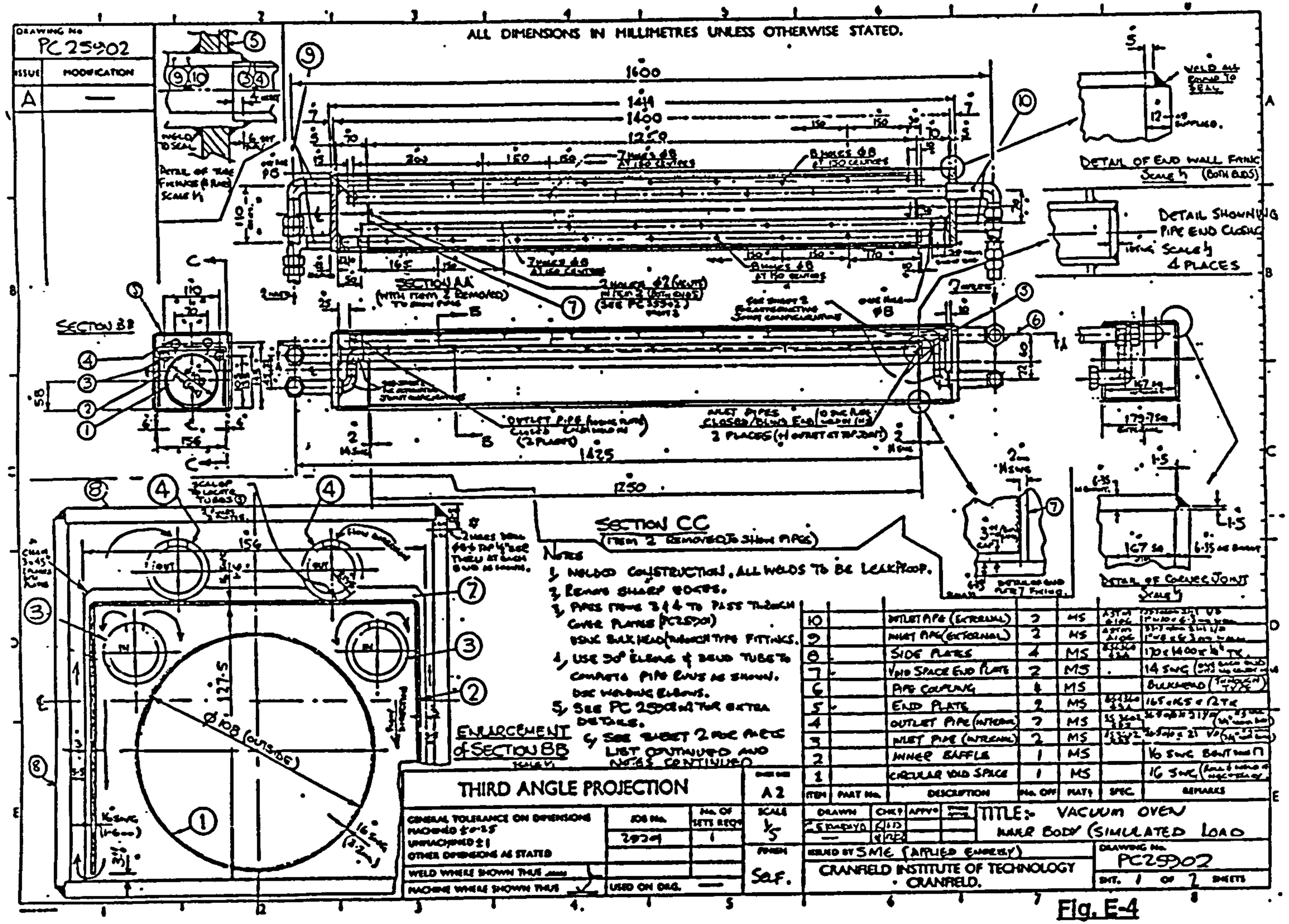
DRAWING No PC25902
ISSUE MODIFICATION
A —
ALL DIMENSIONS IN MILLIMETRES UNLESS OTHERWISE STATED.
SECTION AA (WITH ITEM 2 REMOVED) TO SHOW PIPE
SECTION BB
SECTION CC (ITEM 2 REMOVED TO SHOW PIPES)
ENLARGEMENT of SECTION BB
DETAIL OF END WALL FIXING
DETAIL SHOWING PIPE END CLOSING
DETAIL OF CORNER JOINT
OUTLET PIPE (INTERNAL)
INLET PIPES CLOSED/BLIND END
2 PLACES (1 OUTLET AT BOTTOM)
Ø108 (OUTSIDE)
Ø127.5
1600
1425
1250
NOTES
1. WELDED CONSTRUCTION. ALL WELDS TO BE LEAKPROOF.
2. REMOVE SHARP EDGES.
3. PIPES ITEMS 3 & 4 TO PASS THROUGH COVER PLATES (PC25901) USING BULKHEAD (THROUGH) TYPE FITTINGS.
4. USE 90° ELBOWS & BEND TUBES TO COMPLETE PIPE ENDS AS SHOWN. USE WELDING ELBOWS.
5. SEE PC 25901 & 03 FOR EXTRA DETAILS.
6. SEE SHEET 2 FOR PARTS LIST CONTINUED AND NOTES CONTINUED
THIRD ANGLE PROJECTION
A2
SCALE 1/5
FINISH Self.
GENERAL TOLERANCE ON DIMENSIONS MACHINED ±0.25 UNMACHINED ±1 OTHER DIMENSIONS AS STATED
WELD WHERE SHOWN THUS
MACHINE WHERE SHOWN THUS
JOB No. 2929
No. OF SETS REQD 1
USED ON DRG. —
ITEM PART No. DESCRIPTION No. OFF MATL SPEC. REMARKS
10 OUTLET PIPE (EXTERNAL) 2 MS
9 INLET PIPE (EXTERNAL) 2 MS
8 SIDE PLATES 4 MS 10 x 1400 x 1600 LG
7 VOID SPACE END PLATE 2 MS . 14 SWG
6 PIPE COUPLING 4 MS BULKHEAD (THROUGH TYPE)
5 END PLATE 2 MS 165 x 165 x 12 TK
4 OUTLET PIPE (INTERNAL) 2 MS
3 INLET PIPE (INTERNAL) 2 MS
2 INNER BAFFLE 1 MS 16 SWG
1 CIRCULAR VOID SPACE 1 MS 16 SWG
DRAWN S.E. EMBRYO
CHK'D —
APP'D —
TITLE:- VACUUM OVEN INNER BODY (SIMULATED LOAD
ISSUED BY SME (APPLIED ENERGY) CRANFIELD INSTITUTE OF TECHNOLOGY · CRANFIELD.
DRAWING No. PC25902
SHT. 1 OF 2 SHEETS

Fig. E-4

DRAWING No. PC25902	
ISSUE	MODIFICATION
A	—

ALL DIMENSIONS IN MILLIMETRES UNLESS OTHERWISE STATED.

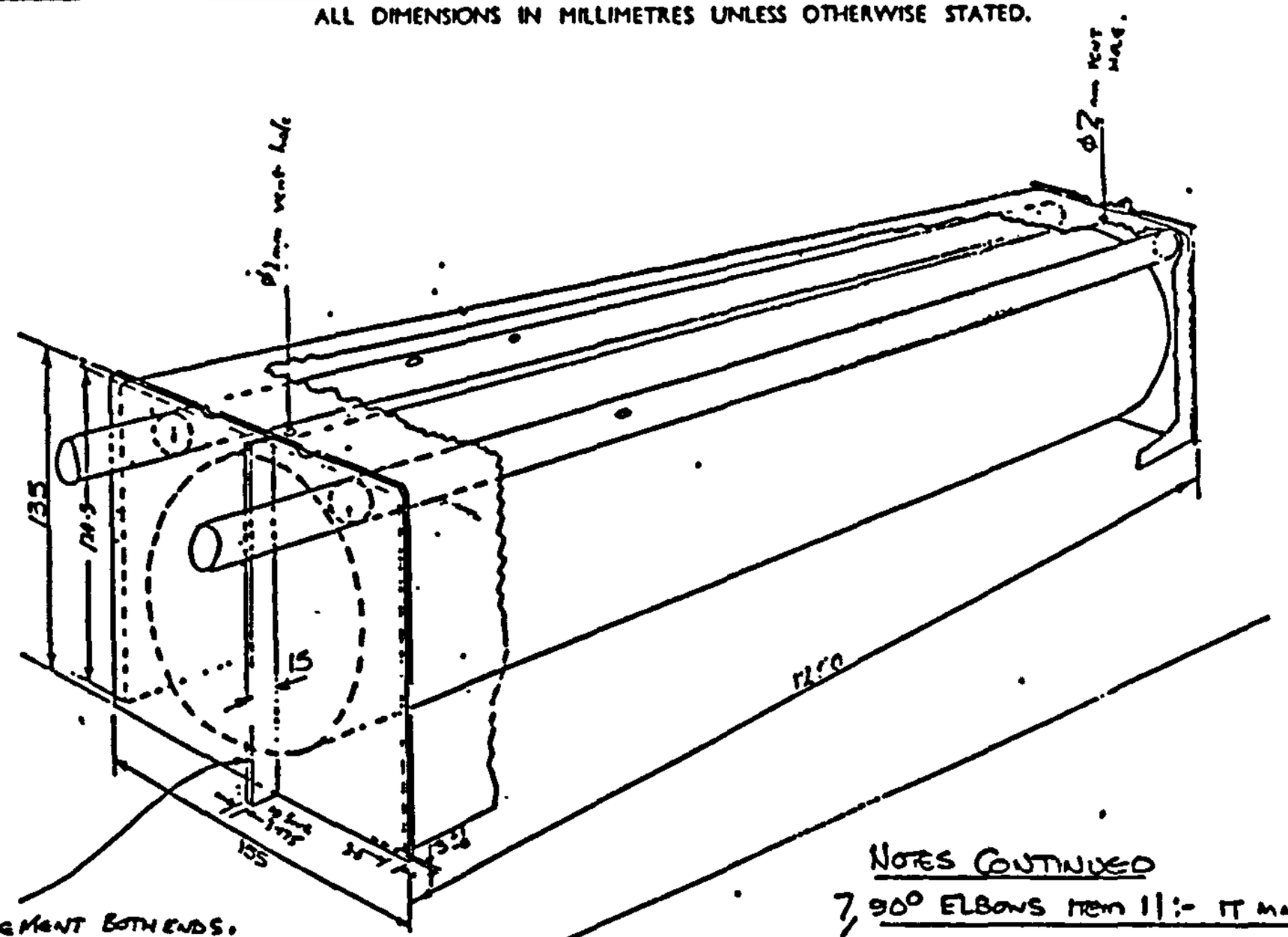

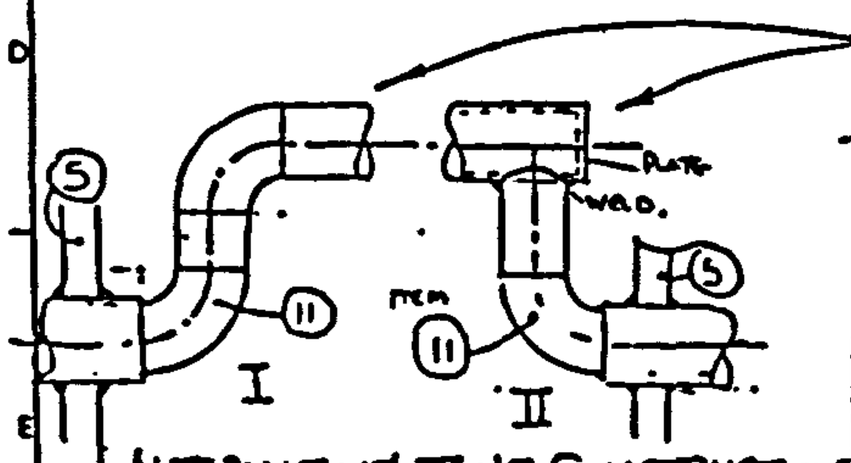

ALTERNATIVE JOINT CONSTRUCTIONS

a) NOTE ELBOW PREFERED AT BEND CLOSEST TO WHERE PIN PASSES THROUGH PLATE ITEM 5.
b) TOP BEND TO BE ALTERNATIVE I, II OR III WHICH-EVER FITS SPACE AVAILABLE.

NOTES CONTINUED

7, 90° ELBOWS ITEM 11:- IT MAY NOT BE POSSIBLE TO FIT 2 ELBOWS IN GAP BETWEEN ITEMS 5 AND 7 EACH END THEREFORE AN ALTERNATIVE CAN BE USED SEE SECTION CC ON PC25902 SHEET 1 AND ALSO LH VIEWS ON THIS DRAWING.

8 SUPPORT INTERNAL TUBES AS NECESSARY

ITEM	PART No.	DESCRIPTION	No. OFF	MATL	SPEC.	REMARKS
12		90° ELBOW	4	MS	BS 1640	1" N/B x 4·56 mm (ST)
11		90° ELBOW	4 SEE NOTE 7	MS	BS 1640	3/4" NB x 2·11 mm (ST)

THIRD ANGLE PROJECTION			SHEET SIZE	A2	
GENERAL TOLERANCE ON DIMENSIONS: MACHINED —; UNMACHINED —; OTHER DIMENSIONS AS STATED; WELD WHERE SHOWN THUS; MACHINE WHERE SHOWN THUS	JOB No. 25201	No. OF SETS REQ'D 1	SCALE NTS	FINISH Self	
	USED ON DRG. —				

DRAWN: Z Edwards 7.4.8 — CHK'D: T.H.B. 7/8/78 — APP'D: — ITEM CONTROL: —

TITLE:- INNER BAFFLE & VOID SPACE

ISSUED BY SMG (APPLIED ENERGY)
CRANFIELD INSTITUTE OF TECHNOLOGY
CRANFIELD.

DRAWING No. PC25902
SHT. 2 OF 2 SHEETS

Fig. E-5

APPENDIX F

COMPUTATION OF GEOMETRIC VIEW FACTORS

F.1. Introduction

The fraction of radiation leaving one surface that reaches another surface depends on the geometric orientation and size of the surfaces with respect to each other and is referred to as the geometric view factor. Other names for the view factor include angle factor, configuration factor or shape factor. The solution of any problem of radiative heat exchange between bodies which see each other requires the knowledge of the surface to surface viewfactor.

Referring to Fig. (F-1), the black body radiation leaving surface 1 and directly incident on surface 2 is

$$Q_{12} = (E_{b1}A_1)^*F_{12} \qquad (F.1)$$

where F_{12} is the view factor from surface 1 to 2.

The assumption is that the radiation leaves the emitting surface uniformly in all directions (i.e. diffuse surface) so that in the absence of an intervening medium, the proportion arriving at another surface depends upon how much of the viewing area is seen.

F.2. Derivation

The intensity of radiation normal to an emitting surface is related to the black-body emissive power by

$$i_n=E_b/\pi, \text{ where } E_b=\sigma T^4 \qquad (F.2)$$

When the direction of the emission is at an angle ϕ to the normal to the surface, the intensity of radiation is expressed by Lambert's cosine law [6]:

$$i_\phi = i_n\cos\phi = E_b\cos\phi/\pi \qquad (F.3)$$

The solid angle subtended by dA_2 at the source dA_1 is given by

$$d\omega_1 = dA_2\cos\phi_2/s^2$$

where s is the interconnecting line at an angle ϕ to the normal to dA_1. The radiation from dA_1 emitted through the small solid angle is then given by

$$dQ_{b(1\text{-}2)}=i_n dA\cos\phi\, d\omega$$

Therefore the radiation incident and absorbed by dA_2 with simplified subscripts is:

$$\begin{aligned} dQ_{b12} &= i_1 d\omega_1 dA_1 \\ &=(i_{n1}\cos\phi_1)\cos\phi_2 dA_2/s^2)(dA_1) \\ &= E_{b1}\cos\phi_1\cos\phi_2 dA_2 dA_1/\pi s^2 \end{aligned} \qquad (F.4)$$

Similarly the radiation incident from dA_2 and absorbed by dA_1 is

$$dQ_{b21} = E_{b2}\cos\phi_2\cos\phi_1 dA_1 dA_2/\pi s^2 \qquad (F.5)$$

which can simply be obtained by reversing the subscripts. Substituting for E_b from (F.2), the net radiation exchange between the two elemental surfaces is:

$$dQ_b = dQ_{b12} - dQ_{b21} = \frac{\sigma \cos\phi_1 \cos\phi_2 dA_2 dA_1}{\pi s^2}\left(T_1^4 - T_2^4\right) \qquad \text{(F.6)}$$

The total Q can then be obtained by integrating over both areas:

$$Q_b = \sigma(T_1^4 - T_2^4) \int_{A_2}\int_{A_1} \frac{\cos\phi_2 \cos\phi_1 dA_1 dA_2}{\pi s^2} \qquad \text{(F.7)}$$

Comparing (F.1) and (F.7)

$$F_{12} = \frac{1}{A_1} \int_{A_2}\int_{A_1} \frac{\cos\phi_2 \cos\phi_1 dA_1 dA_2}{\pi s^2} \qquad \text{(F.8)}$$

and from symmetry of the integral equation,

$$A_1 F_{12} = A_2 F_{21} \qquad \text{(F.9)}$$

The solution of any problem of radiative heat exchange between bodies requires the knowledge of the surface to surface viewfactor. This depends upon whether the double integration of equation (F.8) can be carried out. The analytical determination is especially difficult except for simple geometries. Of course, the integration can be carried out numerically, but the calculation time increases exponentially with the number of surfaces involved, and ascertaining the degree of accuracy can be impossible.

For parallel and for perpendicular rectangular planes, the exact solutions are known. Standard view factor tables and charts are available for some of these as well as for a limited number of different configurations [59]. One method which evolved in evaluating new view factorsis the view-factor algebra, which makes extensive use of reciprocity relations (F.9), and summation rules where complicated arrangement of surfaces with known view factors, are manipulated by superposition of simpler related configurations. But because the starting values obtained from most tables are only to about 6 significant figures, or from charts, at best a 2-figure accuracy, considerable error propagation of 57% or more could arise from an incorrect starting value with an error as low as 0.02%, depending upon the complexity of the resultant algebraic equation [95].

F3. Analytical Solutions

Exact solutions of view factors of rectangular planes which are either perpendicular or parallel to each other are available [102,103].
For perpendicular rectangles (see Fig. F-2), equation (F.8) is written as:

$$F_{12} = \frac{1}{A_1} \int_{ze1}^{ze2} \int_{xe1}^{xe2} \int_{zy1}^{zy2} \int_{y1}^{y2} \frac{\cos\phi_1 \cos\phi_2}{\pi s^2} dy dz_y dx_e dz_e \qquad \text{(F.10)}$$

and for parallel rectangles (see Fig. F-3), it is written as:

$$F_{12} = \frac{1}{A_1}\int_{ze1}^{ze2}\int_{xe1}^{xe2}\int_{zi1}^{zi2}\int_{xi1}^{xi2}\frac{\cos\phi_1\cos\phi_2}{\pi s^2}dx_i dz_i dx_e dz_e \qquad (F.11)$$

To simplify the numerical computation, the variables $\cos\phi_1$, $\cos\phi_2$, and s are expressed in terms of the parallel Cartesian coordinates, and $\cos\phi_1=\cos\phi_2=y/s$.
The distance between centres of the two areas obtained from the direction cosines of the parallel planes is:

$s^2 = (x_e-x_i)^2 + y^2 + (z_e-z_i)^2$

$$\text{thus,}\quad F_{12} = \frac{1}{\pi A_1}\int_{z_i}\int_{x_i}\int_{z_e}\int_{x_e}\frac{y^2}{\left\{(x_e-x_i)^2+(z_e-z_i)^2+y^2\right\}^2} \qquad (F.12)$$

and this gives, after the four integrations: F_{12} =

$$\frac{1}{2\pi A_1}\left\{\begin{array}{l}\left[(xe-xi)\sqrt{y^2+(ze-zi)^2}\right]\tan^{-1}\frac{xe-xi}{\sqrt{y^2+(xe-xi)^2}}+\\ \left[(ze-zi)\sqrt{y^2+(xe-xi)^2}\right]\tan^{-1}\frac{ze-zi}{\sqrt{y^2+(xe-xi)^2}}-\\ \frac{1}{2}y^2 Ln\left\{(xe-xi)^2+(ze-zi)^2+y^2\right\}\end{array}\right\}_{xi1\,zi1\,xe1\,ze1}^{xi2\,zi2\,xe2\,ze2} \qquad (F.13)$$

For inclined planes at an arbitrary angle α (see Fig. F-4), the distance between the centroids of the two areas is:
$s^2 = x_e^2-2x_e y\cos\alpha+y^2+(z_e-z_y)^2$, $\cos\beta_1=(y\sin\alpha)/s$, $\cos\beta_2=(x_e\sin\alpha)/s$,

and F_{12} =

$$\frac{\sin^2\alpha}{A_1\pi}*$$

$$\int_{y1}^{y2}\int_{zy1}^{zy2}\int_{ze1}^{ze2}\int_{xe1}^{xe2}\frac{x_e y}{\left[x_e^2-2x_e y\cos\alpha+y^2+(z_e-z_y)^2\right]^2}dx_e dz_e dz_y dy$$

(F.14)

Three of the integrations have been carried out analytically [103], but the fourth must be done numerically:

$A_1F_{12}=\Sigma\Sigma\Sigma...$

$$\frac{\sin^2\alpha(z_y - z_b)}{2\pi}\int_{y1}^{y2}\left[\begin{array}{l}\dfrac{\cos\alpha(x_e - y\cos\alpha - y\sin^2\alpha)}{\sin^2\alpha(x_e^2 - 2xy\cos\alpha + y^2)^{\frac{1}{2}}} * \\ \tan^{-1}\left(\dfrac{z_y - z_e}{x^2 - 2x_e y\cos\alpha + y^2}\right) + \\ \dfrac{\cos\alpha}{\sin^2\alpha(z_y - z_e)} * \\ \left\{\begin{array}{l}\left(y^2\sin^2\alpha + (z_y - z_e)^2\right)^{\frac{1}{2}} * \\ \tan^{-1}\left(\dfrac{x_e - y\cos\alpha}{\left(y^2\sin^2\alpha + (z_y - z_e)^2\right)^{\frac{1}{2}}}\right) - \\ y\sin\alpha\tan^{-1}\left(\dfrac{x_e - y\cos\alpha}{\sin\alpha}\right)\end{array}\right\} + \\ \dfrac{y}{2(z_y - z_e)} * \\ \left[\mathrm{Ln}\left(\dfrac{x_e^2 - 2xy\cos\alpha + y^2 + (z_y - z_e)^2}{x_e^2 - 2xy\cos\alpha + y^2}\right)\right]\end{array}\right] dy$$

.....(F.15)

The perpendicular plane is a simplified version of the inclined plane. Referring to Fig.F-3, and eqn (F-11), $\cos\phi_1=y/s$, $\cos\phi_2=x_e/s$ and the distance between centres of the two perpendicular areas considered is obtained from $s^2 = x_e^2 + y^2 + (z_e-z_i)^2$ which yields

$$F_{12}=\frac{1}{\pi A_1}\int_{ze1}^{ze2}\int_{xe1}^{xe2}\int_{zy1}^{zy2}\int_{y1}^{y2}\frac{x_e y}{\left(x_e^2+y^2+(z_e-z_i)^2\right)^2}dydz_y dx_e dz_e \qquad (F.16)$$

$$F_{12}=\frac{1}{2\pi A_1}\left\{\begin{array}{l}\left[(z_b-z_y)(x_b^{\,2}+y^2)^{\frac{1}{2}}\right]\tan^{-1}\left(\dfrac{z_b-z_y}{(x_b^{\,2}+y^2)^{\frac{1}{2}}}\right)- \\ 0.25\left(x_b^{\,2}+y^2-(z_b-z_y)^2\right)* \\ \mathbf{Ln}\left\{x_b^{\,2}+y^2+(z_b-z_y)^2\right\}\end{array}\right\}_{y1\,zy1\,xb1\,zb1}^{y2\,zy2\,xb2\,zb2}$$

(F.17)

The evaluation of (F.13) or (F.17)) is done in a series of additions so that the 4 x 2 limits will result in the summation of 2^4 (16) different equations. The insertion of the appropriate preceding arithmetic sign can be accomplished for (F.13) as follows:

$$F_{A1\text{-}A2}=\sum_{m=1}^{2}\sum_{l=1}^{2}\sum_{k=1}^{2}\sum_{j=1}^{2}(-1)^{(j+k+l+m)}F\left(x_{i(j)},z_{i(k)},z_{e(l)},x_{e(m)}\right) \qquad \text{(F.18)}$$

and for (F.17)

$$F_{A1\text{-}A2}=\sum_{m=1}^{2}\sum_{l=1}^{2}\sum_{k=1}^{2}\sum_{j=1}^{2}(-1)^{(j+k+l+m)}F\left(y_{(k)},z_{y(j)},z_{e(l)},x_{e(m)}\right) \qquad \text{(F.19)}$$

F4. Numerical Integration

Although the availability of analytical solutions simplify and reduce the cost of the computation required to only 16 basic functional summations, the vast majority of view factor computations are, however, still done numerically since most of the surfaces are non planar. The apparently simple arbitrarily-inclined plane still required one numerical integration, and further highlights the difficulty in obtaining closed-form representation of geometric view factors.

The problem of obtaining view factors is not that they are inherently difficult to compute numerically, but that the calculation time increases exponentially with the number of surfaces involved. In calculations involving j surfaces, there are j^2 view factors. View factor algebra can only reduce this to j(j-1)/2, or for a 20-node model, there will be a minimum of 190 computations.

The common numerical methods used are based on either the double area integration (AI), or the double line or contour integration. When the surface is not approximated by the diffuse relationship, the Monte Carlo statistical ray tracing technique, can be employed. Although the contour integral method is more accurate and computationally more efficient, it is not suitable for studying the details of the view factors across a plane, and consequently not ideal for obtaining irradiance distribution. The following discussions relate to the AI method which was the main numerical method employed in this study.

F4.1 Double Area Integration

For rectangular surfaces, equation (F.8) is expressed in the required form as either (F.12) - for parallel planes, (F.16) - for perpendicular planes or (F.14), for arbitrarily inclined surfaces. Integration over a rectangular surface area implies integrating first in length and then in depth, which requires four summations over the two surfaces. The surfaces are divided into finite sub-surfaces, the number depending on the accuracy desired. The view factor is then evaluated numerically replacing the quadruple integral with elemental quadruple summations. The following algorithm demonstrates one of the elementary procedures for obtaining view factors numerically from parallel planes.

F4.1.1. Algorithm for parallel planes (see Fig. F-6 and Table F7)

Set the initial dimensions and coordinates of dA1,dA2
Evaluate the coordinates of both centroids
Calculate view factor dA1 to dA2
Increment dA1 along one of the edges, (xe).
    Repeat view factor calculation (i.e. new dA1 to old dA2).
        Sum view factor
If end of xe,
    reset xt to starting value,
    increment dA2 one step along the other edge (ze),
        repeat view factor calculations and summation.
At end xe, all the surface of dA2 scanned, therefore:
    increment dA1 along one of the edges; repeat from start(centroids),
then along the other edge, calculating until all surfaces scanned.

The flow chart is shown (see Table F7). It was found that the most accurate step size on the VAX 8510 was 2. The minimum number of operations from an elemental area 2x2 on the enclosure surface to one side of the inner body was 4x(1400/2)x(176/2)=246400. It is easily seen that a large amount of CPU time was incurred in the process of obtaining the view factors for the 1700x350x350 tunnel oven system. However, for greater clarity the flow chart has not been presented in an optimised version (which took advantage of multiple calculations within DO loops).

Fig. F-1 Direct radiation from surface 1 to 2

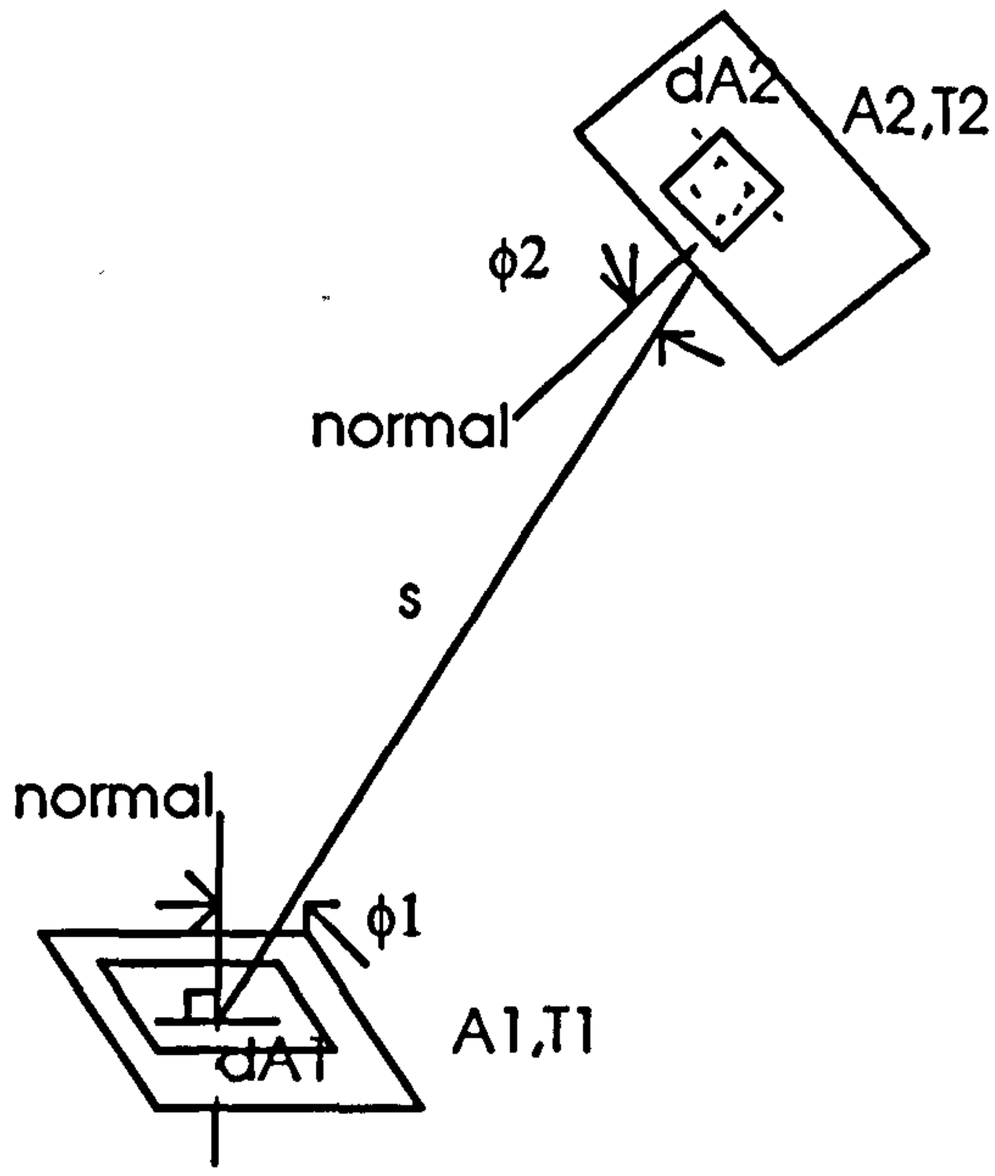

Fig. F-2 Coordinates for perpendicular planes

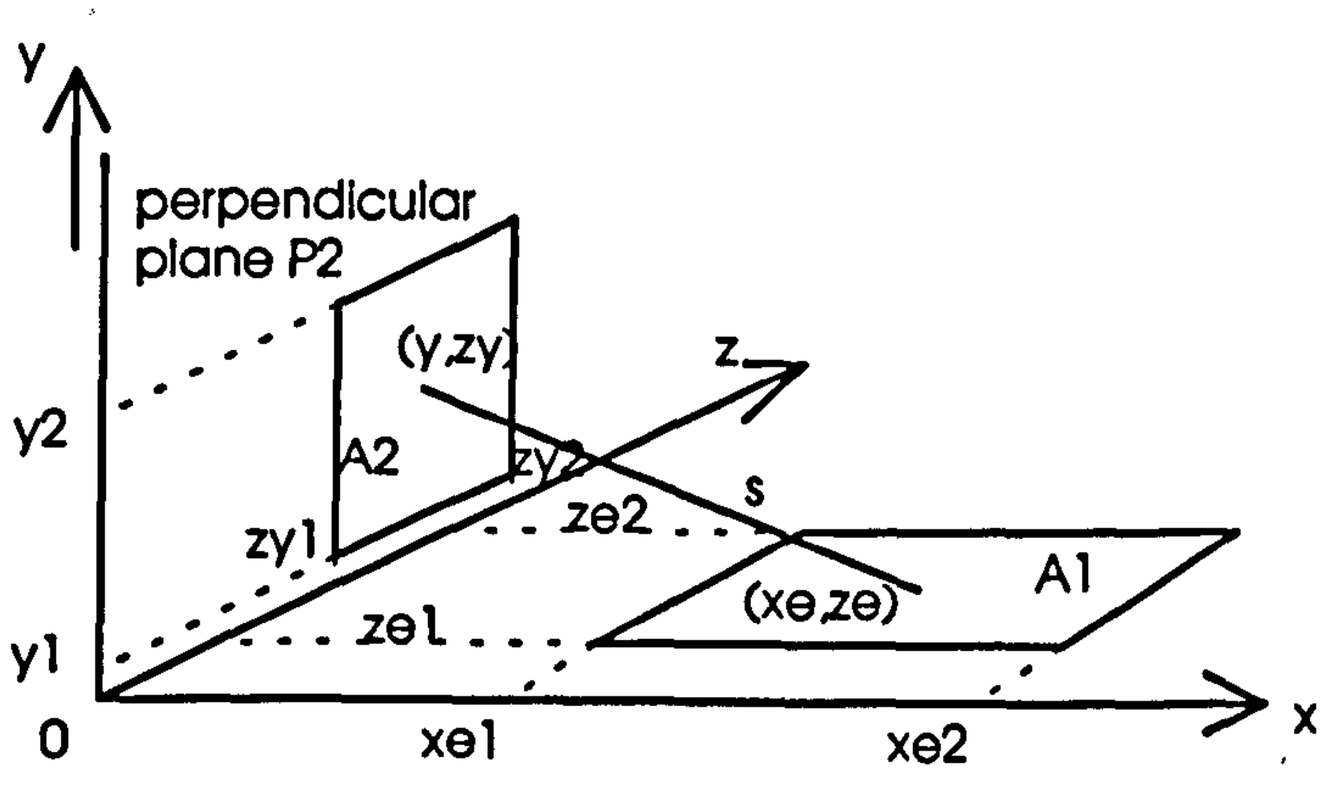

Fig. F-3 Coordinates for parallel planes

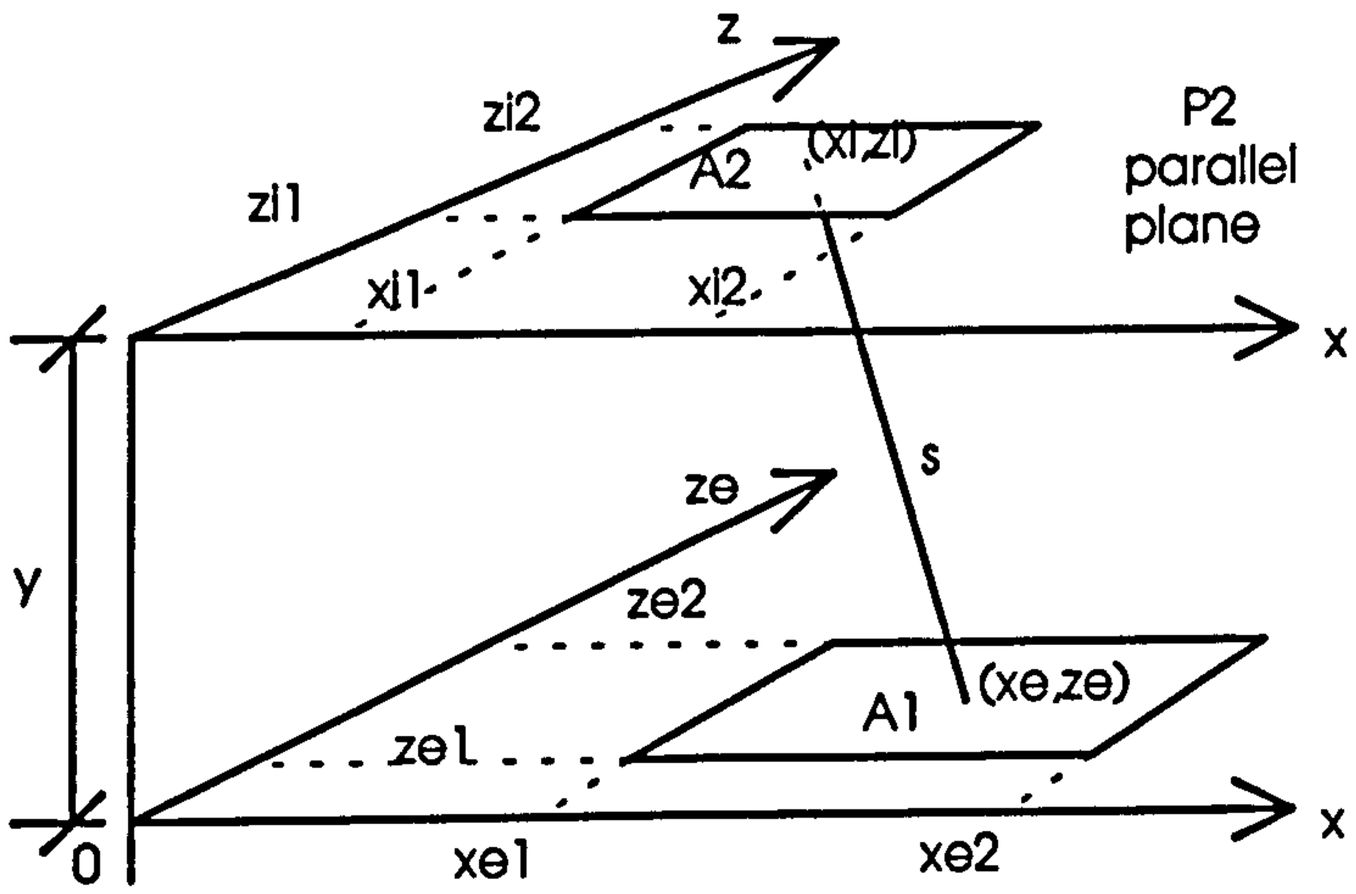

Fig. F-4 Arbitrarily inclined planes

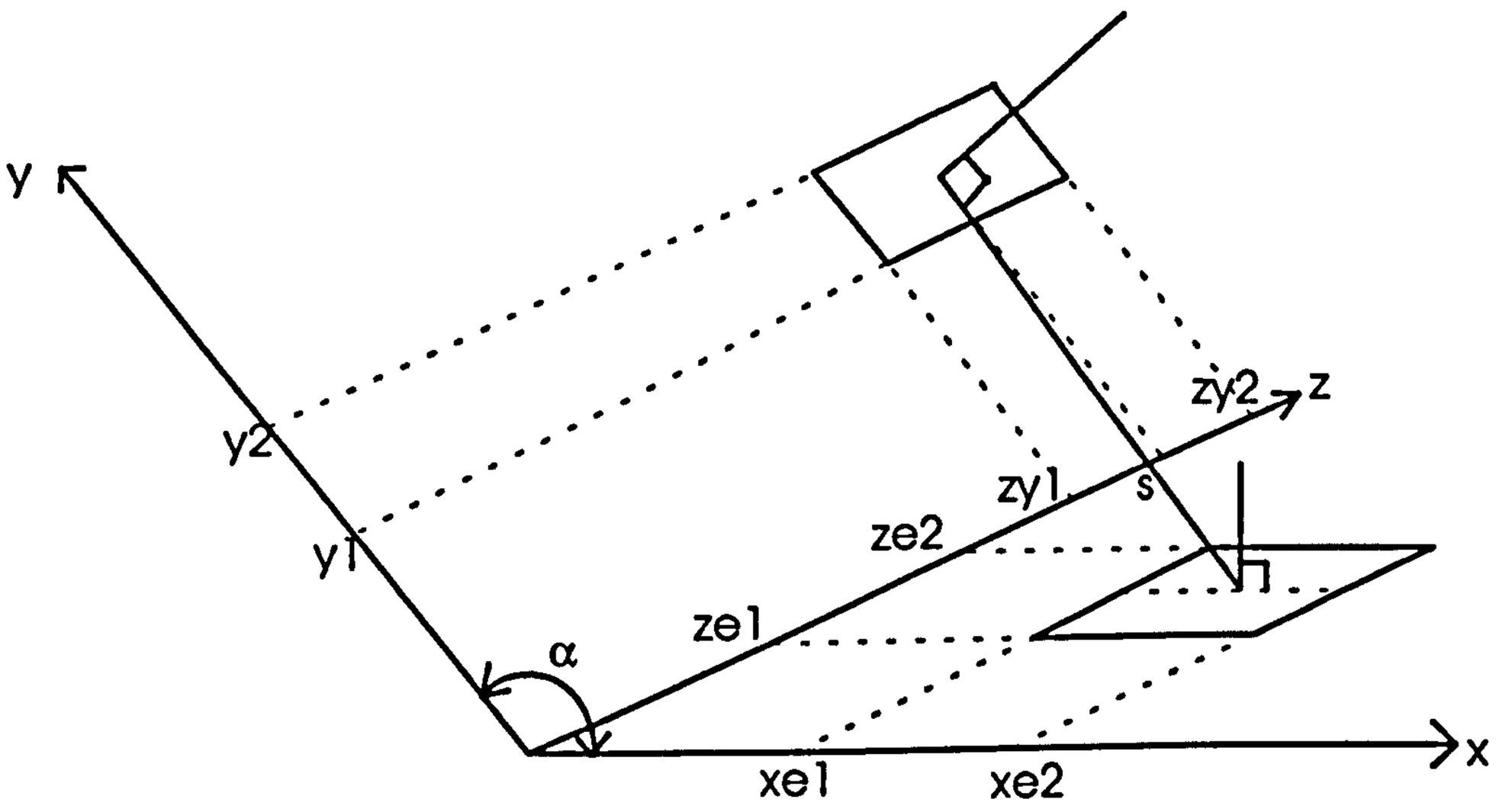

Fig.F-5 NUMERICAL INTEGRATION OF PERPENDICULAR PLANES

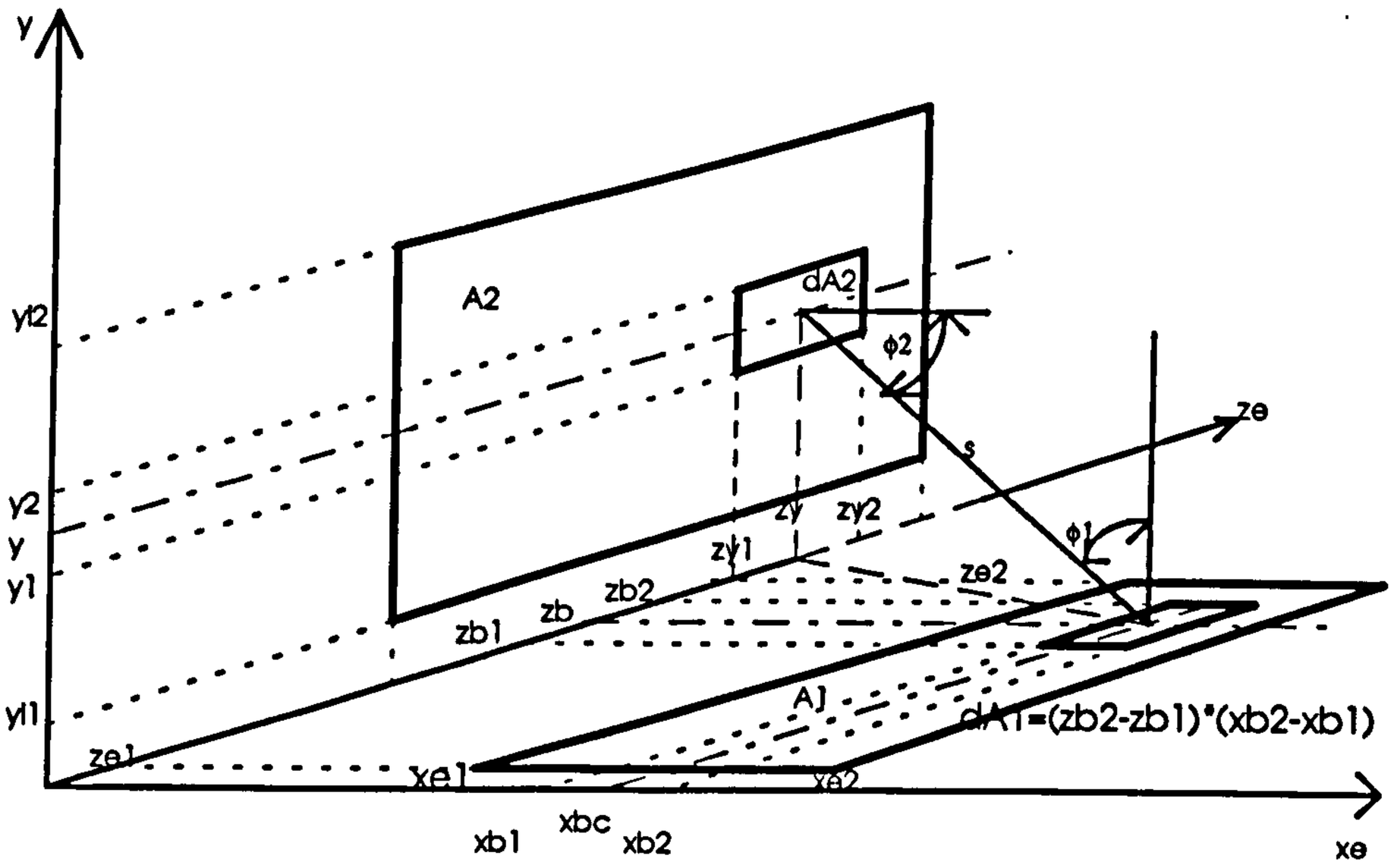

Fig.F-6 NUMERICAL INTEGRATION OF PARALLEL PLANES

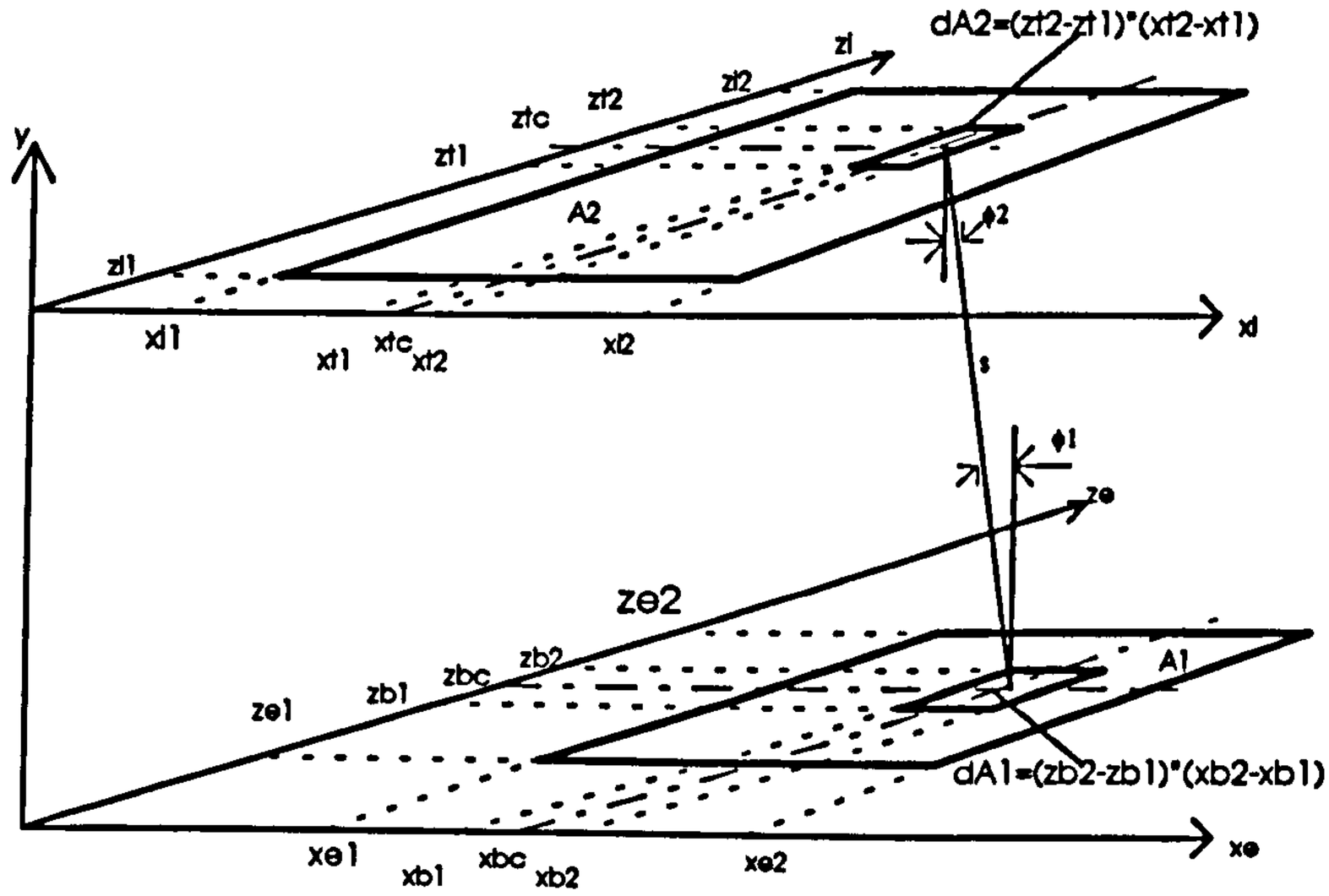

Fig.A7 Flow Chart for Parallel Planes